POST PROCESSING OF CONE PENETRATION DATA FOR ASSESSING SEISMIC GROUND HAZARDS, WITH APPLICATION TO THE NEW MADRID SEISMIC ZONE

A Dissertation
Presented to
The Academic Faculty

by

Tianfei Liao

In Partial Fulfillment
Of the Requirements for the Degree
Doctor of Philosophy in Civil and Environmental Engineering

Georgia Institute of Technology
August 2005

**POST PROCESSING OF CONE PENETRATION DATA FOR ASSESSING
SEISMIC GROUND HAZARDS, WITH APPLICATION TO
THE NEW MADRID SEISMIC ZONE**

Approved by:

Dr. Paul W. Mayne, Advisor
School of Civil and Environmental
 Engineering
Georgia Institute of Technology

Dr. Glenn J. Rix
School of Civil and Environmental
 Engineering
Georgia Institute of Technology

Dr. David Goldsman
School of Industrial and Systems
 Engineering
Georgia Institute of Technology

Dr. James S. Lai
School of Civil and Environmental
 Engineering
 Georgia Institute of Technology

Dr. J. Carlos Santamarina
School of Civil and Environmental
 Engineering
Georgia Institute of Technology

Date Approved: April 28, 2005

To my parents who supported me with their love in all my endeavors.

ACKNOWLEDGMENTS

I wish to express my sincerest gratitude to my advisor, Dr. Paul W. Mayne, for his constant inspiration and encouragement throughout my Ph.D. study. It has been an outstanding experience working with him at Georgia Tech, and the lessons I learned from him will benefit me throughout my career. I am grateful for his guidance and support during this research.

I would like to extend my thanks to other members of my defense committee: Dr. Glenn J. Rix, Dr. J. Carlos Santamarina, Dr. James Lai, and Dr. David Goldsman for their review of my dissertation and insightful comments. Special thanks to Dr. Rix for help with the liquefaction analysis using site response. Although not a committee member, Dr. J. David Frost made very valuable suggestions to this research. His contribution is gratefully acknowledged.

I feel extremely fortunate to have my fellow graduate students, Alec McGillivray and Guillermo Zavala, as my partners in field testing during my Ph.D. study. We together performed more than 180 cone penetration soundings in 10 states in the eastern United States. Their dedication and superior technical skills made every field trip successful. They also provided numerous helpful comments in the course of this research. I am extremely privileged and grateful for their assistance and friendship. A note of appreciation also goes to other colleagues in the geosystems group in Georgia Tech. I am especially grateful to Amr Elhakim, Bo Gao, Catherine Black, Veronica Rebata, Pierre

TABLE OF CONTENTS

LIST OF TABLES

LIST OF FIGURES

LIST OF SYMBOLS AND ABBREVIATION

a'	Attraction = c' cotϕ'
a_{max}	Peak ground acceleration
a_{rock}	Peak acceleration above the input bedrock
B	Normalized porewater pressure = $(u_2 - u_0)/(q_T - \sigma_{v0})$
c'	Effective cohesion intercept
C_c	Virgin compression index.
c_h	Coefficient of consolidation
CHT	Crosshole test
C_N	Normalization factor for stress level
CPT	Cone penetration test
CPTu	Piezocone penetration test
CRR	Cyclic resistance ratio
$CRR_{7.5}$	CRR in the event of earthquake of moment magnitude 7.5
C_s	Swelling index
CSR	Cyclic stress ratio
CSSM	Critical-state soil mechanics
CSW	Continuous surface wave method
D_{50}	Mean grain size
DHT	Downhole test
DMT	Flat dilatometer test
D_R	Relative density
e	Void ratio

$E(X_j)$	Average of all X_j measurements
e_0	Initial void ratio
E_0	Total radiated energy from the earthquake source
e_{max}	Maximum void ratio
e_{min}	Minimum void ratio
ESEE	Embayment Seismic Excitation Experiments
f	Frequency
F	Normalized sleeve friction $= f_s / (q_T - \sigma_{v0})$
FC	Fines content (material passing No. 200 sieve)
f_s	Sleeve friction
g	Acceleration due to gravity ($= 0.8 m/s^2$)
G	Shear modulus
G_{max}	Small strain shear modulus
G_s	Specific gravity of solids
i	Inclination
I_1	The first total stress invariants $= (\sigma_1 + \sigma_2 + \sigma_3)/3$
I_1'	The first effective stress invariants
IBC	International Building Code
I_c	Soil behavior type index
I_h	Arias intensity at the top of the soil profile
I_{hb}	Arias intensity at a given depth
I_R	Rigidity index $= G/\tau_{max}$
I_{xx}	Arias intensity in the x- direction
I_{yy}	Arias intensity in the y- direction

k	Slope of the linear regression
K_0	Earth pressure coefficient at rest
K_{0NC}	K_0 for normally consolidated soil
K_c	Grain-characteristic correction factor
K_D	Horizontal stress index from flat dilatometer test
k_h	Hydraulic permeability
L	Euclidean distance of two data sets
MASW	Multichannel analysis of surface wave
M_c	Slope of critical state line = $6 \sin\phi'/(3 - \sin\phi')$
M_w	Moment magnitude
N	Measured SPT blow counts
N_{60}	SPT blow counts corrected to 60% of efficiency
N_c	Cluster number
NGES	National Geotechnical Experimentation Site
N_m	Cone resistance number
NMSZ	New Madrid Seismic Zone
OCR	Overconsolidation ratio
p'	Mean effective stress = $(\sigma_1' + \sigma_2' + \sigma_3')/3$
PGA	Peak ground acceleration
q	Deviator stress = $\sigma_1 - \sigma_3$
Q	Normalized tip resistance = $(q_T - \sigma_{v0})/\sigma_{v0}'$
q_c	Cone tip resistance
q_{c1N}	Stress-normalized cone tip resistance
q_T	Cone tip resistance corrected for net area ratio

q_{T1}	Stress-normalized tip resistance
R	Hypocentral distance
r^2	Coefficient of determination
r_b	Depth correction factor for Arias intensity
r_d	Stress reduction coefficient
S	Degree of saturation
SASW	Spectral analysis of surface waves
SBT	Soil behavioral type
SCPTu	Seismic cone penetration test
SDMT	Seismic dilatometer
SPT	Standard penetration test
SSL	Steady-state line
S_t	Sensitivity
Stdev(X_j)	Standard deviation of all X_j measurements
s_u	Undrained shear strength
t	Shear wave travel time
t_{50}	Time rate of dissipation
u	Displacement
u_0	Hydrostatic porewater pressure
u_0	Hydrostatic porewater pressure
u_1	Porewater pressure at the face
u_2	Porewater pressure at the shoulder
V_p	Compression wave velocity
V_s	Shear wave velocity

V_{s1}	Stress-normalized shear wave velocity
Y	Yield surfaces
z	Depth
Λ	Plastic volumetric strain potential $= 1 - C_s/C_c$
$(\tau_{max})_h$	Shear stress at depth h
Δd	Difference between the traveling distances
Δt	Arrival time interval between two shear wave signals
ϕ'	Peak friction angle
γ	shear strain
γ_r	Reference shear strain
γ_{sat}	Saturated unit weight
γ_T	Total unit weight
γ_w	Unit weight of water
η	Viscosity
ρ	Density
ρ_T	Total unit mass density
σ_3	Minimum principal stress
σ_{atm}	Atmosphere pressure
σ_p'	Preconsolidation stress
σ_{ref}	Reference confining stress
σ_{v0}	Total overburden stress
σ_{vo}'	Effective overburden stress
σ_0'	Effective confining stress
σ_1	Maximum principal stress

τ	Applied horizontal shear stress
τ_{av}	Average equivalent uniform shear stress
τ_{max}	Maximum measured shear stress
τ_{m0}	Shear stress at approximately 1% shear strain
υ	Poisson's ratio
ψ	State parameter
ζ	Damping ratio
$\ddot{u}_g$	Acceleration at the base of the soil column
$(N_1)_{60}$	Stress-normalized SPT blow counts
$(q_{c1N})_{cs}$	Equivalent clean sand stress-normalized penetration stress
$[C]$	Viscous damping matrix
$[K]$	Stiffness matrix
$[M]$	Mass matrix
$\{I\}$	Unit vector
$\{u\}$	Vector of nodal relative displacements
$\{\ddot{u}\}$	Vector of nodal relative acceleration
$\{\dot{u}\}$	Vector of nodal relative velocities

SUMMARY

The seismic cone penetration test (SCPTu) is the most efficient means for geotechnical site characterization and the evaluation of seismic ground hazards, as it provides up to 5 independent readings in a single sounding: cone tip stress (q_T), sleeve friction (f_s), penetration porewater pressure (u_b), time rate of dissipation (t_{50}), and downhole shear wave velocity (V_s). During SCPTu tests, a very large number of digital measurements are recorded. The overwhelming data provide more detailed information for engineering analysis, but also pose challenges in post-processing of "information overload". In this thesis, software systems including *ShearPro*, *ClusterPro*, and *InSituData*, are developed to automate post processing of these SCPTu data. *ShearPro* is developed to automate the post-processing of the shear wave signals. *ClusterPro* uses the proposed three-dimensional cluster analysis approach for soil stratification. *InSituData* facilitates the post processing of penetration data for seismic ground hazards analysis. A new three-dimensional soil classification chart is also proposed in this thesis to help discern soil layers that may be subject to seismic ground hazards, such as loose liquefied sands and silty sands.

These methods are then applied to SCPTu data collected at previously-identifed paleoliquefaction sites located in the New Madrid Seismic Zone (NMSZ). For liquefaction evaluation, the cyclic stress ratio (CSR) is computed using site response analysis by *DeepSoil* and a measured profile of shear waves derived from the 30-m SCPTU soundings and deep suspension loggings in AR and TN. The natural resistance of the soil to liquefaction, termed the cyclic resistance ratios (CRRs), is evaluated based on

both deterministic procedures and probabilistic procedures. Based on liquefaction evaluation results at selected paleoliquefaction sites, regional CRR criteria for liquefaction are developed for the NMSZ. As even the latest major earthquakes in NMSZ occurred nearly 200 years ago, aging effects might be an important factor to consider in utilizing the liquefaction criteria to assess the seismic parameters associated with the previous earthquakes. The aging effects in the NMSZ were investigated through large scale blast-induced liquefaction tests conducted by the USGS and supplemented by the author by series of CPTs. Then a procedure to estimate seismic parameters associated with previous earthquakes is proposed. It utilizes both the liquefaction criteria based on SCPTu tests and the empirical attenuation relations developed for the corresponding regions. The approach is validated through data evaluation related to the 1989 Loma Prieta earthquakes in California and then applied to previous historic earthquakes in the NMSZ.

CHAPTER I

INTRODUCTION

1.1 Overview

The seismic cone penetration test (SCPTu) is the most efficient means for geotechnical site characterization and the evaluation of seismic ground hazards, as it provides up to 5 independent readings in a single sounding, including: cone tip resistance (q_T), sleeve friction (f_s), porewater pressure (u_1 at the face or u_2 at the shoulder), time rate of dissipation (t_{50}), and shear wave velocity (V_s). During SCPTu field operations, a very large number of digital measurements are recorded, including recorded shear wave trains with 8000 data points at each depth, as well as thousands of data sets of tip resistance, sleeve friction, porewater pressure, and dissipation readings. This research develops new tools and methods to automate post processing of SCPTu data for geostratigraphic profiling, soil parameter determination, and liquefaction evaluation. These tools are then applied to SCPTu data collected in the New Madrid Seismic Zone (NMSZ). In this thesis, new methodologies are suggested for soil stratification and classification, predicting liquefaction potential during future earthquakes, as well as for back-calculating the seismic parameters associated with previous earthquakes. Figure 1.1 presents a graphical illustration of the major components of this research, including post processing of shear wave signals using *ShearPro*, geostratification using *ClusterPro*, interpretation of SCPTu data using *InSituData*, liquefaction evaluation using site response analysis, assessment of aging effects on SCPTu data, and estimation of seismic parameters associated with previous earthquakes.

Figure 1.1 Graphical illustration of seismic ground hazard response in the New Madrid Seismic Zone by seismic cone penetration tests (SCPTu)
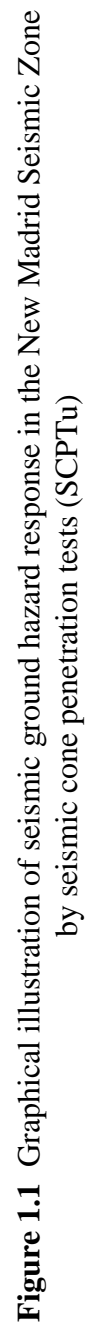
1.2 Seismic Cone Penetration Test (SCPTu)

Seismic cone penetrometers combine the advantages of electronic readings of continuous penetration with a downhole measurement of shear wave velocity (V_s). Cone penetrometers are vertically advanced at the standard rate of 2 cm/sec using hydraulic pushing systems. Readings of tip resistance (q_c), sleeve friction (f_s), inclination (i), and pore pressure (u_2) are taken every 1 to 5 cm by computer, giving unparalleled details on the soil layering profiles, while transient shear wave records and porewater dissipation curves are obtained at 1-m depth intervals during the addition of successive rods.

Typically, the amplitude of each shear wave is recorded at a time interval of 0.025 ms, and thus each shear wave train contains approximately 8000 data for a total recording time of 200 ms. For a 30-meter sounding, a total of 240,000 wave data points and about 15,000 points of readings of depth (z), tip resistance (q_c), sleeve friction (f_s), inclination (i), and pore pressure (u_2) are recorded. At selected depths, piezo-dissipation recordings with time can be made to ascertain the permeability characteristics, thus adding more numbers. The overwhelming data sets provide more detailed information for engineering analysis, but also pose challenges in post-processing of "information overload". In this thesis, software systems including *ShearPro*, *ClusterPro*, and *InSituData*, are developed to automate post processing of these SCPTu data, as illustrated in Figure 1.2.

Of recent, the average shear wave velocity V_s in the top 30 m has paramount significance to seismic structural design. The 2000/2003 IBC (International Building Code) emphasizes the importance of the average V_s in the top 30.5 m (100 ft) by using it to

define sites classification with respect to their seismic vulnerability. The measured V_s

classifies the sites into different categories, which have significant impact on the design

of structures. An accurate measurement of the V_s profile can ensure the correct design for

seismic safety, as well as justify the economic cost.
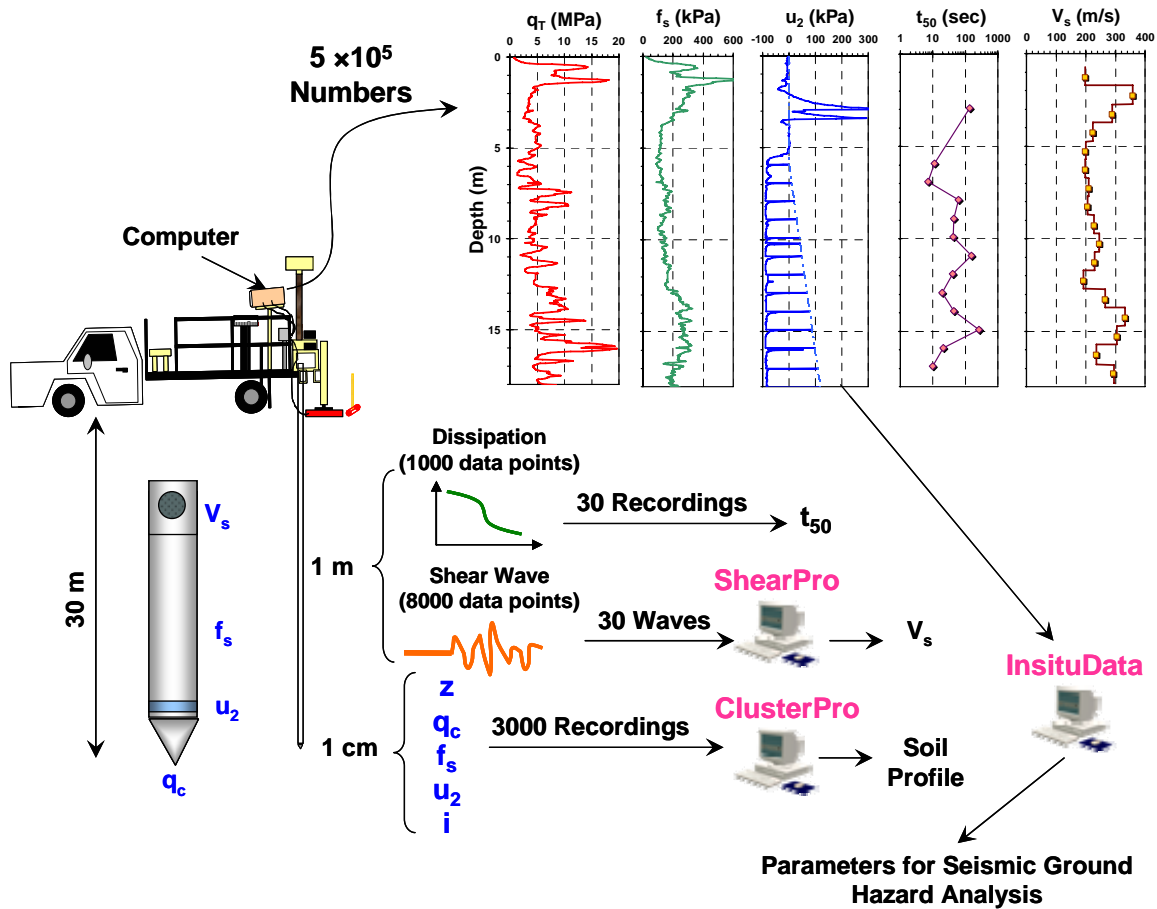
Figure 1.2 Tools for automated post processing of seismic cone penetration data for geotechnical site characterization

In engineering practice, the shear wave velocity (V_s) is usually determined from the

recorded shear wave trains by manually picking the first arrival time of each signal, or

alternatively by selection of the cross-over time of two paired sets of shear wave trains

4

recorded at the same depth but of opposite amplitude (Robertson et al., 1986; Campanella, 1994). These manual methods are time-consuming both in the field and in later data analysis. The derived results of shear wave velocities (V_s) may exhibit poor accuracy, since differences between the successive arrival times or cross-over times are very short. Small errors in hand-picking the arrival times can shift the value of V_s greatly from the correct value. Recently, algorithms for deriving shear wave velocity (V_s) from shear wave signals have been proposed (Campanella & Stewart, 1992; Baziw, 2002; Greening et al., 2003; Theron et al., 2003), and some of these can be implemented on computer to automate the process of deriving V_s from the shear wave signals. In this thesis, a software code (*ShearPro*) is developed to automate and facilitate the post-processing of the shear wave signals.

The CPTu penetration data can be used for stratification and soil classification. It is usually done by visually examining the CPTu data or comparing the data against empirical soil classification charts. The visual method depends largely on the experience of researchers, while the results based on soil classification schemes are associated with the selected charts. Neither of these can provide consistent and objective boundaries between soil layers. Cluster analysis in previous geotechnical research (Hegazy & Mayne, 1998, 2002) helps to delineate the stratigraphy objectively in soil deposits predominantly composed of clay. Since sleeve friction (f_s) in clays is affected by soil sensitivity, the previous clustering relied only on the q_T and u_2 readings. In this thesis, a cluster analysis approach is proposed based on all the three channels of CPTu data: q_T, f_s, and u_2, using normalized forms common to current practice: Q, F, B (Robertson, 1991).

The three-dimensional clustering can be used on any soil type (i.e., clay to silt to sand and mixtures) for stratification purpose. A three-dimensional soil classification chart is also proposed to integrate in the cluster analysis process.

Many soil parameters can be derived from SCPTu data, based on interpretations from analytical, numerical, and empirical relationships. Some computer programs are available to automate this process as listed in Chapter 4. Most of these software programs cost from hundreds to thousands US dollars. Furthermore, the correlations used in these software packages are generally founded on old sometime antiquated methods of analysis (20 years +) as implemented by the software developers. Since new improved relationships are being developed on a frequent basis, the older programs are not able to adapt to the best available methods. New software (*InSituData*) is developed in this thesis to facilitate the post processing of penetration data. For liquefaction analysis, *InSituData* assesses the cyclic resistance ratio (CRR) using both stress-normalized tip resistance q_{T1} (Robertson & Wride, 1998) and/or stress-normalized shear wave velocity V_{s1} (Andrus & Stokoe, 2000). *InSituData* also interfaces directly with Excel and provides more convenience in deriving parameters from in-situ test data, particularly those from SCPTu soundings.

1.3 New Madrid Seismic Zone (NMSZ)

The New Madrid Seismic Zone (NMSZ) is the most extensive seismic region in the eastern United States, as indicated by the U. S. Geological Survey earthquake hazard map in Figure 1.3. Seismic cone penetration tests (SCPTu) were performed by the author at

selected sites in the NMSZ to evaluate the liquefaction potential over the large developed urban, suburban, and rural regions in this region. A number of the specific sites investigated are well-recognized paleoliquefaction locations under study by the USGS and Mid-America Earthquake Center. Moreover, many of the proposed measures discussed herein could also be applied to advantage in other seismic areas of the world.

New Madrid Seismic Zone
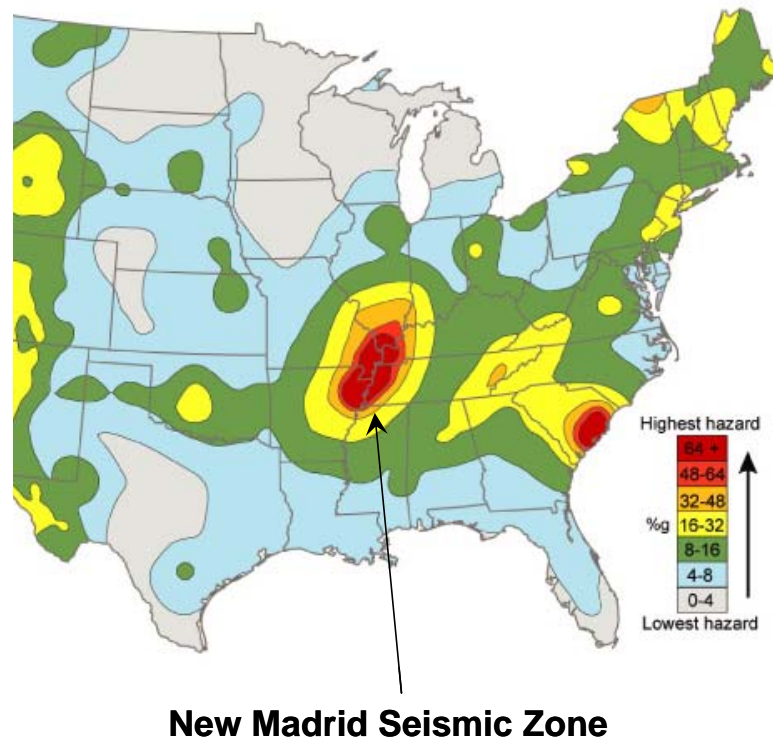
Figure 1.3 U. S. Geological Survey earthquake hazard map for the United States
(http://pubs.usgs.gov/fs/fs-131-02/ fs-131-02-p2.html)

Note: Color coding represents peak ground acceleration (PGA) having a 2 percent
probability of being exceeded in the next 50 years for a firm rock site condition.

Recent paleoliquefaction studies by Tuttle (1999) give improved estimates about the magnitude and location of epicenters of previous earthquakes in the NMSZ. They are used in this thesis to refine the scenario earthquakes for evaluating the liquefaction

potential at the paleoliquefaction sites. In this study, the acceleration on the bedrock is evaluated using the new program SMSIM developed by Boore (2002), and the cyclic stress ratio (CSR) is computed more rigorously using the newly-developed program DEEPSOIL (Park & Hashash, 2004). The CSRs derived from both detailed DEEPSOIL analyses and simple empirical correlations (e.g. Seed & Idriss, 1971) are compared for selected sites in the NMSZ. Specifically, at key paleoliquefaction sites, the obtained CSRs are referenced against the CRRs to assess the liquefaction potential of the test site. The CRRs are evaluated based on both deterministic procedures (e.g. Robertson & Wride, 1998; Andrus & Stokoe, 2000) and probabilistic procedures (e.g. Juang & Jiang, 2000; Juang et al., 2001), using both normalized tip resistance (q_{T1}) and normalized shear wave velocity (V_{s1}). Thus the liquefaction probabilities are also given for the analyzed test sites in this study. Based on the liquefaction evaluation results at the paleoliquefaction sites, regional criteria for liquefaction are developed herein for the NMSZ.

The SCPTu test can serve as a valuable tool for paleoliquefaction studies in the New Madrid Seismic Zone (NMSZ). Since almost all the field test data used in developing the liquefaction criteria are collected after the corresponding earthquakes, the criteria are more appropriate to estimate the seismic parameters associated with previous earthquakes (Chameau et al., 1991a; Olson et., 2001). As even the latest major earthquakes in NMSZ occurred nearly 200 years ago, soil aging effects should be an important factor to consider in utilizing these criteria to assess the seismic parameters associated with the previous earthquakes. Two large-scale blasting tests were conducted by the USGS that

resulted in localized induced liquefaction during the Mississippi Embayment Seismic Excitation Experiments (ESEE). Seismic cone penetration tests (SCPTu) were made before, immediately after, one day, and 8 months later following the large blasts. Considering the variance range caused by soil variability and equipment error, aging effects on field cone penetrometer measurements in NMSZ were not observed to be very substantial. Therefore, soil aging effects are not considered significant for paleoseismology studies in this thesis.

Finally, procedure to estimate seismic parameters associated with previous earthquakes is proposed in this thesis. It utilizes both the liquefaction criteria based on SCPTu tests and the empirical attenuation relations developed for the corresponding regions. The approach is validated through data evaluation related to the 1989 Loma Prieta earthquakes in California and then applied to previous earthquakes in the NMSZ.

1.4 Organization of Thesis

This thesis presents some new techniques for post-processing the SCPTu data, and summarizes some new insights into the seismic response of soils in the NMSZ using enhanced post-processing of SCPTu data.

- Chapter II summarizes the techniques and features of the software, *ShearPro* for deriving shear wave velocity from shear wave signals.

- Chapter III presents the procedures for a three-dimensional cluster analysis for soil stratification, and a three-dimensional soil classification chart that gives consistent

classification results. The software program *ClusterPro* that implements the three-dimensional cluster analysis is also introduced.

- Chapter IV introduces the software, *InSituData*, which is developed to facilitate the post processing of penetration data for seismic ground hazards analysis.

- Chapter V reviews the liquefaction criteria based on tip resistance and shear wave velocity of SCPTu soundings.

- Chapter VI discusses liquefaction evaluation considering local site effects. Case studies are performed at the paleoliquefaction sites in the NMSZ.

- Chapter VII focuses on the aging effects of sands and those observed in the NMSZ during the Embayment Seismic Excitation Experiments (ESEE).

- Chapter VIII proposes an approach to estimate seismic parameters associated with previous earthquakes. It is validated through the 1989 Loma Prieta earthquake and applied to the previous earthquakes in the NMSZ.

- Chapter IX presents the conclusions of this thesis and recommendations for future research.

- Appendix A gives a more detailed introduction about the NMSZ.

- Appendix B discusses the paleoliquefaction sites in the NMSZ, where SCPTu tests have been performed.

- Appendix C gives a brief introduction to the non-paleoliquefaction sites in NMSZ, where SCPTu tests have been performed.

- Appendix D presents the results of liquefaction evaluation for the paleoliquefaction test sites.

- Appendix E is the instructions for using the program *ShearPro* 1.3 to derive shear wave velocity from downhole shear wave signals.

- Appendix F is the instructions for using the program *ClusterPro* 1.0 to do three-dimensional cluster analysis.

- Appendix G is the instructions for using the program *InSituData* 1.0 to process SCPTu data.

CHAPTER II

AUTOMATED POST-PROCESSING OF SHEAR WAVE SIGNALS

2.1 Synopsis

Shear wave velocities (V_s) can be determined by either laboratory or field methods, as illustrated in Figure 2.1 (Schneider, 1999). In the laboratory, the small strain shear modulus (G_{max}) can be measured on undisturbed soil samples using the resonant column, torsional shear, piezoelectric bender elements, as well as triaxial apparatus with internal local strain measurements (Woods, 1994). The shear wave velocity can thereby be determined using $V_s = \sqrt{G_{max}/\rho_T}$, where ρ_T is the total unit mass density. Of note, undisturbed sampling can only be conducted in clayey or silty soils, as clean quartz sands and granular materials are nearly impossible to capture in an undisturbed state. Moreover, the issue of sample disturbance in clays and silts is of paramount concern since the quality of results is greatly affected. The derived magnitude of G_{max} is reduced considerably by disturbances caused by drilling, tube insertions, extraction, sealing with hot was, transportation, extrusion in the lab, trimming, and mounting of the specimens (e.g. Stokoe & Santamarina, 2000). Therefore, for avoidance of these issues, the V_s profile can be measured by field methods, such as crosshole test (CHT), downhole test (DHT), suspension logging, seismic refraction, seismic reflection, and spectral analysis of surface waves (SASW), as shown in Figure 2.1. A more detailed review of various field V_s methods is given by Campanella (1994).

12
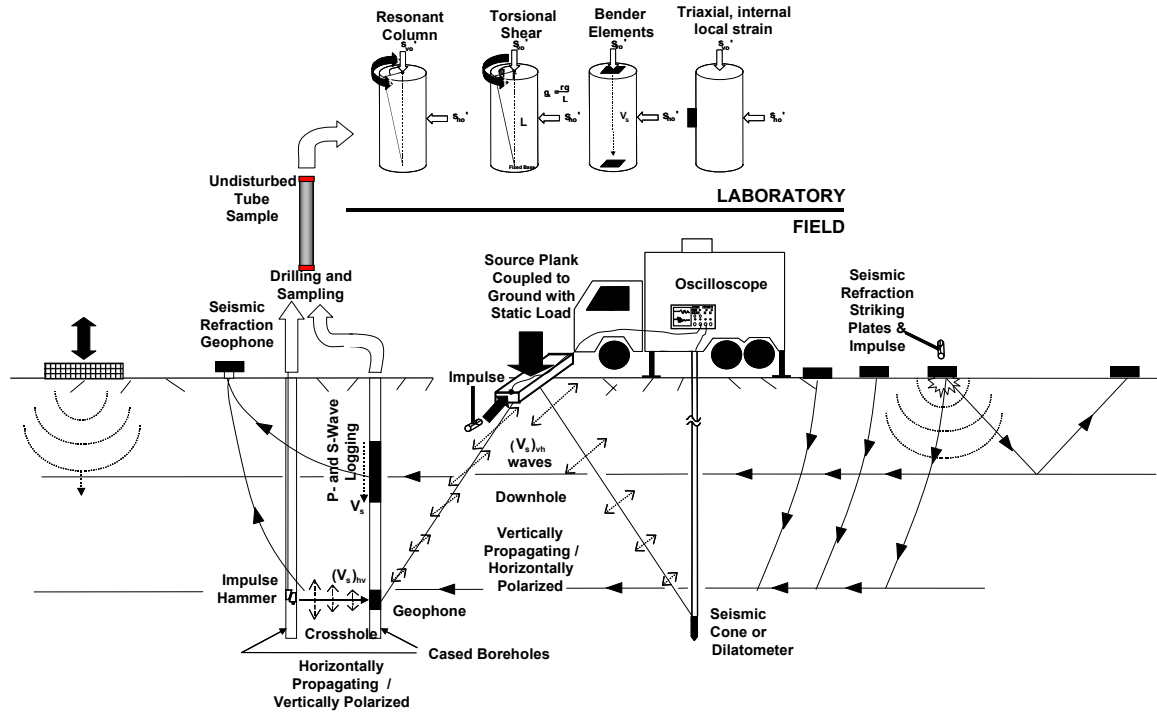
Figure 2.1 Field and laboratory methods to determine shear wave velocity
(Schneider, 1999)

The traditional reference field test for determination of V_s is the crosshole test (CHT), per ASTM D 4484 standards. However, the CHT is a very expensive means to defining the V_s profile, as it requires at least two to three cased boreholes that are subsequently grouted and checked for inclination variances,. A 30 m profile by CHT can cost from US $10k to $15k. The downhole test (DHT) is a reasonable and economical alternative using only a single borehole by conventional drilling and sampling methods. A comparable 30 m downhole test (DHT) would cost about US $6k to $8k. Methods using Rayleigh waves [spectral analysis of surface waves (SASW), continuous surface wave method (CSW), multichannel analysis of surface wave (MASW)] or refracted waves are good alternatives, yet being noninvasive, also require guesswork on the layering sequence or separate borings or soundings to determine the strata depths, thickness, and soil types.

13

Downhole tests (DHT) can be performed in cased boreholes or using direct-push technology, such as the seismic cone penetration test (SCPTu) or seismic dilatometer (SDMT). By processing the shear wave signals from downhole testing, the profile of shear wave velocity V_s with depth can be calculated. The shear wave velocities given by the SCPTu tests have been shown to be comparable to those obtained by crosshole tests in both sand and clay deposits (Robertson et al., 1986). The shear wave velocity is used in deriving the small-strain shear modulus ($G_{max} = \rho_T V_s^2$), which is the initial soil stiffness needed for site amplification analyses in evaluating seismic liquefaction potential. The value of G_{max} is also fundamental in the evaluation of stress-strain behavior and foundation response in soils (Burland, 1989; Tatsuoka & Shibuya, 1991; Mayne, 2001). An objective and quality assessment of the shear wave signals collected by downhole testing can be crucial in obtaining information related to the soil properties.

In most commercial systems, the seismic cone penetration test uses a pseudo-interval time stepping, as illustrated in Figure 2.2. The shear wave velocity V_s is calculated by dividing the incremental traveling distance to the geophone by the incremental arriving time between successive recorded shear waves (Campanella et al., 1986). Several methods exist for calculating the time interval between shear waves. As the DHT was developed more than 30 years ago (e.g. Hoar & Stokoe, 1978), simple data processing schemes were derived because the recordings were analog. The most straight-forward one is to estimate the time that the wave first arrives to the geophone, as shown in Figure 2.3, and the time interval is the difference between the first arrival times of the corresponding

shear waves. But the first arrival time is usually hard to discern and requires much experience. This is because the first arrival point is usually masked by earlier arrival of the faster compression (or P) wave. In addition, the recorded waveforms show additional signals from other waves reflected by the layer interfaces, as well as extraneous noises and electromagnetic interference. Of additional note, the manual processing of data is tedious and time-consuming.
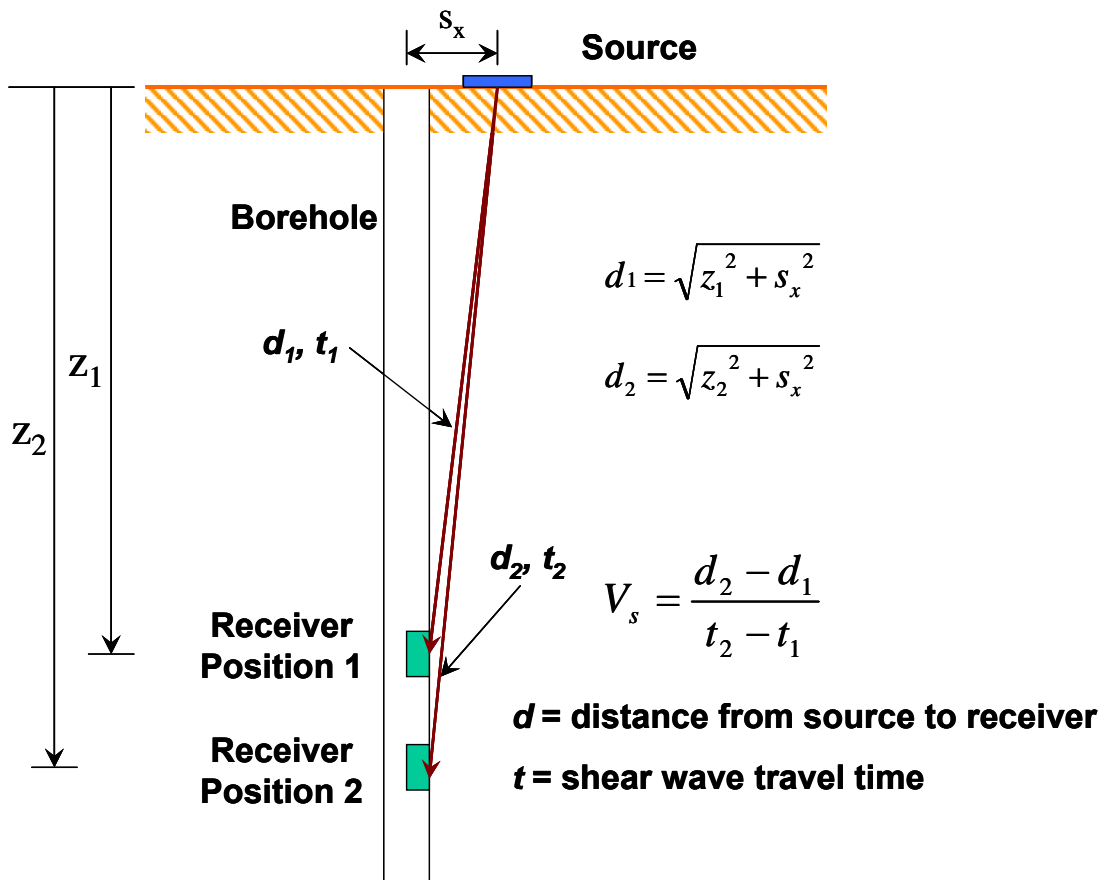
Figure 2.2 Conceptual configuration of downhole seismic test using pseudo-interval time stepping

The cross-over method requires a shear beam source to be hit a minimum of two times: (a) an initial strike and (b) a second strike in the opposite direction. Therefore, two shear

wave trains of opposite amplitude are recorded at the same depth, and the cross-over time is defined as that time that the first clear cross-over of the two shear waves occurs (Robertson et al. 1986). Example shear wave trains recorded after a left and a right strike are shown in Figure 2.3 (a) and (b), respectively, and they are superimposed in Figure 2.3 (c), which indicates the cross-over time of the two waves. Thus, the time interval is the difference between successive cross-over times at consecutive depths. Paired left- and right-strikes, however, require two events. Moreover, since much reliance is placed on the single crossover point, most CPT service firms check the repeatability of each left and right strike, thereby a total of 4 strikes at each depth, prolonging the CPT field testing time. Furthermore, the cross-over method only uses the time information of a single point in the wave train, yet the full wave train can contain thousands of data points, which are not considered in the evaluation. Sometimes, the cross-over time can be shifted because of signal disturbance, particularly if a bad recording is taken on either the left or right strike (Campanella & Stewart, 1992).

With modern data acquisition and digital storage, improved post processing of shear wave arrival times can be made using (a) cross-correlation, and (b) phase-shifting. Cross-correlation is an alternative approach to calculate the time interval by aligning the signal trains in the time axis, and it utilizes considerably more information in the collected shear waves than the first arrival and first cross-over methods (Campanella & Stewart, 1992). The phase-shift method is a frequency-domain technique, which uses the phase difference between signals to measure the travel velocity of the signal. This approach was used to derive the shear wave velocity in bender element experiments (Greening et al., 2003;

Theron et al., 2003), and it can also be applied to analyze the shear wave signals collected by downhole seismic tests. Baziw (2002) suggested the use of forward modeling and the down hill simplex method to derive the shear wave velocity recursively, which considers the refraction of the waves at the soil interfaces, but it is much more complex. It also requires investigation of the geometry of the stratigraphic profile and a good estimation of the wave velocity in each layers, otherwise nonsensical results may occur. In this thesis, the cross-correlation and phase-shift methods are discussed. They are implemented into a stand-alone software program (*ShearPro*) to automate processing of the shear wave signals collected by SCPTu soundings, and/or other downhole tests (DHT, SDMT). The derived V_s results are compared with those obtained by other processing methods.

2.2 Cross-Correlation Method

Cross-correlation is a method that can be easily implemented on a computer to derive the shear wave velocity from raw wave train data. It refers to the correlation of two independent series, and can be used to measure the degree at which the two series are related. Suppose x(*t*) and y(*t*) are two continuous signals with respect to time *t*, the cross-correlation function of x(*t*) and y(*t*) for a time shift *s* is defined as

$$z(s) = \int_{-\infty}^{\infty} x(t)y(t+s)dt \qquad (2\text{-}1)$$

For two signals of the same shape, the cross-correlation function may be used to calculate their difference in their arrival times, which is equal to the time shift that results in the peak of the cross-correlation function.

Originally, the cross-correlation was done in the frequency domain, since it required relatively little computation time compared with that done directly in time domain (Campanella & Stewart, 1992). However, with the computer speed having doubled every eight months, the required computation time in the time domain is insignificant in 2005.
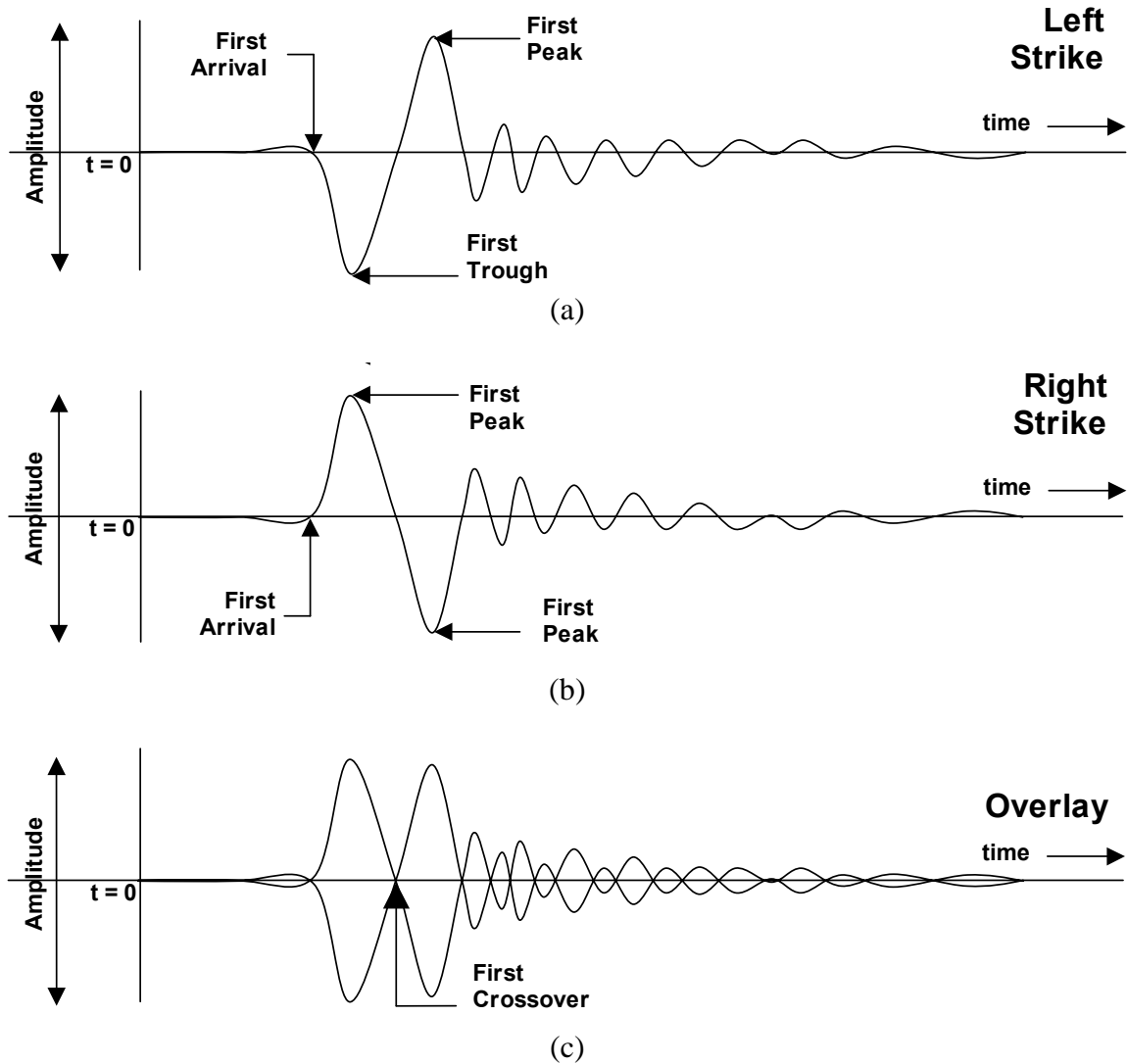
Figure 2.3 First arrival time and first crossover time of shear wave signals: (a) Shear wave train recorded after a left strike; (b) Shear wave train recorded after a right strike; (c) Overlay of the paired shear wave trains in (a) and (b)

18

It is sometimes more advantageous to do cross-correlation in a statistical way in the time domain, since its physical meaning is clear and it can provide some regression parameters to evaluate the quality of the process. Assume N pairs of observations on two shear wave signals in time domain, which are x_i and y_i, where i=1, … , N. If the signal y_i is shifted forward along the time axis for a certain amount of time, which is equal to k times of the sampling interval, the two signals become x_i and y_{i+k}. Therefore, the first N-k data points of signal x_i can be plotted against the last N-k data points of y_i on a scatter plot, and the coefficient of determination (r^2) can be used to evaluate the correlation between them, according to:

$$r^2 = \frac{\left(\sum (x_i - \bar{x})(y_{i+k} - \bar{y})\right)^2}{\sum (x_i - \bar{x})^2 \sum (y_{i+k} - \bar{y})^2}$$

(2-2)

where $\bar{x}$ is the average of the first N-k data points of signal x_i, and $\bar{y}$ is average of the last N-k data points of y_i. The time shift that gives the highest value for the coefficient of correlation r corresponds to the best fit time interval between the signals. Two hypothetical sine waves (signal A and signal B) are presented in Figure 2.4 (a). They are identical in shape, except a time offset between them. The digital observations of these signals are assumed to be the solid dots as shown in this figure. The amplitudes of the digital observations from signal A are plotted against those of the corresponding observations from signal B in Figure 2.4 (b), assuming different amount of time offset Δt. Linear regression is performed for these points, and it can be seen that the coefficient of determination r^2 reaches a maximum value of 1 when the time offset Δt = 2 ms. Therefore, the time offset between signal A and B is 2 ms.
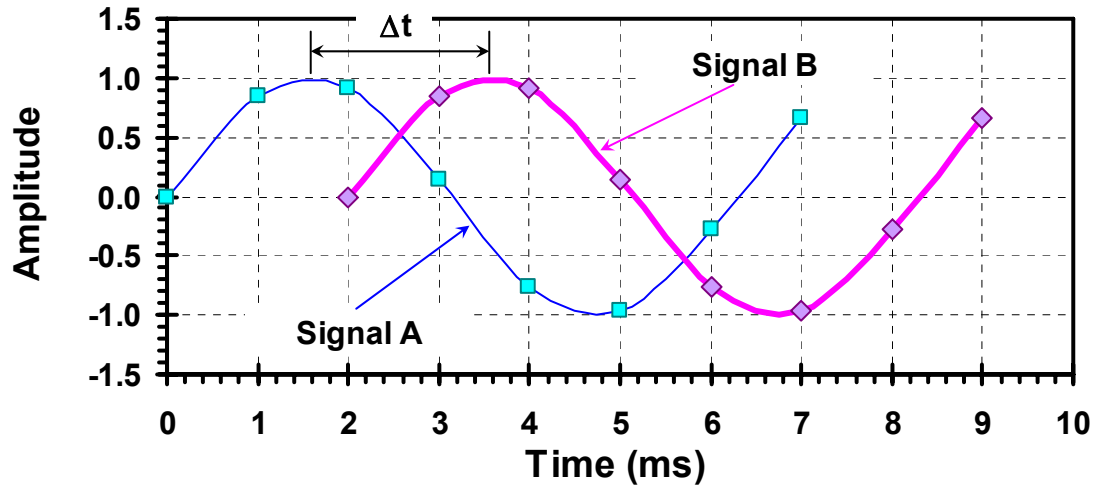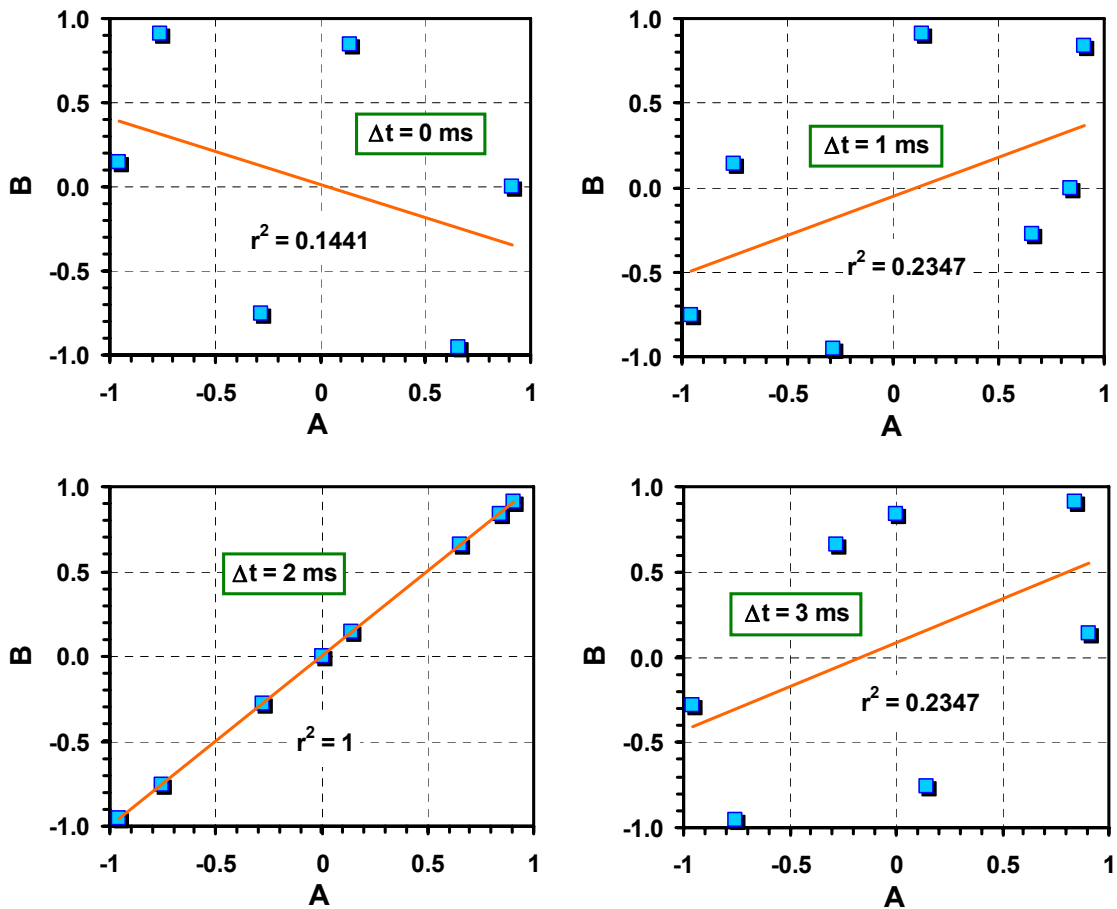
Figure 2.4 Cross-correlation on two hypothetical sine wave signals: (a) The waves in time domain; (b) Scatter plots of amplitude of signal A against that of signal B with a certain amount of time offset

Cross-correlation works well if two signals are of the same shape. In true-interval downhole testing, the initial main wave cycle is very well matched. However, attenuation levels for different frequency components of the shear wave are not the same, and those with high frequencies are more easily attenuated as they travel through the soil media. Thus, the latter parts of the waveform may not match well at all due to different attenuation, as well as due to overlapping signal, from nearby refracted and reflected waves. For pseudo-downhole testing, the seismic source can also influence the signal shape if it is not very repeatable in generating the shear waves. Therefore, it is impossible for two signals collected at different depths to be of the exactly same shape. Realizing the portions of the signal other than the main wave can affect the value of derived shear wave velocity, Campanella and Stewart (1992) proposed use of a window to select a portion of the signal, which is the main shear wave, while clipping off the latter trailing portions of the signal by setting their amplitudes to zero.

2.3 Phase-shift Method

The geophone records the signal generated by the source and transmitted through the soil for a distance. If the damping, refraction, and reflection are not considered, ideally the signals recorded at different depths are the same, except the signal recorded at the greater depth has some delay from the other one, and the delay is the travel time of the wave between the two depths. Assume the signal recorded at a shallow depth is *x(t)*, which is a continuous signal in the time domain, and then its Fourier transform X(*f*) is

$$X(f) = \int_{-\infty}^{\infty} x(t) e^{-j2\pi ft} dt \qquad (2\text{-}3)$$

21

Suppose the delay is a constant time Δt, the signal recorded at a greater depth should be $x(t-\Delta t)$, and the Fourier transform of $x(t-t_0)$ is

$$X'(f) = \int_{-\infty}^{\infty} x(t - \Delta t)e^{-j2\pi ft}\,dt = e^{-j2\pi f\Delta t}X(f) \qquad (2\text{-}4)$$

From this equation, we can see that the delay Δt shifts the phase for the amount of $2\pi f\Delta t$ for each frequency component, which is a function of the frequency f (Brigham, 1988). Since each frequency component would have a phase change when it travels for a certain distance, the phase shift of the sinusoids can be plotted against their frequency, and the slope of the linear regression (k) of the data points should be $2\pi\Delta t$, where Δt is the arrival time interval between two shear wave signals. Therefore, Δt can be derived through the following equation:

$$\Delta t = k /(2\pi) \qquad (2\text{-}5)$$

Figure 2.5 (a) presents a very simple example with two hypothetical signals (A and B). They are identical in shape, except for a time offset between them. Both signals are composed of two frequency wave components in frequency domain, which are $f = 159.2$ Hz and $f = 318.3$ Hz. The two components of the signals are plotted in Figures 2.5 (b) and (c), respectively. The phase difference between the $f = 159.2$ Hz components of the two signals is 2, and that between the $f = 318.3$ Hz components is 4. The phase differences are plotted against the frequencies of the two components in Figure 2.6, and the slope for the line connecting the two points is $k = 0.0126$ sec. Therefore, the time offset between the two signals is 2 ms based on equation (2-5).
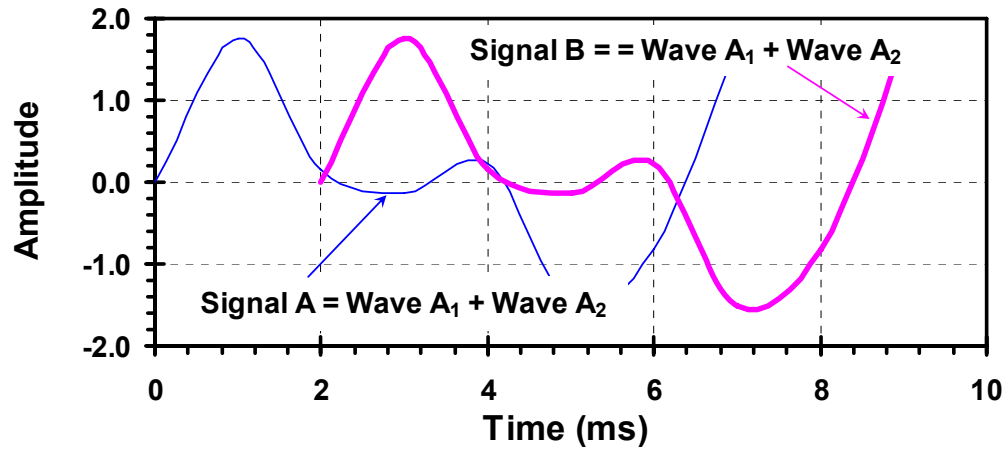
(a)
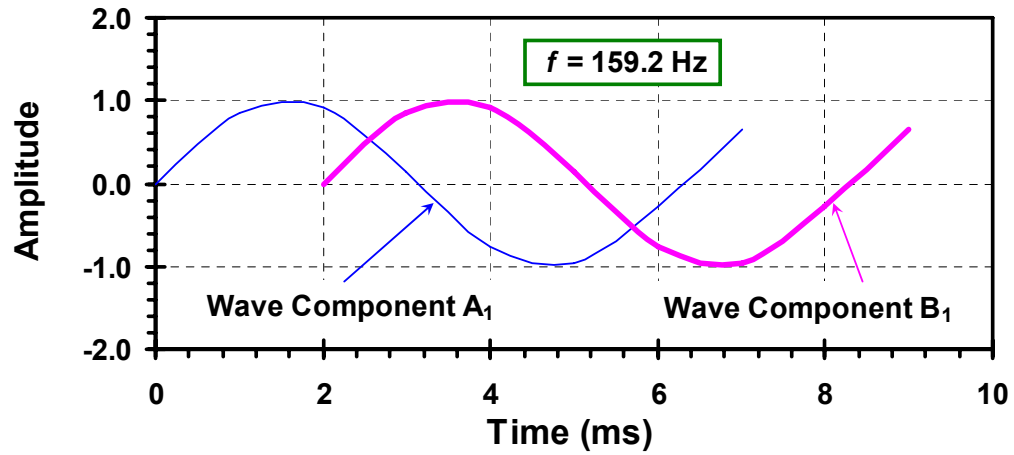
(b)
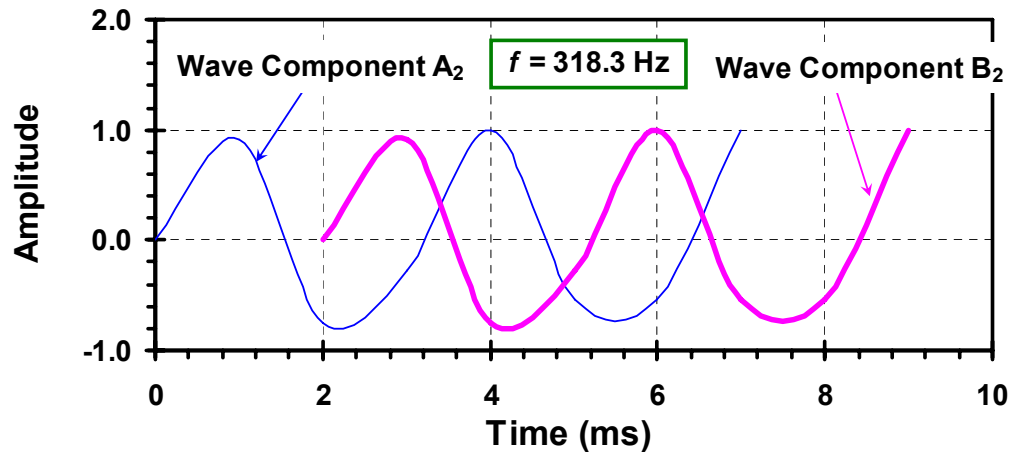
(c)

Figure 2.5 Two hypothetical signals that both have components of frequency f = 159.2
Hz and f = 318.3 Hz: (a) Signals A and B in time domain;
(b) The frequency f = 159.2 Hz components in signal A and B;
(c) The frequency f = 318.3 Hz components in signal A and B.
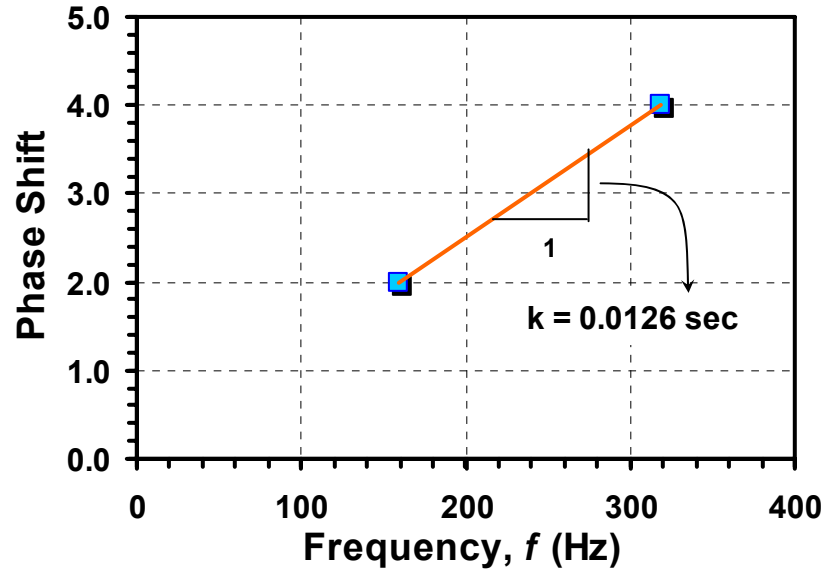
Figure 2.6 Phase shift of the two components between
signal A and B shown in Figure 2.5

2.4 Worked Examples

The cross-correlation and the phase-shift methods are both theoretically robust and
simple. To illustrate these concepts, both methods are applied to process the shear wave
signals collected at two sites, including the Nodena Farm site in Wilson, Arkansas and
the Coca-Cola site in Atlanta, Georgia.

2.4.1 Nodena Farm Site

The Nodena farm site is a paleoliquefaction site located northeast of Wilson, Arkansas
(Tuttle et al., 2000). The site is underlain by layers of interbedded alluvial clay and sand
sediment from the Mississippi River. Additional details about this site are presented in
Appendix B. Figure 2.7 shows the paste-up of the collected shear wave signals at 1-meter
intervals with their amplitudes normalized, that is, the amplitude is divided by the largest

amplitude of the signal in the time domain. The largest wave corresponds to the first

cycle arrival of the shear wave.
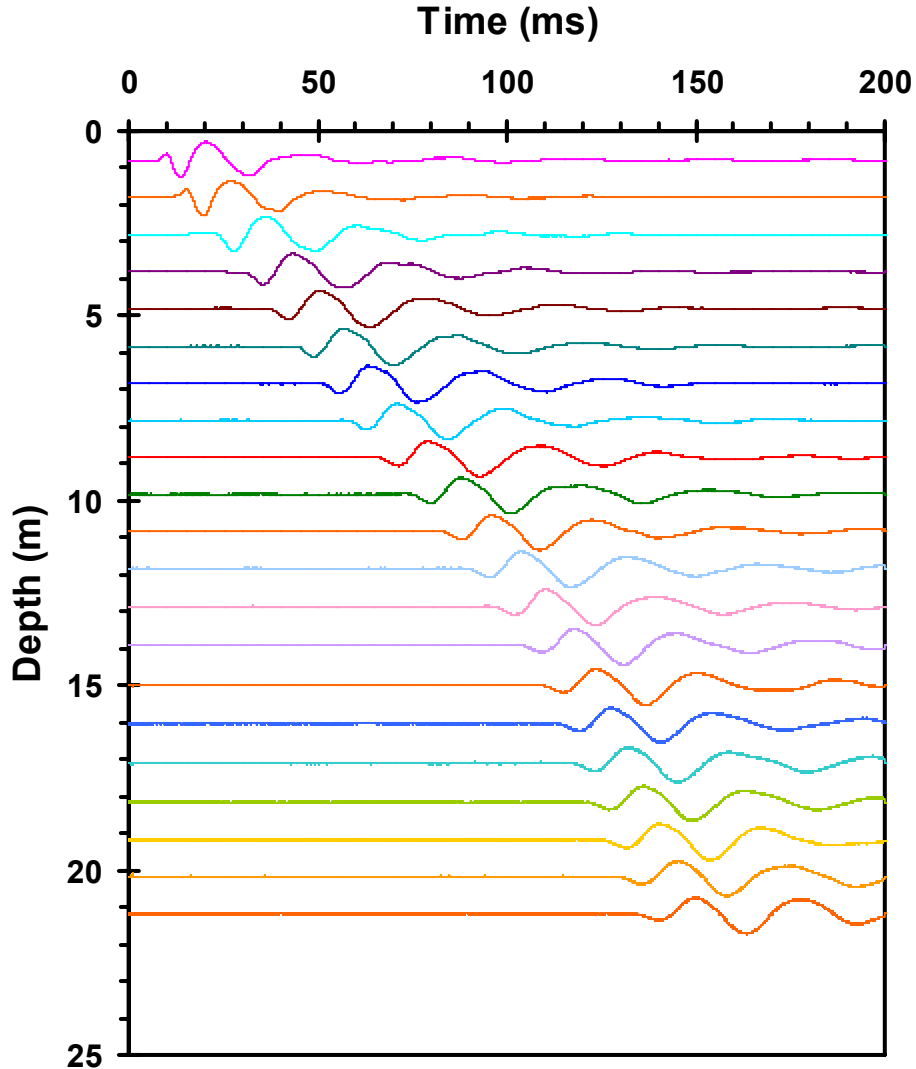
Figure 2.7 Shear waves recorded at one-meter depth interval by a representative SCPTu
sounding performed at the Nodena Farm paleoliquefaction site in Wilson, AR

Figure 2.8 (a) shows the shear wave trains collected at depths of 4.82m and 5.85m from

the seismic piezocone sounding performed at the Nodena Farm site. They have similar

shape, but the shear wave train recorded at the depth of 5.85 m is delayed to some extent

compared with that recorded at the depth of 4.82 m. Figure 2.8 (b) presents the coefficient of determination r^2 calculated from equation (2) during cross-correlation, with different amounts of time shift set between the two wave trains. The time shift is 6.675 ms corresponding to the maximum coefficient of determination $r^2 = 0.9757$.

(a)

(b)
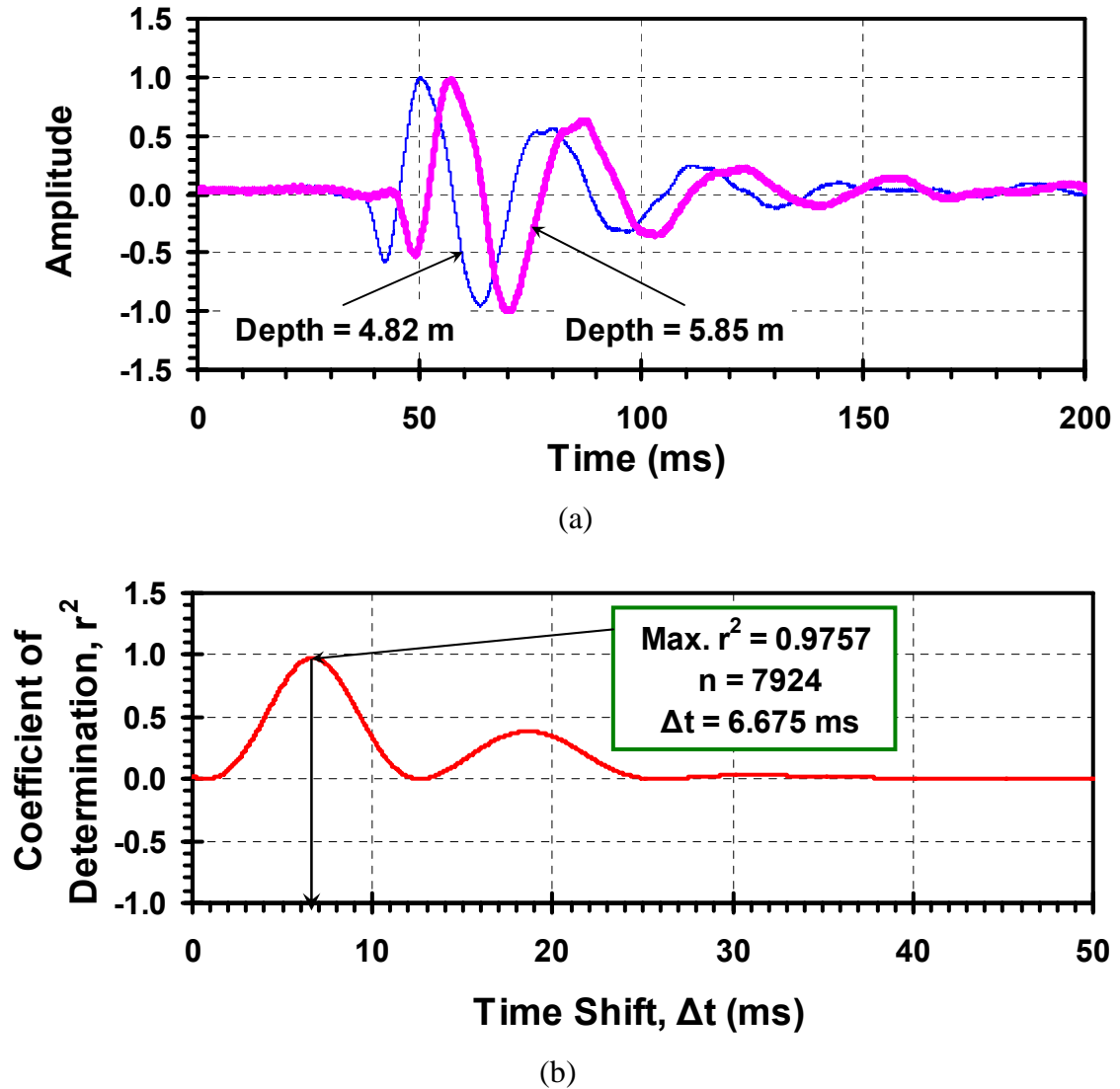
Figure 2.8 Cross-correlating the shear wave signals collected at depths of 4.82m and 5.85m from the SCPTu sounding performed at the Nodena Farm site, Wilson, AR:
(a) Shear wave trains at two consecutive depths;
(b) Coefficient of determination with different time shifts.

For the example shown in Figure 2.8, the distance between the seismic source and the central axis of the cone penetrometer is 0.75 m. Thus, the traveling distance for the shear wave at the depth of 4.82 m $\sqrt{4.82^2 + 0.75^2} = 4.878$ m, and that at the depth of 5.85 m is $\sqrt{5.85^2 + 0.75^2} = 5.898$ m. By dividing the difference between the traveling distances ($\Delta d = 1.02$ m) of the two signals with the time shift ($\Delta t = 6.675$ ms) obtained by the cross-correlation method, the derived shear wave velocity $V_s = \Delta d / \Delta t = 152.8$ m/s. The corresponding mid-depth is 5.34 m.

Phase-shifting of the shear waves will now be applied to the same data set. Fast Fourier transform is applied to the signals shown in Figure 2.8 (a), and their amplitudes in frequency domain are presented in Figures 2.9 (a) and (b), respectively. Most energy of the shear wave signals are concentrated in the frequency range from 20 to 60 Hz, and it is reasonable to believe that frequency components in this range are not significantly altered by noise. Therefore, the phases of the two signals are shown in Figures 2.10 (a) and (b) for the frequency components in the range from 20 to 60 Hz, and the phase differences of the corresponding frequency components are plotted in Figure 2.10 (c). Theoretically, the phase shift should be zero as the frequency converges to zero, and thus the origin is set as the control point for the regression. Linear regression that is forced through the origin is performed on the data points of phase shift, with its equation and coefficient of determination, r^2, also shown in Figure 2.10 (c). Since the measured slope is k = 0.0419, the difference of the arrival time of the two signals is $\Delta t = k/(2\pi) = 0.0419/(2\pi) = 6.67 \times 10^{-3} s = 6.67ms$, and thus the shear wave velocity V_s = 152.9 m/s, which agrees well with that derived using the cross-correlation method. The

coefficient of determination, r^2, indicates the quality of the regression, and the higher the value of r^2, the more accurate the derived shear wave velocity.
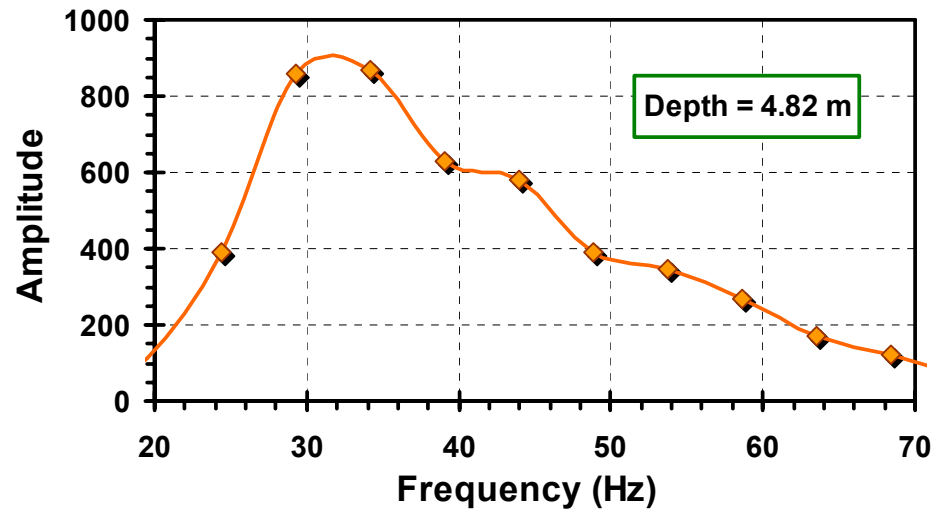
(a)
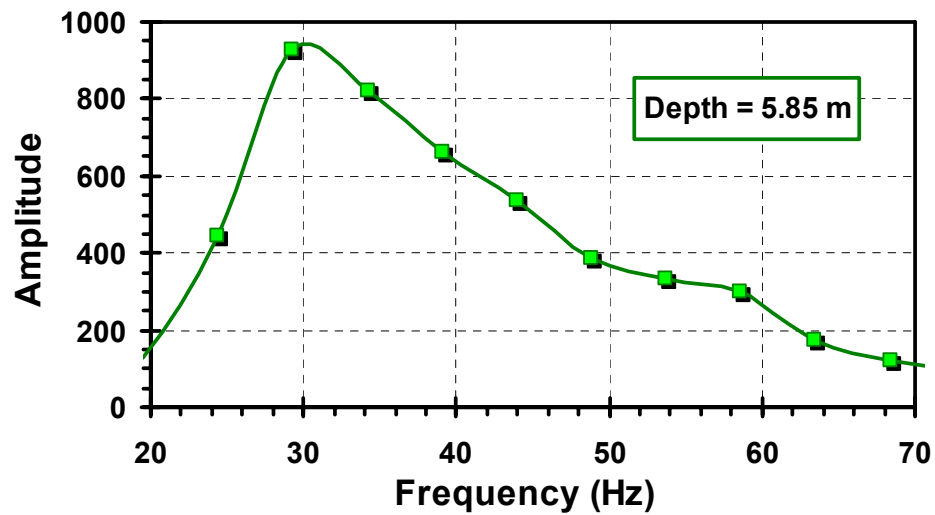
(b)

Figure 2.9 Shear wave signals in frequency domain from a SCPTu sounding performed at the Nodena Farm paleoliquefaction site, Wilson, AR: (a) Shear wave signal in frequency domain at depth = 4.82 m; (b) Shear wave signal in frequency domain at depth = 5.85 m.
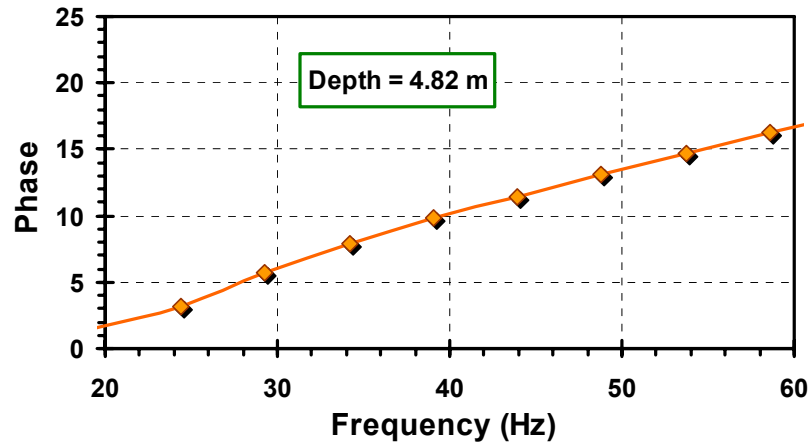
(a)
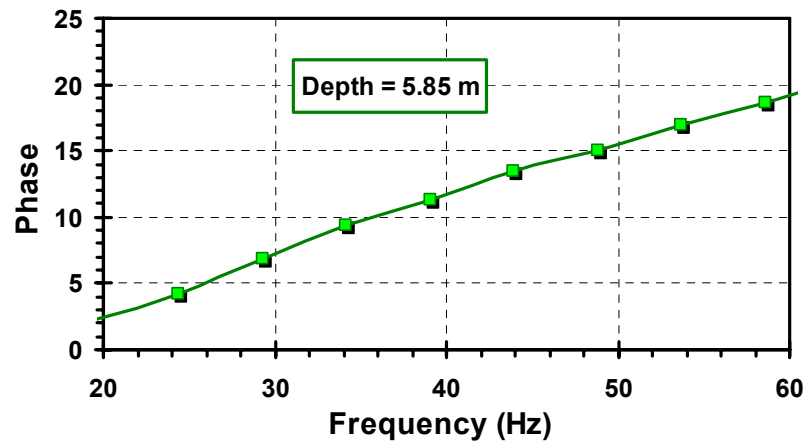
(b)
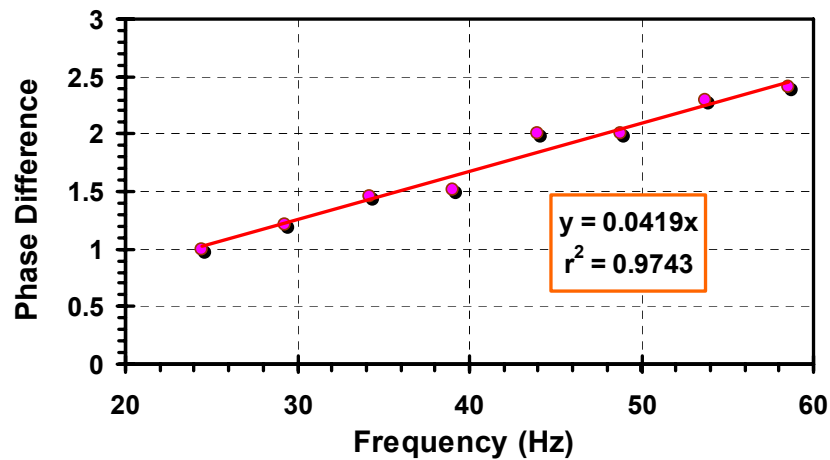
(c)

Figure 2.10 Phase-shifting of shear wave signals collected at depths of 4.82m and 5.85m by a SCPTu sounding performed at the Nodena Farm site, Wilson, AR: (a) Phase of the frequency domain components for shear wave signal at depth = 4.82 m; (b) Phase of the frequency domain components for shear wave signal at depth = 5.85 m; (c) Linear dependency between frequency and phase shift of the two waves.

29
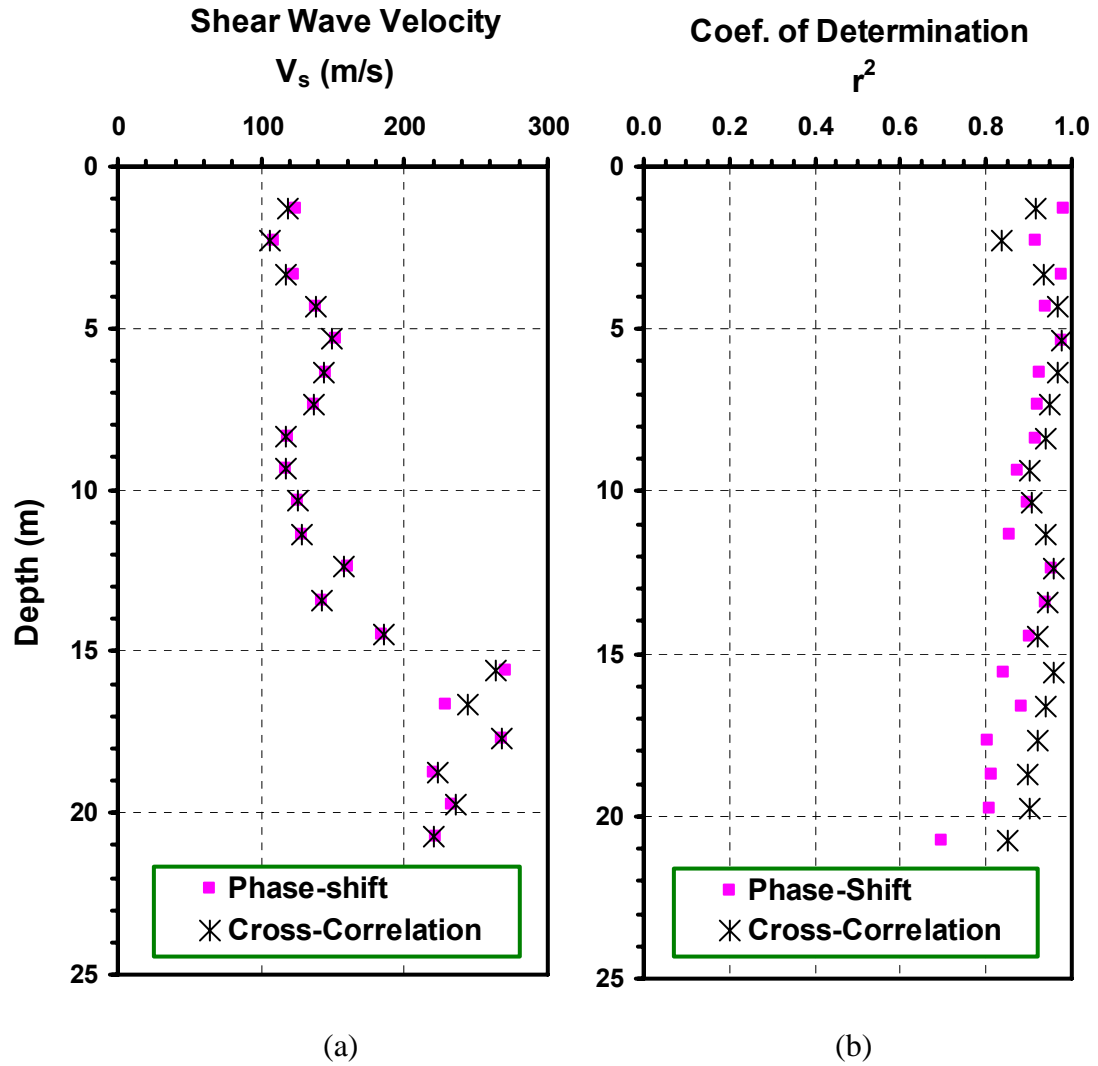
Figure 2.11 Results generated by the cross-correlation and phase-shift methods for the SCPTu data from the Nodena Farm site, Wilson, AR: (a) Shear wave velocity profiles; (b) Coefficients of determination with depth.

Figure 2.11 (a) shows the profiles of V_s calculated by both the phase-shift method and the cross-correlation method for this sounding. The results calculated by these two methods are very consistent. Figure 2.11 (b) presents the coefficient of determination, r^2, used for the cross-correlation method and the phase-shift method. They generally decrease with depth, because as the shear waves travel deeper, the signals become weaker due to the

dissipation of wave energy. Consequently, the shape of the signal and the phase of the frequency components are more likely to be altered by noise, thus affecting the statistical fitting. Over the full depth of 20 m, the coefficient of determination at Nodena site is quite high for the cross-correlation procedure (generally $r^2 > 0.90$), while for the phase-shift method, the r^2 falls to 0.80 at depths below 15 m.

2.4.2 Coca-Cola Site

As another illustrative example, Figure 2.12 shows the paste-up of the shear wave signals collected at a construction site at the headquarters of Coca-Cola Company in Atlanta, Georgia. When the sounding was being performed, some construction activity was ongoing at the site, thus affecting shape of the measured wave trains to some extent. Figure 2.13 (a) shows the shear wave trains recorded at the depths of 4.92 and 5.95 m, and their coefficient of determination, r^2, is plotted versus time shift in Figure 2.13 (b). The time shift Δt is 4.475 ms corresponding to the maximum value of $r^2 = 0.7406$. Since the traveling distance for the two shear wave signals are 4.977 m and 5.997 m respectively, the calculated shear wave velocity V_s is 223.5 m/s.

For the phase-shift method, the amplitudes in frequency domain for the shear wave signals at the depths of 4.92 m and 5.95 m are presented in Figures 2.14 (a) and (b), respectively. The energy of these two shear wave trains are concentrated in the frequency range from 20 to 100 Hz, which is wider than that in the Nodena farm site. Figures 2.15 (a) and (b) present the phases of the frequency components that are in the range from 20

31

to 100 Hz. The phase differences between the corresponding frequency components are plotted in Figure 2.15 (c), and the linear regression that is forced through the origin determines a slope $k = 0.0314$ with coefficient of determination $r^2 = 0.8201$. Therefore, the time shift $\Delta t = k/(2\pi) = 5.00$ ms, and the calculated shear wave velocity V_s is 200.0 m/s.
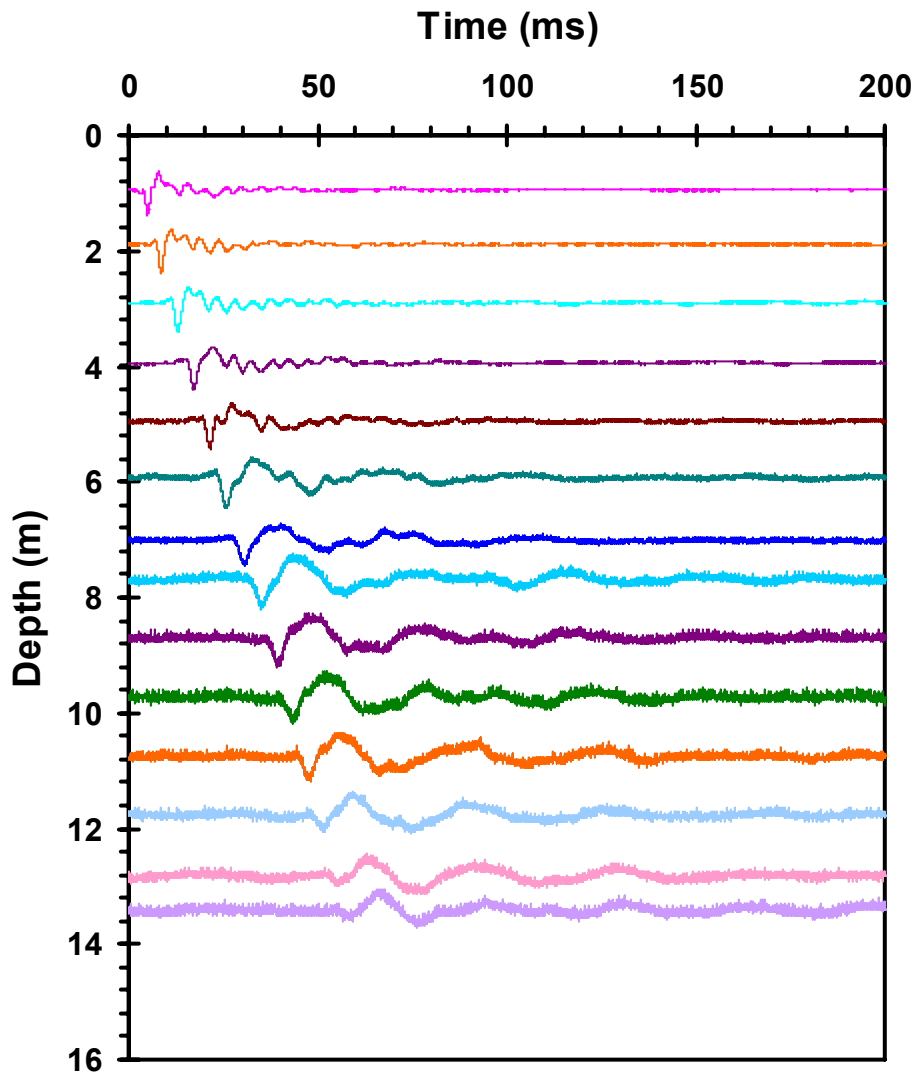
Figure 2.12 Shear waves recorded at one-meter depth intervals by the SCPTu sounding performed at the Coca-Cola Site, Atlanta, GA
Note: Signals include noise from ongoing construction activities
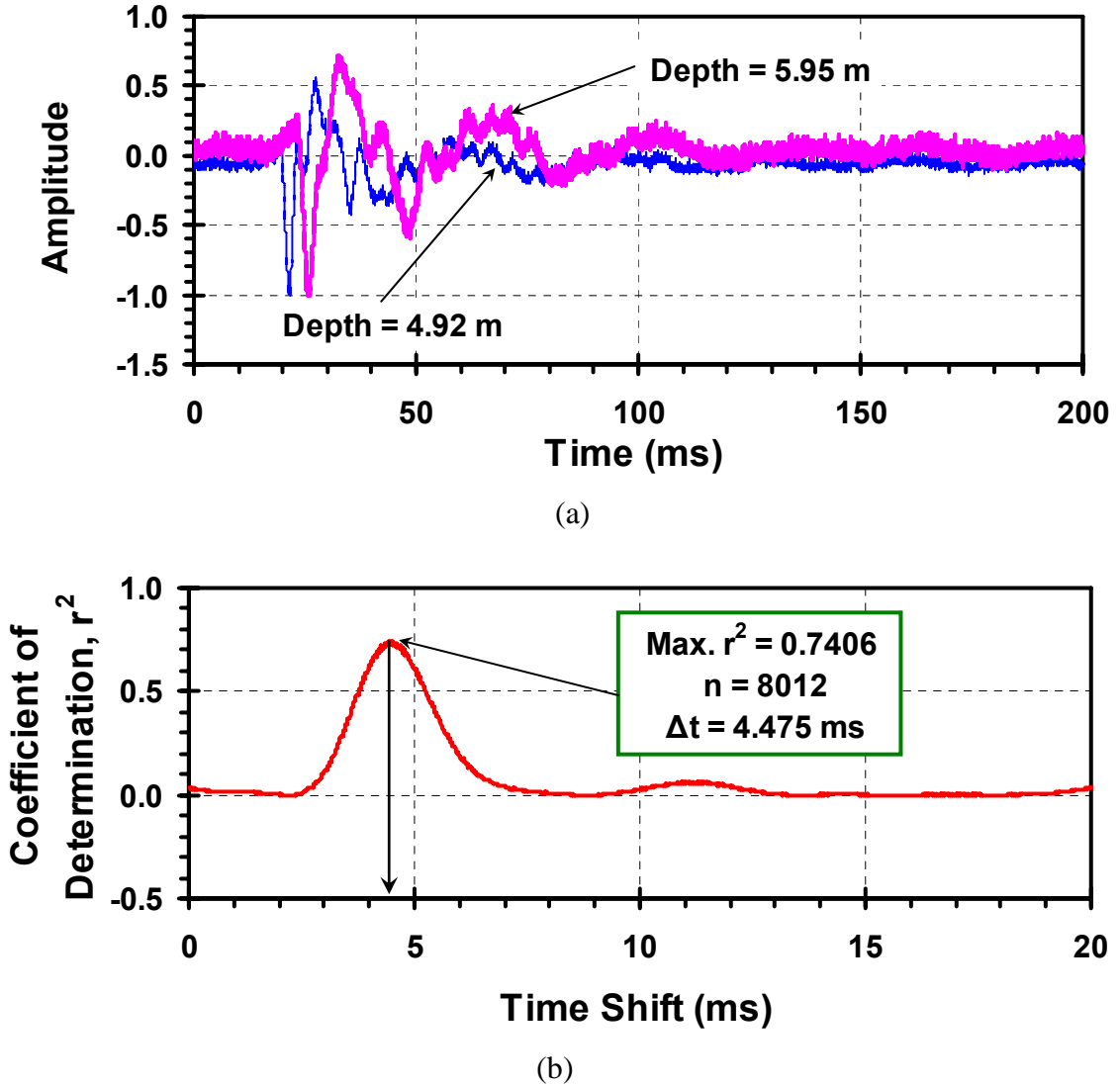
Figure 2.13 Cross-correlating the noisy shear wave signals collected at depth of 4.92m and 5.95m from the SCPTu sounding performed at the Coca-Cola site, Atlanta, GA: (a) Shear wave trains at two consecutive depths; (b) Coefficient of correlation with time shift.

The derived shear wave velocities for the Coca-Cola site calculated by both the cross-correlation method and phase-shift method are shown in Figure 2.16 (a). It can be seen that the results are relatively consistent until the depth exceeds 13 m. Figure 2.16 (b) shows the coefficient of determination, r^2, for both the cross-correlation and phase-shift methods, and similar to the last example, they generally decrease with depth. However,

because of the noisy environment, the values of r^2 are quite lower than those at Nodena site and generally in the range of 0.60 to 0.85.
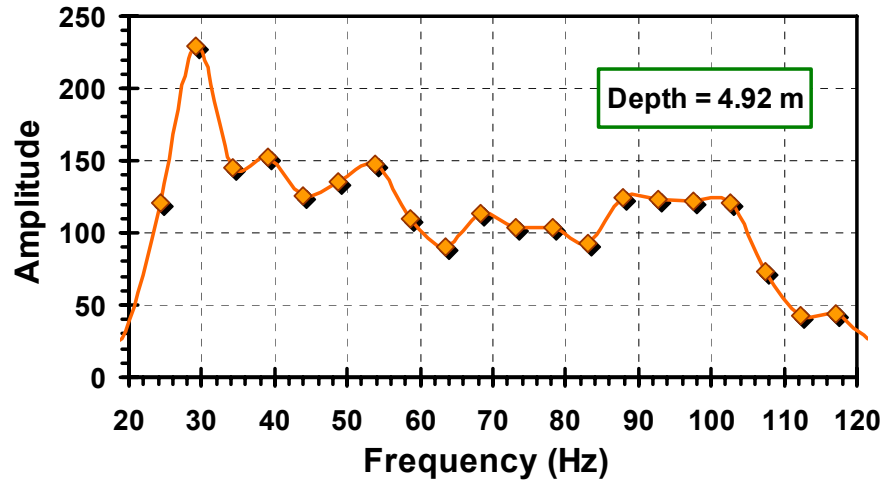
(a)
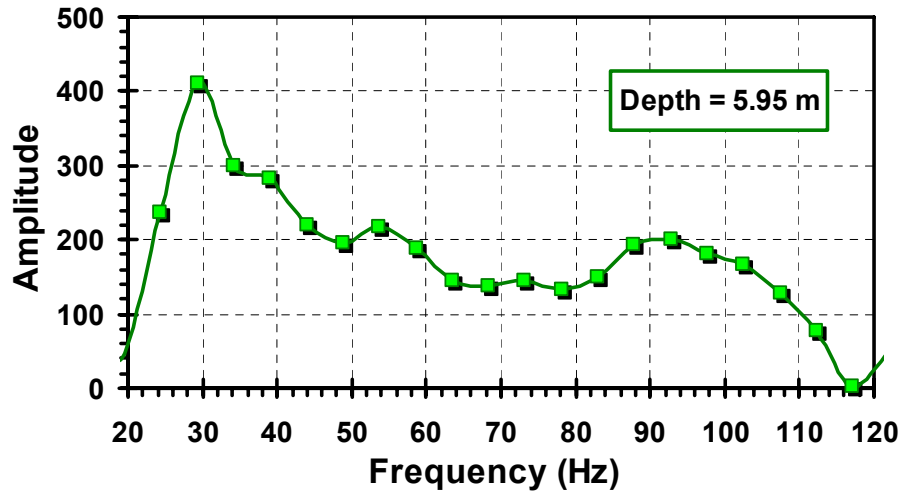
(b)

Figure 2.14 Shear wave signals in frequency domain from a SCPTu sounding performed at the Coca-Cola site, Atlanta, GA: (a) Shear wave signal in frequency domain at depth = 4.92 m; (b) Shear wave signal in frequency domain at depth = 5.95 m.
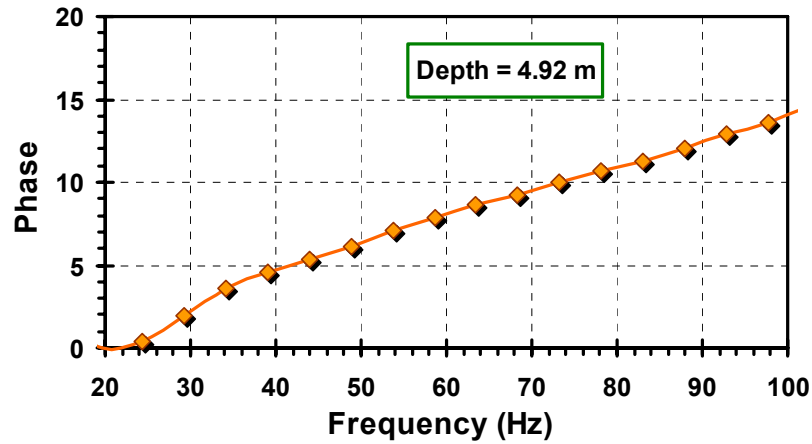
(a)
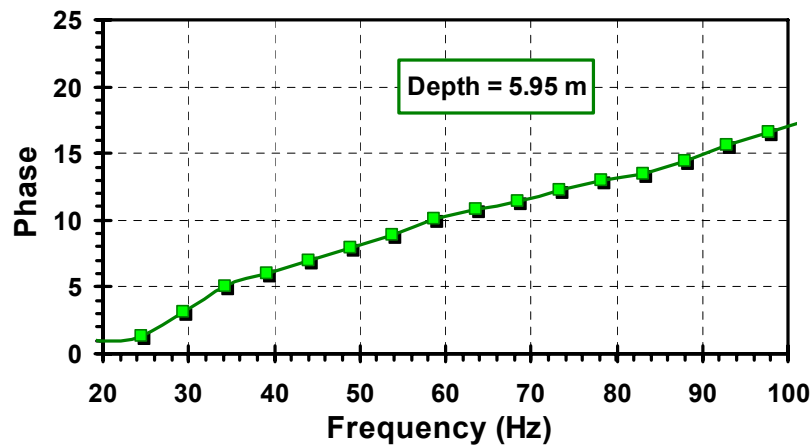
(b)
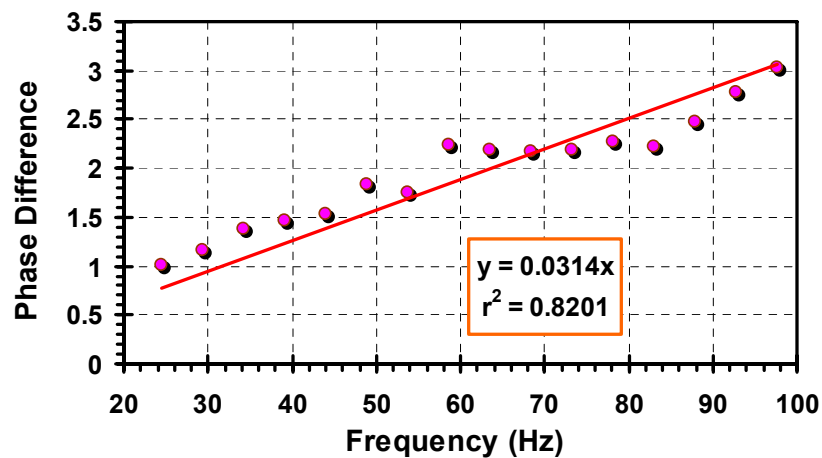
(c)

Figure 2.15 Phase-shifting of shear wave signals collected at depth of 4.92m and 5.95m by an SCPTu sounding performed at the Coca-Cola site, Atlanta, GA: (a) Phase of the frequency domain components for shear wave signal at depth = 4.92 m; (b) Phase of the frequency domain components for shear wave signal at depth = 5.95 m; (c) Linear dependency between frequency and phase shift of the two waves.
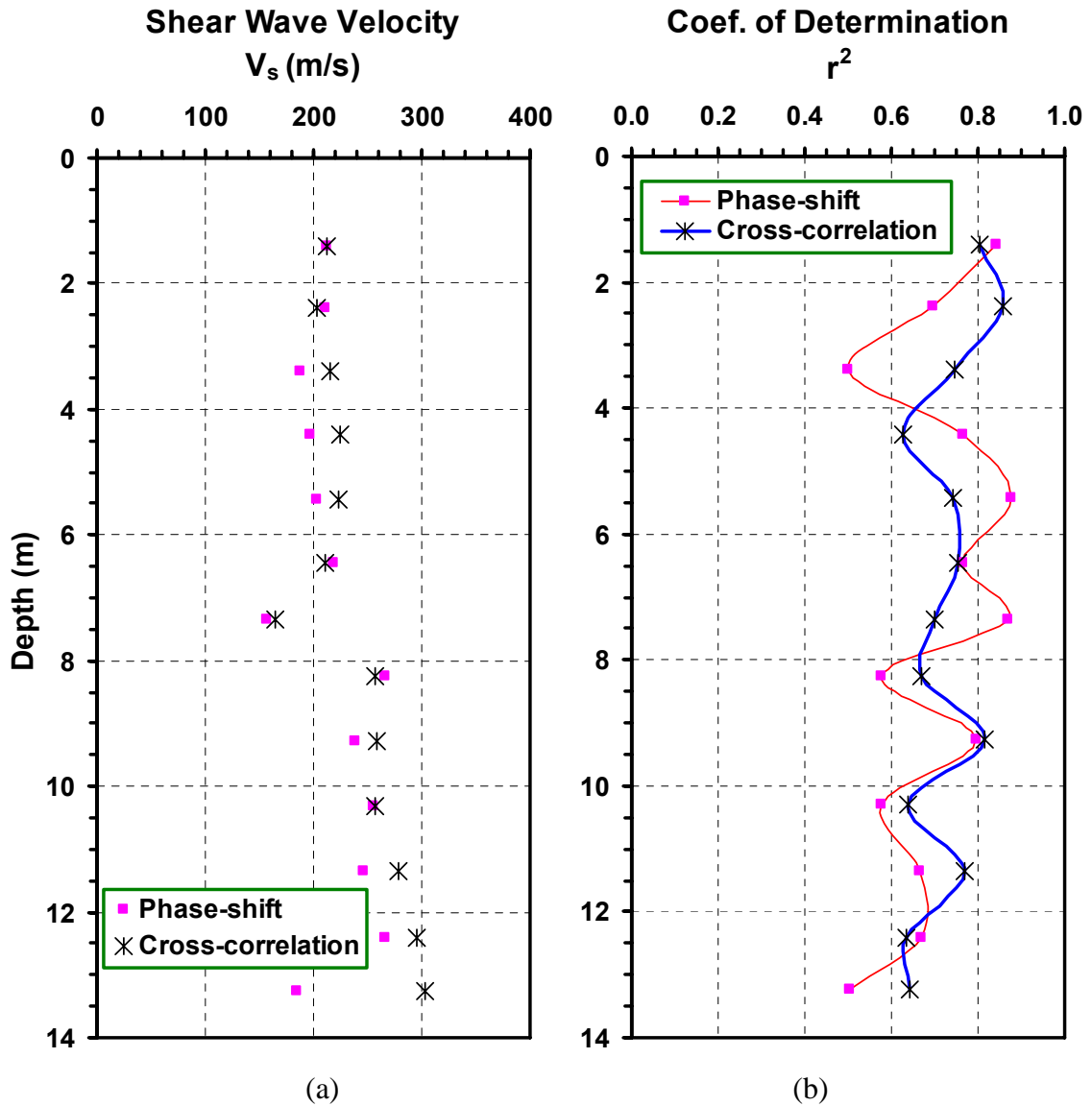
Figure 2.16 Results generated by the cross-correlation and phase-shift methods for the SCPTu sounding performed the Coca-Cola site, Atlanta, GA: (a) Shear wave velocity profile; (b) Coefficient of determination with depth.

2.5 Software to Process Shear Wave Signals -- *ShearPro*

From the two examples shown in last section, as well as other case studies performed by the author, it is noticed that consistent results are generally obtained for the shear wave velocities (V_s) based on both methods. However, the phase-shift method requires a degree of subjective judgment on the frequency range chosen for analysis, which adds

time to the processing as well as uncertainty. Compared with the phase-shift method, the cross-correlation method seems to be free of these disadvantages, and is therefore recommended for use in engineering practice to derive V_s from shear wave signals recorded in downhole seismic tests.

A stand-alone software program (*ShearPro*) is developed to process shear wave signals collected by downhole testing, using the cross-correlation method. It is written with Visual C++ 6.0, and runs in operating systems such as Windows 98/2000/XP. Cross-correlation in fact can be performed using Excel spreadsheets, or other commercial software (e.g. Matlab). However, with Excel, data at 1 m intervals from a 30 m DHT takes about 1 hour for post processing. In contrast, the same data can be handled Matlab in about 30 seconds. However, Matlab requires a sizable purchase (around US $900). Herein, *ShearPro* has been made available as a compiled stand-alone software program which costs only 1 minute to utilize.

ShearPro loads the raw shear wave data files selected by the user, and plots the shear wave trains on the computer screen. As an example, *ShearPro* is used to analyze the shear wave signals collected by a SCPTu sounding performed at the National Geotechnical Experimentation Site (NGES) in Opelika, Alabama. During this sounding, both left strikes and right strikes were applied to the seismic source. As a result, two sets of shear wave signals were recorded, as shown in Figure 2.17 (a) and (b). These are the screen shots after the shear wave data were input into *ShearPro*.
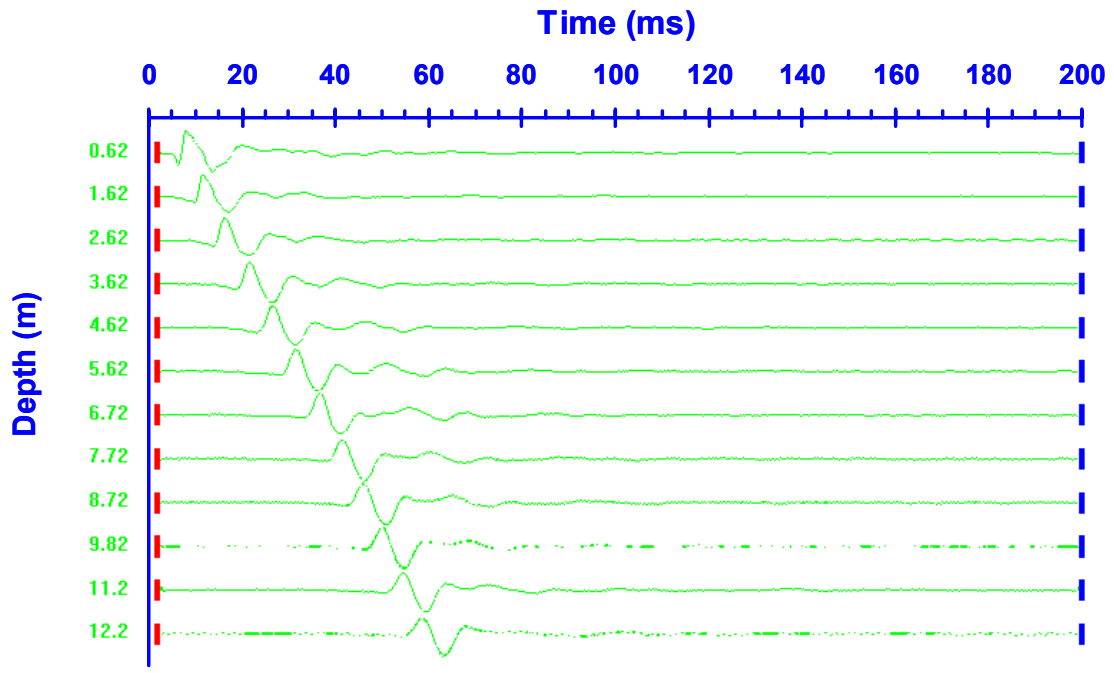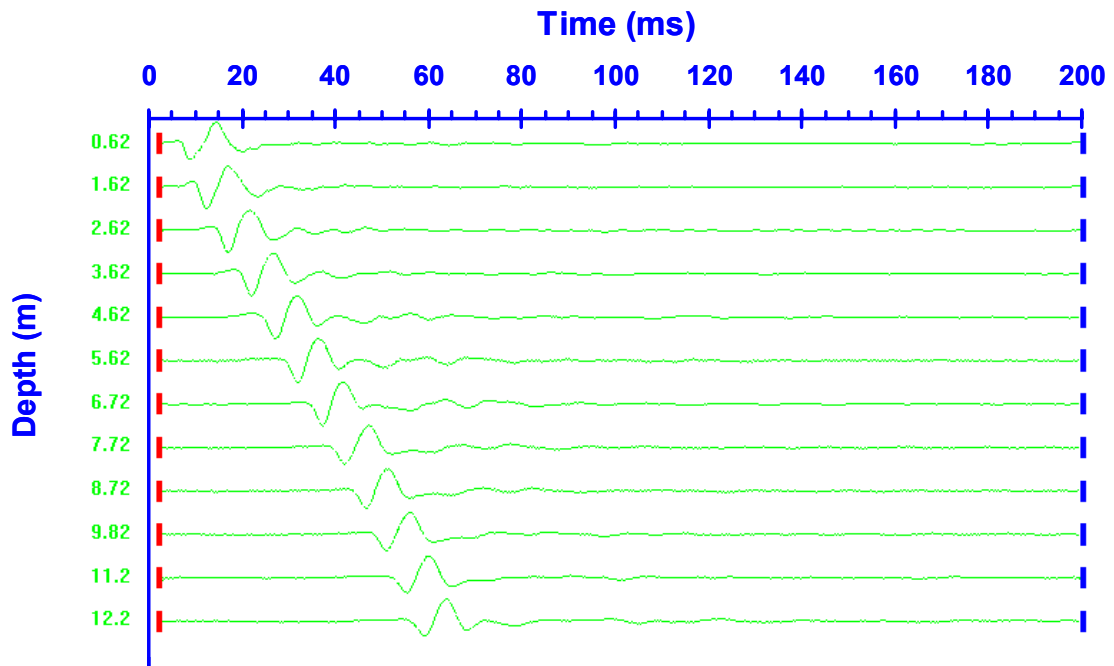
Figure 2.17 Shear wave trains collected at the National Geotechnical Experimentation Site (NGES) at Opelika, Alabama: (a) Left strike on the seismic source; (b) Right strike on the seismic source.
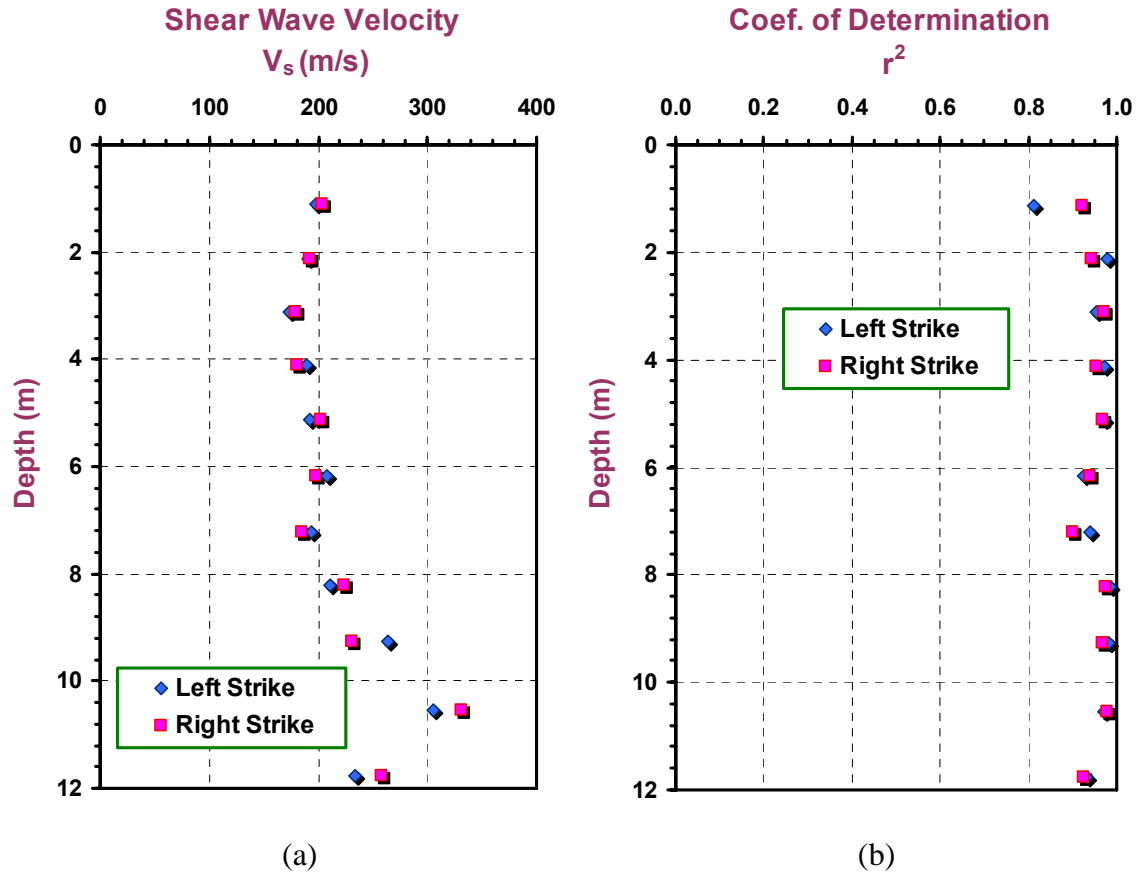
Figure 2.18 Shear wave velocities computed by *ShearPro* using cross-correlation method on the shear wave trains collected at the National Geotechnical Experimentation Site (NGES) at Opelika, Alabama: (a) Computed shear wave velocity for both left strike and right strike; (b) Coefficient of determination for both left strike and right strike.

In traditional DHT by SCPTu, both sets of left- and right- strikes are needed to obtain the V_s profile. The corresponding V_s and r^2 computed by *ShearPro* for the two sets of shear wave signals are presented in Figure 2.18 (a) and (b), respectively. As can be seen from this figure, the V_s and r^2 derived from shear wave signals generated by left and right strikes are quite consistent. Similar results are also observed at some other sites, indicating that using the cross-correlation method, only one set of shear wave trains (generated by either left or right strikes) are necessary. Thus, half the field effort in

collecting shear wave signals can be expended, compared with the routine cross-over method.
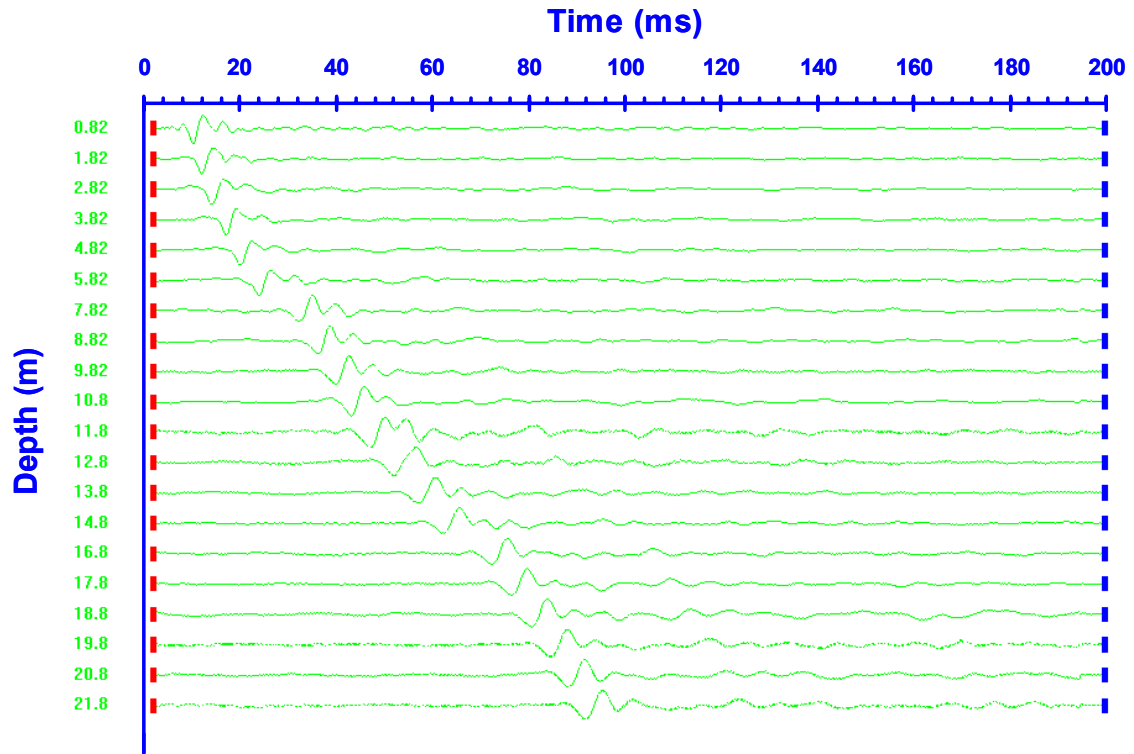
Figure 2.19 Shear wave trains collected at Mobile Infirmary Medical Center, Alabama by seismic cone penetration test (data from Southern Earth Science, Inc., Alabama) Note: Marks on the depth axis represents the depth at which the corresponding shear wave signals are recorded.

As another example, Figure 2.19 presents the shear wave trains from the Mobile Infirmary Medical Center, Alabama. After cross-correlation is applied to these signals, *ShearPro* displays the derived V_s and coefficient of determination (r^2) as shown in Figure 2.20 (a) and (b), respectively. A window technique is implemented in this software in order to limit the amount of wave forms that are matched. The shear wave signals can be trimmed by moving the window bars using a computer mouse, and only the part that remains between the window bars is used to derive time interval for the shear wave. The trimmed shear wave signals from the same site are shown in Figure 2.21. Similarly,

40

cross-correlation can be applied to the trimmed signals, and the V_s profile and coeeficient of determination (r^2) derived from the trimmed signals are presented in Figure 2.22 (a). The values of V_s and r^2 derived both with window and without window are compared in Figure 2.23. Some differences are observed between the shear wave velocities derived with and without window technique. The value of r^2 with window technique is consistently higher than that without window, indicating a higher degree of correlation if the window technique is used.

(a)   (b)
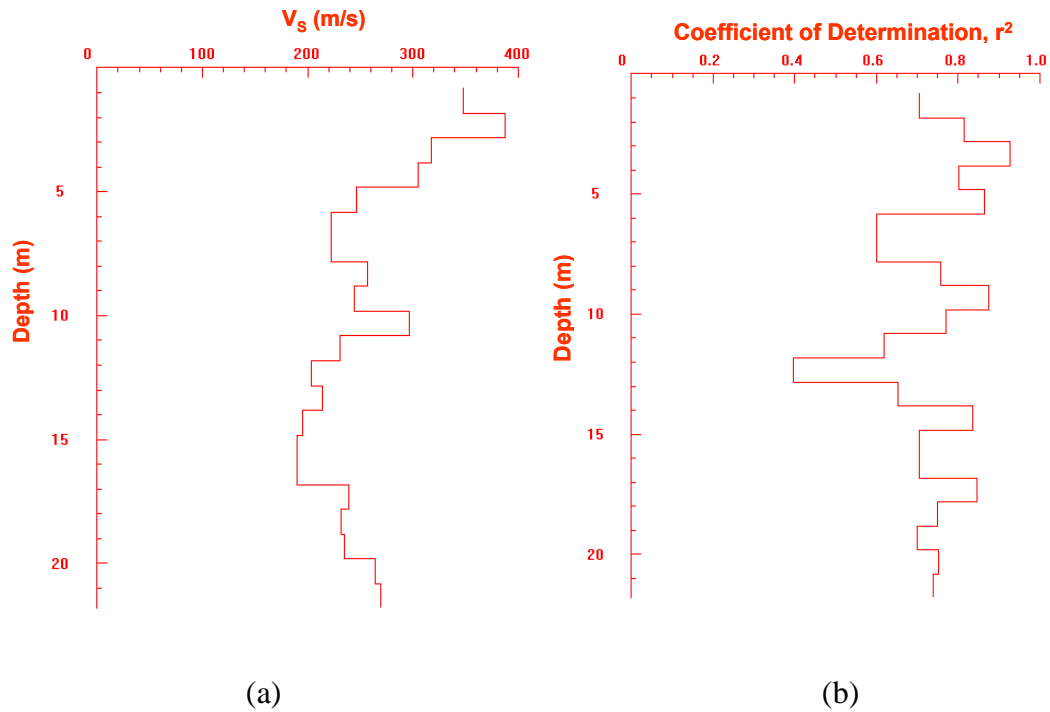
Figure 2.20 Shear wave velocities computed by *ShearPro* using cross-correlation method on the shear wave trains collected at Mobile Infirmary Medical Center, Alabama: (a) Computed shear wave velocity; (b) Coefficient of determination.

Two individuals (Scott and Danny) from Southern Earth Sciences Inc. derived V_s velocities from these signals using the first arrival method. Using the same data set, the V_s velocities were also derived independently using a Matlab program (Zavala & Mayne,

41

2002), that can align the wave trains on computer and get the time shift between waves. The shear wave velocities derived by different methods and different people are shown in Figure 2.24. It can be seen that they agree well, but much effort has been saved by using the program *ShearPro*.
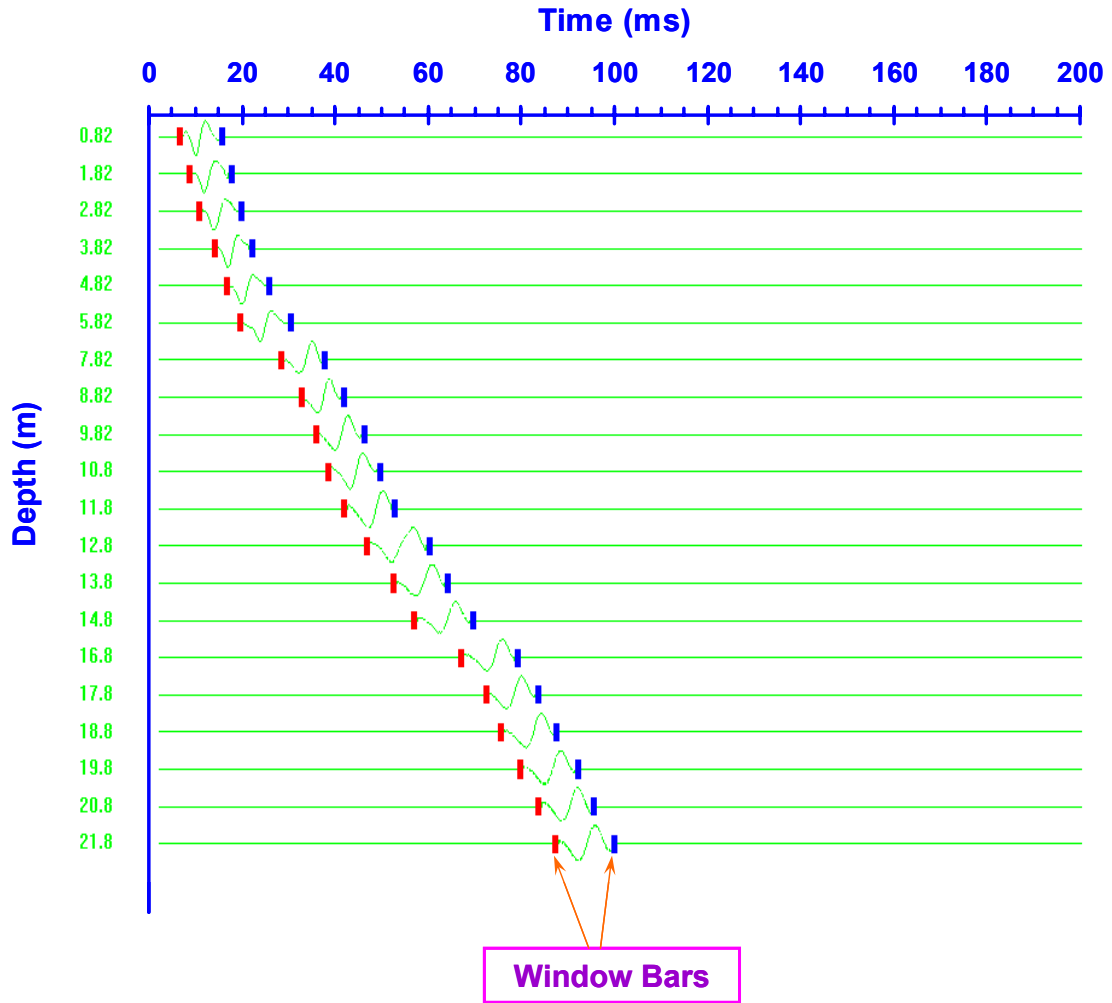
Figure 2.21 Trimmed shear wave trains collected at Mobile Infirmary Medical Center, Alabama by *ShearPro* using window technique proposed by Campanella & Stewart (1992)
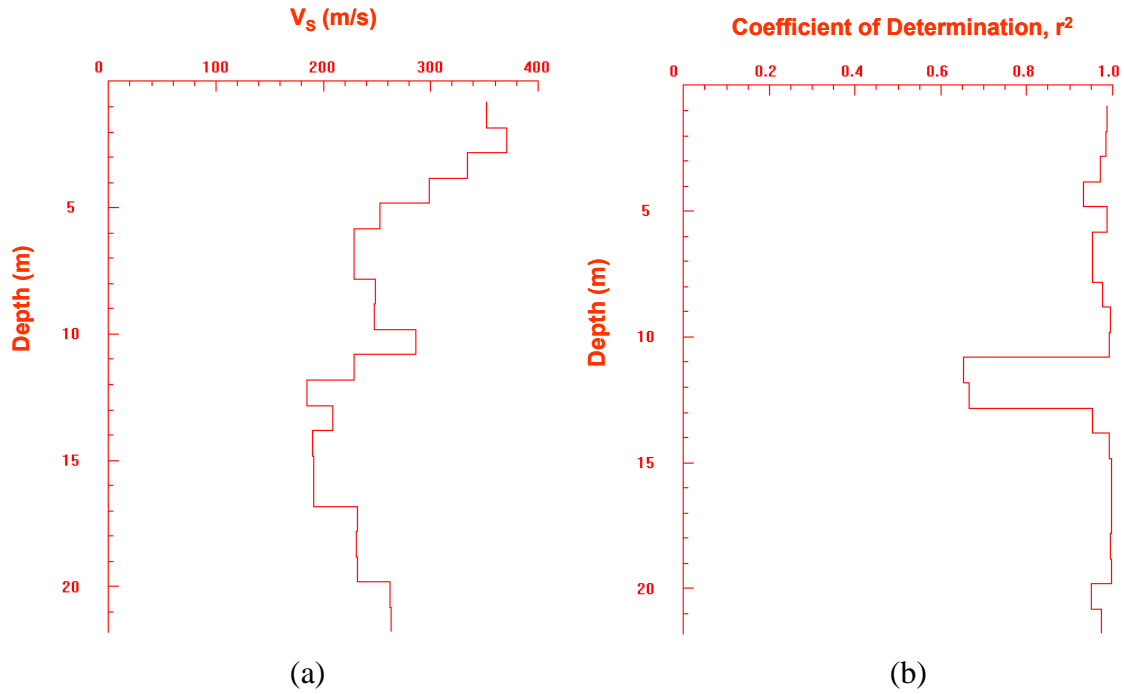
Figure 2.22 Shear wave velocities computed by *ShearPro* using cross-correlation method and windowing of wave trains collected at Mobile Infirmary Medical Center, Alabama: (a) Computed shear wave velocity; (b) Coefficient of determination.
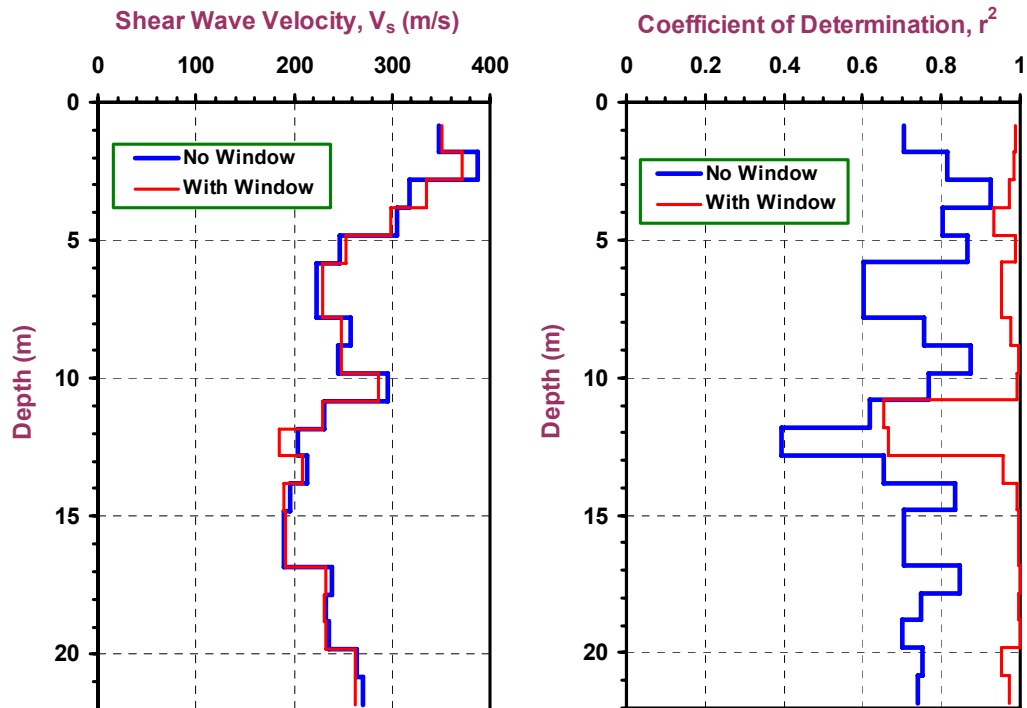
Figure 2.23 Comparison of computed results by *ShearPro* using cross-correlation method with and without the window technique based on the shear wave trains collected at Mobile Infirmary Medical Center, Alabama: (a) Shear wave velocities; (b) Coefficient of determination.

43
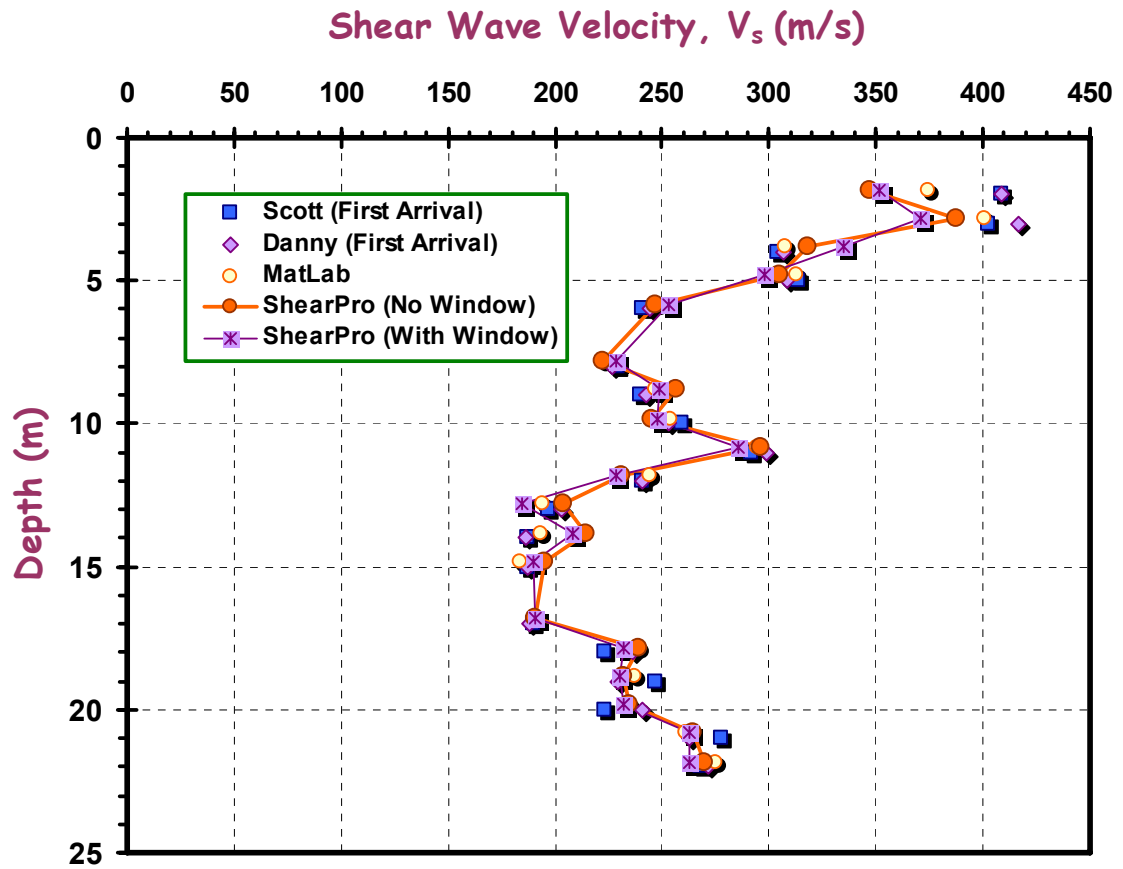
Figure 2.24 Comparison of the shear wave velocities derived by different methods for a set of shear wave trains collected by seismic cone penetration test at Mobile Infirmary Medical Center, Alabama

ShearPro can also output the phase and amplitude information of the frequency components based on Fast Fourier transform of the signals. These can be further analyzed by the user if the phase-shift method is desired.

2.6 Summary

The traditional methods used in engineering practice to derive V_s profiles from shear wave signals from downhole testing are the first arrival method and the cross-over method. They are time-consuming both in the field (as both left and right paired strikes

are required) and in later post-processing (as tedious visual-manual procedures are performed by personnel). Both the cross-correlation method and phase-shift method can be implemented on computer, speeding up the process to derive V_s profiles. With the phase-shift method, some subjective judgment from the user needs to be executed in choosing the frequency range for analysis. With the cross-correlation method, the process of deriving V_s from shear wave signals can be fully automated, and the results are found to agree well with those derived from other methods. Moreover only single wave sets are required (either left or right strikes), therefore reducing field testing times in half. In addition to DHT, SCPTu, and SDMT, these procedures for cross-correlation can also be easily implemented for seismic wave data from crosshole tests, refraction serveys, and other tests. In this thesis, a freely-distributed user-friendly software (*ShearPro*) is developed to process the raw shear wave signals with the cross-correlation method. Automated processing time is quick, therefore the entire data collection phase and analysis are more expedient.

CHAPTER III

STRATIGRAPHIC DELINEATION AND SOIL CLASSIFICATION BY THREE-DIMENSIONAL CLUSTERING OF CPTU DATA

3.1 Outline

Geostratification and soil classification is a first and very important step in site characterization, as it serves as the basis for all subsequent geotechnical analysis and calculations. Since the data collected through cone penetration tests (CPT) are functions of both soil type and soil behavior, they can be used to define the stratigraphy as well as soil classification.

Methods for delineating geostratification from CPT data can be grouped into five categories: visual examination, soil behavioral classification charts, variograms, probability method, and clustering. Currently the visual method and soil classification charts are widely used in engineering practice. With the visual method, the boundaries of the soil layers and the soil types are determined through the engineer's experience. For most cases, simple "rules of thumb" are sufficient: sands exhibit $q_T > 30\sigma_{atm}$ ($1\sigma_{atm} = 100kPa$) and clays $q_T < 20\sigma_{atm}$. Also, for sands, the $u_2 \approx u_0$, whereas for intact clays $u_2 >> u_0$, where u_0 is the hydrostatic porewater pressure. The accuracy of this method is largely dependent on his or her knowledge about the properties of different soils and local geology. Although significant changes in the soil stratigraphy can be picked up by the naked eye, it is usually impossible to detect subtle changes in the geostratigraphy. However, such subtle changes sometimes may correspond to drastic

changes in soil properties, such as plasticity, strength, sensitivity, and/or

overconsolidation ratio (Hegazy & Mayne, 2002).

Table 3.1 Soil classification charts found in literature

(a) Based on tip resistance and sleeve friction

Data Normalization Scheme	Reference
q_c and f_s	Begemann (1965)
q_c and f_s/q_c	Sanglerat et al. (1974)
q_c and f_s/q_c	Schmertmann (1978)
q_c and f_s/q_c	Douglas and Olsen (1981)
f_s/q_c	Vos (1982)
q_c and f_s/q_c	Robertson and Campanella (1983)
q_c and f_s/q_c	Erwig (1988)
$q_{c1} = \dfrac{q_c}{\left(\sigma_{vo}'\right)^n}$ and $FR_1 = \dfrac{f_s / \sigma_{vo}'}{q_c / \left(\sigma_{vo}'\right)^n}$	Olsen and Malone (1988)
q_{c1} and f_s/q_c	Olsen and Mitchell (1995)
Soil index U=f(x, y), and in-situ state index V=f(x, y) $x = 0.1539\left(f_s/q_c\right) + 0.8870\log\left(q_c\right) - 3.35$ $y = -0.2957\left(f_s/q_c\right) + 0.4617\log\left(q_c\right) - 0.37$	Zhang and Tumay (1999)
$q_E = q_T - u_2$ and f_s	Eslami and Fellenius (1997)

(b) Based on tip resistance and porewater pressure

$\left(q_c - \sigma_{vo}\right)/\sigma_{vo}$ and $\left(u_b - u_o\right)/u_o$	Jones et al. (1981)
$\left(q_T - \sigma_{vo}\right)$ and $\left(u_b - u_o\right)$	Jones and Rust (1982)
q_T and $B = \dfrac{u_b - u_o}{q_T - \sigma_{vo}}$	Senneset and Janbu (1985)
q_T and B	Parez and Fauriel (1988)
q_T and B	Senneset et al. (1989)
$q_T/(\gamma_w h)$ and $B = \dfrac{\left(u_b - u_o\right)}{q_T - \gamma_w h}$	Chang-hou et al. (1990)
q_T, B and t_{50}	Jian et al. (1992)

(c) Based on tip resistance, sleeve friction, and porewater pressure

q_T, $FR = f_s/q_T$, and B	Robertson et al. (1986)
$Q = \dfrac{q_T - \sigma_{vo}}{\sigma_{vo}'}$, B, and $F = \dfrac{f_s}{q_T - \sigma_{vo}}$	Robertson (1990, 1991)
Method A: $q_{tn} = \left(q_t - \sigma_{vo}\right)$ and B Method B: q_{tn} and $\left(1/B - f_s/\sigma_{vo}'\right)$	Larsson and Mulabdic (1991)
Q(1-B) and F	Jefferies and Davies (1993)

The reliance on soil classification charts is popular in engineering practice, because it allows a simple deterministic evaluation by either manual methods or utilization of computer. Table 3.1 provides a listing of several soil classification charts found in literature, including the data normalization schemes for their use. They are divided into three groups: a) charts based on tip resistance and sleeve friction; b) charts based on tip resistance and pore pressure; c) charts based on all three channels of CPT data.

One of the most popular set of charts is the soil behavioral type (SBT) developed at University of British Columbia (Robertson et al., 1986; Robertson & Campanella, 1988), as shown in Figure 3.1. Here, all three CPTu readings (q_T, f_s, u_2) are employed indirectly to assess the type of soil with up to 12 different categories possible. In some cases, two different soil types are interpreted since the $q_T - FR$ and $q_T - B$ can provide independent categories. Figure 3.2 shows the soil behavior type classification charts as suggested by Robertson (1990, 1991). Here, the three CPTu readings are normalized and used to categorize nine different soil behavioral types. The collected CPTu data points are compared with the classification charts, and each point is classified as a particular soil type. The soil stratigraphy is then generated by grouping the data points, which are close to each other in depth and belong to the same or similar soil type. Since CPTu soundings provide hundreds or thousands of data points, the number of layers generated through this approach is often overwhelming. Similarly with the visual method, the soil classification charts cannot detect subtle changes in the soil stratigraphy. In addition to the two most commonly-used approaches, there are also statistical methods that use autocorrelation and variograms (e.g. Wickremesinghe, 1989; Hegazy et al, 1996, 1997) or probabilistic

functions (e.g. Zhang, 1994; Zhang & Tumay, 1999) for geostratification. However, neither of these can provide consistent and objective boundaries between soil layers (Hegazy, 1998).

Soil Behavior Type (Robertson et al.,1986; Robertson & Campanella, 1988)		
1 – Sensitive fine grained	5 – Clayey silt to silty clay	9 – sand
2 – Organic material	6 – Sandy silt to silty sand	10 – Gravelly sand to sand
3 – Clay	7 – Silty sand to sandy silt	11 – Very stiff fine grained*
4 – Silty clay to clay	8 – Sand to silty sand	12 – Sand to clayey sand*
		* Overconsolidated or cemented
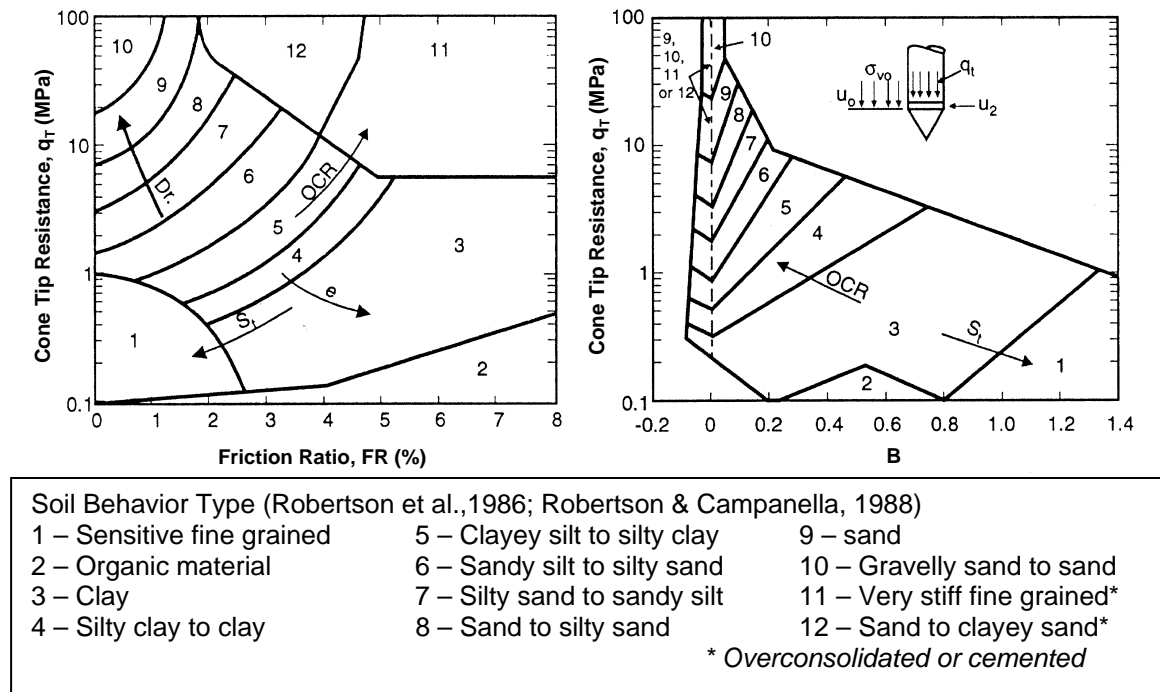
Figure 3.1 Soil behavior classification chart (after Robertson et al., 1986)

$$\text{Note: } FR = \frac{f_s}{q_T}; \ B = \frac{u_2 - u_1}{q_T - \sigma_{v0}}$$

Cluster analysis in previous geotechnical research (Hegazy & Mayne, 1998, 2002) was based on only two channels of CPTu data, that is, q_T and u_2, in terms of their normalized parameters Q and B, respectively. One example is the cluster analysis performed on piezocone data obtained in an offshore deposit at the Troll site in the North Sea (Amundsen et al. 1985). This site consists of firm silty clay from below the mud line down to 45 m. Visual examination of the q_T and u_2 profiles (Figure 3.3) from a representative sounding implies a single uniform clay layer interrupted by an

49

intermediate silty and/or sandy zone between depths of 17 to 20 m. The cluster analysis was conducted "blind" as a "Class A" prediction, with no a priori knowledge on the details at this site. The resulting clustering delineated two different and separate primary layers as shown in Figure 3.3 (f), indicating a major difference in soil types and/or properties above 17.3 and below 20m. The strong demarcation by cluster results are verified by the water content and plasticity measurements presented in Figure 3.3 (d), which show the upper layer is a highly plastic clay underlain by a lean clay. Figure 3.3 (e) provides additional validation from lab fall cone tests defining the upper clay is moderately sensitive ($S_t \approx 6$ to 8) compared with the lower unit which is insensitive ($S_t \approx 2$).

Zone	Soil behaviour type
1.	Sensitive, fine grained;
2.	Organic soils-peats;
3.	Clays-clay to silty clay;

Zone	Soil behaviour type
4.	Silt mixtures clayey silt to silty clay
5.	Sand mixtures; silty sand to sand silty
6.	Sands: clean sands to silty sands

Zone	Soil behaviour type
7.	Gravelly sand to sand;
8.	Very stiff sand to clayey sand
9.	Very stiff fine grained
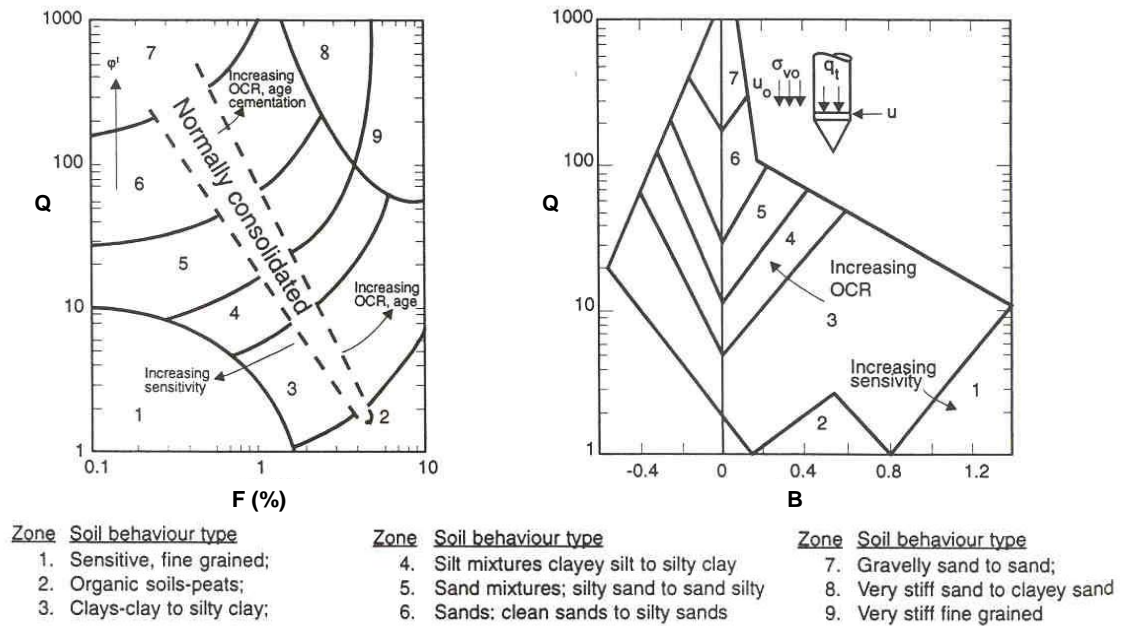
Figure 3.2 Soil behavior classification chart using three normalized CPTu readings
(Robertson, 1990, 1991)

Note: $Q = (q_t - \sigma_{vo})/\sigma_{vo}'$; $B = (u_2 - u_0)/(q_t - \sigma_{vo})$; $F = f_s/(q_t - \sigma_{vo}) \times 100\%$
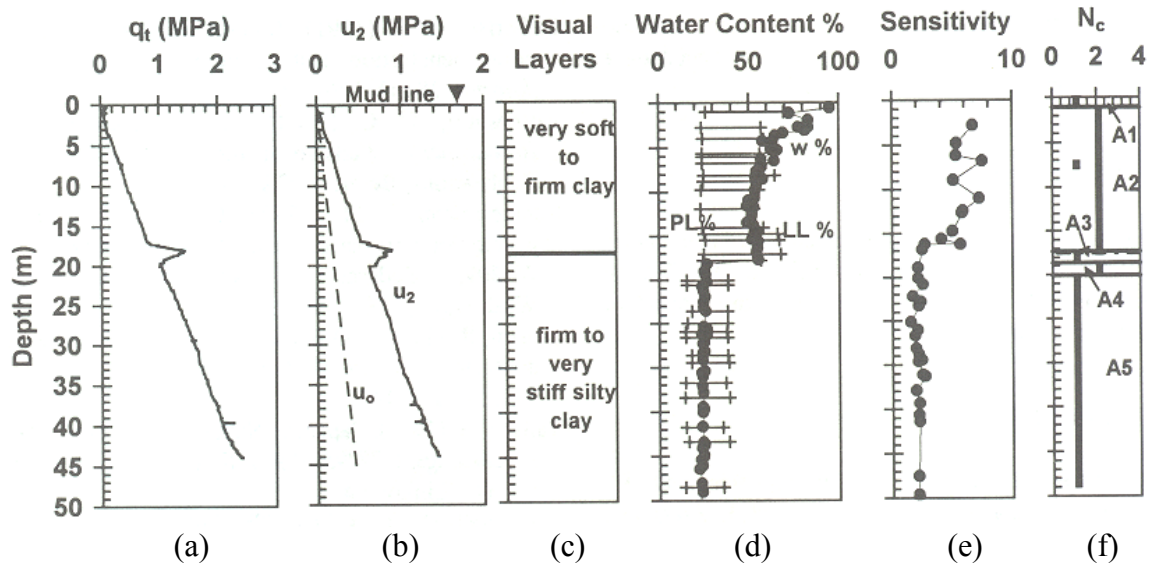
Figure 3.3 Stratification at Troll, North Sea site based on cluster analysis of two channels of data (Hegazy & Mayne, 2002): (a) tip resistance; (b) porewater pressure; (c) soil boring information; (d) index parameters; (e) sensitivity; (f) clustering results.

The cluster analysis based on q_T and u_2 (Hegazy & Mayne, 2002) was previously applied to soundings in soil deposits composed predominantly of clay and silty clay sediments beneath the groundwater table. If soils are located above the water table, the u_2 reading is related to many other factors besides the soil type, such as degree of saturation, capillarity and filter fluid of the cone penetrometer, and cannot properly reflect the soil behavior directly. In fact, in sandy deposits, u_2 is close to the static porewater pressure u_0, making it hardly useful to detect the different facies and/or types of sandy layers. Facciorusso & Uzielli (2004) followed the cluster analysis procedure suggested by Hegazy & Mayne (2002), but used it on the measurement by mechanical cone, which has only the measured tip resistance q_c and sleeve friction f_s (but no u_2 reading), at the harbor area of Gioia Tauro, Italy. The result of cluster analysis at this site agrees well with the boring log obtained nearby. However, measurements from mechanical cones are not as reliable as those from electronic cones, and the measured tip resistance q_c can0not be corrected for

51

porewater pressure effects, due to lack of u_2 measurement. Ziegler & Prokhorova (2004) performed similar cluster analysis based on tip resistance q_T and friction ratio FR, but did not include porewater pressure u_2.

Experience has shown that soil classification can generally be made more reliable using all three channels of CPTu data (Robertson, 1990). The three-dimensional cluster analysis was developed as an improved procedure for stratigraphic delineation. This statistical method can detect the inherent correlation between the CPT data and objectively fuse the data sets into discrete layers.

The soil behavioral classification charts shown in Figure 3.1 and 3.2 were intended to represent a three-dimensional soil classification system that incorporates all three channels of CPT data. However, they consist of two independent charts, and very often soils will fall into different zones on each chart and provide inconsistent classification results, as will become evident in the following example. A SCPTu (Seismic Cone Penetration Test) sounding performed for the new Cooper River bridge in Charleston, South Carolina is presented in Figure 3.4. This area lies in the Atlantic Coastal Plain sediments. As can be seen from this figure, the soil below depths of 20m appears to be more homogeneous than that above 20m, which are a highly variable assortment of Holocene age sediments. Below 20m, the penetration porewater pressure u_2 is much higher than static porewater pressure u_0, while that above 20m show u_2 is close to u_0. The soil below 20m is known as Cooper Marl, which is classified as a stiff calcareous marine clay or silt (CH/MH) (Camp et al., 2002). Although the calcium carbonate content ranges

from about 50% to 80%, this soil is highly plastic with average liquid limit LL ≈ 78, average plasticity index ≈ 38, and average water content ω_n = 48%. Its fines content ranges from about 50% to more than 90%, and the clay fraction (CF) is generally 10% < CF < 30%. Figure 3.5 shows the results of soil classification. Based on the q_T – FR chart of Robertson et al. (1986), the Cooper Marl that is below 20 m is classified as type 8 (Sand to silty sand) and type 9 (Sand), which are the wrong classification. According to the q_T – B chart of Robertson et al. (1986), the data points of Cooper Marl are out of the suggested range where soil data should fall in. Although the Robertson (1990, 1991) Q ~ B chart gives the right classification that most of the soil below 20m is type 3 (clays-clay to silty clay), the Q ~ F chart indicates that most of the soil below 20m is type 5 (sand mixtures: silty sand to sand silty), which classification is clearly incorrect and contradicts that derived from the Q ~ B chart.

In order to provide consistent soil classification results, a three-dimensional chart is proposed herein, which incorporates all three channels of CPTu data. With the proposed three-dimensional soil classification chart, the soil type can be determined during the process of three-dimensional cluster analysis. Both the processes of three-dimensional cluster analysis and three-dimensional soil classification can be automated and implemented by computer.
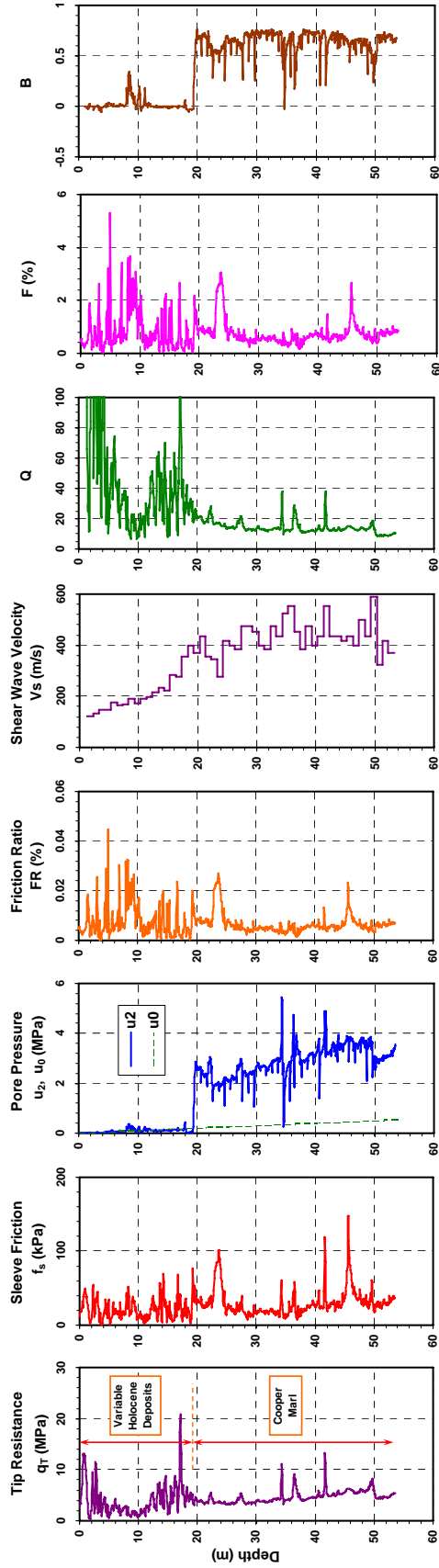
Figure 3.4 Representative SCPTu data from the Cooper River Bridge site in Charleston, SC

Note: $FR = f_s/q_T \times 100\%$; $Q = (q_t - \sigma_{vo})/\sigma_{vo}'$; $B = (u_2 - u_0)/(q_t - \sigma_{vo})$; $F = f_s/(q_t - \sigma_{vo}) \times 100\%$

Figure 3.5 Soil classification results based on the representative SCPTu data from the Cooper River Bridge site in Charleston, SC: (a) Based on the Robertson et al. (1986) charts; (b) Based on the Robertson (1990) charts.
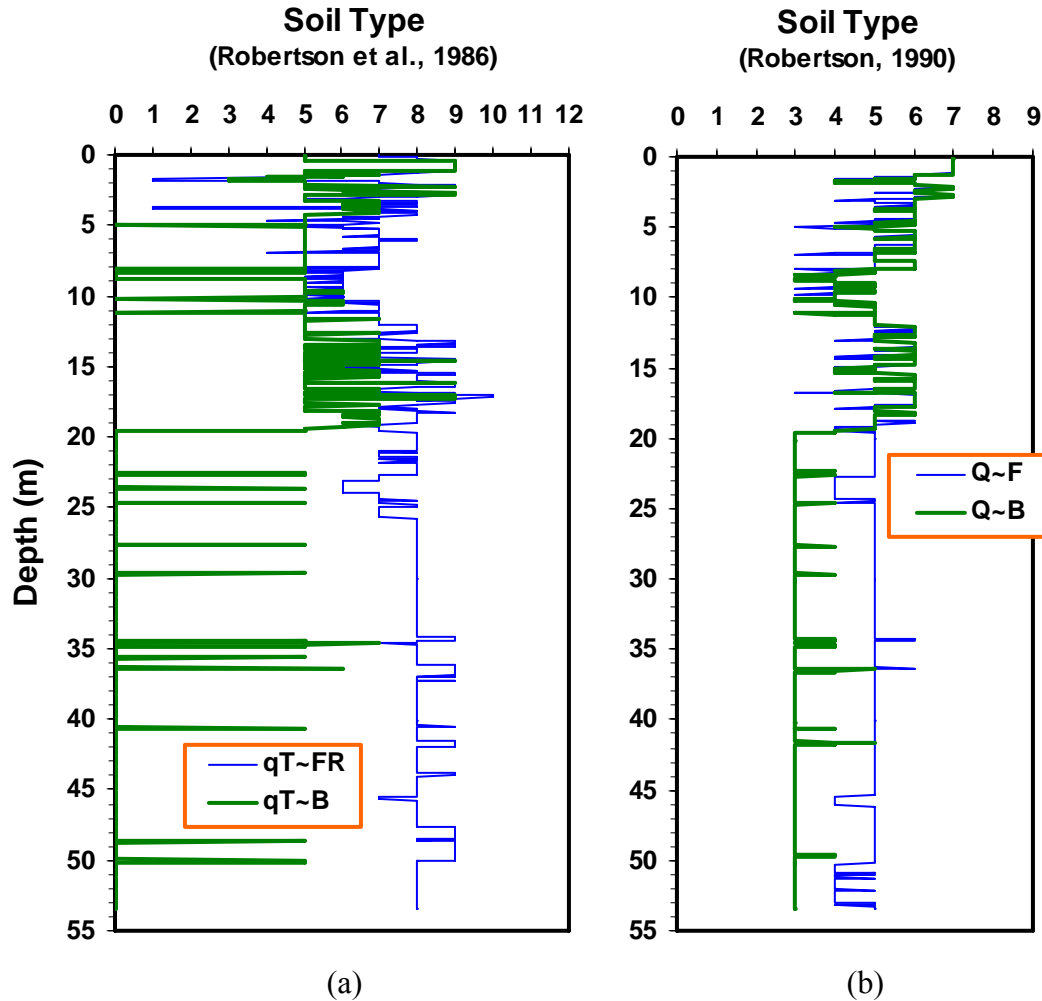
Soil Behavior Type (Robertson et al.,1986)

1 – Sensitive fine grained	5 – Clayey silt to silty clay	9 – sand
2 – Organic material	6 – Sandy silt to silty sand	10 – Gravelly sand to sand
3 – Clay	7 – Silty sand to sandy silt	11 – Very stiff fine grained
4 – Silty clay to clay	8 – Sand to silty sand	12 – Sand to clayey sand

* 0 – Data out of boundary

Soil Behavior Type (Robertson, 1990)

1 – Sensitive, fine grained	5 – Sand mixtures	9 – Very stiff fine grained
2 – Organic soils-peats	6 – Sands	
3 – Clays-clay to silty clay	7 – Gravelly sand to sand	
4 – Silt mixtures	8 – Very stiff sand to clayey sand	

* 0 – Data out of boundary

3.2 Cluster Analysis

Clustering is a numerical statistics method to uncover or discover groups or clusters of homogeneous observations in large data sets (Everitt et. al, 2001). The members of each cluster are similar to each other, but not related to the members in other clusters. Cluster analysis is a very useful tool for classification of a large number of objects or individuals, each of which has a certain number of properties that can be described mathematically. It may reveal the inherent associations in data, which are not previously evident. This method has been applied to sorting and distributions within various fields, such as biology, medicine, and social science. Most recently, it has been applied to internet search engines (e.g. Google, Excite) to find like files or websites of common denomination.

Given a sample of n objects that should be divided into a certain number (N_c) of groups, Romesburg (1984) summarized the steps of cluster analysis:

Step 1. Determine the significant variables that can measure the properties of each of the objects.

Step 2. Since raw data may be recorded at different scales, which can inevitably result in data that have quite different ranges, normalization and standardization should be used to remove the scale effects.

Step 3. A similarity matrix can be formed, which indicates how closely the objects resemble each other numerically. The similarity is usually represented by the distance between objects, which can be mathematically defined in many ways. (Everitt et. al, 2001).

Step 4. Data are divided into correlated groups by clustering techniques. (Everitt et al., 2001).

56

The underlying mathematics of cluster analysis is relatively simple, but extensive computation is required due to the large number of data. Since the similarity between objects can be measured in a number of ways, the produced classification is dependent upon the particular technique used.

A standard electronic CPT sounding provides data about the tip resistance q_T, the porewater pressure u_2, and the sleeve friction f_s of the soil at different depths. All these data records represent complex properties of the soil and are a function of the respective soil types, as well as other facets. Therefore, cluster analysis can be used to classify the soils based on CPT data. It can detect the inherent similarity between the data sets and assist in a rational grouping of the data to define soil layers and types.

3.3 Three-Channel Cluster Analysis

3.3.1 Selection of Variables

Cluster analysis of CPT data in clays suggested by Hegazy & Mayne (1998, 2002) was based on only two readings q_T and u_2, while clustering of sands was done from q_c and f_s data (Facciorusso & Uzielli, 2004). Based on early comparative studies using analog CPT systems with now-antiquated data acquisition and internal electronics (e.g. Lunne et al. 1986). The sleeve friction resistance (f_s) was excluded from Hegazy & Mayne (2002) analysis for the reason that f_s measured by CPT was not as repeatable as q_T and u_2. This was partially due to differences in manufacturer design, e.g. subtraction cone vs. compression penetrometer (Lunne et al., 1986), as well as use of thermally correcting

load cells, type of metal used for penetrometer, wear, and surface roughness (e.g. DeJong and Frost, 2001).
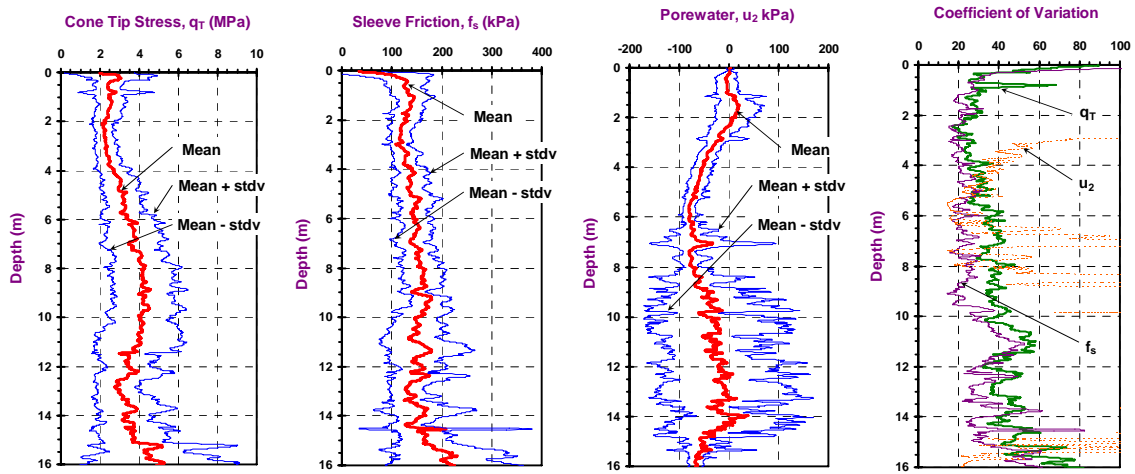
Figure 3.6 Summary of 22 CPTu soundings obtained at the NGES site in Opelika, AL

Today, it is now found that most modern commercial cone penetrometer systems obtain reliable and comparable sleeve friction readings. For example, a total of 22 CPT soundings were performed at the National Geotechnical Experimentation Site (NGES) located in Opelika, Alabama (e.g. Finke et al., 2001). They were performed with commercial cone penetrometers that are of different sizes and manufactured by different companies such as Hogentogler, van den Berg, Fugro, and Vertek. Figure 3.6 shows the mean and standard deviation of each of the three channels of data collected by these soundings, as well as their coefficients of deviation. Within the top 10 m, it can be seen that the standard deviations for all three channels of data are not very large, indicating they are relatively repeatable at the same depth. In fact, the coefficient of variation for the sleeve friction f_s is generally lower than those of the tip resistance q_T and porewater pressure u_2. Therefore, the measurement of the sleeve friction f_s should be at least as reliable as q_T and u_2. Also of note at this NGES is that a special residual kaolin layer or

zone is formed at varying 10 to 15 m depths and of varying thickness, generally between 1 m to 5 m (Finke, 1998). The zone is not uniform and appears quite variable, thus affecting the porewater pressure readings.

Since cluster analysis is performed on a single sounding, it does not require the measurements to be repeatable at the same depth for different cones. As long as the measurements are repeatable for the same cone and they are a function of the specific soil types, they can be included in cluster analysis to delineate the soil stratigraphy.

The friction ratio (FR) is the ratio of sleeve friction f_s to the tip resistance q_T. In sand, FR is usually lower than that in clay, and sands of different fines content exhibit different FR. Therefore, the sleeve friction f_s can indicate the difference between clay and sand, as well as between different types of sand, and it is reasonable to include a third channel, f_s, in the cluster analysis for CPT data. The inclusion of the f_s channel not only removes the constraints of the two-channel approach in classifying sandy deposits, but also mitigates the problem of u_2 readings above the groundwater table as mentioned before. In particular, $u_2 \approx 0$ in dry soils, and u_2 is variable in partially saturated soils, but depends on capillarity, saturation, and filter fluid. Though q_T and u_2 play an important role in distinguishing different types of clayey soils, q_T and f_s give more information about sandy soils. Because of the inclusion of f_s, the cluster analysis can be based on all three channels of CPT data, or any two channels of them. However, experience has shown that more reliable results can be derived if all three channels of CPT measurements (q_T, f_s, and u_2) can be used (Robertson, 1990).

3.3.2 Normalization of Variables

The cone tip resistance q_T, porewater pressure u_2, and sleeve friction f_s measured by CPT soundings can be significantly influenced by the effective confining stress level. Wroth (1984) and Houlsby (1988) suggested normalizing the CPT data with respect to the effective overburden stress in the following format:

$$Q = (q_t - \sigma_{vo})/\sigma_{vo}'$$
(3-1)

$$B = (u_2 - u_0)/(q_t - \sigma_{vo})$$
(3-2)

$$F = f_s/(q_t - \sigma_{vo}) \times 100\%$$
(3-3)

where σ_{vo} is the total overburden stress and σ_{vo}' is the effective overburden stress.

Jefferies & Davies (1991) realized the importance to include all three channels of CPT data in a single chart for soil classification purpose, and proposed to plot the expression Q(1-B) versus F for soil classification purpose (Figure 3.5). In this case, the term Q(1-B) relates to the normalized effective cone resistance, or $Q(1-B) = \dfrac{q_T - u_2}{\sigma_{vo}'} - 1$. The boundaries between the six soil type zones can be approximated as concentric circles, with the center as shown in Figure 3.7. The fines content of the soil types increases with the radius of its boundary circles.

Realizing that the confining stress influences the CPT data differently in different soils, Olsen & Mitchell (1995) suggested normalizing the tip resistance in the following format:

$$q_{cle} = \frac{q_T - \sigma_{v0}}{\left(\sigma_{v0}'\right)^c} = \frac{\left(q_T\right)_{net}}{\left(\sigma_{v0}'\right)^c}$$

(3-4)

$$FR = f_s / q_T \times 100\%$$

(3-5)

where c is a stress exponent that varies with soil type. For clean sands, c ≈ 0.5 to 0.6 while for clays, c ≈ 1. However, this normalization scheme does not consider the porewater pressure readings u_2.
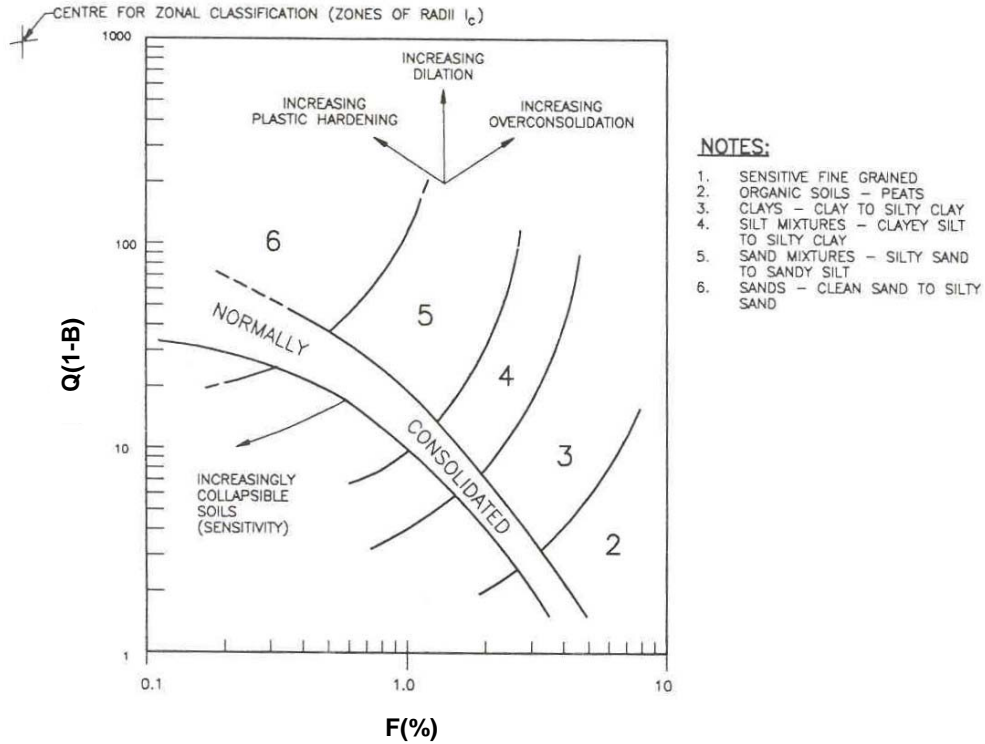
Figure 3.7 Soil Behavior type classification chart (Jefferies & Davies, 1991)

The normalized forms recommended by Wroth (1984) and Houlsby (1988) [equations (3-1) to (3-3)] are used in the soil classification charts proposed by Robertson (1990, 1991). Also, Hegazy & Mayne (1998, 2002) used Q and B in their two-channel cluster analysis. Herein, Q, F, and B are utilized as the three channels of normalized data for conducting

cluster analysis, thus allowing consistency with prior approaches. An example of the derived value of Q, F, and B has been presented in Figure 3.4 for the representative sounding performed at the Cooper River Bridge site in Charleston, SC. The clustering methodology shown herein can be easily adapted to other normalization schemes, if desired.

3.3.3 Standardization of Data

Because the mean and standard deviation of parameters used in cluster analysis can be correlated with their relative influence on the result, it is essential to standardize the parameters for cluster analysis. From the set of soil classification charts shown in Figure 3.2, it can be seen that Q varies in the range from 1 to 1000, F in the range from 0.1% to 10%, B in the range from -0.6 to 1.4. Since these parameters vary over dramatically different ranges, the corresponding means and standard deviations could also be very different in naturally deposited soils.

Hegazy & Mayne (1998, 2002) recommend the "Zscore" procedure to standardize the data. Suppose X_j is a cone variable and x_{ij} is the measurement of X_j at a certain depth indexed by i, the following equation gives the statistical definition of the standardized value of x_{ij}:

$$Zscore(x_{ij}) = \frac{x_{ij} - E(X_j)}{Stdev(X_j)}$$

(3-6)

where $E(X_j)$ is the average of all X_j measurements, $Stdev(X_j)$ is the standard deviation of all X_j measurements. Figure 3.8 shows the q_T and u_2 measurements of a

sounding performed at Amherst, Massachusetts, as well as the derived normalized

parameters (Q and B). A visual examination of the data indicates that the soil stratigraphy

consists of a deep clay deposit underlying a 4-m thick layer of sandy silt and silty clay.

The standardized values of Q and B using Zscore procedure are also shown in Figure 3.8.
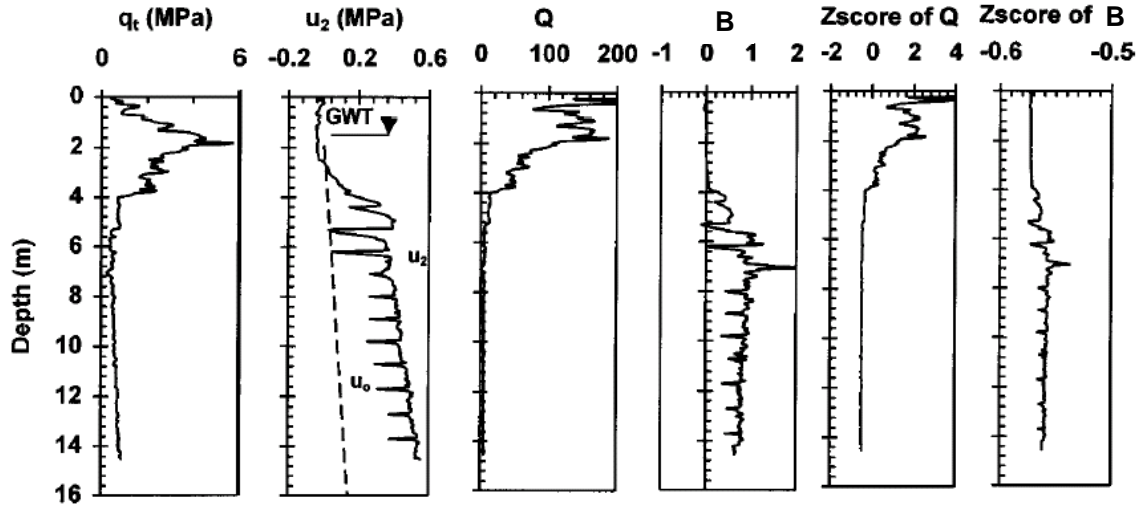
Figure 3.8 CPTu data, normalized parameters, and derived Zscore value for a sounding
performed at Amherst, Mass. Site (Hegazy & Mayne, 2002)

The standardized CPTu data can form a vector $(zscore(Q_i), zscore(B_i))$ for a certain

depth (i), and it can be put in a matrix form as follows:

$$D = \begin{bmatrix} Zscore(Q_1) & Zscore(B_1) \\ Zscore(Q_2) & Zscore(B_2) \\ \vdots & \vdots \\ Zscore(Q_n) & Zscore(B_n) \end{bmatrix} \quad (3\text{-}7)$$

With the inclusion of the normalized friction ratio F in cluster analysis, a vector

$[Zscore(Q_i), Zscore(B_i), Zscore(F_i)]$ can be formed for a certain depth (i), and the CPT

data standardized with the "Zscore" procedure can be looked at in the following way:

$$D = \begin{bmatrix} Zscore(Q_1) & Zscore(B_1) & Zscore(F_1) \\ Zscore(Q_2) & Zscore(B_2) & Zscore(F_2) \\ \vdots & \vdots & \vdots \\ Zscore(Q_n) & Zscore(B_n) & Zscore(F_n) \end{bmatrix} \qquad (3\text{-}8)$$

Standardizing the data using the "Zscore" procedure is statistically viable, but the physical meaning of the parameters in geotechnical engineering generated by the "Zscore" procedure is not clear. Furthermore, equipment errors, such as electric noise, might exist in the collected data. If any of the standardized cone data (Q, B, or F) varies in a very small range, resulting in a small standard deviation, the "Zscore" procedure tends to over amplify the range of the variation. The random errors might thereby be amplified to the extent to affect the analysis results adversely.

In the soil classification charts suggested by Robertson (1990, 1991), the normalized tip resistance (Q) and friction ratio (F) are presented in logarithmic scale, while the normalized porewater pressure (B) is in arithmetic scale. In this thesis, the normalized CPT data are therefore standardized using the scales consistent with those in the soil classification charts.

$$S(Q) = \log_{10} Q \qquad (3\text{-}9)$$

$$S(F) = \log_{10} F \qquad (3\text{-}10)$$

$$S(B) = B \qquad (3\text{-}11)$$

Where S(X) represents the standardized form of the variable X. The CPT data standardized in this way can be looked at in the following way:

$$D = \begin{bmatrix} S(Q_1) & S(B_1) & S(F_1) \\ S(Q_2) & S(B_2) & S(F_2) \\ \vdots & \vdots & \vdots \\ S(Q_n) & S(B_n) & S(F_n) \end{bmatrix} \tag{3-12}$$

The reason for adopting such a standardization scheme will be further explained in the following section.

3.3.4 Similarity Matrix

Hegazy & Mayne (1998, 2002) used the "cosine" procedure to measure the cosine of the angle between the two vectors formed by the standardized data, as shown in Figure 3.9. The similarity between two sets of standardized data (e.g., $[Zscore(Q_i), Zscore(B_i)]$ and $[Zscore(Q_j), Zscore(B_j)]$) at different depths is measured by the cosine of the angle between the two vectors in a two dimensional space, which can be calculated using the following equation:

$$\cos\theta_{ij} = d_{ij} = \frac{\sum_{k=1}^{n} Zscore(x_{ik})Zscore(x_{jk})}{\sqrt{\sum_{k=1}^{n}(Zscore(x_{ik}))^2 \sum_{k=1}^{n}(Zscore(x_{jk}))^2}} \tag{3-13}$$

where n is the number of variables participating in the cluster analysis. And the similarity matrix is of the following form:

$$S = \begin{bmatrix} 1 & \cos\theta_{12} & \cos\theta_{13} & \ldots & \cos\theta_{1n} \\ \cos\theta_{21} & 1 & \cos\theta_{23} & \ldots & \cos\theta_{2n} \\ \cos\theta_{31} & \cos\theta_{32} & 1 & \ldots & \cos\theta_{3n} \\ \vdots & \vdots & \vdots & \vdots & \vdots \\ \cos\theta_{n1} & \cos\theta_{n2} & \cos\theta_{n3} & \ldots & 1 \end{bmatrix} \tag{3-14}$$
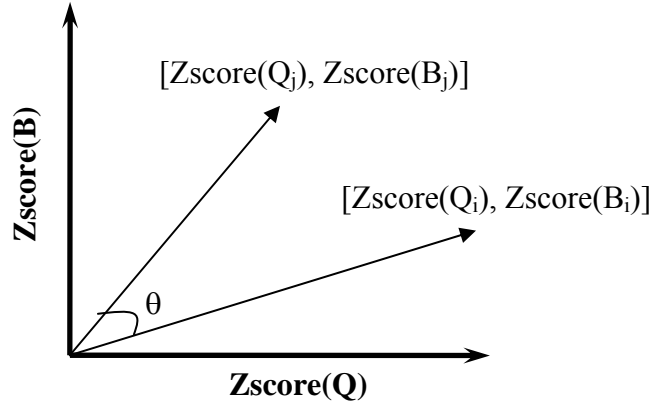
Figure 3.9 The "cosine" procedure measures the cosine of the angle between two vectors formed by the standardized data (Hegazy & Mayne, 2002)

The "cosine" procedure groups data sets that have small angles between their corresponding vectors, but they do not necessarily belong to the same soil type, because the soil type is also related to the length of the vectors.

By using the soil classification charts, it is assumed that soils at different depths belong to the same soil type, if their associated CPT data points are located on the same spot in the charts. The closer the CPT data points are located to each other in the charts, the more similar the associated soils behave. Therefore, the geometric distance (Euclidean distance) can be used to measure the similarity between the CPT data points. The Euclidean distance between the data points is inversely proportional to the similarity of the associated soils.

Since the soil type is a function of all three channels of data (Q, F, and B), a three-dimensional space can be created with the three axes representing the three channels of data respectively, as shown in Figure 3.10. As mentioned above, the normalized tip

resistance and friction are in log scale, while the normalized pore water pressure is in arithmetic scale. The CPT data standardized in the form of equation (3-9) to (3-11) represent the geometric coordinates of the CPT data points in the three dimensional space. The Euclidean distance L of two data sets, $[S(Q_i), S(F_i), S(B_i)]$ and $[S(Q_j), S(F_j), S(B_j)]$, can be computed as following (Figure 3.10):

$$L_{ij} = \sqrt{[S(Q_i) - S(Q_j)]^2 + [S(F_i) - S(F_j)]^2 + [S(B_i) - S(B_j)]^2} \qquad (3\text{-}15)$$

For a CPTu sounding consisting of n sets of data from different depths, an n*n resemblance matrix can be formed with L_{ij} in the entry located on the ith row and j^{th} column.
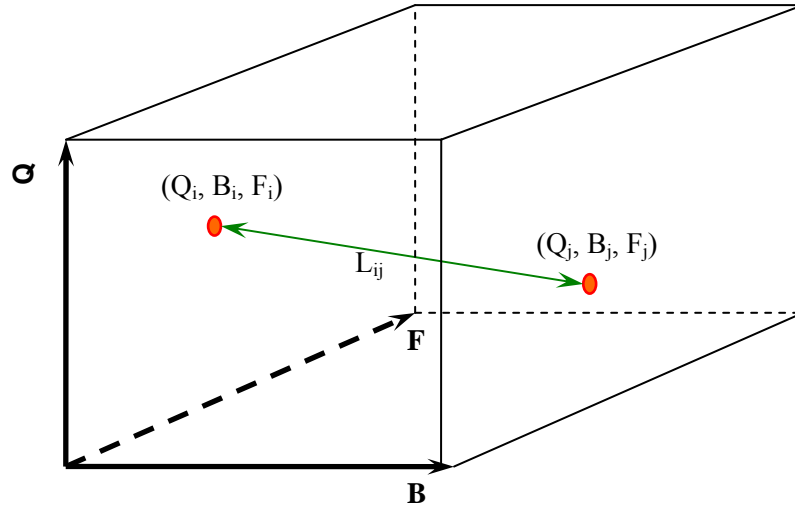
Figure 3.10 Measuring the similarity between data sets using the Euclidean distance L_{ij} between the corresponding CPTu data (Q, B, F) points in three dimensional space

3.3.5 Choice of Clustering Technique

Hegazy & Mayne (1998, 2002) recommended the use of the single-link (nearest neighbor) hierarchical method for the cluster analysis of the CPT data. One similarity matrix, which stores the distance between the data sets at different depths, is computed at the beginning of the cluster analysis. From this single similarity matrix, two individual

data sets are found that are closest at each step. If these two individual data sets are from two separate groups of individuals, the two groups are fused together to form one group. The culminating stage is where all the data sets are in one group. Basically, the criterion to find the two closest groups of individuals is that one individual in one group and another individual in the other group are the closest in the current stage. Because this algorithm uses the distance between the individuals from two different groups to represent the distance between the two groups, it can sometimes fuse very different individuals together, while leaving similar individuals separate.

In order to avoid this situation, whenever two groups of data sets are fused together, the coordinates of the centroid of all the data in these two groups can be computed to represent the newly formed group. Then a new resemblance matrix is formed, where the coordinates of the centroid of the newly formed group is used to compute the distance from it to other groups. Based on this new resemblance matrix, the cluster analysis is further performed to fuse two of the closest groups at this stage. In this algorithm, two groups of individuals are fused together only if their centroids are closest, which effectively eliminate the possibility that very different individuals can be grouped together. Figure 3.11 illustrates the steps in this algorithm. Suppose 5 data points exist in the three-dimensional space (Q, F, B), as shown in Figure 3.11 (a), and the distance between data points 1 and 2 is the shortest among all of them [Figure 3.11 (b)]. Therefore data points 1 and 2 are grouped together, as shown in Figure 3.11 (c). The distances are measured again among data points 3, 4, 5, and the centroid of the group consisting data points 1 and 2. At this stage, the distance between data points 3 and 4 is the shortest

[Figure 3.11 (c)], and they are grouped together as shown in Figure 3.11 (d). Similarly,

this procedure continues in Figure 3.11 (e) and (f), and at the end all the data points are

grouped into one group.
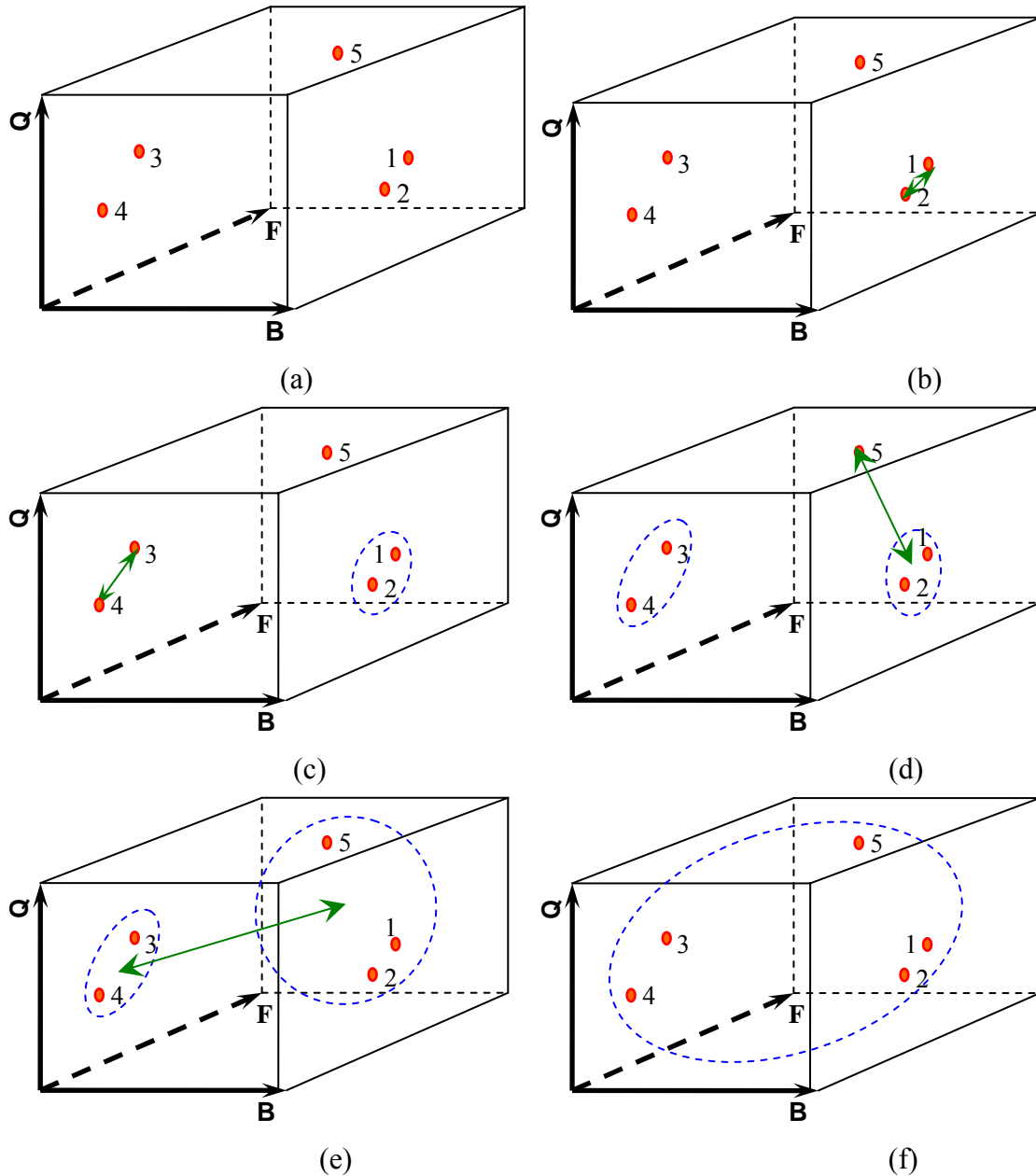
Figure 3.11 Data points grouped together by three-dimensional cluster analysis step by step: (a) Data points in three dimensional space; (b) Data points 1 and 2 have the shortest distance; (c) Data points 1 and 2 grouped together; (d) Data point 3 and 4 grouped together; (e) Data points 1, 2, and 5 grouped together; (f) Data points 1, 2, 3, 4, and 5 grouped together.

3.3.6 Determining the Number of Clusters

A difficulty that exists in all clustering techniques is the final total number of clusters that the data should be fused into (Everitt, 2001). The decision is subjective in the sense that it is the trade off between the desire for detail, which requires a large number of clusters, and the desire for generality and simplicity, which requires a smaller one (Romesburg, 1984). In the extreme case, each row of CPT data can represent one layer, but in engineering practice it is usually overwhelming to keep track of so many layers. And very often what we want is just some general understanding of the soil profile without considering the outlier data, because their contribution to the overall behavior of the soil deposit is limited and usually can be ignored. Based on 25 studied cases of CPTu records with up to 100 assumed clusters, Hegazy & Mayne (1998, 2002) found that the actual number of soil layers can often be accurately represented with the total number of clusters less than 15 and often less than 8.

In the cluster method proposed in this paper, the data points that are grouped together fall in a shape close to a globe in the three-dimensional space. The less the radius of the sphere for a group of data points, the more uniform soil properties this group has. Therefore, by limiting the maximum radius, the uniformity of the soils in each group can be controlled. At the beginning of the cluster process, each data point is one cluster and the largest radius is 0. As cluster analysis proceeds, the data points are fused together step by step, and the largest radius of all the groups of data increases. Therefore, the user can specify the maximum radius for the data groups, and let the cluster process continue until

the largest radius exceeds the specified maximum radius. The number of clusters at this stage is the cluster number corresponding to the specified maximum radius.

3.3.7 *Interpretation of Cluster Results*

The cluster analysis groups the most similar data together at an early stage corresponding to a large number of clusters, while relatively dissimilar data are grouped at late stages corresponding to a small number of clusters. With a larger number of clusters, more detailed features in the vertical profile can be detected. Depending on the definition of the features, they can be interpreted as soil layers, sublayers, seams, lenses, stringers, anomalies, or transition zones between different layers (Hegazy & Mayne, 2002).

It is almost inevitable that some outlier data would exist in the collected CPTu data. Some of them are caused by inaccuracies of the testing equipment or testing procedures errors, such as electrical noise, rod changes, porewater pressure dissipation, as well as random events, such as encountering a stone in the soil matrix or a cemented layer or cap rock. The outlier data caused by these errors can sometimes be recognized through detailed analysis of the testing equipment and testing procedure. However, some outlier data may be the real representation of the soil behavior, and reflect the irregular structure in the soil deposits such as seams, lenses, voids, intrusions, or random events. They are sometimes paramount to certain types of forensic studies. For example, they may indicate the critical surface for slope failure. Since the outliers are so deviant, they have large distances from their neighbor data points, and consequently they remain as independent

layers until the very late stages of cluster analysis. For this reason, cluster analysis can be very useful in detecting the outlier data.

A reasonable definition is needed for the minimum thickness to qualify as a soil layer during cluster analysis. The minimum thickness suggested by Vivatrat (1978) is that it should contain at least 20 points of CPT data, usually between 0.5 and 1 meter for most commercial cone penetrometers (Hegazy & Mayne, 1998). Wickremesinghe (1989) and Zhang (1994) suggested a minimum layer thickness of 0.5m and 0.75m respectively. Using clustering of Q and B in clays, Hegazy & Mayne (1998) chose 0.5m for the minimum layer thickness in their analysis. The author believes that the definition of the minimum thickness depends on the purpose of the analysis. If very thin layers play a significant role in the result, the minimum thickness of the layer should be defined small. Otherwise, it can be defined larger. The thickness of the layers changes with the number of clusters. The user can find the appropriate thickness for the layers by varying the number of clusters to suit the needs of the site investigation.

3.4 Application of Three-Dimensional Cluster Analysis

The clustering of piezocone data (Q, F, B) will be presented for selected sites to define the vertical layering. Results will be compared with available soil boring, sampling and lab test information. For illustration, separate examples are shown for CPTu data in clay, silt, and sand profiles.

3.4.1 Cluster Analysis for the Ariake Clay Site in Japan

The Ariake site, which is located at Hizen-Kashima, Saga Prefecture, on Kyunshu Island, Japan, has long been used as a field test site to study soft clay by the Port and Harbour Research Institute (PHRI) of Japan (Tanaka et al., 2001). Figure 3.12 shows the results of a representative CPTu sounding performed at this clay site, including both the raw reading (q_T, f_s, u_2), the processed friction ratio $FR = f_s/q_T$, and the normalized parameters Q, F, and B. From this figure, it can be seen that the porewater pressure u_2 is two to three times higher than the static pore pressure, indicating the existence of a clayey soil type. In the Ariake clay, all the three channels of data (q_T, f_s, and u_2) increase steadily with depth. The sleeve friction $FR = f_s/q_T$ remains almost constant through the whole soil profile. Small spikes can be seen in the CPTu data at regular depth intervals of about 1 m, indicating the locations where successive rods were added when the sounding was performed (This is a systematic procedural error in data collection). Overall, no apparent change of soil properties can be observed in the vertical soil profile. That is, a visual examination of the profiles reveals no obvious sub-layering at the site with the clay from 2 to 18 m.

Using the procedure specified previously, cluster analysis is performed for this CPTu sounding. The results of the cluster analyses corresponding to the cluster number of $N_c = 9$ is shown in Figure 3.13 (a) and that for $N_c = 20$ is shown in Figure 3.13 (b). They are presented in two formats: the first format is the soil profile with the different clusters representing different soil types, and the second format includes the CPTu data points plotted in the suggested three dimensional space as numbers corresponding to the cluster

in which it belongs. At an assumed $N_c = 9$, most of the data points in the sounding remain in the same cluster, which is cluster 9. The points in clusters 1 to 8 are mostly outlier data corresponding to the procedure errors resulted from change of rods. As N_c increases to 20, the cluster analysis shows two major clusters, cluster 18 and cluster 20. Most of the data points in cluster 18 and cluster 20 correspond to soil above 4.5m and below 4.5m, respectively. Thus, clustering indicates two significant layers in the soil profile with the boundary at a depth of around 4.5m.

Figure 3.14 shows the grain composition versus depth, side by side with the soil stratigraphy delineated by cluster analysis with $N_c = 20$ and 45. The clay content above the depth of 18m is around 40% to 50%, and it sharply increases below 18m. The sand content is relatively high and over 10% in the upper 6m, but for most of the depth between 6m to 18m, the sand content is less than 1%. Below a depth of 18m, the sand content increases significantly to above 40%. From the grain size distribution, the deposit can be divided into three layers: the top 6m is the first layer which has relatively high sand content, the second layer lies between depths of 6m and 18m and it has essentially all fines (particles < 75 µm) low sand content, and below 18m is the third layer which has high sand content. It can be seen that the soil stratigraphy with $N_c = 20$ separated out the first layer at the depth boundary of about 4.5m, and early stages of a third layer > 18 m deep. With $N_c = 45$, further clustering separated out the third layer more clearly. Considering that some inherent horizontal variability exists at the site, the soil stratification given by cluster analysis agrees quite well with that derived from the grain composition.

The CPT data in this sounding contain information about the soil properties at different depths, as well as the procedural and measurement errors, yet they are not visually obvious from the data profiles presented in Figure 3.12. Cluster analysis groups similar data points and separates out the measurement errors, irregularities, and transitional layers as small clusters. Therefore, data points of the major layers remain in the same clusters even as the number of clusters N_c goes quite high. Through the process of cluster analysis, both the general and detailed stratification information can be obtained. A two-dimensional clustering proposed by Hegazy & Mayne (2002) for processing CPTu data has now been extended herein to three channels.
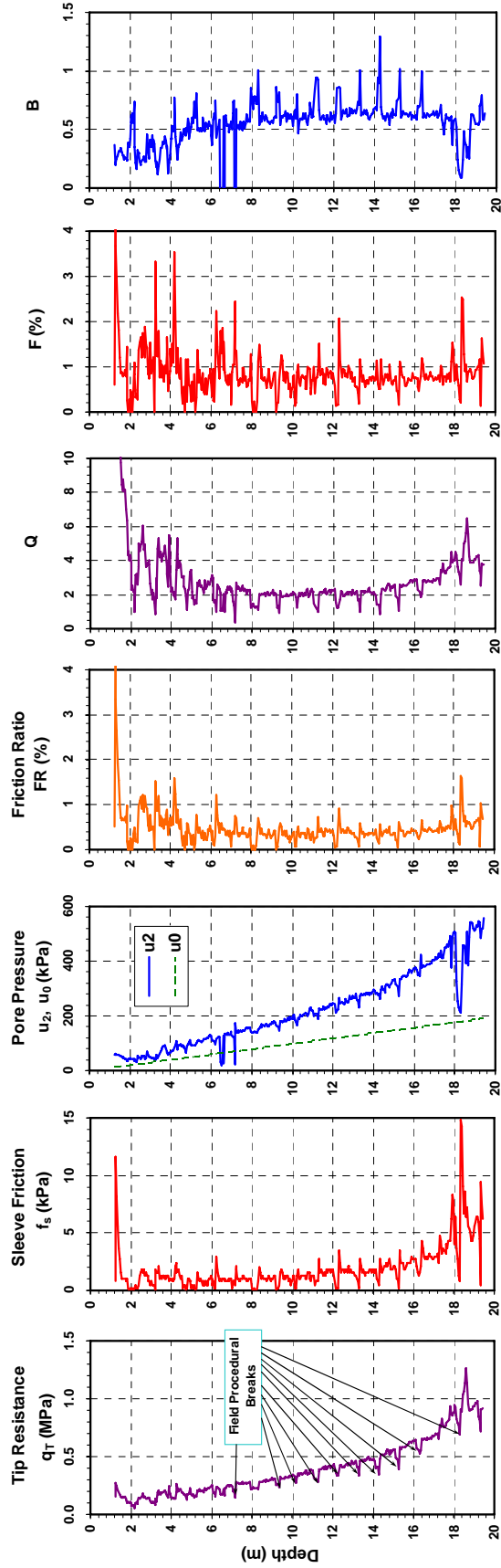
Figure 3.12 Results of representative CPTu sounding performed at the Ariake clay site in Japan (data from Tanaka, 2002)

Note: $FR = f_s / q_T \times 100\%$; $Q = (q_t - \sigma_{vo}) / \sigma'_{vo}$; $B = (u_2 - u_0) / (q_t - \sigma_{vo})$; $F = f_s / (q_t - \sigma_{vo}) \times 100\%$
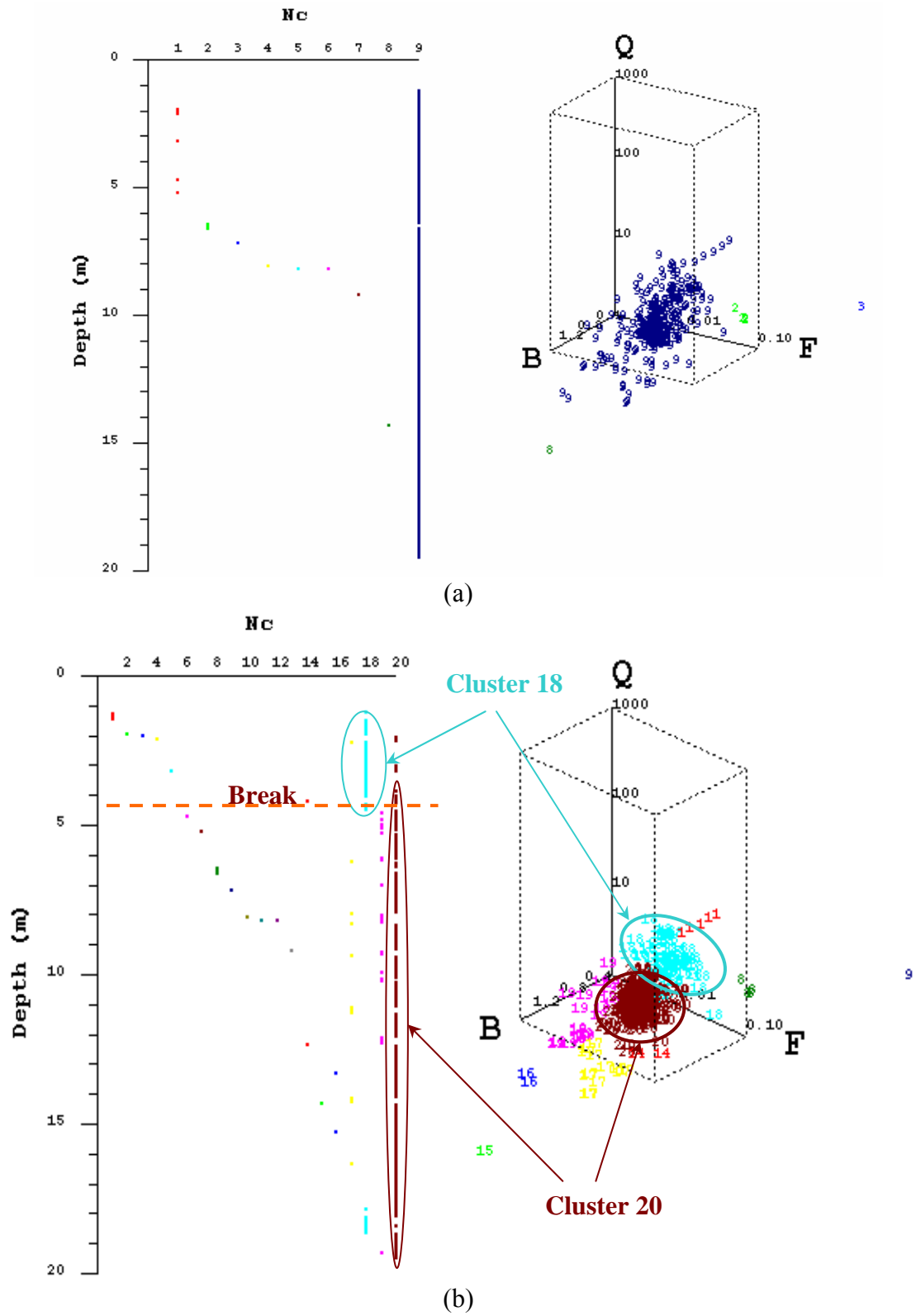
Figure 3.13 Soil stratigraphy delineated by cluster analysis for a representative CPT sounding performed at the Ariake clay site in Japan: (a) $N_c = 9$; (b) $N_c = 20$.
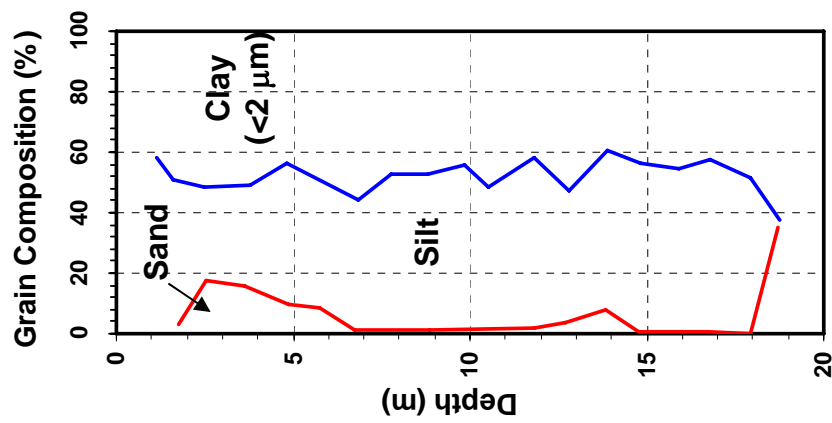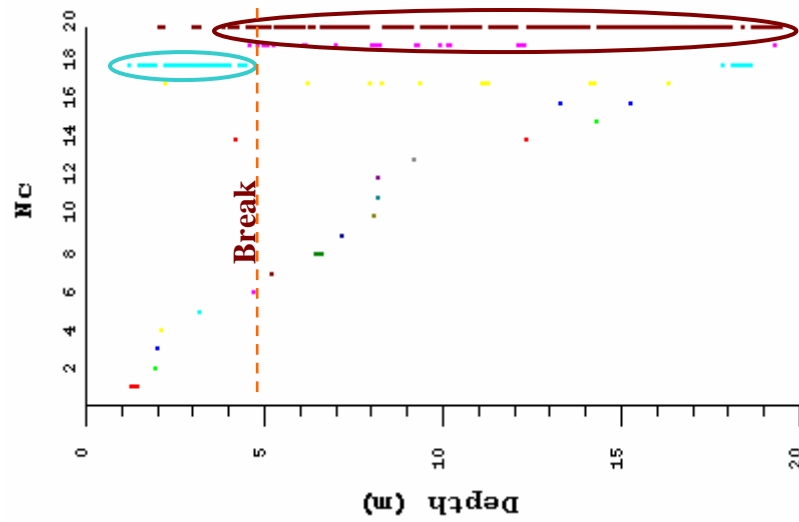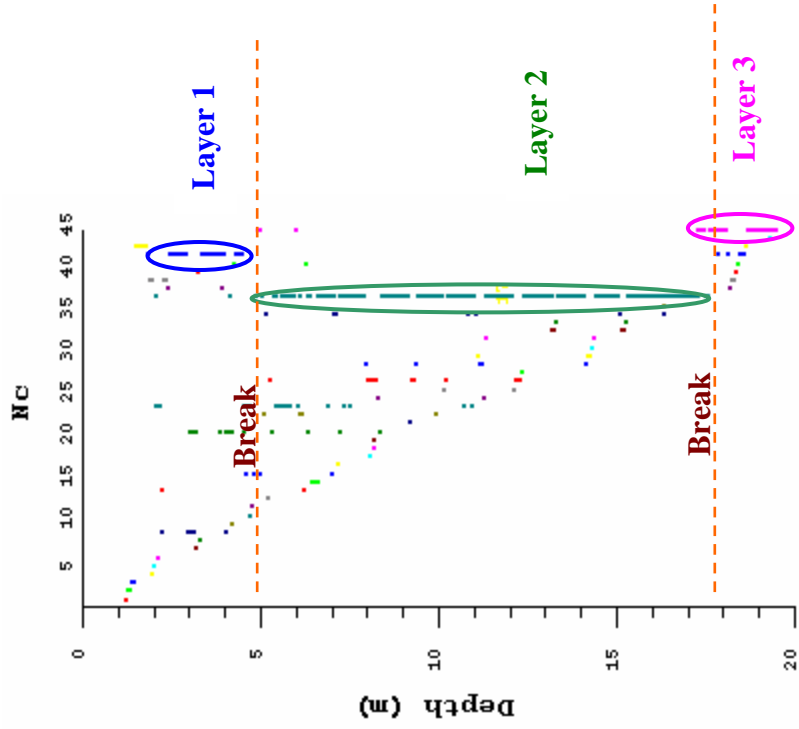
Figure 3.14 Cluster analysis and stratification for the Ariake clay site in Japan: (a) Grain composition vs. depth (after Tanaka et al., 2001); (b) Delineated soil stratigraphy by cluster analysis ($N_c = 20$); (c) Delineated soil stratigraphy by cluster analysis ($N_c = 45$).

3.4.2 Cluster Analysis for Opelika National Geotechnical Experimentation Site (NGES), AL

Extensive in-situ and laboratory tests have been carried out for the NGES site located in Opelika, Alabama, which is located within the Piedmont Geologic Province (Mayne et al., 2000; Mayne & Brown, 2003). Figure 3.15 shows the results of a representative CPTu sounding performed at this site, as well as their corresponding normalized parameters. The tip resistance q_T is about 2 MPa through most of the depth, except in the depth range from 4 to 6 m, where q_T increases up to 8 MPa. The sleeve friction f_s does not change significant with depth, and is in the range from 100 to 200 kPa. Below the depth of 8.5 m is the special residual kaolin layer or zone, as discussed previously. This zone is not uniform, and the porewater pressure readings vary dramatically with depth.

Results of cluster analysis for the representative CPTu sounding at this site are shown in Figure 3.16. At $N_c = 2$, there are two major clusters (cluster 1 and cluster 2) in the soil profile, and they are separated at the boundary of about 2.2 m in depth. The data points that belong to the two clusters are highlighted in the suggested three-dimensional space, and it can be seen that data points in cluster 1 have a higher value of Q than those in cluster 2. Cluster 2 is further separated into two clusters as N_c increases to 6, which are cluster 5 and cluster 6 as shown in Figure 3.16 (b).

In Figure 3.17, the stratigraphy given by cluster analysis with $N_c = 6$ is compared with the results of other in-situ and lab tests. Figure 3.17 (a) shows the mean blow counts N_{60}

79

from 7 SPT tests performed at this site. According to the relationship between mean grain size, D_{50}, and the ratio between CPT tip resistance q_T and SPT blow counts N_{60} suggested by Kulhawy & Mayne (1990), the mean grain size D_{50} can be inferred from the ratio of q_T and N_{60}. The ratio q_T/N_{60} is plotted in Figure 3.17 (b), and the inferred value of D_{50} is presented in Figure 3.17 (c). Lab index tests have been performed on two different sets of soil samples obtained at this site, and the D_{50} values derived from these lab tests are also presented in Figure 3.17 (c). From this figure, it can be seen that the inferred D_{50} values and those obtained from lab tests agree well in the top 11m. Due to inherent variability, the D_{50} values derived from lab tests varies significantly at depths of 12m to 15m, but their average agrees well with the inferred D_{50}. The observed agreement helps to validate the inferred D_{50}. In the top 2m to 3m of the soil profile, D_{50} is low and it is around 0.01mm, indicating fine-grained soil. From depths of 3m to 11m, the soil has a D_{50} of about 0.1mm, indicating granular soil (i.e., fine sand). The value of D_{50} drops to the range of 0.03mm to 0.04mm between the depths of 12m and 15m, indicating fine-grained soil. Figure 3.17 (d) and (e) show the weight percentage of grains passing #200 sieve and the clay fraction derived from lab tests. It is evident that fine grains constitute a larger portion in the soil at the top 2m to 3m than that below it. Based on the grain size distributions, the soil profile for this site can be generated using the Unified Soil Classification System (USCS), and it is shown in Figure 3.17 (f). It agrees well with the soil stratigraphy breaks at depths around 2.2 m and 10.3 m given by cluster analysis with $N_c = 6$ as shown in Figure 3.17 (g).
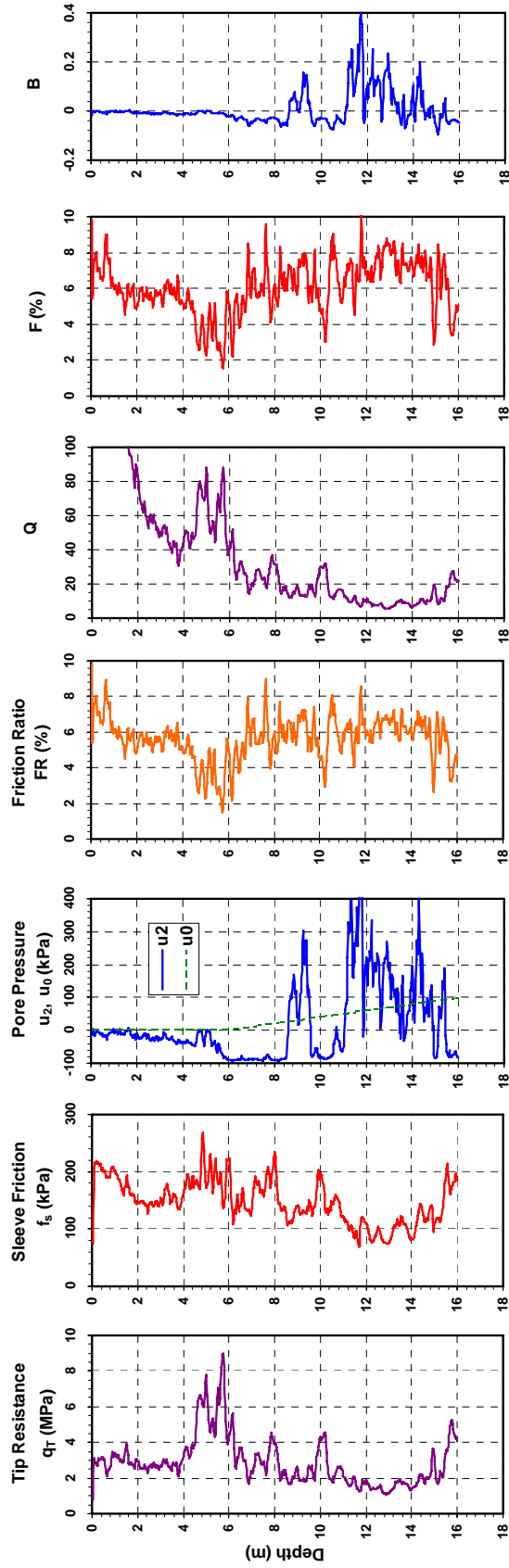
Figure 3.15 Results of a representative CPTu sounding performed at the NGES site located in Opelika, AL

Note: $FR = f_s / q_T \times 100\%$; $Q = (q_t - \sigma_{vo}) / \sigma_{vo}'$; $B = (u_2 - u_0) / (q_t - \sigma_{vo})$; $F = f_s / (q_t - \sigma_{vo}) \times 100\%$
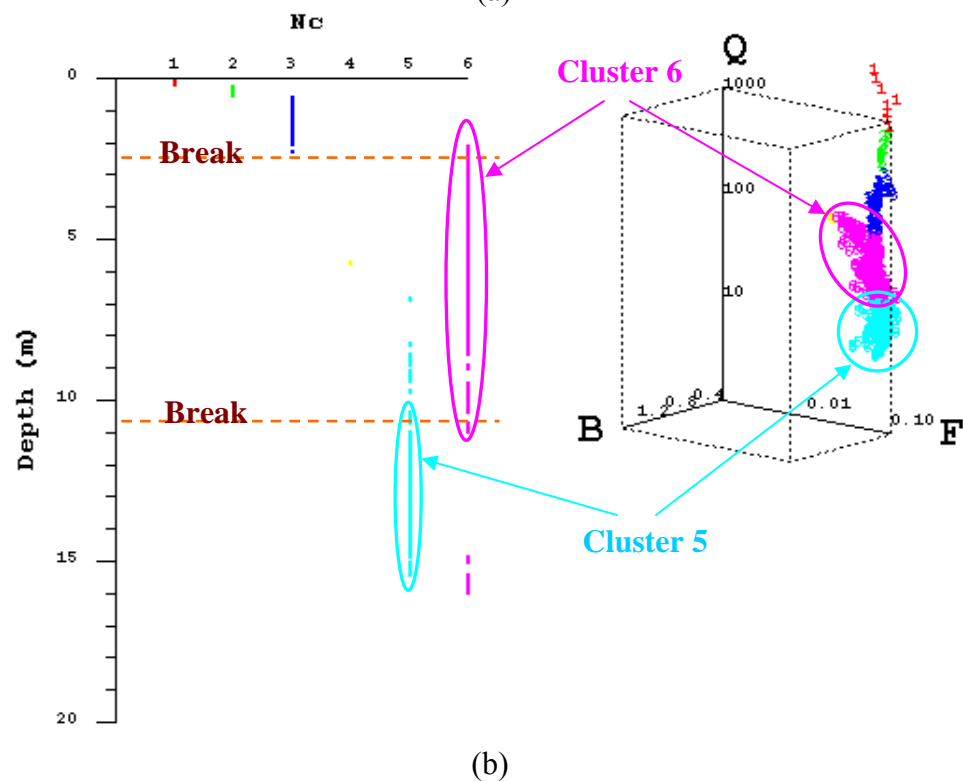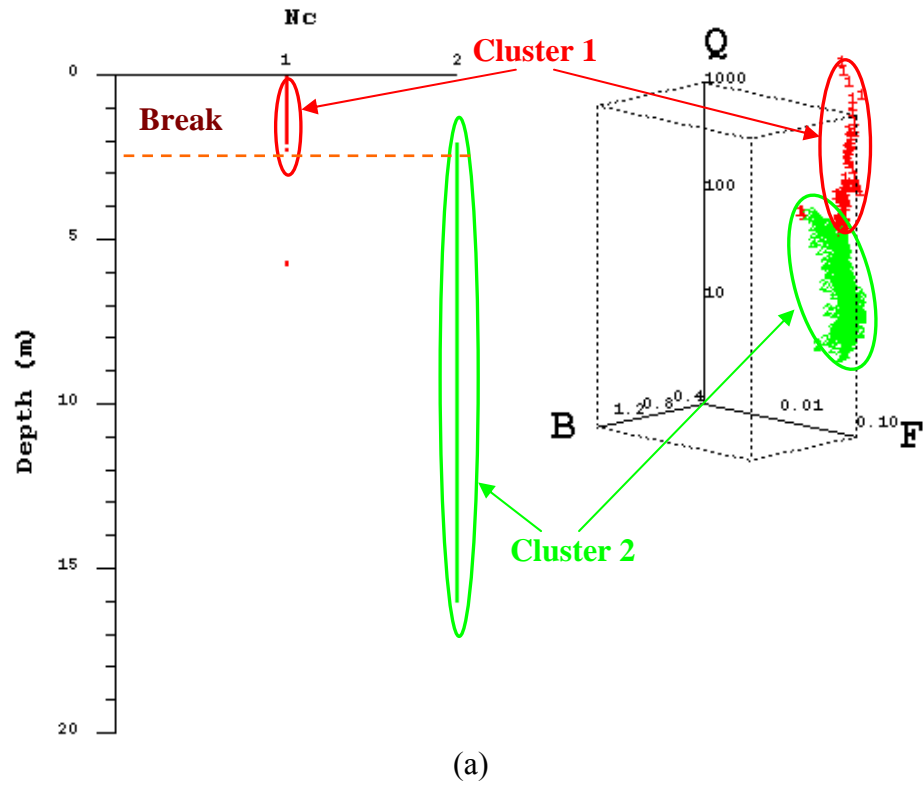
Figure 3.16 Soil stratigraphy delineated by three-dimensional cluster analysis for the representative CPTu soundings performed at the Opelika NGES site: (a) $N_c = 2$; (b) $N_c = 6$.
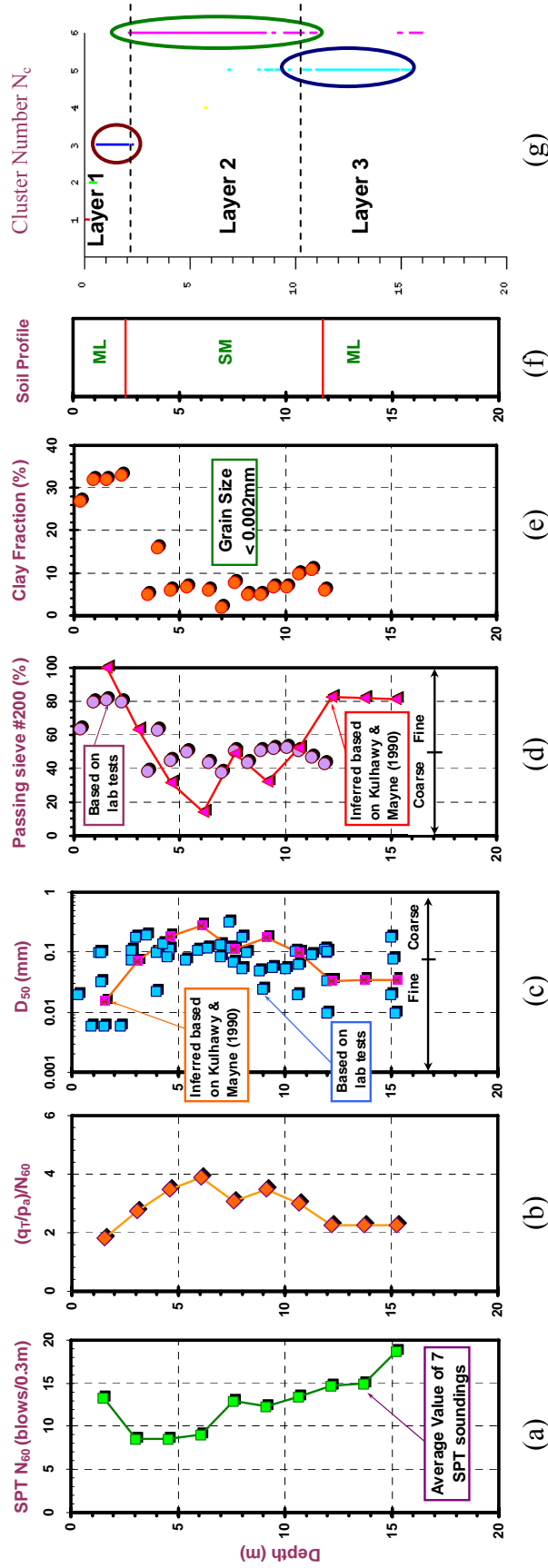
Figure 3.17 Cluster analysis and stratification for the NGES site located in Opelika, AL: (a) SPT N_{60} value; (b) Ratio between CPT tip resistance q_T and SPT N_{60} value; (c) Mean grain size measured from lab tests and inferred from the q_T/N_{60}; (d) Percentage passing #200 sieve; (e) Clay fraction obtained from lab tests; (f) Soil profile based on grain size distribution; (g) Delineated soil stratigraphy by cluster analysis ($N_c = 6$).

83

The Ariake site, Japan in last case study is a clay site, while the NGES site in Opelika, AL is a silt site. In both cases, the results of cluster analysis are confirmed by grain size distribution of the soil. Finally, results for a sand site will be considered.

3.4.3 Cluster Analysis for the Holmen Sand Site at Drammen, Norway

The Holmen site, which is located on Holmen Island in the Drammenford, Norway, has been the main sand research site of Norwegian Geotechnical Institute (NGI). Various in-situ tests have been performed, and many laboratory tests have been carried out on soil samples recovered from boreholes drilled at this site (Lunne et al., 2003). Figure 3.18 shows the results of a typical CPT sounding performed at this site. It can be seen that the tip resistance q_T and the sleeve friction f_s both have relatively high values in the top 2.5m in depth, indicating a layer of sand to gravelly sand. Below 2.5m, q_T and f_s increases steadily with depth, friction ratio FR is nearly constant at about 0.5%, and u_2 is close the hydrostatic porewater pressure u_0. Visually, the soil below 2.5m is a uniform sand deposit. The normalize Q, F, and B are also presented in Figure 3.18 for the Holmen sand site.

Figure 3.19 shows the results of cluster analysis for adopted cluster numbers of $N_c = 5$ and 9. At $N_c = 5$, all the data points corresponding to soil below 2.5m belong to the same cluster (cluster 5). This cluster is separated into two major clusters (cluster 8 and 9) as N_c increases to 9. Cluster 8 is in the depth range from about 4m to 20m, and cluster 9

consists of two major segments, with one from the depth range of 2.5m to 4m and the other from 20m to 24m.

Based on the material index of the soil samples from this site, Lunne et al. (2003) interpret the soil profile as shown in Figure 3.20 (a). The top 2m is a man-made fill of sand and coarser material (gravel, stones), and below it exists a sandy complex. The sandy unit consists of medium to coarse grained sand down to 20m, and fine to medium silty sand below 20m. Figure 3.20 (b) shows the soil unit weight measured by an electrical resistivity probe (ERT) at this site. It can be seen that the unit weight is about 19.0 kN/m^3 down to depths of 18m, and it increases to about 20 kN/m^3 below 20m. Figure 3.20 (c) presents the profile of average overconsolidation ratio (OCR) derived from 6 Marchetti dilatometer tests. The OCR is about 1.0 in the depth range from 5m to 15m, and its value increases sharply to about 3.5 to 4.0 below depths of 18m. Based on the stress history from the dilatometer test, Lunne et al. (2003) divide the deposits into four regions as shown in Figure 3.20 (d). The top 2m is gravelly sand fill, from 2m to 5m is overconsolidated sand, from 5 to 20m is normally to lightly overconsolidated medium-coarse sand, and below 20m is overconsolidated fine-medium sand. This soil profile agrees well with stratigraphy given by cluster analysis with $N_c = 9$ as shown in Figure 3.20 (e). The two segments in cluster 9 correspond to the two overconsolidated layers, and cluster 8 corresponds to the normally to lightly overconsolidated layer, and the small clusters in the top of the soil profile correspond to the gravelly sand fill. The stratigraphy given by cluster analysis also agrees well with the soil profile derived from the soil

85

behavior type index I_c [Figure 3.20 (a)] and the change of the soil unit weight [Figure 3.20 (b)].
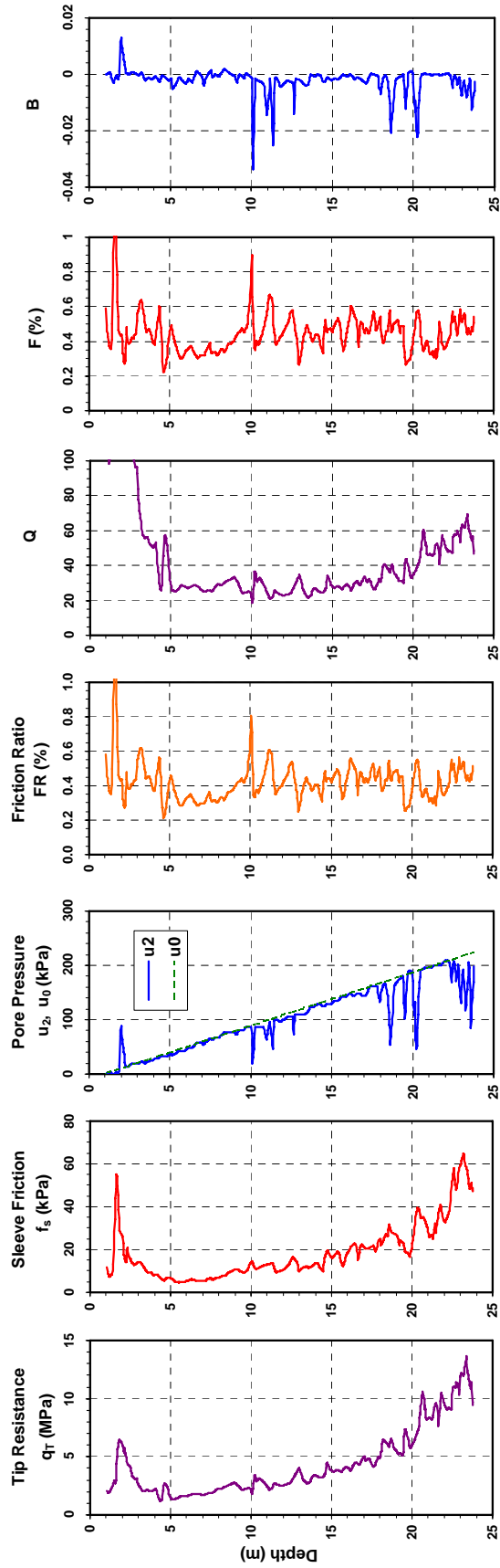
Figure 3.18 Results of a typical CPT sounding performed at the Holmen sand site at Drammen, Norway (data from Lunne et al., 2003)
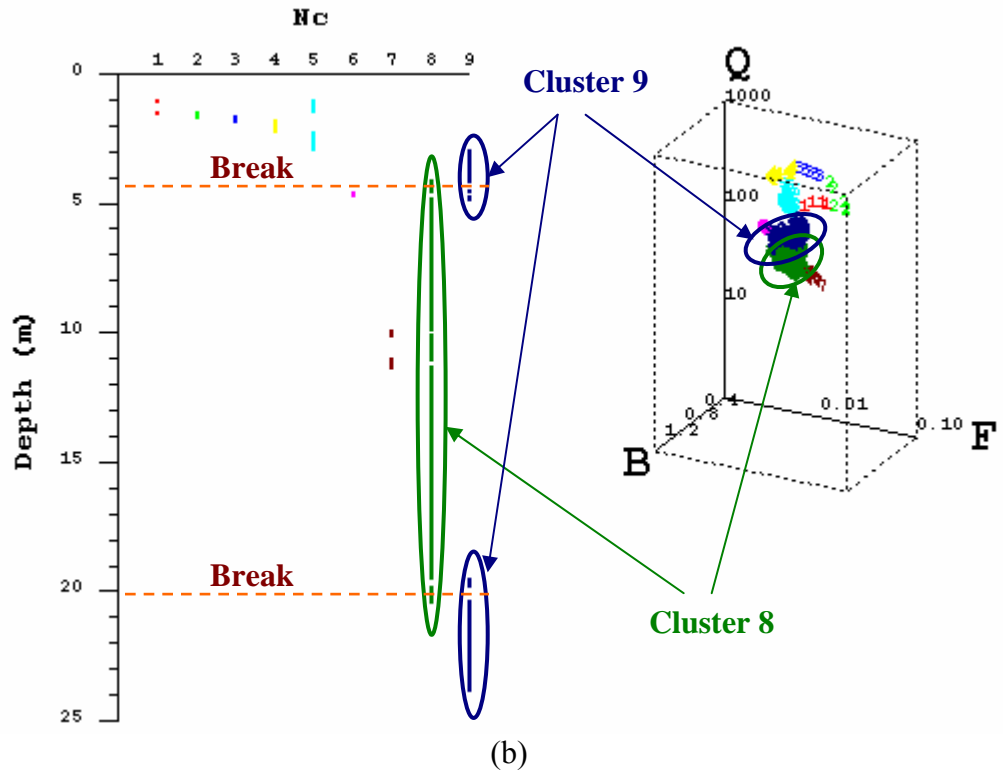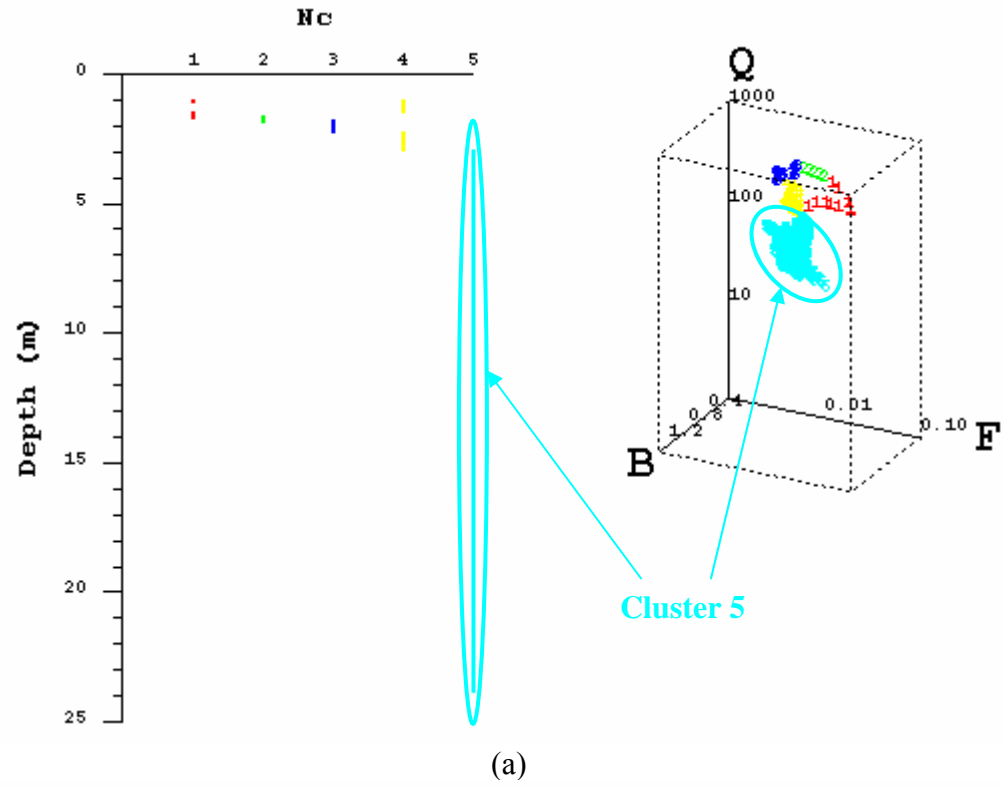
Figure 3.19 Soil stratigraphy delineated by three-dimensional cluster analysis for a representative CPT sounding at the Holmen sand site at Drammen, Norway: (a) $N_c = 5$; (b) $N_c = 9$.
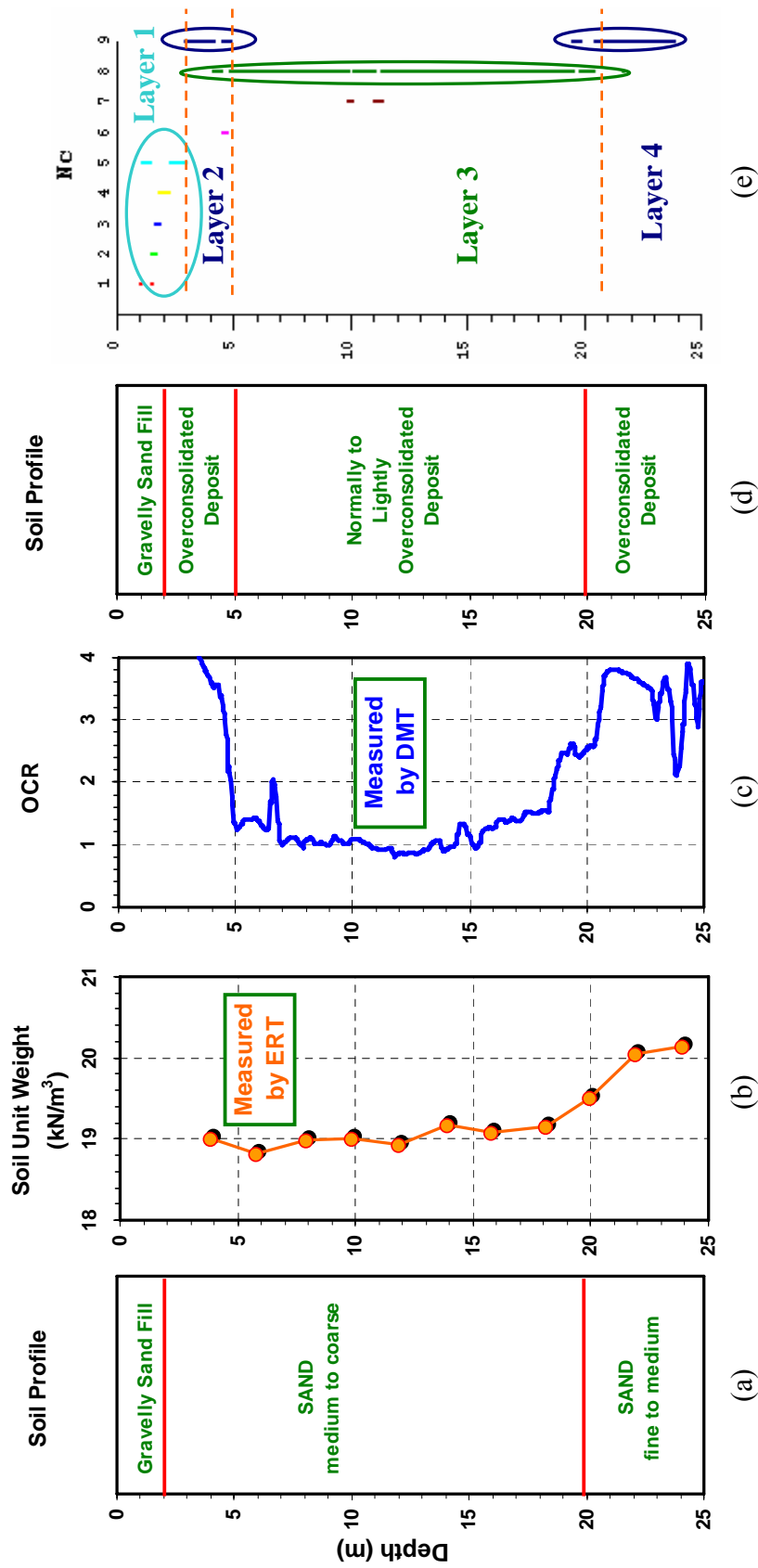
Figure 3.20 Comparison of soil stratigraphy derived from different methods for the Holmen sand site at Drammen, Norway: (a) Soil profile derived from material index (Lunne et al., 2003); (b) Overconsolidation ratio (OCR) derived from dilatometer tests (DMT) (Lunne et al., 2003); (c) Soil unit weight measured by electrical resistivity probe (ERT) (Lunne et al., 2003); (d) Soil profile derived from stress history (Lunne et al., 2003); (e) Delineated soil stratigrphy by cluster analysis (N_c = 9).

3.5 Three-Dimensional Soil Classification Chart

With three-dimensional cluster analysis, the soils can be objectively classified into a certain number of types, but the actual soil type is still unknown. Therefore, a further step is required to characterize the geotechnical properties of each type of soil, where the researcher's expertise or soil classification charts may get involved. Soil stratification by three-dimensional cluster analysis is based on the assumption that the soil types are a function of the set of normalized parameters (Q, F, B), and a specific location in the three-dimensional space Q~F~B corresponds to a specific soil type. Therefore, a three-dimensional soil classification chart is supposed to exist in the three-dimensional space Q~F~B. With a three-dimensional soil classification chart, the process of soil classification can then be integrated with the process of three-dimensional cluster analysis, resulting in a combined process of soil stratification and classification.

A three-dimensional soil classification chart is proposed herein, based on the trends observed from the classification charts developed by other researchers, as well as the author' experience. In the Q ~ F chart of Robertson (1990, 1991) [Figure 3.2 (a)], the boundaries between soil behavior type zones 2 to 7 can be approximated as concentric circles, and the circle radius I_c can be used as the soil behavior type index, that increases with increasing apparent fines content and soil plasticity (Jefferies & Davies, 1993). Jefferies & Davies (1991) suggested the following more generalized equation for the soil behavior type index corresponding to the soil classification chart shown in Figure 3.7,

$$I_c = \sqrt{\{3 - \log[Q(1-B)]\}^2 + [1.5 + 1.3(\log F)]^2} \qquad (3\text{-}16)$$

During liquefaction analysis, Robertson & Wride (1998) assumed B = 0 and defined the soil type index as follows:

$$I_c' = \left[(3.47 - \log Q)^2 + (\log F + 1.22)^2\right]^{0.5} \qquad (3\text{-}17)$$

The simplified relationship between the soil type index and the soil behavior type has been recommended by Jefferies & Davies (1993) and Robertson & Wride (1998), respectively, as shown in Table 3.2.

Table 3.2 Boundaries of soil behavior type

I_c (Jefferies & Davies, 1993)	I_c' (Robertson & Wride, 1998)	Zone	Soil Behavior Type
$I_c' < 1.25$	$I_c < 1.31$	7	Gravelly sand to sand
$1.25 < I_c' < 1.90$	$1.31 < I_c < 2.05$	6	Sands: clean sand to silty sand
$1.90 < I_c' < 2.54$	$2.05 < I_c < 2.60$	5	Sand mixtures: silty sand to sandy silt
$2.54 < I_c' < 2.82$	$2.60 < I_c < 2.95$	4	Silt mixtures: clayey silt to silty clay
$2.82 < I_c' < 3.22$	$2.95 < I_c < 3.60$	3	Clays: silty clay to clay
$3.22 < I_c'$	$3.60 < I_c$	2	Organic soils: peats

Jefferies & Davies (1991) noted that for the cases where B is near zero, the soil classification chart shown in Figure 3.7 is similar to the Q ~ F chart suggested by Robertson (1990, 1991).

In most of the previously developed charts based on Q and B, such as the Robertson (1990, 1991) chart in Figure 3.2 (b), the general trend is that given a certain value of Q, the absolute value of B increases with increasing apparent fines content and soil plasticity. Therefore, it is likely that in a real three-dimensional chart, the apparent fines

content and soil plasticity should increase with the increase of the soil behavior type index I_c or the absolute value of B.

A series of surfaces can be created to indicate the boundaries between the soil types in the suggested three-dimensional space. The boundary surfaces are recommended to be of the shape that can be represented by the following equation:

$$(\log Q - X_0)^2 + (\log F - Y_0)^2 = (I_{c0} - kB)^2 \qquad (3\text{-}18)$$

where k and I_{c0} are parameters that vary with the boundary surfaces. With k and I_{c0} being constant, equation (3-18) represents a circle with (X_0, Y_0) as the center of the circle. It is suggested that $X_0 = 3.47$, $Y_0 = -1.22$. The exact equations of the boundary surfaces between different soil classification zones are listed in Table 3.3:

Table 3.3 Boundary surface equations of soil behavior type

Related Zones for the Boundary Surface	Range for the Value of B	Boundary Surface Equation
7 and 6	$0 < B < 0.655$	$(\log Q - 3.47)^2 + (\log F + 1.22)^2 = (1.31 - 2B)^2$
	$-0.6 < B < 0$	$(\log Q - 3.47)^2 + (\log F + 1.22)^2 = (1.31 + 3.3B)^2$
6 and 5	$0 < B < 1.025$	$(\log Q - 3.47)^2 + (\log F + 1.22)^2 = (2.20 - 2B)^2$
	$-0.6 < B < 0$	$(\log Q - 3.47)^2 + (\log F + 1.22)^2 = (2.20 + 3.3B)^2$
5 and 4	$0 < B < 1.3$	$(\log Q - 3.47)^2 + (\log F + 1.22)^2 = (2.60 - 2B)^2$
	$-0.6 < B < 0$	$(\log Q - 3.47)^2 + (\log F + 1.22)^2 = (2.60 + 3.3B)^2$
4 and 3	$0 < B < 1.4$	$(\log Q - 3.47)^2 + (\log F + 1.22)^2 = (2.95 - 2B)^2$
	$-0.6 < B < 0$	$(\log Q - 3.47)^2 + (\log F + 1.22)^2 = (2.95 + 3.3B)^2$
3 and 2	$0 < B < 1.4$	$(\log Q - 3.47)^2 + (\log F + 1.22)^2 = (4.0 - 0.5B)^2$
	$-0.6 < B < 0$	$(\log Q - 3.47)^2 + (\log F + 1.22)^2 = (4.0 + 2.5B)^2$

Figure 3.21 shows the boundary surface between zone 5 and 4 from different viewpoints. It consists two parts ($B > 0$ and $B < 0$), and each of them is part of a cone surface that is represented by the corresponding equation. The series of the boundary surfaces between zone 2 to 7 are shown in Figure 3.22, and it can be seen that the soil type change from sandy soils to clayey soils with the decrease of Q, the increase of F, and the increase of the absolute value of B.

For B of a certain value, the three-dimensional soil classification chart can be represented in two dimensions (Q versus F), and the cases corresponding to $B = 0.2$ and 0.4 are shown in Figure 3.23. As can be seen from this figure, the radius of the boundary circle decreases with the increase of B, and zone 7 (gravelly sand to sand) disappears when $B = 0.4$. This is reasonable, since as B increases the soil behaves in a way that shows larger apparent fines content and soil plasticity. Figure 3.24 presents the three-dimensional soil classification chart in two dimensions (Q versus B), with $\log(F)$ set to -1 and 0 respectively. In this figure, the boundaries between different soil types move up along the Q axis as F increases, because as F goes up the soil behaves more like fine particulate materials. In the case $\log(F) = -1$, the derived two-dimensional chart (Q versus B) is similar to the $Q \sim B$ chart proposed by Robertson (1990, 1991).

The three-dimensional soil classification chart is visually more complicated than other two-dimensional charts, but it can be implemented on computer easily.
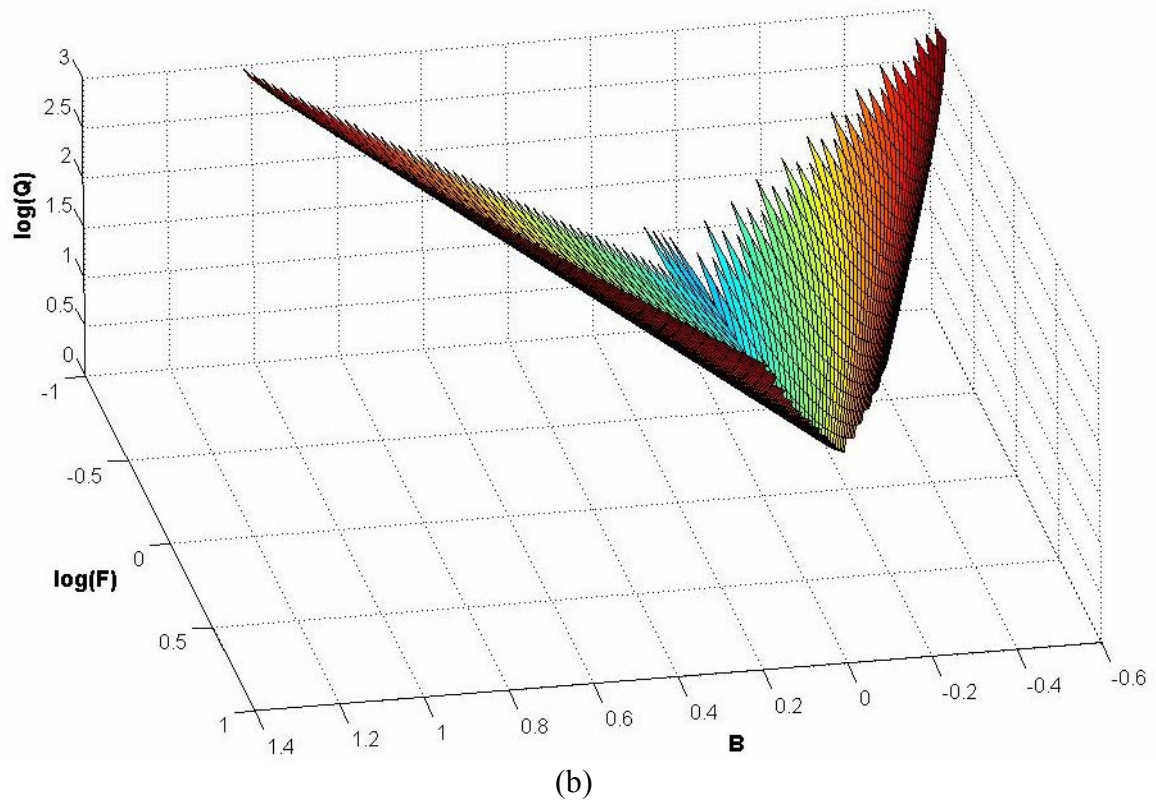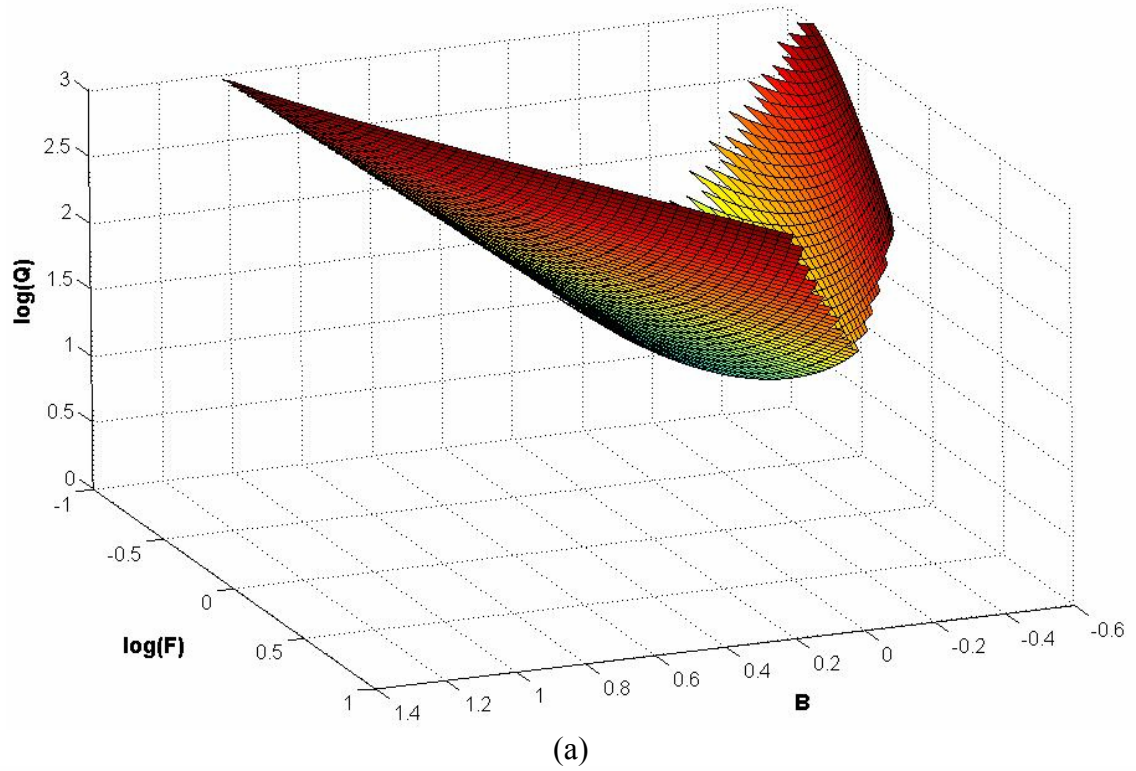
Figure 3.21 The boundary surface between soil classification zone 5 and 4: (a) and (b) represents the surface viewed in different view point.
Note: Color and mesh are used to help visualization of the surfaces.
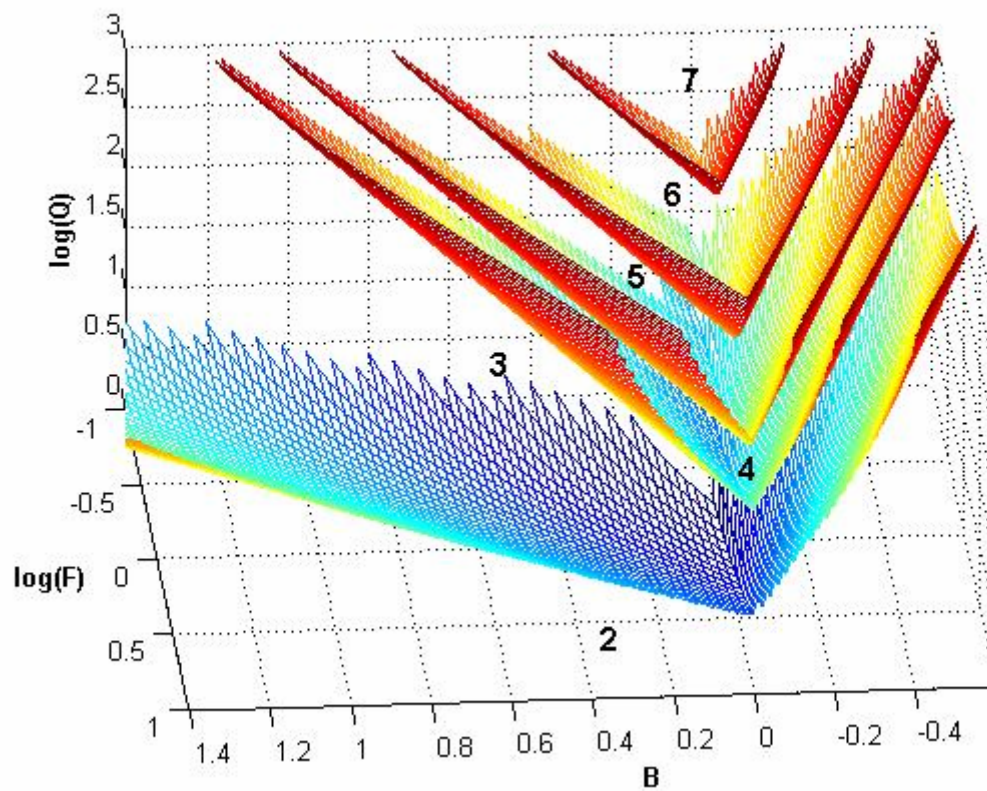
Zone	Soil behavior type
2	Organic soils – peats;
3	Clays – clay to silty clay;
4	Silt mixtures - clayey silt to silty clay
5	Sand mixtures – silty sand to sand silt
6	Sands – clean sands to silty sands
7	Gravelly sand to sand

Figure 3.22 The Boundary Surfaces between Soil Classification Zone 2 to 7
Note: Soil type 1, 8, and 9 are not differentiated with other soil types;
Color and mesh are used to help visualization of the surfaces.
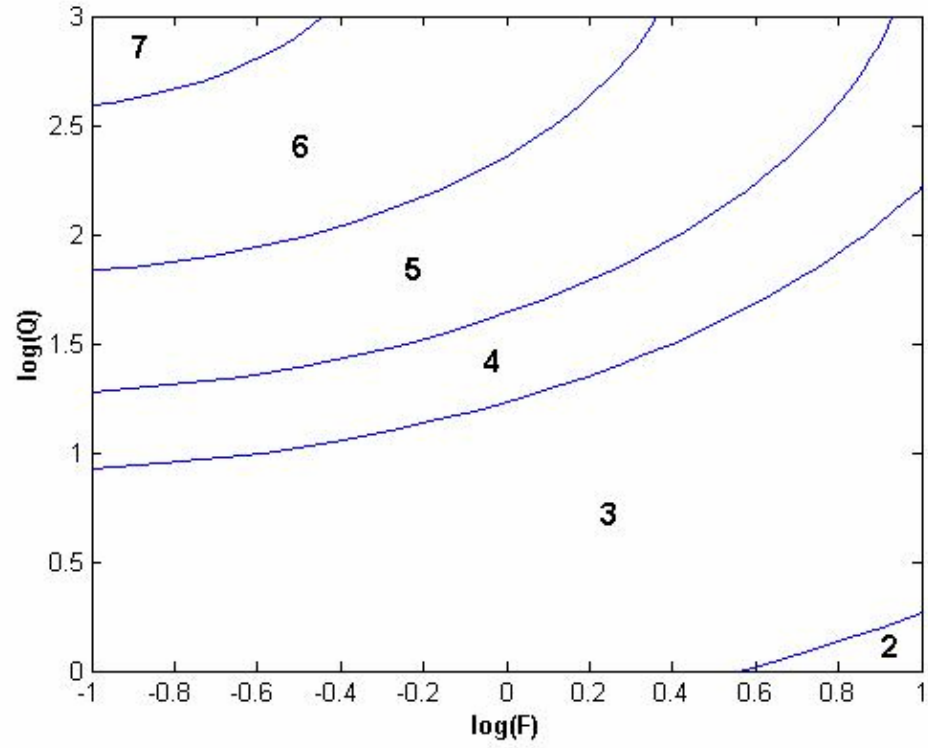
(a)
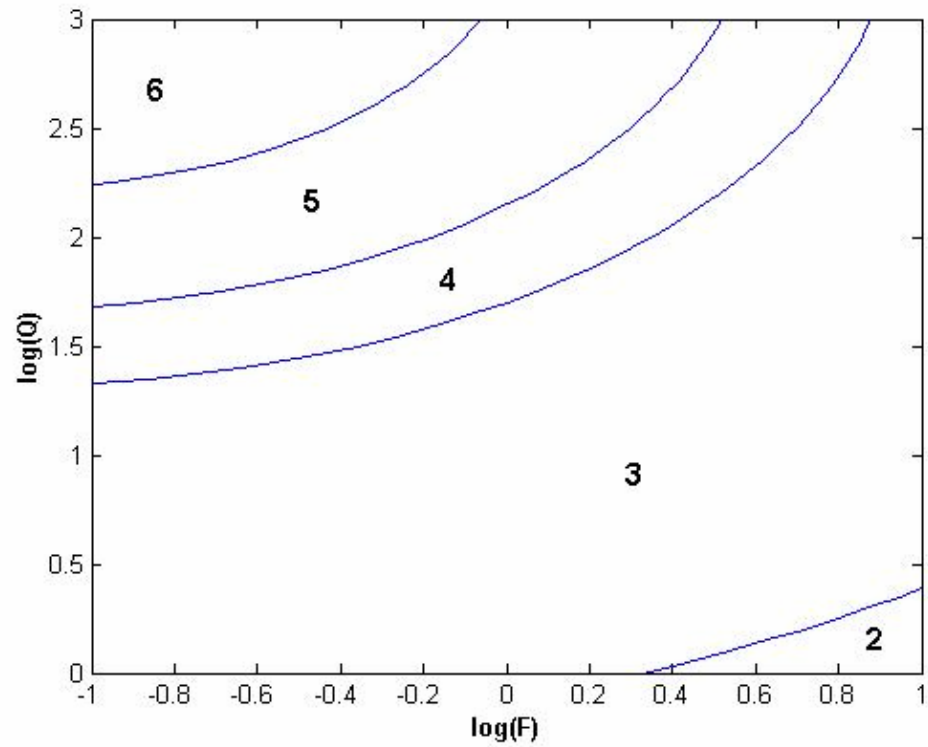
(b)

Figure 3.23 The boundary between soil classification zones given a certain value of B:
(a) B = 0.2; (b) B = 0.4.
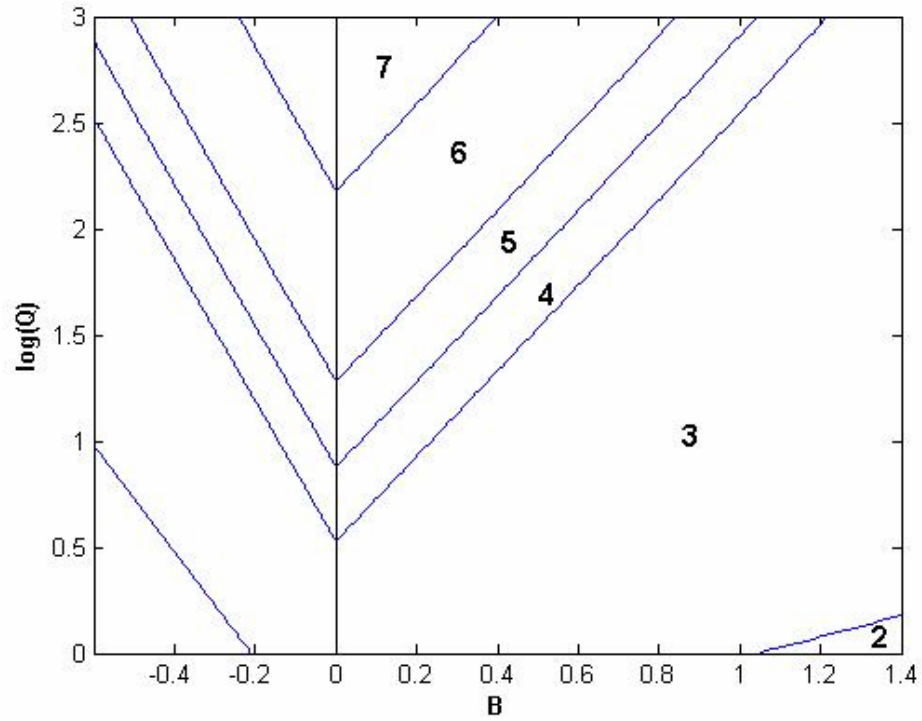
(a)
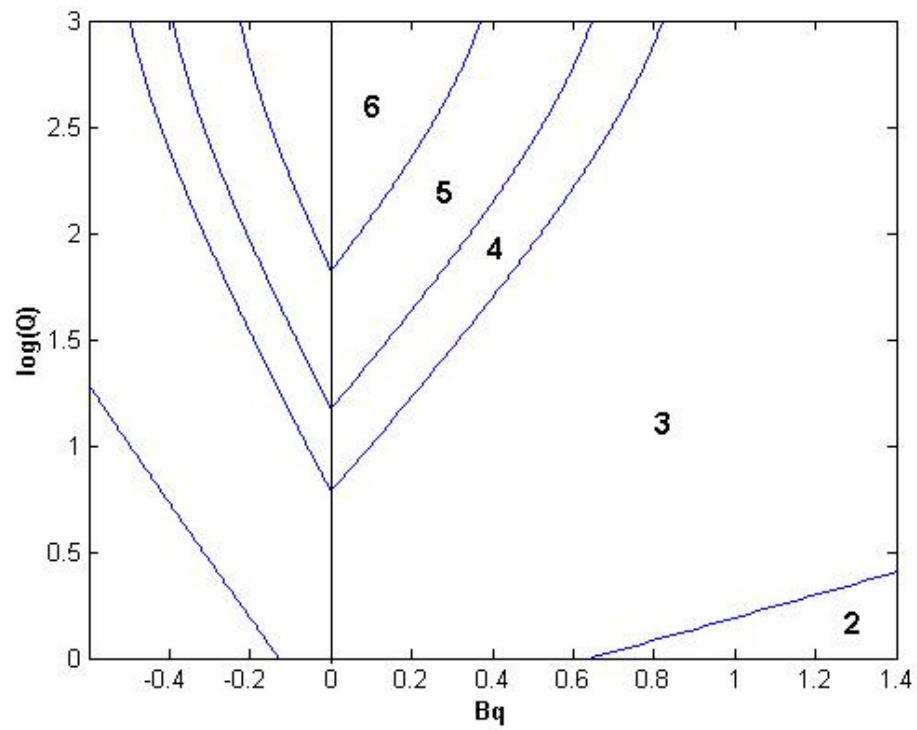
(b)

Figure 3.24 The boundary between soil classification zones given a certain value of log(F): (a) log(F) = -1; (b) log(F) = 0.

3.6 Application of the Three-Dimensional Soil Classification Chart

The proposed three-dimensional soil classification chart is applied to CPT data from the sites on which the three-dimensional cluster analysis have been used, as well as from some other sites which were found problematic in using other soil classification charts.

3.6.1 Soil Classification for Two Offshore Sites in the Canadian Beaufort Shelf

After Robertson (1990) published the original soil classification charts, Jefferies & Davis (1991) used them on two offshore sites in the Canadian Beaufort Shelf. The two sites are Tarsiut P-45 and Sauvrak F-45. The normalized CPTu data (Q, F, B) of four geologic units are from each site are presented in Table 3.4, with units A, B, C, and D belonging to Tarsiut P-45 site, and units E, F, G, and H belonging to Sauvrak F-45. Jefferies & Davis (1991) found that the Q ~ B chart proposed by Robertson (1990) did not work well for these CPTu data. Then Robertson (1991) updated the Q ~ B charts according to these data, but still they do not work satisfactorily for all these data.

Table 3.4 Summary of the soil classification results based on different charts

Geologic Unit Index used by Jefferies & Davis (1991)	Q	F	B	Soil Type			
	Data from Jefferies & Davis (1991)			Soil Samples	Q ~ F Chart (Robertson, 1990)	Q ~ B Chart (Robertson, 1991)	Proposed 3D Chart
A	33	4.5	-0.3	3	4	4	3
B	30	2.5	-0.1	4	4	5	4
C	16	3.5	-0.05	3	3	4	3
D	9.5	2.5	0.25	3	3	3	3
E	30	8	-0.4	3	3	3	3
F	25	8.25	0.1	3	3	5	3
G	14	6.25	-0.35	3	3	3	3
H	9.5	4.5	0.45	3	3	3	3

Table 3.4 lists the soil classification results based on soil samples, the Robertson (1990, 1991) charts, and the proposed 3D chart. As we can see from Table 3.4, some of the soil classification results based on the Q ~ B chart suggested by Robertson (1991) are significantly different from the soil types based on soil samples. The proposed three-dimensional soil classification chart gives more consistent soil classification results.

3.6.2 Soil Classification for the Ariake Clay Site in Japan

The three dimensional soil classification chart is applied to the CPT data collected at the Ariake clay site in Japan (Figure 3.12), and results are compared with soil classification charts proposed by Robertson (1990, 1991) and Jefferies & Davies (1993) in Figure 3.25. The two charts suggested by Robertson (1990, 1991) give inconsistent results for this site, as the Q ~ F chart classified the soils at most of the depth into type 1 (sensitive, fine grained), while the Q ~ B chart classified them into type 2 (organic soils - peats) and type 3 (clays-clay to silty clay). The classification results from the Q ~ F chart are more reasonable, for the Ariake clay is well-known for its high sensitivity. According to the Jefferies & Davies (1993) chart, the soils are type 2 (organic soils - peats) in the depth range from 8m to 17m, while belong to type 2 (organic soils - peats) and type 3 (clays-clay to silty clay) above 8 m and below 17 m. At some depths, the soil type goes to 0 (unable to classify), because the Q(1-B) value becomes negative at these depths due to B value that is over 1. It results from measurement procedural errors in the original CPTu data. The indication of existence of type 2 (organic soils - peats) by the Jefferies & Davies (1993) chart is contradictory to the soil profile derived from soil samples from

this site. The classification result based on the proposed three-dimensional chart is shown in Figure 3.25 (d), and it can be seen that almost the whole deposit belongs to soil type 3 (clays-clay to silty clay). The proposed three-dimensional chart classifies the soil into type 2 to type 7, and does not differentiate type 1 (sensitive, fine grained) from the other soil types. Considering this fact, the classification result based on the proposed three-dimensional chart is reasonable, since the soils at this site consist of about 50% clay particles and 40% to 50% silt particles. The results based on probabilistic soil classification based on Zhang & Tumay (1999) are presented in Figure 3.25 (f). It shows that the probability of sand content increases with depth, while the probability of clay content decreases with the depth, which are not consistent with the grain composition derived from lab tests.

Figure 3.25 Soil Classification for the Ariake Clay site in Japan: (a) Grain composition *vs.* depth (after Tanaka et al., 2001); (b) Soil types based on Robertson (1990); (c) Soil types based on Jefferies & Davis (1991); (d) Soil types based on proposed three-dimensional soil classification chart; (e) Three-dimensional cluster results; (f) Probabilistic soil classification based on Zhang & Tumay (1999).

3.6.3 Soil Classification for the NGES site in Opelika, AL

Similarly, the different soil classification charts are used for the representative CPTu sounding (Figure 3.15) performed at the NGES site in Opelika, AL, with the results shown in Figure 3.26. The Q ~ F chart of Robertson (1990, 1991) classified the soil in the top 2m as type 9 (very stiff fine grained), the depth range from 2m to 11m as type 4 (silt mixtures: clayey silt to silty clay), and below 11m as type 3 (clays-clay to silty clay) with thin layers of type 4. According to the Q ~ B chart, the top 11m is type 6 (sands: clean sands to silty sands), and below 11m is type 5 (sand mixtures: silty sand to sand silty). The Q ~ F chart classified the soils at this site as more fine-grained materials than the Q ~ B chart. The classification result based on Jefferies & Davies (1993) chart is very close to what is given by the Robertson (1990, 1991) Q ~ F chart, since the absolute value of B is low. According to the proposed three-dimensional soil classification chart, the soils in the top 2m and in the depth range between 4m to 11m are soil type 5, while the soils in the depth range between 2m to 4m and below 11m are soil type 4. This agrees well with the soil classification derived from lab tests and other in-situ tests [Figure 3.26 (a)]. The probabilistic soil classification based on Zhang & Tumay (1999) is shown in Figure 3.26 (f). It suggests the soil in the upper 4 m is most likely to be clay, while that in the depth range from 4 to 11 m is more likely to consist of silty materials. Below 11 m, the probability of clay content increases to about 50%. Results of the probabilistic soil classification appears to contradict to the grain size distribution shown in Figure 3.17.
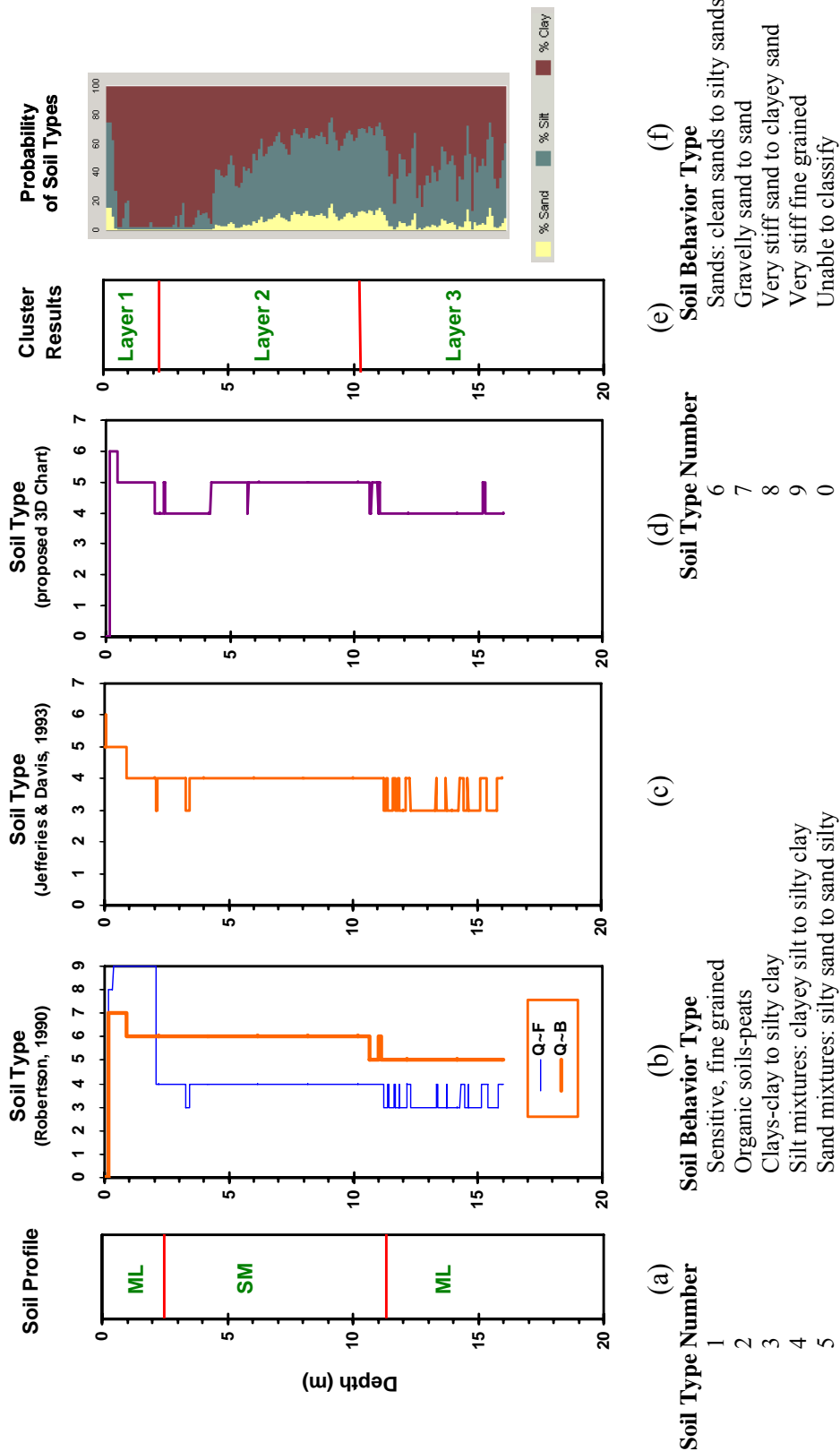
Figure 3.26 Soil Classification for the NGES site in Opelika, AL: (a) Soil profile based on grain size distribution; (b) Soil types based on Robertson (1990); (c) Soil types based on Jefferies & Davis (1991); (d) Soil types based on proposed three-dimensional soil classification chart; (e) Three-dimensional cluster results; (f) Probabilistic soil classification based on Zhang & Tumay (1999).

3.6.4 Soil Classification for the Holmen Sand Site at Drammen, Norway

Figure 3.27 shows the soil classification results for the Holmen sand site at Drammen, Norway. Both the Q ~ F chart and Q ~ B chart of Robertson (1990, 1991) indicate that most of the soils at this site are type 5 (sand mixtures: silty sand to sand silty) with thin layers of type 6 soil (sands: clean sands to silty sands). The Jefferies & Davies (1993) chart and the proposed three-dimensional chart give similar classification results that this site mainly consists of type 6 soil with layers of type 5 soils. Compared with the soil classification results from laboratory index [Figure 3.27 (a)], all the soil classification charts give reasonable results. The probabilistic soil classification shown in Figure 3.27 (f) indicates that the soil above 20 m has relatively high silt content, which is not consistent with the soil profile derived from lab grain size distribution.
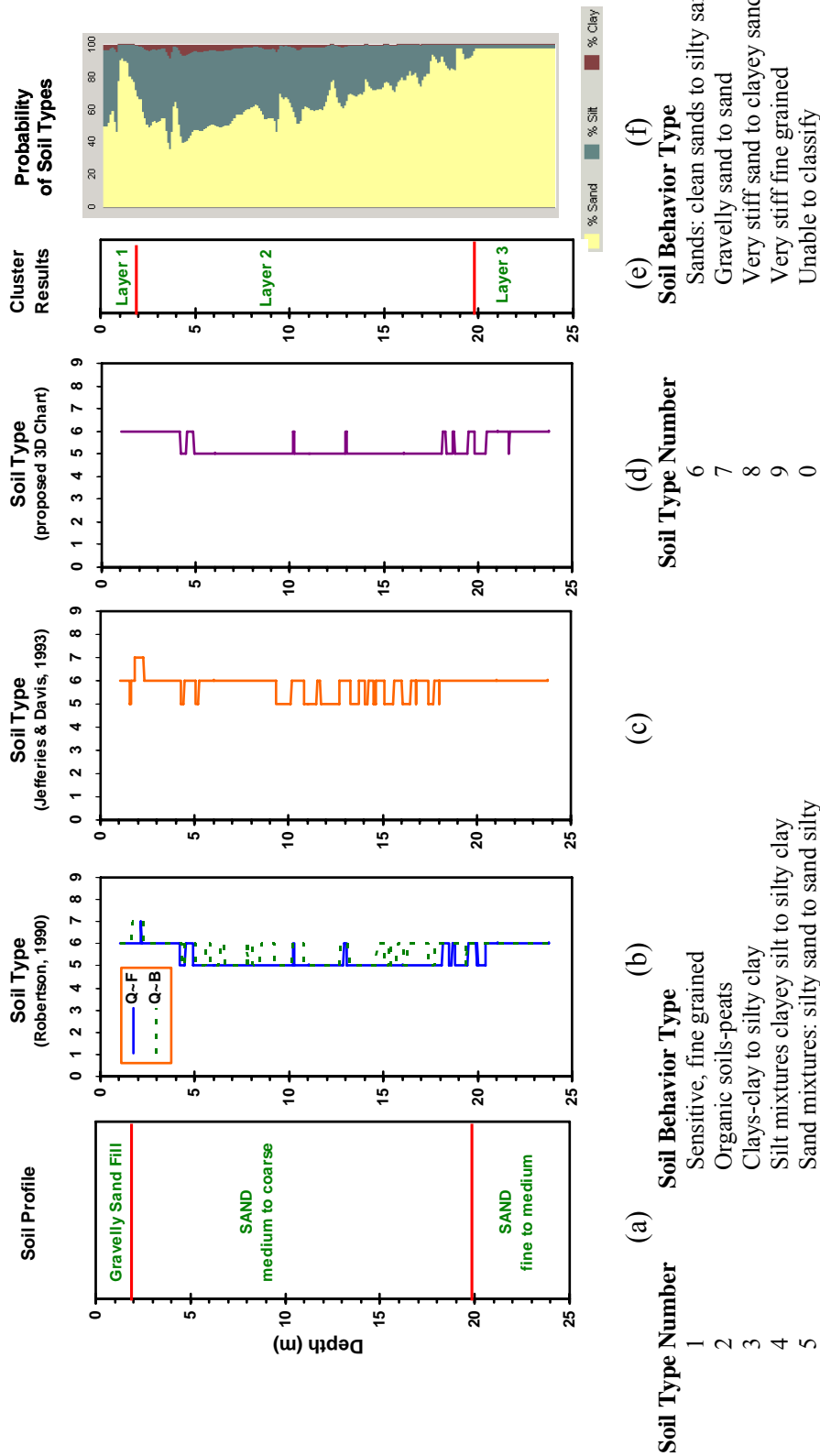
Figure 3.27 Soil Classification for the Holmen Sand Site at Drammen, Norway: (a) Soil profile derived from material index (Lunne et al. based on grain size distribution; (b) Soil types based on Robertson (1990); (c) Soil types based on Jefferies & Davis (1991); (d) Soil types based on proposed three-dimensional soil classification chart; (e) Three-dimensional cluster results; (f) Probabilistic soil classification based on Zhang & Tumay (1999).

3.6.5 Soil Classification for a Representative Sounding Performed in Charleston, SC

For the representative SCPTu sounding (Figure 3.4) performed for at the Cooper River Bridge site in Charleston, SC, the results of cluster analysis and soil classification are presented in Figure 3.28. From cluster analysis with the cluster number $N_c = 9$, the Cooper Marl below 20m was clearly delineated as one layer, which consists different soil than that in the top 20m. Although the Robertson (1990, 1991) Q ~ B chart gives the correct classification for soil below 20m as type 3 (clays-clay to silty clay), the Q ~ F chart indicates that most of the soil below 20m is type 5 (sand mixtures: silty sand to sand silty). The Jefferies & Davies (1993) chart classifies the Cooper Marl soil as type 5 (sand mixtures: silty sand to sand silty) with interleaved layers of type 4 (silt mixtures clayey silt to silty clay), which is not correct. However, the classification result based on the proposed three-dimensional chart consistently suggests that the soil below 20m is type 3, which is the correct classification for Cooper Marl. From this case study, it can be seen that the three-dimensional cluster analysis can delineate the soils into different layers, and the three-dimensional soil classification chart can tell the actual soil type of each layer. Probabilistic soil classification is also performed with this sounding, as shown in Figure 3.28 (e). It incorrectly indicates that the Cooper Marl layer is mostly sand with 10% to 15% of silt.
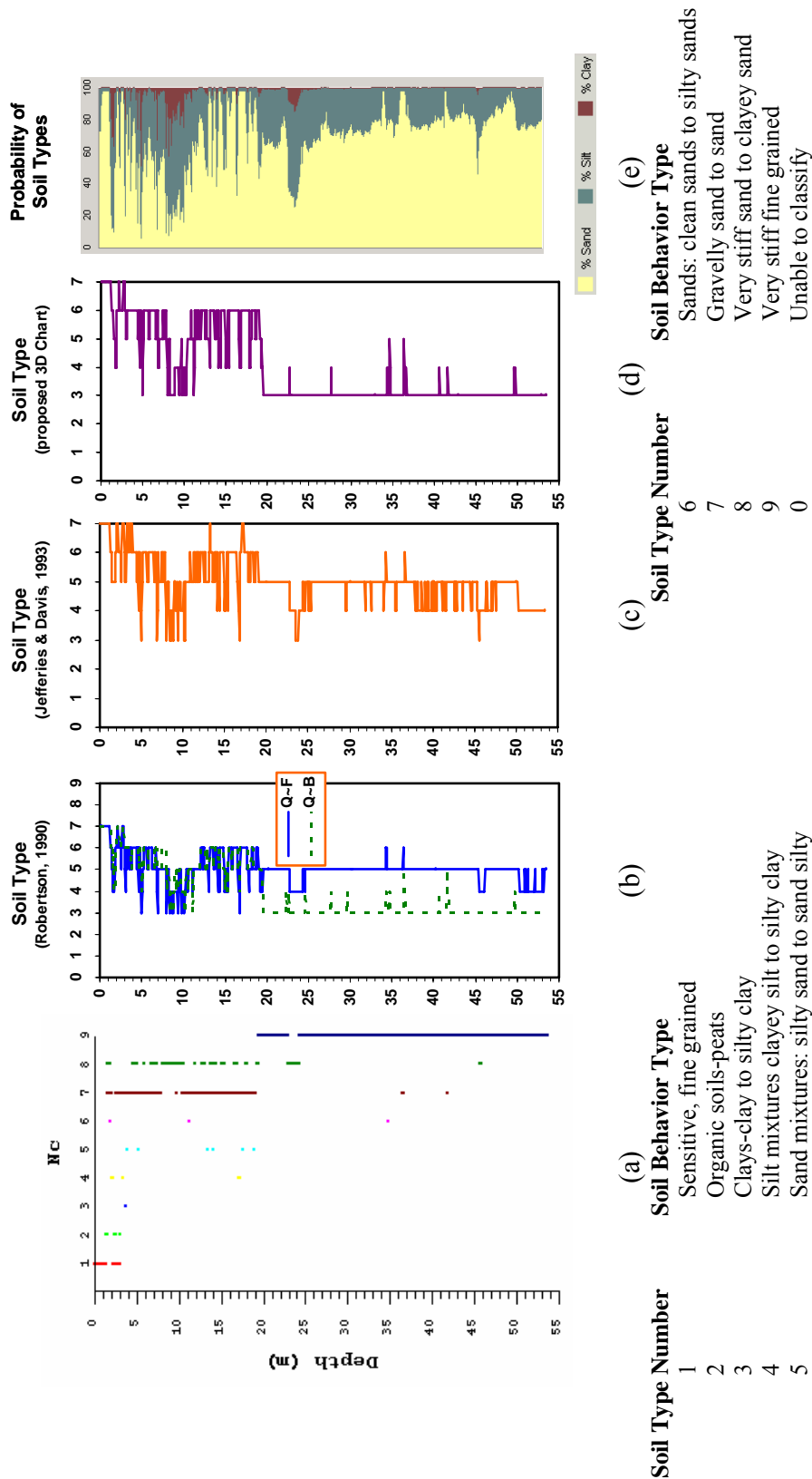
Figure 3.28 Cluster analysis and soil classification based on the CPT data from Charleston, SC: (a) Three-dimensional cluster results; (b) Classified soil types based on Robertson (1990); (c) Classified soil types based on Jefferies & Davis (1991); (d) Classified soil types based on proposed three-dimensional soil classification chart; (e) Probabilistic soil classification based on Zhang & Tummay (1999).

3.7 Summary

The three-channel cluster analysis proposed herein for soil geostratification is based on the normalized CPTu parameters, Q, B, and F, which are derived from the tip resistance q_T, pore pressure u_2, and sleeve friction f_s. Because of the inclusion of all three parameters, this type of cluster analysis can be used on all types of CPTu soundings for layering and stratification purposes. Furthermore, this thesis suggests measuring the similarity between the data points by their Euclidean distance in three-dimensional space, which endows similarity with a clear physical meaning. With cluster analysis, the soils can be classified objectively and the results are independent of the soil classification charts. By grouping similar data points together, cluster analysis can find both the obvious as well as subtle changes between soil types. It can also detect outlier data which are caused by systematic errors or the irregular structure in the soil deposits. The three-dimensional cluster analysis has been used for sites of different materials (clay, silt, and sand). It is found that cluster analysis can group together data points corresponding to soils that have similar grain size distributions. One significant advantage of cluster analysis is that it can detect subtleties in CPT measurements caused by change of soil properties, which are not readily evident by visual examination of the CPT data, or by other available interpretation techniques.

As supplement to the cluster analysis, a three-dimensional soil classification chart is also proposed herein. It is based on the observation of trends in available charts, such as Robertson (1990, 1991) and Jefferies and Davies (1993), as well as the experience of the author in processing CPTu data. Because of the inclusion of all three channels of CPTu

data in a single chart, the three-dimensional soil classification chart shows advantages over charts that are based on only two or one channels of data. The three-dimensional soil classification chart has been found to work quite well for the few selections presented here, but as an empirical chart, it may still need additional calibration in the future research.

The three-dimensional cluster analysis and the proposed three-dimensional soil classification chart can be integrated together in site characterization. The soil stratification can be objectively demarcated by cluster analysis, and then soil type of each layer can be analyzed by using the three-dimensional soil classification chart. Since both the cluster analysis method and the three-dimensional soil classification chart can be implemented on computer, the soil stratification and classification process can be automated, making them much faster and more objective for data handling.

CHAPTER IV

AUTOMATED POST-PROCESSING OF SCPTU DATA: SOIL PROPERTIES

4.1 Overview

Results from seismic cone penetration tests (SCPTu) are increasingly used to interpret site-specific soil properties for geotechnical analysis and design. The penetration data, which include tip resistance q_T, sleeve friction f_s, and porewater pressure u_m, reflect measurements on soil behavior related to a failure state of stress, while the shear wave velocity V_s provides the small strain stiffness corresponding to the nondestructive range (Mayne, 2005). These measurements can be used to characterize the subsurface layering, soil behavioral type, strength properties, stiffness, and stress state, as well as evaluate liquefaction potential. Figure 4.1 depicts the concept for interpretation of soil properties from SCPTu results, and it will be discussed in detail later.

Various correlations have been suggested to determine parameters related to the soil properties. Using these correlations, computer programs have been developed to automate the process of deriving the parameters from the SCPTu data, as listed in Table 4.1. Some of these can only run in a DOS environment, which is inconvenient nowadays since DOS is antiquated operating system. Most of these software programs cost from hundreds to thousands US dollars. Furthermore, the correlations used in the software are limited to old methods of analysis (20 years +) and to those implemented by the software

developers. Since new relationships are being developed on a frequent basis, the older

programs cannot adapt to the best available methods.
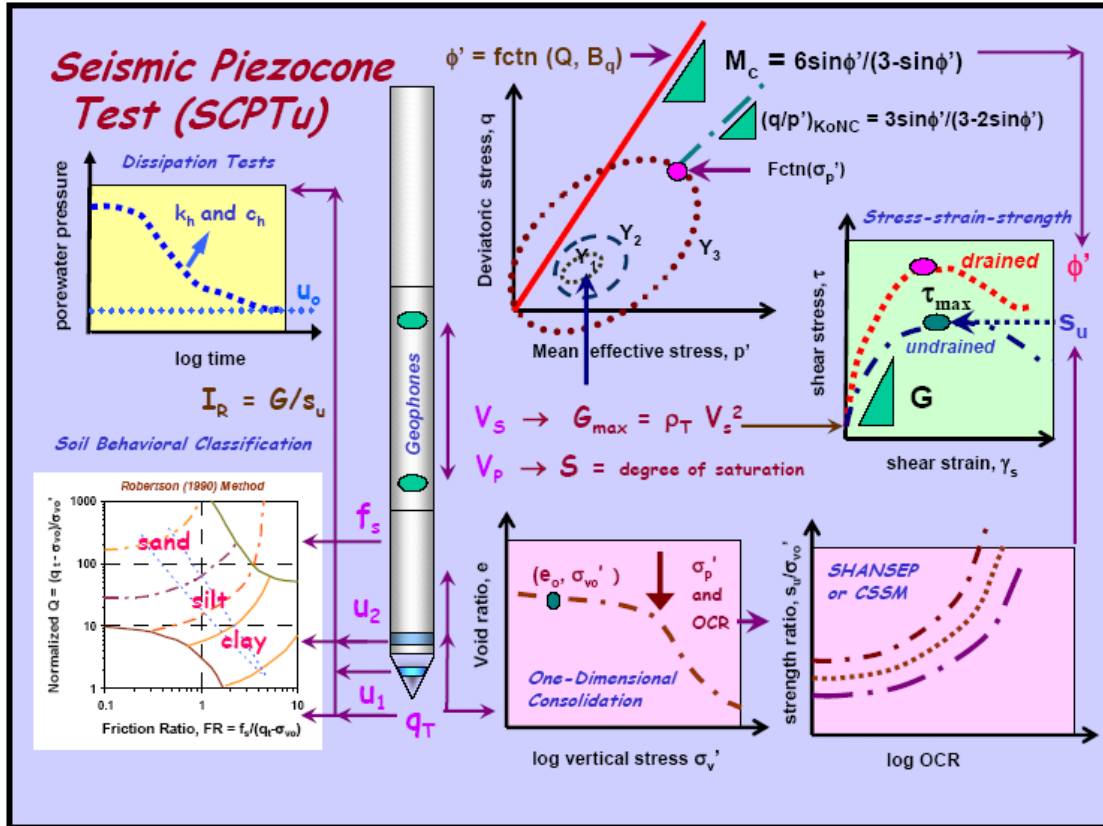
Legend

qT: Cone tip resistance   fs: Sleeve friction
u2: Shoulder porewater pressure   u1: Tip porewater Pressure
Vs: Shear wave velocity   Vp: Compression wave velocity
Gmax: Small-strain shear modulus   ρT: Total unit mass density
S: Degree of saturation   e0: Initial void ratio
σvo': Effective overburden stress   u0: Hydrostatic porewater pressure
ch: Coefficient of consolidation   kh: Hydraulic permeability
IR: Rigidity index   CSSM: Critical-state soil mechanics
Mc: Slope of critical state line   Y1, Y2, Y3: Yield surfaces
G: Shear modulus   su: Undrained shear strength
φ': Peak friction angle   σp': Preconsolidation stress
OCR: Overconsolidation ratio   q: Deviator stress
p': Mean effective stress   K0: Earth pressure coefficient at rest
K0NC: K0 for normally consolidated soil

Figure 4.1 Conceptual framework for interpretation of soil property evaluation from
results of seismic cone penetration test (Mayne, 2005)

Table 4.1 Software developed for post-processing of CPT data

Software	Developer	Operating System	Features	Website & Price
CONEPLOT	University of British Columbia	DOS	Plotting of raw cone data with full control of depth axis (vertical) and parameter scaling with 1 to 6 graphs in portrait or landscape.	http://www.civil.ubc.ca $200
CONEINT	University of British Columbia	DOS	Menu driven program for CPT and CPTU interpretation. Calculates different correlation parameters.	http://www.civil.ubc.ca $350
DCCONE	DC-Software Doster & Christmann	Windows	Plots cone resistance, sleeve friction, and friction ratio	http://www.dc-software.com $450
EDISON	Swedish Geotechnical Institute	Windows	Graphically presents the recorded CPT data and the derived parameters	http://www.geotek.se
INSITU	Geo&soft International	Windows	Calculates parameters, and the results can be exported in Microsoft Word 97 format	http://www.geoandsoft.com $450
CPTask	GeoMil Equipment B.V.	Windows	Calculates parameters from CPTu data and graphically present the results.	http://www.geomil.com
PlotCPT	GeoMil Equipment B.V.	DOS	Calculates and plots parameters	http://www.geomil.com
CPT-pro	Geosoft	Windows	Process multiple soundings in a project, and generate soil profile and site map	http://www.geosoft.com.pl $1500
Static penetrometer	Alpes-Geo-Conseil	Mac	Computes bearing capacity of soil for shallow and deep foundations from CPT data	http://www.alpesgeoconseil.com
Geo-Explorer	Gouda-Geo Equipment	Windows	Record and display data CPT data	http://www.gouda-geo.com $1600
Static Probing	GeoStru Software	Windows	Calculates and plots parameters, and computes bearing capacities of shallow and deep foundations	http://www.geostru.com $300

Nowadays, most engineers would rather make their own Excel spreadsheet, and input the correlation equations by themselves for the purpose of post processing SCPTu data and determining the parameters. It is common to find that engineers dealing with SCPTu data have various Excel spreadsheet templates for different purposes. Geotechnical engineers like Excel spreadsheet, because it has powerful features in both calculation and graphing. However, the disadvantage of Excel is that different templates need to be developed, even if sometimes there are only minor differences.

In this thesis, a free software program (*InSituData*) is developed for post-processing of SCPTu data. It has an interface with Excel but provides much more convenience in the setup, choice of parameters, and post-processing of in-situ test data. Based on SCPTu data, it can classify the soils into different categories, and then derive a much broader suite of soil engineering parameters from the correlations recommended by the author. It can also perform liquefaction analysis based on cone tip resistance (q_T) and shear wave velocity (V_s). *InSituData* also allows the user to easily add new relationships that become available. The software can communicate with Microsoft Excel installed on the user's computer easily, thus allowing the users taking advantages of features of both *InSituData* and Excel.

4.2 Soil Classification

As discussed in Chapter 3, geostratigraphy and soil classification are the basis for all subsequent geotechnical analysis and calculations. In the software *InSituData*, soil

classification is performed based on soil classification charts suggested by Robertson et al. (1986).

4.3 Parameters from SCPTu Data

Mayne (2001, 2005) has summarized selected soil engineering parameters that can be derived from SCPTu data. The specific correlations that are self-contained and implemented within *InSituData* to derive parameters are presented herein.

4.3.1 Unit Weight γ

Compiled data of saturated unit weights (γ_{sat}) and shear wave velocities (V_s) from all types of saturated geomaterials ranging from clays to silts and sands to gravels (Figure 4-2) found the following trend (Mayne, 2001):

$$\gamma_{sat} = 8.32 \log V_s - 1.61 \log z \qquad (4\text{-}1)$$

where γ_{sat} is the saturated unit weight in kN/m^3, V_s in m/s, and z is the depth in meters. Based on such correlation, the saturated unit weight of soils can be calculated.

The shear wave velocity of dry sands has been found to be primarily a function of void ratio (e) and confining stress (σ_0'), based on results of resonant-column tests (Richart et al., 1970). As dry unit weight $\gamma = G_s \gamma_w / (1 + e)$, where G_s is the specific gravity and γ_w is unit weight of water, γ can be estimated by assuming $G_s = 2.7$. The equivalent depth (z) corresponding to the confining stress (σ_0') can be estimated from $z = \sigma_0' / \gamma$. Therefore,

114

dry unit weight (γ) can be correlated with shear wave velocity (V_s) and the depth (z) by the following equation (Figure 4.3):

$$\gamma = 26.9 \log V_s - 7.4 \log z - 42.1 \qquad (4\text{-}2)$$

where γ is in kN/m^3, V_s in m/s, and z is in meters.
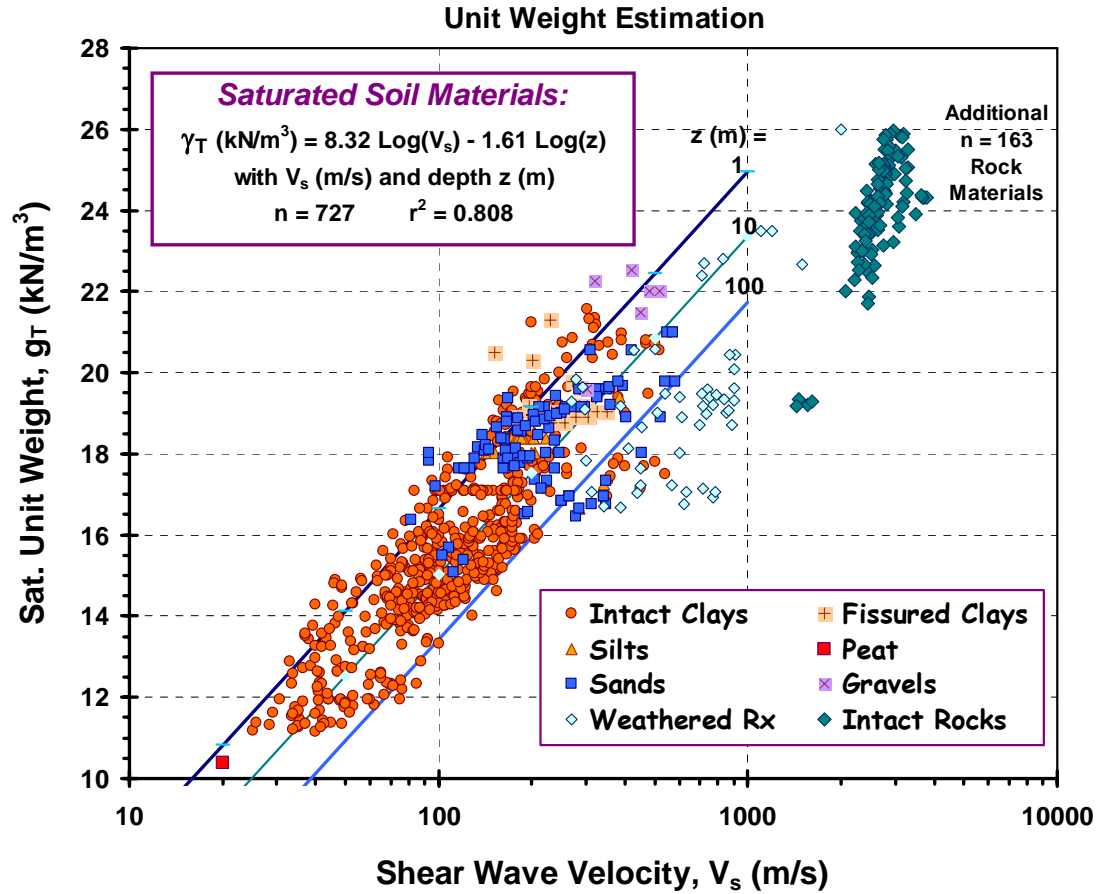
Figure 4.2 Correlation for saturated unit weight from depth and shear wave velocity, V_s (Mayne, 2001)

Hardin and Black (1969) noticed that the correlation among small strain shear modulus G_{max}, void ratio e, and confining stress σ_0', which were originally developed for clean sands, also worked well for normally consolidated clays. As $G_{max} = \rho_T V_s^2$, where

115

$\rho_T = \gamma_T / g$ is total mass density, it is expected that equation (4-2) can also be applied to

dry clays, at least for a first approximation.
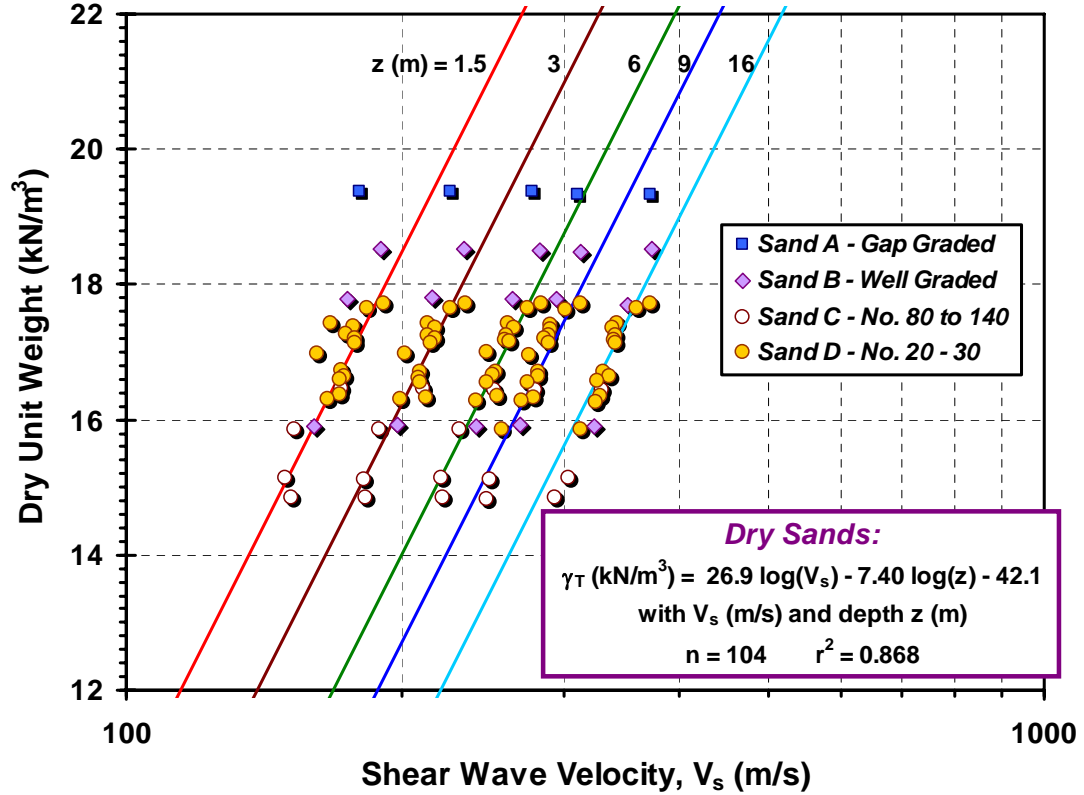
Figure 4.3 Correlation for dry unit weight from depth and shear wave velocity, V_s [data from Richart et al. (1970)]

The total unit weight (γ_T) is equal to saturated unit weight (γ_{sat}) for soils beneath the

groundwater table, and it is equal to dry unit weight (γ) for sands above groundwater

table. As to clayey soils above ground water table, their total unit weight (γ_T) and shear

wave velocity (V_s) are related to the saturation degree caused by capillarity effect (Cho &

Santamarina, 2001). Thus, the situation may be much more complex and different. In

some cases, the clays are fully saturated due to full capillarity.

Since the total unit weight (γ_T) can be estimated from shear wave velocity (V_s), the total and effective overburden stresses (σ_{vo} and $\sigma_{vo}{}'$) can thus be calculated using $\sigma_{vo} = \int_0^z \gamma_T dz$, $u_0 = \gamma_w(z - GWT)$, and $\sigma_{vo}{}' = \sigma_{vo} - u_0$, where γ_w is the unit weight of water, GWT is groundwater table, u_0 is the hydrostatic porewater pressure, and z is the depth. If the measured V_s is not available, its value can be estimated by correlating with tip resistance q_T, which will be discussed in the following subsection.

4.3.2 Shear Wave Velocity V_s

In SCPTu soundings, the shear wave velocity (V_s) is directly measured, using either true- or pseudo-interval at 1-m depth increments. As this is made easier by autoseis sources and post-processing with ShearPro, this is the preferred approach. However, for CPTu soundings with no seismic data, correlation equations are available relating V_s with the CPTu data. Based on studies of two Italian sands (Figure 4.4), Lai & Lo Presti (1988) and Baldi et al. (1989) correlated V_s with q_T and effective overburden stress σ'_{v0} for uncemented and unaged clean quartz sands as follows,

$$V_s = 277(q_T)^{0.13}(\sigma'_{v0})^{0.27}$$
(4-3)

where V_s is in m/s, and q_T and σ'_{v0} are in MPa .

117

Mayne & Rix (1995) compiled both CPTu data and V_s measurements from 31 different clay sites, and proposed the following first-order correlation equation based on a statistical study as shown in Figure 4.5:

$$V_s = 1.75(q_T)^{0.627} \tag{4-4}$$

where V_s is in m/s, and q_T in MPa . They found much better estimates if V_s was evaluated from q_T, void ratio (e_0), and degree of continuity (i.e., intact vs. fissured).
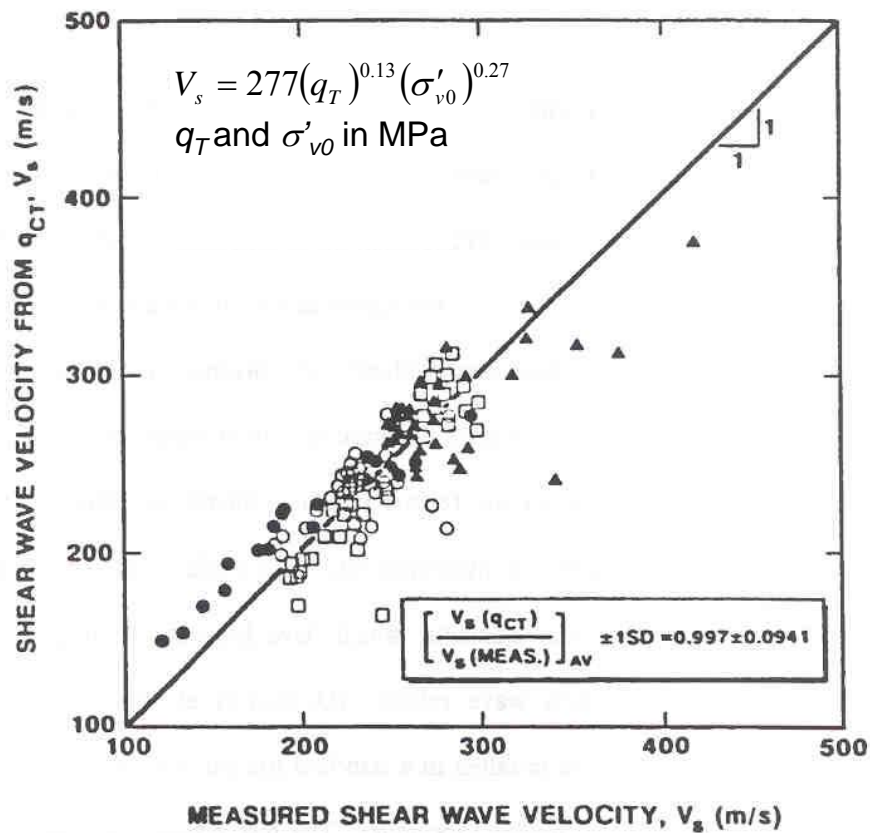
Figure 4.4 Relationship between shear wave velocity and cone tip resistance based on two kinds of Italian sands (Lai & Lo Presti, 1988; Baldi et al., 1989)
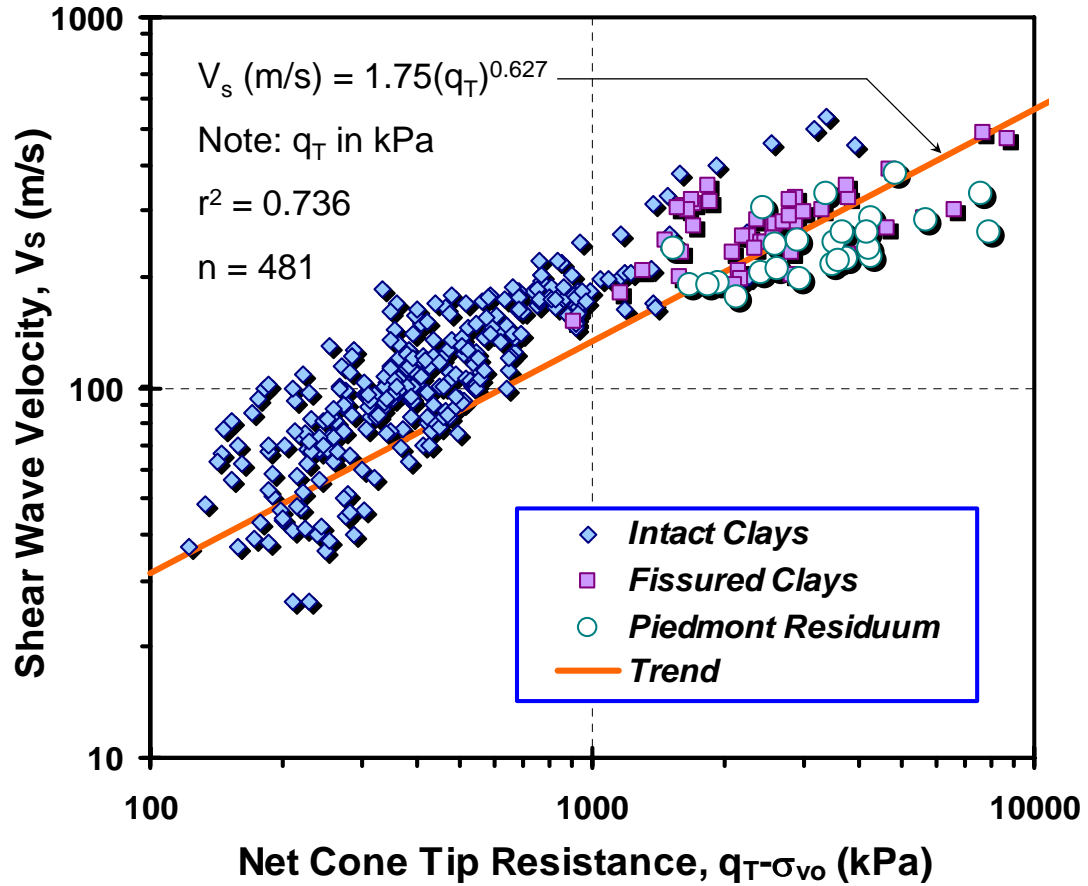
Figure 4.5 Correlation between shear wave velocity and cone tip resistance in clays (Mayne & Rix, 1995)

Based on compiled data from 61 sites including clays, sands, and intermediate soil types, Hegazy & Mayne (1995) suggested the following correlation for all soil types:

$$V_s = \left[10.1\log(q_T) - 11.4\right]^{1.67}\left(100\frac{f_s}{q_T}\right)^{0.3} \quad (4\text{-}5)$$

where V_s is in m/s, and q_T and f_s are both in kPa.

Even though V_s is measured in a downhole manner directly during SCPTu, there are other uses for these correlative relationships. For instance, they can serve as a check to investigate whether the soils are non-cemented or infer whether cementation is present

(e.g. Lunne et al., 1997). Also, in partially saturated soils, the magnitude of V_s can greatly increase during de-saturation (Cho & Santamarina, 2000). Therefore, a more critical situation can be encountered (i.e. fully saturated) when the groundwater table rises and/or in period of heavy rain fall infiltration. In addition, they can aid in a more definitive soil behavioral type, such as charts utilizing Q vs G_{max}/q_T (Lunne et al., 1997).

4.3.3 Normalized Cone Penetration Measurements

Based on equations (3-1) to (3-3), the cone penetration measurements (q_T, u_2, f_s) are normalized to (Q, B, F). These normalized parameters can be used for deriving other parameters, such as soil behavior index I_c and peak friction angle ϕ'.

4.3.4 Soil Behavior Index I_c

The soil behavioral type index I_c can be used to estimate fines content of the soil. It was originally calculated according to equation (3-16) (Jefferies & Davies, 1991), but then modified to equation (3-17) (Robertson & Wride, 1998). The latter equation is used in *InSituData* to derive this parameter, for it is contained within the soil classification scheme proposed by Robertson (1990, 1991) and liquefaction evaluation procedure by Robertson & Wride (1998).

4.3.5 Peak Friction Angle ϕ'

Based on statistical analyses of CPT calibration chamber data corrected for boundary effects, Kulhawy & Mayne (1990) suggested that in clean quartzitic sandy soils, the peak friction angle ϕ' can be approximated by the following equation:

$$\phi' = 17.6^o + 11.0\log(q_{T1}) \tag{4-6}$$

where ϕ' in degrees, $q_{T1} = \left(q_T/\sigma_{atm}\right)\!\Big/\!\left(\sigma_{vo}'/\sigma_{atm}\right)^{0.5}$, σ_{v0}' is the effective overburden stress, and σ_{atm} is atmosphere pressure (σ_{atm} = 1 bar $\approx$ 1tsf $\approx$ 100kPa).

More recently, drained triaxial compression tests have been performed on undisturbed samples of carefully-frozen sands from four river sites (Mimura, 2003). The measured ϕ' values were found to agree well with those inferred from the cone tip resistance based on equation (4-6), as shown in Figure 4.6 (Mayne, 2005). Equation (4-6) also provides excellent agreement with the ϕ' values measured from consolidated triaxial tests on samples recovered from silty sand of the Piedmont geology (Figure 4.7).

In order to interpret ϕ' from SCPTu data in clay, the NTH method has been developed to provide an effective stress-limit plasticity solution for undrained penetration (Senneset et al., 1989). For the classical bearing capacity case, Figure 4.8 shows the theoretical relationship between ϕ' and the cone resistance number N_m that is defined by the following:

$$N_m = \left(q_T - \sigma_{v0}\right)\!\Big/\!\left(\sigma_{v0}' + a'\right) \tag{4-7}$$

where σ_{v0} is the overburden stress, $a' = c'\cot\phi'$ is attraction, and c' is the effective cohesion intercept. For the simplified case where $a' = 0$, N_m equals the normalized cone tip resistance $Q = (q_T - \sigma_{v0})/\sigma_{v0}'$. Mayne (2005) suggested an approximate deterministic expression for normalized porewater pressure values: $0.1 < B < 1.0$ as following:

$$\phi' = 29.5B^{0.121}(0.256 + 0.336B + \log Q) \tag{4-8}$$

which is valid for ranges of friction angle: $20^o \leq \phi' \leq 45^o$.
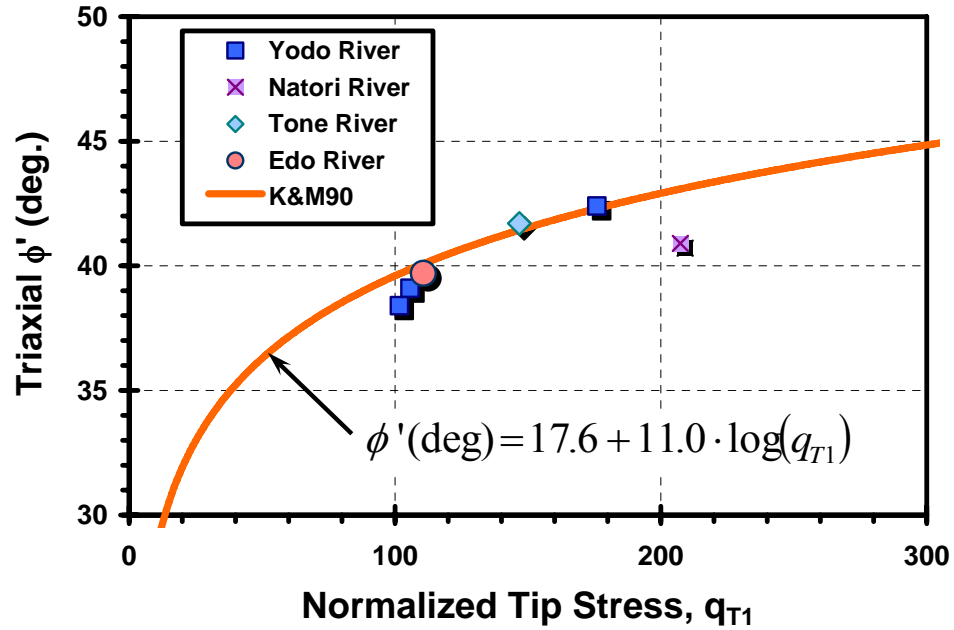
Figure 4.6 Comparison of measured ϕ' from frozen sand samples with that inferred from CPT normalized tip resistance (Mayne, 2005)

Note: $q_{T1} = (q_T/\sigma_{atm})\Big/\left(\sigma_{vo}'/\sigma_{atm}\right)^{0.5}$
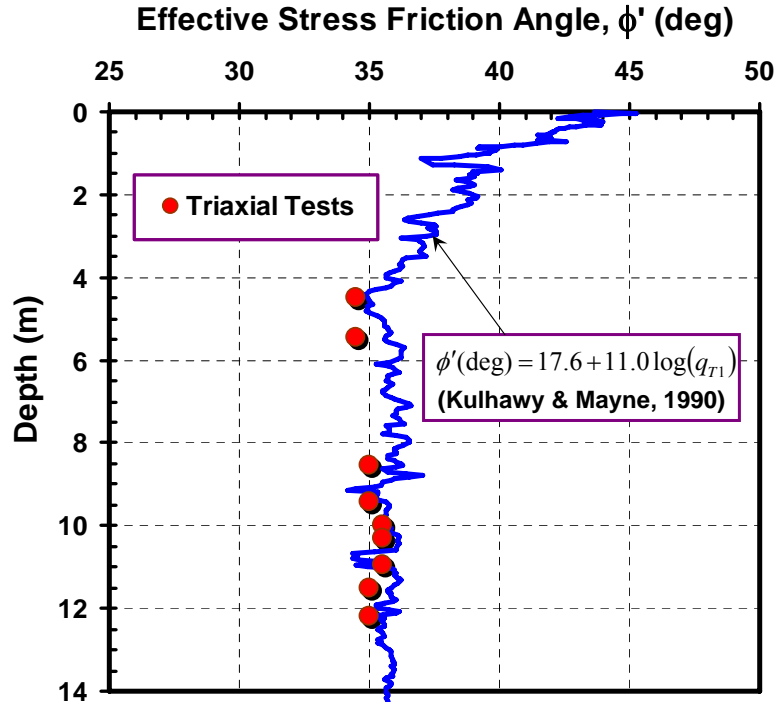
Figure 4.7 CPT profiling of ϕ' in silty sand (30% fines) in Atlanta, Georgia (Mayne, 2001)
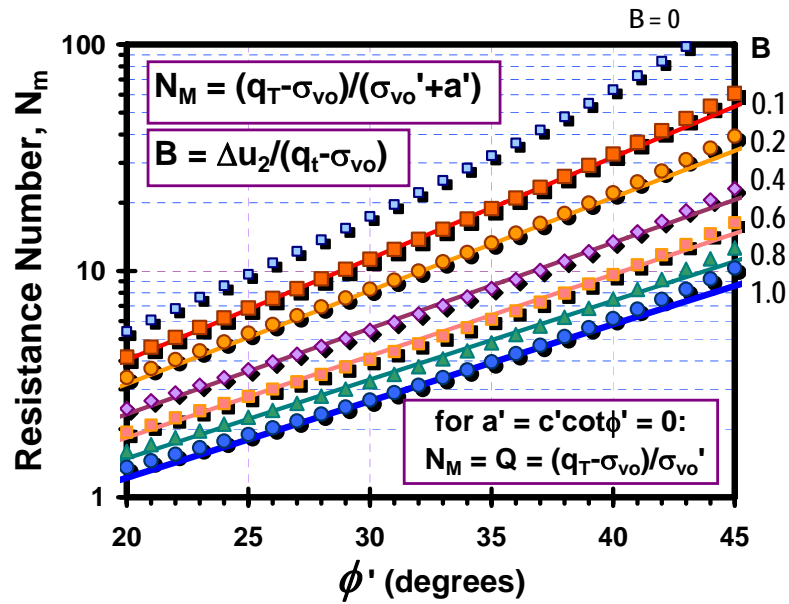
$$For \ \ 0.1 < B < 1.0 \ and \ \ Range \ : \ 20° < \phi' < 45°$$

$$\phi' \approx 29.5 \cdot B^{0.121} \cdot \left[0.256 + 0.336 \, B + \log(N_m) \right]$$

Figure 4.8 Effective ϕ' (dots) from NTH undrained penetration theory (Senneset et al., 1989) and simplified approximation (lines) (Mayne, 2005)

123

4.3.6 Lateral stress coefficient K_0 and overconsolidation ratio OCR

Based on a statistical evaluation of 26 different series of calibration chamber tests, the effective lateral stress σ_{h0}' in clean quartz sands can be estimated from CPTu data using the empirical correlation shown Figure 4.9. Therefore, the lateral stress coefficient K_0 can be expressed by the following equation:

$$K_0 = \frac{\sigma_{h0}'}{\sigma_{v0}'} = 0.19 \left(\frac{q_T}{\sigma_{atm}} \right)^{0.22} \left(\frac{\sigma_{v0}'}{\sigma_{atm}} \right)^{-0.31} OCR^{0.27} \tag{4-9}$$

where σ_{v0}' is the effective overburden stress, σ_{atm} is atmosphere pressure, and OCR is the overconsolidation ratio, defined as the ratio of the preconsolidation stress σ_p' to the existing overburden stress σ_{v0}'.

$$\sigma_{ho}' = 0.30 \, q_T^{0.22} \sigma_{vo}'^{0.69} OCR^{0.27}$$
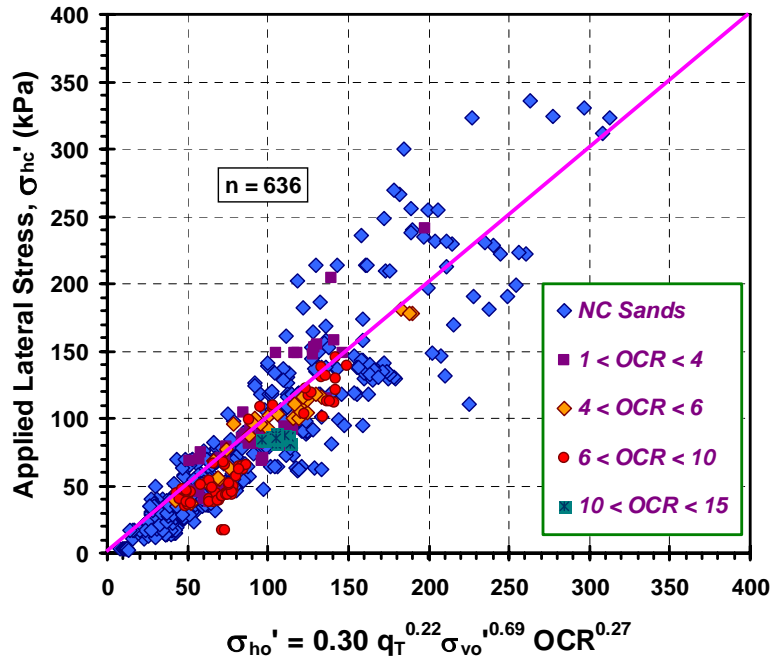
Figure 4.9 CPT calibration chamber relationship for evaluating lateral stresses in unaged clean quartz sands (Mayne, 2001)

Note: σ_{h0}' and σ_{v0}' are in units of kPa and q_T is in MPa

From laboratory studies, the lateral stress coefficient K_0 for soils that are not highly structured or cemented can be calculated from their overconsolidation ratio OCR:

$$K_0 = (1 - \sin \phi')OCR^{\sin \phi'} \tag{4-10}$$

Solving equations (4-9) and (4-10) provides the following solution for OCR in sands (Mayne, 2001):

$$OCR = \left[\frac{0.192}{(1 - \sin \phi')} \frac{(q_T / \sigma_{atm})^{0.22}}{(\sigma_{vo}' / \sigma_{atm})^{0.31}} \right]^{1/(\alpha - 0.27)} \tag{4-11}$$

where $\alpha = \sin \phi'$.

For clays, Mayne (1991) used spherical cavity expansion theory and critical state soil mechanics concepts to relate the OCR to CPT data, and suggested the following equation to evaluate the preconsolidation stress σ_p':

$$\sigma_p' \approx \frac{q_T - \sigma_{v0}}{M\left(1 + \frac{1}{3} \ln I_R\right)} \tag{4-12}$$

where $M = 6\sin \phi'/(3 - \sin \phi')$, and $I_R = G/s_u$ = rigidity index. Adopting representative values of $\phi' = 30^o$ (M=1.2) and $I_R = 100$, equation (4-12) becomes:

$$\sigma_p' = 0.33(q_T - \sigma_{vo}) \tag{4-13}$$

The equation provides excellent agreement with the CPTu-oedometer data involving a variety of different clays, as shown in Figure 4.10. Thus, as a first approximation the OCR in clays can be estimated from the following correlation (Mayne, 2005):

$$OCR = 0.33(q_T - \sigma_{vo})/\sigma_{vo}' \tag{4-14}$$

Since the effective friction angle ϕ' and the OCR can be derived, the lateral stress coefficient K_0 can be estimated using equation (4-10).
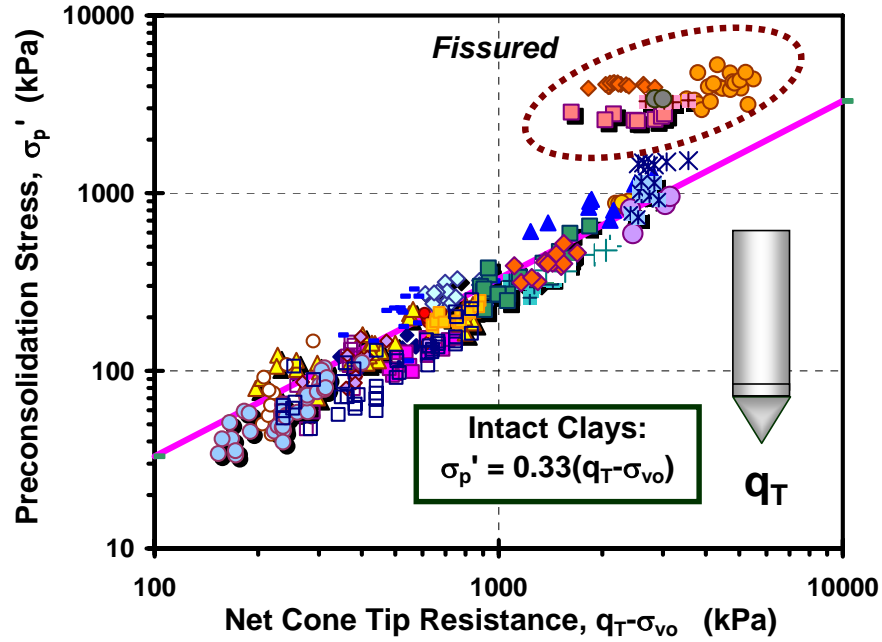
Figure 4.10 Preconsolidation stresses in clay from net tip resistance
(Kulhawy & Mayne, 1990)

4.3.7 Relative Density D_R

Relative density (D_R) only applies to sands with fines content FC < 16%. Based on calibration chamber studies, the relationship between relative density D_R of clean sands and CPTu data is suggested to be of the following form (Kulhawy & Mayne, 1991):

$$D_R = 100\sqrt{\frac{q_{T1}}{Q_F \cdot OCR^{0.2}}} \qquad (4\text{-}15)$$

where D_R is in percentage (%), Q_F is the overall cone factor (average $Q_F = 305$ for 26 types of sands), and $q_{T1} = \left(q_T / P_a\right) \Big/ \left(\sigma_{vo}' / P_a\right)^{0.5}$. Figure 4.11 summarized the calibration chamber studies on the correlation between D_r and the cone tip resistance. The parameter Q_F varies from 280 for high compressibility sands to 332 for low compressibility normally consolidated sands. These relationships can be quantified approximately as following (Kulhawy & Mayne, 1991):

$$D_R = 100\sqrt{\frac{q_{T1}}{305 OCR^{0.2}}} \qquad (4\text{-}16)$$
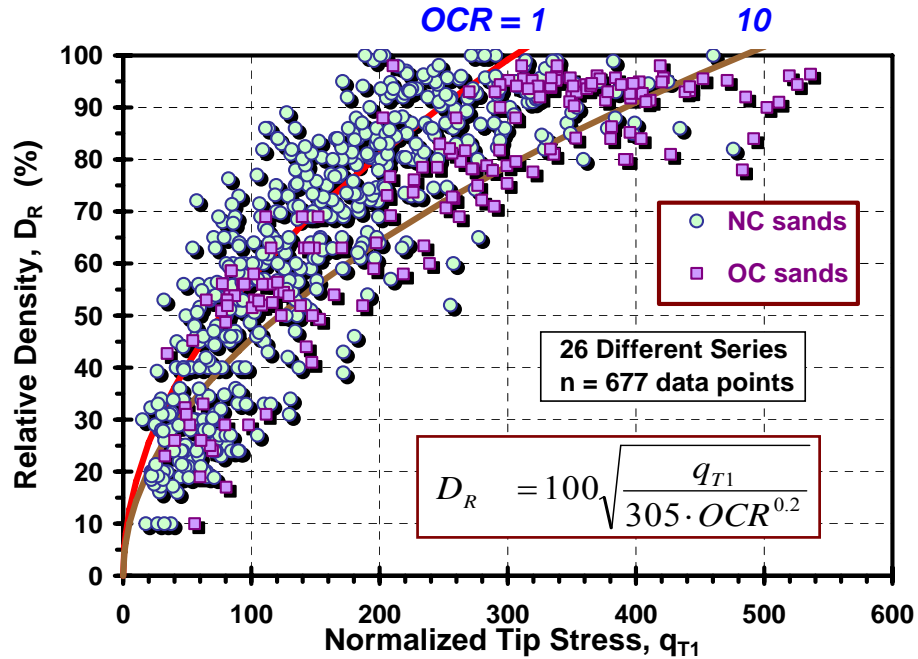
Figure 4.11 Summary of calibration chamber studies on the correlation between relative density and normalized cone tip resistance in clean quartz sands
(after Kulhawy & Mayne, 1990)

4.3.8 Undrained Shear Strength s_u

Based on a critical state soil mechanics approach, Mayne (2005) suggested evaluating the undrained shear strength s_u of clay as following:

$$s_u = \frac{1}{2}\sigma_{v0}{}' \sin\phi' OCR^\Lambda \qquad (4\text{-}17)$$

where the strength mode represents that in direct simple shear (DSS), $\Lambda = 1 - C_s/C_c =$ plastic volumetric strain potential (Wroth, 1984), $C_s =$ swelling index, and $C_c =$ virgin compression index. For "normal" unstructured clays, Λ is about 0.8, and increases to $\Lambda = 1$ for structured and sensitive soils. Figures 4.12 and 4.13 show the dependency of $s_u/\sigma_{v0}{}'$ on ϕ' for normally consolidated and overconsolidated DSS data, respectively. The effect of fissuring is important too, as illustrated in Figure 4.13, as it can reduce s_u by a factor of 2 or more, depending upon the degree of cracks and fissures.
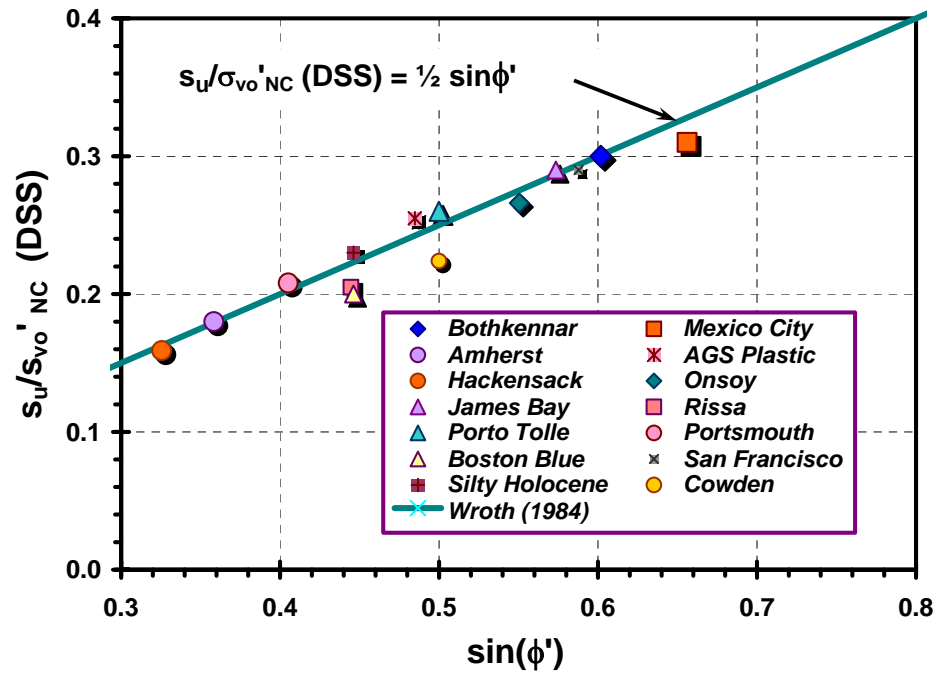
Figure 4.12 Normalized undrained strength with ϕ' for normally consolidated clays (Mayne, 2005)
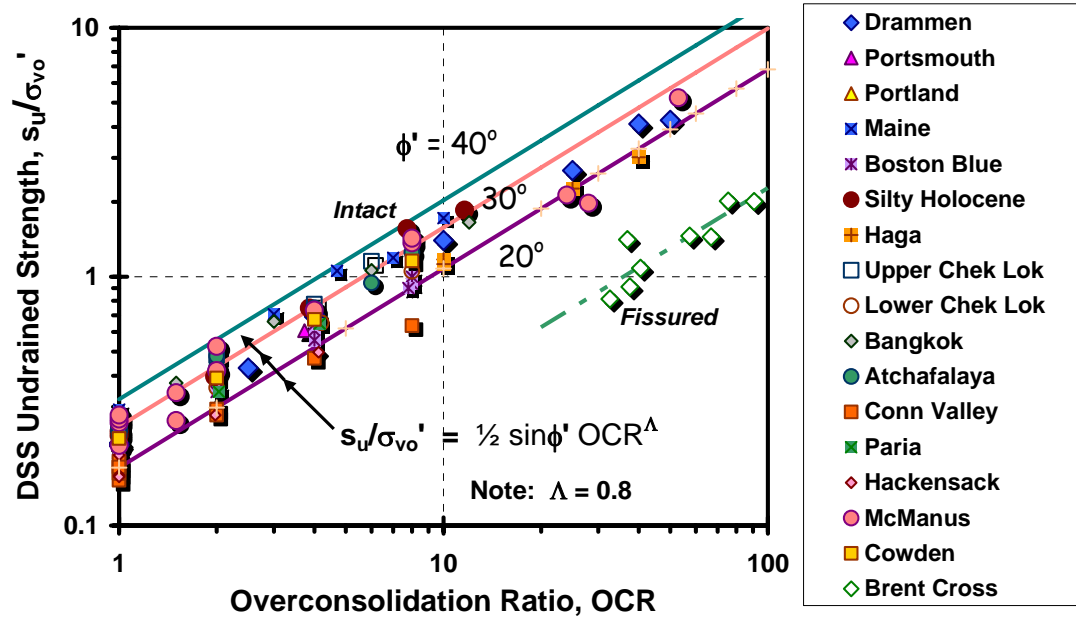
Figure 4.13 Normalized undrained strength with OCR and ϕ' for intact and fissured overconsolidated clays (Mayne, 2005)

4.3.9 Small-Strain Modulus

As mentioned in Chapter 2, the small-strain shear modulus can be derived from the equation $G_{max} = \rho_T V_s^2$, where ρ_T is the unit mass density. The corresponding small-strain Young's modulus can be determined from $E_{max} = 2G_{max}(1+\nu)$, where ν is the Poisson's ratio. The Poisson's ratio ν is about 0.2 for sands and clays under drained conditions, and it is equal to 0.5 for clays and silts for undrained conditions.

4.3.10 *Parameters Related to Liquefaction Evaluation*

The software, *InSituData*, can also compute parameters related to liquefaction evaluation, such as stress-normalized cone tip resistance (q_{c1N}), the grain-characteristic correction factor (K_c) for apparent fines content (FC), equivalent clean sand stress-normalized penetration resistance [$(q_{c1N})_{cs}$], and cyclic resistance ratio (CRR) in the event of earthquake of moment magnitude 7.5 ($CRR_{7.5}$). These parameters will be discussed further in Chapter 5.

4.4 Software to Automate Post-processing of the SCPTu Data - *InSituData*

The software program (*InSituData*) is developed to automate post-processing of cone penetration data. It is written with Visual Basic, and runs in operating systems such as Windows 98/2000/XP. The launcher interface for *InSituData* is shown in Figure 4.14.

Figure 4.14 Launcher interface for the software *InSituData*

The user can input either $CPTu_2$ or $SCPTu_2$ data into the program. The raw data can be loaded into the software from ASCII test type files. After the data file is selected [Figure

4.15 (a)], the content of the file is displayed in the window as shown in Figure 4.15 (b). By specifying the number of title lines in the data file, the header of the file which is not data input can be excluded from loading into the software.Alternatively, *InSituData* can also accept raw data by copying from Excel spreadsheet and paste them in the software.

As an example, the raw SCPTu data (depth, q_c, f_s, u_2, V_s) collected at the Walker site in Marked Tree, Arkansas, is processed here. This site will be discussed in more details later in Chapter 6. Figure 4.16 shows that the raw data are pasted into the software after copying from an Excel spreadsheet. By clicking on the cells in the "Assign Data Columns" window, the columns can be named after the selection of the user from the pull-down list. They can also be named after what is typed in the cells by the user. The units of the data columns are specified here by selecting from the pull-down list. If the names and units of the columns have been set as default, they can be loaded as default. The values of the ground water table (GWT), net area ratio (a_n), and other related information can be specified on the main form of the program.

After the data columns are named, the "Calculate" button in the tool bar of the software is enabled. By clicking this button, the "Calculate Parameters" window pops out [Figure 4.17 (a)]. The water table is input here, and the parameters of interest to the user can be selected for computation. The parameters are calculated using the correlations recommended by the user herein. Figure 4.17 (b) shows the software interface with data columns corresponding to the calculated parameters added in.
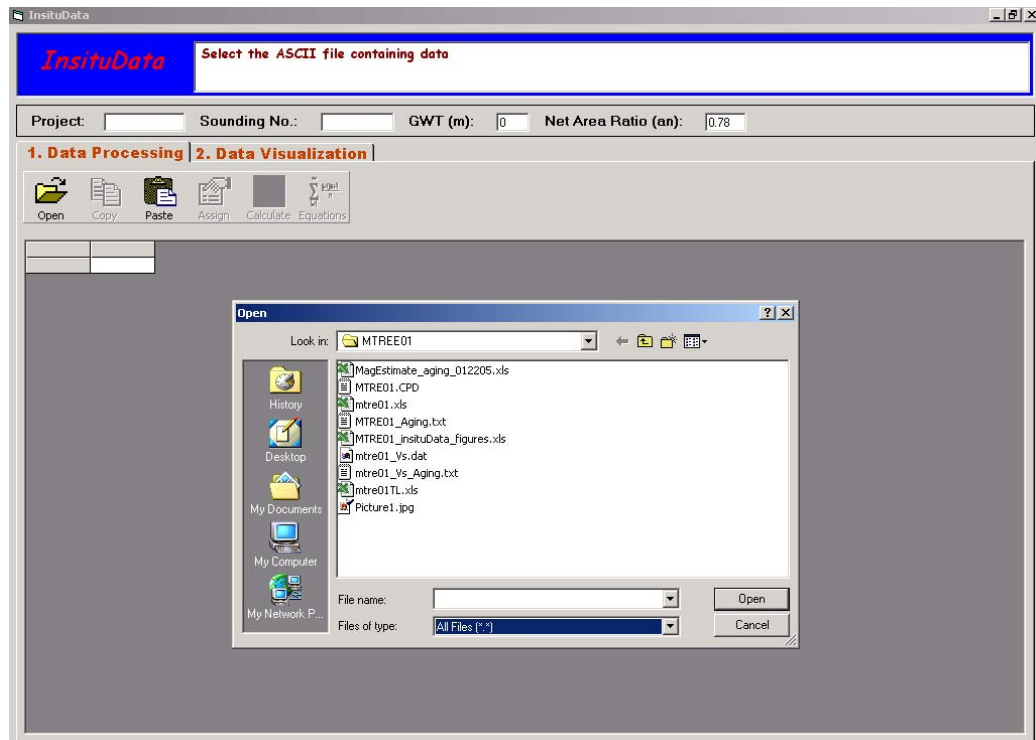
(a)
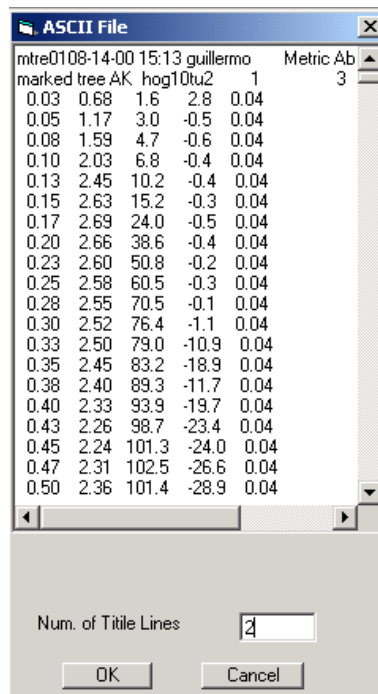
(b)

Figure 4.15 Load raw CPTu data into the software *InSituData*: (a) Open the file containing raw CPTu data; (b) Displaying raw CPTu data
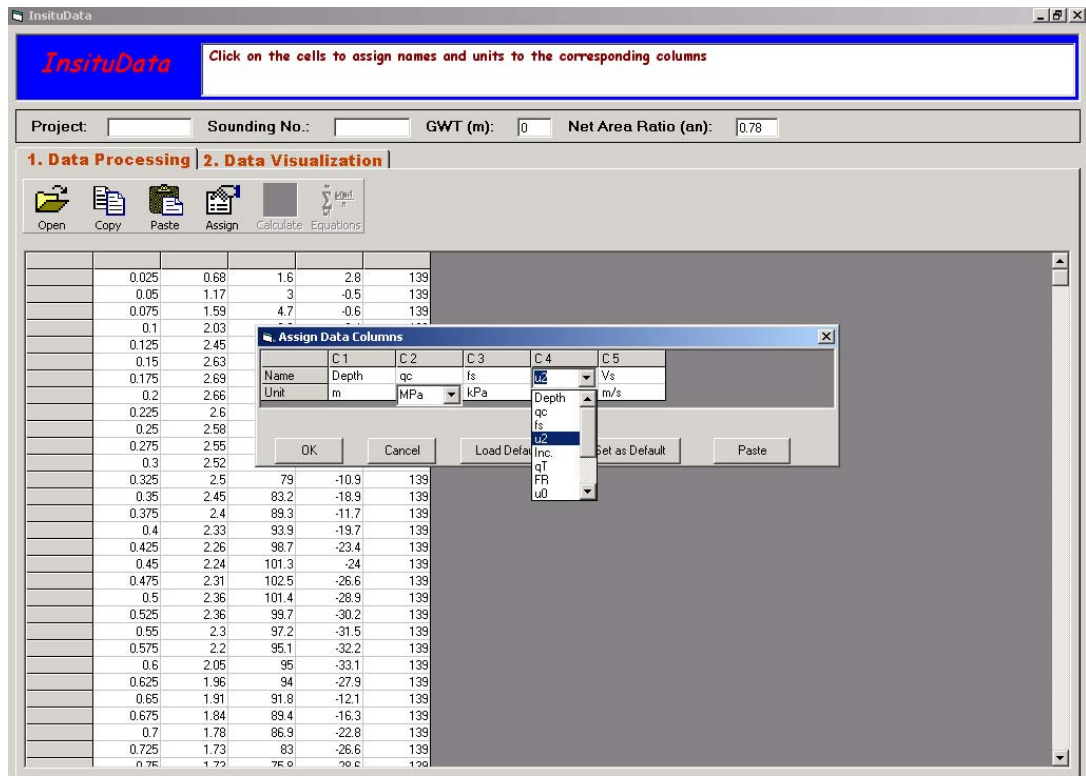
Figure 4.16 Assign names and units to the data columns after they are loaded into the software *InSituData*

To give the user more flexibility, the software allows the user to define the preferred correlation equations (Figure 4.18). The name of the parameter and the formula are input through the "Equations" window. Unlike that in Excel, the equations contained within *InSituData* use variables, making them more straightforward. The user-defined equations can be saved for future use. By selecting the equations saved before, the same parameters can be calculated repeatedly for additional soundings.
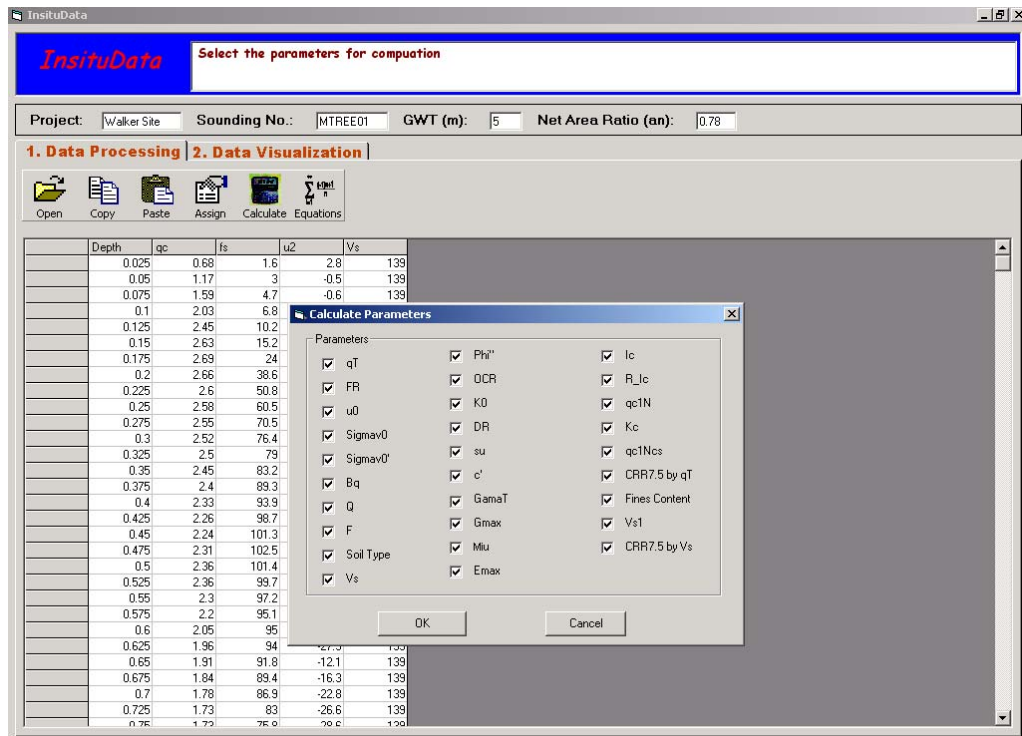
(a)
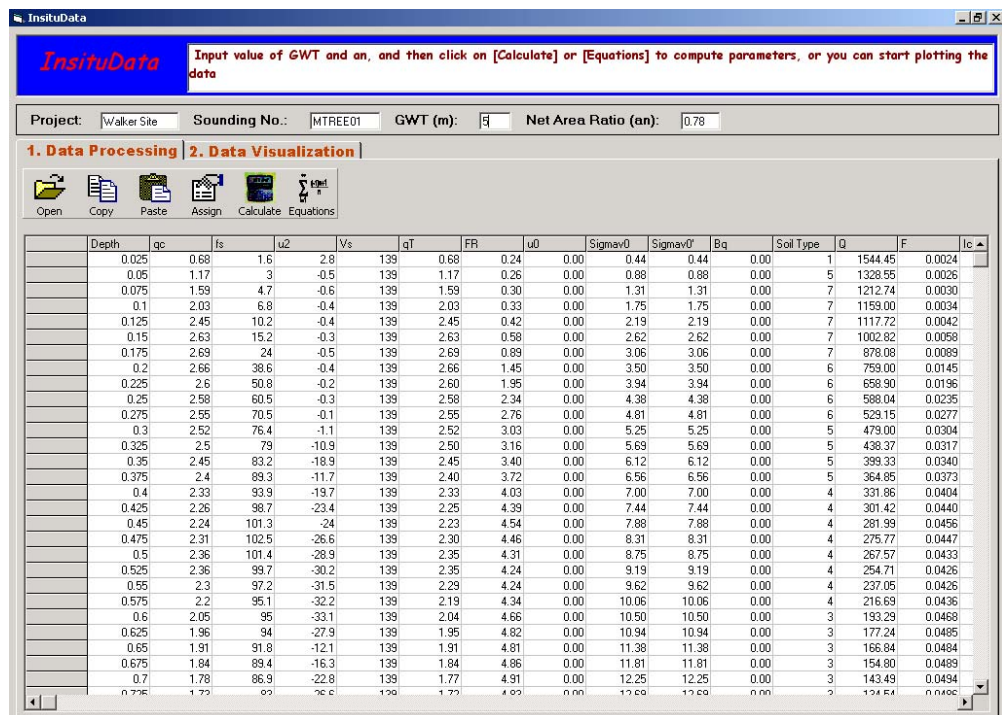
(b)

Figure 4.17 Calculate parameters from the raw CPT data: (a) Select the parameters to calculate; (b) Calculated parameters displayed.
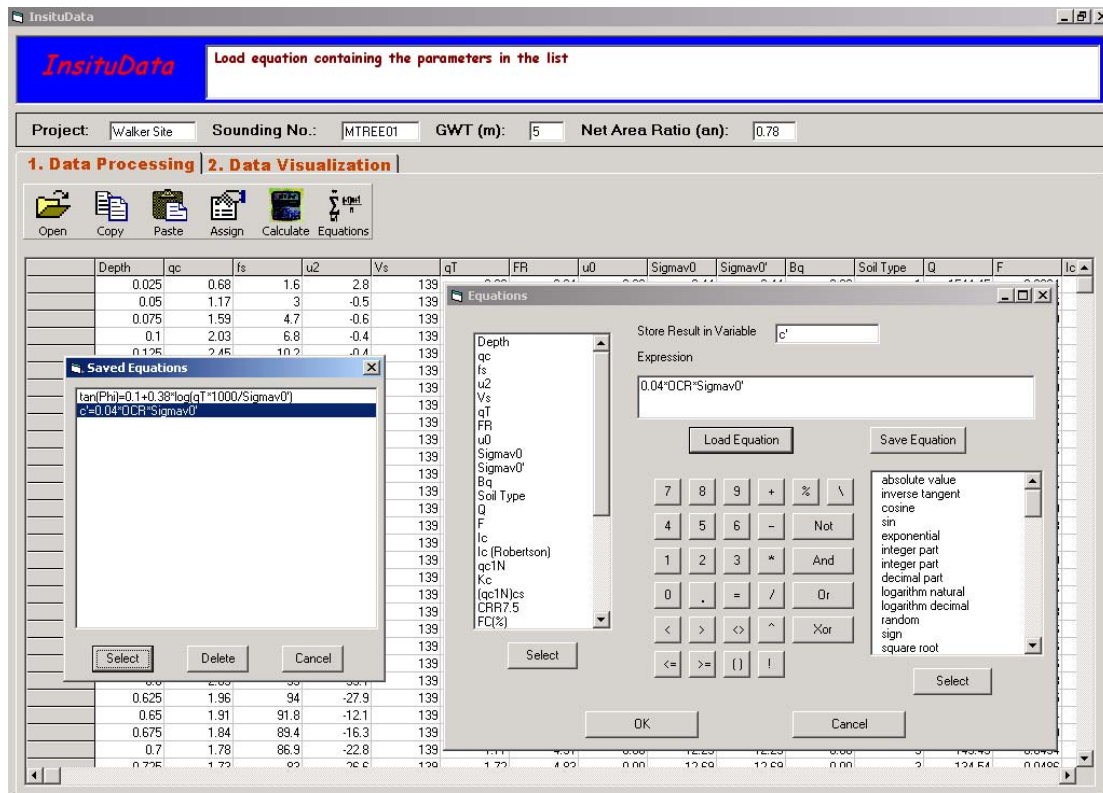
Figure 4.18 Input equations into the software program *InSituData*

The parameters calculated by this software can be plotted in charts similar to those in Excel, as shown in Figure 4.19 (a). Charts can be generated and added as decided by the user. By setting these charts as default, the same charts are presented by default in the future for new raw input soundings. The "Properties" window pops out by double clicking on the charts, and properties of the charts can thus be configured. Configuring the chart properties in this software is similar to that in Excel.

By clicking the "Export to Excel" button on the tool bar, both the data and the charts generated in the software are output to a newly generated Excel spreadsheet. Figure 4.20 shows charts exported to Excel, after the sounding from the Walker site is processed by

the software and parameters are generated based on the correlation equations recommended by the author.
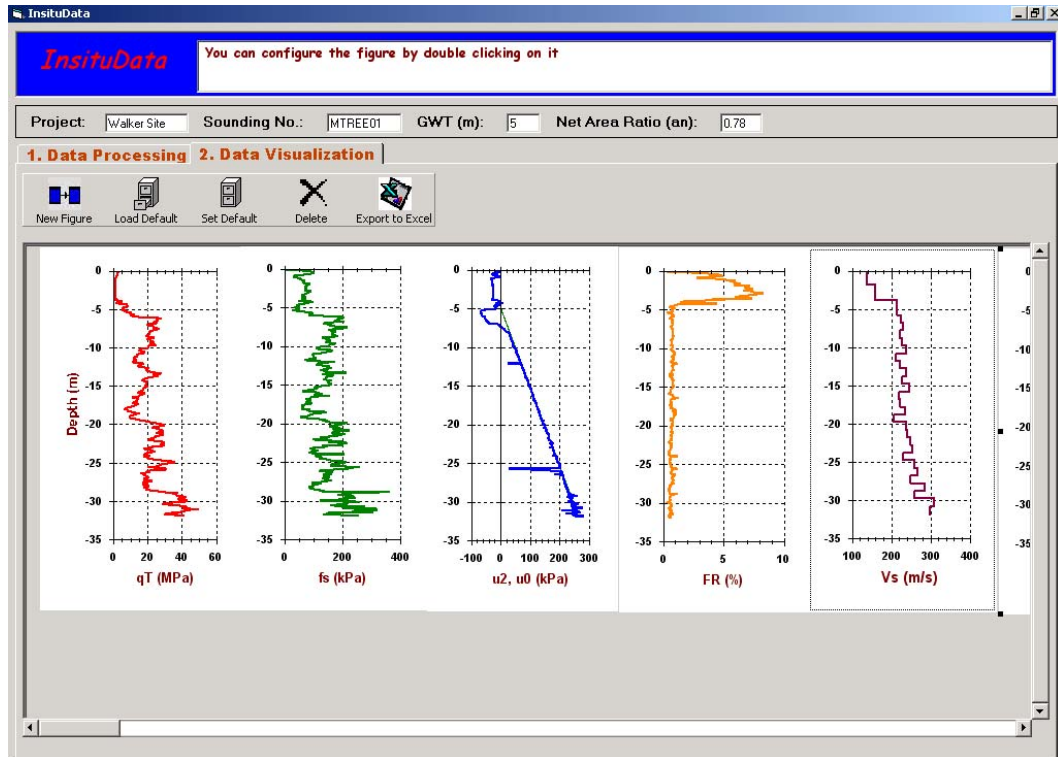
(a)
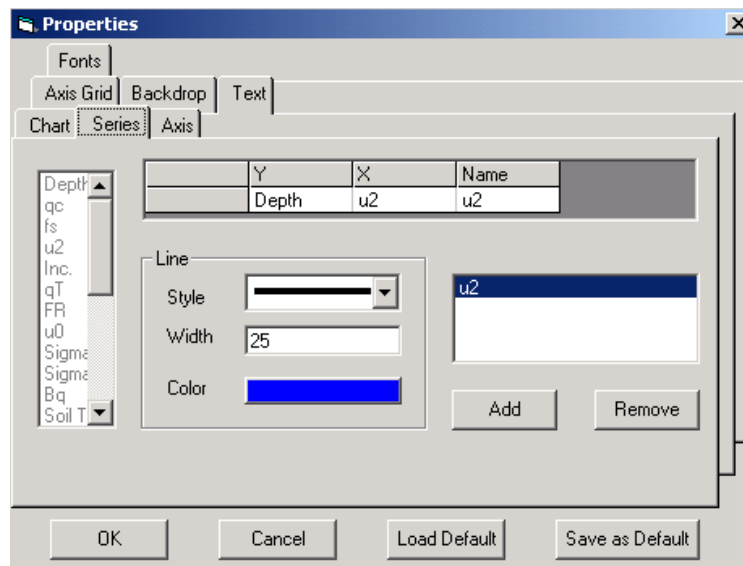
(b)

Figure 4.19 Visualization of SCPTu data and derived parameters in the software *InSituData*: (a) Display of the SCPTu data and derived parameters in separate plots; (b) Configuring of the plots.
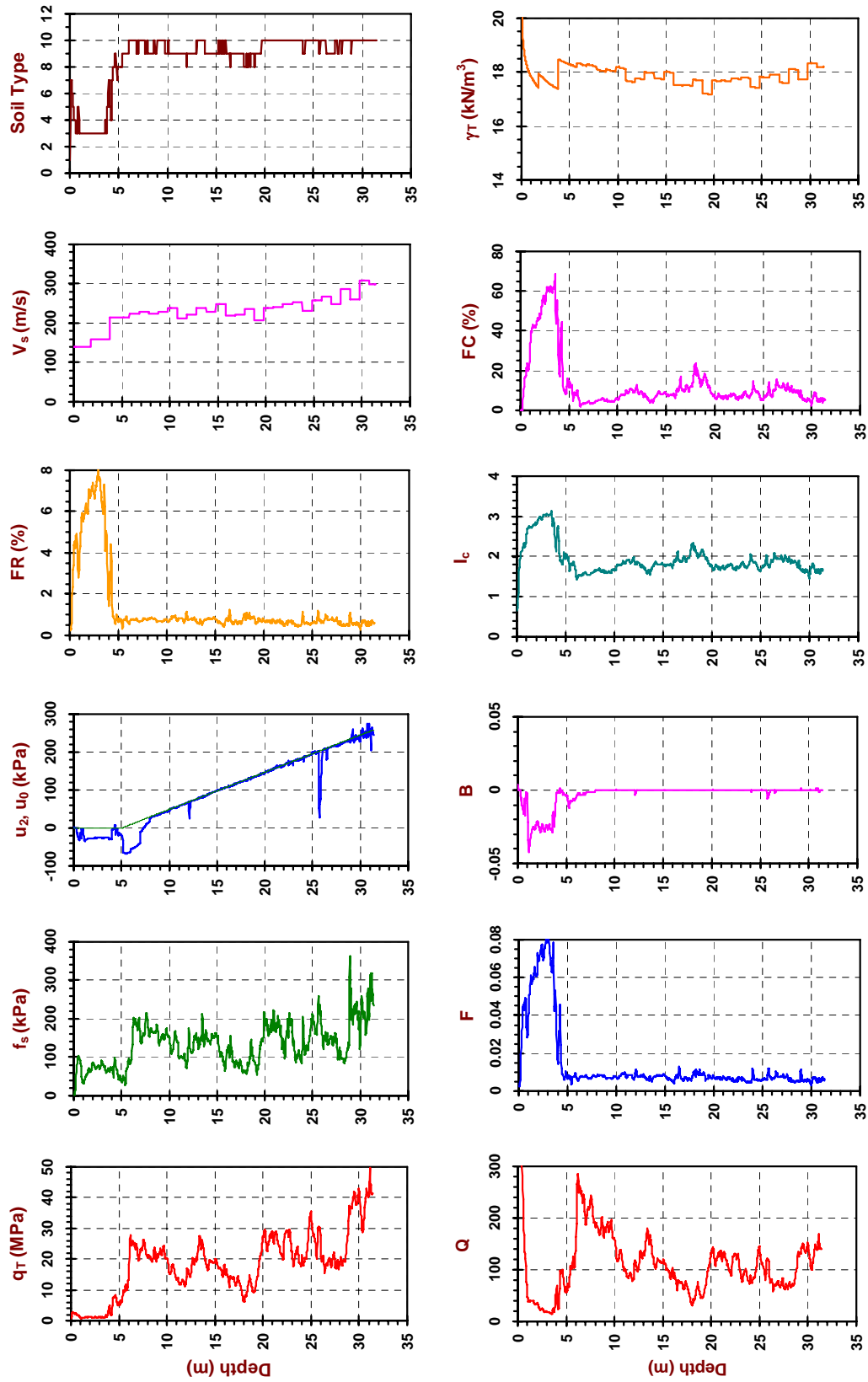
Figure 4.20 Plots of SCPTu data and derived parameters exported to Excel spreadsheet (Data from the Walker site in Marked Tree, AR)
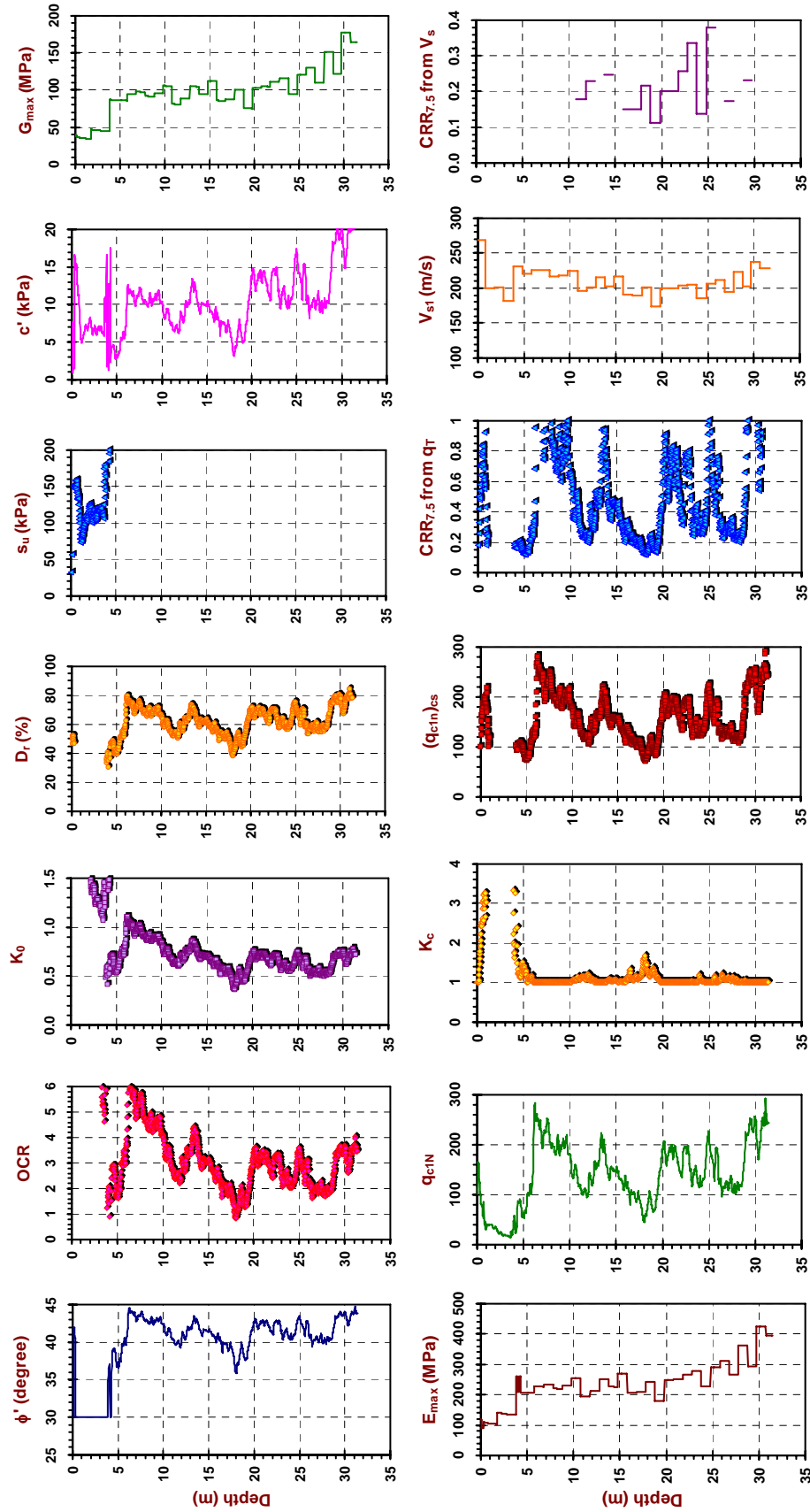
Figure 4.20 Plots of SCPTu data and derived parameters exported to Excel spreadsheet (Data from the Walker site in Marked Tree, AR) (Continued)

138

4.5 Summary

Software codes currently available for processing SCPTu data generally can only compute a small number of soil parameters. These few parameters can only be calculated from correlations implemented by the software developers, and many existing codes utilize older interpretative relationships, not the latest methods. A new free software program (*InSituData*) is developed to automate post-processing of SCPTu data. It provides soil classification and calculates more soil engineering parameters based on methods recommended by the author. It can also perform liquefaction analysis based on cone tip resistance and shear wave velocity. *InSituData* provides a convenient and easy means for the user to enter updated and new equations for CPT interpretation, as they become available. The equations use variables, which is more straightforward and make it easier to detect errors. Due to the popularity of Excel in engineering practice, the software has an interface similar to that of Excel, and can communicate with Excel easily. Finally, *InSituData* is downloadable as freeware and available for general use.

CHAPTER V

LIQUEFACTION EVALUATION METHODS BASED ON
SCPTU SOUNDINGS

5.1 Synopsis

Liquefaction is one of the major disruptions that threaten the safety of civil engineering structures during earthquakes. Figure 5.1 shows the tilted buildings resulted from liquefaction induced by the 1964 Niigata earthquake in Japan, the 1999 Kocaeli (Izmit) earthquake in Turkey, and the 1999 Chi-Chi earthquake in Taiwan, as well as the road cracking from the 2002 Alaska earthquake in the USA. As seismic waves generated by fault rupture propagate towards the ground surface, the structure of near-surface sediments is broken particularly by the cyclic shear waves. Sandy soils that are water-saturated and loosely packed will tend to compact, leading to an increase in porewater pressure. If porewater pressure increases to the point that it equals the overburden stress, the sediment liquefies and can behave like a viscous liquid (Seed and Lee, 1967).

Extensive research has been conducted in the laboratory on the liquefaction response of sandy soils. In laboratory tests, the seismic demanding of the soils is usually expressed in terms of cyclic stress ratio $CSR = \tau / \sigma_0'$, where σ_0' is the effective confining stress. For simple shear test, τ is the applied horizontal shear stress, whereas in triaxial test, $\tau = (\sigma_1 - \sigma_3)/2$, where σ_1 and σ_3 are the maximum and minimum principle stresses, respectively. It is found that for a certain number of stress cycles, the threshold stress ratio that causes initial liquefaction increases with relative density D_R, as shown in Figure

5.2. The relative density D_R in sandy soils has been correlated with results from field tests, such as the blow count N from standard penetration tests (SPT), the tip resistance q_T from cone penetration test (CPT), the horizontal stress index K_D from dilatometer test (DMT), and the shear wave velocity V_s from downhole seismic test (DHT). These in-situ measurements must first be normalized for effective stresses and then serve as a surrogate for in-place relative density.

| (a) | (b) |
| (c) | (d) |
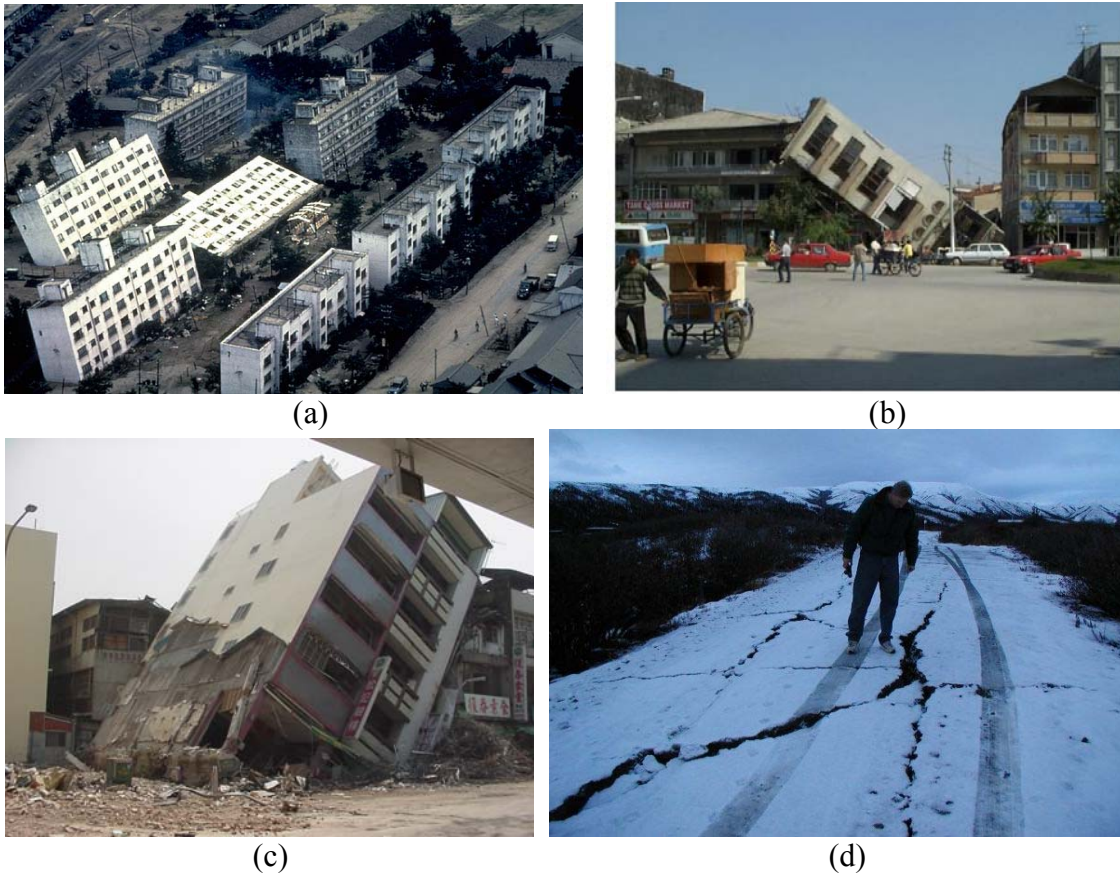
Figure 5.1 Consequences of liquefaction induced by earthquakes: (a) 1964 Niigata earthquake in Japan; (b) 1999 Kocaeli (Izmit) earthquake in Turkey; (c) 1999 Chi-Chi earthquake in Taiwan; (d) 2002 Alaska earthquake in the USA
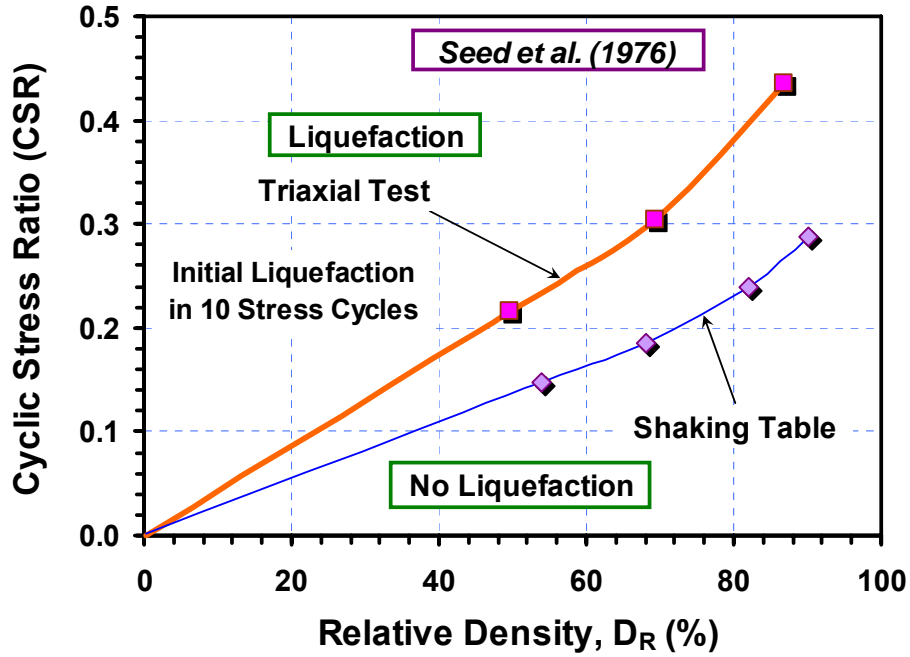
Figure 5.2 Test results of stress ratio to trigger initial liquefaction in shaking table and triaxial test (Seed, 1976)

For the SPT, Figure 5.3 presents the recent empirical correlation between $(N_1)_{60}/D_R^2$ and the void ratio range $(e_{max} - e_{min})$, as expressed by the following equation (Cubrinovski & Ishihara, 2002):

$$\frac{(N_1)_{60}}{D_R^2} = \frac{11.7}{(e_{max} - e_{min})^{1.7}} \qquad (5\text{-}1)$$

where $(N1)_{60}$ is stress-normalized SPT blow counts, e_{max} and e_{min} are the maximum and minimum void ratios, respectively. The void ratio range $(e_{max} - e_{min})$ was found to be correlated with mean grain size D_{50} (mm) as follows (Cubrinovski & Ishihara, 1999):

$$e_{max} - e_{min} = 0.23 + \frac{0.06}{D_{50}} \qquad (5\text{-}2)$$

The correlation between normalized tip resistance q_{T1} and relative density D_R has been shown previously in Figure 4.11 in Chapter 4. Correlations between horizontal stress

index K_D from dilatometer test (DMT) and D_R are also available (e.g., Robertson & Campanella, 1986; Jamiolkowski et al., 2003). Although no direct correlation between normalized shear wave velocity (V_{s1}) and D_R has been established, V_{s1} is found to be related to void ratio e (Robertson & Fear, 1995; Robertson et al., 1995), indicating a link between V_{s1} and D_R. Due to the correlations between the various field test data and D_R, liquefaction criteria can be developed from in-situ field measurements by surrogating D_R in lab testing, as illustrated in Figure 5.4.
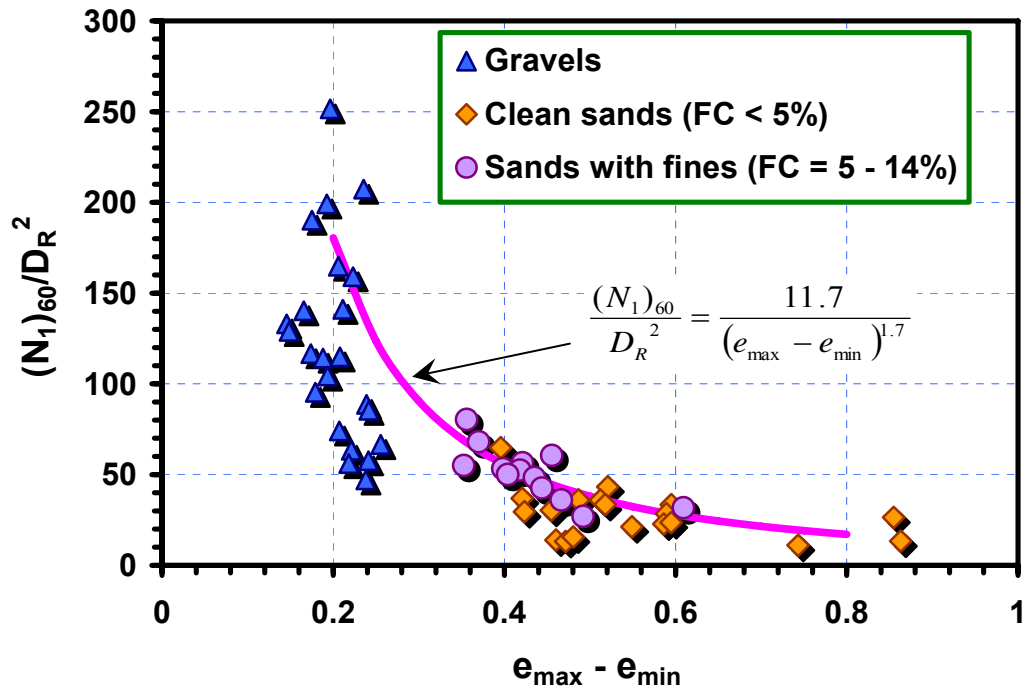
Figure 5.3 Empirical correlation between $(N_1)_{60}/D_R^2$ and $(e_{max} - e_{min})$
(after Cubrinovski & Ishihara, 2002)
Note: The relative density D_R is in decimal.

Many methods have been proposed for liquefaction evaluation based on the results of cone penetration testing, as summarized in Table 5.1. Most of them can be classified into two categories, which include cyclic stress-based procedures and the energy-based procedures. Both types of procedures compare the seismic loading imparted to the soil by the earthquake with the threshold loading that is required to induce liquefaction. If the seismic loading is higher than the threshold loading, liquefaction likely occurs; otherwise, liquefaction is not likely. These procedures are largely based on empirical observations of laboratory and field data, and they are refined as a result of newer studies and increased number of liquefaction case histories.
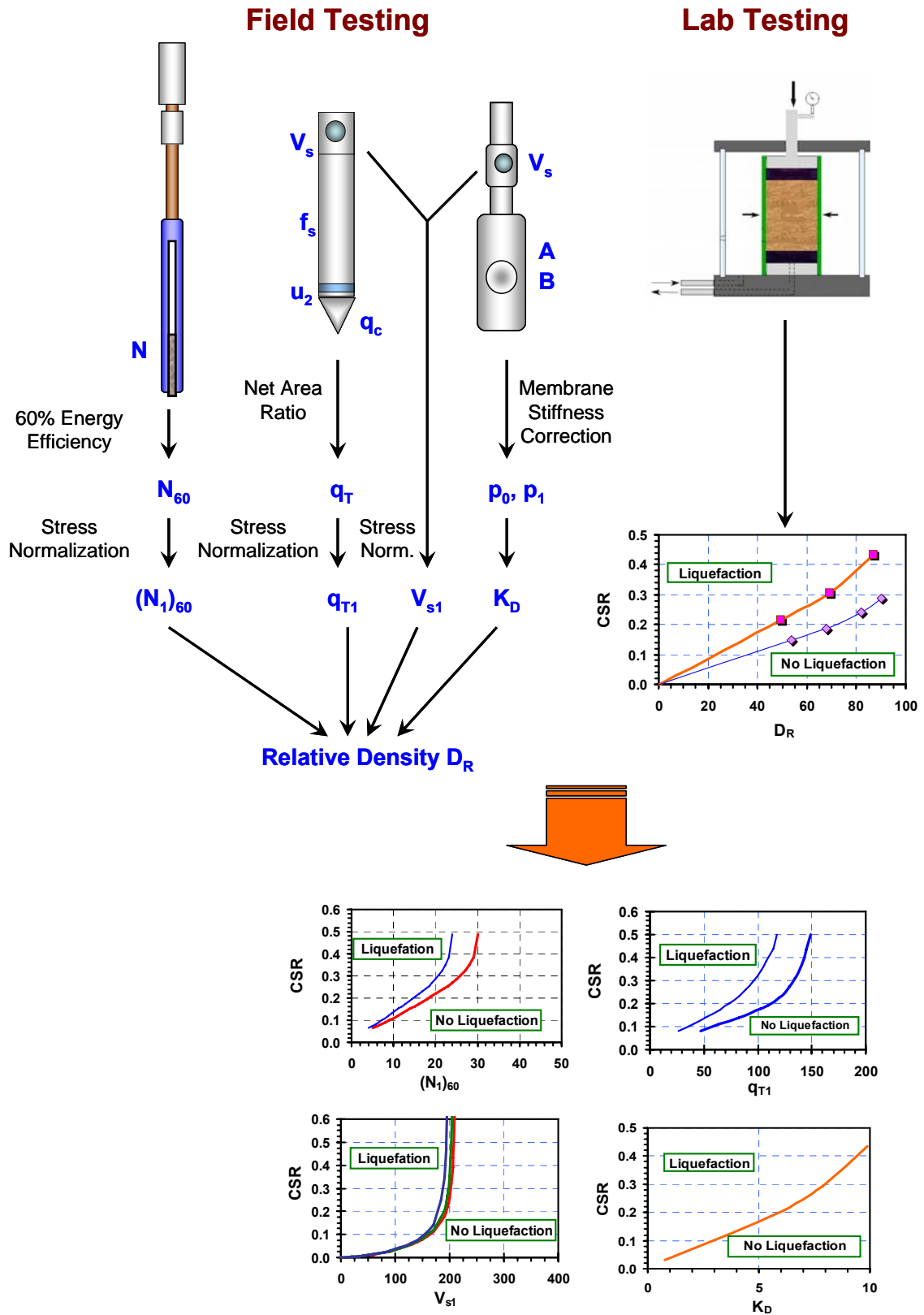
Figure 5.4 Development of cyclic resistance ratio (CRR) curves
from field and lab testing

Table 5.1 Summary of liquefaction evaluation methods based on SCPTu data

Category	Field Data	Reference	Comments
Stress-based	q_T	Seed et al. (1983)	Based on SPT criteria and correlations between q_T and N
		Robertson & Campanella (1985)	
		Seed & de Alba (1986)	
		Shibata & Teparaksa (1988)	Based on database comprising only CPT data
		Mitchell & Tseng (1990)	Based on calibration chamber tests and a penetration resistance theory
		Farrar (1990)	Uses state Parameter, ψ, and relation by Seed & de Alba (1986)
		Suzuki et al. (1995)	Uses q_{T1} and Friction Ratio (FR), with CPT database from Japan
		Olsen & Koester (1995)	Uses q_{T1} and Friction Ratio (FR) from CPT database
		Stark & Olson (1998)	Based on CPT database compiled by Shibata & Teparaksa (1988), USGS, and others
		Robertson & Wride (1998)	Based on database compiled by Suzuki et al. (1995) and Stark & Olson (1998)
		Juang & Jiang (2000)	Relate liquefaction safety factor F_s to liquefaction probability
		Boulanger (2003)	Reevaluated the effect of overburden stress using a theortical framework
		Carraro et al. (2003)	Based on laboratory chamber testing of clean to silty sands with nonplastic fines
	V_s	Seed et al. (1983)	Based on SPT criteria and correlations between V_s and N
		Robertson et al. (1992)	Based on database comprising V_s data from seismic regions
		Kayen et al. (1992)	
		Lodge (1994)	
		Andrus & Stokoe (2000)	
		Juang et al. (2001)	Relate liquefaction safety factor F_s to liquefaction probability
Energy-based	q_T	Kayen & Mitchell (1997)	Uses Arias intensity and field case histories

5.2 Stress-based Procedures

5.2.1 Cyclic Stress Ratio (CSR)

In the stress-based procedures, the level of seismic loading caused by the earthquake is expressed in terms of the cyclic stress ratio (CSR), which is defined by Seed & Idriss (1971) as following

$$CSR = \frac{\tau_{av}}{\sigma'_{vo}} \qquad (5\text{-}3)$$

τ_{av} is the average equivalent uniform shear stress, and σ'_{v0} is the effective vertical stress. Based on an analysis of a number of time-histories of shear stress in soil deposit obtained in laboratory, Seed & Idriss (1971) found that τ_{av} is about 65% of the maximum measured shear stress, τ_{max}. The CSR can therefore be derived from the following equation:

$$CSR = 0.65 \frac{\tau_{max}}{\sigma'_{vo}} \qquad (5\text{-}4)$$

Assuming that the soil column above a soil element at depth h behaves as a rigid body, the maximum shear stress developed during an earthquake can be assessed from the following relationship (Seed & Idriss, 1971):

$$\left(\tau_{max}\right)_h = \left(\frac{a_{max}}{g}\right)\sigma_{vo}r_d \qquad (5\text{-}5)$$

where $\left(\tau_{max}\right)_h$ is the shear stress at depth h, g is acceleration due to gravity, σ_{v0} is the total vertical stresses, and r_d is a stress reduction coefficient that accounts for the

flexibility of the model soil column. Therefore, for the conventional simplified procedure of liquefaction evaluation, the cyclic stress ratio is expressed as:

$$CSR = \frac{\tau_{av}}{\sigma'_{vo}} = 0.65\left(\frac{a_{max}}{g}\right)\left(\frac{\sigma_{vo}}{\sigma'_{vo}}\right)r_d \qquad (5\text{-}6)$$

The 1996 National Center for Earthquake Engineering Research (NCEER) and 1997 NCEER/National Science Foundation (NSF) workshops on the evaluation of soil liquefaction resistance (Youd et al., 2001) recommends that the value of r_d to be the average of the values suggested by Seed & Idriss (1971), as shown in Figure 5.5. It can be approximated as following (Robertson & Wride, 1997):

$$r_d = 1.0 - 0.00765\ z \qquad \text{for } z < 9.15 \text{ m} \qquad (5\text{-}7\ a)$$

$$r_d = 1.174 - 0.0267\ z \qquad \text{for } 9.15 < z < 23 \text{ m} \qquad (5\text{-}7\ b)$$

$$r_d = 0.744 - 0.008\ z \qquad \text{for } 23 < z < 30 \text{ m} \qquad (5\text{-}7\ c)$$

$$r_d = 0.5 \qquad \text{for } z > 30 \text{ m} \qquad (5\text{-}7\ c)$$

where z is depth in meters.

5.2.2 Cyclic Resistance Ratio (CRR) Based on SPT Blow Counts N

The threshold loading required to induce liquefaction is quantified as a function of the cyclic resistance ratio (CRR), which in turn is correlated to field data, such as the SPT blow counts N, the tip resistance q_T, or the shear wave velocity V_s. The CRR is used to compare the available soil resistance with the level of ground shaking represented by the cyclic stress ratio (CSR). Therefore, if the CSR value is higher than the CRR, the soil will

likely liquefy; otherwise, it will not. Various researchers have proposed ways to evaluate the cyclic resistance ratio (CRR).
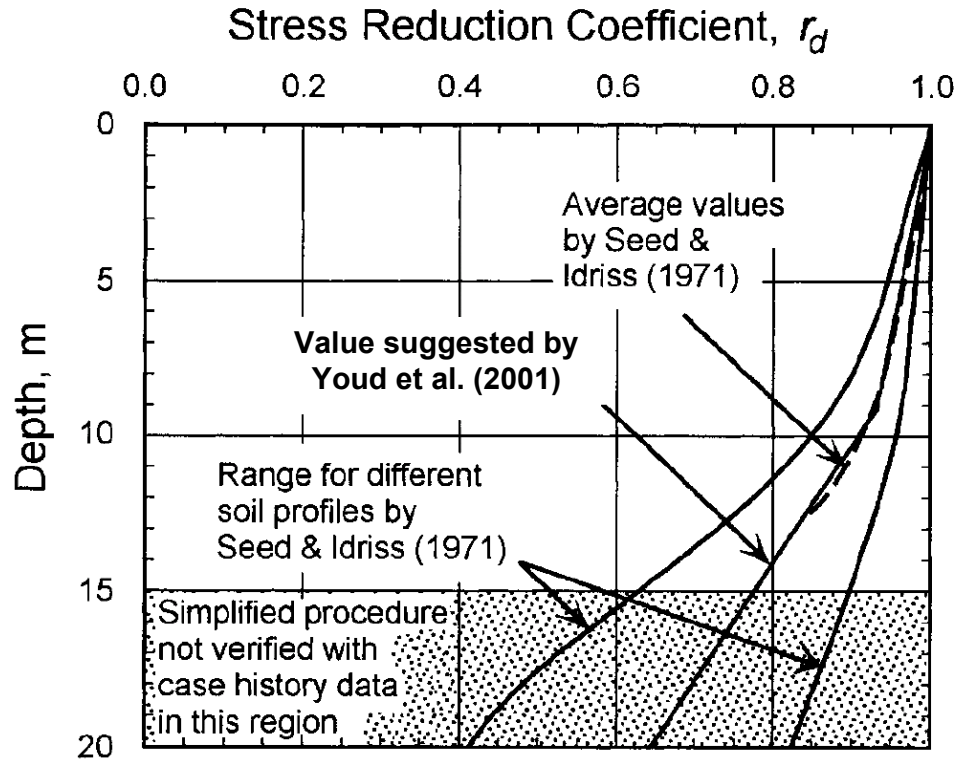
Figure 5.5 Stress reduction coefficient versus depth curves developed by Seed and Idriss (1971) and suggested by Youd et al. (2001)

Since the standard penetration test (SPT) has been the most widely used field testing method, abundant test data enabled the development of liquefaction critera based on the SPT blow count N (e.g. Tatsuoka et al., 1980; Tokimatsu and Yoshimi, 1983; Seed et al., 1985; Ishihara, 1993; Fear and McRoberts, 1995; Cetin et al., 2004). The N value is the number of repetitive blows required to drive the sampler 30 cm during the SPT test. The value of N is usually corrected to N_{60} corresponding to 60% energy efficiency before used in analysis due to variation of systems. Since the value of N_{60} varies with stress

level, overburden stress normalization factors are usually used to provide a consistent point of reference. The stress-normalization of N_{60} takes the form:

$$(N_1)_{60} = C_N \cdot N_{60} \tag{5-8}$$

where $(N_1)_{60}$ is the value corresponding to a reference stress of one atmosphere (σ_{atm}), and C_N is the normalization factor for overburden stress. The normalization factor C_N is a function of the effective overburden stress at the depth where the penetration value was obtained. A comprehensive review of different C_N recommendations can be found in Kulhawy & Mayne (1990). The simplest expression for C_N is as follows (Liao & Whitman, 1986):

$$C_N = \left(\sigma_{atm} / \sigma_{v0}' \right)^{0.5} \tag{5-9}$$

where σ_{atm} is atmosphere pressure, and σ_{v0}' is effective overburden stress.

By adding new data into the SPT liquefaction database compiled by Seed et al. (1985), Cetin et al. (2004) suggested the cyclic resitance ratio (CRR) curves as shown in Figure 5.6. The CRR increases with normalized SPT blow counts $(N_1)_{60}$, consistent with the trend observed in Figure 5.2 that the CRR increases with relative density D_R. The CRR also increases with the fines content (FC).
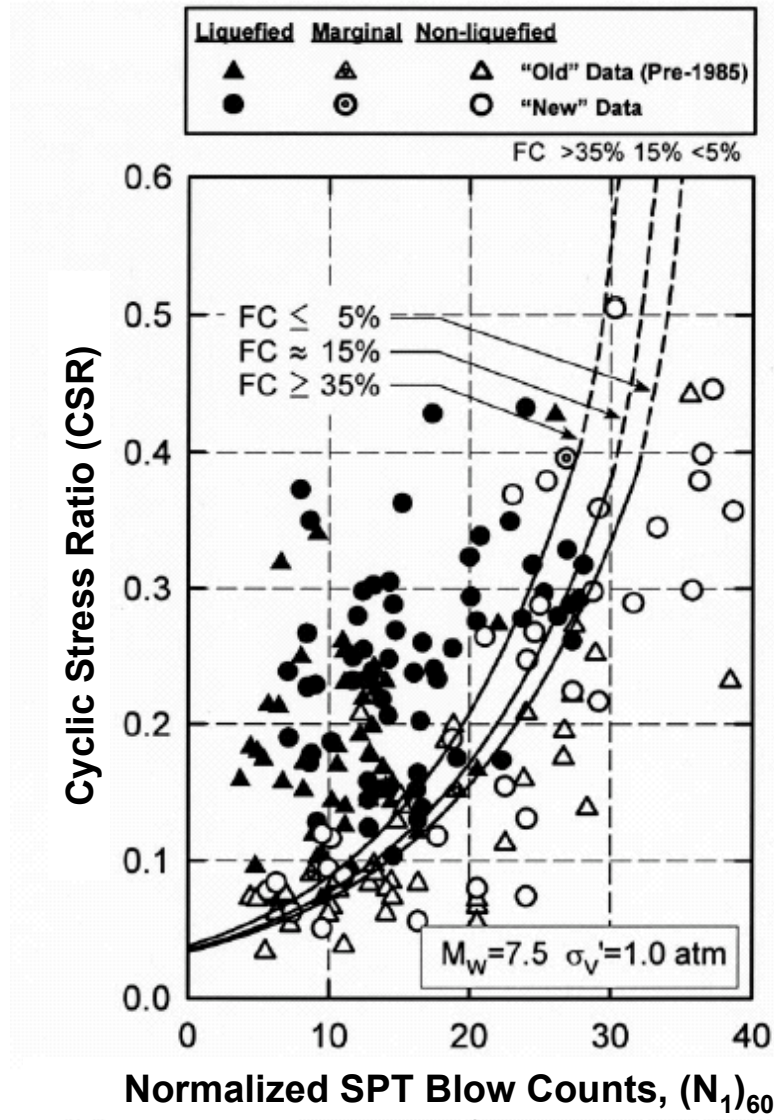
Figure 5.6 SPT liquefaction case histories and suggested cyclic resistance ratio (CRR) curves (Cetin et al., 2004)

5.2.3 Cyclic Resistance Ratio (CRR) Based on Cone Tip Resistance q_T

Cone tip resistance q_T measured by CPT soundings can be normalized with resprect to the overburden stress in the same way as SPT blow counts N_{60}:

$$q_{T1} = C_N \cdot q_T \qquad (5\text{-}10)$$

where q_{T1} is the value corresponding to a reference stress of one atmosphere (σ_{atm}), and C_N is the normalization factor for overburden stress.

Due to the scarcity of SCPT liquefaction database, the early liquefaction criteria based on SCPT data were developed from the SPT liquefaction database by correlating with SPT N value. Figure 5.7 shows that the ratio of q_c and N is a function of mean grain size (D_{50}). The average relationships between q_{T1} and $(N_1)_{60}$ in SPT tests are approximately $q_{T1} = 4$ to 5 $(N_1)_{60}$ for clean sands and $q_{T1} = 3.5$ to 4.5 $(N_1)_{60}$ for silty sands (Schmertmann, 1978). Since the CRR based on $(N_1)_{60}$ has already been developed from the SPT liquefaction case history database, the correlation between CRR of sands and normalized cone tip resistance q_{T1} could thus be derived as shown in Figure 5.8 (Seed et al., 1983). The shaded areas correspond to the possible relation between CRR and stress-normalized cone tip resistance q_{T1} for both silty sands with mean grain size $D_{50} < 0.15$ mm and clean sands with $D_{50} > 0.25$ mm.

Based on correlations between cone tip resistance q_T and SPT blow count N, Robertson & Campanella (1985) proposed the CPT-based liquefaction potential assessment relationship for sands ($D_{50} > 0.25$ mm) and silty sands ($D_{50} < 0.15$ mm), as shown in Figure 5.9. It is verified using CPT data from Canada, Japan, China, and the USA.

With a more varied database, Seed and de Alba (1986) improved values of q_{T1}/N_1 for sands with different mean grain sizes D_{50}. By cross-correlating SPT and CPT data, a

correlation between CRR and q_{T1} with respect to grain diameter D_{50} is developed as shown in Figure 5.10 based on SPT liquefaction database.

In order to reduce the uncertainties from the intermediate correlation between SPT blow counts and CPT tip resistance, Shibata & Teparaska (1988) developed a direct database comprising only CPT data. The derived CRRs of sands with different grain diameter D_{50} are shown in Figure 5.11.
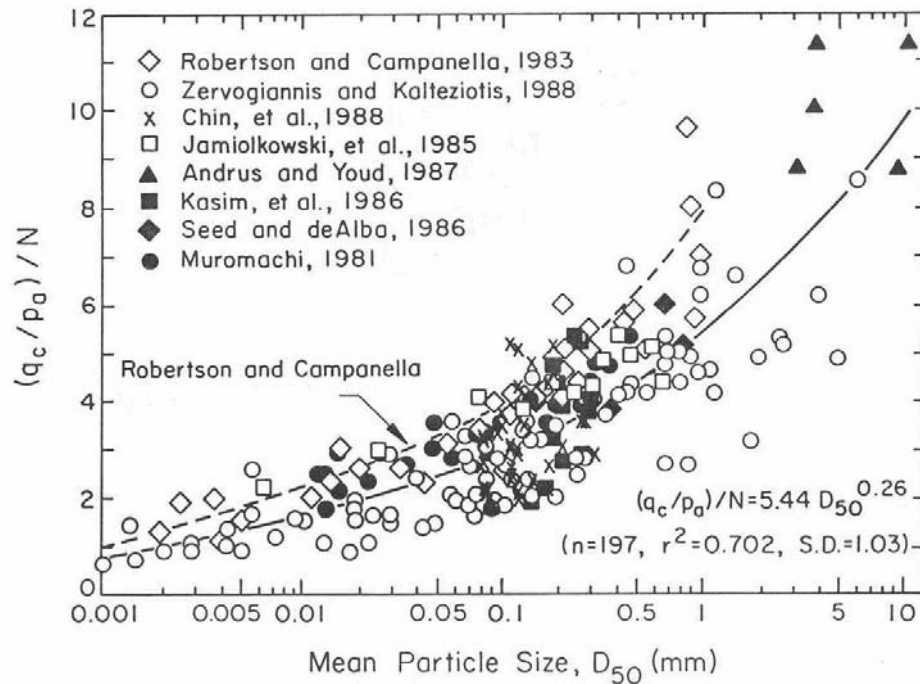
Figure 5.7 Variation of q_c/N with mean grain size (Kulhawy & Mayne, 1990)
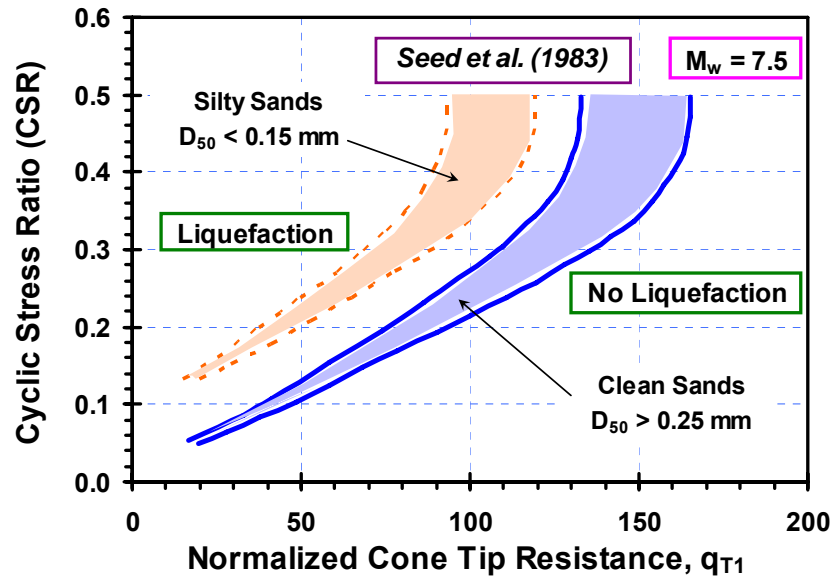
Figure 5.8 Correlation between cyclic resistance ratio $(CRR)_{7.5}$ for earthquake of moment magnitude 7.5 and normalized cone tip resistance q_{T1} estimated from SPT N value according to Seed et al. (1983)
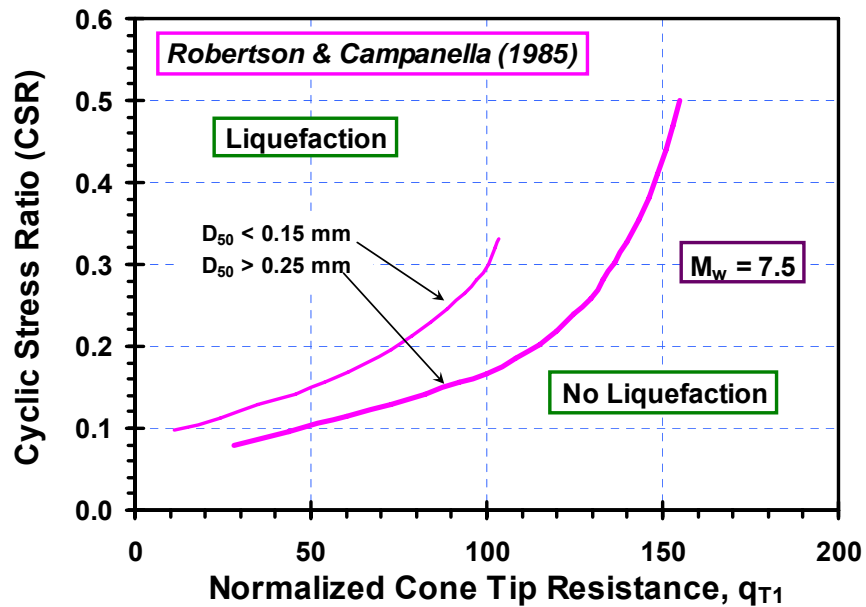
Figure 5.9 Correlation between cyclic resistance ratio $(CRR)_{7.5}$ for earthquake of moment magnitude 7.5 and normalized cone tip resistance q_{T1} according to Robertson & Campanella (1985)

154
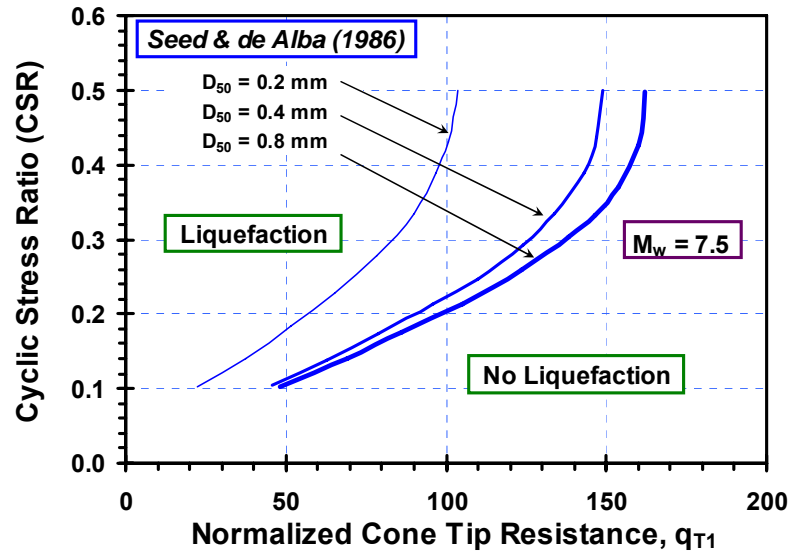
Figure 5.10 Correlation between cyclic resistance ratio (CRR)$_{7.5}$ for earthquake of moment magnitude 7.5 and normalized cone tip resistance q$_{T1}$ according to Seed & de Alba (1986)
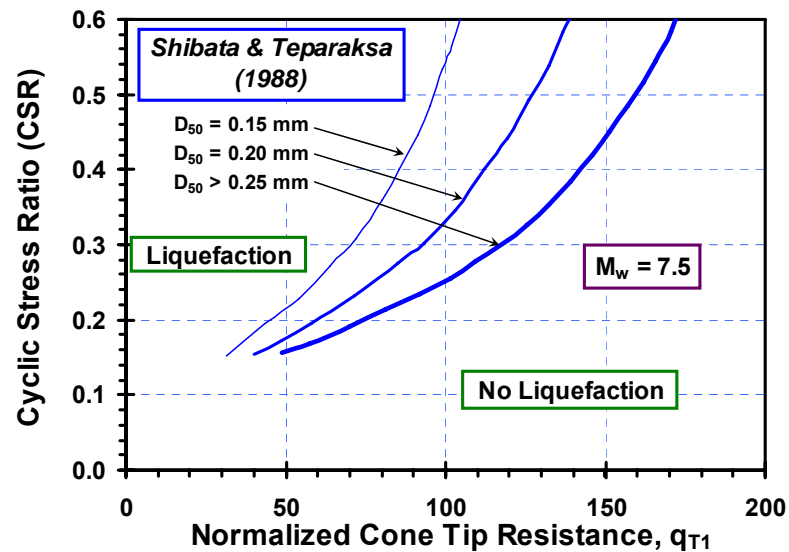
Figure 5.11 Correlation between cyclic resistance ratio (CRR)$_{7.5}$ for earthquake of moment magnitude 7.5 and normalized cone tip resistance q$_{T1}$ according to Shibata & Teparaksa (1988)

155

Mitchell and Tseng (1990) calibrated a penetration resistance theory using calibration chamber test results for various clean sands, and then used this theory to compute field cone tip resistance for soil states at which liquefaction occurred in laboratory liquefaction. The derived correlation between CRR and cone tip resistance is also plotted for different grain diameter D_{50} in Figure 5.12 (Mitchell and Tseng, 1990).
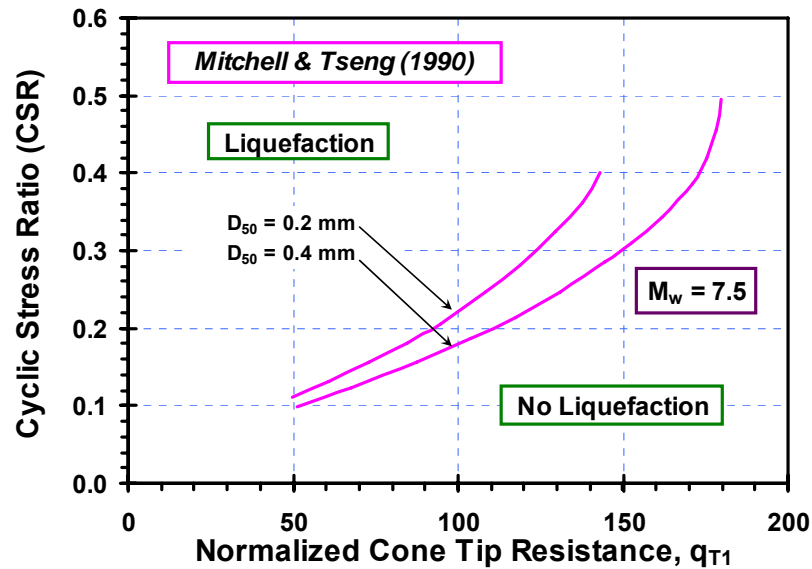
Figure 5.12 Correlation between cyclic resistance ratio $(CRR)_{7.5}$ for earthquake of moment magnitude 7.5 and normalized cone tip resistance q_{T1} according to Mitchell & Tseng (1990)

The concept of the state parameter (ψ) for sands is depicted in Figure 5.13 (Been & Jefferies, 1985). In critical state soil mechanics, the state of soil is a function of mean normal stress and void ratio. The state parameter ψ is the difference in void ratio between the compression line (initial state) and steady static line (failure). If the soil state has a position below the steady-state line (SSL), the state parameter (ψ) is negative; otherwise, it is positive. By evaluating the steady-state lines for sands used in CPT

chamber testing, Been et al. (1985) found the correlation between the state parameter (ψ) and tip resistance q_T, as shown in Figure 5.14. The state parameter (ψ) can be determined from q_T as follows:

$$\psi = -0.092\ln[0.032(\frac{q_T - I_1}{I_1'} + 17)]$$ (5-9)

where I_1 and I_1' are the first total and effective stress invariants (mean normal stress),

$$I_1' = \frac{1}{3}\left(\sigma_1' + \sigma_2' + \sigma_3'\right) = \frac{\sigma_{v0}'}{3}\left(1 + 2K_0\right),$$ and the stress units are all in kPa.

State Parameter for A

λ = Slope of Steady State Line and Virgin Compression Line
e_{ss} = Void Ratio on Steady State Line
e = Void Ratio at Initial State
ψ = State parameter

$$I_1 = \frac{1}{3}\left(\sigma_1 + \sigma_2 + \sigma_3\right)$$

Slope - λ

Slope - λ

A

λ-line

$e = e\lambda - \lambda \log I_1$

SSL

VOID RATIO

e_{ss}

$e\lambda$

MEAN NORMAL STRESS, I_1, kPa
(Log Scale)
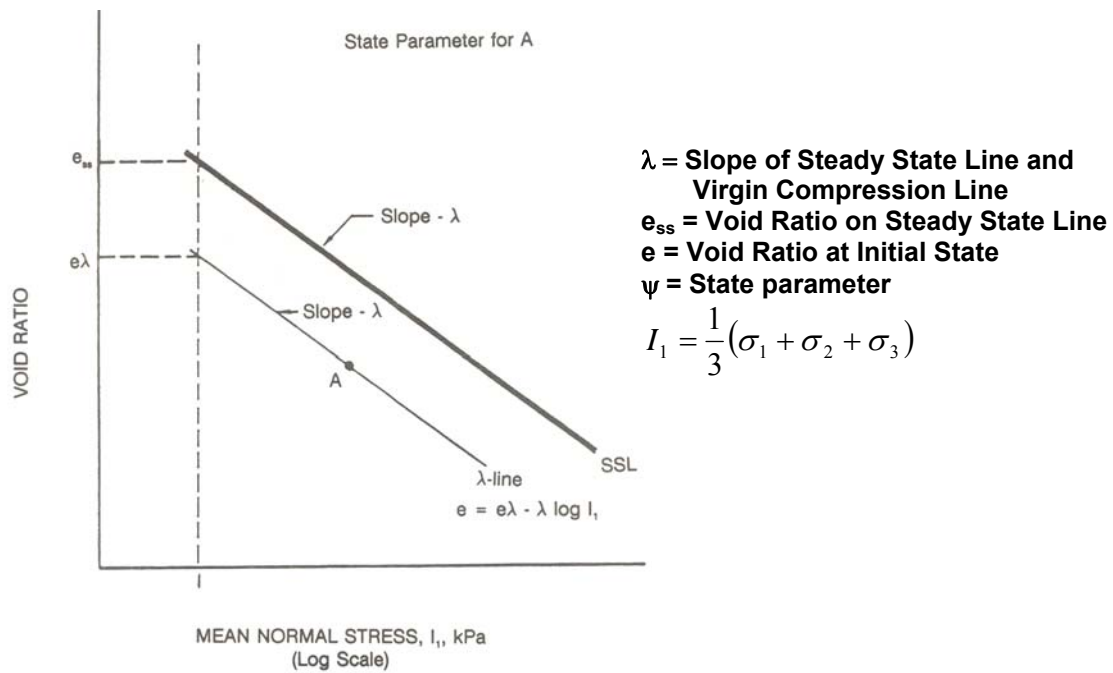
Figure 5.13 Definition of the state parameter ψ (Been & Jefferies, 1985)

The correlation between CRR and q_{T1} suggested by Seed & de Alba (1986) (Figure 5.10) was used by Farrar (1990) to derive the correlation between CRR and the state parameter (ψ). The value of q_{T1} of clean sands was converted to the state parameter (ψ) by

assuming $K_0 = 0.5$, with typical sand unit weight and groundwater location at the ground

surface, as shown in Figure 5.15. The derived curve by assuming $K_0 = 1.0$ is also plotted

in this Figure.
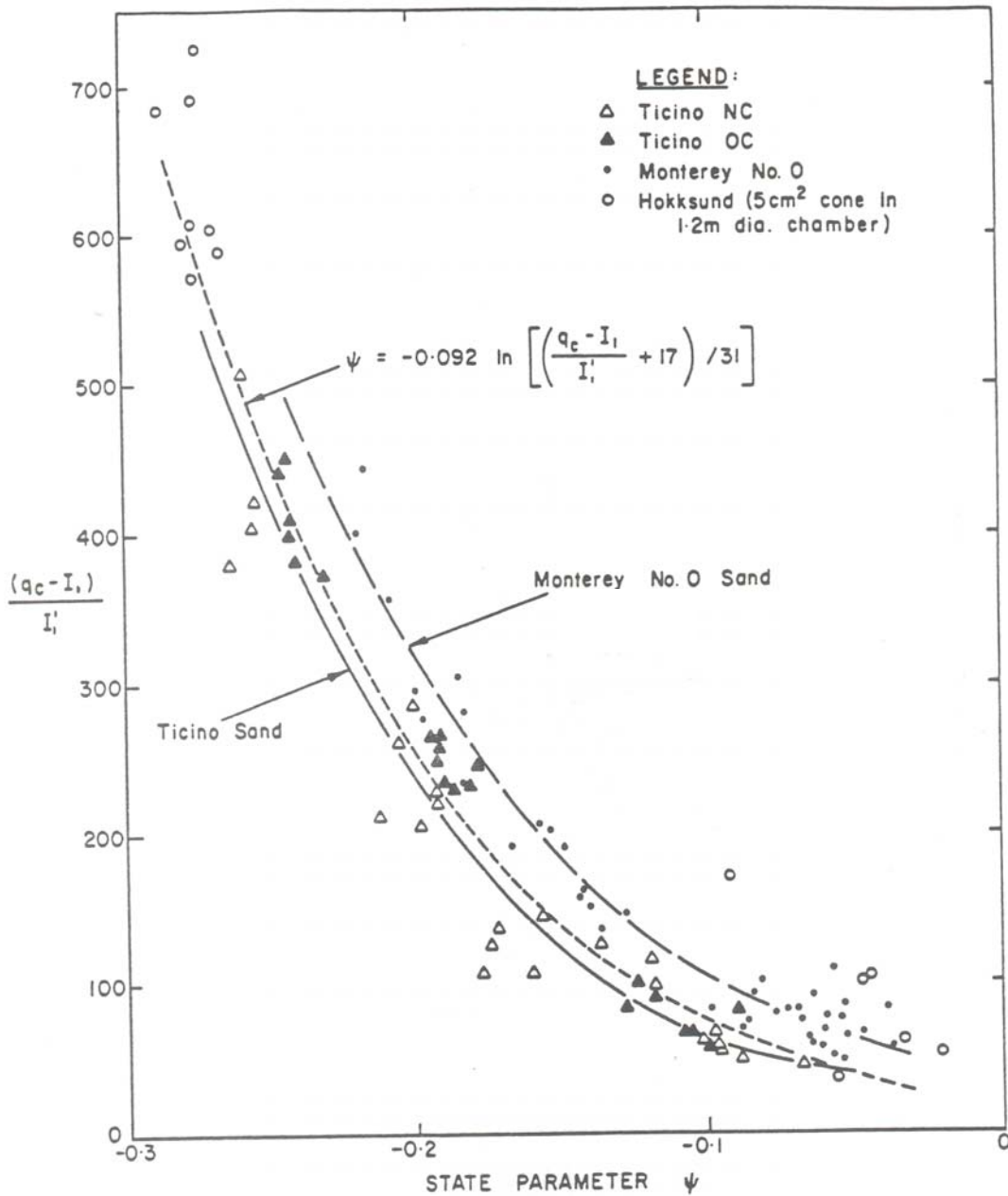
Figure 5.14 Correlations between normalized cone tip resistance and state parameter
(Been et al., 1985)
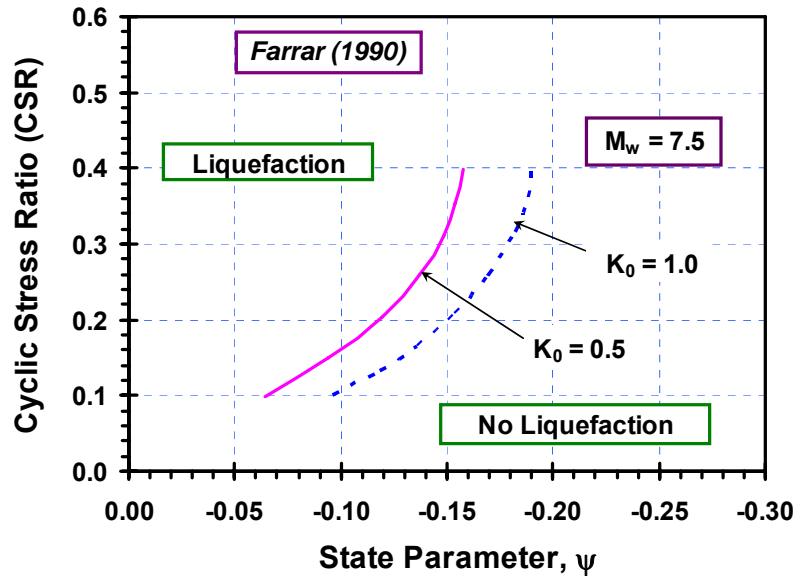
Figure 5.15 Correlation between cyclic resistance ratio $(CRR)_{7.5}$ for earthquake of moment magnitude 7.5 and state parameter according to Farrar (1990)

From CPT data obtained at 47 sites in eight regions in the Hokkaido and Hyogo prefectures in Japan, Suzuki et al. (1995) found that boundaries separating liquefiable from non-liquefiable conditions at a certain level of CSR are well defined, if the test data are expressed in terms of stress-normalized cone tip resistance (q_{T1}) and friction ratio (FR). The derived boundaries at CSR = 0.15 and CSR = 0.25 are shown in Figure 5.16. Based on cyclic laboratory tests and trends of CPT-predicted SPT equivalent clean sand blow counts, Olsen & Koester (1995) also developed the boundary contours of CRR based on q_{T1} and FR, as shown in Figure 5.17. With this approach, the soil index, such as D_{50}, is not required to predict liquefaction resistance.

By adding new field CPT data into the database originally developed by Shibata & Teparaksa (1988), Stark & Olson (1995) suggested a revised relationship between CRR and q_{T1} for sands with respect to different fines content (FC), as shown in Figure 5.18.

159
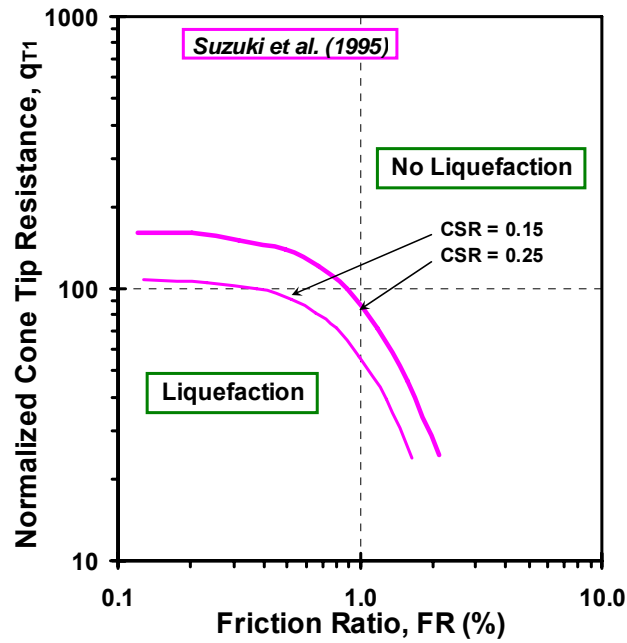
Figure 5.16 Prediction of cyclic stress ratio (CSR) based on two channels of CPT measurements according to Suzuki et al. (1995)
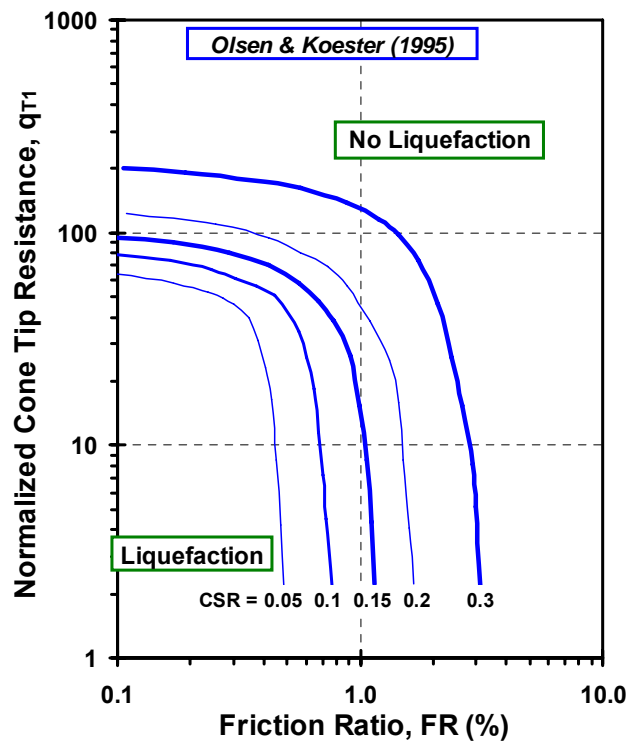
Figure 5.17 Prediction of cyclic stress ratio (CSR) based on two channels of CPT measurements according to Olsen & Koester (1995)

160
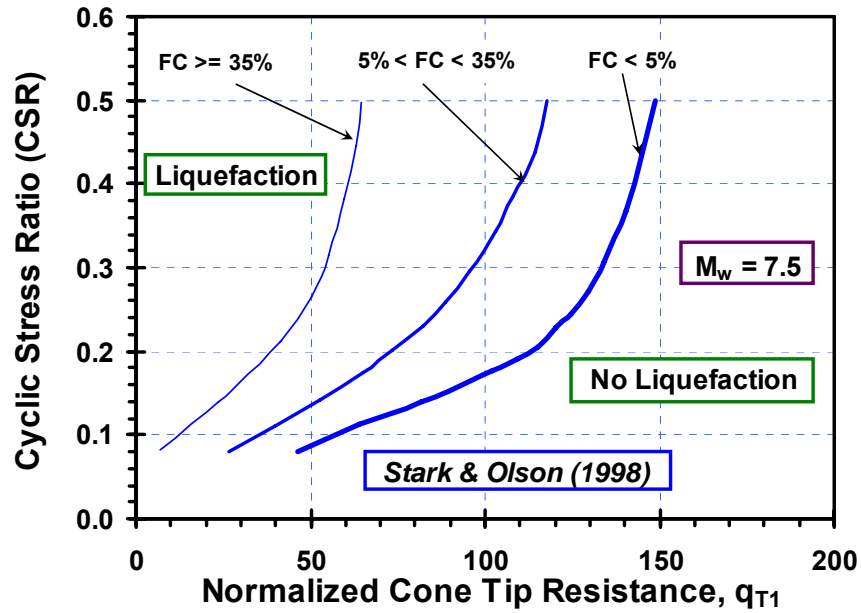
Figure 5.18 Correlation between cyclic resistance ratio (CRR)$_{7.5}$ for earthquake of moment magnitude 7.5 and normalized cone tip resistance q_{T1} according to Stark & Olson (1998)
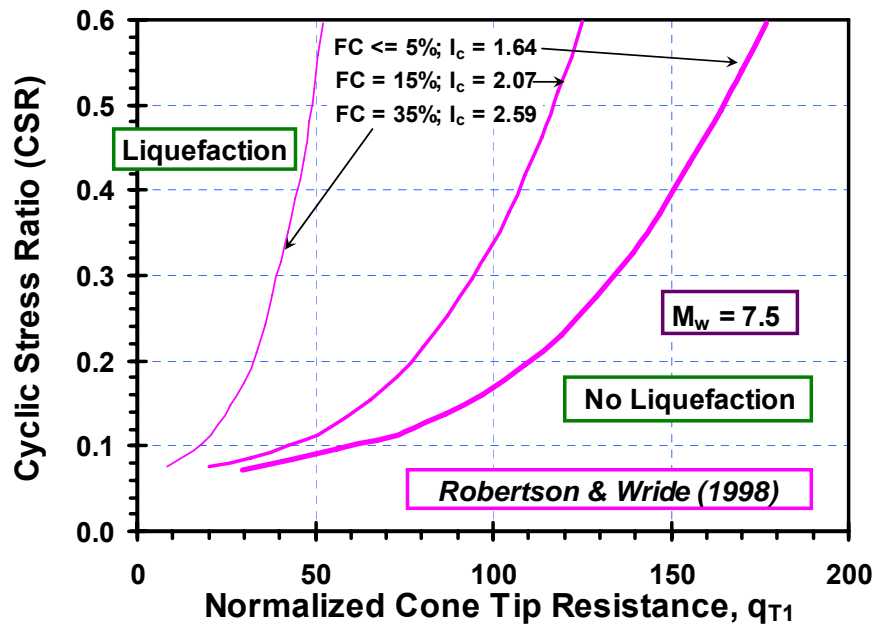
Figure 5.19 Correlation between cyclic resistance ratio (CRR)$_{7.5}$ for earthquake of moment magnitude 7.5 and normalized cone tip resistance q_{T1} according to Robertson & Wride (1998) for sands of varying fines content (FC)

161

Robertson & Wride (1998) recommended a new CRR vs. normalized tip resistance q_{T1} with respect to fines content (FC) and soil behavior type index (I_c) as shown in Figure 5.19. The tip resistance q_T can be normalized to q_{c1N} (or q_{T1}) for effective overburden stress using the normalization factor given by equation (5-7). For silty sands, the stress-normalized cone tip resistance q_{c1N} (or q_{T1}) is further normalized to the adjusted tip resistance $(q_{c1N})_{cs}$, which is its equivalent clean sand value. This is achieved using the following relationship:

$$(q_{c1N})_{cs} = K_c q_{c1N} \qquad (5\text{-}11)$$

where K_c is the grain-charateristic correction factor for the apparent fines content and is empirically calculated from soil behavior type index I_c, as shown in Figure 5.20. For clean sands, $(q_{c1N})_{cs} = q_{c1N}$.
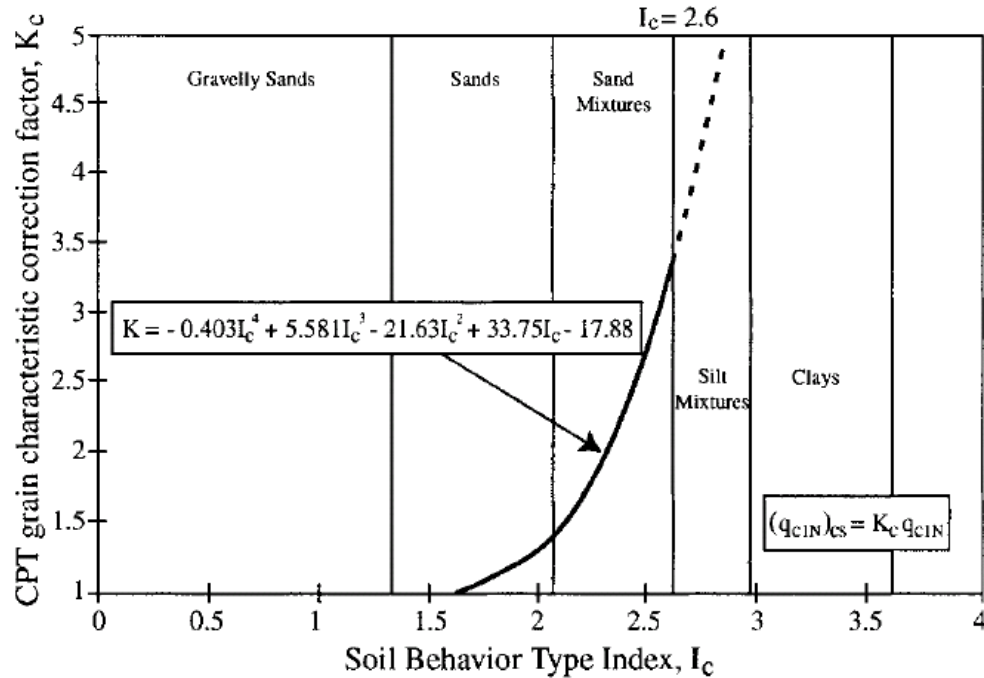
Figure 5.20 Grain-characteristic correction factor K_c for determination of clean-sand equivalent cone tip resistance (Youd et al., 2001; Robertson & Wride, 1998)
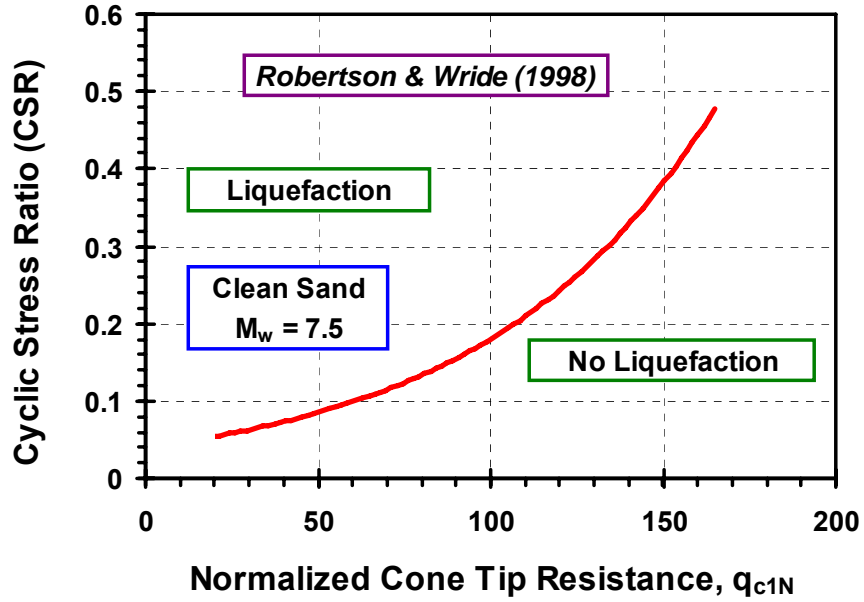
Figure 5.21 Correlation between cyclic resistance ratio (CRR)$_{7.5}$ for earthquake of moment magnitude 7.5 and normalized cone tip resistance q_{T1} according to Robertson & Wride (1998) for clean sand

The level of ground motion (CSR) and the adjusted tip resistance $(q_{c1N})_{cs}$ are compared with the cyclic resistance ratio (CRR) to determine whether liquefaction will or will not occur. The CRR for clean sand for an earthquake moment-magnitude of 7.5 is presented in Figure 5.21. It can also be calculated by the following equation (Robertson & Wride, 1998; Youd et al., 2001):

$$CRR_{7.5} = 93\left[(q_{c1N})_{cs}/1000\right]^3 + 0.08, \quad \text{if } 50 \le (q_{c1N})_{cs} < 160 \qquad \text{(5-12 a)}$$

$$CRR_{7.5} = 0.833\left[(q_{c1N})_{cs}/1000\right] + 0.05, \quad \text{if } (q_{c1N})_{cs} < 50 \qquad \text{(5-12 b)}$$

Carraro et al. (2003) developed curves of CRR versus stress-normalized cone resistance q_{T1} from a combination of analysis and laboratory testing. The CRR as a function of relative density was determined from cyclic triaxial tests performed on samples isotropically consolidated to atmospheric pressure (i.e. 1 atm = σ_{atm}). The stress-

normalized cone resistance q_{T1} was estimated for the relative densities at which the soil liquefaction tests were performed, based on cavity expansion analysis. The test data and the derived CRR curves for clean sands and silty sands are presented in Figure 5.22. These appear to be quite contradictory to the CRRs curves suggested by other researchers, as the fines content move the CRRs to the right. This study indicates the liquefaction resistance decreases due to the presence of fines, perhaps because of the nonplastic nature of the fines added to the sand mixture, although boundary effects in limited chamber sizes may also have affected the results.
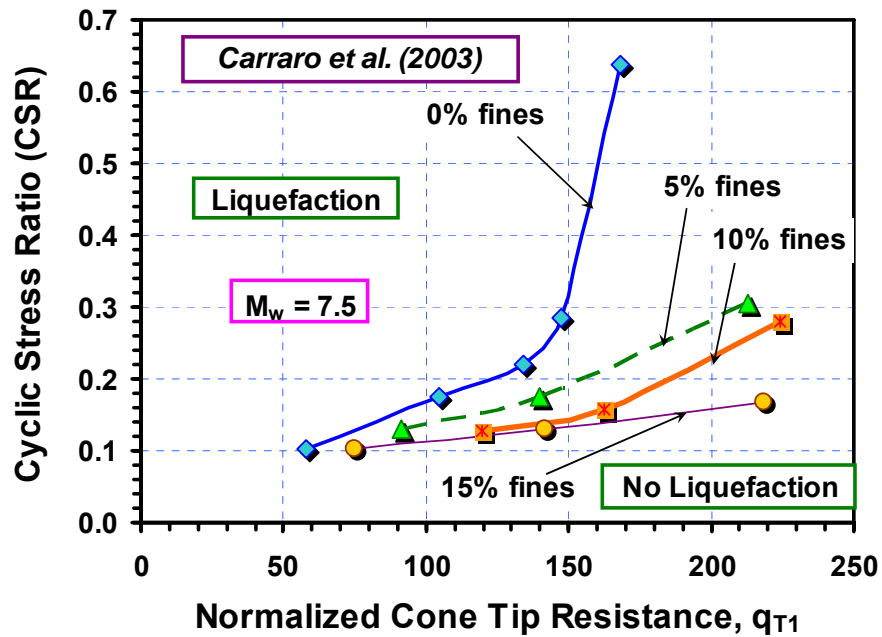
Figure 5.22 Correlation between cyclic resistance ratio (CRR)$_{7.5}$ for earthquake of moment magnitude 7.5 and normalized cone tip resistance q_{T1} according to laboratory tests performed by Carraro et al. (2003)

Since the normalization factor for effective overburden stress (C_N), is limited to $\sigma_{v0}'/\sigma_{atm}$ less than about 5.5, Boulanger (2003) reevaluated the effect of overburden stress on liquefaction evaluation using a theoretical framework, and suggested

relationships between CRR and tip resistance q_T for $\sigma_{v0}'/\sigma_{atm}$ up to 10, as shown in Figure 5.23. This study is useful for evaluating the liquefaction potential of foundation soils under high dams, which have high confining stresses due to the weight of dams.
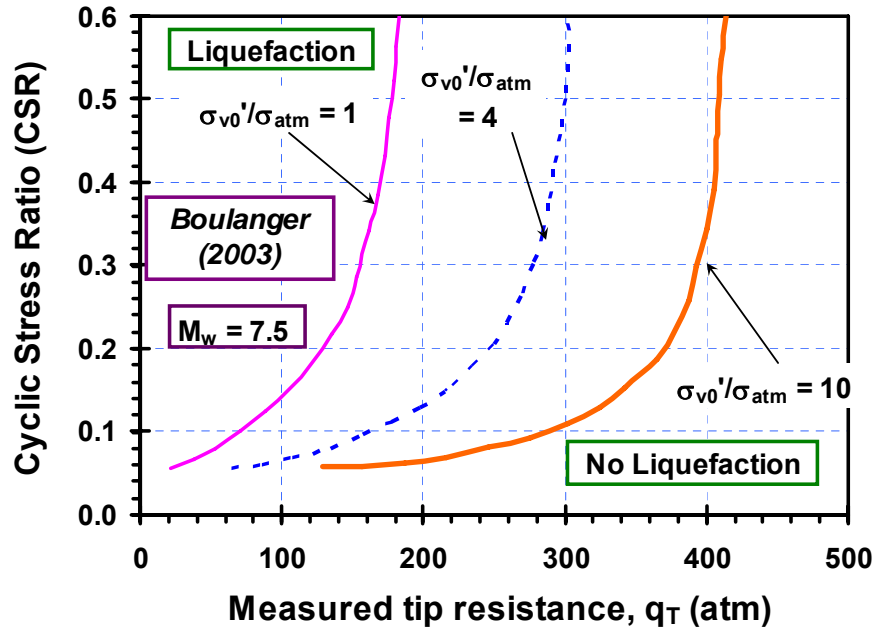
Figure 5.23 Correlation among cyclic resistance ratio (CRR)$_{7.5}$ for earthquake of moment magnitude 7.5, effective overburden stress σ_{v0}', and measured cone tip resistance q_T (Boulanger, 2003)

Figure 5.24 compares the CRR curves based on normalized tip resistance q_{T1}, with those developed from CPT liquefaction case histories shown as thicker lines. The curves for clean sands are shown in Figure 5.24 (a), and it can be seen that they generally fall in a relatively narrow range. The upper boundary of the range suggested by Seed et al. (1983) predicts liquefaction occurrence at relatively higher CSR level than the other curves. The CRR curves for silty sands show more discrepancy at relatively high CSR range [Figure 5.24 (b)], with the curve suggested by Robertson * Wride (1998) predicting liquefaction occurrence at the highest CSR level.
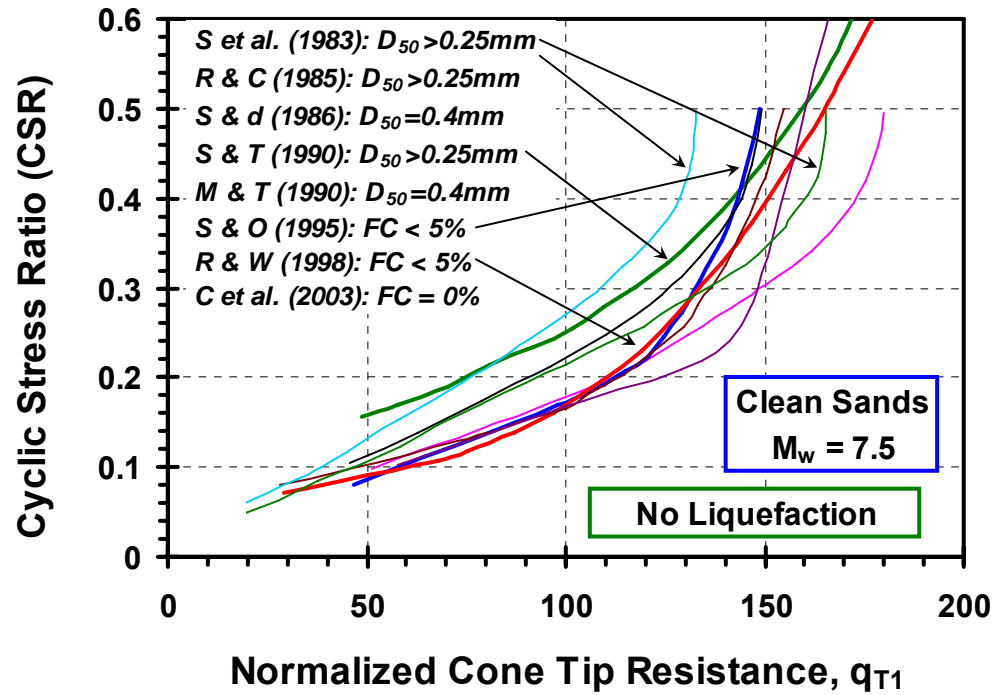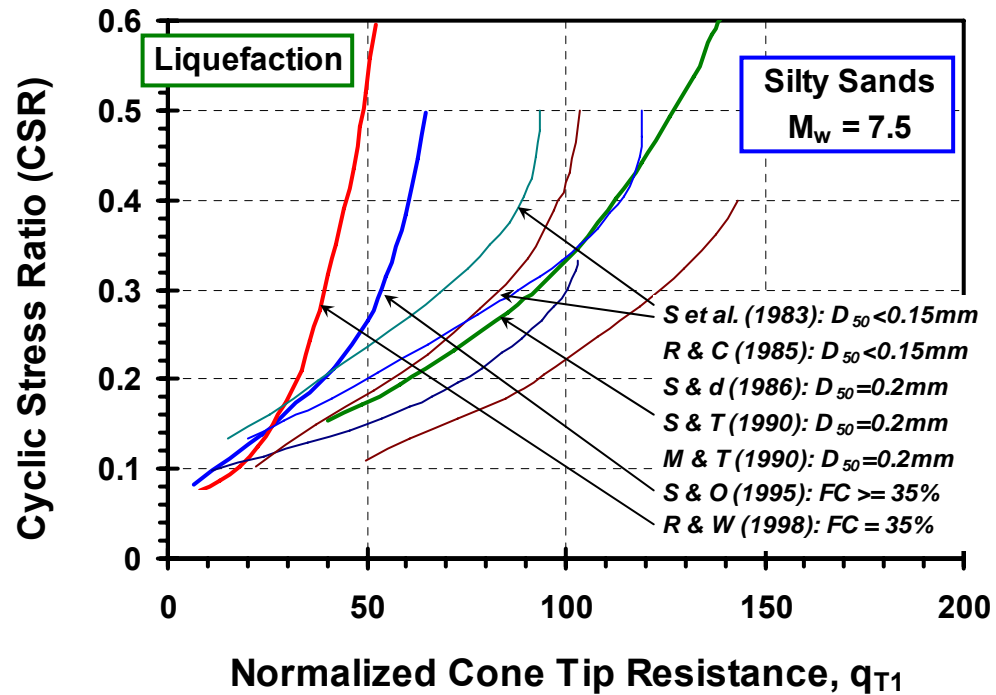
Figure 5.24 Comparison of the CRR curves suggested by various researchers:
(a) Clean sands; (b) Silty Sands.

166

5.2.4 Cyclic Resistance Ratio (CRR) Based on Shear Wave Velocity V_s

The CRR can also be evaluated from the shear wave velocity V_s. An approximate relationship between the shear wave velocity V_s and stress-normalized SPT blow count N_1 for depths up to 15m, was suggested as following by Seed et al. (1983):

$$V_s \approx 60\sqrt{N_1} \qquad (5\text{-}13)$$

where V_s is in m/s. With this relationship, the correlation between CRR of sandy soils and V_s can be derived from the CRR based on SPT liquefaction case history database, as shown in Figure 5.25.
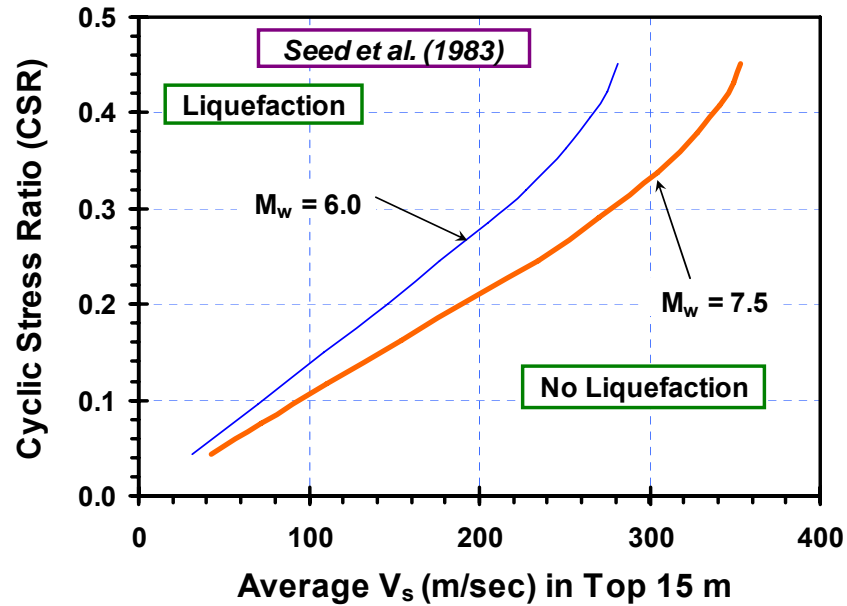
Figure 5.25 Correlation between cyclic resistance ratio and average shear wave velocity V_s in top 15 m (Seed et al., 1983)

Since the shear wave velocity V_s is approximately a function of the effective overburden stress σ_{v0}' to the power of 0.25 (Hardin & Drnevich, 1972), Robertson et al. (1992) suggested the following stress-normalized form:

$$V_{s1} = V_s / \left(\sigma_{v0}' \right)^{0.25} \qquad\qquad (5\text{-}14)$$

where V_s is in *m/s* and σ_{v0}' in *atm*.

Based on V_s measurement and liquefaction observation in the Imperial Valley of California during the 1987 Superstition Hill earthquake (M = 6.6), Robertson et al. (1992) proposed a correlation between stress-normalized shear wave velocity (V_{s1}) and the CRR, as shown in Figure 5.26. Also based on liquefaction case histories, CRR curves were proposed by Kayen et al. (1992) and Lodge (1994) (Figure 5.27). Compared with these two relationships, the one developed by Robertson et al. (1992) is the least conservative.
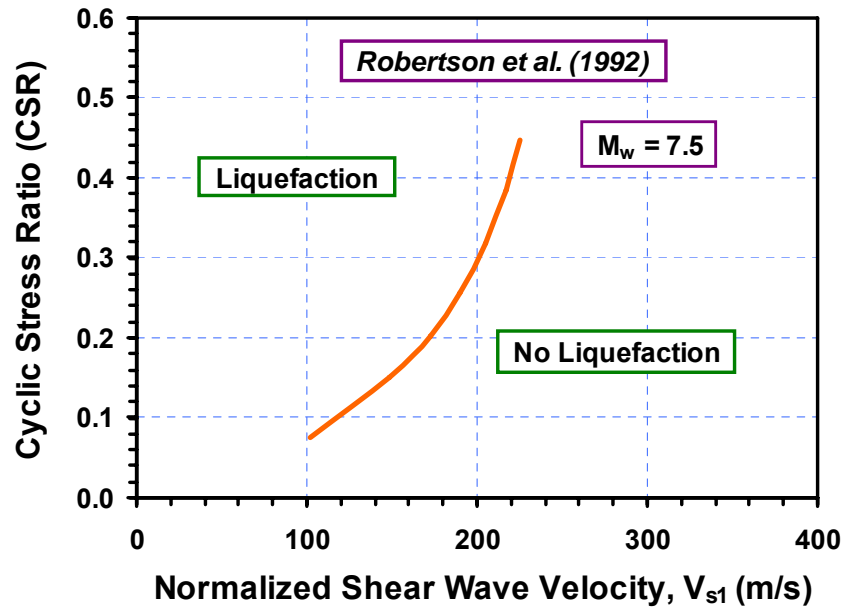
Figure 5.26 Correlation between cyclic resistance ratio (CRR)$_{7.5}$ for earthquake of moment magnitude 7.5 and normalized shear wave velocity V_{s1} according to Robertson et al. (1992)

Based on case history data of measured V_s from 26 earthquakes and more than 70 measurement sites, Andrus & Stokoe (2000) established CRR curves based on V_s in soils ranging from fine sand to sandy gravels with cobbles. The CRR for an earthquake moment-magnitude of 7.5 is found from (Andrus & Stokoe, 2000; Youd et al., 2001):

$$CRR_{7.5} = a\left(V_{s1}/100\right)^2 + b\left[1/\left(V_{s1c} - V_{S1}\right) - 1/V_{s1c}\right] \qquad (5\text{-}15)$$

where $a = 0.03$, $b = 0.9$, V_{s1} is the overburden stress-normalized shear-wave velocity, and V_{s1c} is a limiting asymptote value. From statistical database analyses, Andrus & Stokoe (2000) determined the following values for sands and gravels related to fines contents: $V_{s1c} = 220$ m/s for FC $\leq 5\%$; $V_{s1c} = 210$ m/s for FC $= 20\%$; and $V_{s1c} = 200$ m/s for FC $\geq 35\%$. The suggested CRR curves for soil with different fines content (FC) are shown in Figure 5.28.
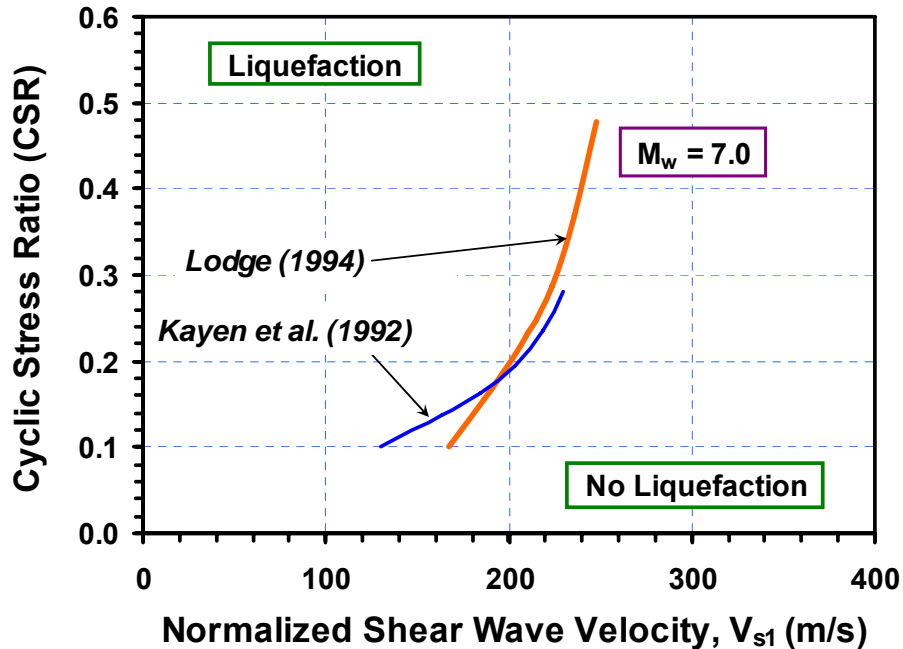
Figure 5.27 Correlation between cyclic resistance ratio (CRR)$_{7.0}$ for earthquake of moment magnitude 7.0 and normalized shear wave velocity V_{s1} according to Kayen et al. (1992) and Lodge (1994)

169
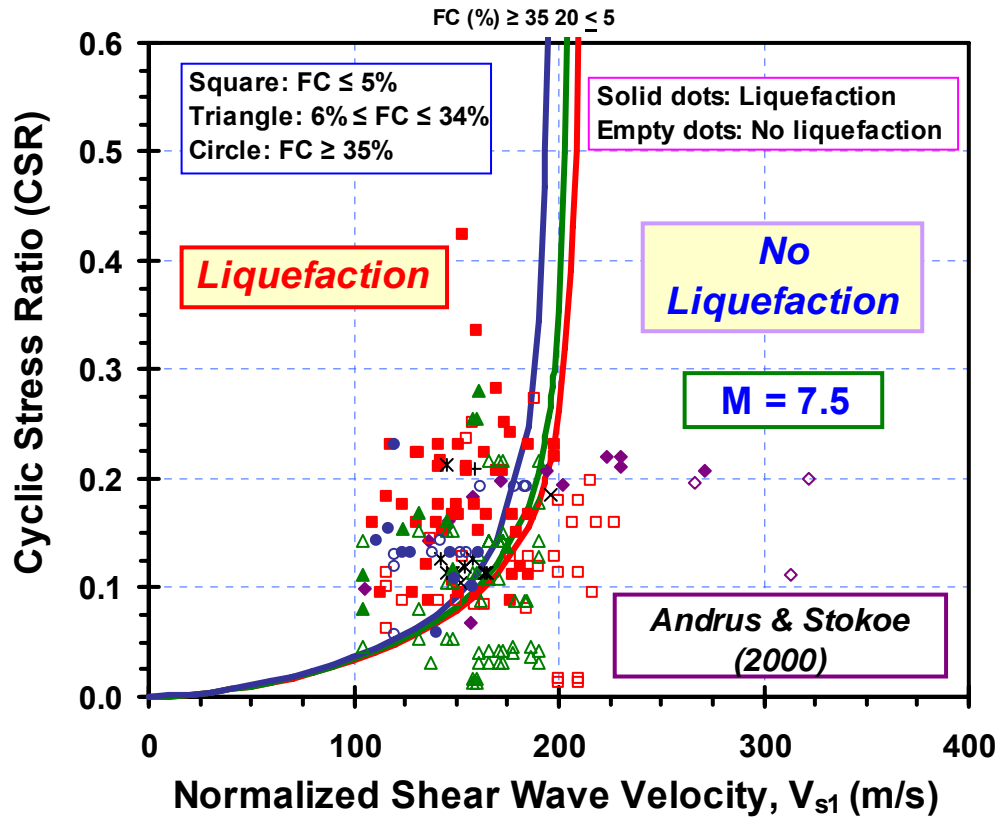
Figure 5.28 Correlation between cyclic resistance ratio and normalized shear wave velocity, V_{s1} (Andrus & Stokoe, 2000)

Note: $V_{s1} = V_s / (\sigma'_{v0})^{0.25}$, where V_s is in *m/s* and σ'_{v0} is the effective overburden stress in *atm*.

From the cone tip resistance q_T and shear wave velocity V_s, most of the correlations only give the value of $CRR_{7.5}$, which represents the liquefaction resistance in the event of earthquake of moment magnitude $M_w = 7.5$. For earthquake of magnitude other than 7.5, Seed and Idriss (1982) introduced correction factors termed ''magnitude scaling factors (MSFs)''. The MSFs are traditionally applied to CRR. Figure 5.29 presents a summary of different MSFs developed by various researchers. The NCEER workshops (Youd et al., 2001) suggested that for earthquakes of magnitudes <7.5, the range of MSFs falls in the

170

shaded area in Figure 5.29, while the MSFs recommended by Idriss should be used for earthquakes of magnitudes >7.5.
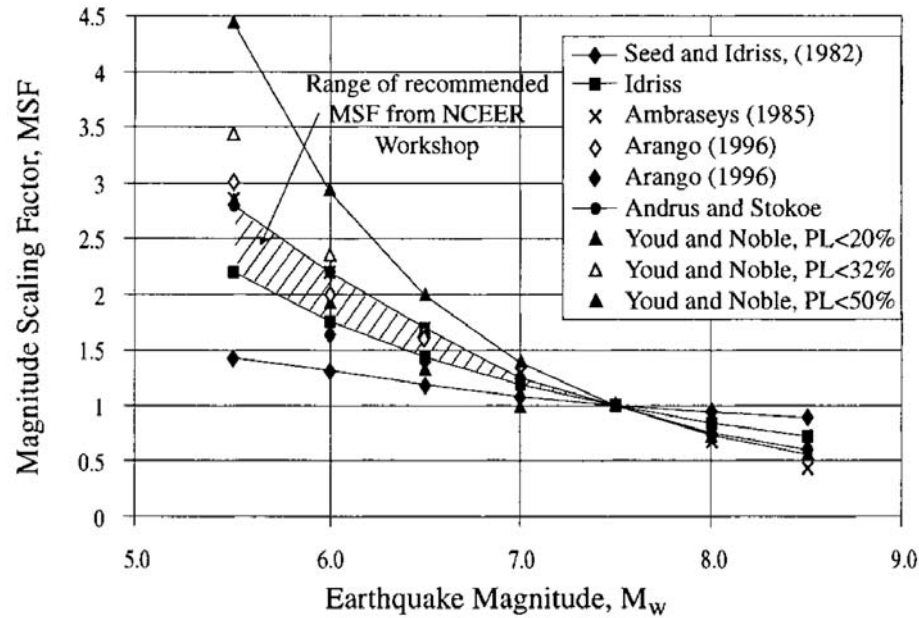
Figure 5.29 Magnitude scaling factors (MSF) derived by various researchers (Youd et al., 2001)

5.2.5 Probabilistic Cyclic Resistance Ratio (CRR)

All the aforementioned methods to evaluate CRR are conventional deterministic approaches, which give only a binary evaluation of liquefaction potential. To assess the degree of liquefaction severity, calculated factor of safety (F_s) can be defined as $F_s = $ CRR/CSR for a particular earthquake magnitude and set of data. A calculated FS = 1 corresponds to "initial liquefaction" whereas FS = 0.5 indicates severe quick sand.

In more recent evaluations, CRR curves of different probabilities of occurrence have been developed from the original databases. Based on the SPT liquefaction database from

which the deterministic CRR curves were developed, probabilistic curves for CRR have been proposed by Liao et al. (1988), Liao (1996), Youd & Noble, 1997, and Cetin et al. (2004). The probabilistic CRR curves suggested by Cetin et al. (2004) are shown in Figure 5.30.
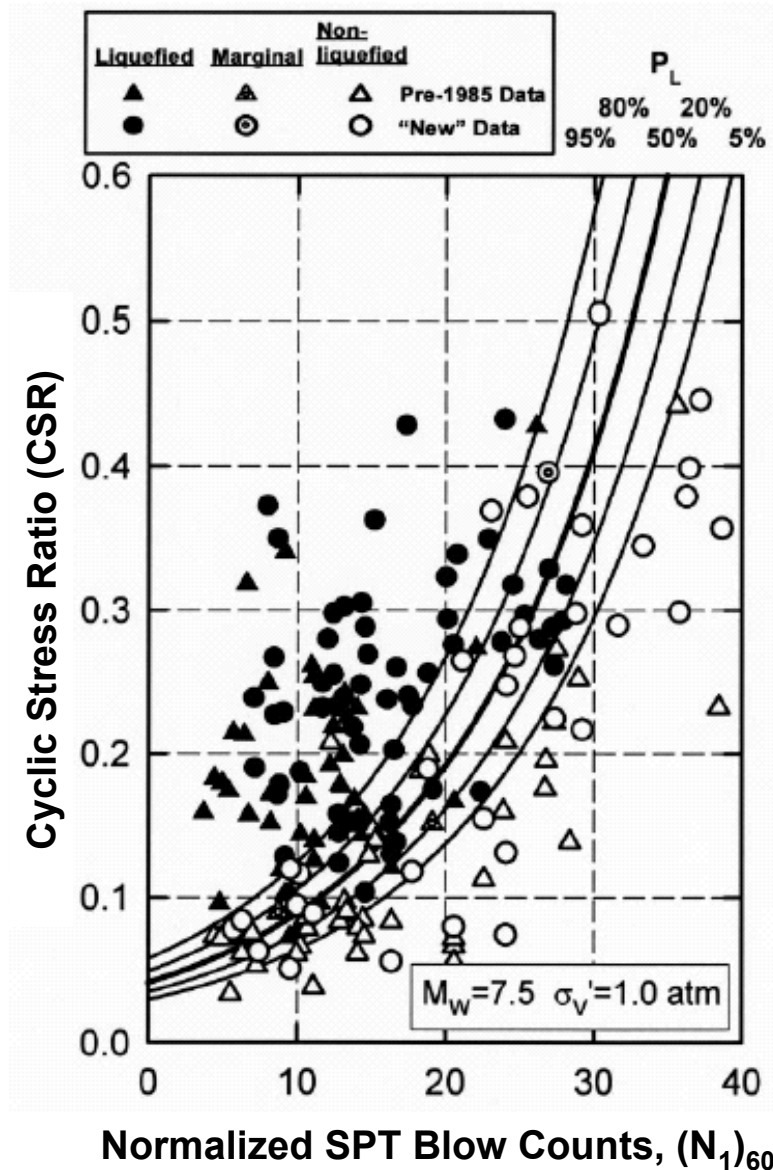
Figure 5.30 SPT liquefaction case histories and suggested probabilistic cyclic resistance ratio (CRR) curves (Cetin et al., 2004)

Based on stress-normalized cone tip resistance q_{T1}, a mapping function was proposed (Chen & Juang, 2000; Juang & Jiang, 2000) to relate the safety factor F_s to the liquefaction probability P_L based on a database of 225 CPT-based cases compiled by Juang & Jiang (2000):

$$P_L = 1/\left[1 + \left(F_s/1.0\right)^{3.34}\right] \tag{5-16}$$

Based on the shear wave velocity, there is a similar mapping function (Juang et al., 2001):

$$P_L = 1/\left[1 + \left(F_s/0.72\right)^{3.1}\right] \tag{5-17}$$

Curves of CRR for different probabilities of liquefaction based on stress-normalized tip resistance q_{T1} are presented in Figure 5.31. This provides a more rational means of assessing the likelihood of liquefaction for a particular CSR and soil resistance measured by the stress-normalized tip resistance q_{T1}. The CRR curves at different probabilities ranging from 10% to 90% are given in Figure 5.32 for stress-normalized shear wave velocity V_{s1}.

173
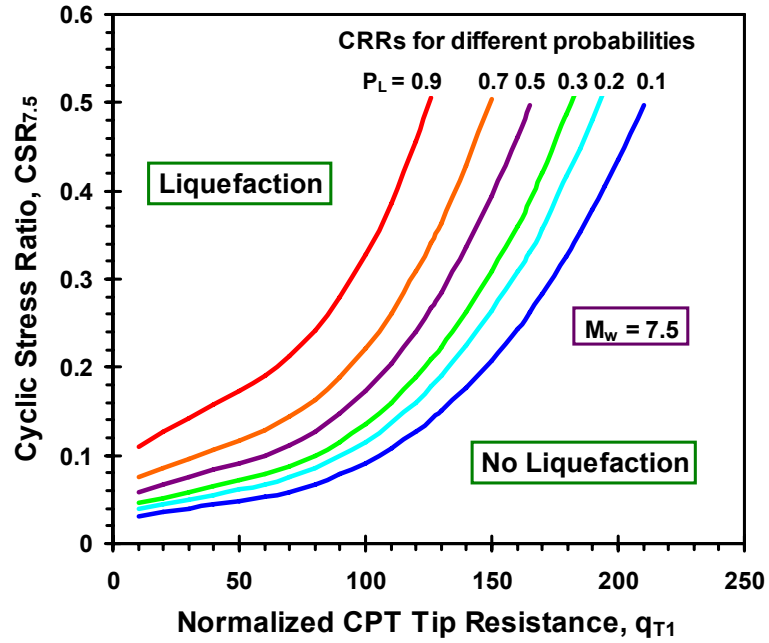
Figure 5.31 Cyclic resistance ratios (CRRs) for clean sands based on tip resistance at different levels of probability (Juang & Jiang, 2000)
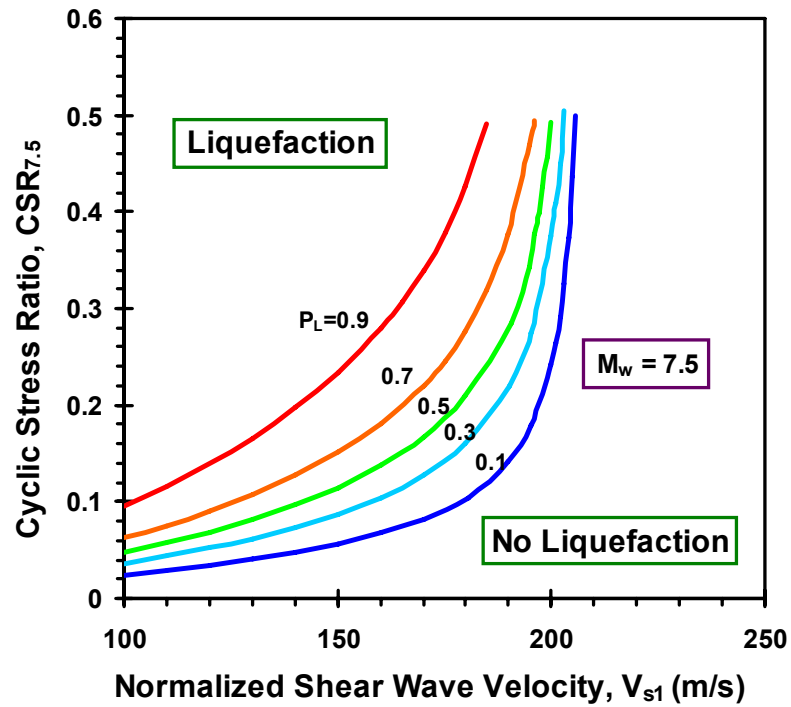
Figure 5.32 Cyclic resistance ratios (CRRs) for clean sands based on shear wave velocity at different levels of probability (Juang et al., 2001)

174

5.3 Energy-based Procedures

Numerous energy-based procedures have been proposed for liquefaction evaluation (e.g. Davis & Berrill, 1982; Law et al., 1990; Liang et al., 1995; Kayen & Mitchell, 1997). In these approaches, the seismic loading is quantified with the energy released during earthquakes, and it is compared with the threshold loading of soil liquefaction in terms of energy.

Some of the procedures use the Gutenberg-Richter energy correlation as the basis to estimate the seismic loading imparted to the soil. The energy relation is given as following (Gutenberg & Richter, 1956):

$$E_0 = 10^{1.5M + 1.8} \tag{5-18}$$

where E_0 is the total radiated energy from the earthquake source (kJ), and M is the magnitude of earthquake in Richter scale. With different assumptions on energy dissipation, expressions to derive seismic loading are suggested by Davis & Berrill (1982), Berrill & Davis (1985), Law et al. (1990), and Trifunac (1995). Based on the SPT liquefaction database from earthquake case histories, the same researchers proposed the boundary curves, which separate the liquefied and non-liquefied cases, with respect to the stress-normalized SPT blow counts, N_1.

In contrast with these studies, Kayen & Mitchell (1997) uses Arias intensity (I_h) to measure the earthquake shaking intensity quantitatively. Arias intensity represents the total energy per unit weight in a given direction that is absorbed by an idealized set of single degree of freedom oscillators (Arias, 1970). Arias intensity (I_h) is calculated by

integrating the acceleration time histories, and is the sum of Arias intensity in the x- (I_{xx})

and y- (I_{yy}) directions:

$$I_h = I_{xx} + I_{yy} = \frac{\pi}{2g}\int_0^{t_0}a_x^2(t)dt + \frac{\pi}{2g}\int_0^{t_0}a_y^2(t)dt \qquad (5\text{-}19)$$

where I_h is the Arias intensity of the earthquake motion at the top of the soil profile (m/s),

$a_x(t)$ and $a_y(t)$ are the horizontal acceleration time histories in the x- and y-direction

(m/s^2), t_0 is the acceleration due to gravity (m/s^2), and g is the acceleration due to gravity

(m/s^2).

Similar to the stress-based procedure, the Arias intensity typically decreases with depth.

A depth correction factor, r_b, analogous to r_d used in the stress-based procedure is

necessary to relate the Arias intensity of surface motions to that at depth in a profile:

$$I_{hb} = I_h \cdot r_b \qquad (5\text{-}20)$$

where I_{hb} is the Arias intensity of the earthquake motions at a given depth in the profile.

Based on analysis of synthetic seismograms propagated through soil profiles using the

SHAKE 1-D equivalent linear program, Kayen & Mitchell (1997) gave the average and

standard deviation of the value of r_b. The average value of r_b can be calculated from the

following equations:

$$r_b = 1.0 - 0.07z \qquad \text{when } z \le 6 \text{ m} \qquad (5\text{-}21 \text{ a})$$

$$r_b = 0.76 - 0.03z \qquad \text{when } 6 \text{ m} \le z \le 10 \text{ m} \qquad (5\text{-}21 \text{ b})$$

$$r_b = 0.46 \qquad \text{when } z > 10 \text{ m} \qquad (5\text{-}21 \text{ c})$$

where z is in meters.

Based on SPT liquefaction case histories, the boundary curve expressed in terms of Arias intensity (I_{hb}) with respect to SPT N value normalized to effective overburden stress of 1 atmosphere [$(N_1)_{60}$] was developed as reasonable separation of the data sets, as shown in Figure 5.33 (Kayen & Mitchell, 1997).
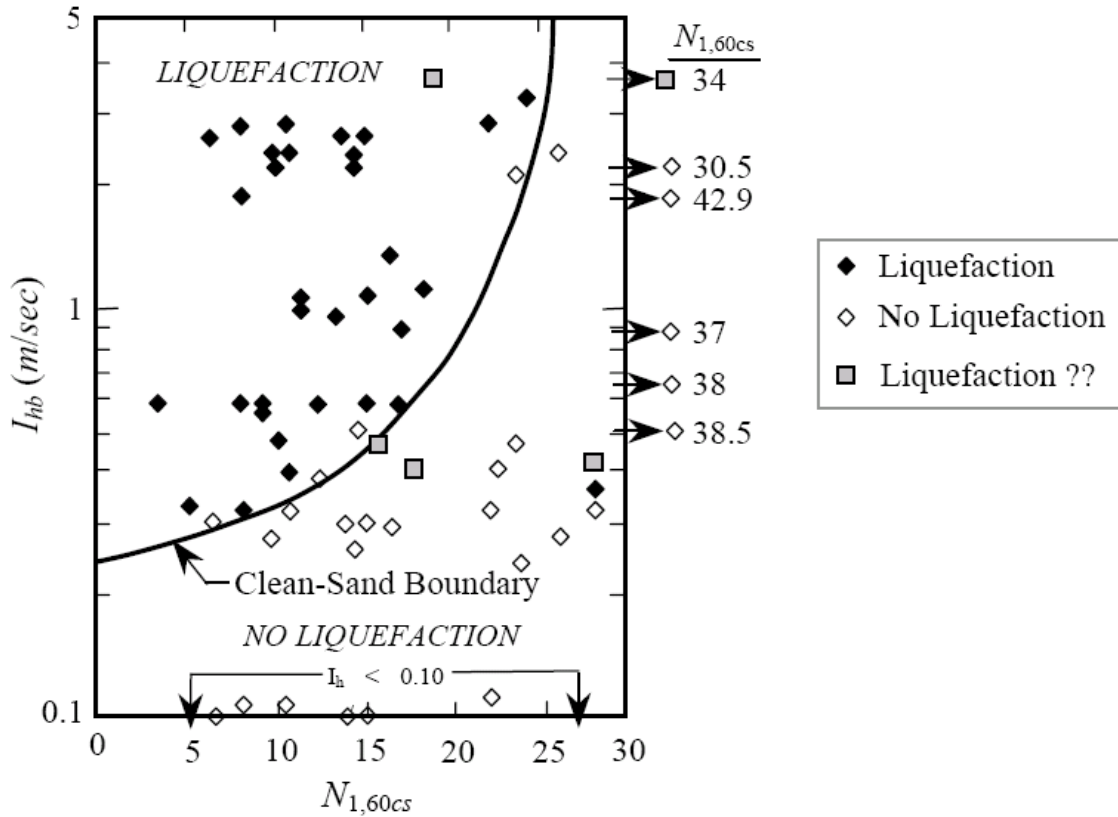
Figure 5.33 Arias intensity liquefaction field data and boundary curves suggested by Kayen & Mitchell (1997) based on SPT N value

Similarly, Figure 5.34 presents the boundary curves expressed in terms of Arias intensity (I_{hb}) with respect to normalized cone tip resistance (q_{T1}), based on 28 field case histories where strong ground motion data were available (Kayen & Mitchell, 1997). Considering the number of field case histories is limited, this approach is considered quite

approximate (Schneider, 1999). Therefore, the stress-based approach is used for liquefaction evaluation in this thesis.
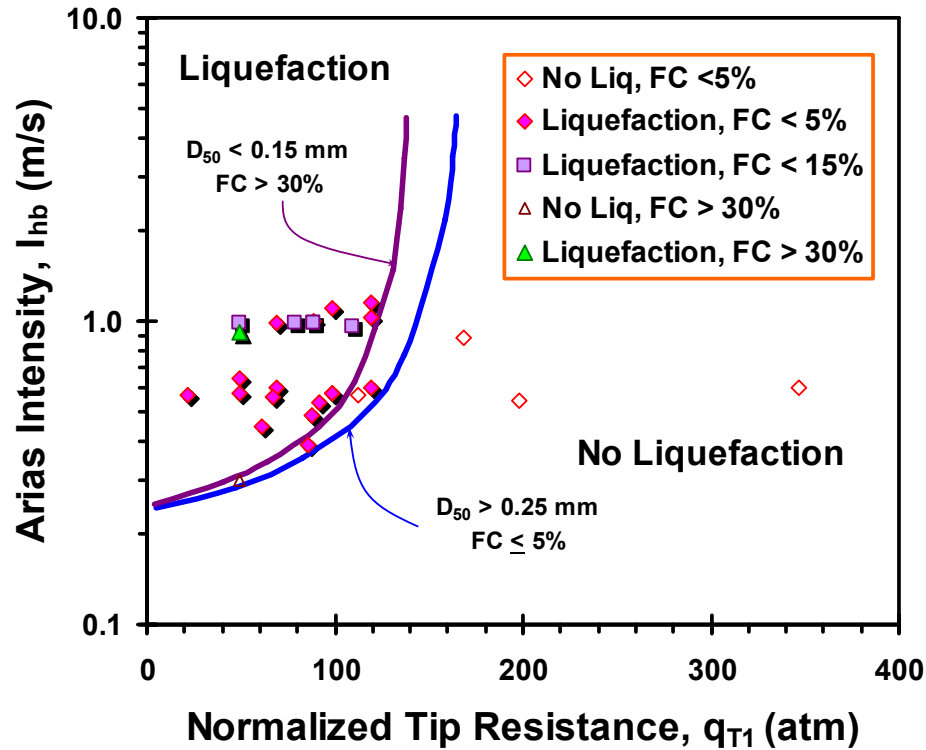
Figure 5.34 Arias intensity liquefaction field data and boundary curves suggested by Kayen & Mitchell (1997) based on CPT tip resistance

5.4 Summary

A review of liquefaction evaluation methods based on SPT N value and SCPTu data is performed herein, with emphasis on the stress-based approaches. In stress-based approaches, deterministic and/or probabilistic curves can be used with the stress-normalized tip resistance q_{T1} (or q_{c1N}) and normalized shear wave velocity V_{s1} in evaluating the CRR. Comparison of CRR curves developed by various researchers shows that those for clean sands agree relatively well, but significant discrepancy exists for silty sands. The CRRs are generally found to increase with fines content, but lab tests

performed by Carraro et al. (2003) showed CRRs decreases with fines content, probably due to the nonplastic nature of the added fines. As to the energy-based approach, the CRR based on Arias intensity is discussed. Due to the limited case histories for developing this approach, the Arias intensity approach is considered to be quite approximate.

CHAPTER VI

LIQUEFACTION EVALUATION BY SCPTU SOUNDINGS
IN NMSZ

6.1 Outline

The Mississippi embayment is the key geologic feature that overlies the New Madrid

Seismic Zone (NMSZ). The embayment is a deep soil-filled syncline or a trough-like

depression that plunges southward along the course of Mississippi River, extending

from southern Illinois to the Gulf of Mexico, as shown in Figure 6**.**1 (a). Paleozoic

rock forms the bedrock floor of the Mississippi embayment and the thickness of its

upper sediments varies from a few meters at the southern tip of Illinois to more than

1000 m in Arkansas and Tennessee near Memphis, as shown in Figure 6.1 (b). The

soil sediments consist of layers of clay, silt, sand, gravel, chalk, and lignite ranging in

age from Cretaceous at lower depths to recent Holocene at shallow depths. The

uppermost surficial soils consist primarily of clean to slightly silty sands with

occasional to frequent silty clay layers. Figure 6.2 illustrates by color shading the

thickness of the sediments synthesized from well-logging and reflection profiles. The

Mississippi embayment continues south into Mississippi, and the sediment thickness

here increases to 1600 m. Such deep soil columns are much greater than typical

overburden profiles found in the well-known seismic regions of California and

Alaska.

During earthquakes, shear waves from the underlying rock propagate upward through

the soil column. The magnitude of ground shaking can be represented by the

maximum acceleration (a_{max}), or peak ground acceleration (PGA), and is required

input for a liquefaction evaluation of a particular site based on in-situ tests. The value of a_{max} can be estimated from empirical correlations with earthquake magnitude, distance from the seismic energy source, and local site conditions. By estimating the PGA (or a_{max}) from empirical correlations, the cyclic stress ratio (CSR) can be inferred from the simplified procedure outlined in Chapter 5 using equation (5-6).
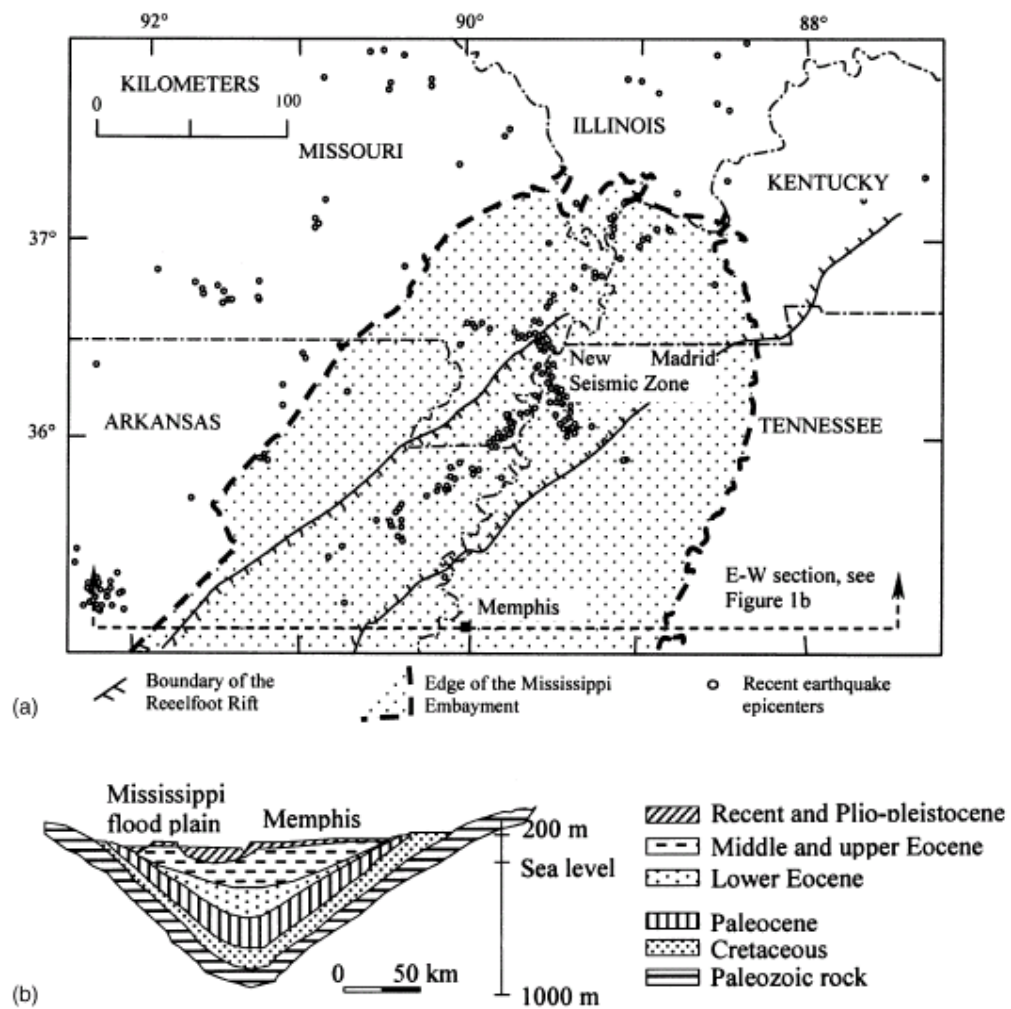
Figure 6.1 The Mississippi embayment: a) Plan view of the Mississippi embayment; b) E-W section through Memphis (Ng et al., 1989; Hashash & Park, 2001).
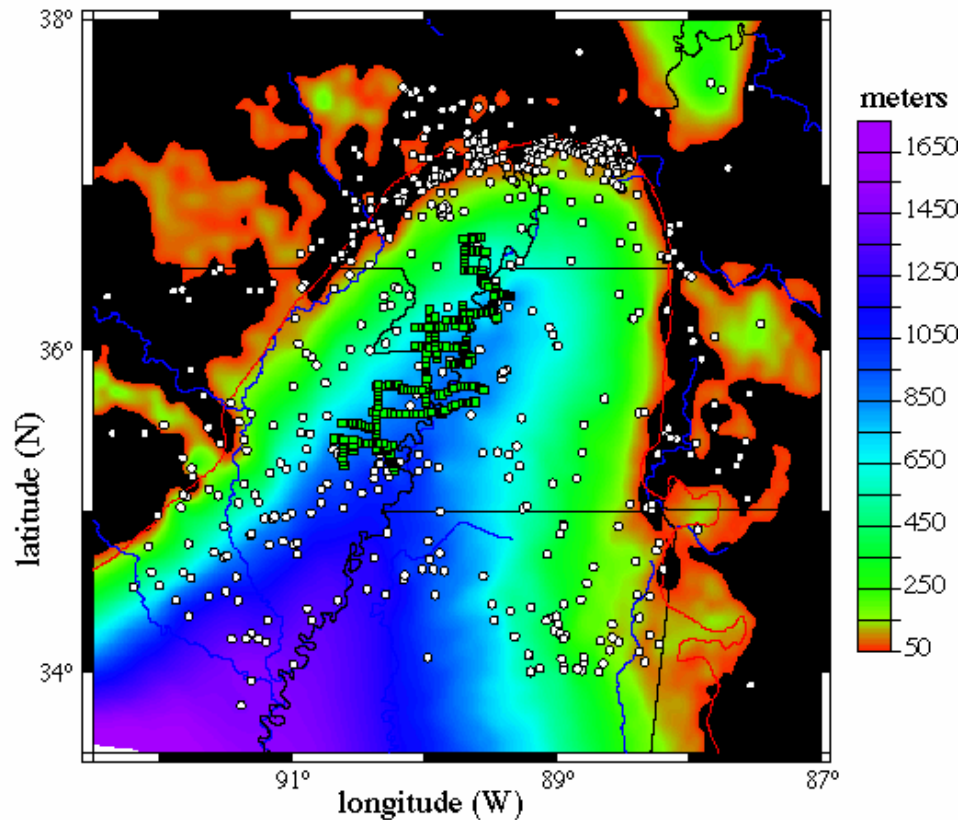
Figure 6.2 The thickness of the Mississippi Embayment sediments from log wells
and reflection profiles shown by color shading
(http://www.ceri.memphis.edu/usgs/model/sedthick.shtml)

However, the local site effects can significantly affect the site response during earthquake shaking. The level of excitation at the ground surface can be less than, equal to, or greater than that at the rock depth, depending upon the specific soil stiffness, damping, layering, and local site effects. The local geologic and soil conditions have been found to influence the intensity of ground motion significantly. For example, ground motions were recorded at six stations along a 6.4-km section in San Francisco during a nearby earthquake of moment magnitude $M_w \approx 5.3$ in 1957 (Idriss & Seed, 1968). The stations were located close to each other, but the recorded peak ground acceleration (PGA) varied from 0.05g to 0.12g due to the variation of thickness of the underlying soil columns (Idriss & Seed, 1968). Similar local site

effects have also been observed during many other earthquakes, such as the 1985 Michoacan earthquake in Mexico (Stone et al., 1987) and the 1989 Loma Prieta earthquake in California (Seed et al., 1990).

Based on a statistical study on 147 sets of earthquake-induced ground motions recorded at sites underlain by different types of soil profiles, Seed et al. (1976) suggested the generalized PGA attenuation relationships for sites of rock, stiff soils, and deep cohesionless soils (Figure 6.3). The overall trends suggest that the PGA at sites of both stiff soils and cohesionless soils are greater than on rock when peak accelerations are small (a_{max} < 0.1 g), and are smaller at higher acceleration levels (a_{max} < 0.1 g). Idriss (1990) developed generalized PGA relationships for soft soil sites (Figure 6.4) based on data from Mexico City and the San Francisco Bay area, as well as on site response analysis. Soft sites are more likely to amplify the peak acceleration above the input bedrock motion at low acceleration levels (a_{rock} < 0.4 g), and the amplification decreases with acceleration level on bedrock. For a_{rock} > 0.4 g, the PGA is lower than the acceleration level on bedrock.

The empirical peak acceleration attenuation relationships aforementioned are almost exclusively developed from earthquakes outside of the NMSZ. Due to the deep soil deposit feature and the long recurrence period of major earthquakes in the NMSZ, the recordings of strong ground motions are not available for developing its own empirical attenuation relations. Boore & Joyner (1991) constructed a generic deep-soil column for deep soil sites in eastern North America, by averaging the shear wave velocities compiled from a number of deep soil sites and assigning the damping ratio to the layers that are reasonably consistent with those inferred in the Mississippi

embayment. Accounting for the effect of this generic deep-soil column, a stochastic

model was used to estimate motions at deep soil sites for a number of distances and

magnitudes. Then, the following equation was derived from these motions to estimate

the PGA or a_{max}:

$$\log(a_{max}) = 3.663 + 0.448(M_w - 6) - 0.037(M_w - 6)^2 - 0.016(M_w - 6)^3 - \log R - 0.0022R \quad (6-$$

$$1)$$

where a_{max} in cm/s^2, R is the hypocentral distance (km) or distance from the site to the

hypocenter, and M_w is the moment magnitude of the earthquake. This relationship can

represent the average soil conditions in the Mississippi Embayment for moment

magnitudes ranging from 5 to 8.5 and distances R from 10 to 400 km (Boore &

Joyner, 1991). Alternatively, the PGA can be estimated from the NEHERP maps of

earthquake ground motion for an earthquake of a certain magnitude.
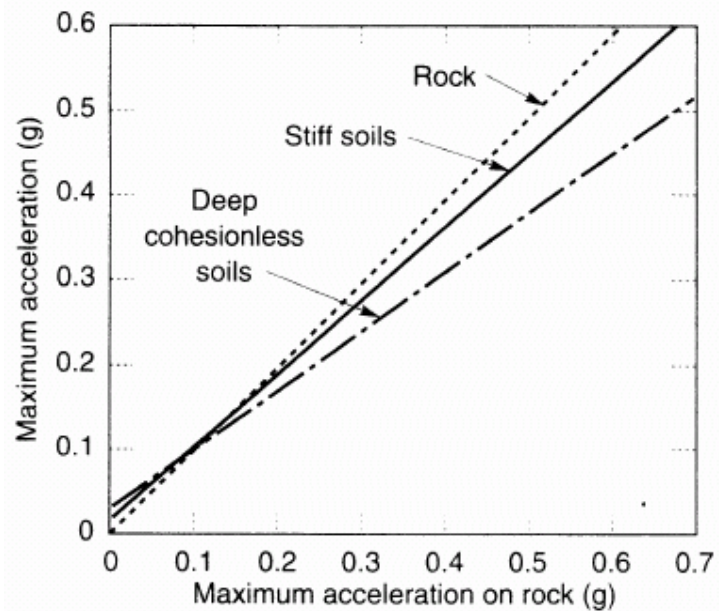
Figure 6.3 Relationship between peak accelerations at rock outcrop and soil sites
based on 147 sets of earthquake-induced ground motions (Seed et al., 1976)
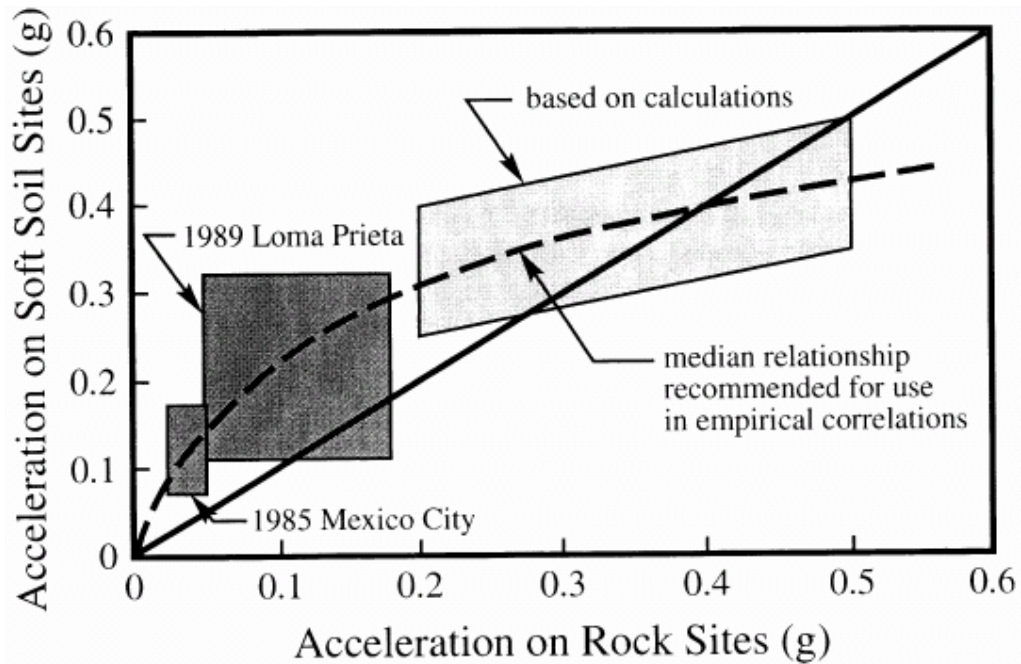
Figure 6.4 Relationship between peak accelerations on rock and soft soil sites based on data from Mexico city and the San Francisco Bay area, as well as on site response analysis (Idriss, 1990)

With equation (6-1), the PGA can be estimated for sites in NMSZ for certain earthquakes, and then the cyclic stress ratio (CSR) can be calculated using the simplified procedure. It provides an approximate solution for the seismic loading. Since this procedure does not account for local site effects, the result can be different from reality. In this situation, site response analysis is commonly used to account for local site effects and to determine the response of the soil deposit to the motion of the bedrock immediately beneath it. Figure 6.5 illustrates the procedure for liquefaction evaluation based on SCPTu soundings and site response analysis. The bedrock motion resulted from an earthquake is generated numerically, and then the propagation of the ground motion from the bedrock to the ground surface is simulated by software conducting site response analysis. The cyclic stress ratio (CSR) can thus be obtained and compared with the cyclic resistance ratio (CRR) that can be derived from SCPTu soundings. In this thesis, site response analysis is applied to the paleoliquefaction sites

185

in the NMSZ for liquefaction evaluation. Base on the results, regional criteria of liquefaction evaluation based on SCPTu data are developed for the NMSZ.
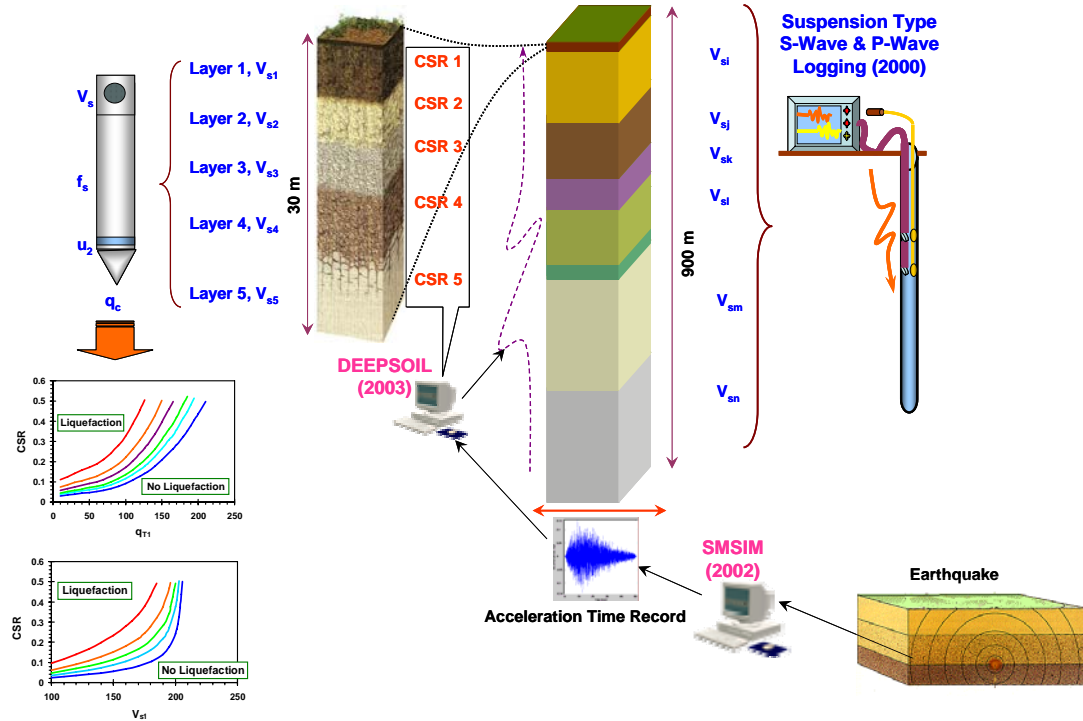
Figure 6.5 Liquefaction evaluation based on SCPTu soundings and site response analysis

6.2 Evaluation of Cyclic Stress Ratio by Site Response Analysis

One-dimensional (1D) analysis is commonly employed for site response analysis. It assumes that all soil layers are horizontal and that the response is predominantly caused by shear waves propagating vertically upward from the underlying bedrock.

The bedrock motion is generated by seismic hazard analysis using the program SMSIM developed by Boore (2002). This program uses a stochastic approach to generate synthetic bedrock motion, given the earthquake magnitude and source-to-site distance. In this thesis, the ground motion relations proposed by Atkinson & Boore

(1995) for eastern North America are chosen as input source and path model for the SMSIM program.

The 1D equation of motion for vertically propagating shear waves through an unbounded medium can be written as:

$$\rho \frac{\partial^2 u}{\partial t^2} = G \frac{\partial^2 u}{\partial z^2} + \eta \frac{\partial^3 u}{\partial z^2 \partial t} \qquad (6\text{-}2)$$

where ρ = density, u = displacement, z = depth below the ground surface, G = shear modulus, t = time, and η = viscosity.

In site response analysis, there are two main numerical methods for solving different equation (6-2): (1) equivalent linear analysis method solved in frequency domain, and (2) nonlinear analysis performed in time domain. The equivalent linear approach to one-dimensional ground response analysis has been implemented in computer programs such as SHAKE (Schnabel et al., 1972) and RASCALS (Silva, 1992). Newer versions of SHAKE are available as EDUSHAKE (http://www.proshake.com) and SHAKE2000 (http://www.shake2000.com). Although the equivalent linear analysis is computationally simple, it is essentially an approximation to the actual nonlinear process of seismic ground response. Nonlinear analysis, on the other hand, uses direct numerical integration in the time domain and can more accurately simulate the nonlinear behavior of soils. Table 6.1 lists some of the most commonly-used computer programs for nonlinear one-dimensional ground response analysis.

Table 6.1 Computer programs for nonlinear one-dimensional ground response
analysis (after Kramer, 1996; Luna, 2004)

Program	Soil Model	Method	Stress	Reference
CHARSOIL	Ramberg-Osgood	Characteristics	Total	Streeter et al. (1973)
MASH	Martin-Davidenkov	Finite Element	Effective	Martin and Seed (1978)
DESRA-2	Hyperbolic	Finite Element	Effective	Lee and Finn (1978)
TESS1	HDCP (Hardin-Drnevich-Cundall-Pyke)	Finite Element	Effective	Pyke (1985)
DYNA1D	Nested yield surface	Finite Element	Effective	Prevost (1989)
SUMDES	Hypoplasticity	Finite Element	Effective	Li et al. (1992)
D-MOD	M-K-Z (Matasovic, Konder, and Zelasko)	Finite Element	Effective	Matasovic (1993)
DESRAMOD2	Hyperbolic	Finite Element	Effective	Vucetic (1998)
DESRA-MUSC	Hyperbolic	Finite Element	Effective	Qiu (1998)
DEEPSOIL	Modified Hyperbole	Finite Element	Effective	Park & Hashash (2004)

A new 1D nonlinear time domain site response analysis model (DEEPSOIL) has been developed by Park (2003) and Park & Hashash (2004). This model incorporates several improvements over conventional 1D nonlinear time-domain analysis.

In time domain analysis, the wave propagation equation (6-2) can be written as:

$$[M]\{\ddot{u}\} + [C]\{\dot{u}\} + [K]\{u\} = -[M]\{I\}\ddot{u}_g \qquad (6-3)$$

where $[M]$ = mass matrix; $[C]$ = viscous damping matrix; $[K]$ = stiffness matrix; $\{\ddot{u}\}$ = vector of nodal relative acceleration; $\{\dot{u}\}$ = vector of nodal relative velocities; $\{u\}$ = vector of nodal relative displacements, $\ddot{u}_g$ = acceleration at the base of the soil column, and $\{I\}$ is the unit vector.

The viscous damping matrix $[C]$ represents damping at very small strains where many soil models are primarily linear, and it is assumed to be proportional to the mass and stiffness matrices:

$$[C] = a_0[M] + a_1[K] \qquad (6-4)$$

where a_0 and a_1 are scalar values. In traditional analyses, viscous damping is supposed to be frequency independent. However, in time domain analysis, the ground motion is not decomposed to a sum of harmonic components, and it is impossible to make the viscous damping frequency independent.

Park and Hashash (2004) suggests that scalar values a_0 and a_1 can be computed as following, assuming the damping ratio is constant throughout the soil profile:

$$\begin{bmatrix} \zeta_m \\ \zeta_n \end{bmatrix} = \frac{1}{4\pi} \begin{bmatrix} \dfrac{1}{f_m} & f_m \\ \dfrac{1}{f_n} & f_n \end{bmatrix} \begin{Bmatrix} a_0 \\ a_1 \end{Bmatrix}$$ (6-5)

where m and n are two significant natural modes, f_m and f_n are the corresponding natural frequency values, and ζ_m and ζ_n are the corresponding damping ratios. Equation (6-5) results in equal damping ratios at the two selected modes. In order to specify more than two frequencies/modes, equation (6-4) can be extended as following:

$$[C] = [M] \sum_{b=0}^{N-1} a_b \left[[M]^{-1}[K] \right]^b$$ (6-6)

where N is the number of frequencies/modes incorporated. Assuming a constant damping ratio throughout the soil profile, the scalar value of a_b is define as follows:

$$\zeta_n = \frac{1}{4\pi f_n} \sum_{b=0}^{N-1} a_b \left(2\pi f_n \right)^{2b}$$ (6-7)

The viscous damping formulation in equation (6-5) reduces the artificial damping introduced numerically through uncontrolled frequency-dependent viscous damping (Park and Hashash, 2004).

DEEPSOIL also incorporates a confining stress-dependent nonlinear soil model. It is based on the modified hyperbolic model developed by Matasovic and Vucetic (1995):

$$\tau = \frac{G_{max}\gamma}{1 + \beta\left(\dfrac{G_{max}}{\tau_{mo}}\gamma\right)^s} = \frac{G_{max}\gamma}{1 + \beta\left(\dfrac{\gamma}{\gamma_r}\right)^s} \qquad (6\text{-}8)$$

where τ = shear stress; γ = shear strain; G_{max} = initial shear modulus; τ_{mo} = shear stress at approximately 1% shear strain; $\gamma_r = \tau_{mo}/G_{max}$ is the reference shear strain; and β and s are two parameters to adjust the shape of the backbone curve to represent a wider range of measured soil behavior. In order to allow coupling between confining stress and shear stress, Park and Hashash (2004) proposed the following stress-dependent reference strain:

$$\gamma_r = a\left(\frac{\sigma_{vo}{}'}{\sigma_{ref}}\right)^b \qquad (6\text{-}9)$$

where a and b are curve fitting parameters, $\sigma_{vo}{}'$ is effective vertical stress, and σ_{ref} is a reference confining stress. Park and Hashash (2004) also suggested the following equation to describe the dependency of zero strain equivalent damping ratio on confining pressure:

$$\xi = \frac{c}{\left(\sigma_{vo}{}'\right)^d} \qquad (6\text{-}10)$$

where c and d are material parameters and $\sigma_{vo}{}'$ is the effective vertical stress.

The influence of confining stress (or effective mean principal stress) is very important on cyclic behavior of soils for deep soil sites, but it has been generally neglected in most site response analysis studies, because many sites have relatively shallow depths

to bedrock (Park, 2003). With the confining stress dependent nonlinear soil model, DEEPSOIL can more accurately predict the ground motions, particularly in NMSZ where the soil column extends to depths of 1000 m or more.

The 1D nonlinear time domain site response analysis model (DEEPSOIL) is implemented in a program also called DEEPSOIL (Park, 2003). It inputs the bedrock motion and soil properties, such as shear wave velocity, unit weight, shear modulus degradation curves and damping curves, and it outputs the time-history of ground motion, shear stress, and shear strain for each soil layer. Compared with the simplified procedure, in which the cyclic stress ratio (CSR) is approximately assessed from the estimated maximum ground surface acceleration, the computed time-history of shear stress is more appropriate for the liquefaction evaluation. It takes account of the local site effects and nonlinearity properties of soils, and includes information on both the amplitude and duration of the ground shaking. It is a fact that the cyclic shear stress for liquefaction evaluation is addressed as the CSR, which is the ratio of the average equivalent uniform shear stress τ_{av} to the overburden stress σ_{vo}'. With seismic response analysis (i.e. DEEPSOIL), the CSR can be derived directly from equation (5-4) without the assumption of rigid soil column that exists in the simplified procedure. Thus the stress reduction coefficient r_d is not needed to account for the flexibility of the soil column, reducing the uncertainty of the liquefaction analysis results.

6.3 Shear Modulus in Mississippi Embayment

Nonlinear seismic response analysis by DEEPSOIL requires the input of dynamic soil properties for each layer, including shear wave velocity (V_s), shear modulus reduction curve (G/G_{max}), and damping ratio (ζ).

Based on geologic age of near-surface deposits, Romero et al. (2001) classified the Mississippi embayment into two broad categories as shown by Figure 6.6: (1) Holocene-age deposits (called Lowlands) that are located along the floodplains of the Mississippi River and its tributaries; (2) Pleistocene-age deposits (called Uplands) that are found in the interfluve terrace regions. By aggregating and synthesizing various near-surface V_s profiles in this region, generic shear wave velocity profiles for the two geologic categories were developed up to a depth of 70 m, as shown in Figure 6.7 (a). The Lowlands profile shows lower shear wave velocity than the Uplands profile, for the Holocene-age deposits were found to be loose in the alluvial plains. The generic V_s profile for deep soils extending from 70 m to 1000 m [Figure 6.7 (b)] is developed from V_s estimated from various models, which relate the depth of soil to V_s by assuming V_s is a certain function of depth z (i.e. $V_s = f(z)$) (Romero, 2001).

Recent explorations in the Mississippi Embayment provided measured V_s profiles of deep soil sites, which locations are shown in Figure 6.8. An exploratory well for hydrocarbons was drilled at Keiser located in northeast Arkansas, and went to a final depth of 887.4 m before meeting hard limestone. Upon completion of the well, geophysical logging was performed. Based on the measured velocity of P-wave, also known as compression wave, Rix (2004) inferred the V_s profile as shown in Figure 6.9 (a). The logs in the top 75.7m were not used, because they were affected by the

presence of the surface steel casing. Also plotted on Figure 6.9 (a) is a set of shear wave velocity V_s and compression wave velocity V_p profiles directly measured by downhole logging during advancement of a water well in Memphis, TN. The logs go from 15.8 m to a depth of 425.2 m. The wave velocities in Figure 6.9 (a) show unrealistic fluctuations, which are probably resulted from measurement errors. The technique of moving averages is applied to the data, and the average value of wave velocities at depth intervals of 5 m is assumed to be their approximate value at the corresponding median depth. The wave velocities smoothed with moving average are presented in Figure 6.9 (b).
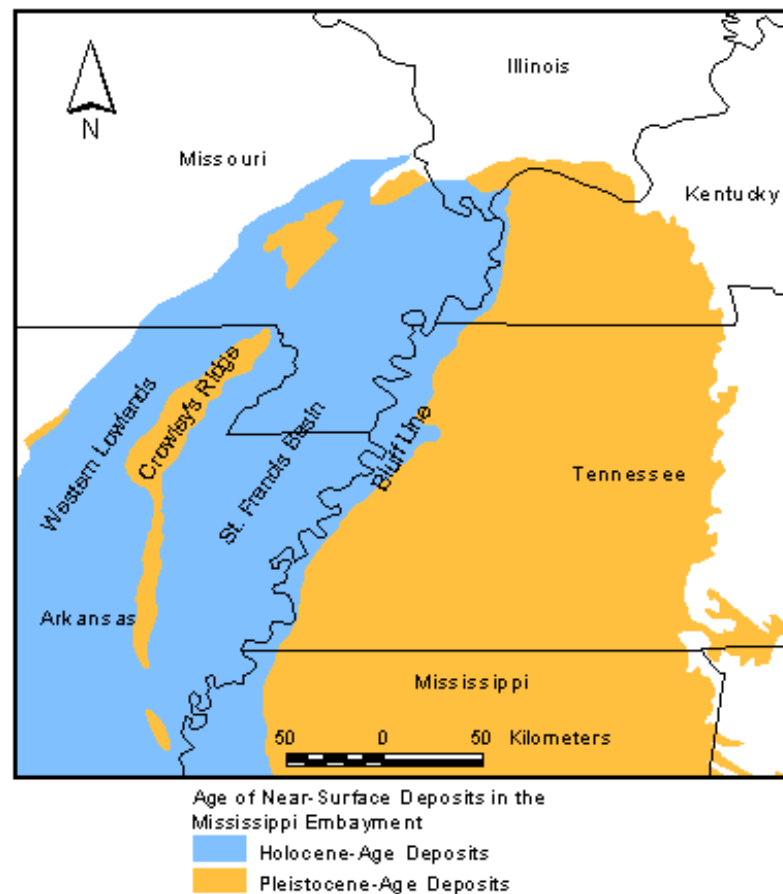
Figure 6.6 Age of near-surface geologic deposits in the Mississippi embayment
(Romero, 2001)

An approximate V_s profile can be created for the deep soil sites in the NMSZ. The V_s in the top 30 m can be obtained from the SCPTu test, and those between the depth of 30 m and 425.2 m are the real V_s data collected by downhole logging in Memphis, TN. While those below 425.2m are the V_s inferred from the P wave velocity from downhole logging at Wilson Well, Keiser, AR. Figure 6.10 compares the composite of measured suspension-type V_s from downhole logging and the generic V_s values suggested by Rix & Romero (2001). From this figure, it can be seen that the measured V_s follows the general trend of the generic V_s profile.
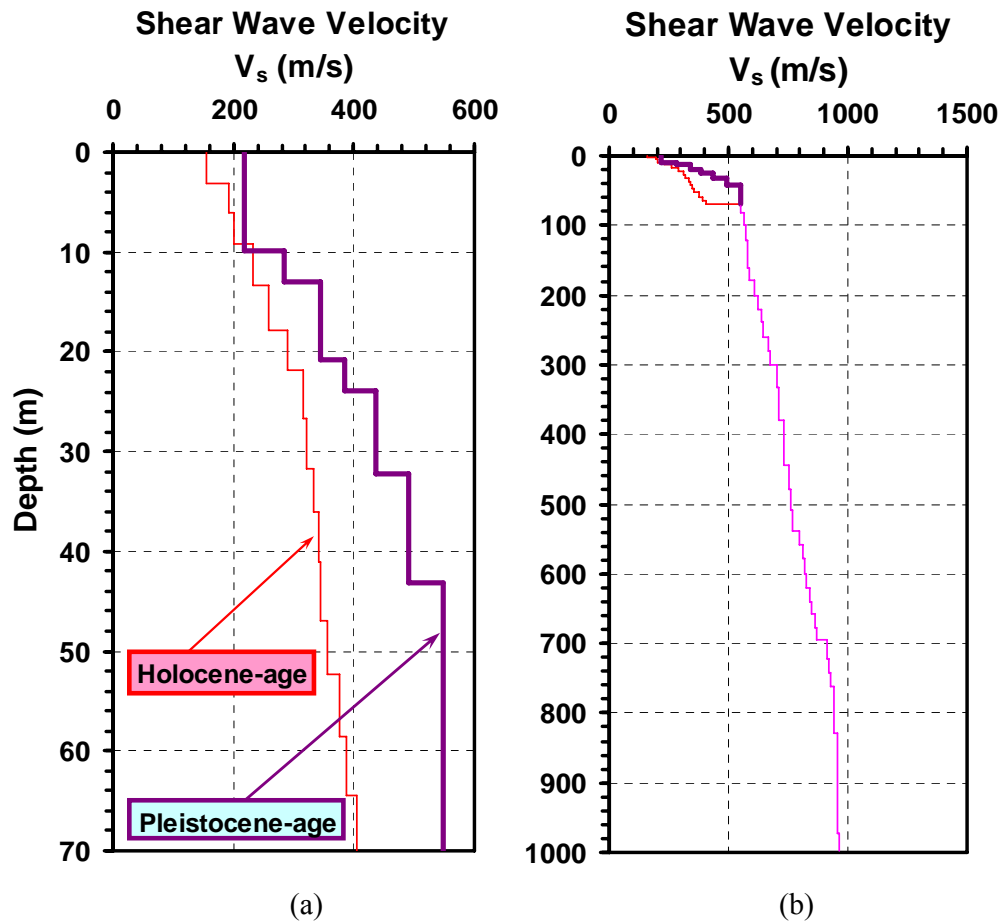
Figure 6.7 Generic shear wave velocity profiles and simplified stratigraphy of Mississippi embayment: a) up to 70m; b) up to 1000m (Romero, 2001)

Figure 6.8 Map showing the recent locations where deep shear wave velocity V_s and compression wave velocity V_p profiles were acquired

For a specific site, the V_s in the top 30 m can be accurately measured in a downhole manner by a SCPT test. In fact, this shallow depth is of paramount significance to seismic evaluation. The 2000 IBC (International Building Code) emphasizes the importance of the average V_s in the top 30.5 m (100 ft) by using it to define sites with respect to their seismic vulnerability, as listed in Table 6.2. The measured V_s classifies the sites into different categories, which has significant impact on design of

structures. Accurate measurement of V_s can ensure the correct design for seismic safety, as well as justify the economic cost.
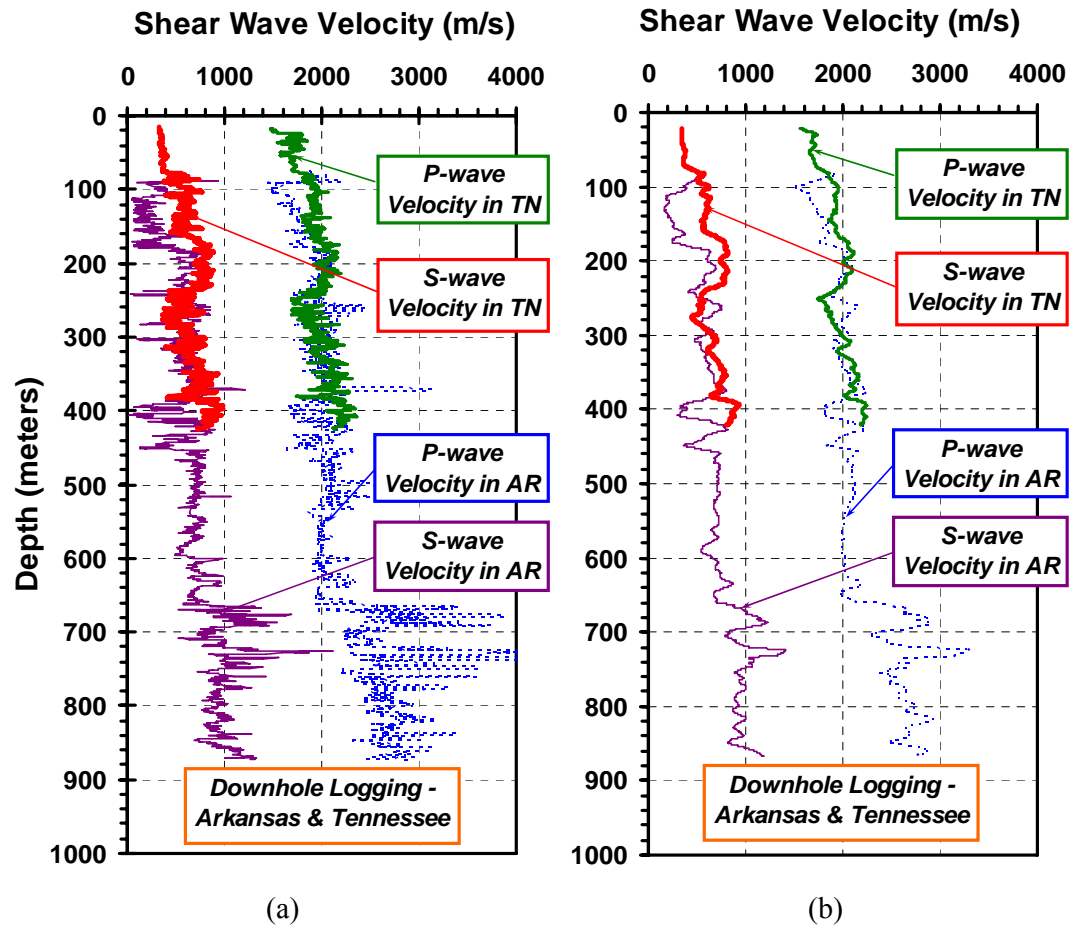
Figure 6.9 Shear wave velocity and compression wave velocity from Keiser, AR and Memphis, TN: (a) Unsmoothed wave velocities; (b) Smoothed wave velocities

Table 6.2 Site class definitions by average shear wave velocities (IBC, 2000)

Site Class	Soil Profile Name	Average shear wave velocity $\overline{V}_s$ (m/s) in top 30.5 m
A	Hard rock	$\overline{V}_s > 1524$ m/s
B	Rock	762 m/s $< \overline{V}_s \leq 1524$ m/s
C	Very dense soil and soft rock	366 m/s $< \overline{V}_s \leq 762$ m/s
D	Stiff soil profile	182 m/s $< \overline{V}_s \leq 366$ m/s
E	Soft soil profile	$\overline{V}_s < 182$ m/s
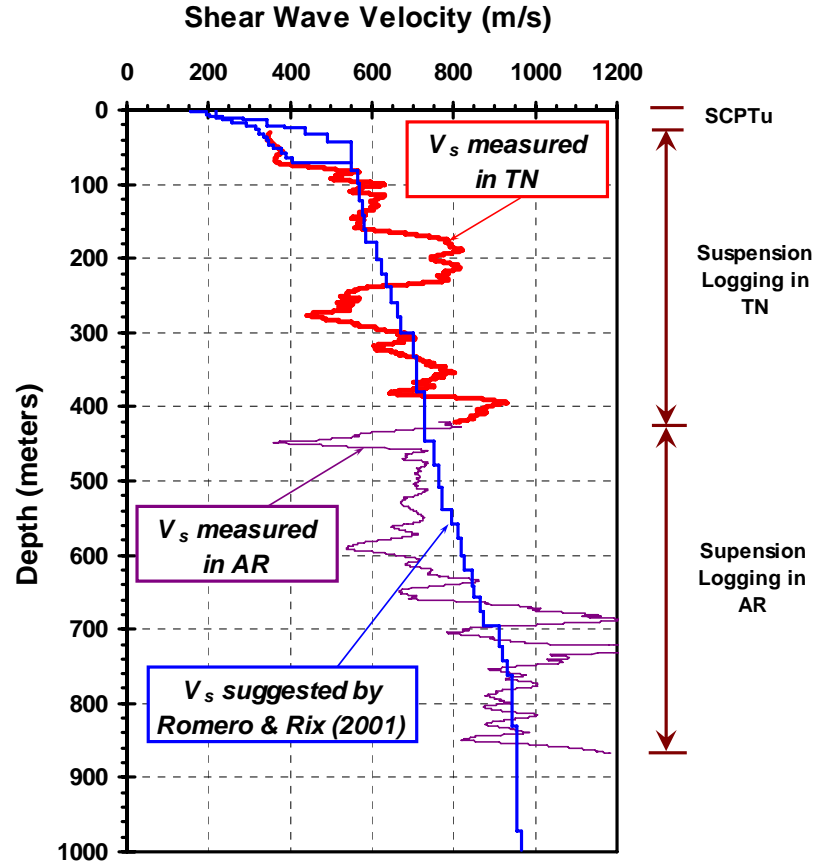
Figure 6.10 Composite of measured suspension-type shear wave velocity from downhole logging in comparison with the generic shear wave velocity developed by Rix & Romero (2001) for the Mississippi Embayment

For detailed site amplification analysis, the composite V_s profile shown in Figure 6.10 can be input into the program DEEPSOIL. The composite V_s profile combines the shallow near-surface V_s measured by SCPT (i.e., upper 30 m), the V_s profile from S-wave logging measured in Memphis, TN to 425 m, and the inferred V_s values for depths up to 900 m from P-wave velocity logging at the Arkansas site. With shear wave velocity V_s and the saturated unit mass density ρ_T, the small-strain shear modulus G_{max} can be derived ($G_{max} = \rho_T V_s^{\,2}$), as discussed in Chapter 4.

The small strain stiffness (G_{max}) is a reference benchmark and needs to be reduced with higher levels of strain. The Electric Power Research Institute (EPRI, 1993) developed generic depth-dependent modulus reduction (G/G_{max}) and damping (D) curves for the deep soil sediments of the Mississippi embayment, as shown in Figure 6.11. They are based on results of resonant column/torsional shear and large-scale triaxial chamber laboratory tests, as well as literature review of available dynamic curves. Park (2003) simulated the EPRI dynamic curves by set value to the material parameters as shown listed in Table 6.3. The simulated curves are compared with EPRI curves in Figure 6.11, which shows a relatively good match.

Table 6.3 Value of material parameters used in the simulated dynamic curves
(after Park, 2003)

Parameters	β	s	σ_{ref}	a	b	c	d
Value	0.7	0.8	0.18 MPa	0.05	0.4	Chosen to match small strain damping of EPRI curves	0.0
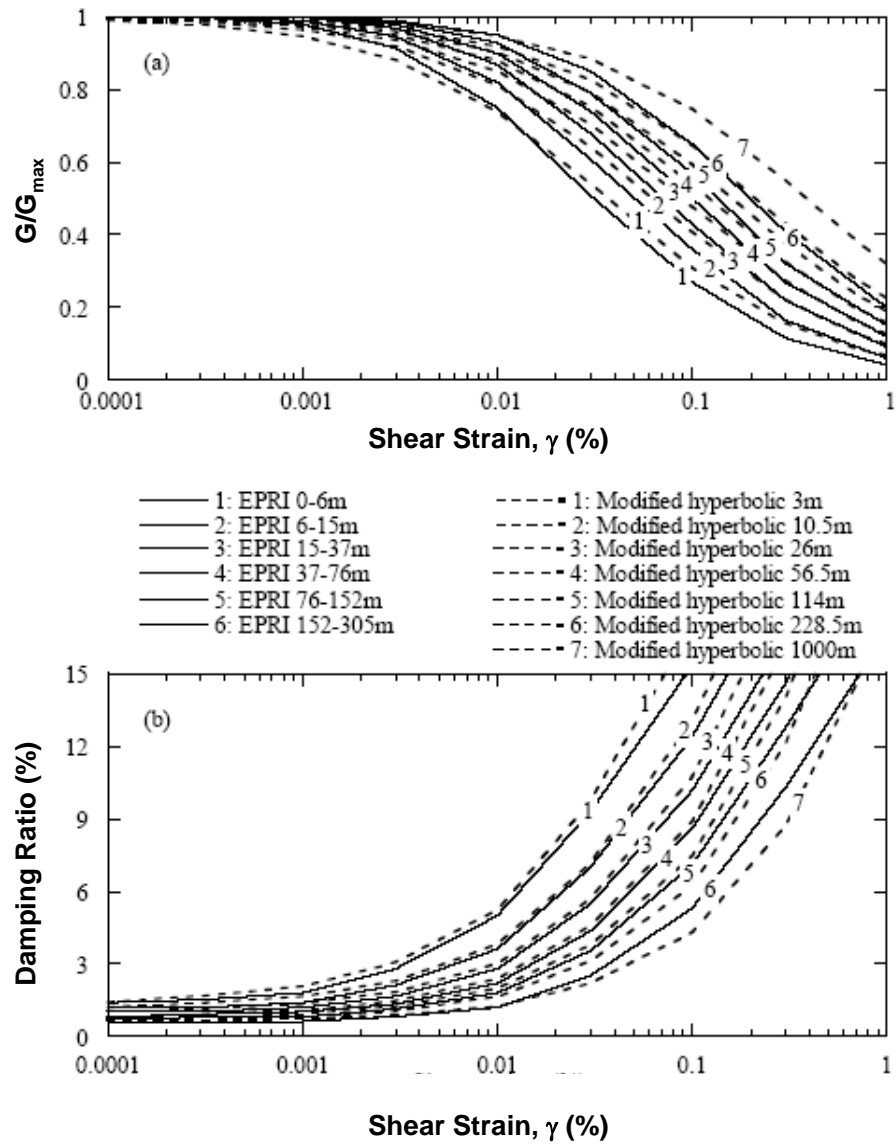
Figure 6.11 Comparison of modulus degradation and damping curves suggested by EPRI (1993) and those developed to match EPRI curves (Park, 2003)

6.4 Scenario Earthquakes for Strong Ground Motion in NMSZ

In order to develop seismic hazard maps for Memphis, Shelby County, Tennessee, Cramer et al. (2004) assumed two scenario earthquakes for median ground motions. The first one is a $M_w = 7.7$ earthquake on the southwesterly trend line of seismicity of the NMSZ (Figure A.1 in Appendix A). The second is a $M_w = 6.2$ earthquake at Marked Tree, Arkansas at the southern end of the southwest-trending arm of seismicity of the NMSZ.

Site investigation have given well-constrained age estimates for a number of liquefaction features associated with previous earthquakes in the NMSZ. Tuttle (1999) has summarized these results from paleoliquefaction sites in a chronology shown in Figure 6.12. Findings from the chronology indicated that besides the 1811-1812 earthquakes, major earthquakes also occurred around 1530, 900, and 490. The liquefaction fields attributed to the 1811-1812 A.D., 1530 A.D., and 900 A.D. events, were interpreted, as shown in Figure 6.13 (Tuttle, 1999). The corresponding estimated earthquake magnitudes are also shown in the figure. The spatial distributions of liquefaction features that formed during these earthquake events are represented as the zones enclosed by the ellipses shown in the figure. The liquefied areas during 1530 A.D. and 900 A.D. earthquakes are similar to those that formed during 1811-1812 A.D. (Tuttle, 1999), showing a pattern consisting two to three major earthquake events.

Assuming the epicenters of the earthquakes are at the center of the ellipses, the epicenters corresponding to the 1530 A.D. and 900 A.D. earthquakes are plotted in Figure 6.14. As can be seen from this figure, the epicenters can be clustered into two

200

groups, which are located in the two areas enclosed in the two ellipses plotted on the figure, respectively. The area in the north has four epicenters with the corresponding earthquake magnitudes ranging from 7.8 to 8.0, and the area in the south has three epicenters corresponding to two magnitude 7.6 earthquakes and one magnitude 8.1 earthquake.
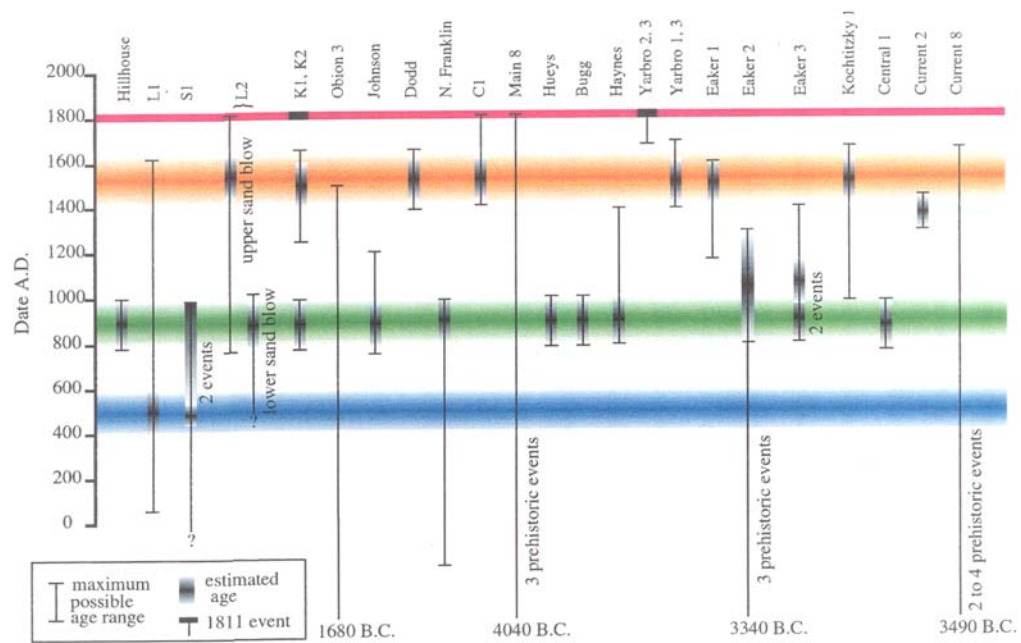
Figure 6.12 Chronology for the liquefaction features found at sites in the New Madrid region (Tuttle, 1999)

201
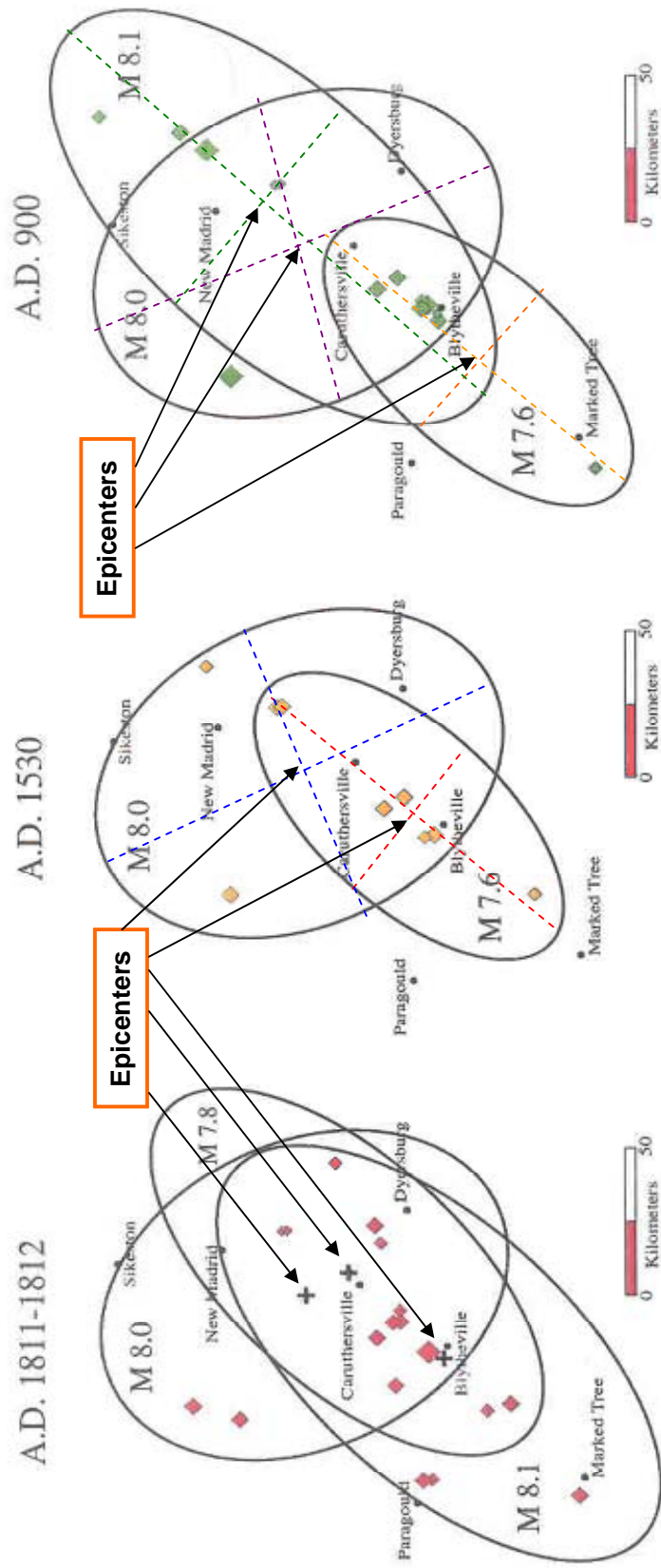
Figure 6.13 Interpretations of distribution of liquefaction features attributed to historic earthquakes in 1811-1812, 1530, and 900 (after Tuttle, 1999)
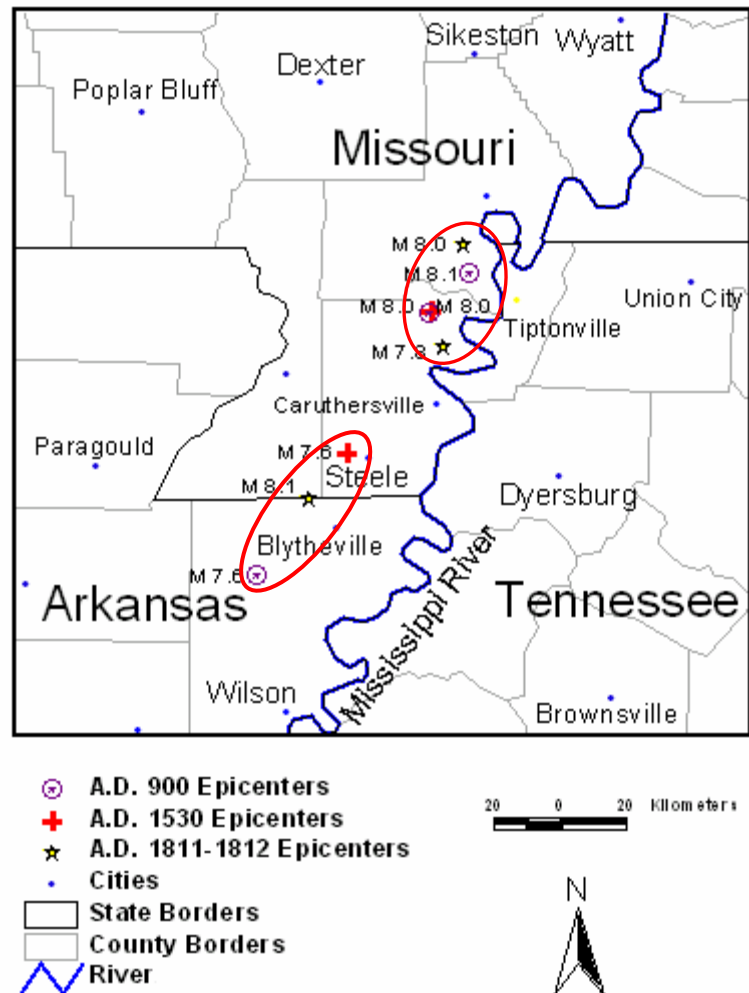
Figure 6.14 Estimated epicenters of earthquakes in 1811-1812, 1530, and 900

This leads to the thought that the major earthquake events followed similar patterns with regard to the magnitude, epicenter, and liquefaction fields. It is reasonable to surmise that the major earthquakes in the future might follow the same pattern too. Therefore, two scenario earthquakes can be assumed for strong ground motion. Their epicenters are located in the center of the two areas enclosed by the ellipse shown in Figure 6.14, and their moment magnitude can be assumed as 8.0.

6.5 Liquefaction Evaluation for Paleoliquefaction Sites in NMSZ

Sites of the liquefaction features caused by previous major earthquakes have been identified in the NMSZ, and the magnitude and epicenters of the corresponding earthquake events have been estimated by paleoliquefaction studies (e.g. Tuttle, 1999). Curiosity warrants a look at the liquefaction analysis results for these paleoliquefaction sites, in the event of the same earthquake events that caused liquefaction hundreds of years ago.

6.5.1 Liquefaction Evaluation at Walker Site of Marked Tree, AR

A series of CPT tests was performed at the Walker paleoliquefaction site that is located near Marked Tree, AR. Figure 6.15 presents a vicinity map showing the location of this site. A notable feature of the Walker site is its well-preserved Indian Mound, as shown in Figure 6.16. This site was selected for a paleoseismology study because sand blows were found in association with a Native American occupation horizon, suggesting that the sand blow was prehistoric in age (Tuttle et al., 2000). The study included a large scale surface resistivity survey to locate anomalies indicating the exact location of the feeder dikes (Wolf et al., 1996; Barnes, 2000).

From the contour plot of the resistivity data from the west side of the Indian mound (Figure 6.17), a northwest-southeast trending anomaly with high resistivity (green) can be seen, reflecting a sudden lateral change in sediment composition. The high gradient of resistivity values indicates sand, which is of high resistivity, had been injected into

overlying clay or finer-graned deposits, which is of low resistivity. Similarly, Figure 6.18 shows the contour plot for the south side of the Indian Mound, isolated areas of high resistivity suggest the existence of liquefaction features. After the orientation of the sand dikes and related sand blow were defined by geophysical survey, the sand dikes were trenched to examine stratigraphic relations and to document the liquefaction features and the cultural horizon (Tuttle, 1999). The locations of the two trenches are shown as white rectangles in Figure 6.17 and 6.18. Both trenches are approximately 5 m in length and 1 m in width. Excavation trench 1 is orientated across the northwest-southeast trending geophysical anomaly to the west of the Indian Mound. The exposed portion of a sand blow and its associated sand dike are shown in Figure 6.19. The fine- to medium-grained sand dike crosscuts mud and sandy mud layers containing pottery shreds, charcoal, and deer bones. Based on radiocarbon dating of charcoal sample C2 found in the sandy mud layer below the sand blow, the liquefaction features were formed after A.D. 1420. Excavation trench 2 located to the south of the Indian Mound is oriented across the northwest-southeast trending geophysical anomaly seen in the resistivity contour plot (Figure 6.18). It intersected two fine- to medium-grained sandy dikes and a portion of their associated sand blow, as shown in Figure 6.37. Similar to those exposed in excavation trench 1, the sand dikes crosscut the top layers, and sand blow material has been deposited on top of the sandy mud and muddy fine sand layers. Radiocarbon dating of charcoals C2 and C3 provided calibrated dates of 1530 A.D.-1550 and A.D. 530-660, respectively. The similarity of the sand dikes exposed in excavation trenches 1 and 2 suggests the liquefaction features formed during the same event. On the basis of radiocarbon dating and artifact analysis, the sand blows and related dikes are thought to

have formed during a large New Madrid earthquake circa 1530 A.D. (Tuttle et al., 2000; Barnes, 2000).

At a later date (Aug. 2000), CPT testing was performed in two linear arrays perpendicular to the main direction of the sand dikes, as shown by Figure 6.16. The 14 soundings include 2 seismic cone penetration tests with u_2 measurement (SCPTu$_2$), 8 cone penetration tests with u_2 measurement (CPTu$_2$), and 4 cone penetration tests with u_1 measurement (CPTu$_1$). The intention of these series was to provide information on the subsurface stratigraphy and source sands, explore lateral variability, and evaluate the potential for re-liquefaction.
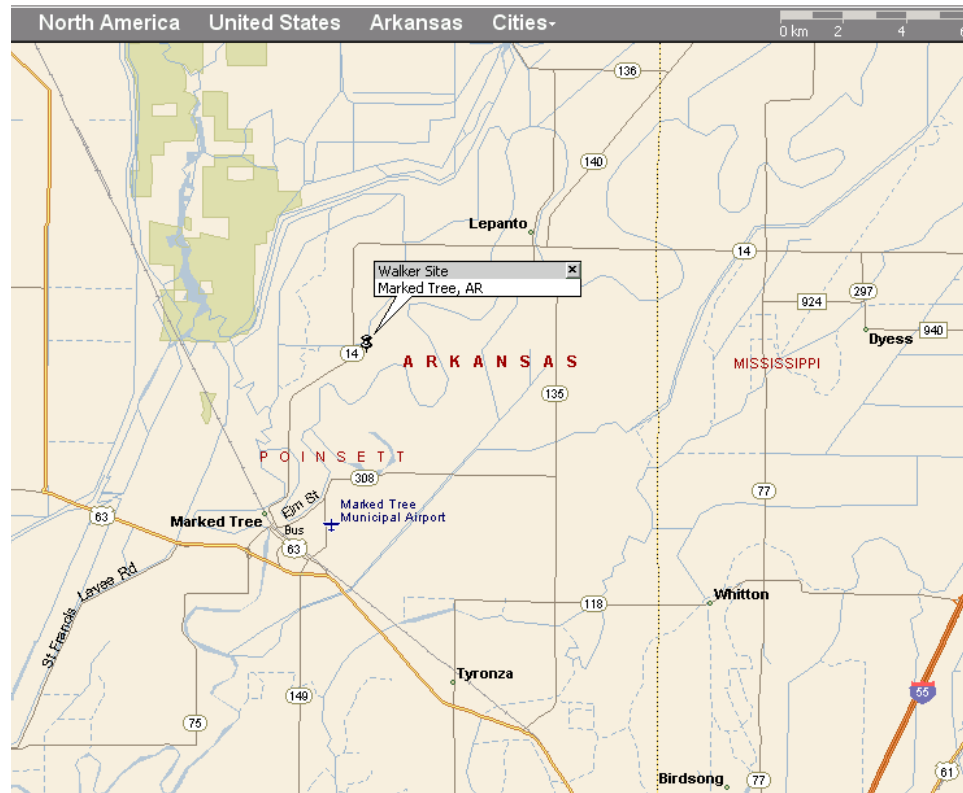
Figure 6.15 Map showing location of the Walker paleoliquefaction site in Marked Tree, Arkansas
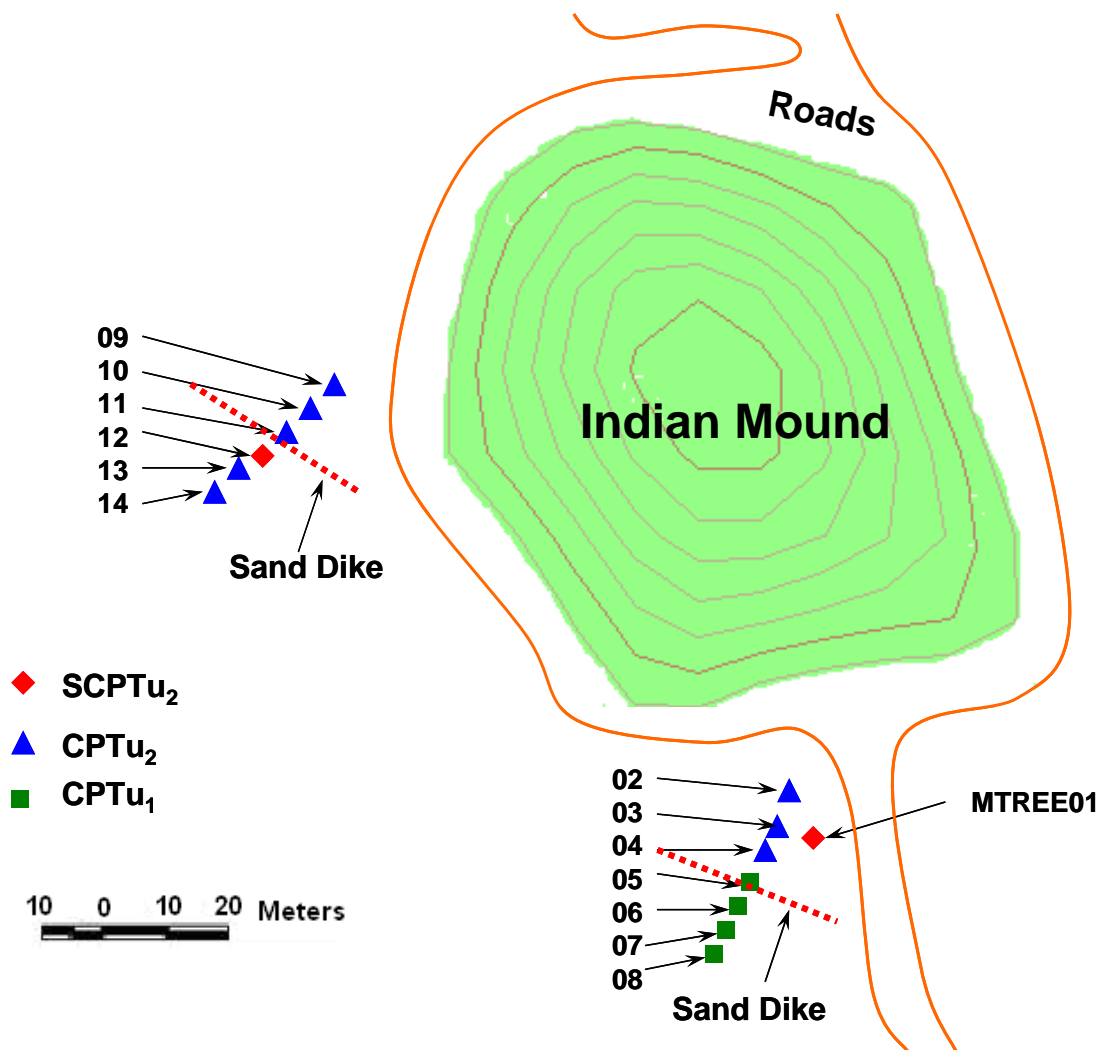
Figure 6.16 Overview of the sounding locations at the Walker paleoliquefaction site in Marked Tree, AR
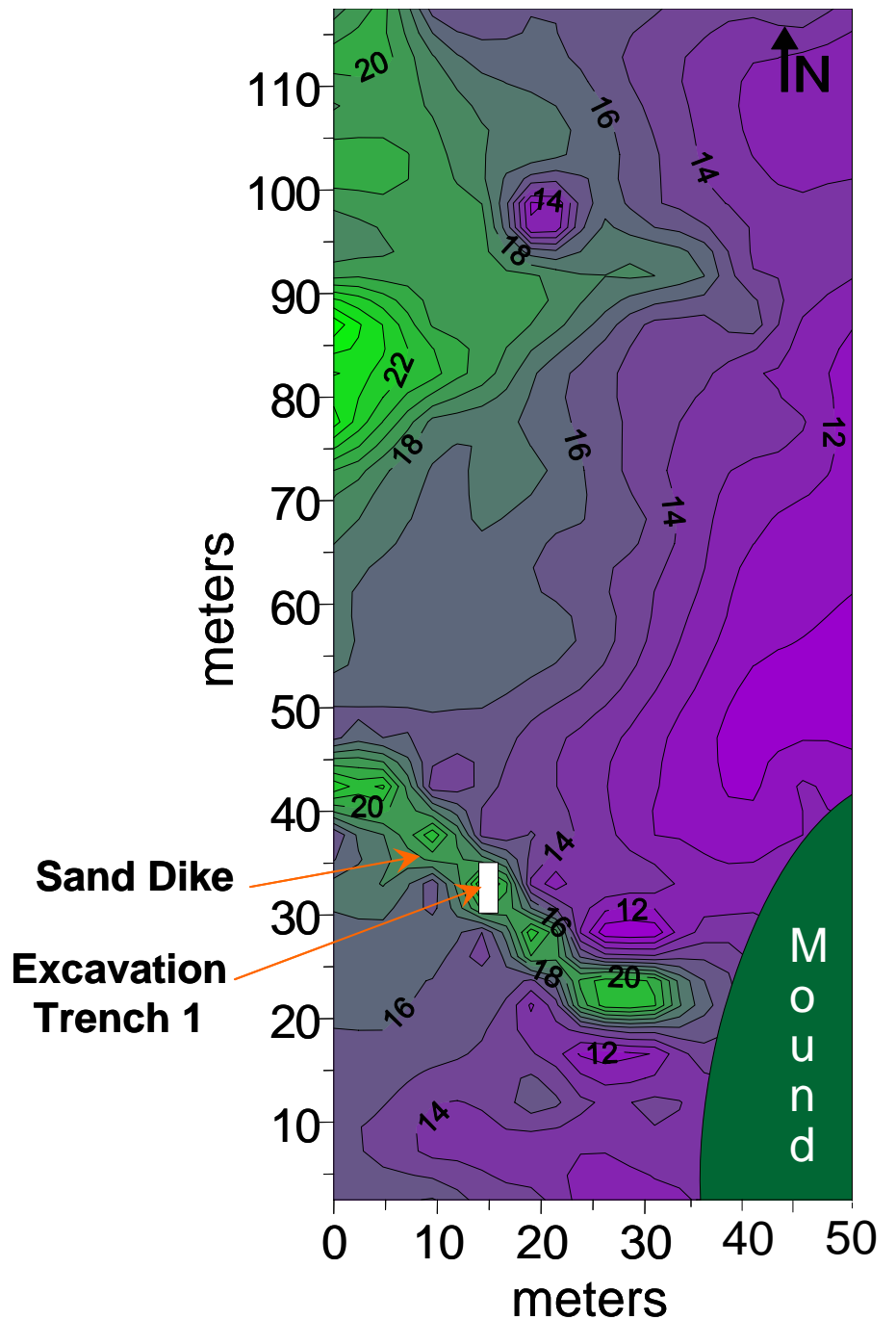
Figure 6.17 Resistivity survey results (in ohm-m) from the west part of the Walker site (Barnes, 2000)

Note: The northwest-trending sand blow and associated sand dike are indicated by high resistivity values (green). White rectangle indicates the location of excavation trench 1 which was oriented across the northwest-trending geophysical anomaly.
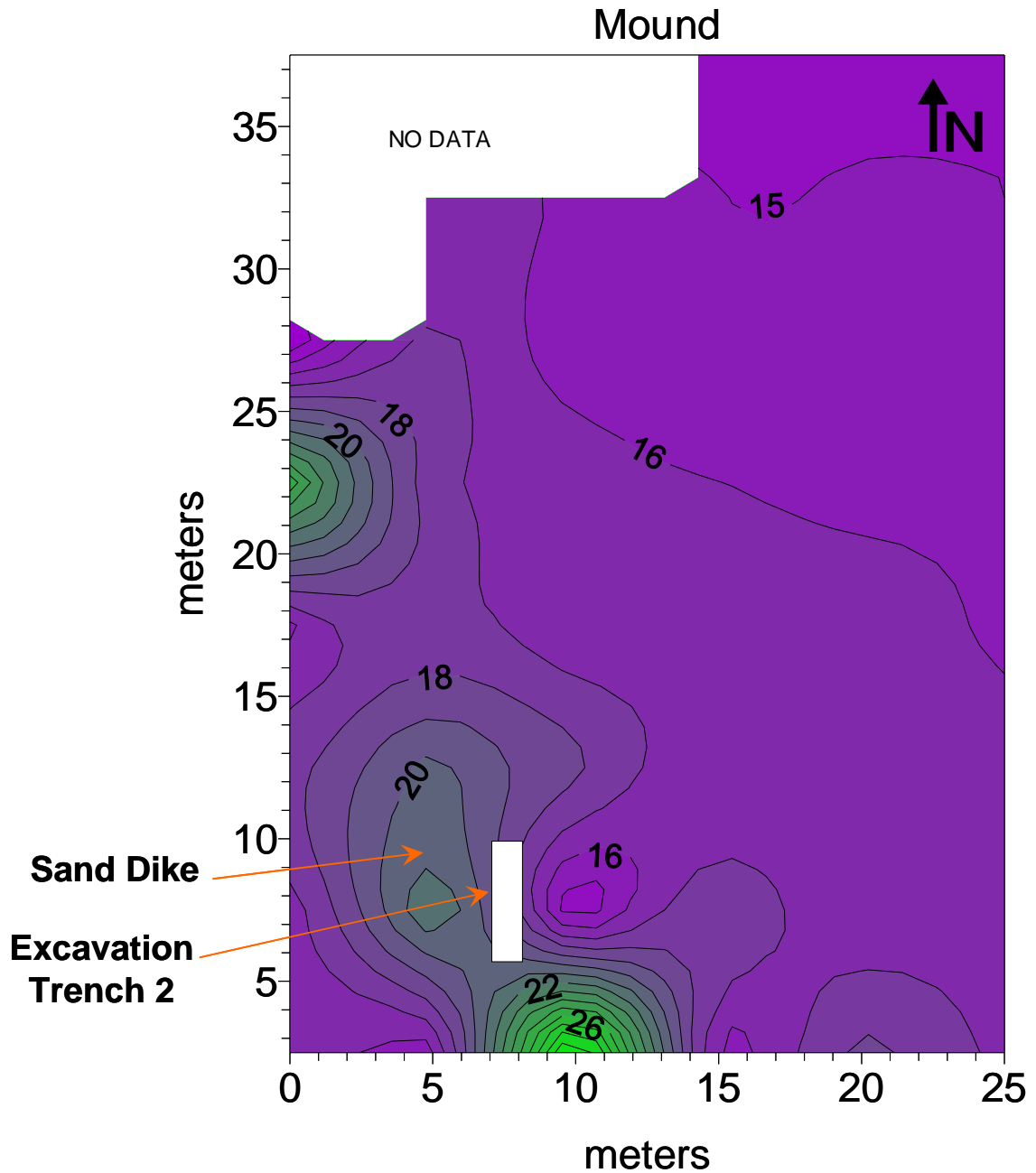
Figure 6.18 Resistivity survey results (in ohm-m) from the south part of the Walker site (Barnes, 2000)

Note: The northwest-trending sand blow and associated sand dike are indicated by high resistivity values (green). The white rectangle denotes the position of excavation trench 2, which was oriented on the northwest-trending geophysical anomaly.
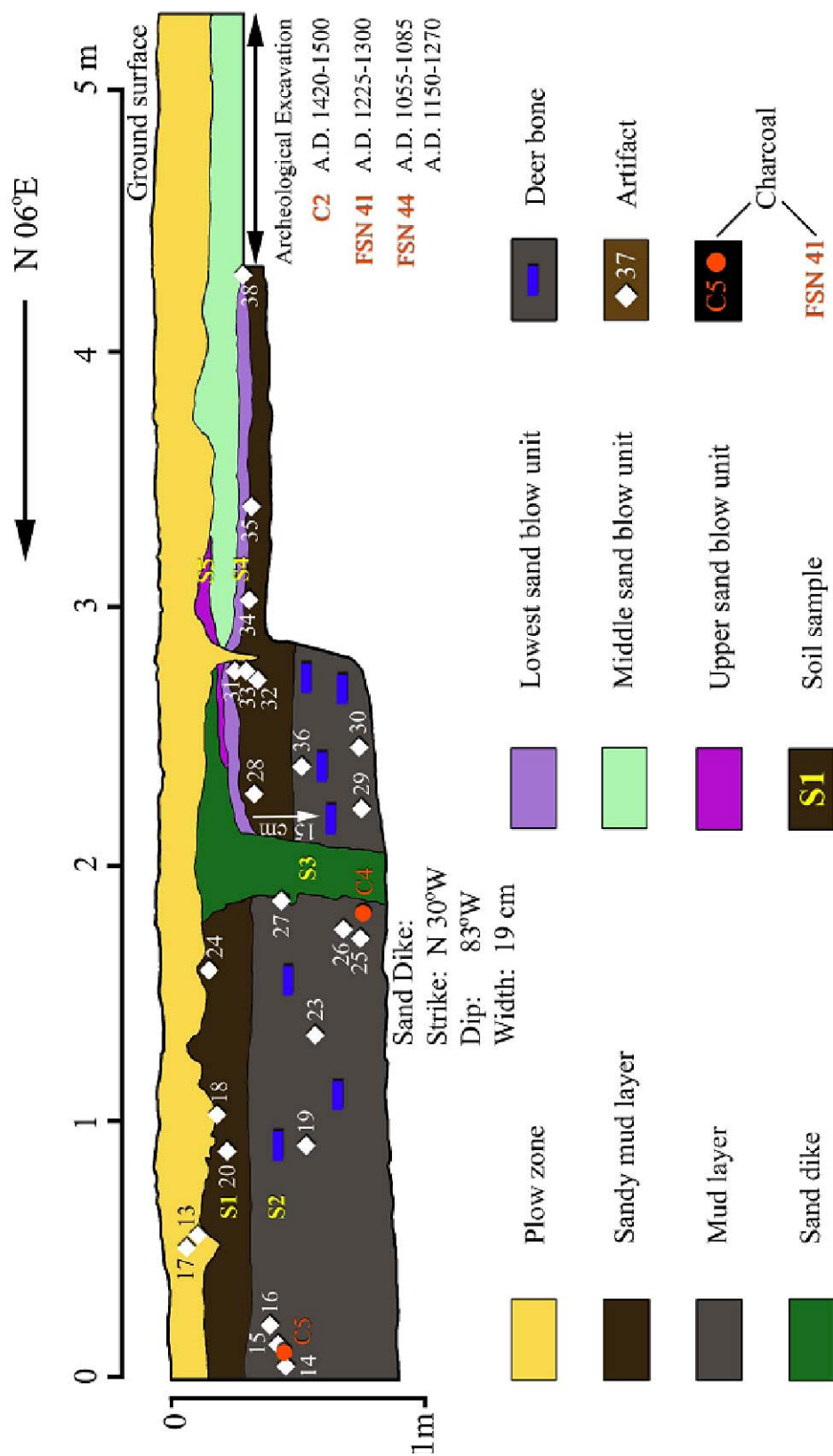
Figure 6.19 Log of east wall of excavation trench 1 at Walker site (Barnes, 2000)

210

Figure 6.20 Log of east wall of excavation trench 2 at Walker site (Barnes, 2000)

Figure 4.20 in Chapter 4 has shown the results from a representative SCPTu$_2$ sounding (No. MTREE01) advanced to a depth of 32 meters at the Walker site, as well as the derived parameters and soil profile. The soil profile indicates a clayey layer in the upper 4 meters underlain by an extensive deposit of relatively clean sand layers. The profile corresponds similarly with the boring and geological log of a nearby site reported by Liu et al. (1997).

The Walker site is very close (15km) to Keiser, AR, where the 887.4m-deep well logging was performed, and therefore the deposit over the Walker site should be approximately as thick as that over the Keiser site. The approximate V$_s$ shown in Figure 6.10 is applied to the Walker site. For nonlinear analysis in DEEPSOIL, the thickness of the delineated soil layer controls the maximum frequency that can be propagated by the layer as following:

$$h = \frac{V_s}{4 f_{max}}$$
(6-11)

where h is the thickness of the soil layer, V$_s$ is the shear wave velocity of the layer, and f$_{max}$ is the maximum frequency that can be propagated. Based on the recommendation of Park (2003) with f$_{max}$ = 25 Hz, the depths of the soil layers (h) can thus be calculated. Figure 6.21 shows the V$_s$ profile input into DEEPSOIL, as well as the derived saturated unit weight γ_T and small-strain shear modulus G$_{max}$ based on the equations suggested in Chapter 4. The symbols on this figure represent the average value of V$_s$, γ_T, and G$_{max}$ for the corresponding soil layers.
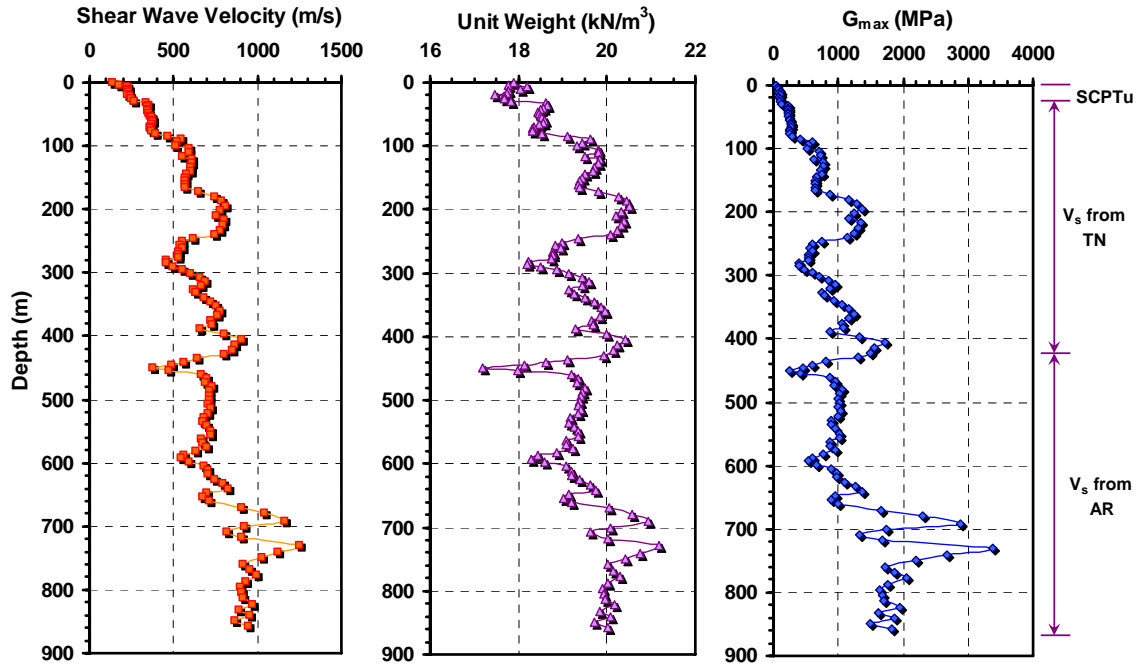
Figure 6.21 The shear wave velocity profile and derived unit weight and small-strain shear modulus for the Walker site at Marked Tree, AR

The 1530 A.D. earthquakes include two major earthquake events of moment magnitude 7.6 and 8.0, and their estimated epicenters are about 73km and 110km from the Walker site, respectively (Figure 6.22). For the magnitude 7.6 earthquake, one representative synthetic time-history response is generated for the Walker site using the program SMSIM, as shown in Figure 6.23. The bedrock motions are input into the DEEPSOIL program, and the time-history of the stress in each layer can be computed, hence, the CSR that is plotted in Figure 6.24. The computed a_{max} of the surface ground motion is 0.16g.
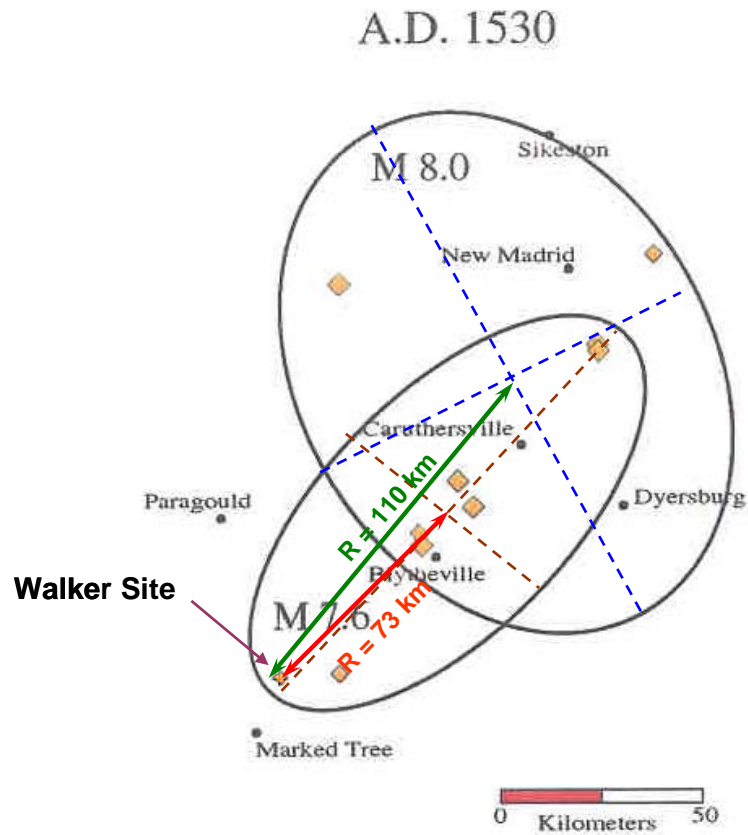
Figure 6.22 Distance from the Walker site to the estimated epicenters of the seismic events that occurred around 1530 A.D. in NMSZ (after Tuttle, 1999)
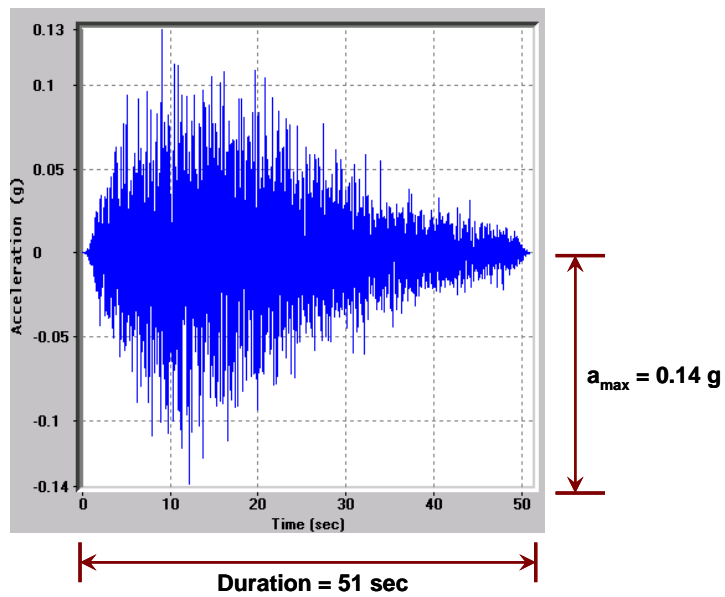
Figure 6.23 Example time-history of bedrock motion generated for the Walker site under the M 7.6 earthquake occurring around A.D 1530 using the program SMSIM

Using the Boore & Joyner (1991) attenuation relations shown in equation (6-1), the estimated a_{max} at the Walker site is 0.15g, which is very close to that obtained from seismic response analysis by DEEPSOIL. The CSR calculated using the simplified procedure is also presented in Figure 6.24. It can be seen that the CSRs derived from the two approaches are very close.
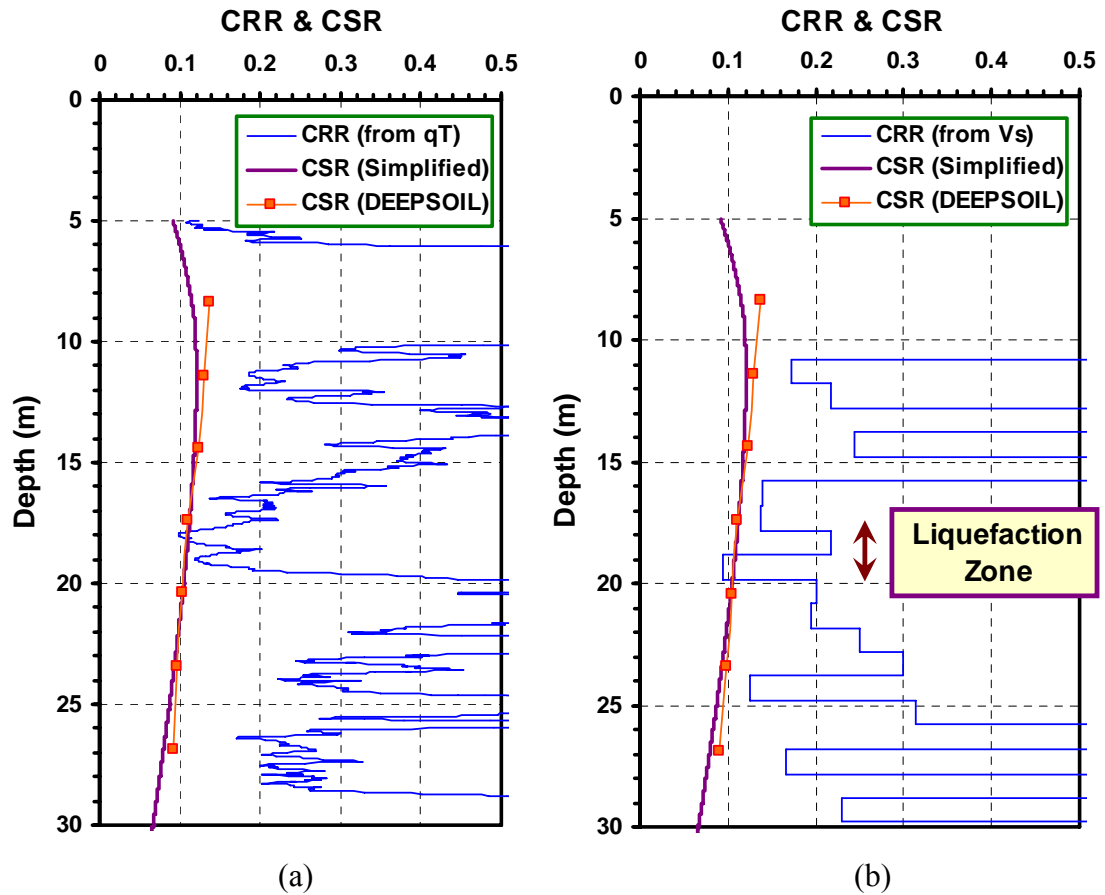
Figure 6.24 Liquefaction analyses by deterministic approaches for the Walker site sounding ($M_w = 7.6$, epicentral distance = 73 km): (a) Based on normalized cone tip resistance; (b) Based on normalized shear wave velcotiy.

Based on the deterministic approaches proposed by Robertson & Wride (1998) and Andrus & Stokoe (2000), the CRRs can be derived from both q_T and V_s, and these are

shown respectively in Figure 6.24. Liquefaction is likely whenever the CRR value is less than the CSR value. The gaps in the CSR data represent soil layers that are not susceptible to liquefaction due to their classification (e.g., clayey soils for which liquefaction analyses are not relevant). Comparison between the CSRs and the CRRs shows that liquefaction is likely to occur in the depth range from 18 to 20 m.

Similarly, the CRR probability curves (Chen & Juang, 2000; Juang & Jiang, 2000; Juang et al., 2001) can be applied to the CPT data from the Walker paleoliquefaction site. The probabilistic procedure is presented as the different liquefaction probabilities versus the corresponding depth in Figure 6.25. The probability is analyzed based on the independent stress-normalized tip resistance and the shear wave velocity, respectively. For each approach, two probability curves are presented, which are derived from the CSRs calculated using the simplified procedure and the DEEPSOIL procedure, respectively. The computed probability for the depth range from 17 to 20 m is from 20% to 60% for q_{T1} and 16% to 36% for V_{s1}. As this site has clear evidence of prior liquefaction, the results seems somewhat low.

The same process can be applied to investigate the liquefaction potential of the Walker site under the 1530 A.D. earthquake of magnitude 8.0, which epicenter is 110 km away (Figure 6.22). Similarly, a time history of bedrock motion is generated by the program SMSIM corresponding to such an earthquake, as illustrated in Figure 6.26. The average a_{max} on the ground surface computed by DEEPSOIL is 0.17 g. However, based on the Boore & Joyner (1991) attenuation relations, the a_{max} at ground surface is 0.1g. Figure

6.27 shows the CSR computed by DEEPSOIL, the CSR by the simplified procedure, as well as the CRR based on q_T and V_s respectively. From the CSR by the simplified procedure, the Walker site is not liquefiable under such an earthquake event. But the comparison between the CRRs and the CSR computed by DEEPSOIL shows that liquefaction would occur in the depth range of 16m to 20m, as well in the depth range from 11m to 12m. Figure 6.28 shows the liquefaction probability based on q_T and V_s respectively, and it can be seen that the CSR computed from DEEPSOIL generally gives higher probability of liquefaction than that calculated using the simplified procedure. Both the probabilities derived from DEEPSOIL and the simplified procedure suggest that the depth range from 15 to 20m has the highest liquefaction potential.

(a)   (b)
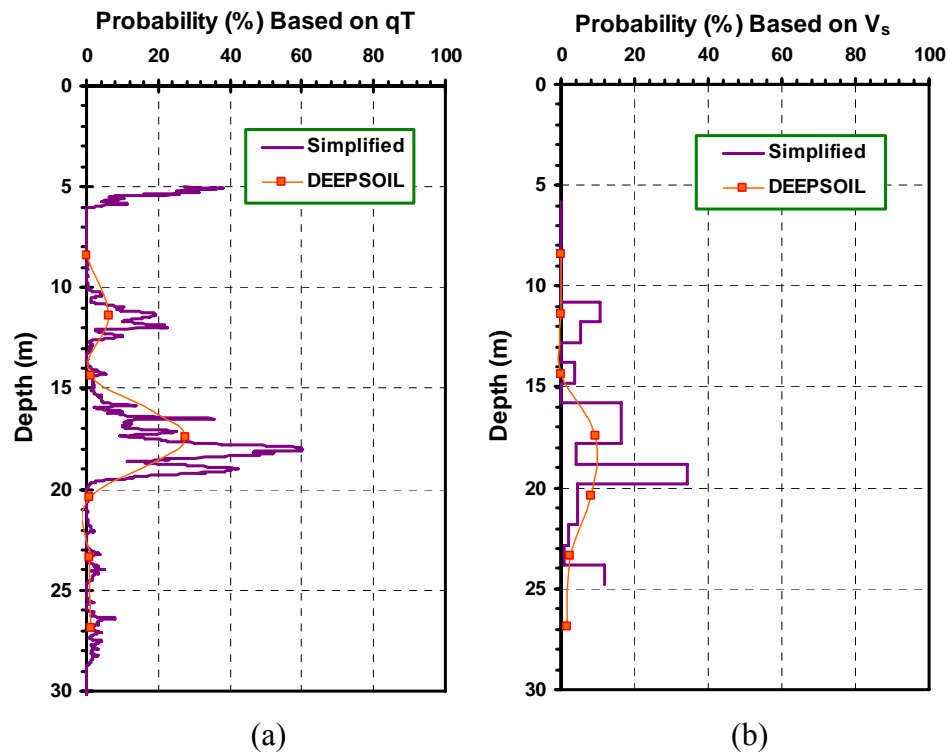
Figure 6.25 Liquefaction analyses by probabilistic approaches for the Walker site sounding ($M_w = 7.6$, epicentral distance = 73 km): (a) Based on normalized cone tip resistance; (b) Based on normalized shear wave velocity.

217
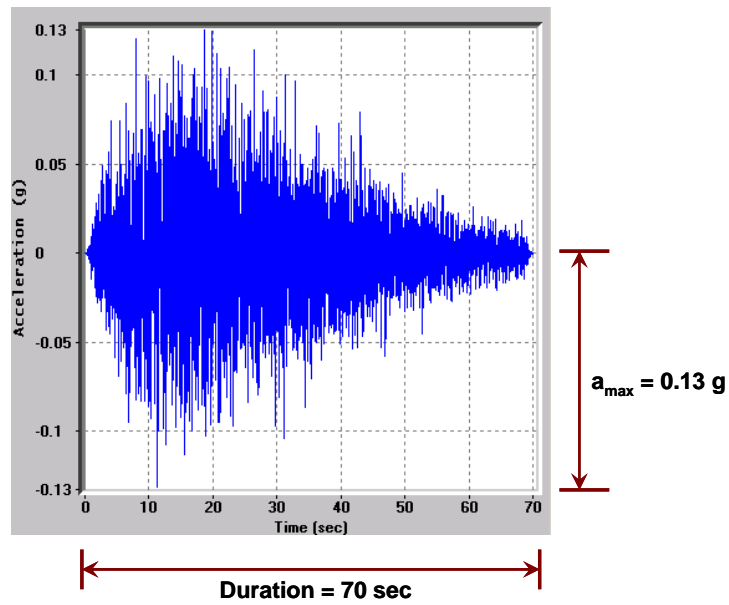
Figure 6.26 Time-histories of bedrock motion generated for the Walker site under the M 8.0 earthquake occurring around A.D 1530 using the program SMSIM

(a)   (b)
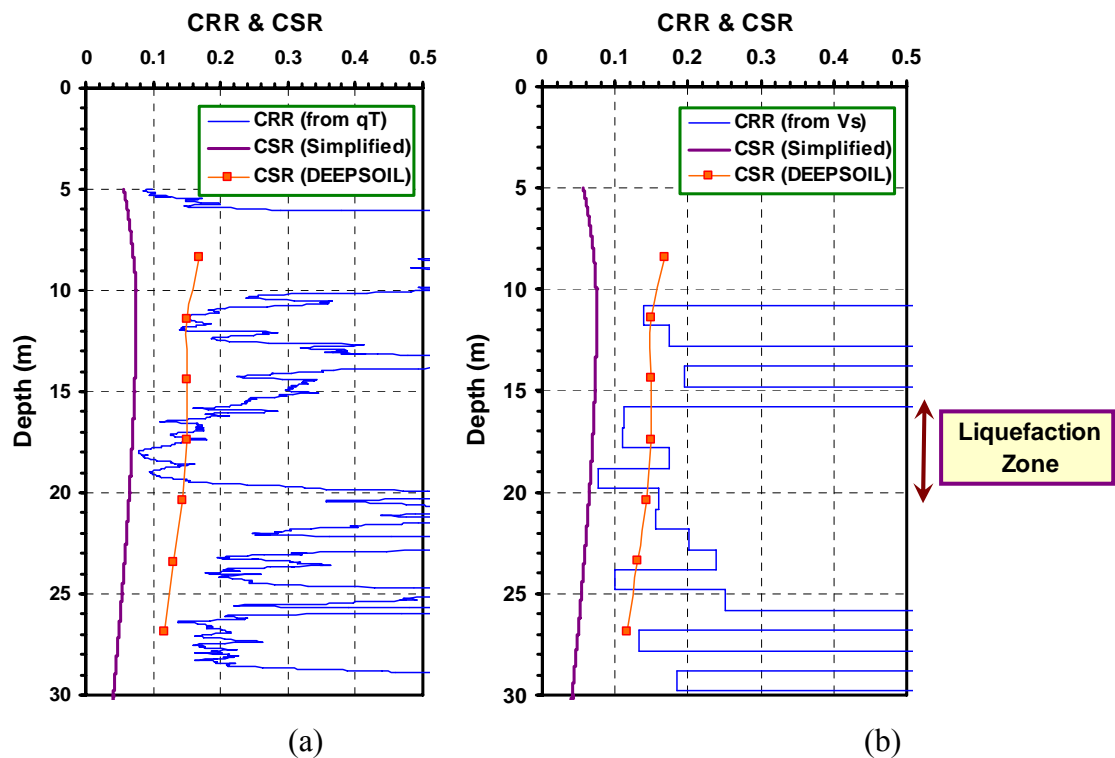
Figure 6.27 Liquefaction analyses by deterministic approaches for the Walker site sounding ($M_w = 8.0$, epicentral distance = 110 km): (a) Based on normalized cone tip resistance; (b) Based on normalized shear wave velcotiy.

218
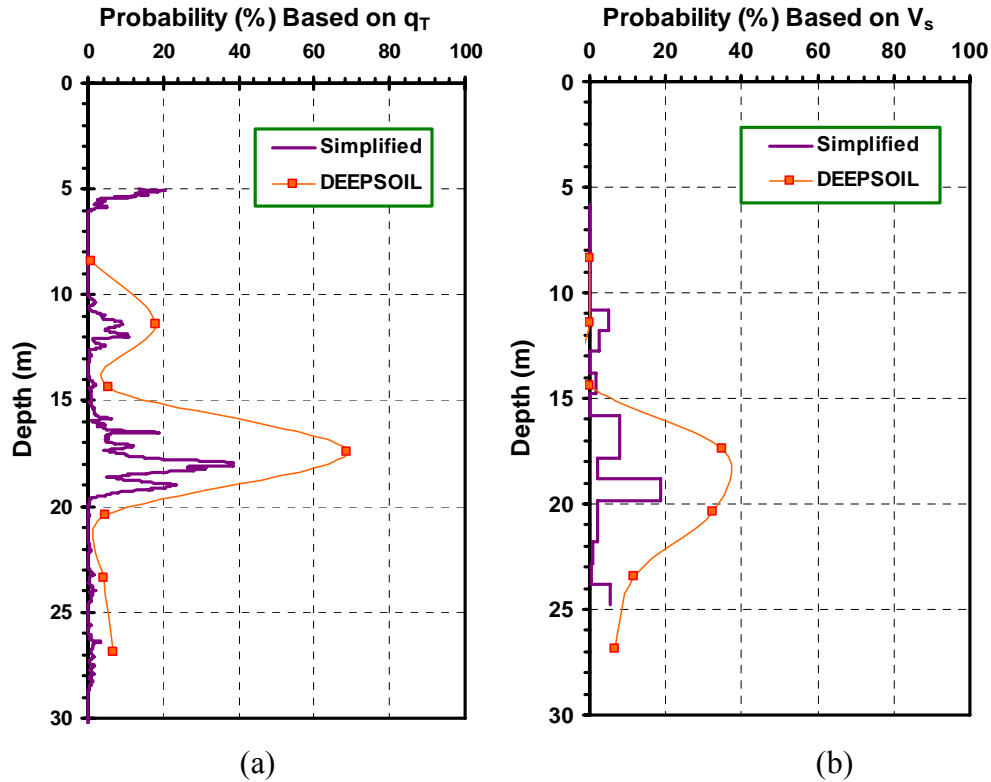
Figure 6.28 Liquefaction analyses by probabilistic approaches for the Walker site sounding ($M_w = 8.0$, epicentral distance = 110 km): (a) Based on normalized cone tip resistance; (b) Based on normalized shear wave velcotiy.

Liquefaction analysis at the Walker site shows that the CRRs derived from q_T and V_s are quite consistent, though the two procedures were developed independently. For the magnitude 7.6 earthquake event, both the simplified procedure and the DEEPSOIL procedure give similar results of CSRs. By comparing the CRRs and CSRs, it is found that liquefaction would likely occur. For the magnitude 8.0 event, the DEEPSOIL procedure gives higher CSR and peak ground acceleration than the simplified procedure does. Based on the DEEPSOIL procedure, this site would liquefy during this event, while contradictory conclusions can be drawn according to the simplified procedure.

6.5.2 *Liquefaction Evaluation at Hillhouse Site of Wyatt, MO*

The Hillhouse site is located at Wyatt, Missouri, as shown in Figure 6.29. An aerial photograph of the Hillhouse site and its surrounding features is presented in Figure 6.30. The site is about 3.25 km west of the Mississippi River and 0.5 km south of Brewer Lake. The resistivity contour plot (Figure 6.31) shows a broad area of high resistivity anomalies (green), indicating existence of liquefaction features (Barnes, 2000). Also shown in this figure are two trenches excavated for archeological investigation and dating purposes. Figure 6.32 presents the excavation log of trench 1, which exposed a sand blow deposit near the surface and a sand dike of 1.03 m wide. A sand dike of 32 cm wide is also observed from excavation trench 2 (Figure 6.33). According to radiocarbon dating of the deposits and analysis of artifacts found at this site, the liquefaction features were formed during the 900 A.D. earthquakes (Tuttle, 1999). This site is also the most northern site that has found liquefaction features attributed to the 900 A.D. earthquakes (Tuttle, 1999).

The results of a SCPT sounding performed at this site are shown in Figure 6.34. The soils in the top 5m are clay, overlying a layer of silt mixture between 5m and 10m. Below 10m, the soils are clean sands. Figure 6.35 presents the parameters derived from the CPT data, as well as the soil profile.

Based on the color shading of the soil deposit thickness shown in Figure 6.2, the total depth of soil deposits at the Hillhouse site is about 400m thick. An approximate V_s profile can therefore be created for this site. The V_s in the top 24.7m is taken from the SCPTu test, and those between the depths of 24.7m and 400 m are the real Vs data

collected by downhole logging in Memphis, TN. The V_s profile and the derive profiles of

unit weight γ_T and small-strain shear modulus G_{max} are similar to those in the top 400 m

shown in Figure 6.21.
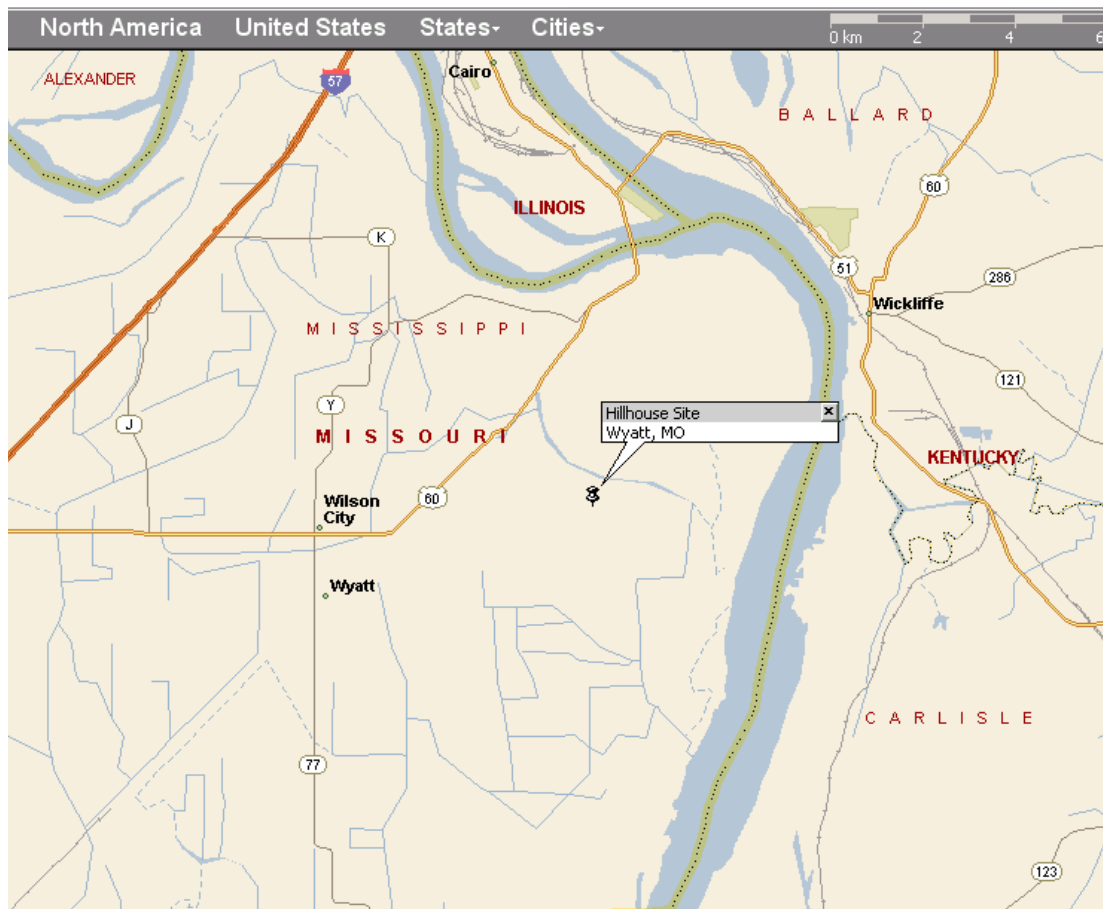
Figure 6.29 Map showing location of the Hillhouse paleoliquefaction site in Wyatt, Missouri

Figure 6.30 Aerial photograph of the Hillhouse site and surrounding features
(Barnes, 2000)
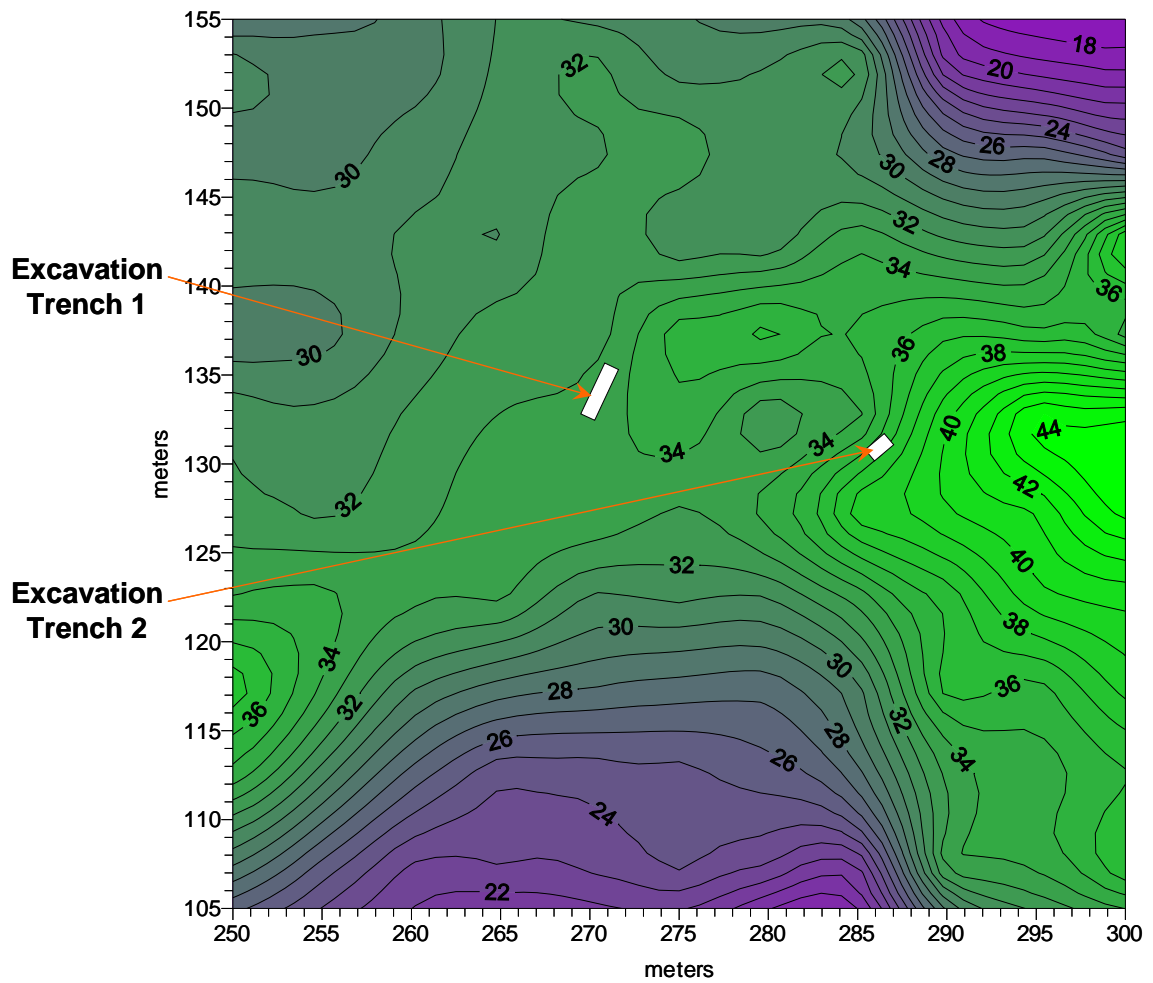
Figure 6.31 Resistivity survey results (in ohm-m) at the Hillhouse site
(Barnes, 2000)

Note: The broad zone of high resistivity (green) trends may indicate the orientation of
multiple liquefaction features. Yellow rectangles indicate areas of extreme high
resistivity. White-filled rectangles indicate the location of excavation trenches.
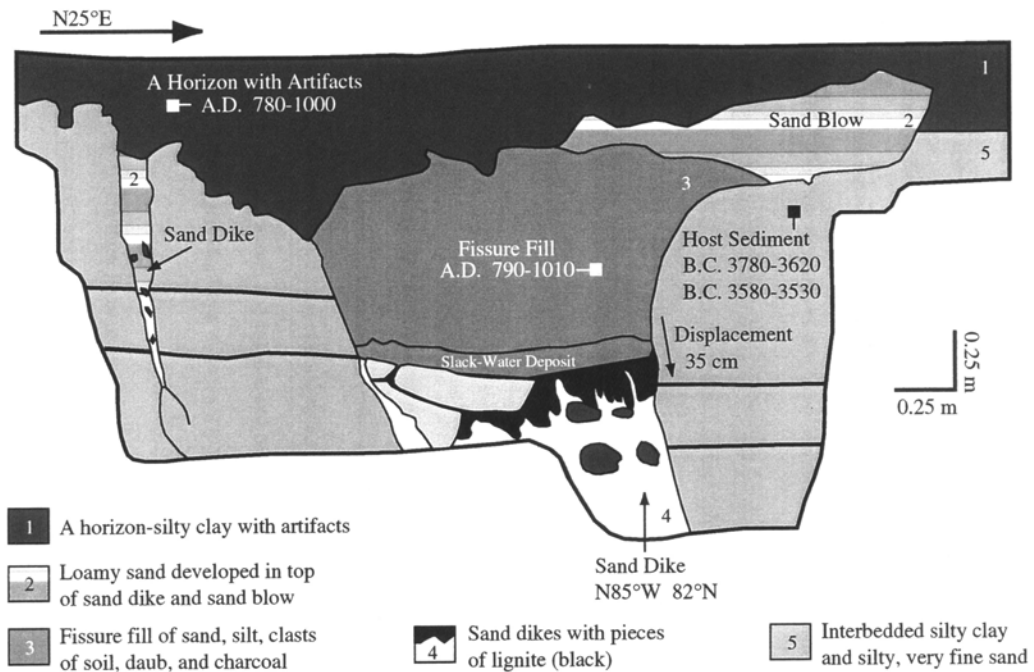
Figure 6.32 Log of excavation trench 1 at the Hillhouse site exposing sand dikes
(Tuttle, 1999)
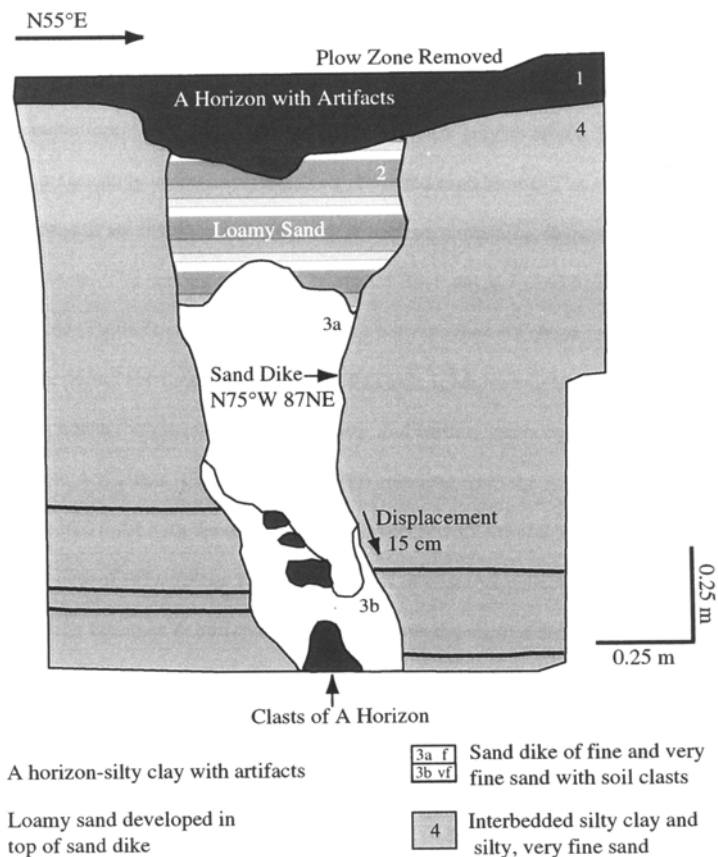
Figure 6.33 Log of excavation trench 2 at the Hillhouse site exposing a sand dike
(Tuttle, 1999)
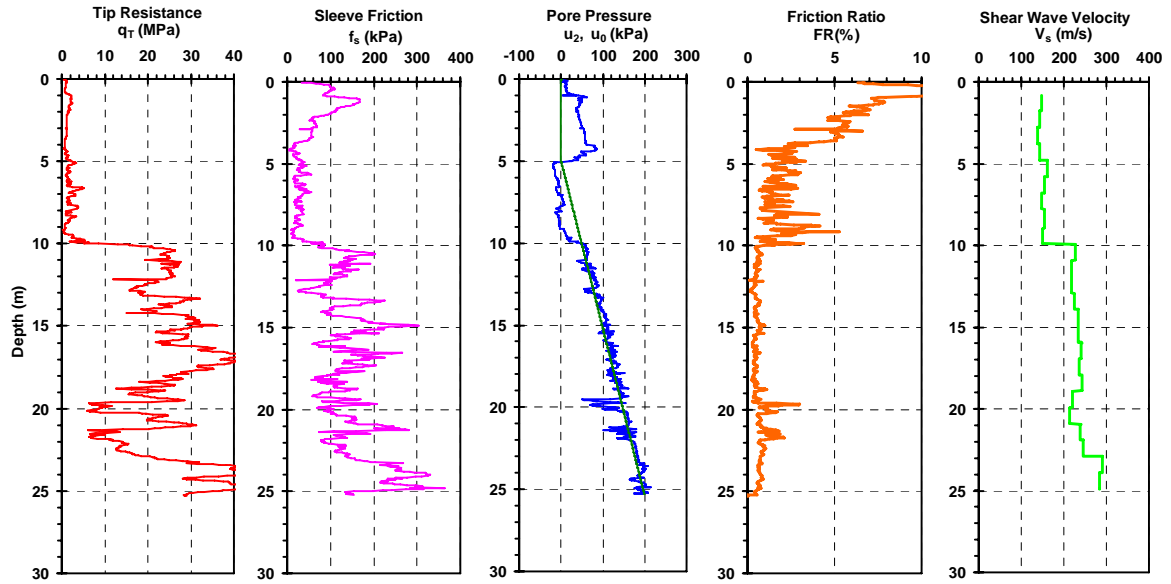
Figure 6.34 Representative SCPTu results at Hillhouse paleoliquefaction site near Wyatt, MO

The 900 A.D. earthquakes consist of three individual earthquake events with magnitudes of 8.1, 8.0, and 7.6. The M_w = 8.1 earthquake has the maximum magnitude and the shortest epicentral distance (65km) to the Hillhouse site (Figure 6.36), and therefore generates the strongest bedrock motion at this site. Figure 6.37 shows an example of time-histories of bedrock motion generated for this site using the program SMSIM. The average a_{max} at the ground surface computed by DEEPSOIL is 0.19 g, and it is 0.18g according the the Boore & Joyner (1991) attenuation relations.

225
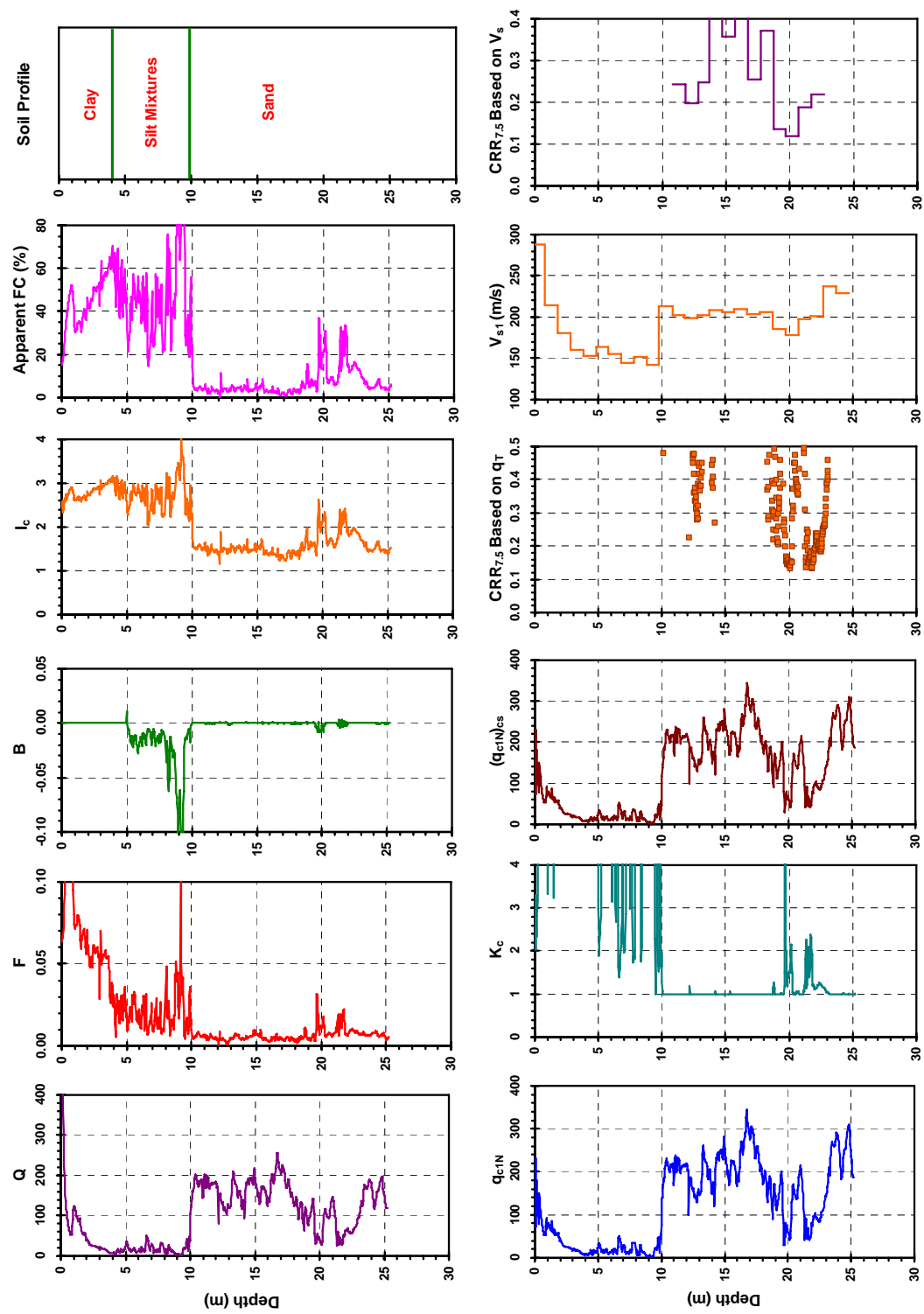
Figure 6.35 Parameters and soil profile derived from the SCPTu data collected at Hillhouse site at Wyatt, Missouri

226
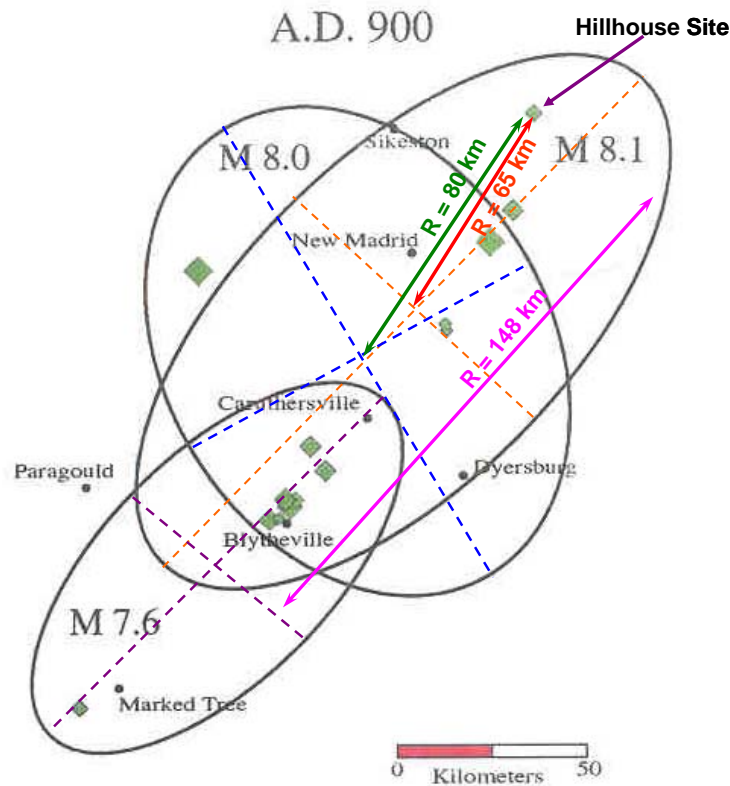
Figure 6.36 Distance from the Hillhouse site to epicenters of the seismic events that occurred around 900 A.D. in NMSZ [Modified from Tuttle (1999)]
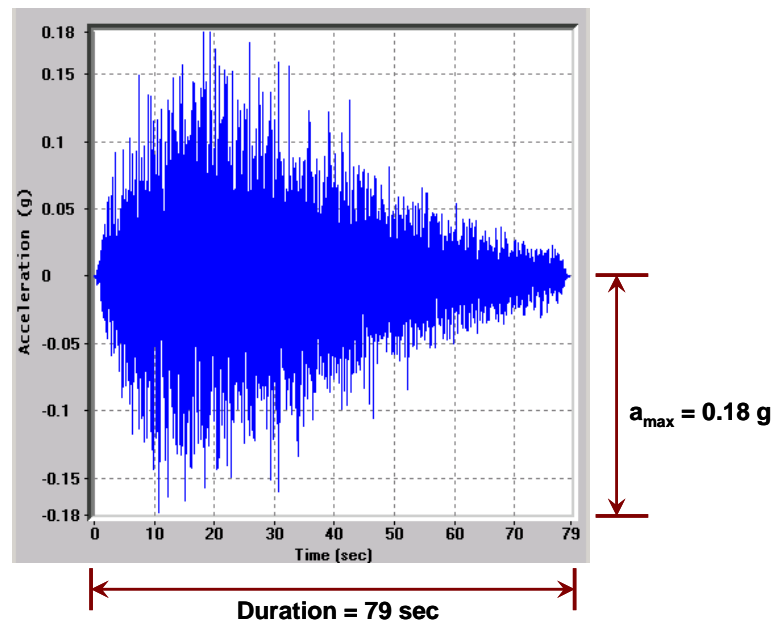
Figure 6.37 Time-history of bedrock motion generated for the Hillhouse site under the $M_w = 8.1$ earthquake occurring around 900 A.D. using the program SMSIM

227

Similar to the analysis performed for the Walker site, the CSRs calculated by the simplified procedure and the DEEPSOIL procedure are plotted with the CRRs based on q_T and V_s in Figure 6.38. The comparison between CSRs and CRR based on q_T suggests that liquefaction is likely to occur in the depth ranges from 19.5 to 20.5 m and from 21 to 22.5 m. While the comparison between CSRs and CRR based on V_s suggests that liquefaction is likely to occur in the region from 19 to 21m. The same zones are also found to have the highest potential for liquefaction from the probabilities shown in Figure 6.39.
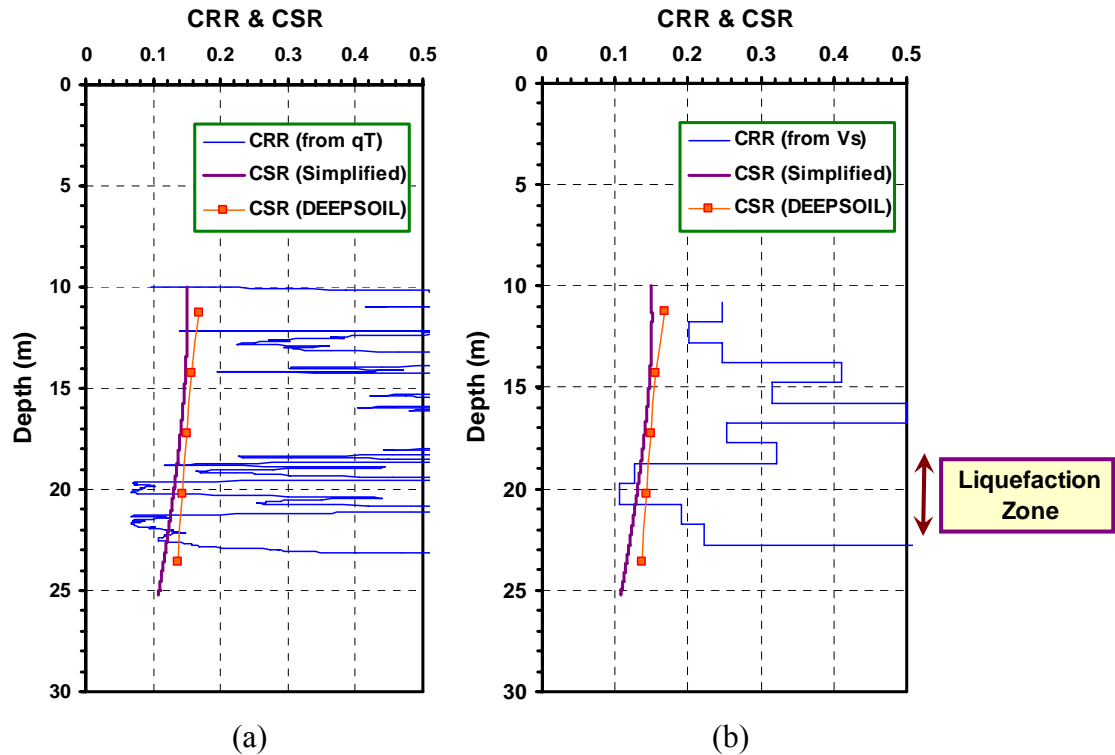
Figure 6.38 Liquefaction analyses by deterministic approaches for the Hillhouse site ($M_w = 8.1$, epicentral distance = 65 km): (a) Based on normalized cone tip resistance; (b) Based on normalized shear wave velcotiy.
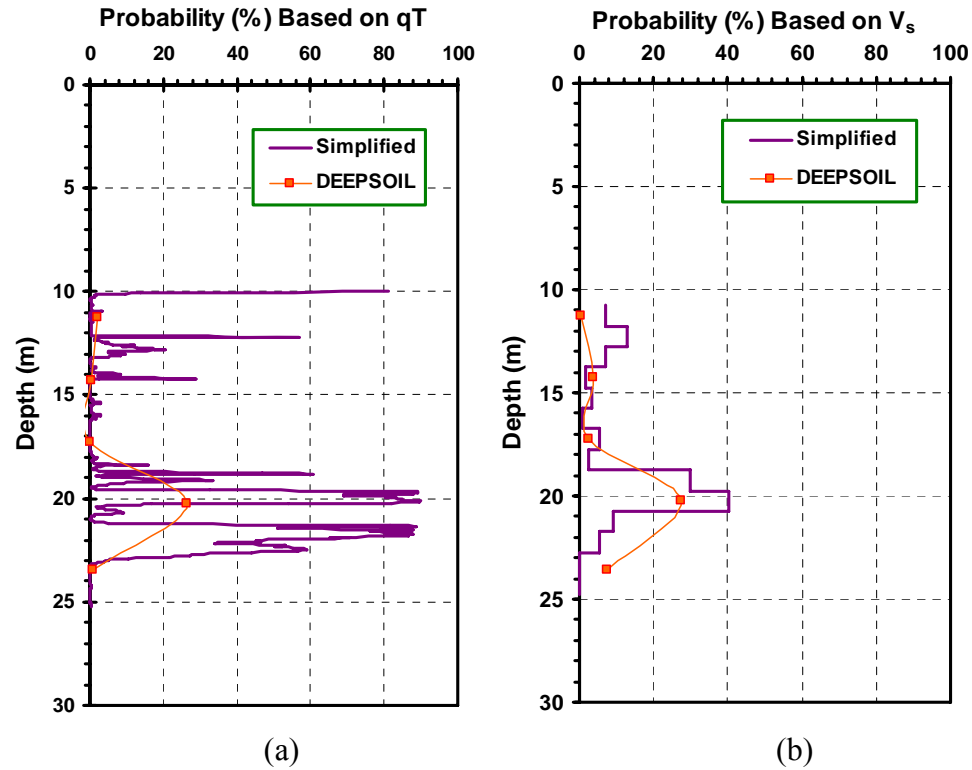
Figure 6.39 Liquefaction analyses by probabilistic approaches for the Hillhouse site (M_w = 8.1, epicentral distance = 65 km): (a) Based on normalized cone tip resistance; (b) Based on normalized shear wave velcotiy.

The CRRs derived from the q_T and V_s data collected at the Hillhouse site show similar trends, which are consistent with what has been observed from the analysis for the Walker site. The value of the CSRs calculated using the simplified procedure and the DEEPSOIL procedure are very close. The comparison between the CSRs and CRRs shows that the CSRs are higher than the CRRs in some depth ranges, where liquefaction is consider likely in the event of such earthquakes.

6.6 Development of Regional Liquefaction Criteria for the NMSZ

In last section, liquefaction evaluation has been performed for two paleoliquefaction sites in the NMSZ (Walker site, AR and Hillhouse site, MO), assuming the same magnitude of

large earthquakes that liquefied these sites occur again. This liquefaction procedure has also been applied to the Yarbro site, Bugg site, Hueys site, Dodd Farm site, Johnson Farm site, and Nodena site. The results are presented in Appendix D.

For each site, a liquefaction zone is delineated based on the comparison of the CRRs and CSRs, as shown in the corresponding figures. Although liquefaction might have also occurred at other depths, the selected liquefaction layer is the one that has most likely liquefied. Information on the liquefaction zones of the paleoliquefaction sites is presented in Table 6.4, including the estimated mean CSRs, q_{T1}, V_{s1}, as well as earthquake magnitude. Using the magnitude scaling factor (MSF), the CSRs corresponding to earthquake magnitude $Mw = 7.5$ can be derived, and they are denoted as CSR7.5 here. Therefore, the CSR7.5 that have liquefied the sites can be plotted against the adjusted cone tip resistance $[(q_{T1})_{cs}]$, which is the equivalent q_{T1} in clean sands, and the normalized shear wave velocity (V_{s1}), as shown in Figures 6.40 and 6.41. The CSRs in Figure 6.40 are calculated using the simplified approach, while those in Figure 6.41 are obtained through site response analysis. Based on the CRR curve suggested by Robertson & Wride (1998), which is plotted on both Figure 6.40 (a) and 6.41 (a), most of the data points from the paleoliquefaction sites are non-liquefiable, which is incorrect given the clear evidence of previous liquefaction at these sites. The CRR curve suggested by Andrus & Stokoe (2000) is also compared with the data points in Figure 6.40 (b) and 6.41 (b), and in both figures, data points from three of the liquefaction sites fall on the side of no liquefaction. It seems that the CRR curves suggested by both Robertson & Wride

230

(1998) using q_{T1} and Andrus & Stokoe (2000) using V_{s1} underestimate the liquefaction potential of sandy soils in the NMSZ.

The lower boundaries of the data points corresponding to the paleoliquefaction case histories in the NMSZ are plotted in Figures 6.40 and 6.41. If data fall below the suggested lower boundaries, it is unlikely that the soil would liquefy. Therefore, they are taken as the suggested new CRR curves for the NMSZ. Comparing the CRR curve suggested by Robertson & Wride (1998) and the CRR curves suggested for the NMSZ [Figure 6.40 (a) and Figure 6.41 (a)], the newly suggested CRR curves predicts liquefaction at lower CSR. The same conclusion can be drawn from the comparison of the CRR curve suggested by Andrus & Stokoe (2000) and the CRR curves suggested for the NMSZ [Figure 6.40 (b) and Figure 6.41 (b)]. The regional CRR curves developed using the simplified approach (Figure 6.40) predicts liquefaction at lower CSR than those developed from site response analysis (Figure 6.41).

Table 6.4 Information on the liquefaction zones of the NMSZ paleoliquefaction sites

Site	M_w	R (km)	MSF	CSR (s.)	$CSR_{7.5}$ (s.)	CSR (D.)	$CSR_{7.5}$ (D.)	q_{T1}	$(q_{T1})_{cs}$	V_{s1} (m/s)
Walker	7.6	73	0.96	0.11	0.11	0.11	0.1056	80	80	185
Walker	8.0	110	0.85	0.07	0.06	0.15	0.1275	80	80	185
Hillhouse	8.1	65	0.82	0.13	0.11	0.14	0.1148	120	120	180
Yarbro	8.1	5	0.82	N/A	N/A	0.52	0.4264	80	80	200
Bugg	7.6	25	0.96	0.52	0.50	0.3	0.288	160	160	200
Hueys	7.6	25	0.96	0.4	0.38	0.3	0.288	130	130	180
Dodd	7.6	8	0.96	N/A	N/A	0.45	0.432	150	170	200
Johnson	8.1	28	0.82	0.41	0.34	0.28	0.2296	160	160	180
Nodena	7.6	48	0.96	0.2	0.20	0.16	0.1536	150	150	210

Note: s. = simplified; D. = DEEPSOIL
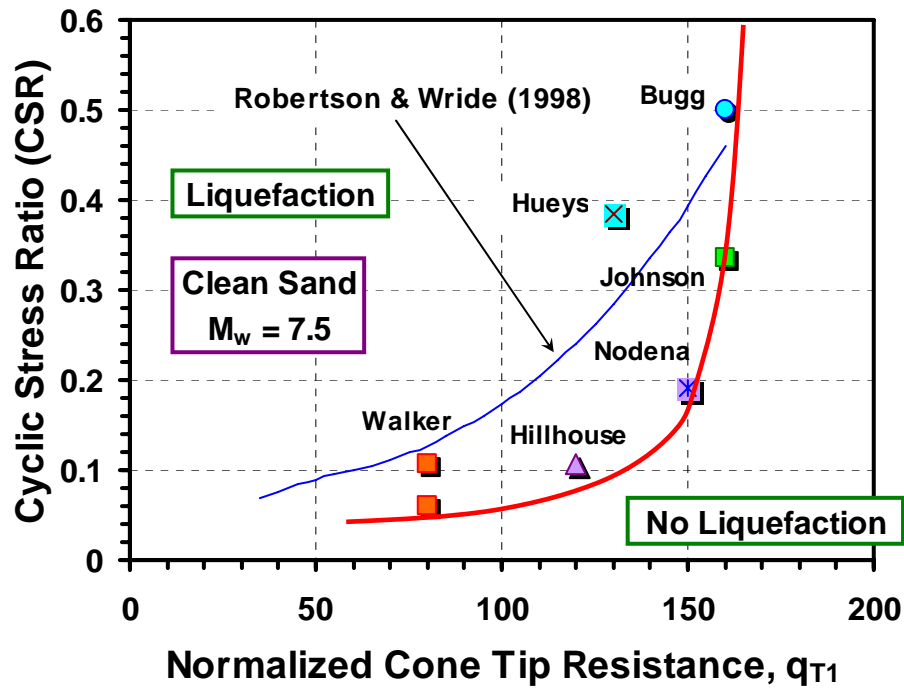
(a)
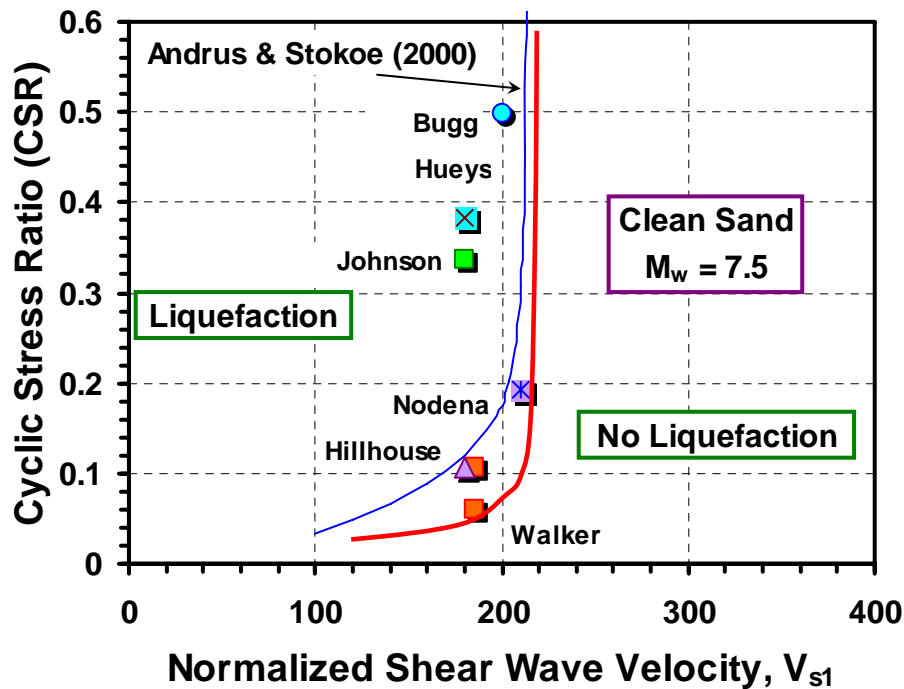
(b)

Figure 6.40 CRR$_{7.5}$ curves for clean sands developed from simplified approach and SCPTu data in the NMSZ: (a) Based on normalized cone tip resistance; (b) Based on normalized shear wave velocity.
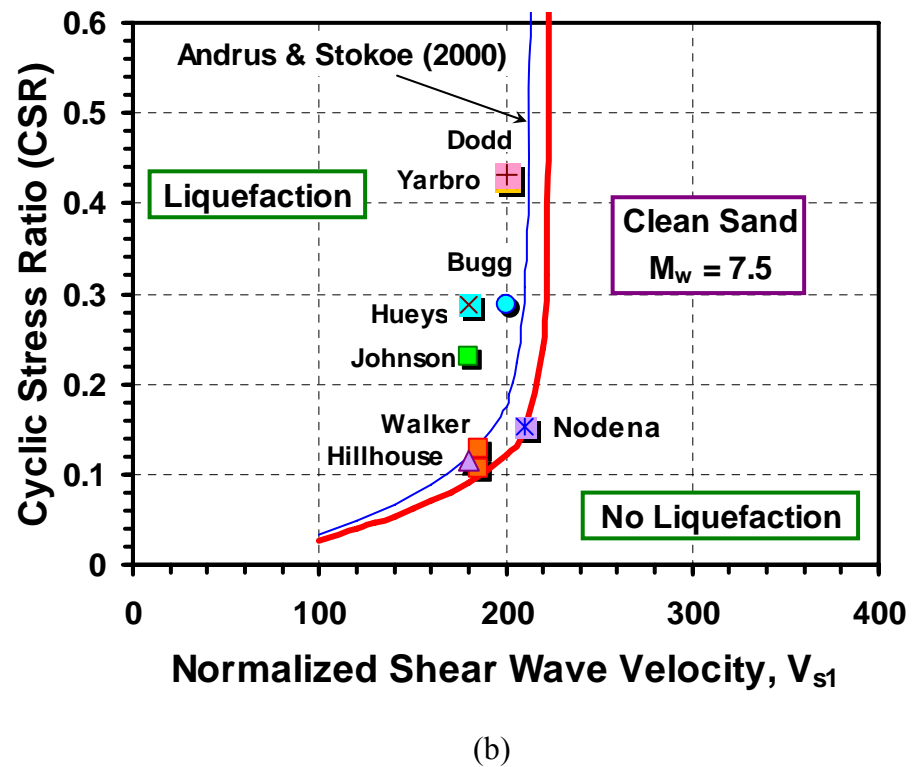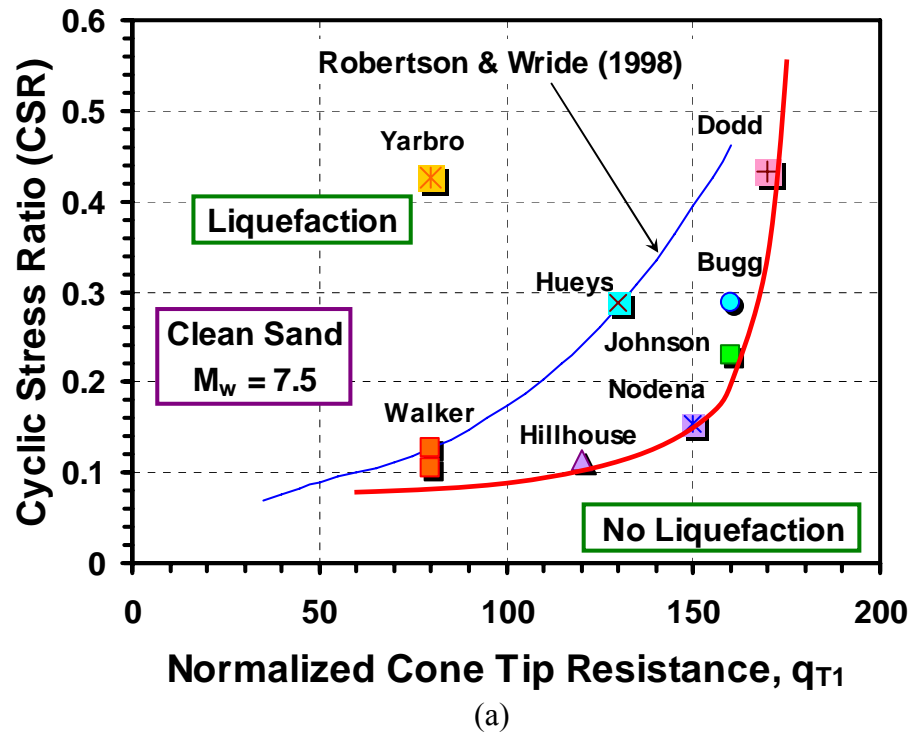
Figure 6.41 CRR$_{7.5}$ curves for clean sands developed from site response analysis and SCPTu data in the NMSZ: (a) Based on normalized cone tip resistance; (b) Based on normalized shear wave velocity.

233

Andrus & Stokoe (2000) suggested the following formula to fit the CRR curves based on normalized shear wave velocity V_{s1}:

$$CRR_{7.5} = a(\frac{V_{s1}}{c})^2 + b(\frac{1}{V_{s1}^* - V_{s1}} - \frac{1}{V_{s1}^*}) \qquad (6\text{-}12)$$

where a, b, and c are curve fitting parameters, and V_{s1}^* is limiting upper value of V_{s1} for liquefaction to occur. The same equation can be adopted to fit the regional CRR curves for the NMSZ. For the CRR curve based on V_{s1} and site response analysis [Figure 6.41 (b)], a = 0.025, b = 0.06, c = 100, and $V_{s1}^* = 225$ m/s. Equation (6-12) can be modified to the following form to fit the regional CRR curve based on normalized tip resistance q_{T1}:

$$CRR_{7.5} = a(\frac{q_{T1}}{c})^2 + b(\frac{1}{q_{T1}^* - q_{T1}} - \frac{1}{q_{T1}^*}) \qquad (6\text{-}13)$$

where q_{T1}^* is limiting upper value of q_{T1} for liquefaction to occur. The regional CRR curve based on q_{T1} and site response analysis [Figure 6.41 (a)], a = 0.005, b = 0.7, c = 30, and $q_{T1}^* = 175$.

6.7 Summary

Deterministic and/or probabilistic curves can be used with the stress-normalized tip resistance q_{c1N} (or q_n) and normalized shear wave velocity V_{s1} in evaluating the CRR. Based on the pattern of the epicenters and magnitudes of previous earthquakes, two scenario earthquake events are suggested for liquefaction evaluation in the NMSZ in the case of strong ground motions. With selected scenario earthquakes, the PGA can be estimated from empirical attenuation relations, and then the CSR can be estimated using the simplified procedure. With the availability of the profile of the dynamic soil properties, such as V_s, the CSR can alternatively be computed from seismic response

analysis. The seismic response analysis is carried out by the nonlinear analysis program DEEPSOIL herein, which is developed to account for the effects of deep soil deposits on site response. The CSR calculated this way is thought to be more reliable than that derived from the empirical simplified procedure. Redundancy information results from the CRRs derived from two independent readings and the CSRs calculated by two independent approaches, but it provides a higher level of confidence in the conclusions on liquefaction hazards.

The liquefaction methods are applied to the paleoliquefaction sites in the NMSZ, assuming the same level of large earthquakes that liquefied these sites occur again. These sites include the Walker site, AR and Hillhouse site, MO discussed in this chapter, and the Yarbro site, Bugg site, Hueys site, Dodd Farm site, Johnson Farm site, and Nodena site presented in Appendix D. From the liquefaction analysis performed for these sites, it is found that CRRs derived from q_T and V_s have similar trends. The CSRs computed by the DEEPSOIL procedure can be close to or quite different than those calculated using the simplified procedure. Although liquefaction evidence has shown that these sites liquefied during the earthquake events, the analysis results generally show lower probabilities of liquefaction than expected. Based on the analysis of the liquefaction zones at these paleoliquefaction sites, regional liquefaction criteria for the NMSZ have been developed. Comparison between the newly developed criteria and those suggested by other researchers show that the soils in the NMSZ are more prone to liquefaction upon the same seismic loading.

CHAPTER VII

AGING EFFECTS ON SCPTU MEASUREMENTS IN NMSZ

7.1 Overview

The last major earthquakes in the NMSZ occurred approximately 200 years ago. It is commonly thought that aging effects increase soil strength and stiffness with the passage of time, although no significant change of density is observed (Schmertmann, 1991). The resistance to liquefaction [e.g. cyclic resistance ratio (CRR)] of sandy soils is also found to increase with time. Seed (1976) performed laboratory tests on identical sand samples that have been subjected to sustained loads for time ranging from 0.1 to 100 days prior to testing, and found that the cyclic resistance ratio (CRR) for initial liquefaction increases with the time, as shown in Figure 7.1. Since tests on samples of much longer time are virtually impossible, the CRRs of undisturbed sand samples that have subjected to a long time of sustained pressure are compared with those of freshly deposited samples of the same sand (Figure 7.1). The obtained data also indicated an increase of CRR with time.

As a consequence of destructuration and increased porewater pressures caused by seismic ground motions, the earthquake-induced liquefaction might decrease the soil strength and stiffness due to obliteration of pre-earthquake aging effects. However, when saturated sandy soils are subjected to seismic cyclic loading, the relatively loose soil tends to rearrange its grains into a denser packing, and the liquefied deposit may be densified as the excess porewater pressure dissipates during subsequent reconsolidation, which could result in increased soil strength and stiffness. Therefore, the pre- and post-earthquake

236

SCPTu data that represent the soil strength and stiffness might be different, because of the obliteration of aging features and post-liquefaction densification. Following liquefaction, the aging process restarts on normally consolidated sands. Hundreds of years of aging can possibly increase the soil strength and stiffness. Figure 7.2 illustrates the conceptual effects of aging and earthquake-induced liquefaction on cone tip resistance (q_T).
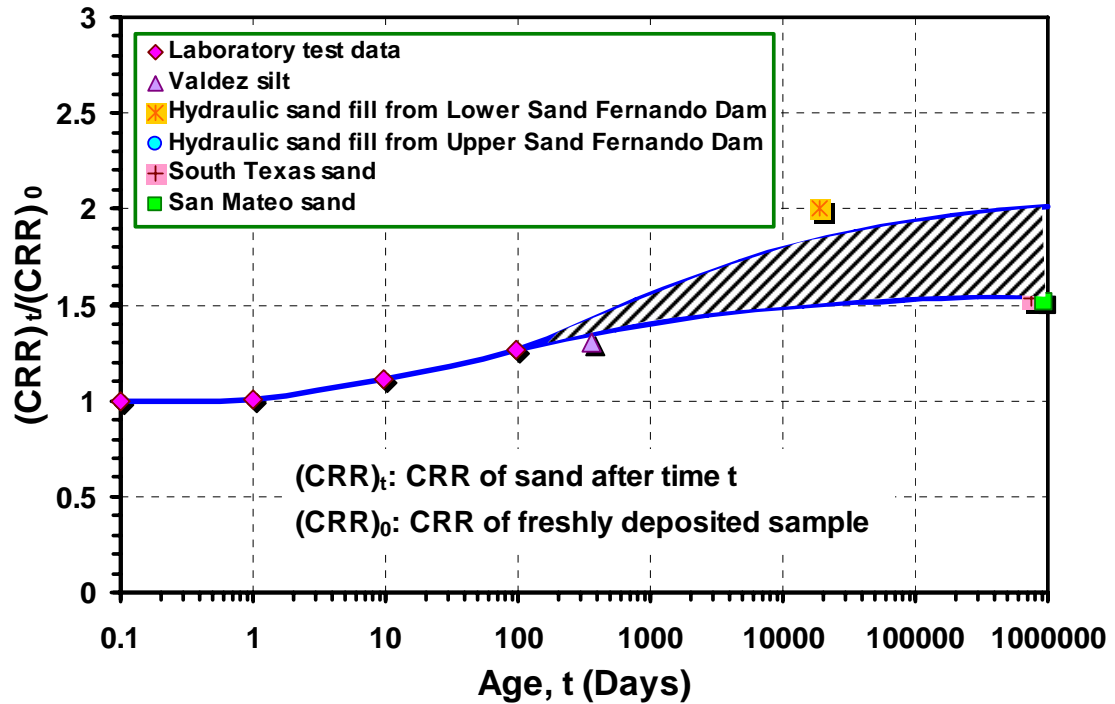
Figure 7.1 Influence of period of sustained pressure on stress ratio causing initial liquefaction (Seed, 1976)

Chameau et al. (1991a) studied the liquefaction response of fill soils along the waterfront area of San Francisco after the 1989 Loma Prieta earthquake. The comparison of in-situ data obtained prior to and after the earthquake showed that the cone tip resistance q_T increased significantly following the earthquake event at some of the investigated sites.

The same phenomena were observed in the SPT data and shear-wave velocity V_s. Figure

7.3 shows the average cone tip resistance q_T measured in 1979 before the earthquake and

that in 1990 after the earthquake event in 1989 at the Yerba Buena Cove (YBC) site in

San Francisco, CA (Chameau et al., 1991a). An obvious increase can be seen in these

data, but it is unknown if the increase is caused solely by aging effects following a

restructuring of the soil or because of post-liquefaction densification and/or aging with

time. This chapter focuses on the aging effects on cone tip resistance q_T and shear wave

velocity V_s, which are directly related to soil strength and stiffness. During two large-

scale blasting tests carried out in the NMSZ, series of SCPTu tests were performed to

evaluate the local aging effects.
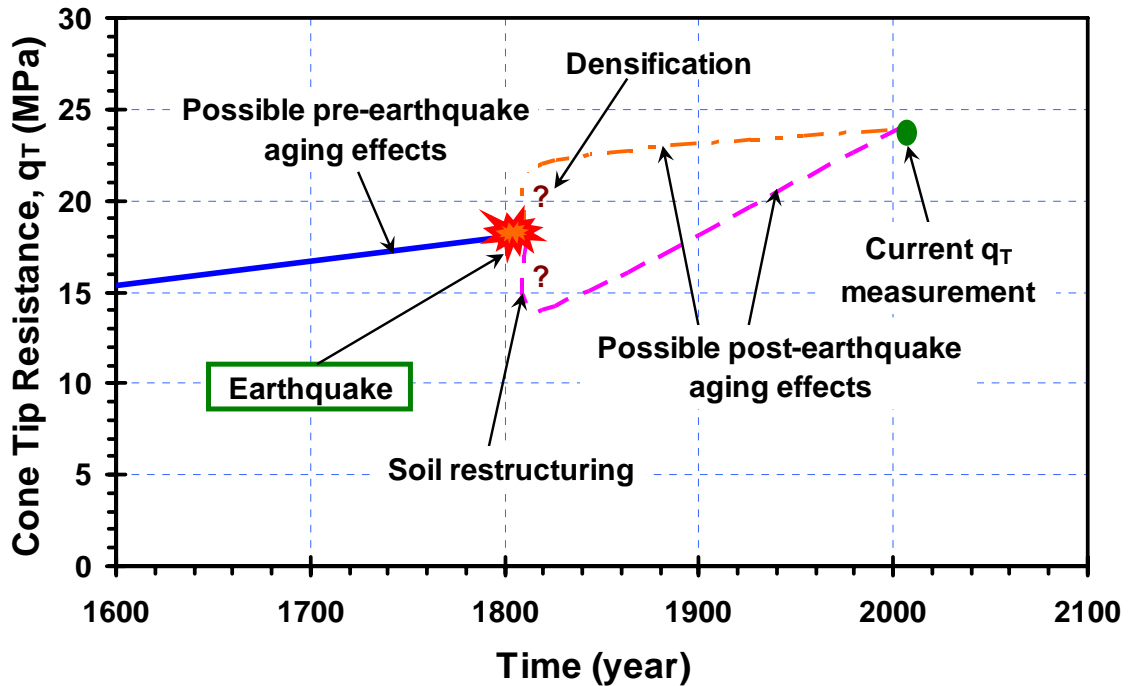
Figure 7.2 Conceptual effects of aging and earthquake-induced liquefaction on cone tip resistance
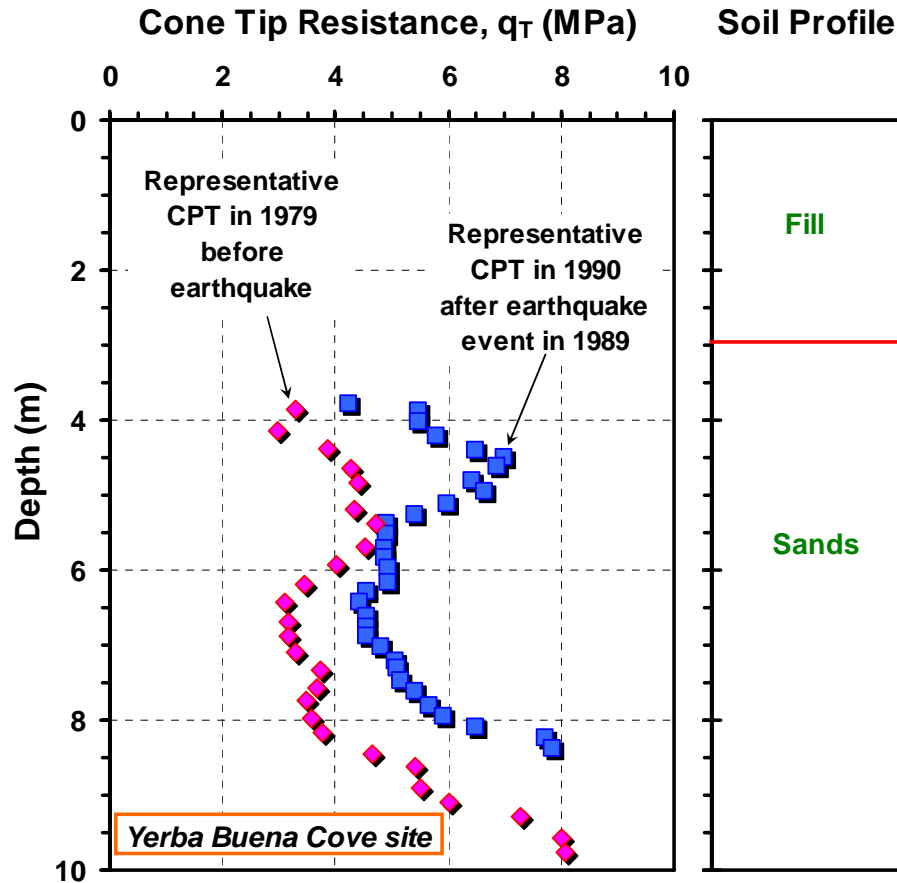
Figure 7.3 Average cone tip resistance measured at the YBC site before and after the 1989 Loma Prieta earthquake (Chameau et al., 1991a)

7.2 Prior Studies of Aging Effects on Cone Tip Resistance

7.2.1 Lab Studies

Dowding & Hryciw (1986) performed a laboratory study and observed aging effects in saturated sand with and without blast densification. The sand, which was fine and poorly graded, and had an initial relative density of $D_r = 50\%$, was contained in a sand tank of 1 m in height and 1m in diameter. Before blasting, the observed increase of tip resistance q_T is consistent between different locations of the penetration tests, and the aging effects seem to be uniform throughout the sand tank. However, after blasting was detonated in

the center of the sand tank, the q_T in the sand near the center axis of the tank increased more significantly than that located further away.

The most systematic laboratory study of aging effects on penetration resistance is that conducted by Joshi et al. (1995). Two types of sands, River sand and Beaufort Sea sand, were used in this study, and their physical characteristics are listed in Table 7.1. They were aged under one or more of the following conditions: dry state, submerged in distilled water, or submerged in sea water. Penetration resistances obtained from series of small-scale penetration tests were taken at 1 day, 1 week, and other times up to 2 years after placement of the sands. According to these data, Joshi et al. (1995) proposed the following equation to estimate the aging effects on penetration resistance, for an aging period of 10 days or more:

$$\frac{P_t}{P_1} = a(t)^b \tag{7-1}$$

where t is the aging period in terms of days, P_t is the penetration resistance at time t, P_1 is the penetration resistance measured on the first day after the sand is placed, and a and b are constants related to the environmental conditions of the sands. The values of a and b suggested by Joshi et al. (1995) are given in Table 7.2. Figure 7.4 plots the experiment data of River sand in dry state and in distilled water, as well as their conceptual behavior described by equation (7-1). Analogously, equation (7-1) can be used to express changes in cone penetration resistance as following:

$$\frac{(q_T)_t}{(q_T)_1} = a(t)^b \tag{7-2}$$

where $(q_T)_t$ and $(q_T)_1$ are the cone penetration resistance at time t and on the first day.

240

Table 7.1 Physical characteristics of the sands used by Joshi et al. (1995)

	River Sand	**Beaufort Sea Sand**
Mean Grain Size, D_{50} (mm)	0.42	0.34
Uniformity coefficient, UC	2.39	2.67
Minimum density (kN/m^3)	14.6	14.3
Maximum density (kN/m^3)	16.6	16.3
Particles shape characteristics	More angular, less rounded	Less angular, more rounded, with some flaky particles

Table 7.2 Values of constants a and b suggested by Joshi et al. (1995)

Environmental Condition	**a**	**b**
Dry state	0.90	0.06
Distilled water	0.75	0.15
Sea water	0.70	0.17
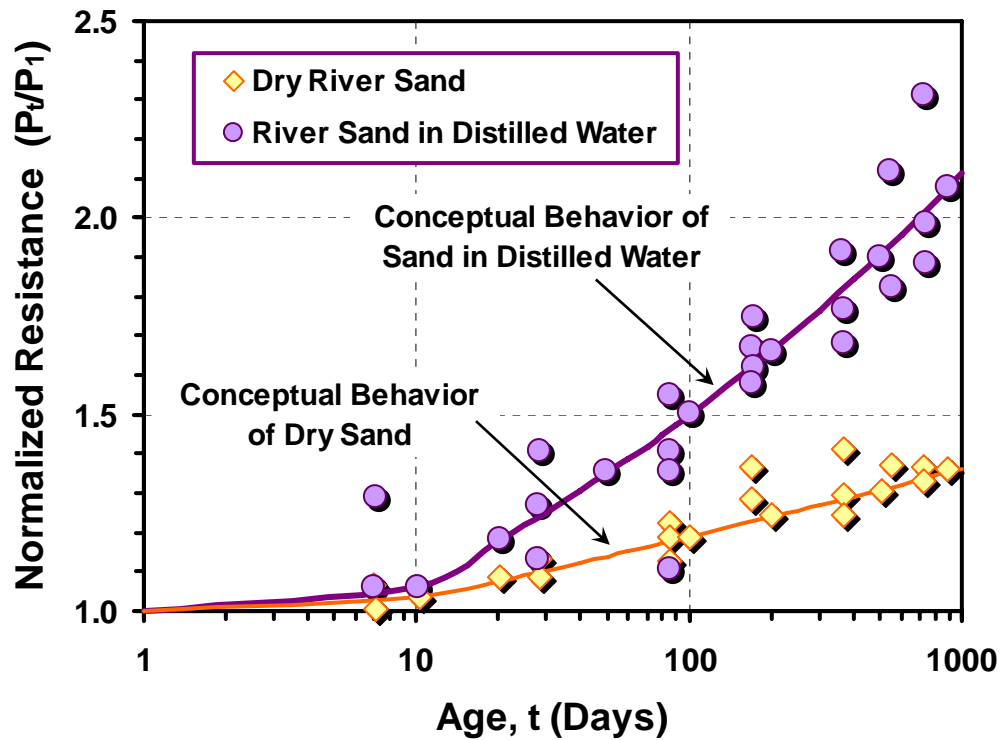
Figure 7.4 Behavior of penetration resistance of dry river sands and river sands in sea water (after Joshi et al., 1990)
Note: P_t is the penetration resistance at time t, P_1 is the penetration resistance on the first day after the sand is placed.

Baxter & Mitchell (2004) performed a similar series of lab tests on two types of sands: Evanston beach sand and Density sand. Evanston beach sand is the same sand used by Dowding and Hryciw (1986) in their laboratory experiment to observe time-dependent increases in penetration resistance after blasting. It is a tan, subangular, poorly graded fine sand from a Lake Michigan beach in Evanston, Illinois. Density sand is a white, rounded, poorly graded, fine to medium sand and it is commercially available from Humbolt Inc. Samples of these two sands were prepared with a certain relative density (40 or 80%) using different pore fluid (distilled water, ethylene glycol, CO_2 saturated water, and air). They were put in an environment of a certain temperature (25 ^{o}C or 40 ^{o}C) for a period of time range from 30 to 118 days. This study did not observe noticeable increases in mini-cone penetration resistance of sands.

7.2.2 Field Case Histories

Most observations of aging effects in sands are from ground improvement projects, in which soils have been improved by ground modification techniques such as subsurface blasting, vibrocompaction, and dynamic compaction. Often, during ground modification of loose sands, liquefaction is typically induced in the saturated sands as a manifestation of the intended densification process. Of particular interest are projects that utilize underground blasting, as the induced shock from the exposion(s) can mimic wave propagations. The generated waves may bear similarities with ground motions comparable to those imparted by earthquakes. A summary of field case histories found in literature, in which aging effects of sands were reported, is presented in Table 7.3.

Table 7.3 Summary of case histories related to aging effects observed in the field

Site	Material	Means of ground improvement	Observed Phenomenon	Reference
Water power project close to Volga River,	Quartz sand	Hydraulically placed fill	SPT blow counts N almost linearly increased from 2.1 to 4.4 in four months	Denisov et al. (1963)
Beside the Volga River	Saturated fine sand to sandy silt	Blasting	SPT resistance of loose sand increased due to blasting, while that of dense sand decreased	Denisov & Dudler (1967)
Nagoya, Japan	Man-made sand	Fill	Decreasing damage rate with age during the Tonankai earthquake in 1944	Ohsaki (1969)
Jebba Dam	Fill material and natural sand	Vibrocompaction	The time dependent increase, measured between day 9 and day 24 after vibrocompaction, was approximately 68% for the fill and 33% for the sand	Mitchell and Solymar (1984); Solymar (1984)
Jebba Dam, Nigeria	Alluvium comprising fine- to coarse-grained, round to subangular quartzitic sands	Hydraulic fill	CPT tip resistance increased significantly with time	Mitchell & Solymar (1984); Mitchell (1986)
Jebba Dam, Nigeria	Alluvium comprising fine- to coarse-grained, round to subangular quartzitic sands	Blasting	Post-blast CPT resistance increased with time	Mitchell & Solymar (1984); Mitchell (1986)
Jebba Dam, Nigeria	Alluvial sand with uniform, fine to coarse quartzitic sand	Dynamic compaction	A substantial increase in CPT tip resistance after compaction.	Solymar & Reed (1986)
Field data in Japan and full-scale lab tests	Recent fill sites and natural sand deposits	Fill and natural deposit	SPT blow counts N increases with age	Skempton (1986)
St. Johns River Power Parke, Jacksonville, Florida	Uncemented loss, relatively clean quartz sand	Dynamic Compaction	Significant increase in CPT tip resistance due to dynamic compaction	Schmertmann et al. (1986)
St. Johns River Power Plant near Jacksonville, Florida	Very low to dense, fine quartz sand	Blasting	The increase of CPT tip resistance is a function of time after densification, and the rate and magnitude appear to depend on the size of initial disturbance.	Schmertmann et al. (1986)
Bay Farm Island, California	Hydraulic fill	Dynamic Compaction	The average CPT tip resistance increased by 10%	Petraborg (1987)

Table 7.3 Summary of case histories related to aging effects observed in the field (Continued)

Site	Material	Means of ground improvement	Observed Phenomenon	Reference
Canadian Beaufort Sea	Slight silty quartz sand	Hydraulic fill	No aging effects are observed	Jefferies et al. (1988)
Fort McMurray, Canada	Oil sand	Blasting	SPT blow counts increased dramatically	Handford (1988)
Pointe Noire, Canada	Clean, medium to coarse sand that are extremely loose	Dynamic Compaction	Enormous increase in average CPT resistance after dynamic compaction, and additional 20% increase within the next 8 days after compaction.	Dumas & Beaton (1988)
Harriet's Bluff, Georgia	Loose to medium dense, uniformly graded, fine sand	Blasting	The CPT tip resistance decreased in the first couple of days, and then it did not show appreciable change after 30 days.	Hryciw and Dowding (1988)
Gray Beverages, Annacis Island, British Columbia, Canada	Deltaic and alluvial deposits	Vibrocompaction	Due to the large variation in the results of the CPT resistance, no consistent increase or decrease was observed.	Massarsch & Vanneste (1988); Brown (1989)
Zeebrugge Harbour, Belgium	Dumped sea sand that is clean and rather uniform.	Hydraulic fill and then blasting	The average tip resistance increased 56% during the first year after placement; The tip resistance decreased one hour after blasting, and then it increased significantly with time.	Carpentier et al. (1985); Van Impe & Meyus (1990)
Thap Sahao Dam, Thailand	Ranging from a fine sandy silt to a well graded gravelly sand	Dynamic Compaction	The SPT blow count was found to continue to increase significantly with time after compaction.	Gambin (1987); Fitzhardinge (1990)
Annacis Island, Vancourver, Canada	Hydraulic fill dredged from the Fraser River	Vibrocompaction	For the loose sand fill, the cone tip resistance increased from about 5 MPa to 20 MPa.	Campanella et al. (1990)
Canadian Beaufort Sea	Fill material with fines content less than 2%	Blasting	The CPT tip resistance increased immediately after blasting, as well as with time.	Jefferies (1991)
Hong Kong	Deep hydraulic fill	Vibrocompaction	The cone resistance increased markedly in one year after the compaction	Massarsch & Heppel (1991)
Geeley, Colorado	Poorly graded gravelly to fine sand	Blasting	Both the tip resistance and sleeve friction increased after an initial decrease following blasting	Charlie et al. (1992)

Table 7.3 Summary of case histories related to aging effects observed in the field (Continued)

Site	Material	Means of ground improvement	Observed Phenomenon	Reference
Chicopee Industrial Park, Massachusetts	Loose to very loose saturated alluvial sands	Blasting	The tip resistance increased significantly between two weeks and five months after blasting	La Fosse & von Rosenvinge (1992)
Chek Lap Kok airport in Hong Kong	Hydraulically placed sand fill	Vibrocompaction	A clear increase in CPT tip resistance is observed	Ng et al. (1996)
Treasure Island in San Francisco Bay	Loose to firm sand fill over San Francisoc Bay mud clays	Blasting	CPT tip resistance dropped following blasting, and then increased significantly	Ashford et al. (2004)

Significant aging effects in clear sands have been observed in conjunction with the foundation densification program for Jebba Dam in Nigeria (Mitchell & Solymar, 1984; Solymar, 1984). This rockfill dam is an embankment of 42 m in height and founded on an alluvial sand deposit, that has a maximum thickness of 70 m. The sands are comprised of medium to coarse silica sand particles that are subrounded to rounded in shape. Blasting and vibrocompaction were used to densify the loose to medium-dense portions of river sands that are located as deep as 40m. Observations following blast-densification in the Jebba Dam foundation showed that the cone penetration resistance immediately following ground densification decreased, due to the destrucacturation of the aging effects (Mesri et al., 1990). The decrease was not caused by the unfinished dissipation of seismically-induced extra porewater pressure, for any excess pore pressures would be fully dissipated in the medium to coarse sands within a few minutes (Mitchell & Solymar, 1984). However, the post-liquefaction aging effects at Jebba increased the soil strength quickly. Figure 7.5 shows the cone tip resistance measured at the Jebba Dam site before and after explosives were detonated nearby. It represents the typical loss of cone

tip resistance due to blast disturbance, followed by significant increases observed during this project (Mitchell & Solymar, 1984). At the Jebba Dam site, a significant increase of cone tip resistance with time was also observed after the foundation was densified using vibrocompaction, as well as after sandy hydraulic fill was placed.
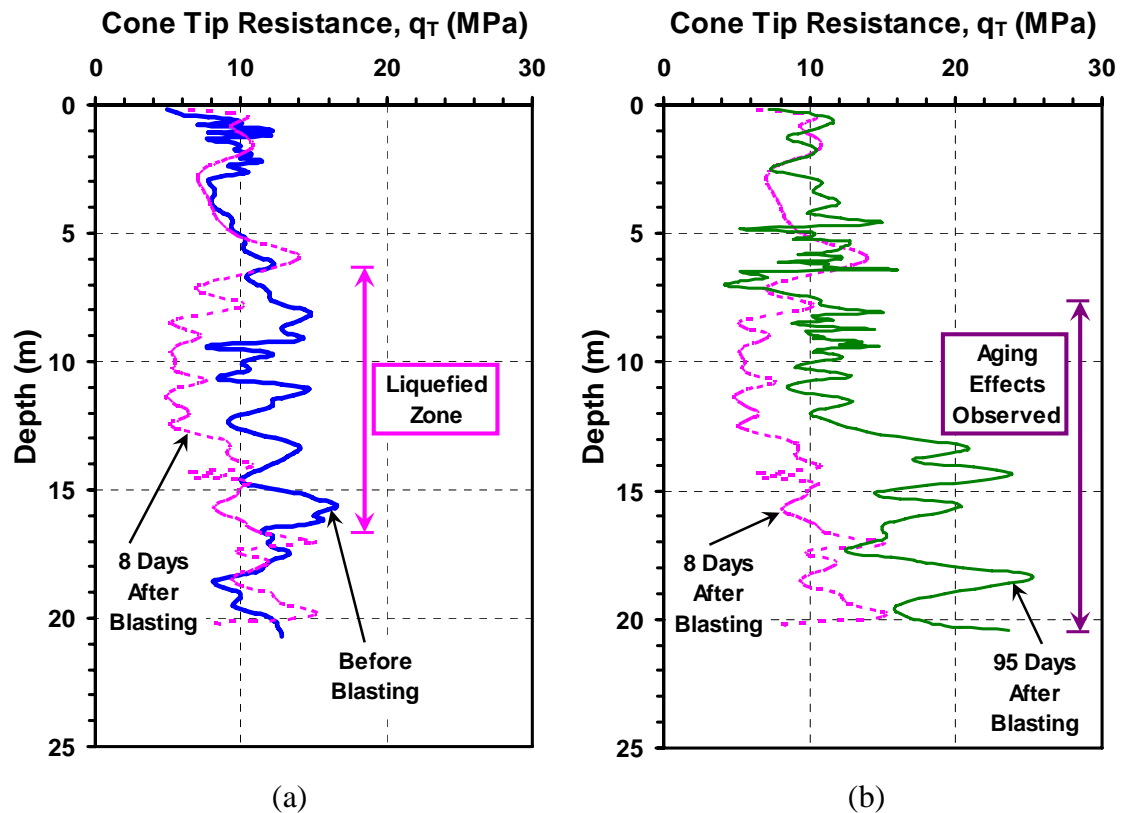
Figure 7.5 Aging effects on cone tip resistance at Jebba Dam site in Nigeria:
(a) Data before and 8 days after blasting; (b) Data collected 8 days after and 95 days after blasting (after Mitchell & Solymar, 1984)

Blast-induced liquefaction was initiated for the Cooper River Bridge in Mount Pleasant, South Carolina. Two sets of blast events were set off, and each of them consisted of a sequence of timed blasts. Piezometers clearly showed dramatically elevated porewater pressures following the blasts. Water was also observed to flow to the ground surface after these events. Series of CPTu tests were performed before, during, and after the blasting events. The measured cone tip resistances are presented in Figure 7.6.

Comparing the CPTu data measured before and just after the blast events, obvious decrease of tip resistance q_T is observed after every event in the depth range from 3.3 to 5.6 m, which delineates the liquefied sand zone. From this figure, it can be seen that q_T in the liquefied sand zone increased significantly one month after the second blast event, and it even surpassed its value before the blasting in depth range from 4.6 to 5.2 m, but it did not fully resume to original q_T values in zone 3.5 m to 4.6 m.

Ashford et al. (2004) performed blast testing at Treasure Island in San Francisco Bay. Treasure Island was constructed by hydraulic and clamshell dredging, and consists of loose to firm sand fill over San Francisoc Bay mud clays. The island serves as a National Geotechnical Experimentation Site (NGES) and full details are given elsewhere (e.g. Benoit, 2000; Faris & de Alba, 2000). The blasting site was excavated to a depth of 1.2m in order to minimize the cap effect caused by the nonliquefiable soil at the ground surface. The porewater pressure transducer implemented at the site indicated that the porewater pressure was dramatically increased immediately after the blasting was set off, while the surface manifestation of liquefaction (sand boils and water flows) occurred 3 to 5 minutes after the blasting. Figure 7.7 shows the results of CPTu soundings performed prior to blasting, 2 days after blasting, and 42 days after blasting. The results clearly indicate that the penetration resistance measured 2 days after blasting decreased compared with that measured before blasting, but the penetration resistance and sleeve friction measured 42 days later showed significant increase over those measured before blasting (Ashford et al., 2004). As to the friction ratio, its value does not seem to be significantly changed by the blasting and time effects.
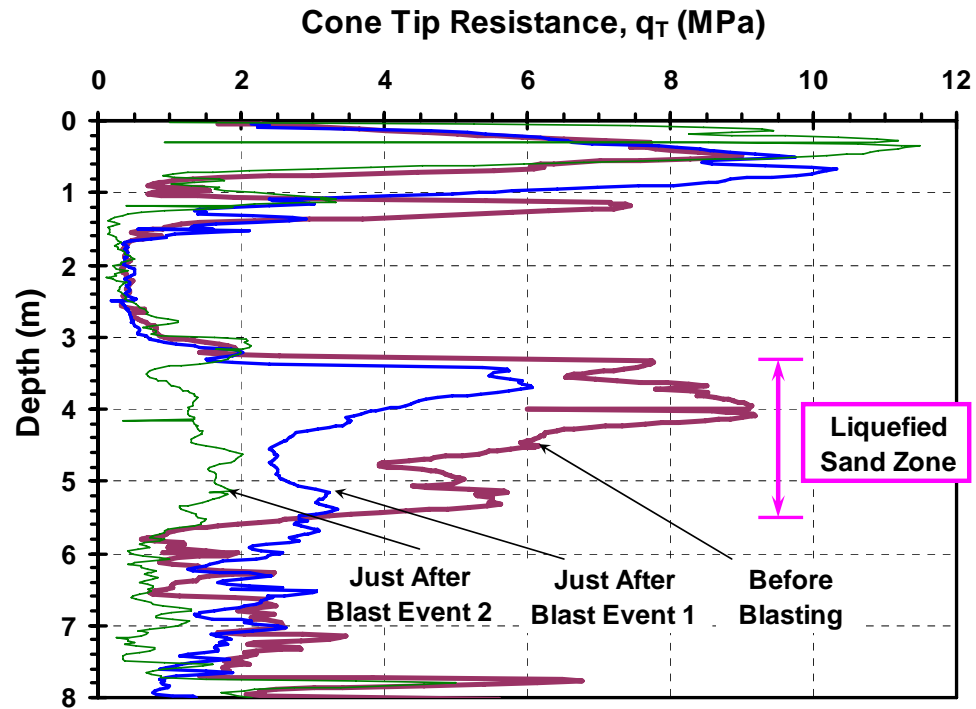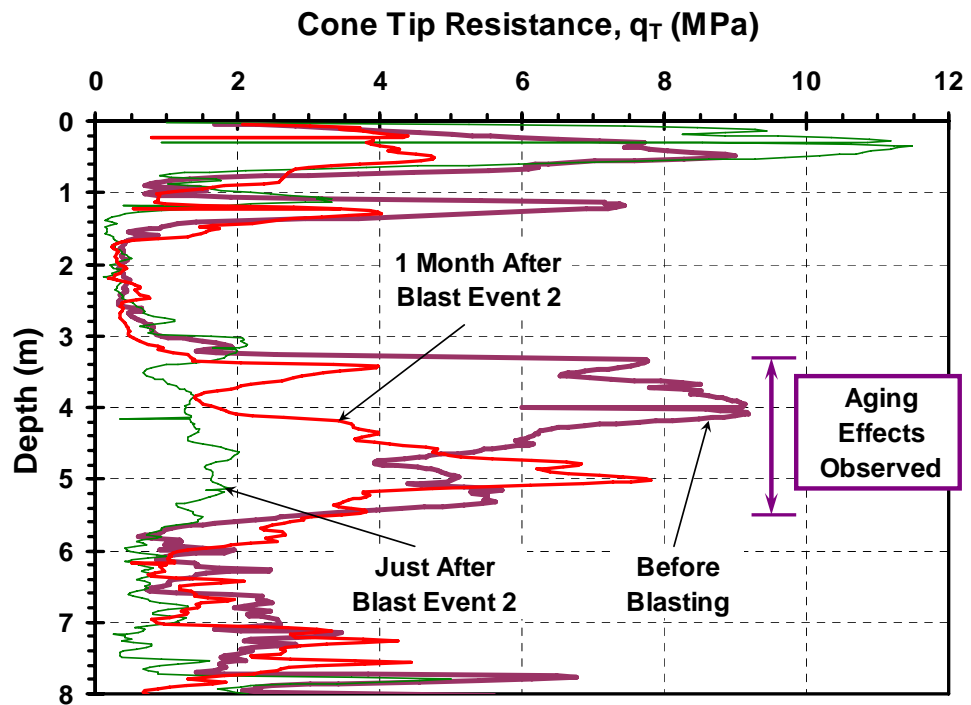
Figure 7.6 CPT soundings performed before, during, and after blast events at Cooper River Bridge site in Mount Pleasant, South Carolina [Data from Camp (2004)]
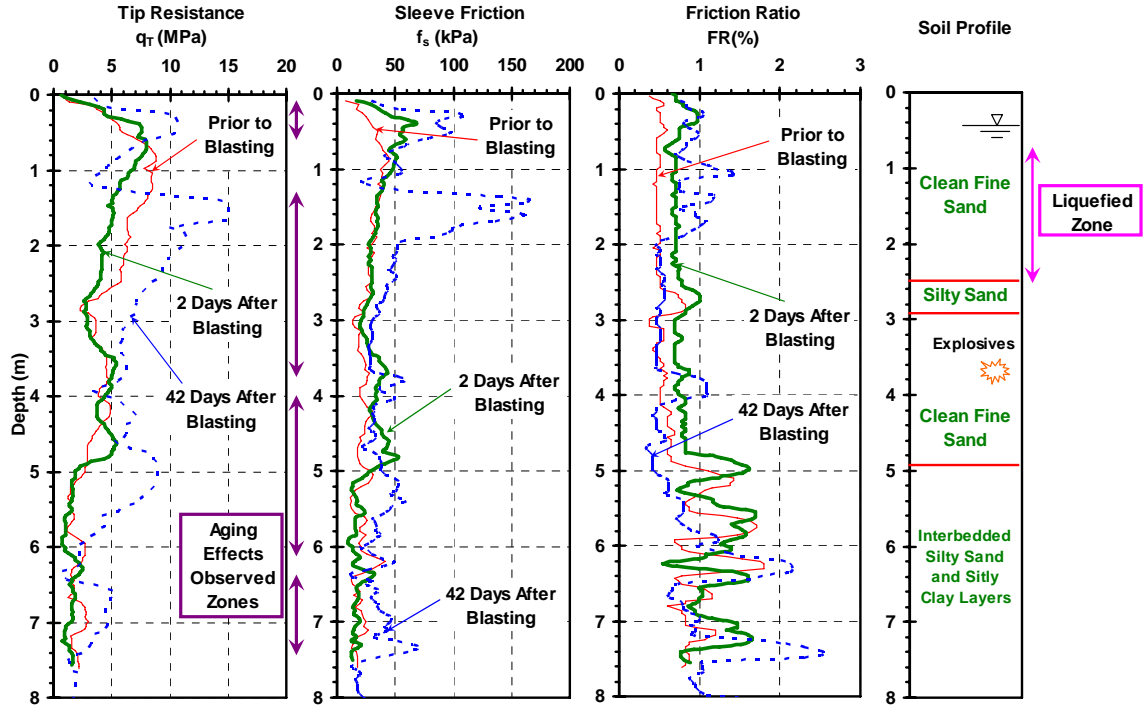
Figure 7.7 CPT results at induced liquefaction study site prior to, 2 days after, and 42 days after blasting at the Treasure Island in San Francisco Bay (Ashford et al., 2004)

7.2.3 *Estimation of Aging Effects on q_T Based on Field Case Histories*

Based on considerations of secondary compression, Mesri et al. (1990) suggested the following expression for estimating the increase of q_T in the short-term aging timeframe:

$$\frac{(q_T)_t}{(q_T)_R} = \left(\frac{t}{t_R}\right)^{C_D C_\alpha / C_C} \tag{7-3}$$

where $(q_T)_R$ is a reference cone tip resistance at a reference time $t_R > t_p$, and $(q_T)_t$ is the cone tip resistance at any time $t > t_R$. The parameter C_D reflects the densification effect, and is related to the procedure of densification and the increase of relative density D_r. The value of C_D is in the range from 10 to 15 for blasting densification, while in the range from 4 to 8 for dynamic compaction. The parameter C_α is the secondary compression

index and C_c is the virgin compression index. In the absence of laboratory compressibility data, Mesri et al. (1990) suggested typical values of C_α/C_c to be 0.04 for inorganic clays, and in the range of 0.02 to 0.03 for silts and sands.

Based on data from case studies, as well as q_T data obtained following a blast densification in a sandy alluvium, Charlie et al. (1992) suggested that q_T with time fits the following empirical equation:

$$\frac{(q_T)_{N\ weeks}}{(q_T)_{1\ week}} = 1 + K \log N \tag{7-4}$$

where N is the number of weeks since the sands are disturbed, and K is an empirical constant related to the air temperature during the measurements of q_T. However, Jefferies & Rogers (1993) disagreed with the air temperature estimated by Charlie et al. (1992), and pointed out the relationship of K with temperature is not significant. The observed values of K vary from 0.02 to 1 for the limited number of cases considered. With such a huge range, a forward prediction of the aged q_T following liquefaction would be highly unreliable.

As to the aging effects in geologic time, very few long-term data are available. Based on data compiled by Skempton (1986) supplemented with other studies, Kulhawy & Mayne (1990) and Jamiolkowski et al. (1988) proposed relationships between SPT penetration resistance, relative density, and the passage of time. Affected similarly by the compressibility of the soil and the effective horizontal stress, the q_T from the SCPTu and the N-value from the SPT can be correlated, and the ratio q_T/N is constant, given a certain

mean grain size (Robertson et al., 1983; Kulhawy & Mayne, 1990). Figure 7.8 shows the equivalent tip resistance with time converted from the relationships proposed by Kulhawy & Mayne (1990) and Jamiolkowski et al. (1988) respectively. Also shown in this figure are the data of CPT tip resistances obtained from 7 sites during the Canadian Liquefaction Experiment (CANLEX) project (Wride et al., 2000). The sand deposits at these sites range in age from approximately 1 month to approximately 4000 years (Wride et al., 2000), and a trend line is drawn through these data, indicating the possible aging effects on cone penetration resistance in a long term. Since these sands may have been affected by a number of other variables, such as overconsolidation, desiccation, groundwater fluctuations, and creep (Wride et al., 2000), the observed trends may reflect factors other than just aging.

By extending the trend line of the CANLEX data (Figure 7.8) to very young age, the tip resistance, normalized by relative density, for one day old sand is about 100. Therefore, the tip resistance, normalized by the reference tip resistance of one day old, can be derived for the CANLEX data, and they are plotted on Figure 7.9. Similarly, the tip resistance, normalized by relative density, for one day old sand can be obtained by extending the curves suggested by Kulhawy & Mayne (1990) and Jamiokowski et a. (1988) (Figure 7.8). Thus their corresponding curves of the tip resistance, normalized by the reference tip resistance of one day old, can be derived, as shown in Figure 7.9. Also plotted on Figure 7.9 is the prediction of aging effects based on equation (7-2) suggested for sands in fresh water environment by Joshi et al. (1995), as well as the prediction based on equation (7-3) suggested by Mesri et al. (1990), with the parameters suggested

for sands. From this figure, it can be seen that aging effects vary significantly among these proposed prediction schemes. The equation suggested by Joshi et al. (1995) fits the CANLEX data relatively well.
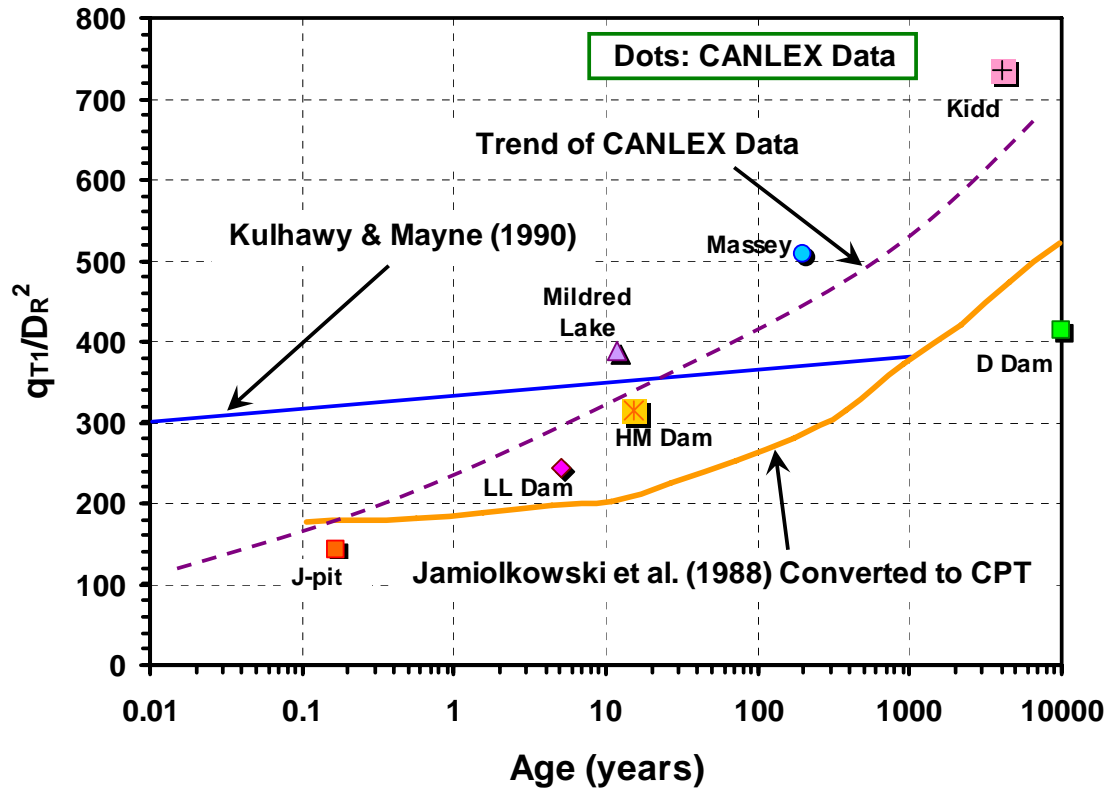
Figure 7.8 Possible aging effects on cone penetration resistance normalized by relative density [after Wride et al. (2000)]

Note: D_R is relative density in decimal, and q_{T1} is overburden-stress normalized tip resistance.

Except for the relationship suggested by Jamiolkowsi et al. (1988), the other three curves shown in Figure 7.9 suggest the logarithm of $(q_T)_t/(q_T)_1$ generally increases linearly with the logarithm of time t:

$$\log\left[(q_T)_t/(q_T)_1\right] = k\left[\log(t) - \log\left(\frac{1}{365}\right)\right] \tag{7-5}$$

where k is the slope of the linear relationship, t is in the unit of years. The value of k is about 0.05, 0.15, 0.20 corresponding to the curves suggested by Kulhawy & Mayne (1990), Joshi et al. (1995), and Mesri et al. (1990), respectively. The value of k should be related to many factors, such as sand type, pore fluid, sand origin, and method of destructuration. A hypothesis is made here for deriving the value of k:

$$k = \frac{k_1 + k_2 + k_3 + k_4}{4} \tag{7-6}$$

where k_1, k_2, k_3, k_4 are the hypothetical influence factors of sand type, pore fluid, sand origin, and method of destructuration. Values are assigned to them intuitively, and are listed in Table 7.4. Figure 7.10 shows the hypothetical behavior of cone tip resistance with time for different sands.
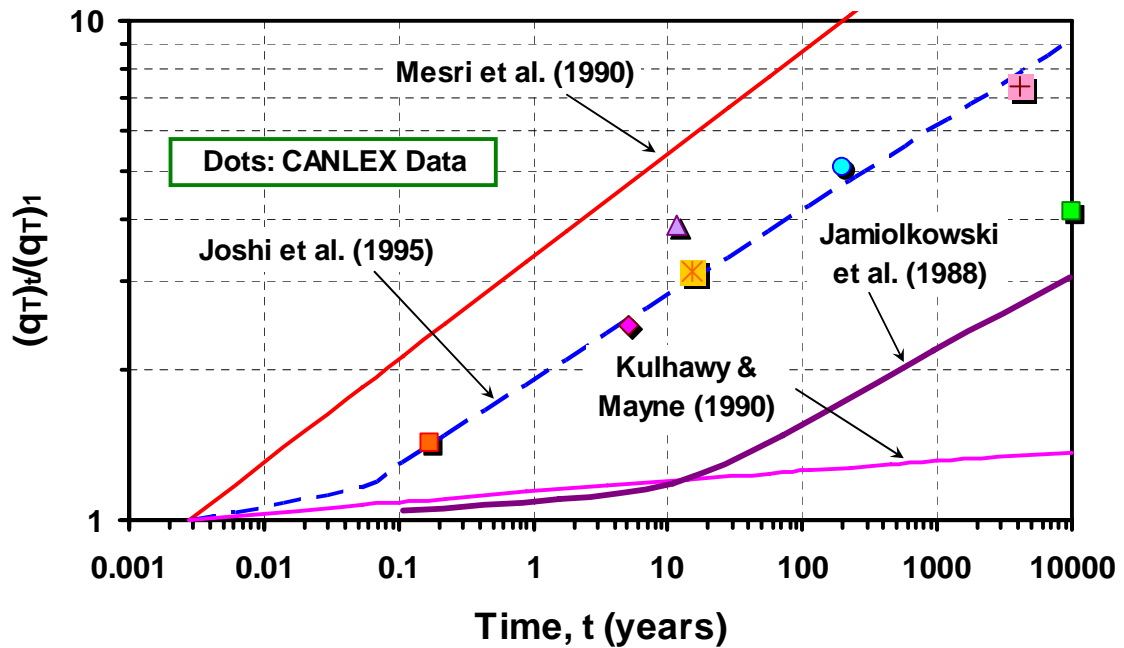
Figure 7.9 Comparison between the predictions proposed by Mesri et al. (1990) and Joshi et al. (1995)

Note: $(q_T)_t$ and $(q_T)_1$ are the cone penetration resistance at time t and on the first day after sand is deposited

253

Table 7.4 Hypothetical influence factors of sand type for aging effects
on cone tip resistance

Sand Type		Pore Fluid		Origin		Destructuration	
Sand Type	K_1	Pore Fluid Type	K_2	Origin	K_3	Method of Destructuration	K_4
Clean sand	0.05	Dry	0.05	Man-made (e.g. Crushing)	0.05	Fill	0.05
Silty Sand	0.08	Fresh water	0.08	Aeolin	0.08	Earthquake	0.08
Clayey Sand	0.12	Salt water	0.1	Sediment	0.1	Vibration	0.08
		Water with $CaCO_3$	0.12			Dynamic Compaction	0.08
		Water in fine silica	0.15			Subsurface Blasting	0.12
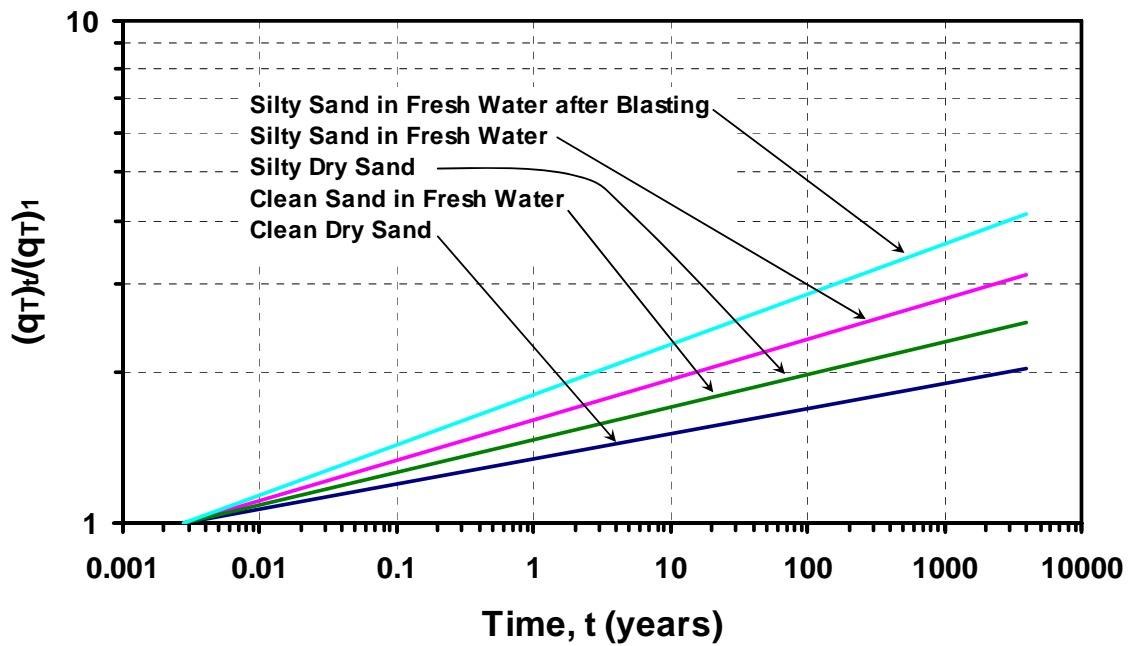
Figure 7.10 Hypothetical behavior of cone tip resistance with time for different sands

7.3 Aging Effects on Shear Wave Velocity

7.3.1 Lab Studies

The small-strain shear modulus G_{max} can be derived from the shear wave velocity V_s from

$G_{max} = \rho_T\, V_s^2$, where ρ_T is the total unit mass density and g is acceleration due to

gravity. From lab resonant column tests, Afifi & Woods (1971) found that G_{max} of air-dry

sands increased linearly with the logarithm of time as shown in Figure 7.11 (a), although the density does not change. Figure 7.11 (b) presents the back-calculated ratio of shear wave velocity V_s at time t and that at 1 minute. The increase of V_s most closely follows a linear relationship with the logarithm of time (Anderson & Stokoe, 1978). A coefficient of shear modulus increase with time is proposed to express the time effect of G_{max}:

$$I_G = \Delta G_{max} / \log_{10}(t_2/t_1)$$ (7-7)

where t_2 and t_1 are respective times, and ΔG_{max} is the change in G_{max} from t_1 to t_2 (Anderson & Stokoe, 1978). The value of I_G equals the increase of G_{max} per log cycle of time, and for air-dry sands it is typically in the range of 2% to 5% of the G_{max} measured approximately one day after aging starts (Afifi & Woods, 1971). From Figure 7.11 (b), the increase of V_s per log cycle of time is about 0.42%.

Using laboratory bender elements, Human (1992) performed a study on the aging effects of shear wave velocity. With different confining stresses, void ratio, stress anisotropy and preparation methods, a series of sand samples were aged for up to 29 days, and their V_s were measured with time, as shown in Figure 7.12. It was found that the change of V_s with time in dry sands generally follows the following form:

$$\frac{V_t}{V_i} = 1 + V_\alpha \log \frac{t}{t_i}$$ (7-8)

where V_t is the shear wave velocity at time t, V_i is the initial shear wave velocity at time t_i, and V_α is a constant. The reported V_α ranges from 0.6% to 1.1%, and Human (1992) noticed that it corresponds to an increase in G_{max} of 1.2% to 2.1% per log cycle of time, lower than the corresponding range of 2% to 5% suggested by Afifi & Woods (1971).

Although systematic aging effect is observed in dry sands, no apparent increase in V_s was found for saturated samples in this study. However, according to tests performed by Hardin & Richart (1963), the V_s of wet sands is 10% less than that of dry sands.
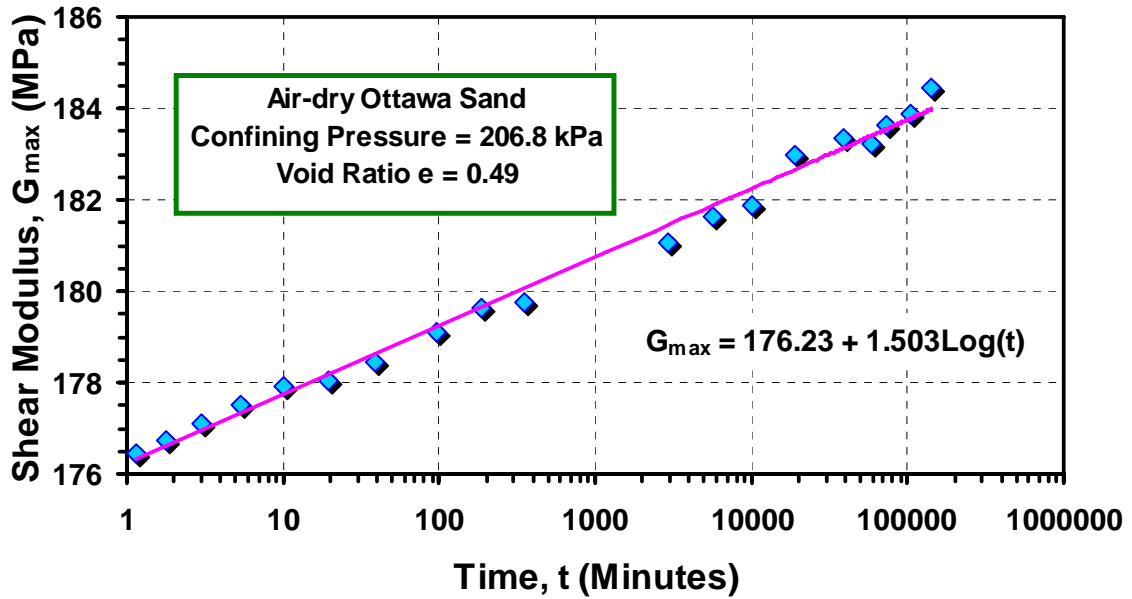
(a)
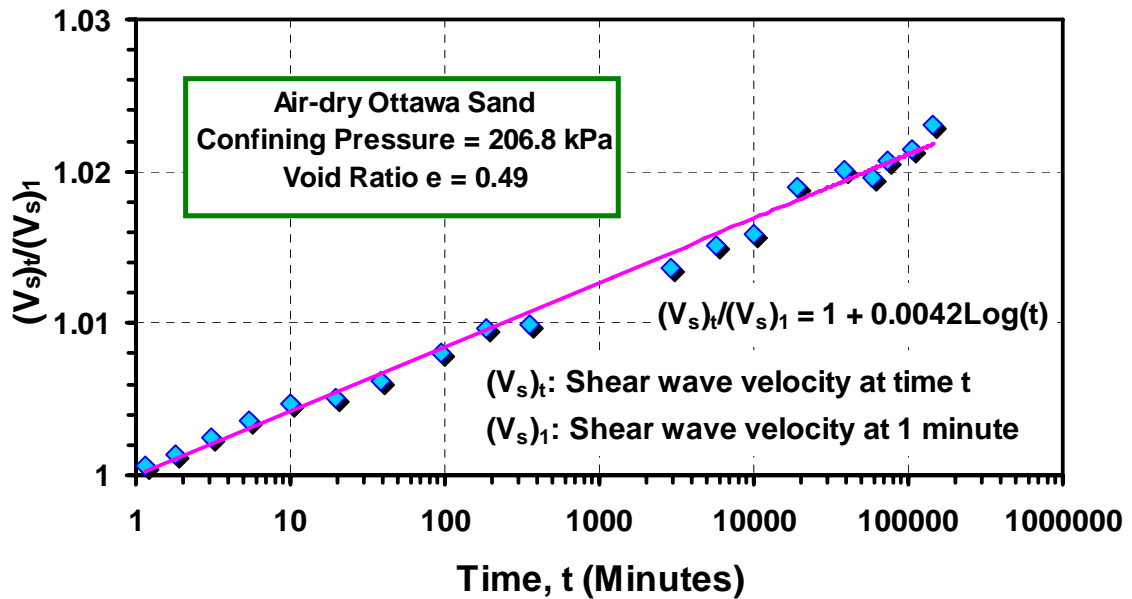
(b)

Figure 7.11 Aging effects on shear modulus for air-dry Ottawa sand at constant confining pressure [after Afifi & Woods (1971)]
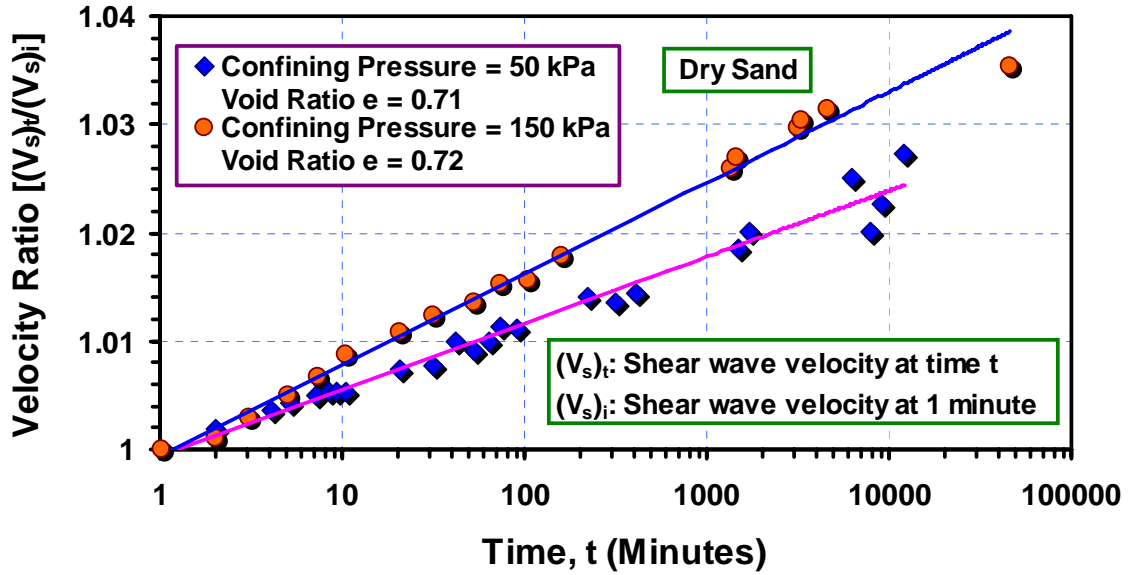
Figure 7.12 Aging effects on shear wave velocity in dry sand with increasing level of confining stress (Human, 1992)

7.3.2 Field Studies

The shear wave velocity of sands has been recognized to increase with time. Stokoe & Santamarina (2000) reported a pilot study of blast densification aimed to densify a loose fine silty sand layer located about 7 to 11 m below the ground, as shown in Figure 7.13. Also presented in this figure is the comparison of the shear wave velocities measured before blasting and at different times after blasting. The shear wave velocities measured 1 day after blasting was significantly lowered compared with that measured before blasting, and from the measurement made 7 days and 10 months after blasting, the shear wave velocity increased significantly with time.

As to the aging effects on V_s in geologic time, Wride et al. (2000) presented a set of data of shear wave velocities, normalized for relative density, collected from the CANLEX sites as shown in Figure 7.14, illustrating the possible aging effects on V_s in geologic

time. These data follow a good linear relationship in a log-log scale, with the logarithm of the normalized shear wave velocity increasing about 4.9% per log cycle of time. The aging effects on V_s suggested by Wride et al. (2000) are much more significant than those found in the laboratory experiments, and it is difficult to judge which can be used for the NMSZ.
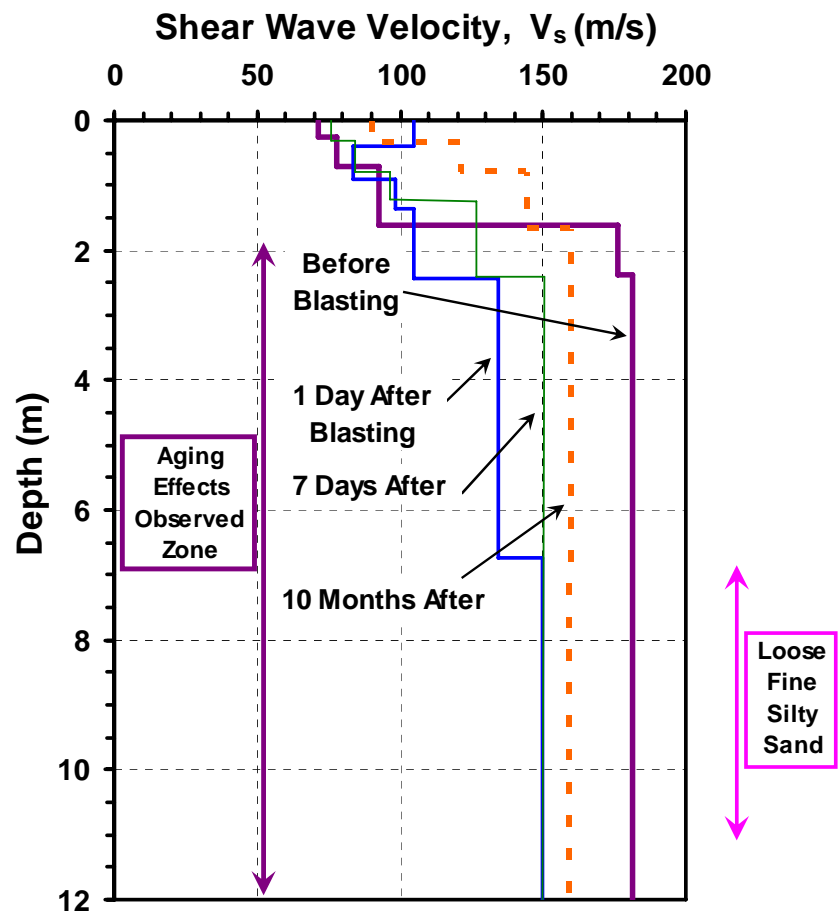
Figure 7.13 Shear wave velocities measured before and after a blasting
(Stokoe & Santamarina, 2000)
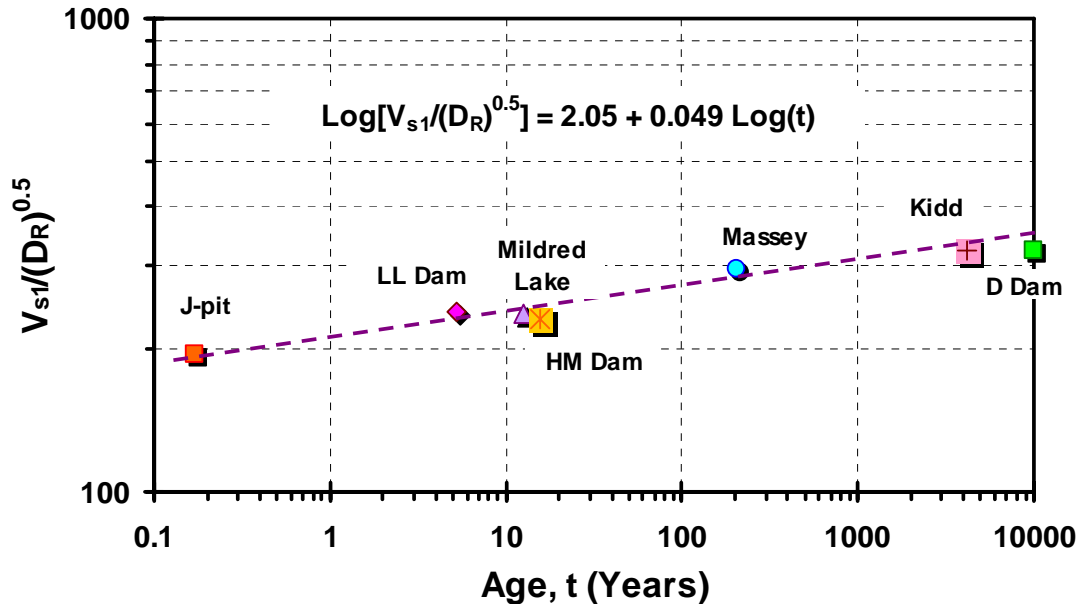
Figure 7.14 Data of shear wave velocity with time from CANLEX project
(Wride et al., 2000)
Note: V_{s1} is stress-normalized shear wave velocity, and D_R is relative density in decimal.

7.4 Uncertainty of CPT measurements in NMSZ

In order to compare the measurements taken at different time, it is important to know the relative uncertainty of the measurements. The uncertainty of the in-situ measurements taken by CPT is associated with both the horizontal variability of the soils and equipment errors used to perform the test. Because of the inherent lateral variability of the soils, measurements from different soundings might vary significantly or moderately, depending on the distance between test locations, geologic setting, and/or environmental factors. The random or systematic errors of the equipment would result in differences between the measured value and the real value of parameters intended to measure.

A series of CPT tests was performed at the Walker paleoliquefaction site near Marked Tree, AR, as discussed previously in Chapter 6. The CPT testing was performed in two

linear arrays as shown in Figure 6.16 in Chapter 6. The intention of these series was to provide information on the subsurface stratigraphy and source sands, explore lateral variability, and evaluate the potential for re-liquefaction.

The average, maximum, and minimum value of CPT measurements in array 1 and array 2 are presented in Figure 7.15 and 7.16 respectively. The profiles mainly consist of clay and silt for the upper 4 m in array 1 and the upper 5 m in array 2, and the remainder of the profiles to depths of at least 16 meters indicates the presence of sand. The soundings in each array were performed about 5 meters apart, and the horizontal variability of the soils plus equipment errors are reflected in the differences of the CPT measurements within these soundings. A statistical study was carried out for the average measurement of tip resistance and sleeve friction in the sand layer from 7 m to 13 m. The reason to choose this depth range is that it consists of a relatively uniform sand layer and the CPT measurements are available in all the presented soundings. Tables 7.5 lists the average value of the readings (q_T, f_s and FR) in the depth range from 7m to 13m of soundings in array 1 and array 2, and their statistics are shown in Table 7.6. Both sounding MTREE02 and MTREE13 were excluded from this analysis, because they were stopped prematurely at shallow depths due to excessive inclination.

Comparing the statistics for the two arrays, it can be seen that array 2 has a more significant variance for the average value of CPT measurements in the depth range from 7m to 13m, with COVs (Coefficient of Variance) for q_T and f_s in the range from 11% to 16%, twice as high as those for array 1. The COV for FR of both arrays are about 8%,

and it seems that the range of variation of FR is not significantly different between the two arrays. The ratio of the average q_T and f_s between any two soundings is within the range from 0.8 to 1.25 in array 1, and from 0.7 to 1.5 in array 2. These reflect a more significant horizontal variability of the soils where soundings in array 2 are performed.

Table 7.5 Average value of CPT measurements from 7m to 13m at Walker Site in Marked Tree, Arkansas

	Sounding	q_T (MPa)	f_s (kPa)	FR (%)
Array 1	Marktree 1	18.62	143.04	0.77
	Marktree 3	19.24	118.31	0.62
	Marktree 4	19.86	126.76	0.64
	Marktree 5	19.18	131.50	0.69
	Marktree 6	19.09	128.06	0.67
	Marktree 7	20.85	146.94	0.71
	Marktree 8	21.69	135.08	0.61
Array 2	Marktree 9	22.48	163.78	0.73
	Marktree 10	21.58	159.23	0.75
	Marktree 11	19.94	141.14	0.71
	Marktree 12	17.11	128.85	0.76
	Marktree 14	17.70	109.77	0.63

Table 7.6 Statistics of CPT measurements from 7m to 13m at Walker Site in Marked Tree, Arkansas

	Item	q_T	f_s	FR
Statistics of Array 1	Average	19.79	132.81	0.67
	Stdev	1.100	9.836	0.057
	COV (%)	5.556	7.406	8.467
	Max/Min	1.16	1.24	1.26
	Min/Max	0.86	0.81	0.80
Statistics of Array 2	Average	19.76	140.55	0.72
	Stdev	2.34	22.21	0.054
	COV(%)	11.87	15.80	7.54
	Max/Min	1.31	1.49	1.22
	Min/Max	0.76	0.67	0.82
Statistics of Array 1 and Array 2	Average	19.78	136.04	0.69
	Stdev	1.63	15.75	0.058
	COV(%)	8.25	11.58	8.34
	Max/Min	1.31	1.49	1.26
	Min/Max	0.76	0.67	0.80
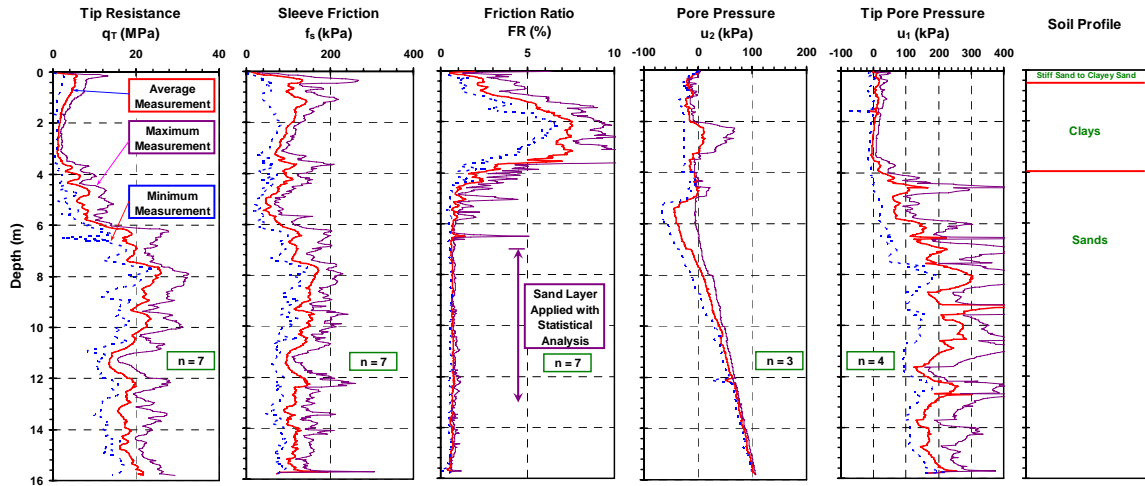
Figure 7.15 Presentation of CPT measurements from array 1 at Walker site in Marked Tree, Arkansas
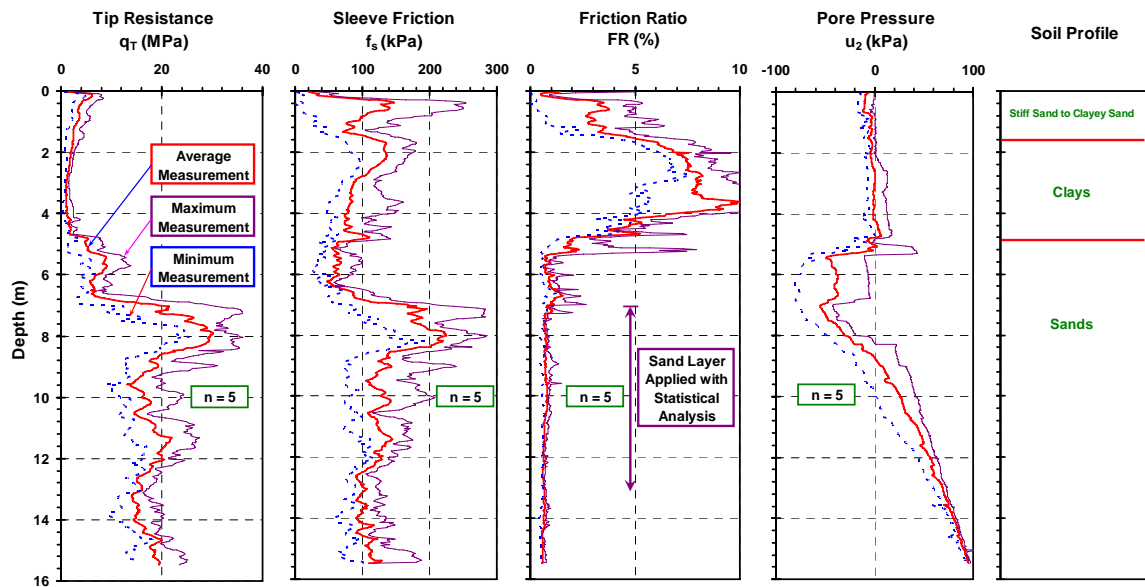
Figure 7.16 Presentation of CPT measurements from array 2 at Walker site in Marked Tree, Arkansas

7.5 CPT Tests Performed During Embayment Seismic Excitation Experiments

7.5.1 Test Sites

During the Embayment Seismic Excitation Experiments (ESEE), two test sites were selected to detonate underground explosives to generate surface waves. The first site was

located in the southern NMSZ near Marked Tree, AR, and the second site selected in the northern NMSZ near Tiptonville, TN, as shown in Figure 7.17. Figure 7.18 illustrates the setup of the explosive boreholes. Each borehole was drilled with a diameter of 0.56 m and to a depth of 48.8 m. The upper 24.4 m was lined with steel casing for facilitating the placement of explosives. The southern site was configured with 1180 kg (2600 lbs) of ammonium nitrate explosives, which were emplaced in a single borehole. The northern explosion received 2268 kg (5000 lbs), which are equally emplaced in two boreholes that were situated 28.3 m away from each other. The explosives in the two boreholes were detonated simultaneously during that experiment.

The seismic CPT tests were performed before blasting, approximately 1 day after, and 8 months after the blasting at both sites. In addition, at the TN site, a SCPTu was conducted within 2 to 3 hours after blasting. They are located in a small area of 1 m^2 situated about 31 m away from both the boreholes at the southern site, and about 32 m from the borehole at the northern site.

7.5.2 *Test Results at Arkansas ESEE Site*

The southern ESEE site is located less than 20 km away from the Walker site in Marked Tree, AR. Figure 7.19 presents results of the SCPTu sounding performed prior to the ESEE event, as well as the interpreted soil profile. The soil profile at the ESEE site is similar to that at the Walker site, with a 2.5 m thick clayey layer underlain by a thick layer of clean sand to depths exceeding 20 m. Figure 7.20 compares the data from soundings performed at different times. The values of q_T and f_s measured 40 hours after

blasting generally decreased, compared with the measurements before the blasting. The decrease is especially significant in the depth range from 4 to 12 m. The shear wave velocity V_s also decreased in the depth range from 2 to 10.5 m. Decreases of these measurements very likely resulted from the blasting-induced liquefaction. Figure 7.21 compares the q_T and f_s measured 40 hours and 229 days after the blasting. The tip resistance q_T increased with time in the depth range from 5 to 9 m, which is within the suspected liquefied zone. The sleeve friction f_s showed increase with time below depth of 3.5 m. The shear wave velocity V_s consistently decreased with time along almost all the depths. It is contradictory to expectation based aging effects, and the reasons are unknown.

Figure 7.17 Locations of the Embayment Seismic Excitation Experiment (ESEE) sites in Marked Tree, Arkansas and Tiptonville, Tennessee
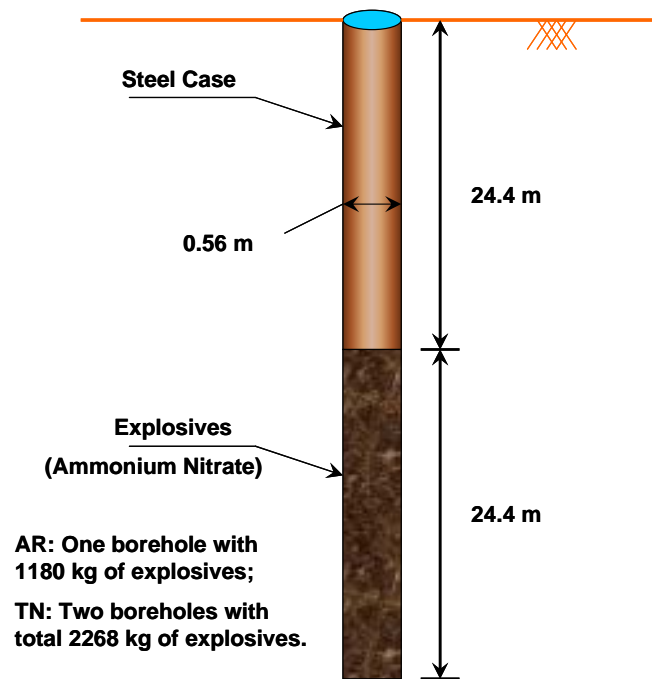
Figure 7.18 Setup of the explosive borehole in ESEE experiments
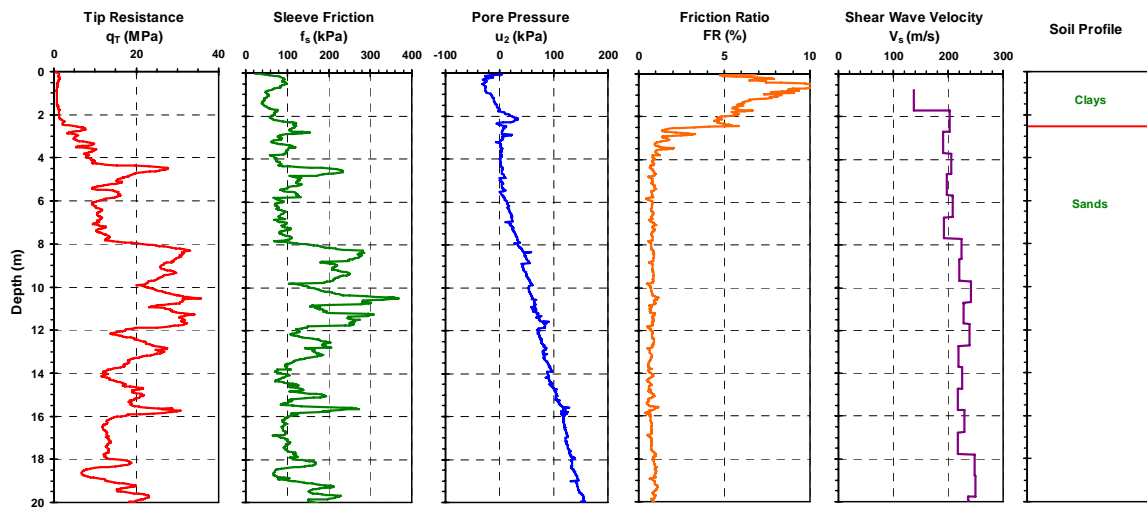
Figure 7.19 SCPTu data and interpreted soil profile prior to ESEE Marked Tree, AR event
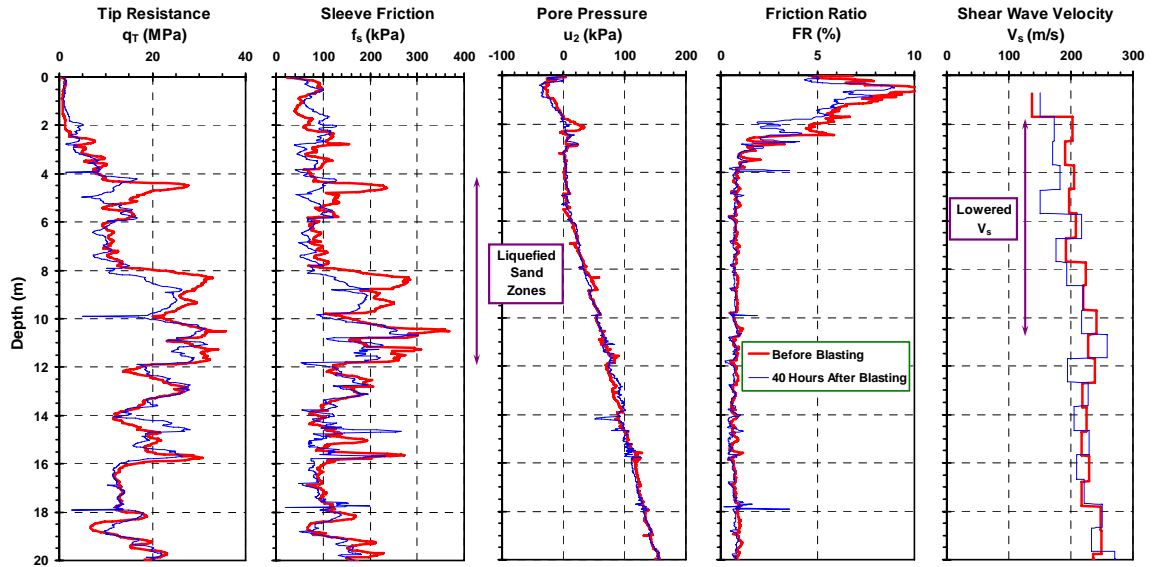
Figure 7.20 SCPTu data collected before and 40 hours after ESEE Marked Tree, AR event
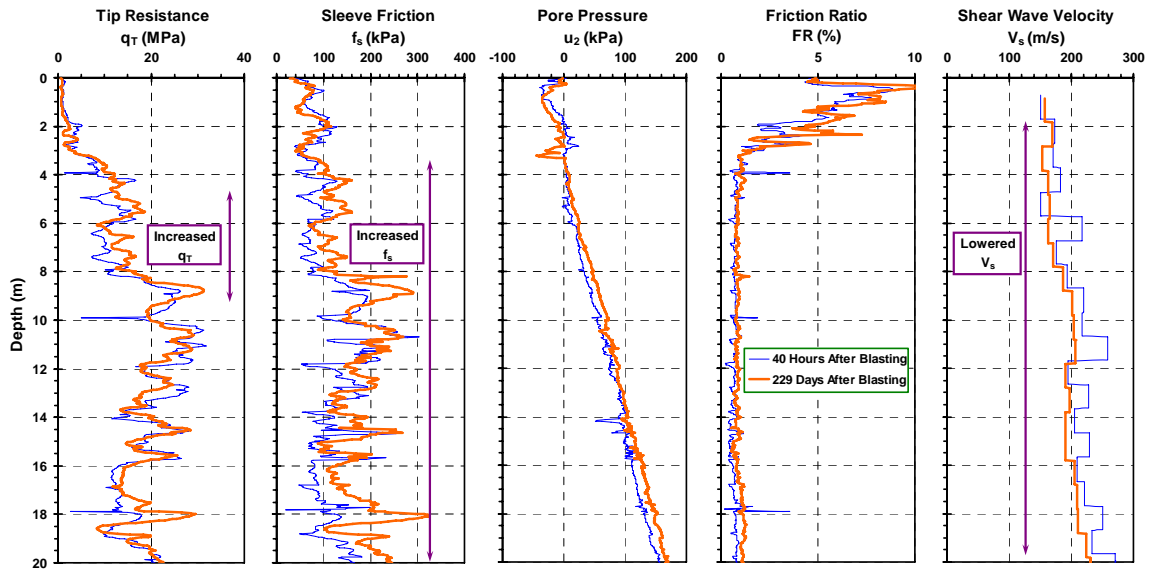
Figure 7.21 SCPTu data collected 40 hours and 229 days after ESEE Marked Tree, AR event

In order to have a better look at the variations between these SCPTu measurements, the average values of q_T, f_s, u_2 and FR in a depth interval of every 1 m are calculated, and they are presented in Figure 7.22. The average value of porewater pressure (u_2) and

266

friction ratio (FR) do not seem to have changed due to the earthquake. Some differences can be seen between the q_T, f_s and V_s, but they are not significant and no consistent trend is observed.
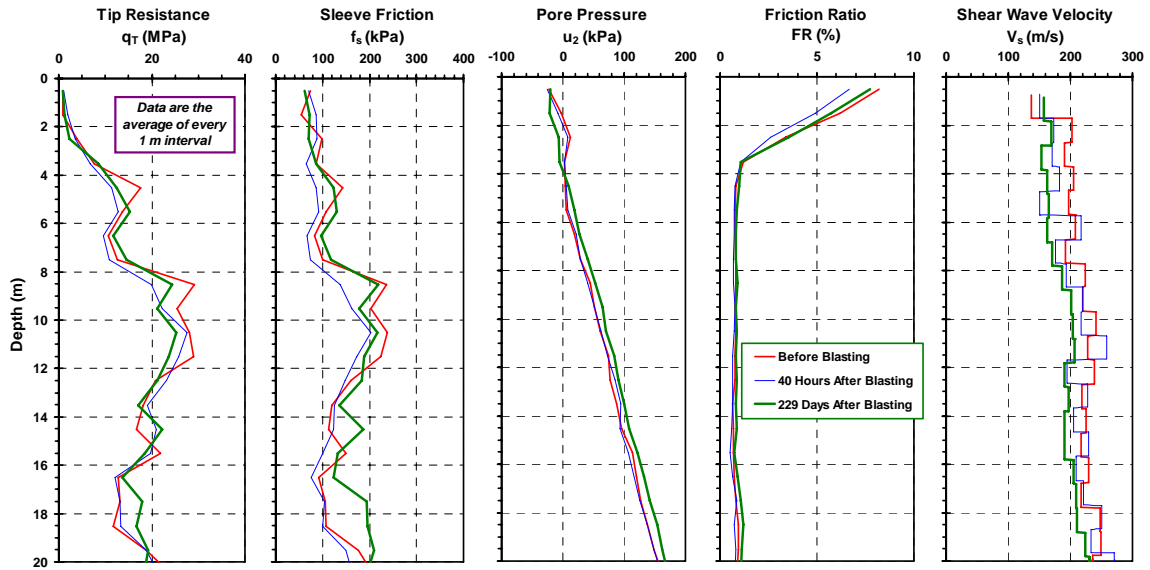
Figure 7.22 Average SCPTu data in every 1 meter interval (Data collected before and after ESEE Marked Tree, AR event)

As a more objective approach to evaluate how significantly the CPT data at this site are influenced by the blasting and aging effects, statistical analysis is applied to the sand layer within the depth range from 8m to 14m. Similar to the sand layer selected for statistical study at the Walker site, this sand layer is relatively uniform, and it is within approximately the same depth range and has the same thickness as the sand layer at the Walker site. Table 7.7 lists the average values of q_T and f_s for this sand layer in the soundings performed at the ESEE site in Marked Tree, and the ratios between these average values from different soundings are listed in Table 7.8. The q_T ratio $(q_T)_m/(q_T)_n$ is defined as the ratio of the average q_T measured at time m and that measured at time n.

The f_s ratio $(f_s)_m/(f_s)_n$ is defined similarly. The q_T and f_s ratios between the sounding performed 40 hours after the blasting and that before the blasting are 0.9 and 0.8 respectively. Both ratios are still in the range that can result from horizontal variability and equipment errors, because the q_T ratio at the Walker site is between 0.76 and 1.31, and the f_s ratio is between 0.67 and 1.49. However, they are at the lower end of the range. Considering that the soundings at this ESEE site are performed in a relatively smaller area than those at the Walker site, it is highly likely that the value of q_T and f_s dropped due to the simulated earthquake. The q_T and f_s ratios between the soundings performed 229 days after the blasting and that 40 hours are well within the ranges of the ratios observed at the Walker site. Therefore, the changes in q_T and f_s in sand due to aging effects are not significant compared with that caused by horizontal soil variability and equipment errors. The q_T and f_s ratios between the sounding performed 229 days after the blasting and that before the blasting are also well within the possible ranges, and thereby hard to tell if the q_T and f_s have recovered to the level before blasting after 229 days.

Table 7.7 Average CPT Measurements from 8m to 14m at ESEE Marked Tree, AR Site

Sounding	q_T (MPa)	f_s (kPa)
Before	25.12	196.54
40 Hours After	22.87	157.54
229 Days After	22.09	186.71

Table 7.8 The Ratio between the Average CPT Measurements from 8m to 14m at ESEE Marked Tree, AR Site

Ratio	$(q_T)_m/(q_T)_n$	$(f_s)_m/(f_s)_n$
40 Hours After/Before	0.91	0.80
229 Days After/Before	0.88	0.95
229 Days After/40 Hours After	0.97	1.19

7.5.3 Test Results from Tennessee ESEE Site

The ESEE Mooring site is located in Tiptonville, TN about 120km north of the Walker site. Figure 7.23 shows the SCPTu results collected at the Tiptonville site before blasting, as well as the interpreted soil profile. The soil profile consists of a sandy layer from ground surface to 4 m, and a clayey layer from 4 m to 9 m, underlain by a substantial sand layer from 9 m to 17 m. Figure 7.24 presents data at the Tiptonville site obtained approximately 2 hours after blasting, in comparison with data collected before blasting. Both the pre- and post-blasting data consist of some spikes in the upper and bottom sand layers, indicating the existence of some thin clayey lenses. In the depth range from 10 to 16m, the immediate post-blasting measurements of q_T, f_s, and V_s show significant decreases compared with their corresponding pre-blasting value. Such decrease is also observed in the depth range from 2 to 4 m in the silty sandy layer.

The seismic CPT measurements made at approximately 2 hours after, 20 hours after, and 64 hours after blasting are compared in Figure 7.25. In the depth range from 11 to 14 m, the q_T, f_s, and V_s measured 20 hours after blasting showed significant increase over those measured 2 hours after blasting. However, the value of q_T and f_s measured 64 hours after blasting decreased to the same level as those measured 2 hours after blasting. (Note: V_s is not measured 64 hours after blasting). It is therefore suspected that the differences of the measurements in this irregular zone are caused by lateral horizontal variability, instead of aging effects. The measurements taken 229 days after blasting are compared with those taken 2 hours after and 20 hours after blasting in Figure 7.26. The value of q_T and f_s measured 229 days after blasting showed increased in the depth range from 11 to 17 m,

but it is probably caused by lateral variability. There are both increase and decrease in the

value of V_s at different depth ranges (Figure 7.26).
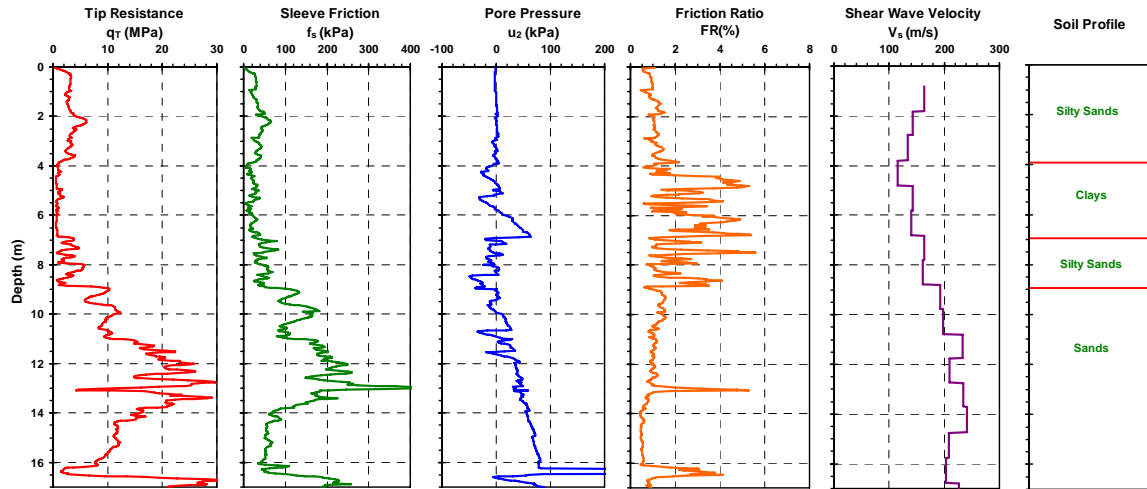
Figure 7.23 SCPTu data and interpreted soil profile prior to ESEE Tiptonville, TN event
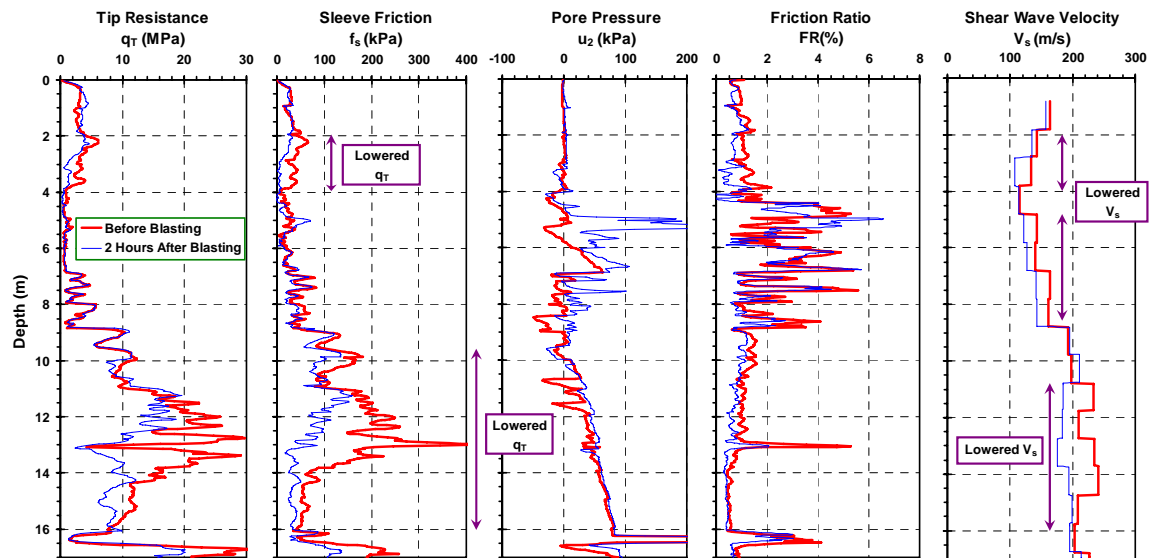
Figure 7.24 SCPTu data collected before and 2 hours after ESEE blasting event in Tiptonville, TN
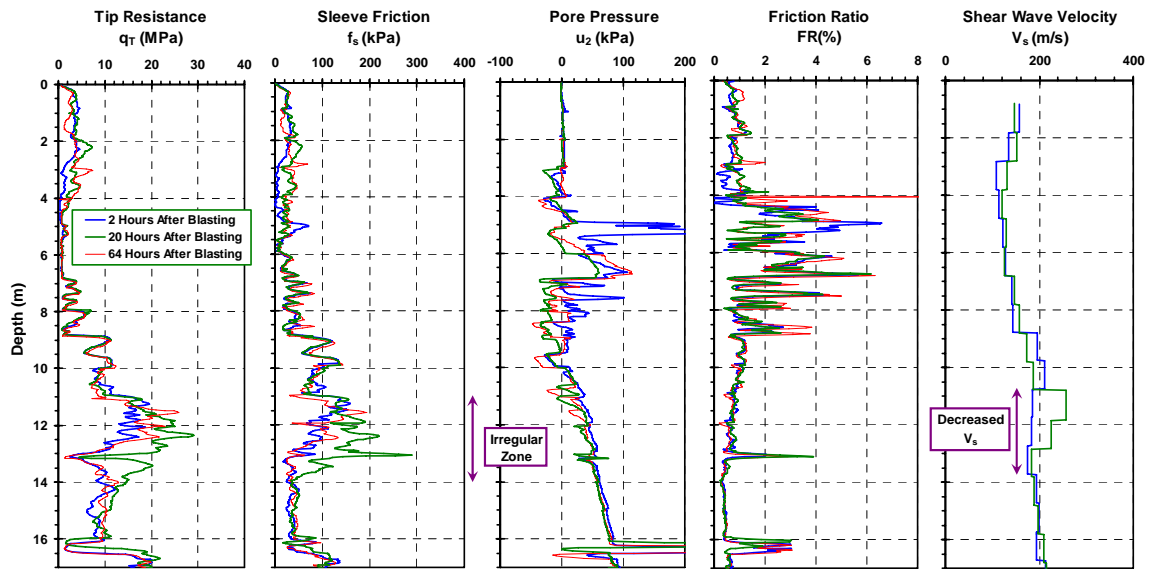
Figure 7.25 SCPTu data collected 2 hours, 20 hours, and 64 hours after ESEE blasting event in Tiptonville, TN
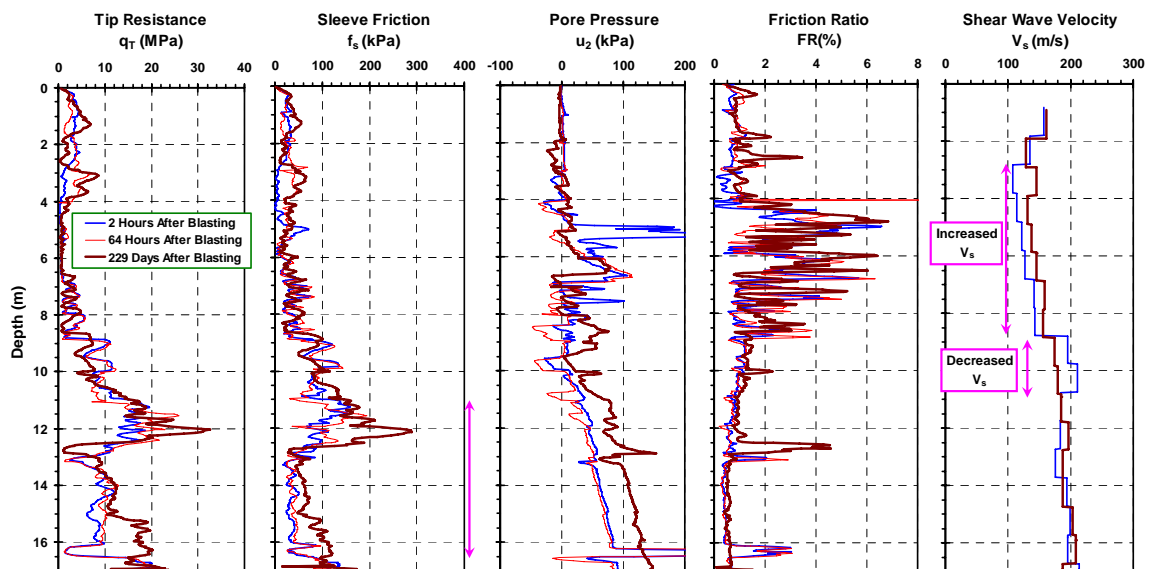
Figure 7.26 SCPTu data collected 2 hours, 20 hours, and 229 days after ESEE blasting event in Tiptonville, TN

The average values of q_T, f_s, u_2, FR, and V_s in a depth interval of every 1 m are calculated for the soundings performed after earthquakes, as shown in Figure 7.27. No evident nor consistent changes are observed between them, indicating that the aging effects on the CPT measurements are not particularly significant in these materials following the ESEE explosives-induced liquefaction.
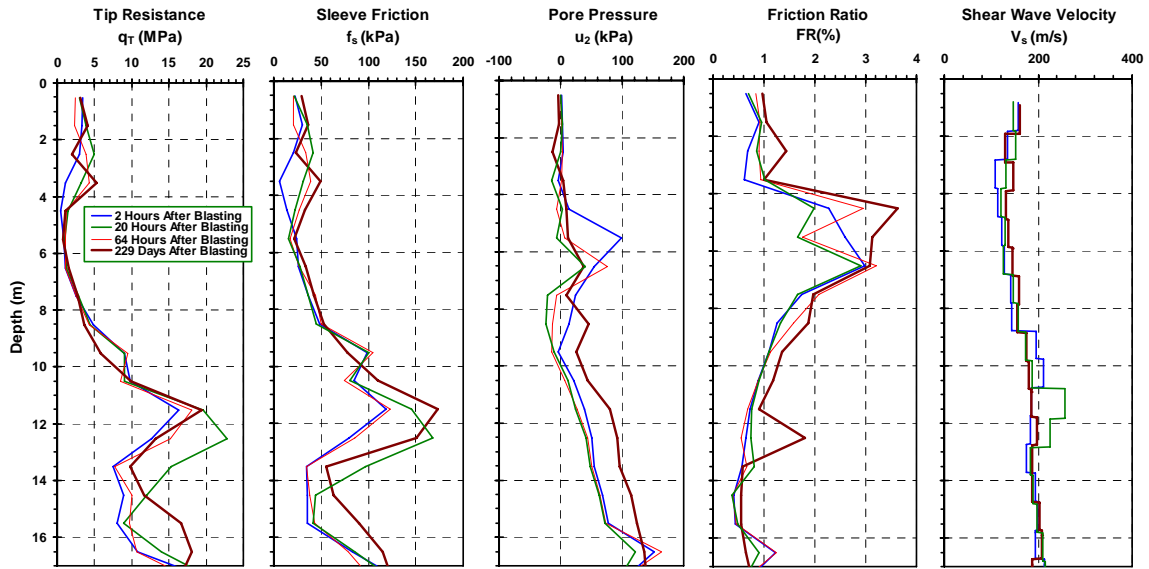
Figure 7.27 Average SCPTu data of every 1 meter interval (Data collected before and after ESEE Tiptonville, TN event)

7.6 Summary

Age of sand may affect its penetration resistance and shear wave velocity profile, thus influence its behavior during large seismic events. Aging effects in sands is a complicated problem, and is suspected to be related to many factors, such as pore fluid, sand type, grain shape, relative density, and effective confining stress. Only a few systematic lab experiments have been performed to investigate aging effects, because of the time-consuming nature of the experiments. Even among the few lab experiments, contradictory conclusions have been drawn by different researchers. For example, Joshi

272

et al. (1995) showed penetration resistance increased with time, whereas Baxtor & Mitchell (2004) did not. Although aging effects are observed in many field testing cases, the data are reported primarily from ground modification projects where the intention is to densify the soils. It appears that the influence of aging effects on soil strength and stiffness has to be site-specifically addressed. A hypothetical equation is proposed for estimating the behavior of cone tip resistance with time. Values of the parameters used in this equation are related to sand type, pore fluid, sand origin, and the method of destructuration.

The Embayment Seismic Excitation Experiments (ESEE) provided an opportunity to research on the aging effects in the NMSZ. During the ESEE experiments, it is observed that the SCPTu measurements, including q_T, f_s, and V_s, just after the blasting were lowered to some extent in the liquefied zones. This observation is consistent with what are reported by many other researchers, such as Mitchell and Solymar (1984) and Stokoe and Santamarina (2000). This phenomenon caused a destructuration of the sand into a normally-consolidated state. However, in contrast to the significant time-dependent gain of strength reported for some sand sites previously (e.g. Schmertmann, 1991; Mitchell and Solymar, 1984; Mesri et al.; 1990), the SCPTu soundings from the ESEE experiments do not show significant or appreciable aging effects. This may be due in part to the freshwater environment, rounded to subrounded particle size of the quartz sands, and fairly significant inplace relative density.

CHAPTER VIII

ESTIMATING SEISMIC PARAMETERS ASSOCIATED WITH PREVIOUS EARTHQUAKES BY SCPTU SOUNDINGS IN NMSZ

8.1 Synopsis

Upon liquefaction, saturated loose sands tend to flow upward and vent to the ground surface. Vented sand deposits that formed at the ground surface due to previous earthquakes in the NMSZ have been widely observed (e.g. Obermeier, 1998). Figure 8.1 illustrates the tremendous extent of liquefaction caused by the 1811-1812 earthquakes. However, measured strain rates, which indicate how fast the lithosphere is being deformed during plate tectonic movement, in the NMSZ are relatively low (Newman et al., 1998). As a result, the recurrence interval of large earthquakes in NMSZ is relatively long, and is suggested to be hundreds of years (Tuttle & Schweig, 1995). Since even the most recent large earthquakes occurred nearly two hundred years ago, their surface traces, such as sand boils, subsidence, and dikes, have been modified by erosion, farming, vegetation, and other manifestations, thus making them very difficult to identify. Therefore, paleoliquefaction features, which are formed during past earthquakes and kept within the soil stratigraphy, are often used to analyze the previous seismic activities.

The geological methodologies for paleoliquefaction studies include aerial photography, site reconnaissance, and site excavation. Sand blows appear as light colored patches in the field and have different impact on the plant growth from the surrounding soils, making them easy to be identified by aerial photos, despite the disturbance of topsoil by

agriculture practices (Tuttle & Barstow, 1996). It is usually assumed that sand blows of large size are located in the area where strong ground shaking occurs. However, liquefaction is triggered by the full or partial collapse of the sand-grain structure caused by the ground shaking during earthquakes. Then, the locally-liquefied material will cause stress redistribution in the surrounding soil mass, inducing larger scale liquefaction (Gu, et al., 1993). This process is not only related to the characteristics of earthquakes, but also the local site conditions, such as the layering and related soil properties. Evidence found from some recent earthquakes confirms that the distribution of liquefaction features can be irregular (Tuttle, 1999).

Through reconnaissance along cutbanks of rivers or ditches, some of the paleoliquefaction features buried below the ground surface, such as sand dikes and sills, may be discovered. Information derived through aerial photos and reconnaissance is limited, and not sufficient for fully understanding the soil behavior during liquefaction. In order to investigate the liquefaction features in detail, some important paleoliquefaction sites have been carefully excavated to expose the buried sand structure and features, thereby allowing the liquefaction events to be radiocarbon-dated and the liquefaction mechanism to be better investigated. Nonetheless, the cost of site excavation is very high, limiting its widespread scale and use. Recently, geophysical methods, such as ground penetrating radar (GPR) (Liu & Li, 2001) and resistivity surveys (Barnes, 2000), have been used to identify the liquefaction and deformation features in the NMSZ. In addition, several geotechnical methods have been used in paleoliquefaction studies to back-calculate the seismic parameters associated with previous earthquakes (e.g. Martin &

Clough, 1994; Pond, 1996). In this thesis, a new methodology for estimating these parameters has been proposed. It has been applied to the1989 Loma Prieta earthquake in California, as well as previous earthquakes that occurred in the NMSZ.
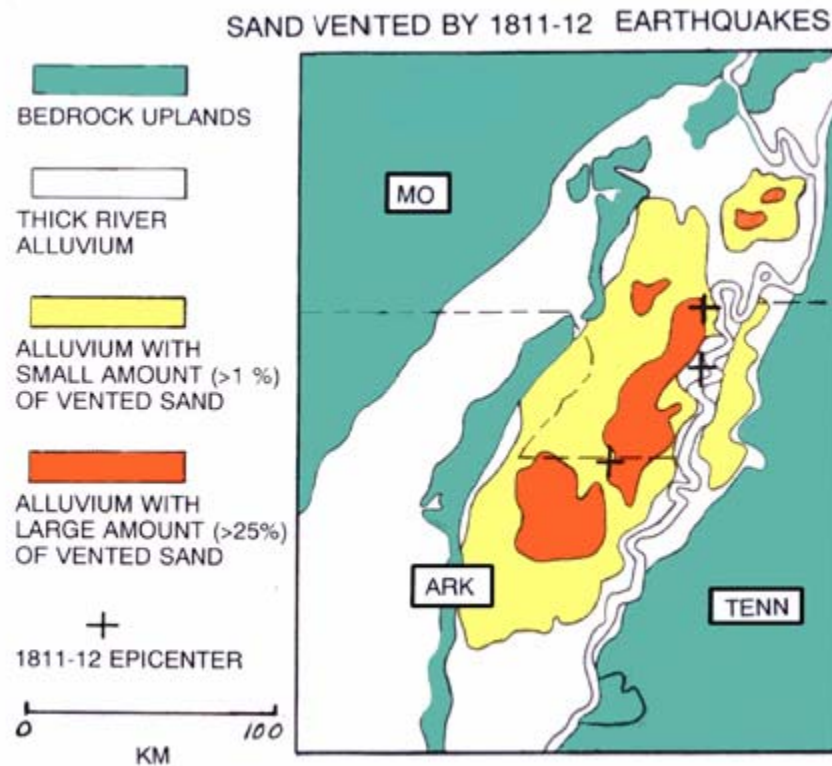
Figure 8.1 Tremendous extent of liquefaction caused by the 1811-1812 earthquakes in the New Madrid Seismic Zone (Obermeier, 1998)

8.2 Methods to Estimate Seismic Parameters

A very important task of the paleoliquefaction studies is the estimation of seismic parameters associated with previous earthquakes. Obermeier & Pond (1999) and Tuttle (2001) summarized a number of techniques which can be used for back-calculating the degree of shaking and magnitudes of earthquakes from paleoliquefaction features. They include: (1) the simplified procedure based on the relationship between the peak ground

acceleration (PGA) and the penetration resistance of soils, typically the blow counts of the standard penetration test (SPT) (Seed et al., 1983, 1984, 1985) (Figure 8.2); (2) the cap thickness method based on the relation between the thickness of liquefied layer and the overlying non-liquefied cap for certain PGA (Ishihara, 1985) (Figure 8.3); (3) the liquefaction severity index (LSI) method based on the relationship between the LSI and the epicentral distance (Youd & Perkins, 1987); (4) the magnitude-bound method based on the relationship between the magnitude and the maximum epicentral distance of surface evidence of liquefaction (Ambraseys, 1988); (5) the energy-stress method based on the relation between the seismic energy intensity and penetration resistance of soils (Pond, 1996); and (6) the comparison approach that reconstructs the paleoearthquake event by comparing the paleoliquefaction features with those resulting from other earthquakes in the same region (Tuttle, 2001).
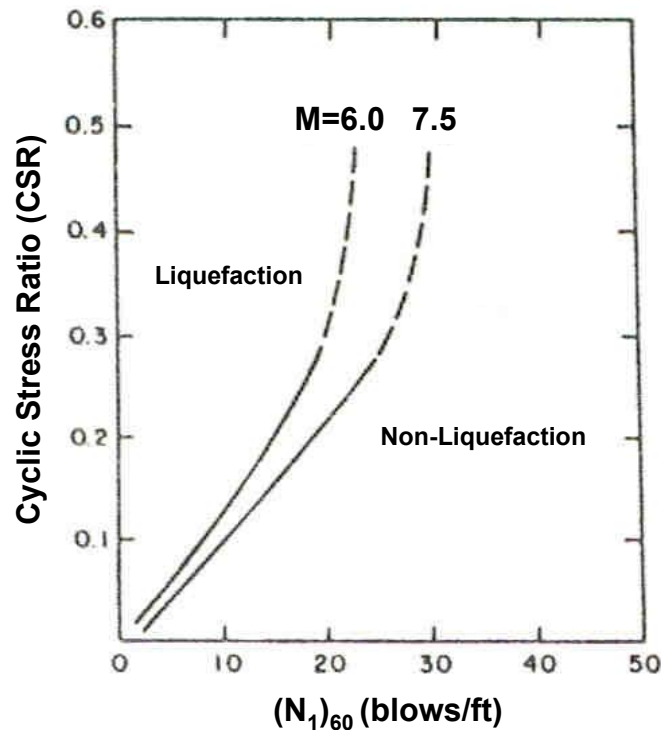
Figure 8.2 Boundary curve for discriminating occurrence and non-occurrence of liquefaction based on SPT blow counts (after Seed et al., 1984)
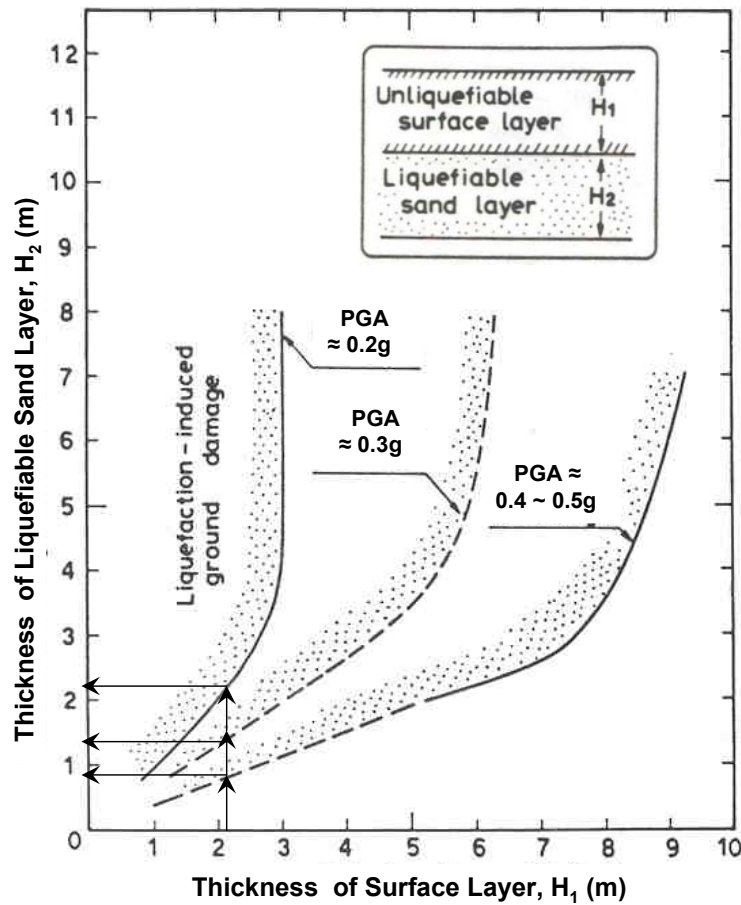
Figure 8.3 Boundary curves for site identification of surface effects of liquefaction (Ishihara, 1985)

Using both the simplified procedure and the cap thickness method, Martin & Clough (1994) conducted research to estimate the seismic parameters associated with the large historic earthquake that occurred near Charleston, South Carolina in 1886. Field testing by SPT and CPT was performed at sites that experienced different degrees of liquefaction at different distances to the epicenter of the earthquake. It was assumed that at sites where liquefaction evidence was nonexistent, the peak ground acceleration (PGA) during the 1886 earthquake did not exceed the threshold values, which could trigger liquefaction and thus formed the upper bound of the PGAs at these sites. At sites where liquefaction

evidence was marginal, the 1886 PGAs were taken approximately equal to the threshold values. Based on SPT data collected in the field, Martin and Clough (1994) used the simplified procedure to derive a relationship between the PGA and the percentage of the liquefiable layer that would be susceptible to liquefaction. This process is conceptually illustrated in Figure 8.4. Assuming a certain threshold peak ground acceleration (a_{max}), the critical $(N_1)_{60}$ value for liquefaction occurrence is back-calculated using the simplified procedure (Seed et al., 1971). It is then compared with the measured stress-normalized SPT blow counts $(N_1)_{60}$ to determine the thickness of the liquefied layer in case of the assumed a_{max} (Figure 8.4), thereby allowing the calculation of the percentage of layer liquefied. The thickness of the liquefied layer in the event of a certain a_{max} can also be derived from Figure 8.3. The thickness of liquefiable layer can be derived corresponding to the thickness of the unliquefiable surface layer and the assumed peak ground acceleration (PGA), as illustrated by the arrows in this figure.

As an example, Figure 8.5(a) shows the relationship between the PGA and percentage of layer liquefied for the Hollywood Site in Charleston, South Carolina, based on the criteria proposed by Seed et al. (1984) (Figure 8.2). The same relationship can be derived using the cap thickness method, as shown in Figure 8.5(b). The threshold acceleration that triggers liquefaction is the lowest value of PGA at which both methods agreed, and Figure 8.5(c) shows that the threshold acceleration for the Hollywood site is about 0.25g for an $M_w = 7.5$ earthquake.

The cap thickness method was developed from data collected from two major earthquakes in Japan and China (Ishihara, 1985). Thus, its validity for other earthquakes and other regions still needs to be justified. More recent analysis found the criteria are valid only for liquefaction sites that are not susceptible to ground oscillation or lateral spreading (Youd & Garris, 1995).
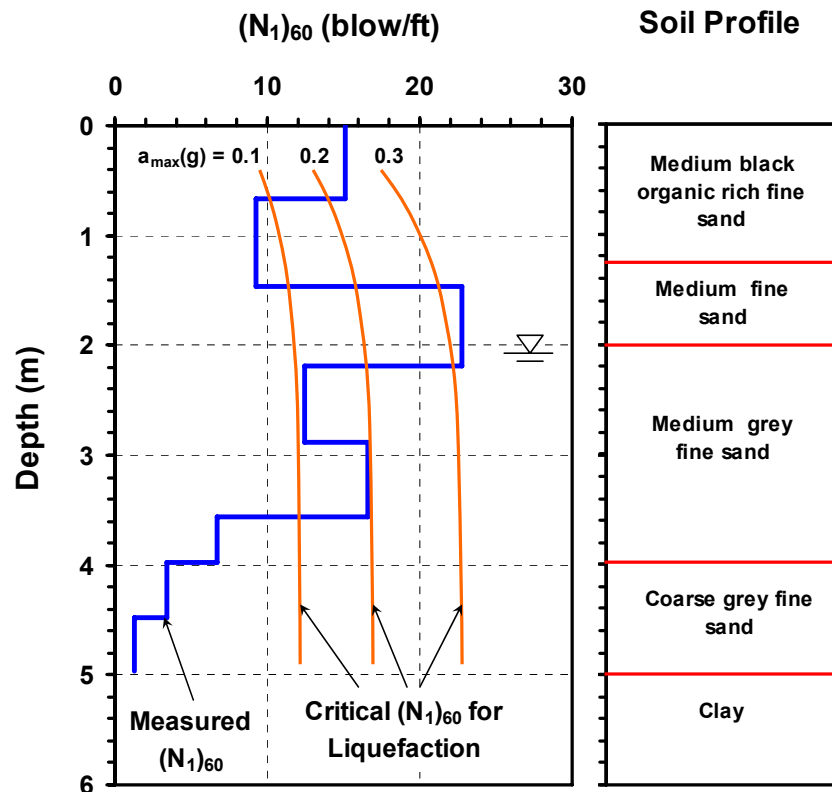
Figure 8.3 Conceptual illustration of the process in deriving the thickness of liquefiable layers in case of a certain peak ground acceleration (a_{max})

Note: SPT data and soil profile are from the Hollywood site in Charleston, South Carolina (Martin & Clough, 1990)
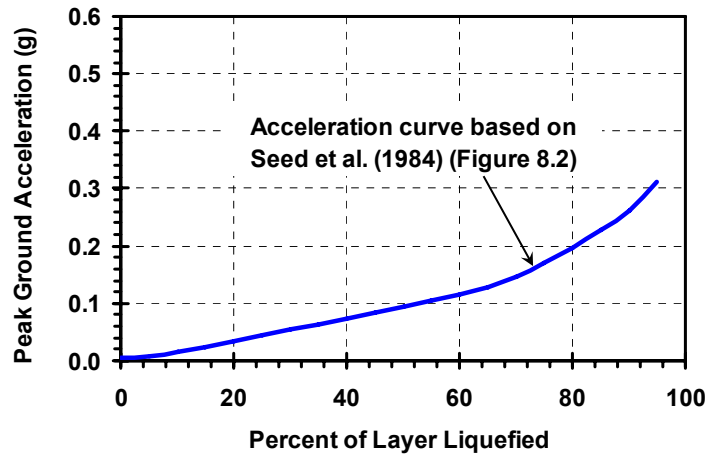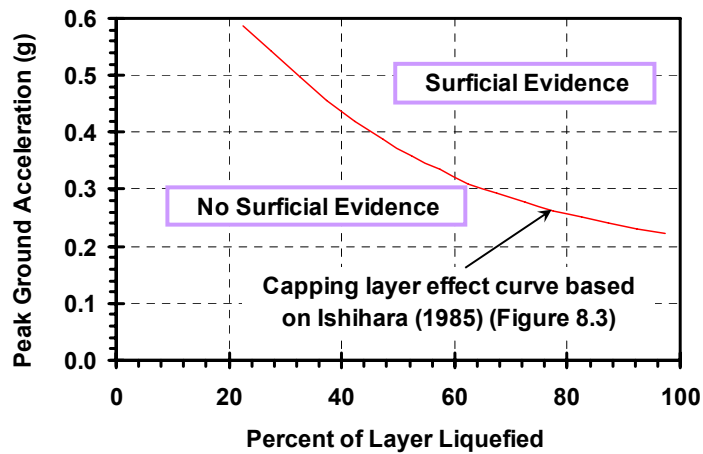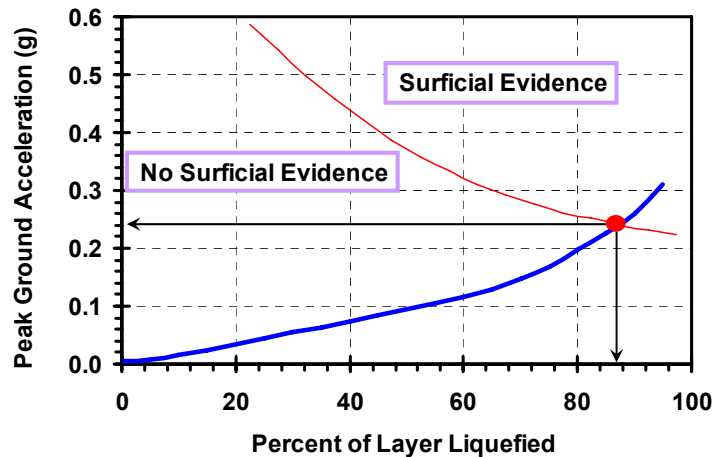
Figure 8.5 Liquefaction analysis for the Hollywood site in Charleston, SC with an earthquake of $M_w = 7.5$ (after Martin & Clough, 1994): (a) Acceleration curve based on Seed et al. (1984); (b) Capping layer effect curve based on Ishihara (1985); (c) Superimposed plot showing threshold acceleration (Crossover Point)

281

The liquefaction severity index (LSI) method and the magnitude-bound method correlate the earthquake magnitude with its damage effect at a certain distance. Since the soil properties of the investigated sites are not considered, errors in these methods are inherent. Soils of different properties might behave significantly differently when subjected to the same type of earthquake vibration. Furthermore, they are based empirically on the interplate earthquakes that have occurred in the western USA, Japan, and China, but the geology and the tectonic setting in the NMSZ are quite different with intraplate events. Earthquakes of the same magnitude would result in liquefaction and related ground displacement at greater distances in the eastern North America than in the western North America, because of the lower attenuation for seismic energy in eastern North America (Youd et al., 1989).

Although the magnitude-bound method has been calibrated for use in the central USA from paleoearthquakes in the Wabash Valley region of Indiana-Illinois (Obermeier et al., 1993; Pond, 1996), further case studies are needed in order to verify it. Based on the relation between energy dissipation and the porewater pressure development during undrained cyclic loading of saturated sands, the energy-stress method is very similar to the simplified procedure, except it uses seismic energy instead of the PGA to evaluate the site's susceptibility to liquefaction. Pond (1996) developed an energy model that estimates the seismic energy intensity at a site from the earthquake magnitude and hypocentral distance, but further verification is needed (Obermeier & Pond, 1999). Finally, the comparison approach is based on the geologic principle that the deposits and structures resulting from modern geologic processes are comparable to those from past

geologic events in the same region (Tuttle, 2001). Since the recurrence period of large earthquakes is long in the NMSZ, essentially no seismic events can be used as reference. Therefore, this method requires not only large amounts of work in finding and investigating the remnant liquefaction features, but also great expertise in analyzing and synthesizing the scantly available information to infer seismic parameters and data.

By judging if the soil at a given site has liquefied or not during earthquakes, the simplified procedure relates the peak ground acceleration (PGA) with the soil properties, which are represented by penetration resistance of the field tests. Although this relationship is also based upon case histories collected outside of eastern North America, it focuses on the mechanical properties of soils under ground shaking, and therefore will be less sensitive to geologic and tectonic setting of the investigated region. The widely-used SPT N-value has been used to provide an evaluation of the resistance of soils to liquefaction. However, the test is quite variable due to energy inefficiency amongst different drillers and equipment. As an alternative, the seismic cone penetration test (SCPTu) can provide better quality data. In addition, both normalized tip resistance (q_{T1}) and shear wave velocity (V_{s1}) are obtained from the same sounding, and therefore allow for the independent assessments on liquefaction potential. The SCPT is best qualified to fulfill the task of paleoliquefaction analysis as the V_s profile obtained is also needed for evaluating site-specific ground shaking (i.e., CSR or a_{max} = PGA) from amplification analysis. Hence, the SCPTu test is used herein to evaluate the seismic parameters associated with the previous earthquakes that occurred in NMSZ.

283

8.3 Methodology for Estimating Seismic Parameters by SCPTu Test

Existing correlations for evaluating liquefaction potential based on in-situ tests were developed almost exclusively from post-earthquake data (Chameau et al., 1991a; Olson et al., 2001). However, pre- and post-earthquake measurements can be significantly different, as discussed in Chapter 6. Since the existing liquefaction correlations are based on in-situ data measured after earthquakes, they are more appropriate for back-calculation of the seismic parameters associated with previous earthquakes.

The seismic loading is typically expressed in terms of cyclic stress ratio (CSR) that represents the normalization of cyclic shear stresses to effective overburden stress (Seed & Idriss, 1971):

$$CSR = \frac{\tau_{ave}}{\sigma'_{vo}} = 0.65 \left(\frac{a_{max}}{g} \right) \left(\frac{\sigma_{vo}}{\sigma'_{vo}} \right) r_d \qquad (8\text{-}1)$$

where a_{max} is the peak ground acceleration (PGA) generated by the earthquake of interest, g is the acceleration of gravity, σ_{vo} and σ'_{vo} are the total and effective vertical stresses respectively, and r_d is a stress reduction coefficient that accounts for the flexibility of the model soil column.

As mentioned in previous chapters, the cyclic resistance ratio (CRR) at the time when a previous earthquake occurred can be evaluated from either q_T or V_s data, using the criteria proposed by Robertson & Wride (1998) and Andrus & Stokoe (2000), respectively. During an earthquake of moment magnitude M_w, the CRR of the site can be derived from the following equation:

$$CRR = MSF*CRR_{7.5} \qquad\qquad (8\text{-}2)$$

where $CRR_{7.5}$ is the cyclic resistance ratio of soils in the event of an earthquake with M_w = 7.5, and the moment scaling factor (MSF) represents the effect of duration of ground shaking resulted from earthquakes. The value of MSF decreases with the increase of the magnitude, for the duration of ground shaking increases with the earthquake magnitude. The relation of MSF with earthquake moment magnitude suggested by Youd et al. (2001) is used herein.

During earthquake shaking of loose saturated sands, there is no likely liquefaction when CSR < CRR. Liquefaction occurs when CSR > CRR. Liquefaction is triggered and termed "marginal liquefaction", when CSR = CRR. By substituting both Equation (8-1) and (8-2) into CSR = CRR, the minimum peak ground acceleration (PGA) that triggers liquefaction can be derived from the following equation:

$$\left(\frac{a_{max}}{g}\right)_{min} = \frac{MSF \cdot CRR_{7.5}}{0.65 r_d}\left(\frac{\sigma'_{vo}}{\sigma_{vo}}\right) \qquad\qquad (8\text{-}3)$$

Since the MSF decreases with earthquake magnitude, it is expected that the critical PGA or a_{max} triggering liquefaction decreases with the increase of the earthquake magnitude.

The PGA can alternatively be estimated through empirical attenuation correlations of a_{max} with earthquake magnitude, distance from the seismic energy source, and local site conditions. By combining the peak acceleration attenuation relations for rocks motions with the amplification ratios at soft soil sites (i.e. the ratios of peak acceleration at a soft soil site divided by the corresponding peak accelerations at a nearby rock site), Idriss

(1991b) derived the following attenuation relations for estimating the peak acceleration at soft soil sites:

For $M_w \leq 6$

$$Ln(a_{max}) = e^{(1.673-0.137M_w)} - e^{(1.285-0.206M_w)}Ln(R+20) \qquad \text{(8-4 a)}$$

and, for $M_w > 6$

$$Ln(a_{max}) = e^{(2.952-0.350M_w)} - e^{(2.015-0.328M_w)}Ln(R+20) \qquad \text{(8-4 b)}$$

where a_{max} is in g's, Ln is the natural logarithm, M_w is the moment magnitude of the earthquake, and R is the hypocentral distance to the source in km. Idriss (1991b) suggested that the standard error associated with above equations is magnitude-dependent and can be estimated using the following equations:

$$\varepsilon = 1.39 - 0.14M_w \quad \text{for } M_w < 7.25 \qquad \text{(8-5 a)}$$

$$\varepsilon = 0.38 \qquad \qquad \text{for } M_w \geq 7.25 \qquad \text{(8-5 b)}$$

Based on the estimated shear strength of soft soils under dynamic conditions, Idriss (1991b) also suggested that a maximum limiting value of 0.6 g can be applied to the PGA derived from the empirical correlations. Figure 8.6 shows the mean PGA and the mean ± one standard deviation of PGA versus the closest distance to the source in the event of an earthquake of moment magnitude 7.0. The PGA recorded at soft soil sites during the 1989 Loma Prieta earthquake is also plotted in the figure, and it can be seen that equations suggested by Idriss (1991b) for calculating the mean PGA at soft soil sites provide a reasonable estimate of the recorded values during the 1989 Loma Prieta earthquake.
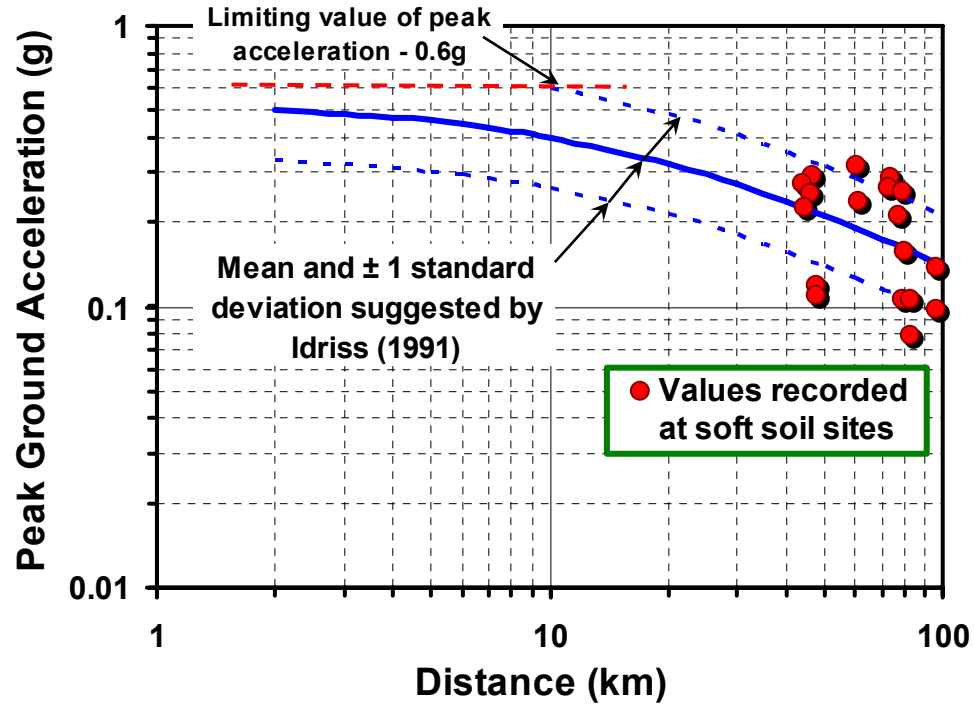
Figure 8.6 Comparison of peak ground acceleration of motions recorded during the 1989 Loma Prieta earthquake at soft soil sites and those derived from the attenuation relations suggested by Idriss (1991b)

For eastern North America, Boore & Joyner (1991) proposed the following equation to estimate the PGA, as discussed in Chapter 6:

$$\log(a_{max}) = 0.672 + 0.448(M - 6) - 0.037(M - 6)^2 - 0.016(M - 6)^3 - \log R - 0.0022R \quad \text{(8-6)}$$

where a_{max} is in g's. This relationship can represent the average soil conditions in the Mississippi Embayment for moment magnitude ranging from 5 to 8.5 and hypocentral distances from 10 to 400 km (Boore & Joyner, 1991). The use of equation (8-6) for estimating PGA for different moment magnitudes is illustrated in Figure 8.7. The estimated PGA increases with the earthquake magnitude, and decreases with the hypocentral distance.
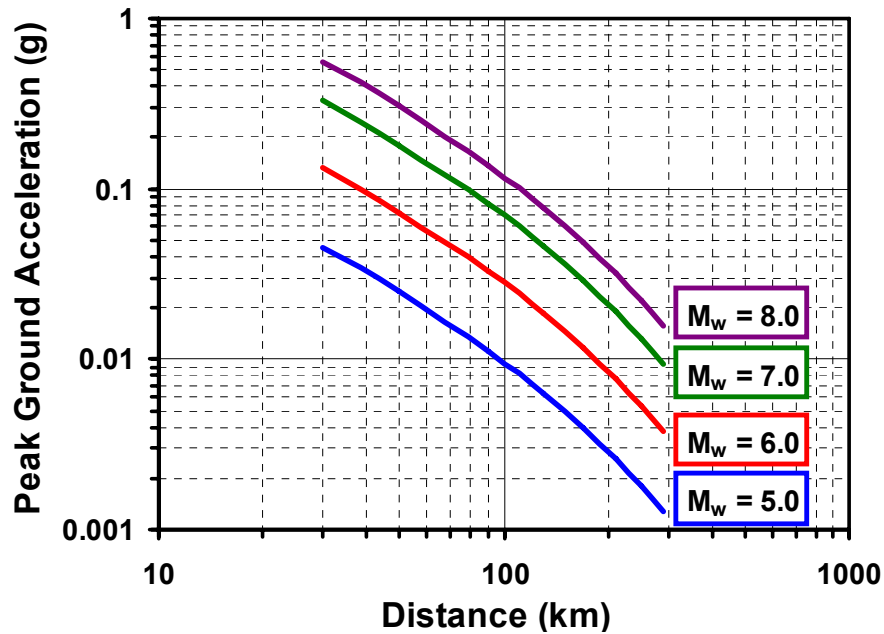
Figure 8.7 Estimated peak ground acceleration at ground surface of deep-soil sites in eastern north America (after Boore & Joyner, 1991)

The critical PGA triggering liquefaction, which is derived through liquefaction evaluation, monotonically decreases with the magnitude, while the PGA calculated using the attenuation relations monotonically increases with the magnitude. The magnitude of an earthquake event and the threshold acceleration that triggers marginal liquefaction are the value of M_w and PGA at which both relations agree. Therefore, sites of marginal liquefaction have great significance to the paleoliquefaction studies, since marginal liquefaction indicates that the driving forces caused by earthquake are equal to the resisting strength of the soil (Stark, 2001). Because CRR can be derived from both q_T and V_s, CSR and the PGA the sites have experienced can thus be back-calculated. During an earthquake event, the liquefied sites that have the greatest distance to the epicenter are also significant for estimating the seismic parameters. Generally, with the increase of distance to the epicenter, the driving force of the earthquake attenuates, and the extent of

the liquefied features decreases. When the distance exceeds the limit of the liquefaction field, no liquefied sites can be found. The liquefied sites that have the greatest distance to the epicenter are located close to the boundary of the liquefaction field. Therefore, it is reasonable to believe that the M_w and PGA that triggered liquefaction at these liquefied sites were not significantly higher than, if they were not close to, the M_w and critical PGA for this site to liquefy.

8.4 Validation of the Methodology through 1989 Loma Prieta Earthquake

In order to validate the methodology proposed above, the procedure is applied to back-calculate the seismic parameters associated with the Loma Prieta earthquake that occurred on October 17, 1989. This earthquake resulted from a slip along a 45-kilometer segment of the San Andreas fault where it traverses the Santa Cruz Mountains. This earthquake is a moderate event with a moment magnitude M_w = 6.9 to 7.0, and its epicenter is located in the Santa Cruz Mountains, approximately 18 km from Santa Cruz and 96km south of San Francisco (Figure 8.8). Also shown in Figure 8.8 are the sites where liquefaction-induced damage occurred due to the 1989 Loma Prieta earthquake.

8.4.1 Moss Landing Site

During the 1989 Loma Prieta earthquake, extensive liquefaction occurred at several locations within the area of Moss Landing located on Monterey Bay in California. This area is underlain by Holocene alluvium with thickness up to 60 m, and the deposit is generally soft near the surface. Boulanger et al. (1997) suggested this area to be a soft soil

site. The numerical simulations performed by Woodward-Clyde (1990) and Mejia et al. (1992) suggest that the peak horizontal acceleration on a hypothetical rock outcrop at Moss Landing should be about 0.15g. Using the relationship proposed by Idriss (1991a) for amplification of peak horizontal accelerations on soft soils relative to rock, the peak horizontal acceleration at the Moss Landing area should be about 0.2 to 0.3 g, which is consistent with the level of damage to contents of buildings and with intensity of ground motions felt by people in the area (Boulanger et al., 1997).

Slope inclinometers were installed along the shoreline edge of Moss Landing area prior to the Loma Prieta earthquake, and readings were made before the earthquake in April and June 1989, as well as after the earthquake on November 30, 1989 (Harding, 1988). Lateral displacements were noticed during this time period, and they were attributed to the earthquake effects, since prior measurements and observation showed the shoreline slope was not deforming measurably. The deflection measured by one of the inclinometers is shown in Figure 8.9, along with data from a CPTu sounding performed 1.5 m away from the inclinometer. The soil profile in this figure is interpreted by Boulanger et al. (1997) based on the CPTu signature and soil samples from an adjacent SPT boring performed 3.0 m away from the inclinometer. The primary deformation occurred between depths of about 2.0 and 4.5m, and the ground surface moved about 28 cm to the east and 10 cm to the north. After analyzing the CPTu results and the index data of the soil samples, Boulanger et al. (1997) concluded that the deformations resulted from liquefaction in two sand layers which are located between the depths of 2.1 m to 3.6 m and 4.2 m to 4.6 m, respectively.
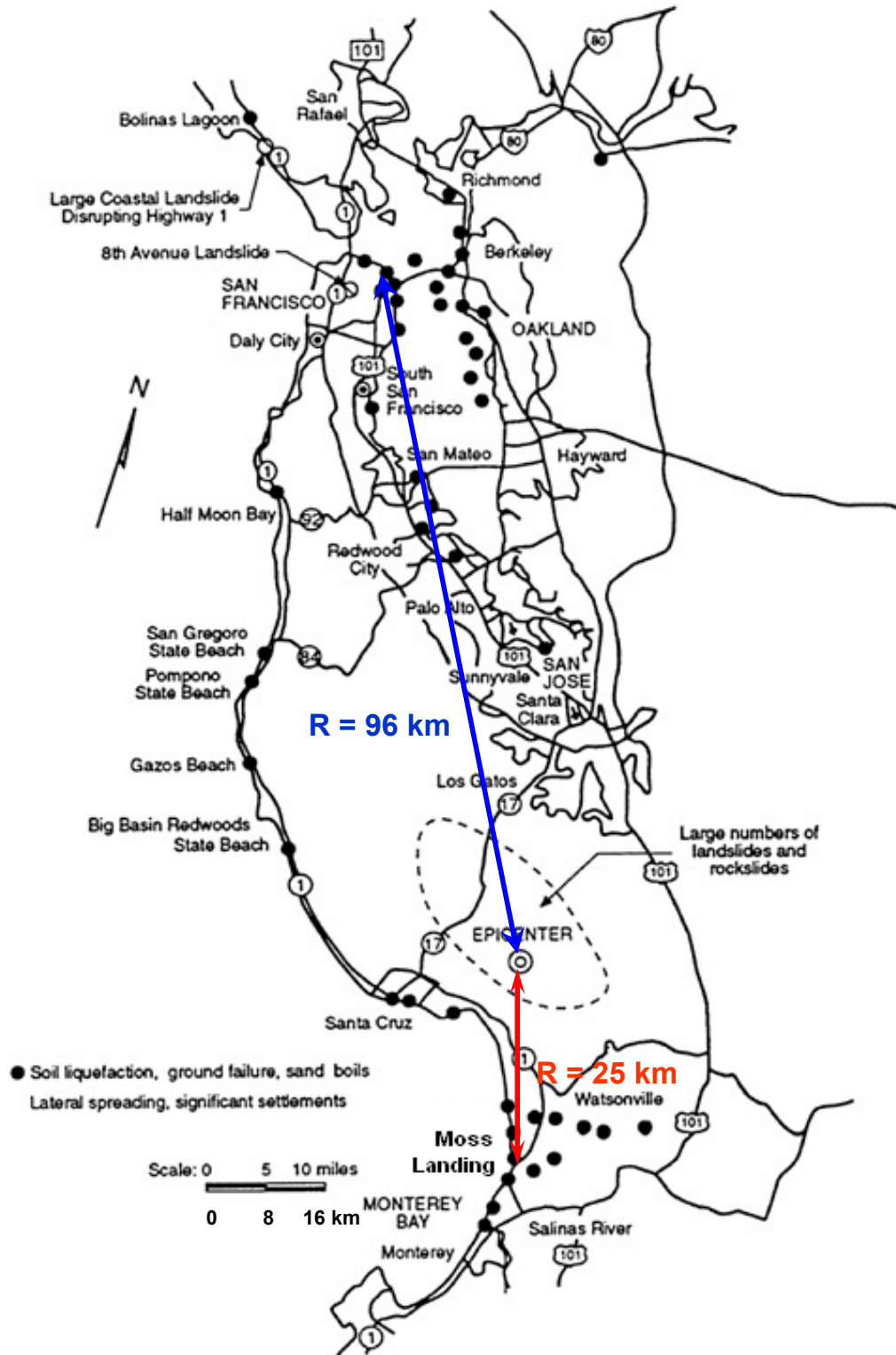
Figure 8.8 Regional map of liquefaction-induced damage due to the 1989 Loma Prieta earthquake (after Seed et al., 1991)
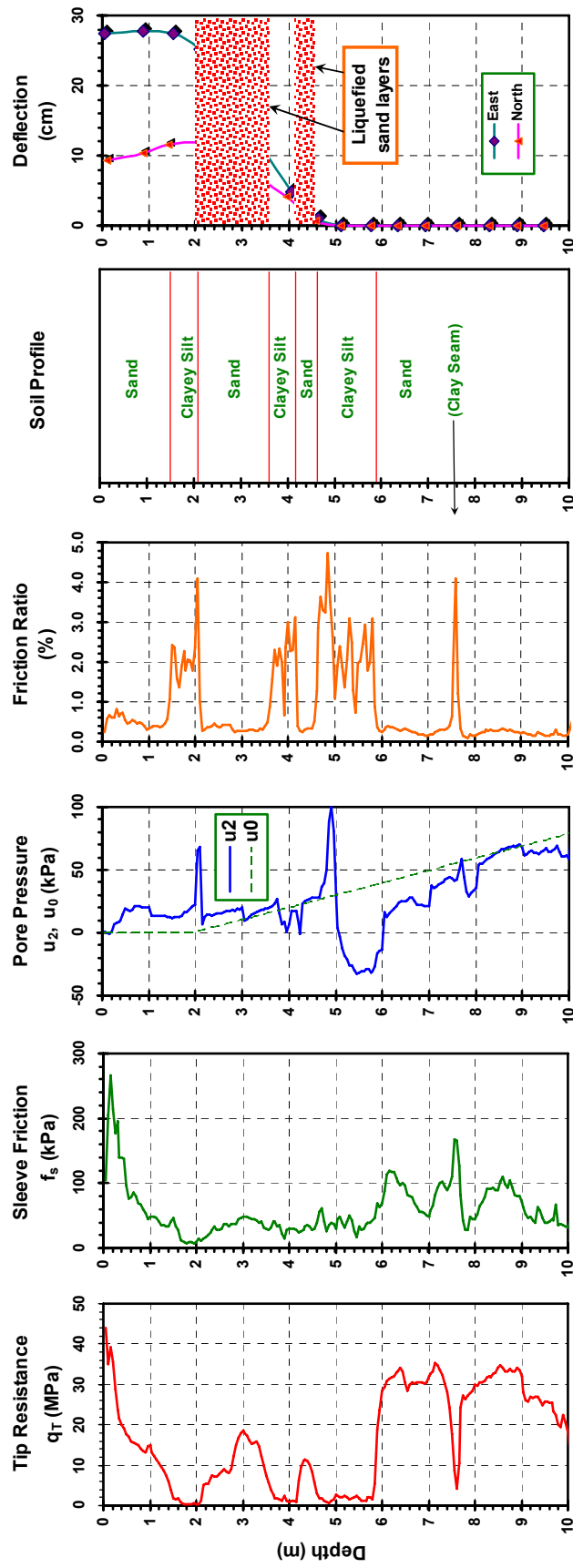
Figure 8.9 Representative CPT sounding performed at Moss Landing, CA, and deflection measured by a nearby inclinometer due to the 1989 Loma Prieta earthquake (after Boulanger et al., 1997)

292

Figure 8.10 shows the parameters derived from this CPTu sounding, which include the normalized tip resistance Q, the normalized friction ratio F, the normalized porewater pressure B, tip resistance corrected for overburden stress q_{c1N}, soil behavior type index I_c, apparent fines content FC, correction factor for tip resistance K_c, equivalent clean sand normalized penetration resistance $(q_{c1N})_{cs}$, and cyclic resistance ratio for $M_w = 7.5$ $CRR_{7.5}$. Assuming a certain magnitude, the critical PGA that can cause marginal liquefaction can be calculated using equation (8-3), and those based on q_T of the sounding performed at Moss Landing are shown in Figure 8.11. The assumed magnitudes are from $M_w = 5.5$ to 8.0 taken in 0.5 steps, and for each assumed magnitude, the minimum critical PGAs are at the depth of 3.5m, 4.2m, and 4.5m, all of which are within the two sand layers that have been identified as having liquefied by Boulanger et al. (1997). The minimum critical PGAs are plotted versus the magnitude in Figure 8.12. These decrease with the increase of the magnitude, since the duration of ground shaking is usually longer for larger earthquakes, which requires a lower PGA to trigger liquefaction. Also plotted in Figure 8.12 is the attenuation relationship of the mean PGA and the mean PGA ± 1 standard deviation versus the magnitude based on equation (8-4) and (8-5), with the knowledge that Moss Landing is about 25 km away from the epicenter of the earthquake (Figure 8.8). The minimum critical PGA curve meets the curve for mean PGA - standard deviation at the point of $M_w = 6.95$ and PGA = 0.19 g, while it meets the mean PGA + standard deviation at the point of $M_w = 5.75$ and PGA = 0.3 g. They indicate that in the event of marginal liquefaction at this site, the earthquake is likely of magnitude in the range from 5.75 to 6.95, and the PGA at this site is likely to be in the range from 0.19 g to 0.3 g. The data point corresponding to the mean values of these ranges is close to

293

crossover point of the minimum critical PGA curve and the attenuation relation curve for
the mean PGA, which corresponds to $M_w = 6.4$ and PGA = 0.24 g.
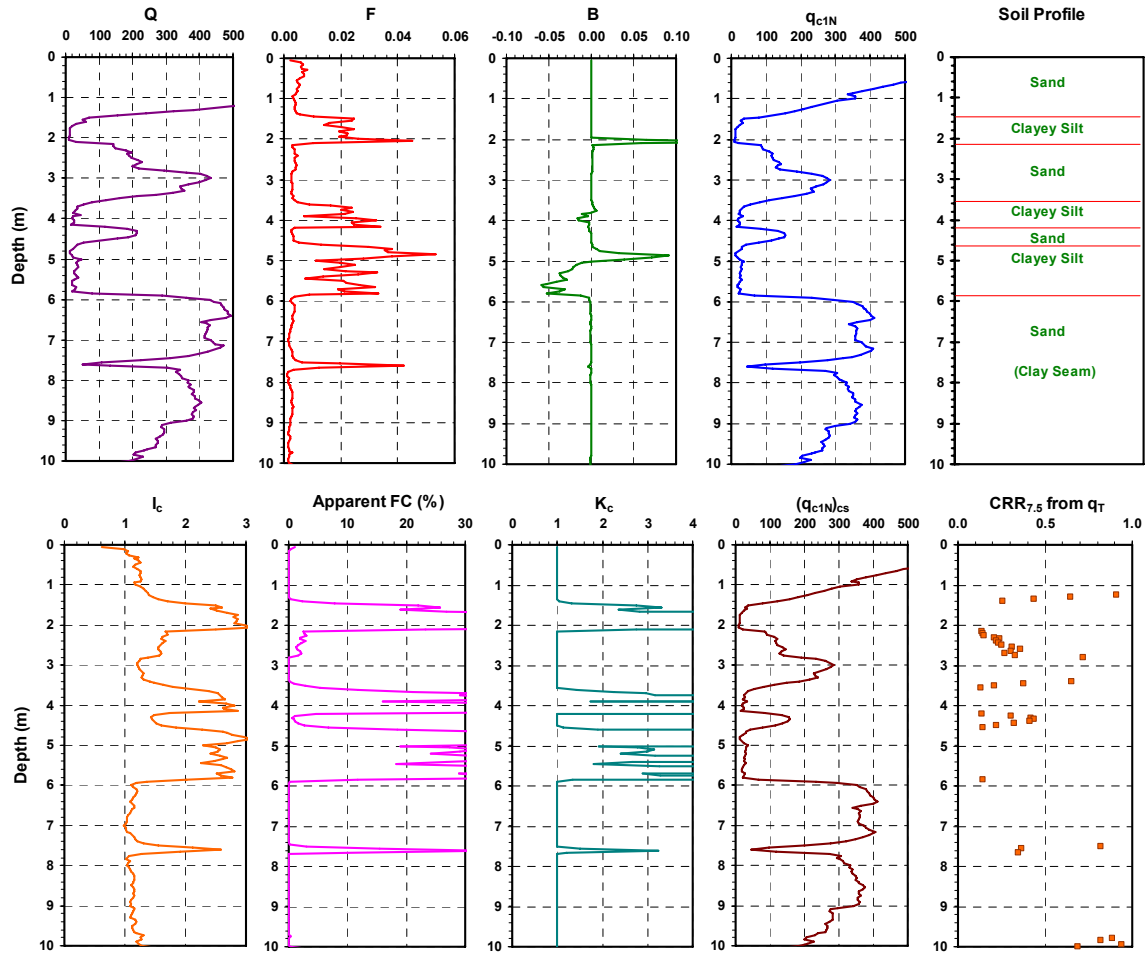
Figure 8.10 Parameters and soil profile derived from the representative CPT sounding
performed at Moss Landing, CA after the 1989 Loma Prieta earthquake

Figure 8.11 Critical peak ground acceleration corresponding to earthquakes of different magnitude, based on tip resistance of the representative CPT sounding performed at Moss Landing, CA after the 1989 Loma Prieta earthquake

Figure 8.12 Relations between moment magnitude and critical peak ground acceleration triggering marginal liquefaction at the Moss Landing Site, superimposed with the attenuation relation

Evidence has confirmed that the Moss Landing site is a liquefied site. It is of moderate distance to the epicenter among the liquefied sites as shown in the regional map of liquefaction-induced damage in Figure 8.8. Therefore, the Moss Landing site should have experienced CSR greater than CRR of the local soils, hence, greater PGA than the critical PGA that triggers marginal liquefaction. The M_w and PGA corresponding to the crossover point of the minimum critical PGA curve and the attenuation relation curve for the mean PGA (Figure 8.12) can serve as the mean of lower boundaries of the magnitude of the 1989 Loma Prieta earthquake and the PGA at this site has experienced during this event. Thus using the proposed methodology, the 1989 Loma Prieta earthquake is very likely to have a magnitude greater than 6.4, and the PGA at this site is very likely to be over 0.24 g. These estimations are consistent with the real magnitude (M_w = 6.9 to 7.0) of

the 1989 Loma Prieta earthquake and the PGA of 0.2 to 0.3 g at Moss Landing estimated by Boulanger et al. (1997).

8.4.2 Yerba Buena Cove Site

The Yerba Buena Cove (YBC) site is the primary work site during the study of liquefaction response of the fill soils along the waterfront area of San Francisco, CA after the 1989 Loma Prieta earthquake (Chameau et al., 1991a). Since the YBC site is one of the few liquefied sites that have the greatest distance to the epicenter (Figure 8.8), the PGA this site experienced during the earthquake should be close to the critical PGA that can trigger marginal liquefaction. Figure 8.13 presents the results of the CPTu sounding performed at the YBC site after the earthquake in March of 1990, as well as the soil profile interpreted by Chameau et al. (1991a). The YBC site consists of approximately 3 m of gravel fill overlying a dune sand deposit of 5 m in thickness. The dune sand is underlain by a thick Bay mud layer, 18 to 21 m thick, which rests above the bedrock.

Figure 8.14 presents the parameters that are derived from this CPTu sounding, and it can be seen that the dune sand layer has relatively low $CRR_{7.5}$. The back-calculated critical PGA corresponding to earthquakes of assumed magnitudes ranging from 6.0 to 8.0 is presented in Figure 8.15, and the minimum critical PGA appears to be situated at about the depth of 6.6 m. Similar to the Moss Landing site, the minimum critical PGA is plotted against M_w in Figure 8.16, superimposed with the attenuation relations suggested by Idriss (1991b). The crossover points between the minimum critical PGA and the mean

PGA ± 1 standard deviation curves suggest that the M_w of the causative earthquake is likely to be in the range from 6.5 to 7.35, and the PGA the YBC experienced during the earthquake is in the range from 0.11 to 0.17 g. The M_w and PGA corresponding to the crossover point of the minimum critical PGA curve and the attenuation relationship for the mean PGA (Figure 8.16) can serve as the mean of the estimated M_w and PGA. Thus, using the proposed methodology, the 1989 Loma Prieta earthquake is very likely to have a magnitude around 6.95, and the PGA at this site is very likely to be 0.13 g. The estimated M_w is consistent with the real magnitude (M_w = 6.9 to 7.0) of the 1989 Loma Prieta earthquake. The estimated PGA is also close to the computed PGA, which is about 0.17 g, based on numerical simulation carried out by Chameau et al. (1991b).
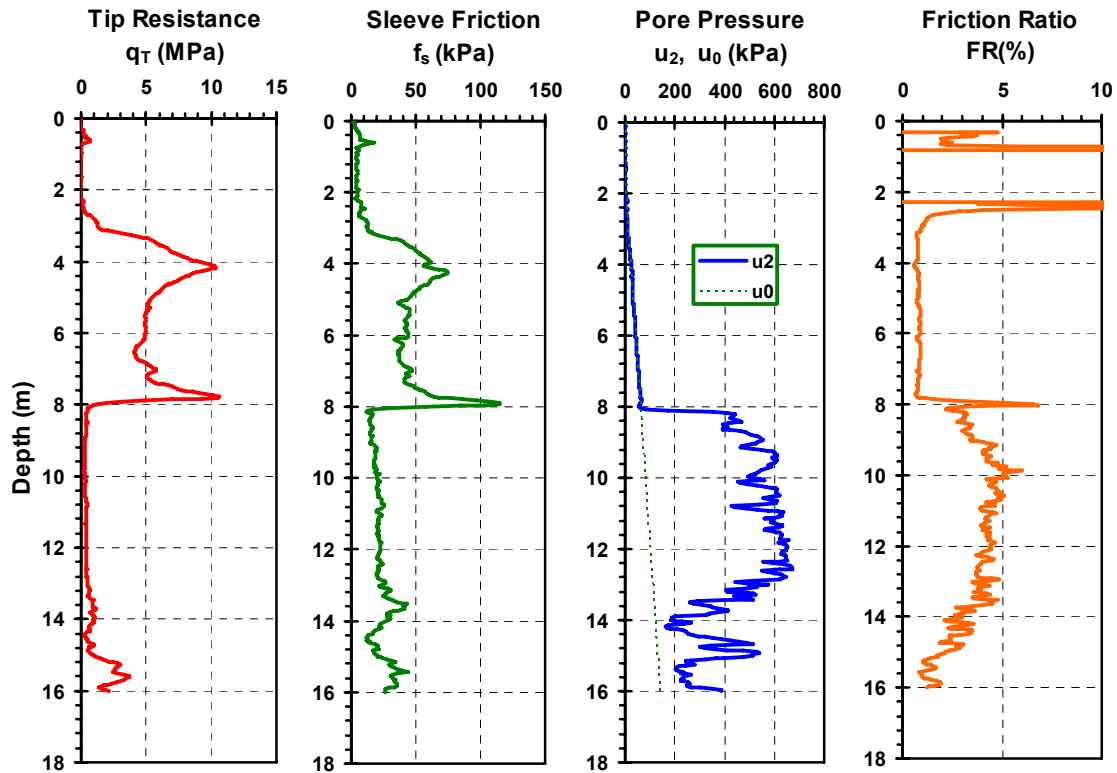
Figure 8.13 Representative CPT sounding performed at Yerba Buena Cove site located in San Francisco, CA after the 1989 Loma Prieta earthquake (data from Chameau et al., 1991b)
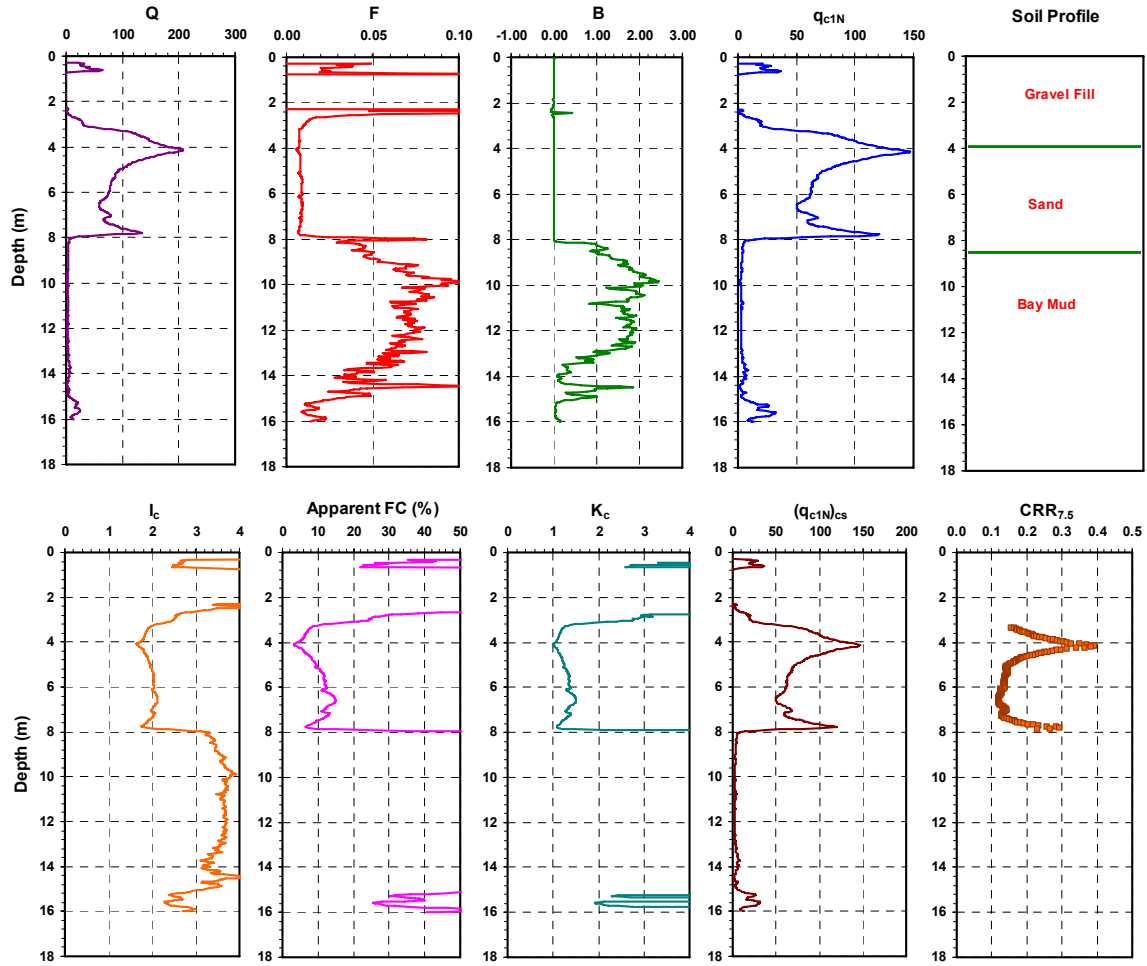
Figure 8.14 Parameters the soil profile derived from the representative CPT sounding performed at Yerba Buena Cove site located in San Francisco, CA after the 1989 Loma Prieta earthquake

The proposed methodology has been successfully applied to the Moss Landing site and the YBC site, both of which are the major sites where researchers investigated the liquefaction response of soils using CPTu tests, following the 1989 Loma Prieta earthquake. Based on the post-earthquake CPTu data from the Moss Landing site, the proposed methodology gives reasonable lower boundaries for the M_w of the earthquake and the PGA this site experienced during the earthquake. Using the CPT sounding performed at the YBC site after the earthquake, the M_w and the PGA derived from the

proposed methodology are close to the real values. Although Idriss (1991b) suggested significant standard deviation in the attenuation relations for soft soil sites, the use of the mean PGA in attenuation relations was successful in matching the estimated M_w with the real M_w of the earthquake.

Figure 8.15 Critical peak ground acceleration corresponding to earthquakes of different magnitude, based on tip resistance of the representative CPT sounding performed at Yerba Buena Cove site located in San Francisco, CA after the 1989 Loma Prieta earthquake
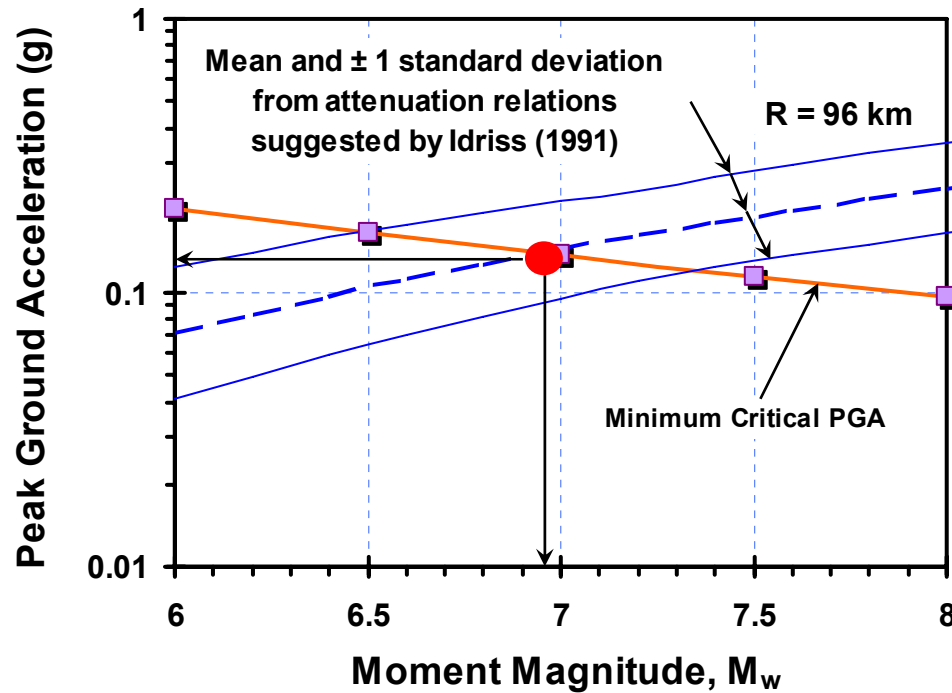
Figure 8.16 Relationship between moment magnitude and critical peak ground
acceleration triggering marginal liquefaction at the Yerba Buena Cove site, superimposed
with the attenuation relation

8.5 Validation and Application of the Methodology in the NMSZ

By observing the sedimentary characteristics of sand blows and large dikes in the NMSZ,

Tuttle (1999) concluded that the liquefaction features found in the region resulted from a

few very large earthquake events, instead of many smaller events. The large earthquakes

of similar magnitude as those in 1811-1812 also occurred around 1450 AD, 900 AD, and

490 AD (Tuttle, 1999). These earthquakes consisting of multiple individual earthquake

events occurred a long time ago, when no seismograph records were yet available, thus

making paleoliquefaction analysis more complicated in the NMSZ.

8.5.1 *Wolf River Site*

The Wolf River site is a paleoliquefaction site (Broughton et al., 2001) located east of Memphis, TN, and north of Colliersville, TN, and situated on the north bank of the Wolf River. As shown in Figure 8.17, the distance between the Wolf River site and the epicenters associated with the three big earthquakes in 1811-1812 are R = 100 km, R = 135 km, and R = 155 km, respectively. Figure 8.18 presents a more detailed map showing the location of the Wolf River site.

At this location, CPT soundings were performed in areas having evidence of marginal liquefaction, as well as in non-liquefied areas (Obermeier, 2002). As shown in Figure 8.19, seven soundings were performed at the Wolf River site. Soundings WOLF1 to WOLF4 were performed at sites where no liquefaction was observed, while WOLF5 to WOLF7 were at sites with only very small dikes extending upward into the overlying layers, which are the evidence of marginal liquefaction caused by the great New Madrid earthquakes of 1811-1812 (Van Arsdale, 1998). The soundings performed at sites of marginal liquefaction can be used to estimate the M_w of the earthquake and the PGA this site experienced. In addition, those CPTs that were performed at sites where there was no apparent liquefaction evidence provide a basis to estimate the upper boundaries of the M_w and PGA.

Figure 8.17 Map showing the epicenters of the 1811 -1812 earthquake events and their distance to the Wolf River site near Memphis, TN
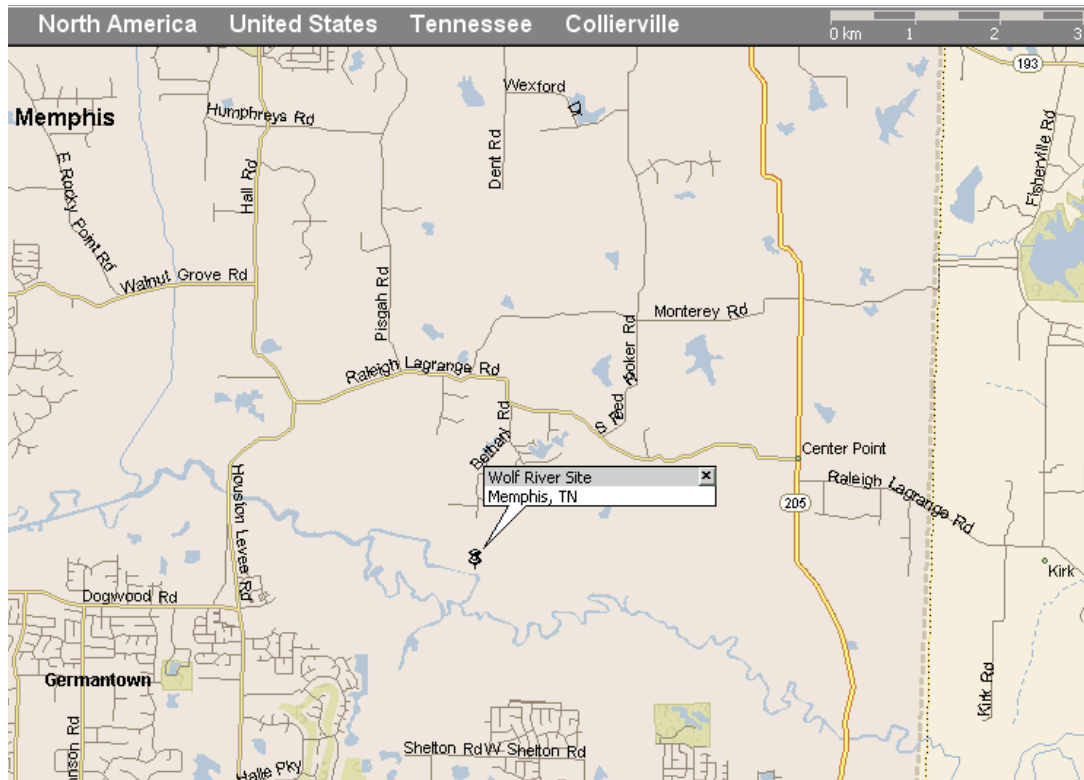
Figure 8.18 Map showing the location of the Wolf River site in Memphis, Tennessee
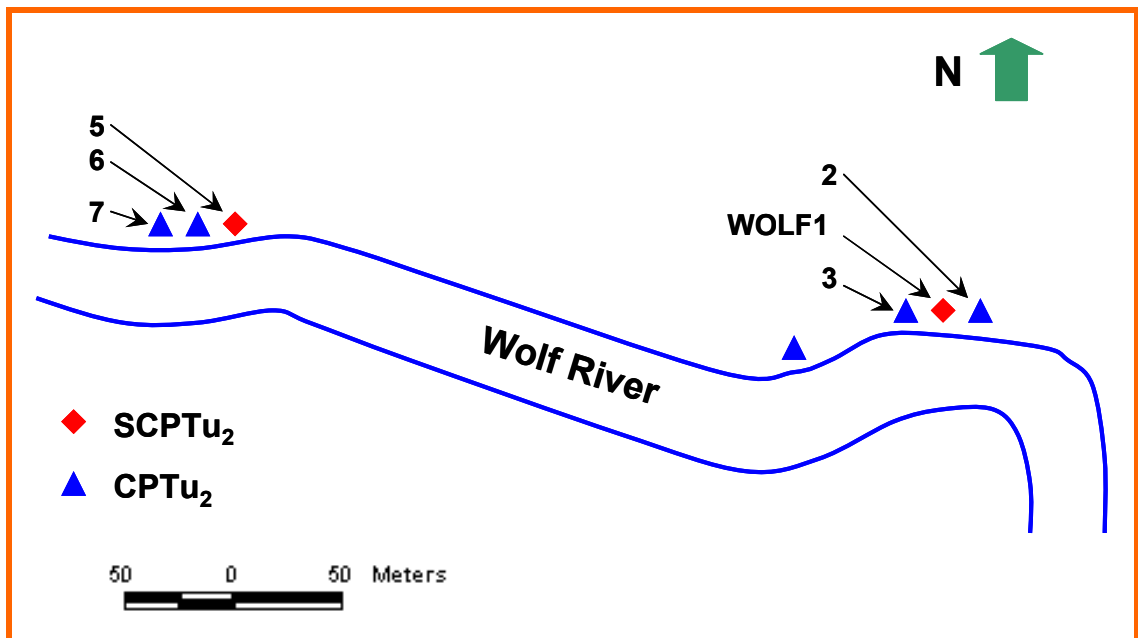
Figure 8.19 Overview of the CPT Locations at Wolf River test site, TN

Figure 8.20 shows the SCPTu data for the sounding WOLF5. Apparently, two sand layers exist in the depth ranges from 3.5 m to 10.2 m and from 17 m to 28 m, for their measured porewater pressure u_2 is close to the static porewater pressure u_0 and their friction ratio FR is relatively low, around 2%. Figure 8.21 presents the parameters and soil profiles derived from this sounding, including the normalized shear wave velocity V_{s1} and the $CRR_{7.5}$ derived from shear wave velocity, as well as the soil profile based on cluster analysis and the soil classification chart proposed by Robertson (1990). The top 3 m of soil profile consists of fine-grained materials, underlain by an upper sand layer of about 7 m in thickness, where the $CRR_{7.5}$ derived from both q_T and V_s are relatively low. Small sand dikes, which formed the evidence of marginal liquefaction at this site, were found to erupt from the underlying sand layer into the top layer.
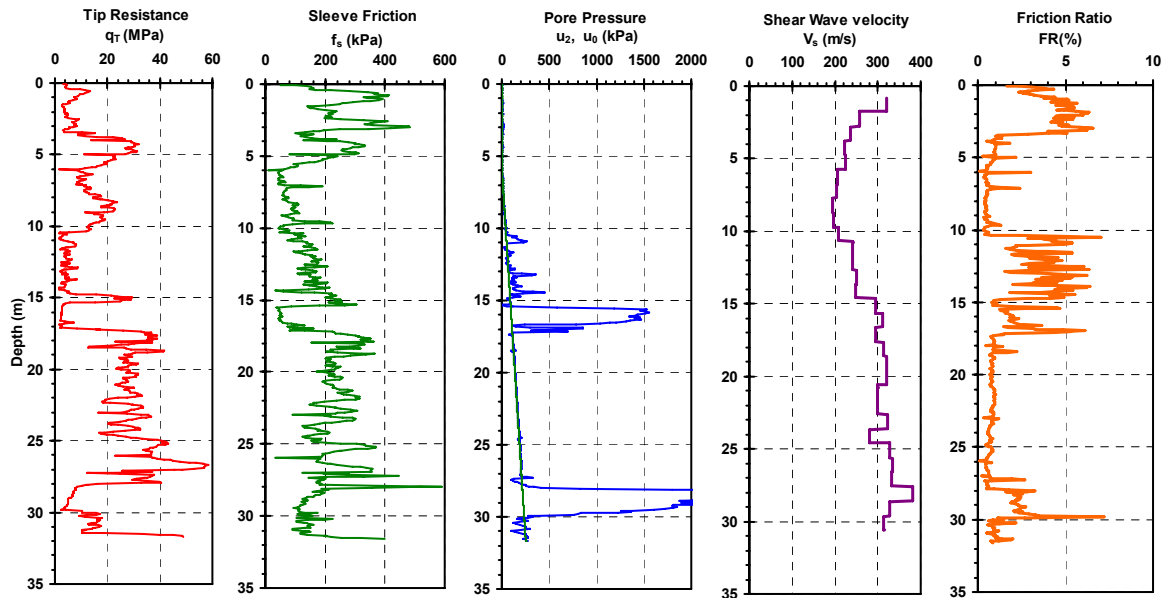
Figure 8.20 Results of the sounding (WOLF5) performed along Wolf River, Memphis, Tennessee
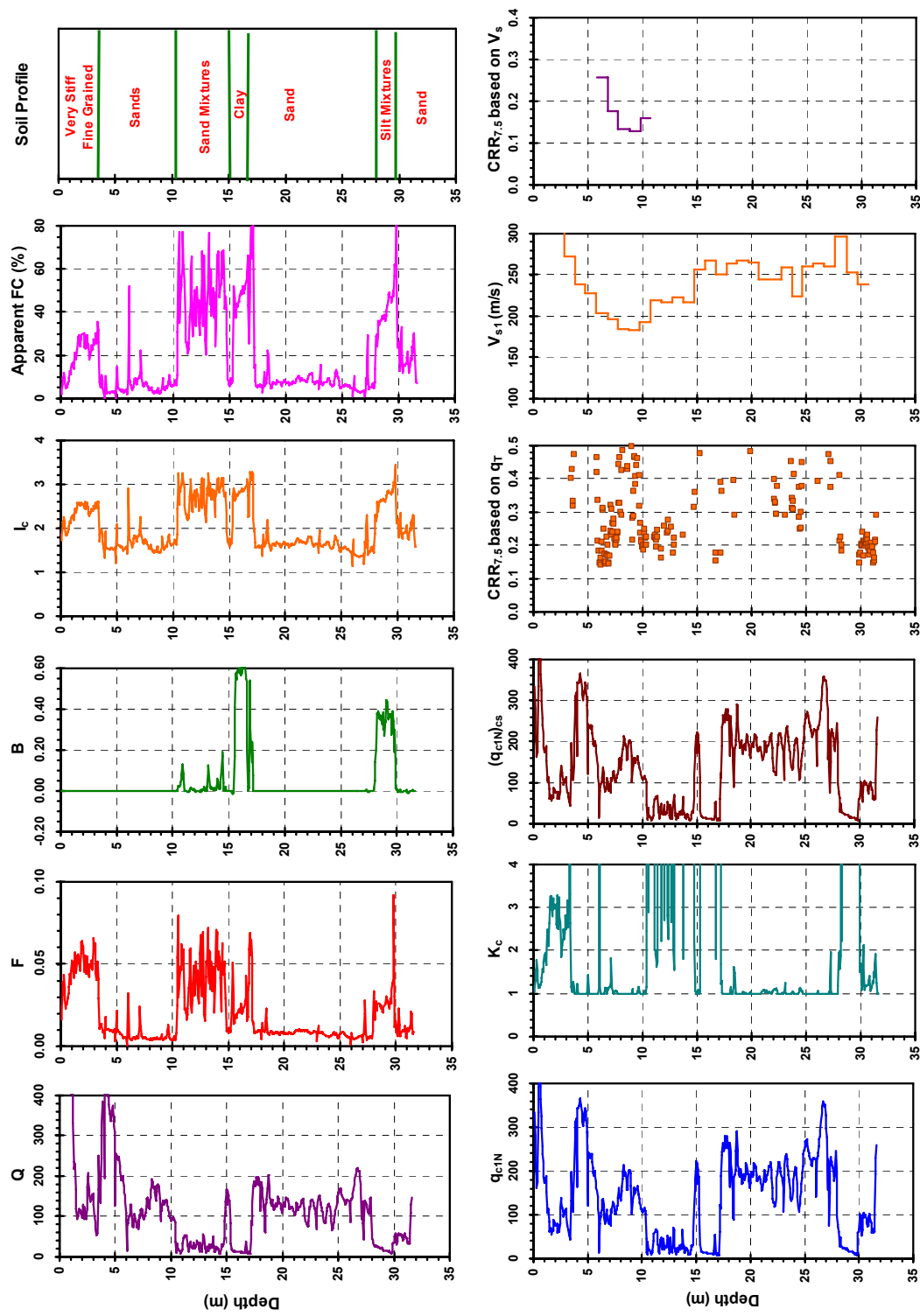
Figure 8.21 Parameters derived from data of the sounding (WOLF5) performed along Wolf River, Memphis, TN

306

Assuming earthquakes of different magnitudes ranging from $M_w = 7.0$ to 8.5, Figure 8.22 shows the critical PGA that could trigger liquefaction at the corresponding depth based on q_T and V_s. The minimum critical PGAs derived from both approaches are within the sand layer in the depth range from 3.5 to 10.2 m. Figure 8.23 plots the minimum critical PGA curves derived from q_T and V_s, respectively. Since the distance from the epicenters to the Wolf River site is known, the attenuation relations suggested by Boore & Joyner (1991) for deep soil sites in eastern north America can also be plotted in Figure 8.23. Here, only the case for R = 100 km is plotted, for the attenuation relation curves with R = 135 km and R = 155 km do not intersect the minimum critical PGA curve at reasonable magnitude. The minimum critical PGA curves intersect the attenuation relation curve for R =100 km at the magnitude of 8.2 and 8.3, and the corresponding PGAs are about 0.125 g. It indicates that the marginal liquefaction features at this site are attributed to the December 16, 1811 earthquake event, which epicenter is 100 km away. The estimated M_w using the proposed methodology agrees with that suggested by Johnston (1996), who believed the December 16, 1811 earthquake event is of magnitude 8.1 ± 0.3 based on contemporary records of structure damage and human reaction.
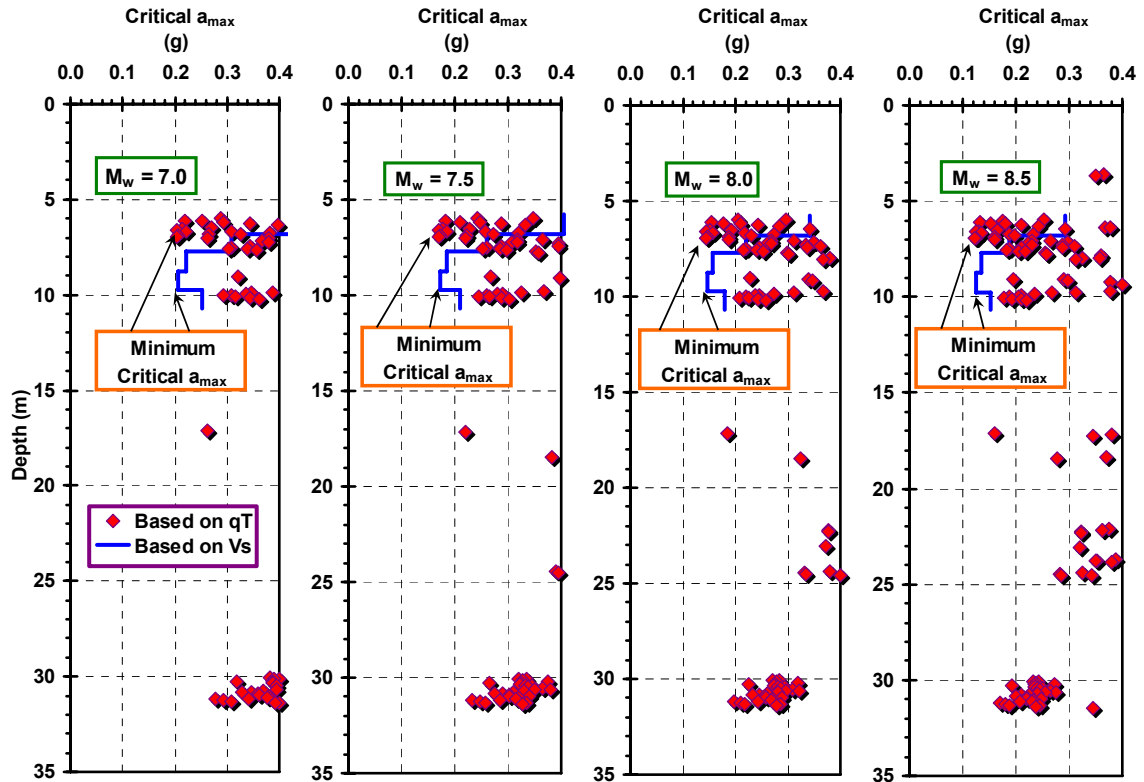
Figure 8.22 Critical peak ground acceleration corresponding to earthquakes of different magnitude, based on the tip resistance and shear wave velocity of the WOLF5 sounding performed along Wolf River, Memphis, TN
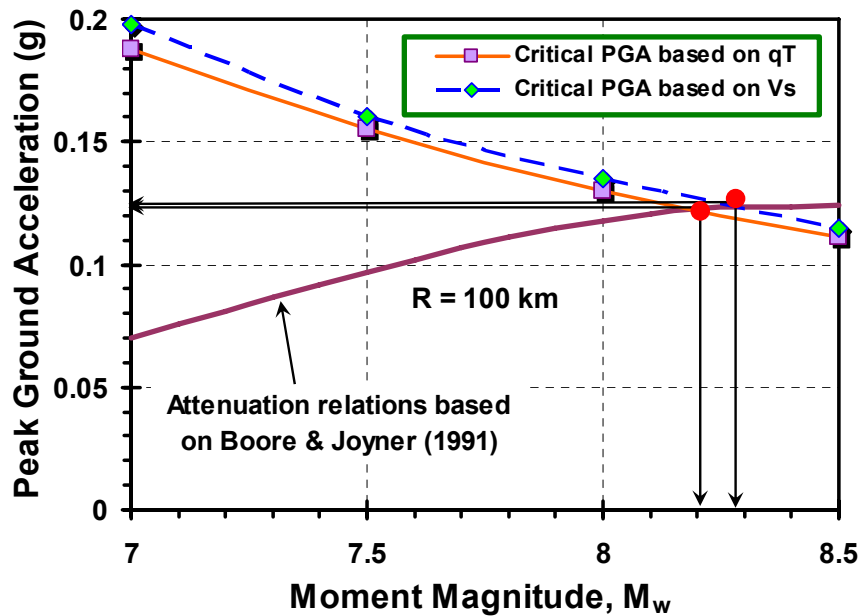
Figure 8.23 Relations between moment magnitude and critical peak ground acceleration of possible previous earthquake triggering liquefaction at the WOLF5 site, superimposed with attenuation relations

The SCPTu sounding WOLF1 was performed where no apparent liquefaction evidence was found. Figure 8.24 presents the data from this sounding, and the measured porewater pressures u_2 are significantly higher than the static porewater pressure u_0 in the depth range from 14 to 19 m, indicating a clayey a layer. In the depth range from 4 to 14 m and from 19 to 24 m, the q_T is relatively high, the u_2 is close to the u_0, and the FR is relatively low, indicating sandy layers. Figure 8.25 shows the parameters and soil profile derived from the sounding and the interpreted soil profile. The $CRR_{7.5}$ derived from both q_T and V_s suggest that the two thick sand layers as shown in the soil profile are most prone to liquefaction.
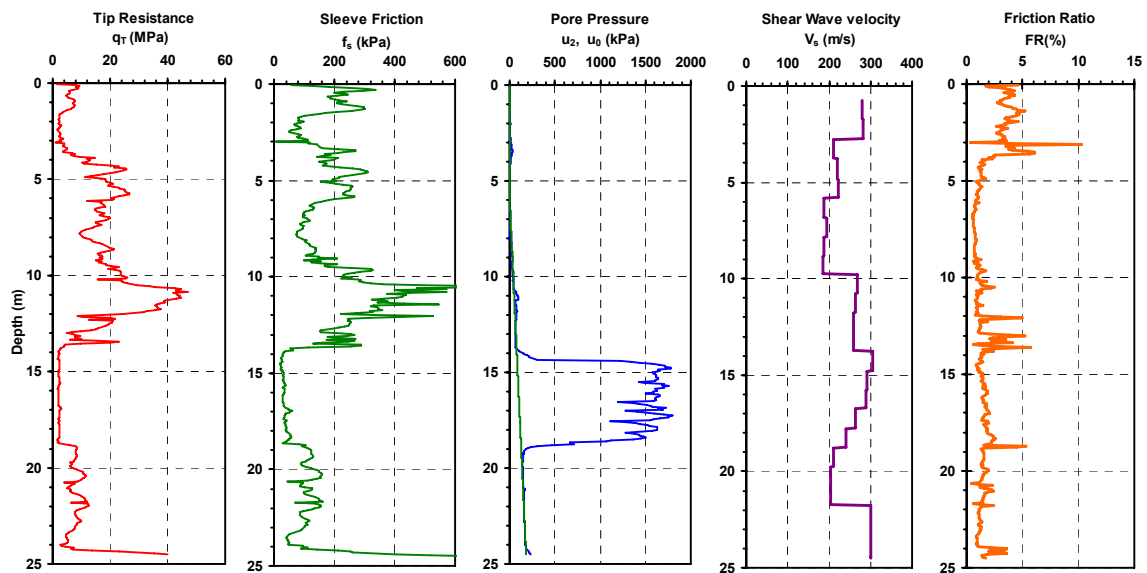
Figure 8.24 Data representation for the sounding (WOLF1) performed along Wolf River, Memphis, TN

Figure 8.26 shows the critical PGA in the event of earthquakes of different magnitudes from $M_w = 7.0$ to 8.5. The minimum critical PGA seems to be within the sand layer in the depth range from 19 to 24 m. Similar to the previous case studies, the minimum critical PGA curves are superimposed with the attenuation relation in Figure 8.27. Since only the attenuation relation curve with respect to $R = 100$ km intersects the minimum critical PGA curves at magnitudes in reasonable range, the other attenuation curves associated with $R = 135$ km and $R = 155$ km are not plotted in this figure. The two crossover points between the minimum critical PGA curves and the attenuation curve correspond to $M_w = 8.25$, PGA =0.122 g and $M_w = 8.4$, PGA = 0.127 g, respectively. Because no liquefaction evidence was found at the location where this sounding was performed, the magnitudes and PGAs associated with the crossover points can serve as the upper boundaries of the real values. If the average value of the two crossover points is used, the upper boundaries for the M_w of the December 16, 1811 earthquake event is about 8.3 and that for the PGA of the Wolf River site is 0.125 g. The derived upper boundary of the M_w is also consistent reasonably well with the M_w suggested by Johnston (1996).
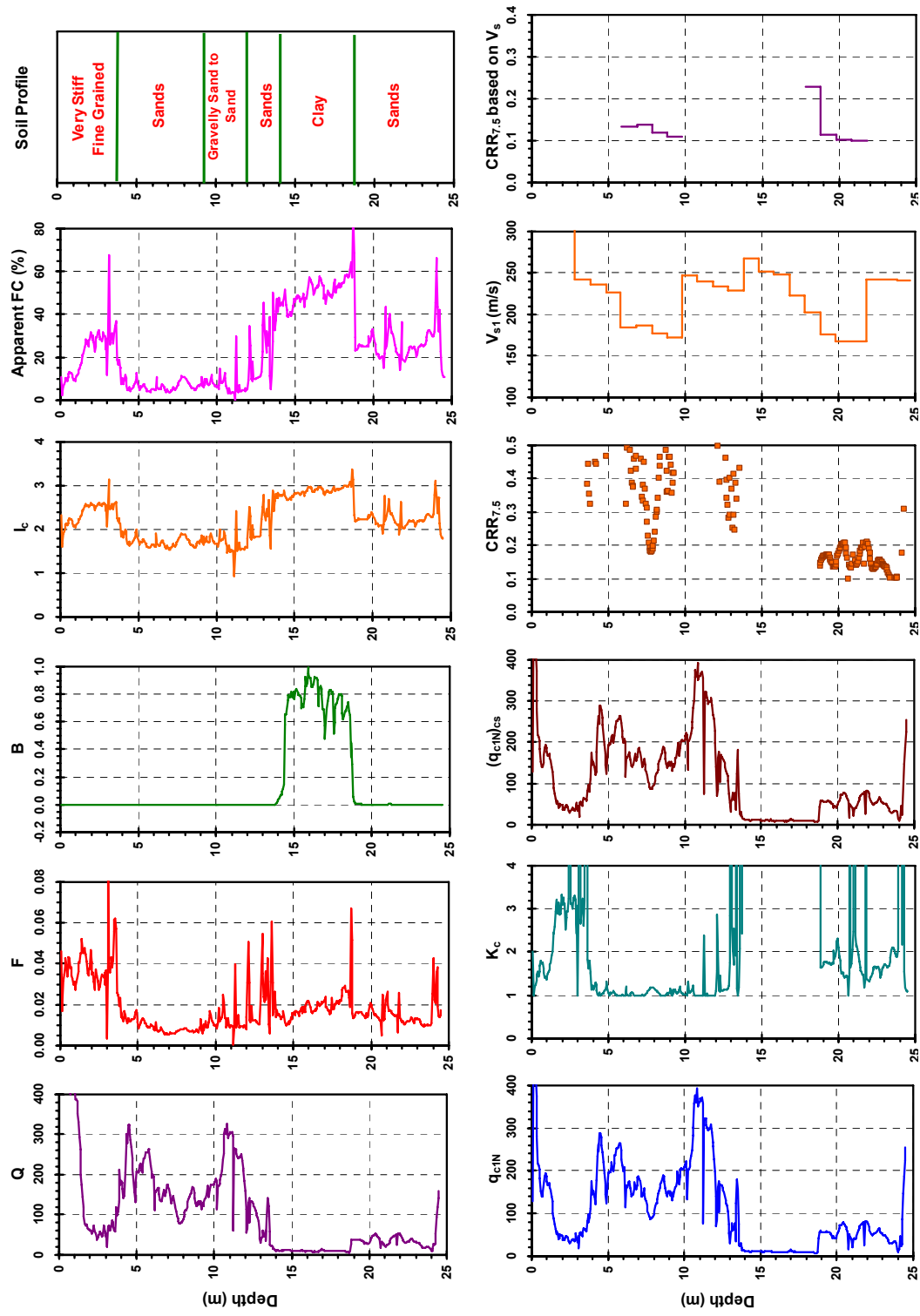
Figure 8.25 Parameters and soil profile derived from the sounding (WOLF1) performed along Wolf River, Memphis, TN
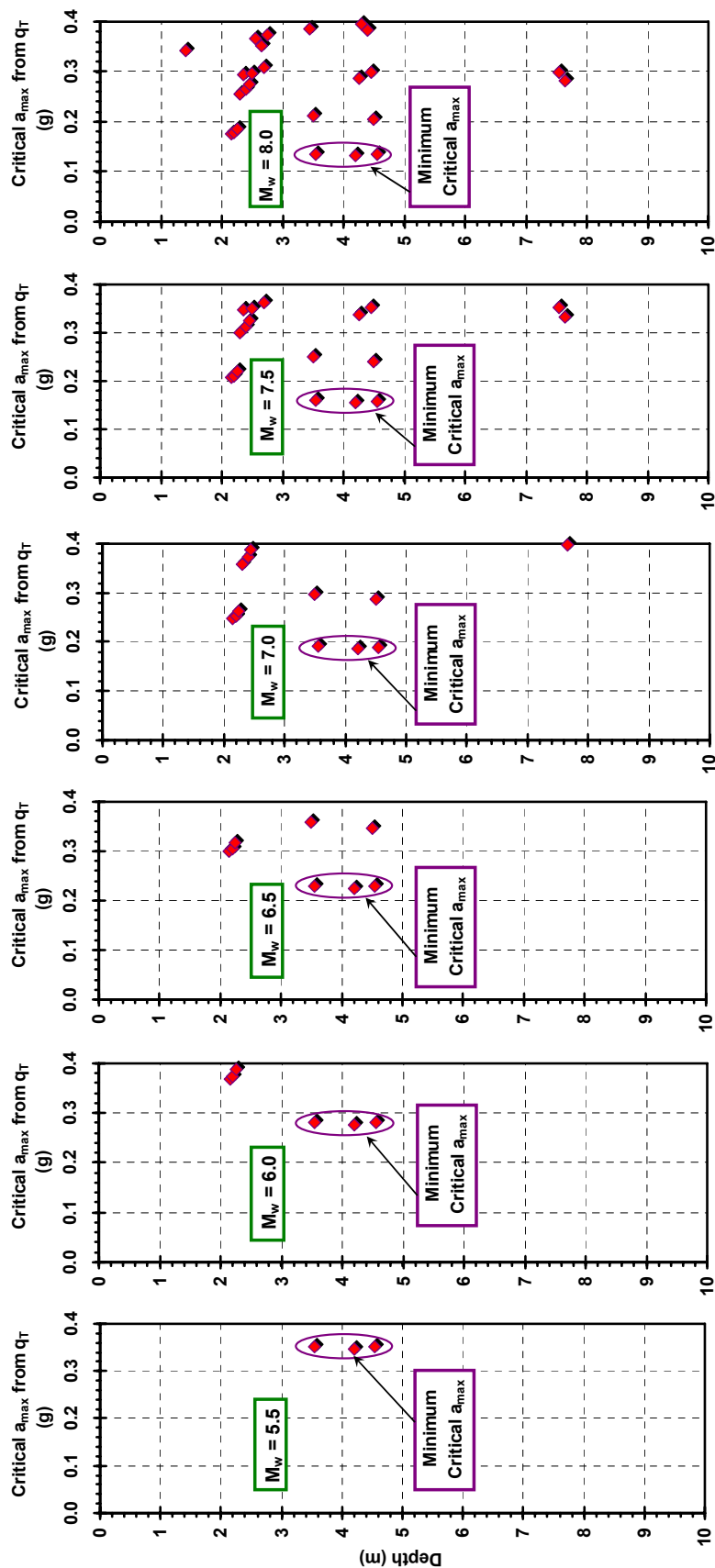
311
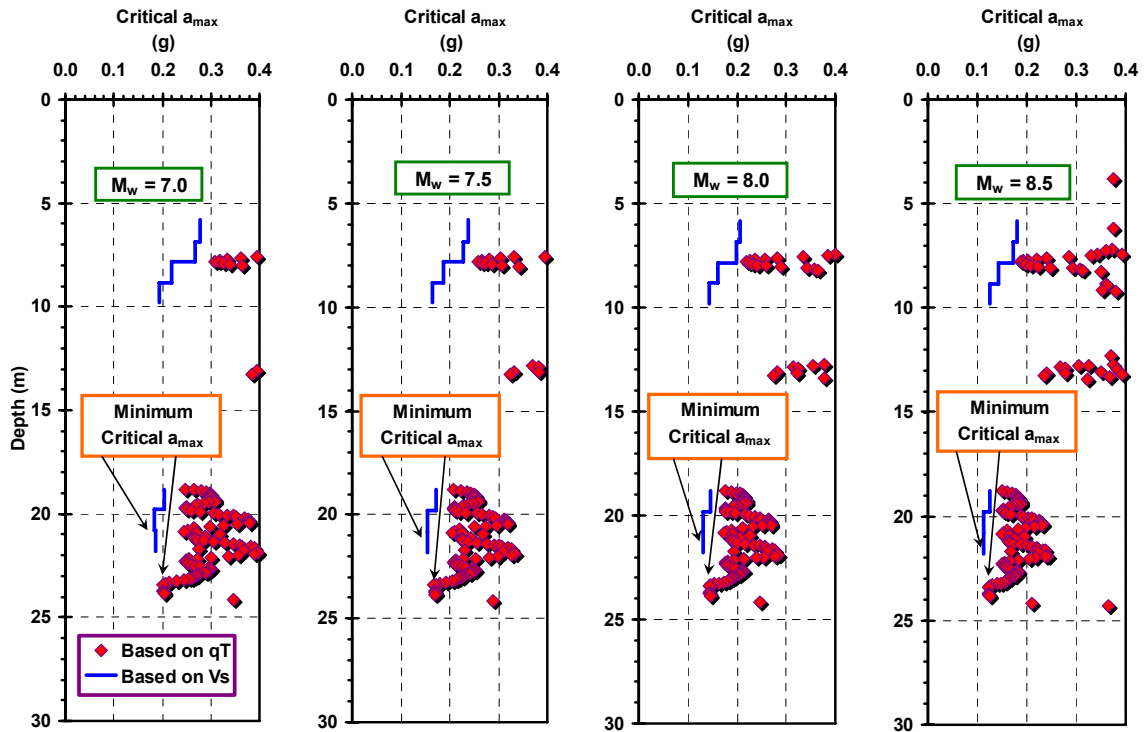
Figure 8.26 Critical peak ground acceleration corresponding to earthquakes of different magnitude, based on the tip resistance and shear wave velocity of the sounding (WOLF1) performed along Wolf River, Memphis, TN
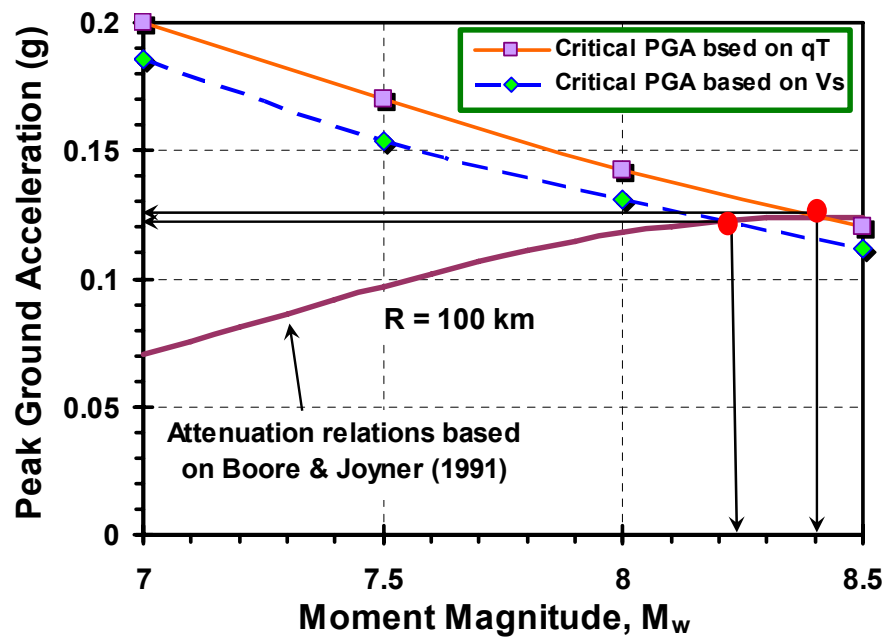
Figure 8.27 Relationships between moment magnitude and critical peak ground acceleration of possible previous earthquake triggering liquefaction at the WOLF1 site, superimposed with attenuation relations

8.5.2 Walker Site

The Walker paleoliquefaction site near Marked Tree, Arkansas has been discussed previously in Chapter 5. On the basis of radiocarbon dating and artifact analysis, the sand blows and related dikes at this site can be attributed to the large New Madrid earthquakes that occurred in circa 1530 A.D.. Although the full extent of the 1530 A.D. liquefaction field has not yet been determined, this is the southernmost known occurrence of sand blows of this age. Therefore, the estimated M_w and PGA based on this site should be close to the real values.

Figure 6.22 in Chapter 6 has shown the magnitude and interpreted liquefaction fields for two seismic events circa 1530 A.D.. The epicenters of the corresponding earthquakes are assumed to be located at the centers of the liquefaction fields. The Walker site is approximately is 73 km and 110 km to the estimated epicenters of the two A.D. 1450 events, which were estimated to be of magnitude 7.6 and 8.0, respectively, by Tuttle (1999) based on the comparison of liquefaction features caused by previous and modern earthquakes.

Figure 4.20 in Chapter 4 presented the data from a representative SCPTu sounding (MTREE01) advanced to a depth of 32 meters at the Walker site, as well as the derived parameters and soil profile. From the back-calculated critical PGA based on q_T and V_s (Figure 8.28), the minimum value occurs around the depth range from 18 to 20 m. The minimum critical PGA curves and the attenuation relation for R = 73 km are superimposed in Figure 8.29, and the crossover points indicate M_w = 7.6 and PGA = 0.16

313

g. The attenuation relation for R = 110 km is not shown in this figure, for it does not intersect the minimum critical PGA curve at reasonable magnitude. Therefore, the liquefaction features at the Walker site was likely caused by the earthquake event which epicenter is 73 km away. Notably, the estimated magnitude by the proposed methodology agrees well with that suggested by Tuttle (1999).
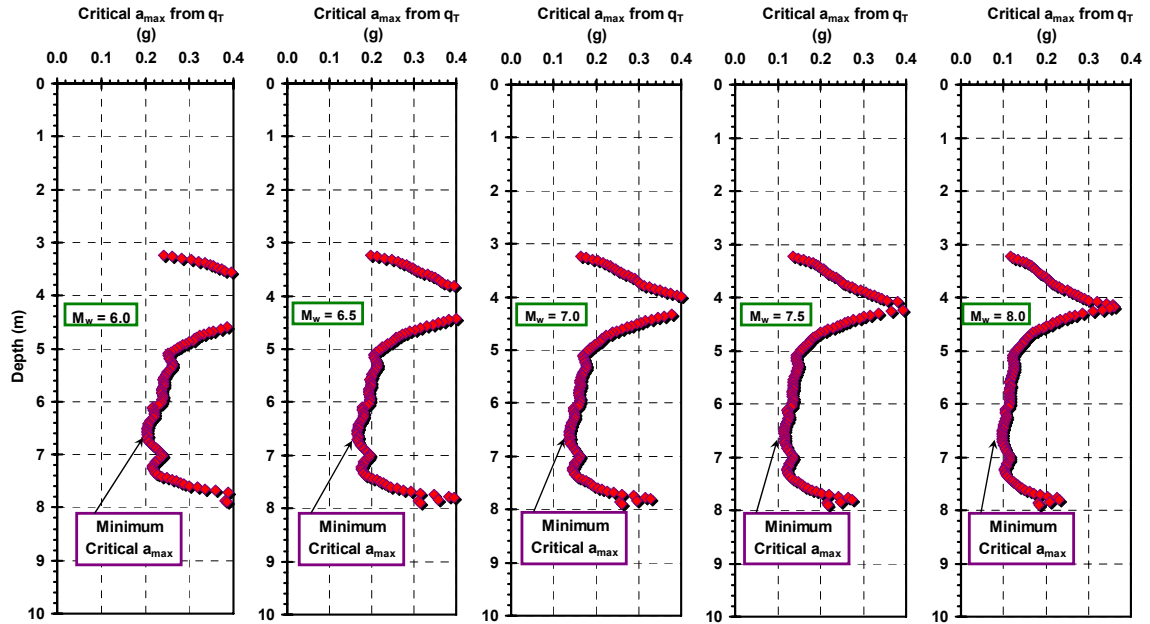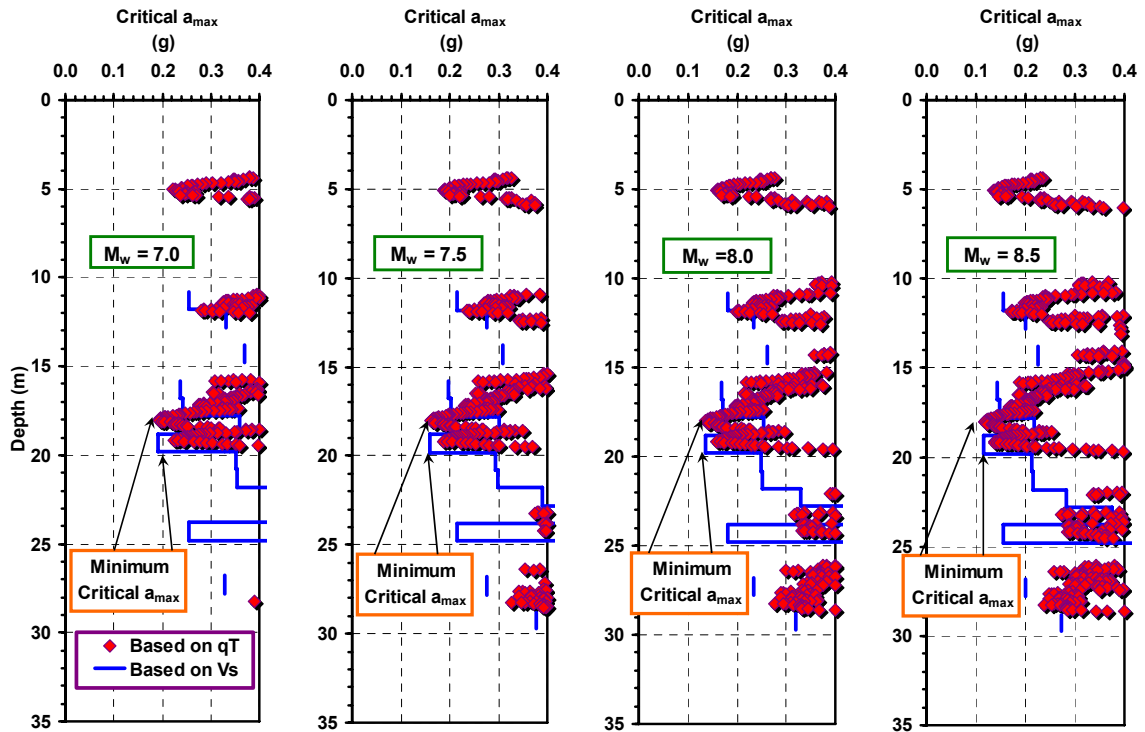

Figure 8.28 Critical peak ground acceleration corresponding to earthquakes of different magnitude, based on the tip resistance and V_s profile from SCPTu sounding MTREE01
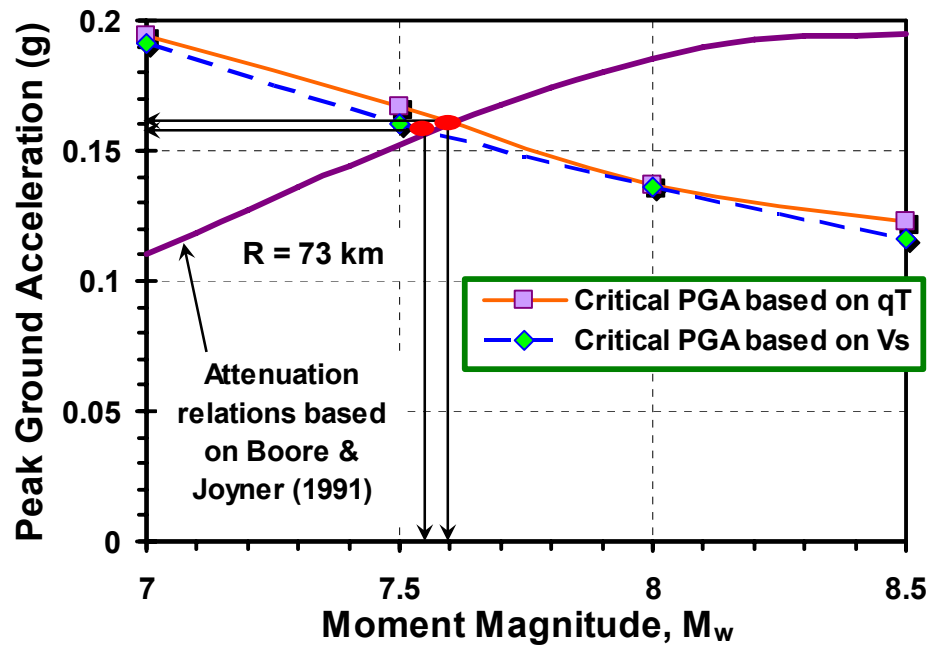
Figure 8.29 Relationship between moment magnitude and PGA of possible previous earthquake triggering liquefaction at the Walker site based on the MTREE1 sounding, superimposed with attenuation relations

8.5.3 Hillhouse Site

The Hillhouse paleoliquefaction site located at Wyatt, MO has also been discussed previously in Chapter 5. According to radiocarbon dating of the deposits and analysis of artifacts found at this site, the liquefaction features are formed during the 900 A.D. earthquakes (Tuttle, 1999), and it is the most northern site that has found liquefaction features attributed to the 900 A.D. earthquakes. These facts indicate that the CSR was probably only slightly higher than the CRR at this site when the liquefaction features were formed around 900 A.D..

As shown in Figure 6.36 in Chapter 6, the 900 A.D. earthquakes consist of three individual earthquake events with the magnitudes of 8.1, 8.0, and 7.6. The Hillhouse site is 65, 80, and 148 km away from the estimated epicenters. Figure 6.34 and 6.35 in Chapter 6 have shown the results of a SCPTu sounding performed at this site, as well as the derived parameters and the interpreted soil profile.

The critical PGAs derived from both q_T and V_s are presented in Figure 8.30, and the minimum critical PGA occurs around the depth of 20 m. Figure 8.31 (a) and (b) shows the minimum critical PGA curves superimposed with the attenuation relations for R = 65 km and R = 80 km, respectively. The attenuation relation for R = 148 km does not intersect the minimum critical PGA curve at reasonable magnitude, and thus is not shown here. The crossover points in both Figure 8.31 (a) and (b) indicate that the liquefaction features could possibly be caused by either or both of the earthquake events which epicenters are 65 km and 80 km away. For the earthquake with R = 80 km, the estimated M_w = 7.9, which agrees well with the M_w = 8.0 suggested by Tuttle (1999). However, for the earthquake with R = 65 km, the estimated M_w = 7.55, which is lower than the M_w = 8.1 suggested by Tuttle (1999). The difference between the estimated magnitudes might be attributed to that the fact that a 10-m thick unliquefiable layer is on top the liquefiable sand layer at this site (Figures 6.34 and 6.35 in Chapter 6). Because of the cap effect of the unliquefiable layer, extra seismic loading was required to form liquefaction features, such sand blow and sand dikes.
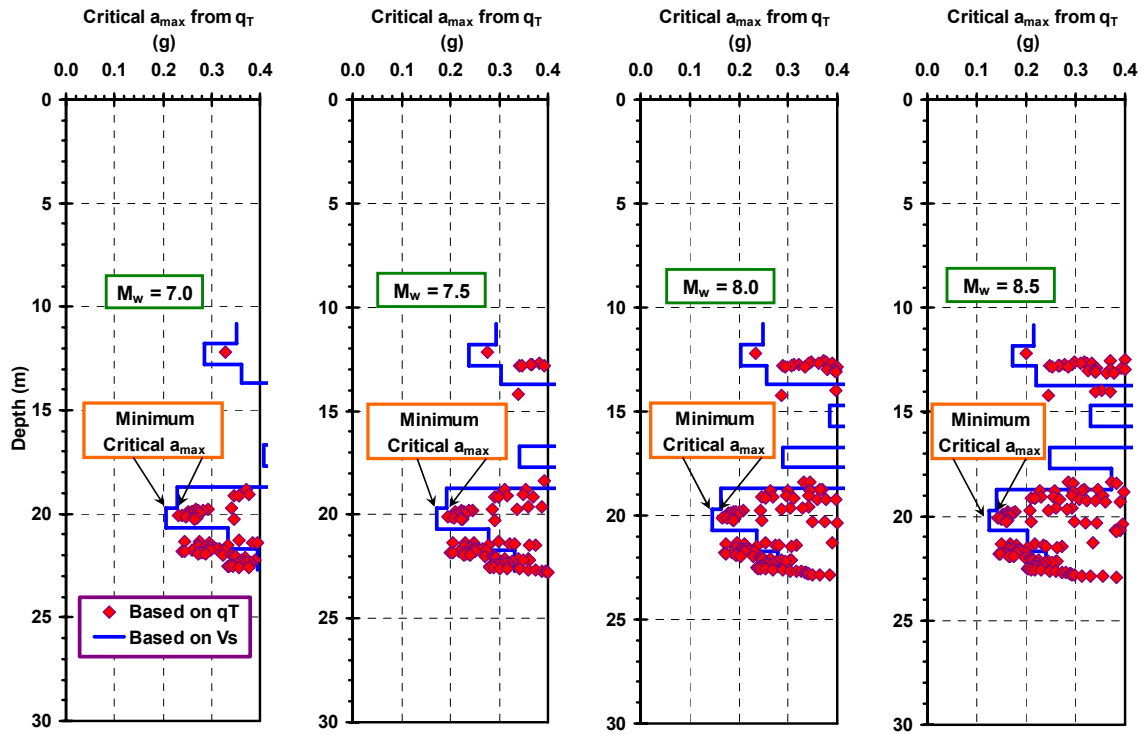
Figure 8.30 Critical peak ground acceleration corresponding to earthquakes of different magnitude, based on the tip resistance and V_s profile from the representative SCPT sounding performed at Hillhouse paleoliquefaction site in Wyatt, Missouri
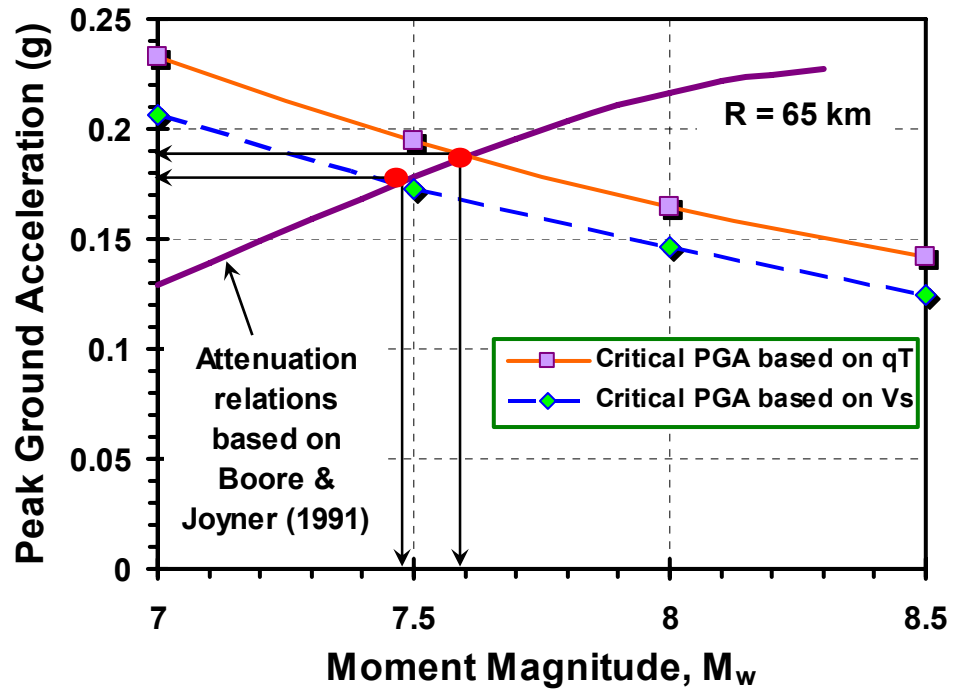
(a)
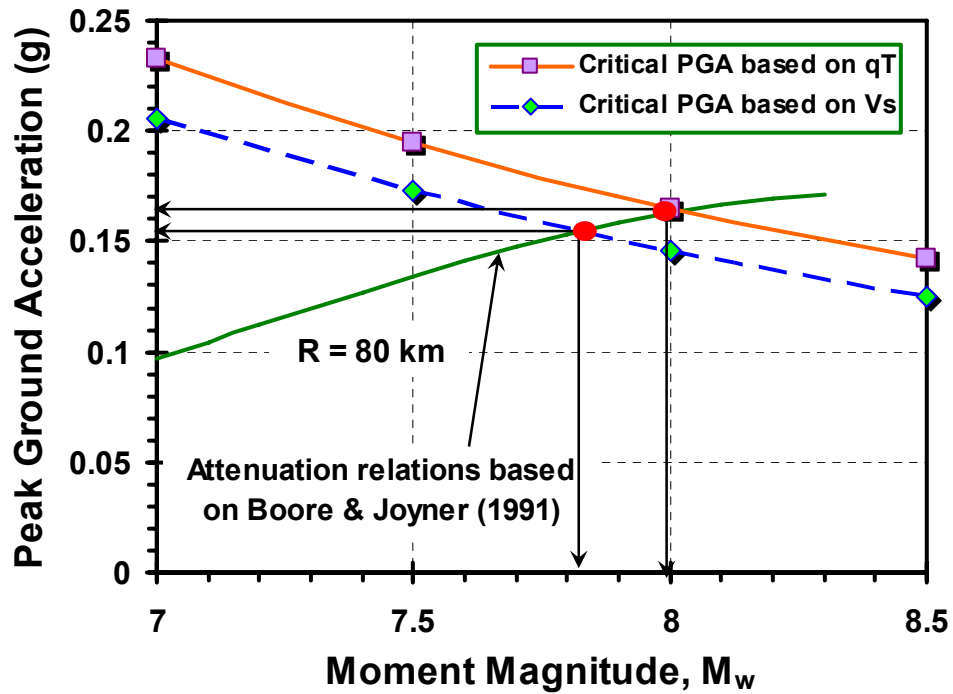
(b)

Figure 8.31 Relationship between moment magnitude and PGA of possible previous earthquake triggering liquefaction at the Hillhouse site in Wyatt, Missouri, superimposed with the attenuation relations: (a) R = 65 km; (b) R = 80 km.

8.6 Summary

Due to the relatively long recurrence interval of large earthquakes in the NMSZ, the historic and pre-historic earthquakes, especially the liquefaction features resulting from these earthquakes, are often used to extend our understanding of the seismic activities in this region. The lack of seismograph readings from the last large events in 1811-1812 compounds the problem. Some geotechnical methods, such as the simplified procedure based on in-situ data, have been proven very useful for estimating the seismic parameters associated with previous earthquakes.

Criteria have been developed to evaluate the capacity of the soil to resist liquefaction (i.e. CRR) based separately on the cone tip resistance q_T or shear wave velocity V_s. Since all the test data used in developing the criteria are collected after the corresponding earthquakes, the criteria are more appropriate for estimating the seismic parameters associated with previous earthquakes.

A new methodology is proposed to estimate the seismic parameters (moment magnitude M_w and peak ground acceleration PGA) associated with previous earthquakes, using the simplified procedure based on SCPTu data and the attenuation relationships developed for the corresponding seismic areas. This methodology is initially validated through the paleoliquefaction studies at two sites associated with the 1989 Loma Prieta earthquake (Moss Landing and Yueba Puena Cove). After verification, the procedures are applied to estimate the M_w and PGA for the major previous earthquakes in the NMSZ. Three sites are constrained: Wolf River site, TN (1811 – 1812 events); Walker site, AR (1530 A.D. events), and Hillhouse site, MO (900 A.D. events). Although the methodology is

319

theoretically simple, the estimated earthquake magnitudes and associated PGAs agree quite well with the records and values estimated by other methods.

CHAPTER IX

CONCLUSIONS AND RECOMMENDATIONS FOR
FURTHER STUDIES

9.1 Conclusions

The SCPTu is an efficient way to assess soil stratigraphy, soil properties, and liquefaction potential in seismically active areas. In this thesis, software tools were developed to automate post-processing of SCPTu data, and new methods were proposed for soil stratification and classification, liquefaction evaluation, and paleoliquefaction studies. They have been applied to the series of cone penetration tests performed in the NMSZ.

The in-situ shear wave velocity V_s provides the small-strain moduli (G_{max}), which is required for both site amplification analyses and soil liquefaction studies. In this thesis, the cross-correlation method and the phase-shift method are discussed and applied to derive V_s from downhole test. Both methods can be implemented on computer, and can obtain V_s more accurately and much faster than the first arrival and cross-over methods, which are presently done manually in engineering practice. Compared with the cross-correlation method, the phase-shift method requires some degree of subjective judgment from the user. The software (*ShearPro*) utilizes the cross-correlation method to automate the process of deriving V_s. After data files of shear wave signals are loaded into *ShearPro*, it outputs the derived V_s and corresponding coefficient of determination r^2 that indicates the quality of cross-correlation between signals.

Cluster analysis is an efficient statistical way to analyze the stratigraphic vertical profiling of geomaterials. In this thesis, the constraints of the two-channel approach proposed by Hegazy & Mayne (2002) are analyzed, and a new three-dimensional cluster analysis approach is developed based on three channels of data including tip resistance, sleeve friction, and porewater pressure. The applicability to soil formations of clay, silt, and sand is now generalized.

A new algorithm for cluster analysis on CPTu data is proposed, which simplifies the computation procedure, as well as provides physical meaning to the clustering. It can detect the depth of soil boundaries, layers, and sublayers, as well as the systematic errors and random outliers. The method is also capable of detecting soil lenses, seams, transitions, as well as important changes within the stratigraphy. Current CPT soil behavioral charts (e.g., Robertson et al., 1986; Robertson, 1990) often exhibit conflicts between the $Q \sim F$ domain and $Q \sim B$ domain. In a number of cases, CPT service companies rely solely on the $Q \sim F$ charts and have incorrectly identified stiff clays as "sand". A three-dimensional soil classification chart that gives consistent classification results is proposed in this thesis to avoid these difficulties. Illustrative soil profiles from real examples derived by the three-channel cluster analysis and the three-dimensional soil classification chart agree well with soil boring data and available lab testing.

Various soil parameters can be inferred from SCPTu data, based on interpretative correlations. The software (*InSituData*) is developed in this thesis to automate this process. It can derive parameters based on the correlations recommended and

implemented by the author, as well as on the user-defined equations. This software can also visualize the parameters in charts similar to those in EXCEL. Both the data and charts can be exported to an EXCEL spreadsheet. Compared with other available software, this software has a friendly user interface, and gives more flexibility to users in processing the SCPTu data.

Geotechnical site characterization using seismic cone penetration tests (SCPTu) in the New Madrid Seismic Zone (NMSZ) serves multiple purposes, including: (1) identifying soils with high potential to liquefaction; (2) providing data for site-amplification analysis; and (3) obtaining information for ongoing paleoliquefaction studies. The data collected by the SCPTu sounding can be processed to give the soil stratigraphy and a direct liquefaction evaluation of test sites. In this thesis, the cyclic stress ratio (CSR) is derived using both the simplified stress-based procedure (e.g., Seed & Idriss, 1971) and the program DEEPSOIL (Park & Hashash, 2004). For the DEEPSOIL procedure, the bedrock motion at a specific site is generated using the program SMSIM (Boore, 2002), and DEEPSOIL simulates the propagation of the shear waves from the bedrock to ground surface. The cyclic resistance ratios (CRR) calculated from the tip resistance q_T and shear wave velocity V_s can both be used for the liquefaction evaluation at a single site. The redundancy information provides a higher level of confidence in conclusions. Both the deterministic and probabilistic approaches of liquefaction analysis are now available, and are used to detect zones susceptible to liquefaction. Based on the analysis of the liquefaction zones at these paleoliquefaction sites, regional liquefaction criteria for the NMSZ have been developed. Comparison between the newly developed criteria and

323

those suggested by other researchers show that the soils in the NMSZ are more prone to liquefaction upon the same seismic loading.

Existing correlations to evaluate liquefaction susceptibility based on in-situ tests were developed almost exclusively from data measured post-earthquakes. However, only pre-earthquake data are available to evaluate the liquefaction susceptibility during future earthquakes. The pre- and post-earthquake data might be significantly affected by liquefaction and aging effects. In order to find out these influences, SCPTu tests were performed before and after simulated earthquakes in the NMSZ. Blast-induced liquefaction was observed in some sand zones, where q_T, f_s, and V_s were significantly lowered by the induced-liquefaction. However, subsequent CPT soundings showed no significant aging effects at these test sites.

Since almost all the field test data used in developing the liquefaction criteria are collected after the corresponding earthquakes, the criteria are more appropriate to estimate the seismic parameters associated with previous earthquakes. A new methodology is proposed in this thesis to estimate the seismic parameters associated with previous earthquakes, using the simplified procedure based on SCPTu data and the attenuation relationship developed for corresponding seismic areas. This methodology is validated through two paleoliquefaction studies from the 1989 Loma Prieta earthquake and then applied to the major previous earthquakes in the NMSZ. The estimated earthquake magnitude and peak ground acceleration (PGA) agree quite well with the records and those suggested by other methods.

9.2 Recommendations for Further Studies

As computer software, *ShearPro*, *ClusterPro*, and *InSituData* can always be improved. In this thesis, effort is put in developing user-friendly interfaces, but additional features can be added in the interface to make them more convenient to use. In *ShearPro*, print options can be added to enable printing out the filtered/unfiltered shear wave trains and graph of V_s versus depth. For the current version of *InSituData*, the data column names and settings of plots have only one default option. The users would have more flexibility and convenience, if more options can be saved. Additional correlations can be added to the software, and then the user would be able to choose from the recommended correlations to derive parameters.

Clustering is a very promising technique for soil stratification based on in-situ data. Three channels of CPTu data are used in the three-dimensional cluster analysis discussed herein. There is the possibility that cluster analysis could be expanded to more channels of data, such as for use in four-channel resistivity soundings (RCPTu), seismic soundings (SCPTu), and other tests.

Regional liquefaction criteria for the NMSZ have been developed from analysis of the SCPTu data collected at the paleoliquefaction sites in this region. These empirical criteria can be refined through more case studies. Its correctness can be verified through earthquakes in the future. Although the recurrence interval of large earthquakes is long, small earthquakes occur quite often in the NMSZ, which may provide opportunities for the verification.

No obvious aging effects were observed from the blast-induced liquefaction experiments in the NMSZ during the time of 229 days. More tests at the tests sites may substantiate the conclusion. Since aging effects are indeed observed during some laboratory tests and ground improvement projects, future work can concentrate on finding the difference between these sites, which might be associated with aging effects. A hypothetical equation is proposed for estimating the behavior of cone tip resistance with time. Values of the parameters used in this equation need to be calibrated through case studies.

A new methodology has been proposed to estimate the seismic parameters associated with previous earthquake. Since it is based on empirical methods for liquefaction evaluation and ground motion attenuation, more case studies in the future would be helpful in refining this methodology.

APPENDIX A

NEW MADRID SEISMIC ZONE

A.1 Introduction

As the most extensive seismic region in the eastern United States, the New Madrid Seismic Zone (NMSZ) is located within the central Mississippi Valley, covering northeast Arkansas, western Tennessee, southeast Missouri, western Kentucky, and southern Illinois (Figure A.1). During 1811 and 1812, three largest earthquake events occurred in this region, and they are estimated to have moment magnitudes of 8.1, 7.8, and 8.0 (Johnston, 1996). Their dates of occurrence and epicenter locations are listed in Table A.1.

Table A.1 Occurring date, estimated magnitude, and epicenter of the three largest events during the 1811-1812 earthquake sequence (Nuttli, 1979; Johnston, 1996)

Occurring Date	Magnitude	Epicenter
16 Dec 1811	M 8.1 ± 0.3	Northwest of Blytheville, Arkansas
23 Jan 1812	M 7.8 ± 0.3	North of Caruthersville, Missouri
07 Feb 1812	M 8.0 ± 0.3	Southwest of New Madrid, Missouri

The New Madrid seismic zone is named after the town of New Madrid, Missouri, which is the closest town to the epicenters of these earthquakes. Another two major earthquakes occurred on January 4, 1843 and October 31, 1895, and they were estimated to both have moment magnitude over 6.0 (Johnston & Schweig, 1996).

The New Madrid Seismic Zone (NMSZ) is located within the North America tectonic plate. Although it is not situated at a plate boundary, it is the most prominent intraplate seismic zone within the North America plate. The seismic activities occur primarily along the New Madrid fault system (Figure A.1), which consists of three legs, and has been identified as a left-stepping, right-lateral strike-slip fault zone (Schweig & Van Arsdale, 1996). On average, more than 200 earthquake events are located in the fault zone annually, most of which are too small to be felt (moment magnitude $M_w < 2.5$), but every 18 months or so, the fault releases a shock that is capable of local minor damage ($M_w > 4.0$) (http://www2.semo.edu/ces/CES2.HTML).
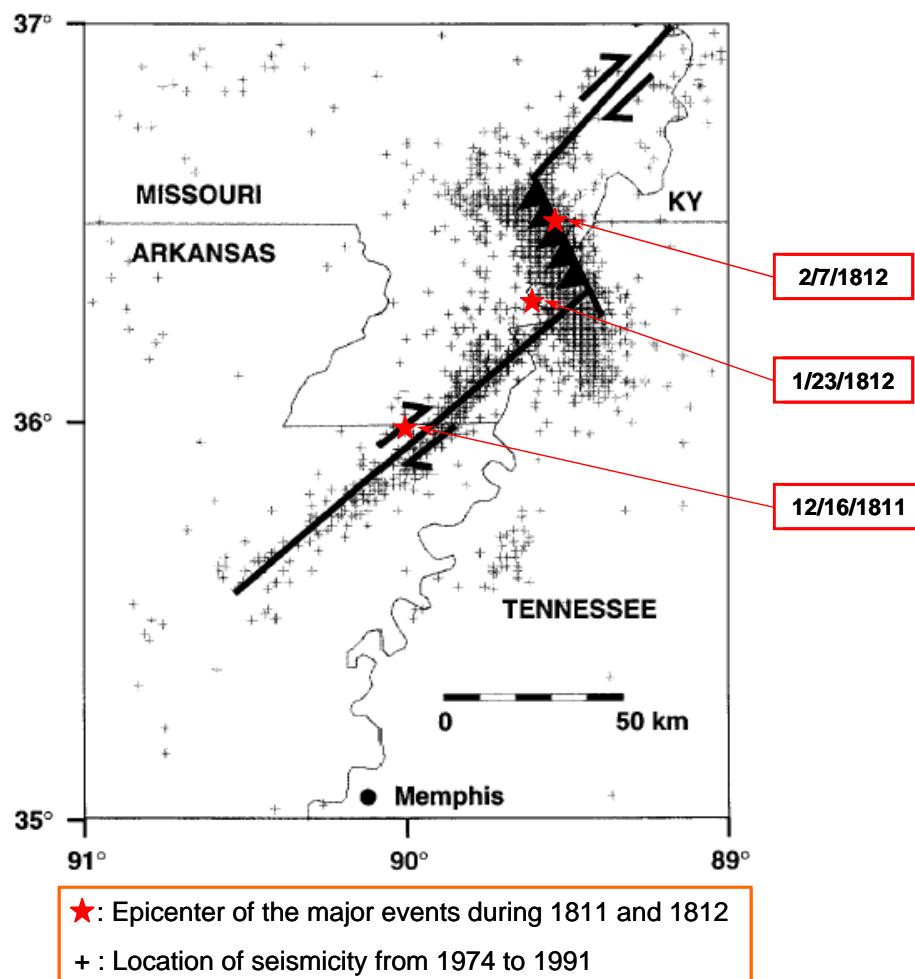
Figure A.1 The fault in the New Madrid Seismic Zone (Schweig & Van Arsdale, 1996)

In 1811-1812, there were very few residents and man-made structures in the New Madrid Seismic Zone (NMSZ), whereas nowadays this region has become home to millions of people and includes several big cities, such as Memphis, Tennessee and St. Louis, Missouri. Recent studies and educational campaigns have led to the public awareness on the inevitable recurrence of these significant seismic events and subsequent loss of life and damage. Research has shown that there is a 90% probability for a magnitude 6 to 7 earthquake to occur within the next 50 years (Schweig et. al., 1995).

Compared with even the 1994 Northridge, California earthquake that exhibited a moment magnitude of 6.7, the 1895 earthquake in NMSZ with a moment magnitude of only 6 affected a much larger area of the USA, as shown in Figure A.2, because of the different geology east and west of the USA (Filson et al., 2003). Since the Northridge, California earthquake killed 67 people and caused $40 billion of property destruction, it is expected that the effects of an earthquake with the same magnitude in the NMSZ could be far worse (Filson et al., 2003). Efforts are definitely necessary for evaluating the level of seismic hazards in this area in order to help protect the life and property.

Recent studies have uncovered that wide-spread liquefaction features in the NMSZ, such as sand blows and sand dikes (Obermeier, 1998; Tuttle, 1999). They resulted from previous earthquakes in this region. Upon liquefaction, the underground sands may erupt to the ground surface and redeposit as sand blows (Figure A.3). Sand blows are connected to sand dikes, which are sediment-filled cracks through which sand and water flowed. Sand sills are the sand deposits intruded below layer of low permeability, and

they usually take the form of lenses that are connected to sand dikes (Tuttle, 1999). Since even the most recent large earthquakes occurred nearly two hundred years ago in the NMSZ, their surface traces, such as sand boils, subsidence, and dikes, have been modified by erosion, farming, vegetation, and other manifestations. Thus, they are very difficult to identify except at special pristine and undisturbed location. Therefore, paleoliquefaction features as shown in Figure A.4, which are formed during the past earthquakes and kept in the soil stratigraphy, are often used to analyze the previous seismic activities, such as their magnitudes, location of epicenters, as well as peak ground acceleration (PGA) at specific sites.
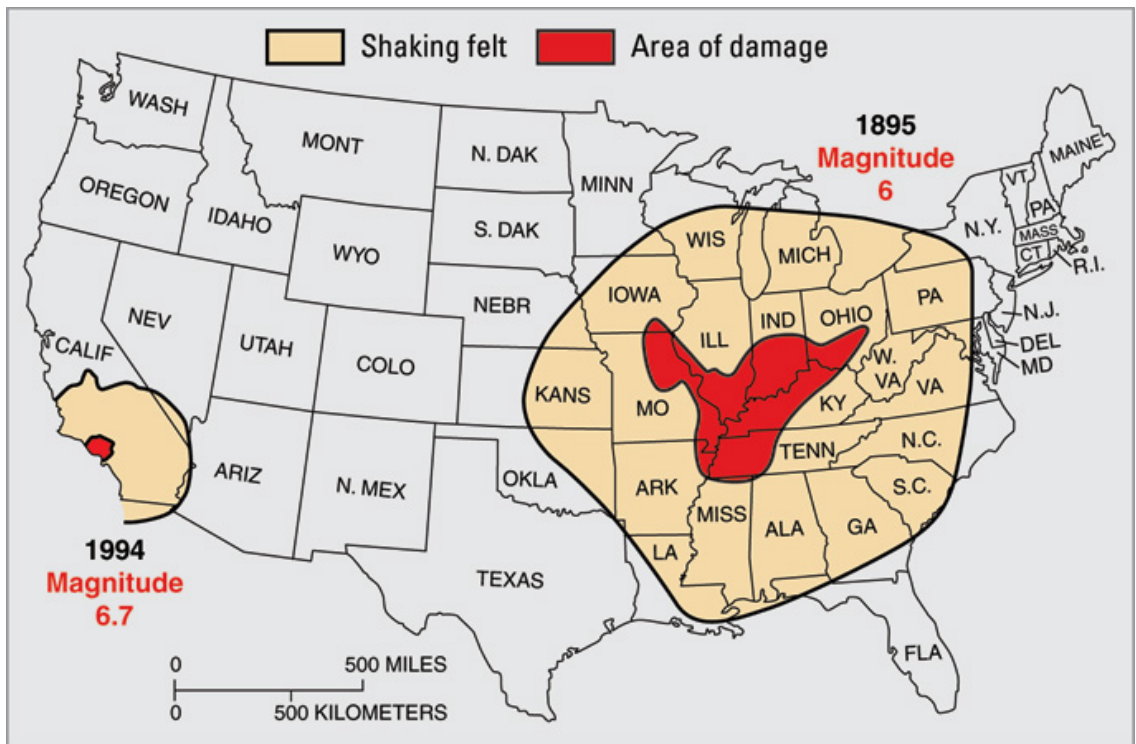
Figure A.2 Areas affected by earthquakes in the USA (Filson et al., 2003)
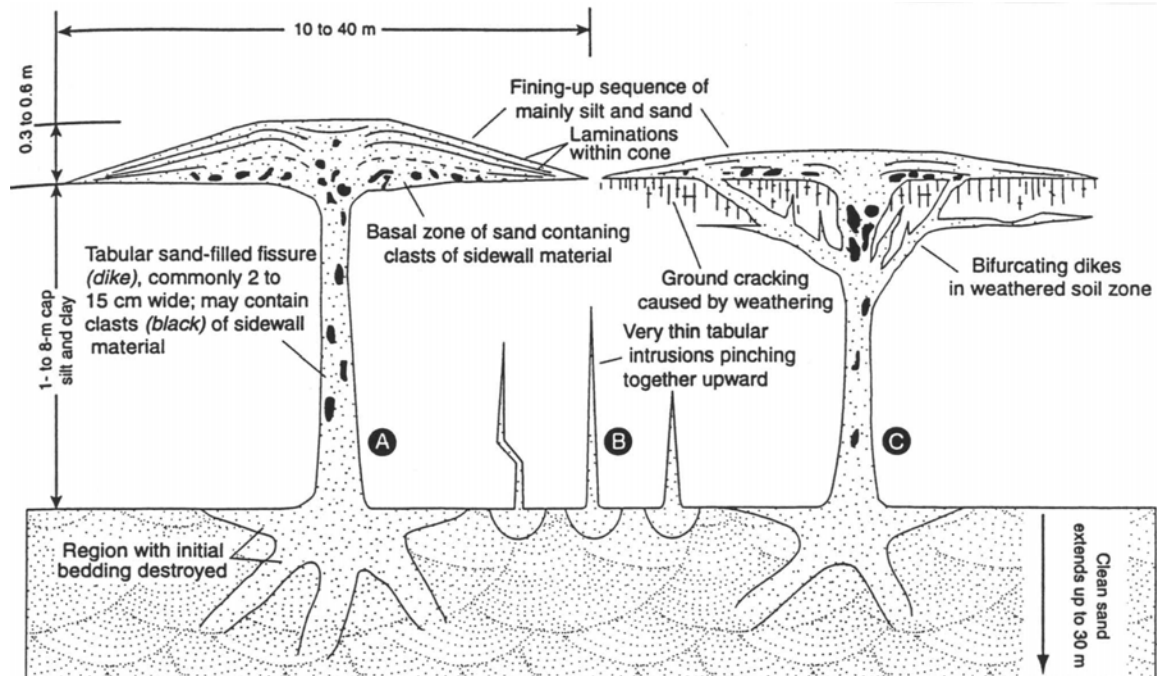
Figure A.3 Schematic cross section of sand blow and related liquefaction features (Obermeier and Pond, 1999): A: Sand dike with sand blow on the surface; B: dikes that pinch together as liquefied soil flow upwards; C: dike characteristics often associated with fractured zone of weathering that develops in highly plastic clays.

One important issue is the historic fact that sites that have experienced liquefaction during a prior earthquake event will likely liquefy again in subsequent ground shaking events of similar magnitude (Youd, 1988; Yasuda & Tohno, 1988). Seismic cone penetration tests (SCPTu) were performed in the NMSZ to evaluate the liquefaction potential over the large developed urban, suburban, and rural regions in this region. Many of the proposed measures discussed herein could also be applied to advantage in other seismic areas of the world.
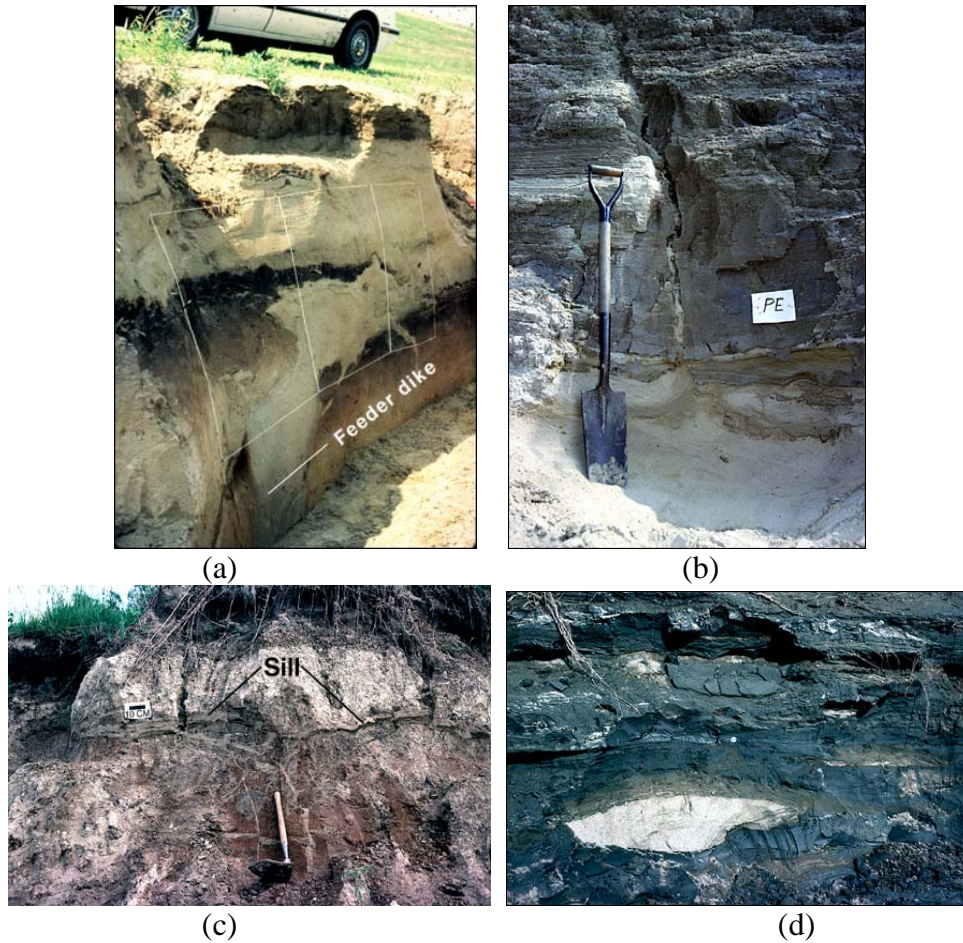
Figure A.4 Photos of liquefaction features in the field (Obermeier, 1998): (a) Vertical section showing vented sand (white sand) with feeder dike; (b) Typical small dike in vertical section; (c) Typical sill that is parallel to the ground surface and is as much as 10 cm thick; (d) The white sand is a thick, dome-shaped sill between blue clay beds

A.2 Test Sites in the New Madrid Seismic Zone

Previously, cone penetration tests (CPT) and seismic cone penetration tests (SCPTu) have been performed by Hryciw (1992) and Schneider (1999) in the NMSZ. Figure A.5 shows locations of CPT, SCPT, and dilatometer test (DMT) tests performed in the heart of the NMSZ by Hryciw (1992), and the analysis results showed that the stress-normalized tip resistance (q_{T1}) and stress-normalized shear wave velocity (V_{s1}) generally decrease with the extent of the paleoliquefaction features found around the sites.
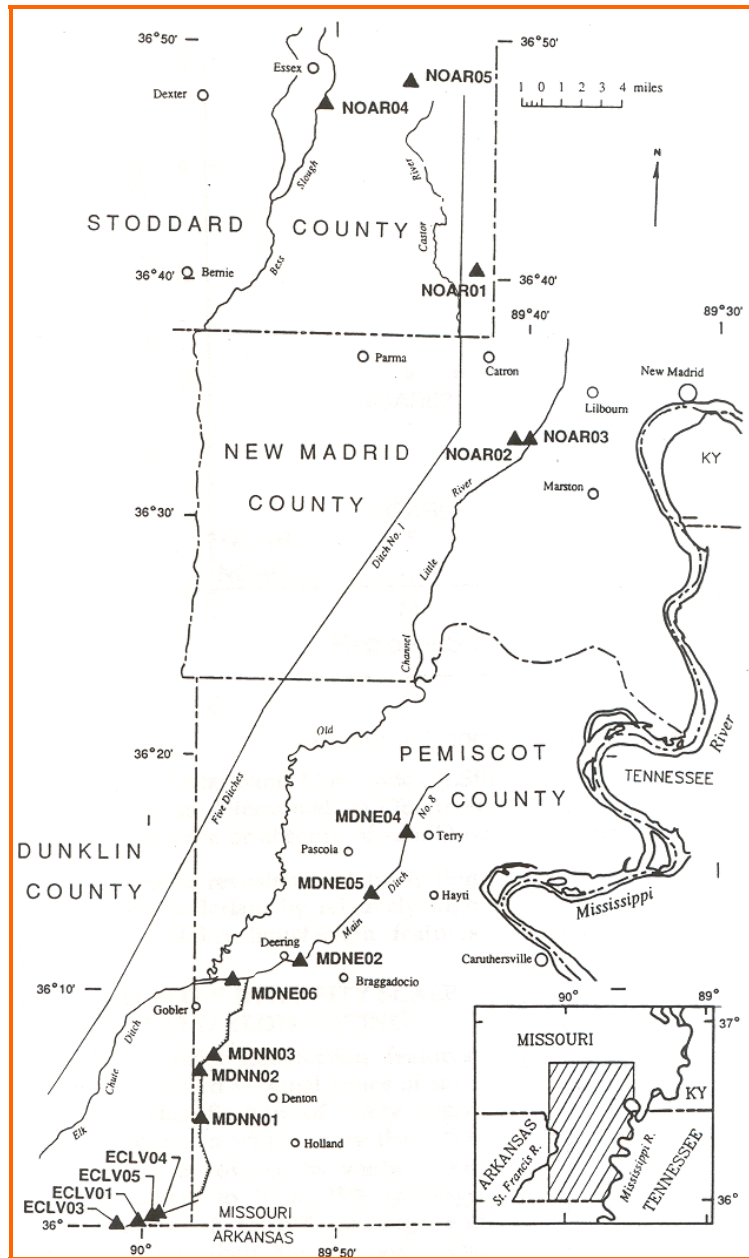
Figure A.5 Locations of CPT, SCPT, and DMT tests performed by Hryciw (1992)
Note: The black triangles represent the test locations.

Since 1998, more cone penetration tests were conducted for the purpose of mapping seismic ground hazards and soil properties in the NMSZ. Field programs have been completed at sites previously mapped by researchers working with the U.S. Geological Survey (USGS), Mid-America Earthquake Center (MAEC), and Center for Earthquake

Research & Information (CERI). Figure A.6 shows the location of the CPT soundings that have been performed in this area since 1998. The tests before 2000 were performed by Schneider (1999), and the results have been discussed in Schneider & Mayne (2000) and Schneider et al. (2001). The test sites can be classified into two categories: paleoliquefaction sites where evidence of prior liquefaction has been found, and non-paleoliquefaction sites where no apparent liquefaction evidence has been observed. Most of the paleoliquefaction sites were mapped by Tuttle (1999) and Tuttle et al. (1999, 2000). Appendix B summarizes all the soundings that are performed at the paleoliquefaction sites. Tests are performed at the non-paliqoliquefaction sites for various purposes, and they are summarized in Appendix C. Although the CPT tests performed at both kinds of sites can help predict the liquefaction response of the soils in future earthquakes, those performed at the paleoliquefaction sites can also be useful for the research in paleoseismology, which is to study the earthquake effects currently preserved in the geologic record in order to extend our knowledge and enhance our understanding of seismic activities (Tuttle, 2001).

Figure A.6 Representative CPT locations in New Madrid Seismic Zone

APPENDIX B

PALEOLIQUEFACTION TEST SITES IN NMSZ

Table B.1 summarizes the cone penetration soundings performed at paleoliquefaction sites in the NMSZ since 1998, including test dates, location and coordinates of the test sites, penetration depth, ground water table, and the sounding type. The tests before 2000 were performed by Schneider (1999). The paleoliquefaction features for most of the test sites are summarized in Tuttle (1999) and Tuttle et al. (1999, 2000). Each of these test sites will be introduced in the following sub-sections, including paleoliquefaction features, test location, test results, as well as inferred soil parameters.

B.1 Shelby Farms Paleoliquefaction Site

The Shelby Farms site located in Memphis, TN (Figure B.1) contains a sand dike mapped by researchers from the University of Memphis (Broughton et al., 2001). Although it is believed that the sand dike was originated from the New Madrid earthquakes, the exact time when it was formed is unknown (Schneider, 1999). A SCPTu sounding was performed approximately 20 m from the sand dike. An aerial photo showing the location of the SCPTu sounding is presented in Figure B.2. The results of this 31-m deep sounding and the inferred soil parameters are shown in Figure B.3.

B.2 Yarbro Excavation Paleoliquefaction Site

Yarbro excavation is a large borrow pit located north of Blytheville (Figure B.4), and its aerial photo is presented in Figure B.5. Liquefaction features have been exposed in walls

of the borrow pit, as well as in walls of islands within the pit. Tuttle (1999) presented the liquefaction features at locations Y1, Y2, and Y3 in the borrow pit. Sand blow and related dikes and sills were exposed at location Y1 (Figure B.6). The sand blow is about 35 cm thick and 3.8 m in width. It consists of medium and fine sand, underlying laminated silt and surrounding the based of a dead tree. The wall at location Y2 exposed a portion of a very large sand blow, which is estimated to be at least 75 m wide and 140 m in length (Figure B.7). As exposed on this wall, the sand blow is up to 55 cm thick and composed of layers of silty sand, fine sand, and medium sand. Figure B.8 shows a photo of the wall at location Y3, where two stacked sand blows were exposed. The lower sand blow composed of medium sand is about 30 cm thick and of limited lateral extent. The upper sand blow is about 2 m thick, and consists of layers of silty sand, fine sand, and medium sand.

Calibrated dates are yielded from radiocarbon-dating of organic materials and soil samples from these locations, and they are with the logging figures. Based on the dating information, Tuttle (1999) suggested that the 1530 event led to the formation of moderate size liquefaction features, and the 1811-1812 events caused the formation of very large liquefaction features, the extrusion of more than 20,000 m^3 of sand, which is now being removed from the excavation pit for use in construction. A SCPTu sounding was performed close to the excavation pit, as shown in Figure B.5. The results of this sounding and the inferred soil parameters are shown in Figure B.9.

B.3 Bugg Site

The Bugg site is located north of Blytheville, Arkansas and very close to the Yarbro excavation site (Figure B.4). A 65 m-long trench exposed sand blow and related sand dikes at this site, as shown in Figure B.10. The sand blow is up to 1.1 m thick, and composed of a layer of fine sand overlain by medium sand. Archeological investigation and radiocarbon dating lead to the interpretation that the sand blow at this site is attributed to the 900 A.D. earthquakes (Tuttle, 1999).

Two SCPTu soundings were performed at this site, as shown in Figure B.11. The first (BUGG01) was adjacent to the exposed liquefaction feature, and the second (BUGG02) was located in an area of no liquefaction features. Figure B.12 and B.13 show the results and inferred soil parameters from these two soundings, respectively.

B.4 Dodd Farm Site

The Dodd Farm site is located southwest of Caruthersville, Missouri, and north of Steele, Missouri (Figure B.14). A trench was excavated across a sand blow at this site, and its logging is shown in Figure B.15. The sand bow deposit is at least 14 m across and up to 1 m thick, consisting of layers of coarse, medium, and silty find sand. The two sand dikes are 5 m and 1.2 m wide. Radiocarbon dating and archeological analysis indicate that liquefaction features at this site are probably formed between 1400 AD and 1670 AD, and likely to be attributed to the 1530 AD earthquakes (Tuttle, 1999).

Three cone penetration soundings were performed at this site, as shown in Figure B.16. Results from two SCPTu sounding and the inferred soil parameters are shown in Figure B.17 and B.18.

B.5 3MS617 Site

The 3MS617 site is located northeast of Blytheville, Arkansas, and close to the Hueys site (Figure B.4). An archeological dig was underway at the time when cone penetration tests were performed at this site. Trenches were being mapped, and artifacts were being collected for ongoing dating process. Three soundings were performed adjacent to an uncovered sand blow that is approximately 1-meter wide (Schneider, 1999), and their locations are shown in Figure B.19. Results of the SCPTu sounding (3MS617-A) and the inferred soil parameters are presented in Figure B.20.

B.6 Johnson Farm Site

The Johnson Farm site is located southwest of Caruthersville, Missouri and north of Steele Missouri (Figure B.14). Two perpendicular and intersecting trenches were excavated in the sand blow at this site. The east-west oriented trench was 68 m long, and its logging is presented in Figure B.21. The main dike shown in this figure is about 47 cm wide, and consists of medium to fine sand. The sand blow close to the dike is about 25 cm thick, and composed of fine sand. The north-south oriented trench was 18 m long, intersecting the other trench at its western end. Logging of this trench (Figure B.22) shows a sand blow deposit up to 1 m thick over a feeder dike of 32 cm in width. The sand blow is composed of silty, very fine sand overlain by medium to coarse sand, and the

dike consists of silty, very fine sand. Information from radiocarbon dating and archeological study suggests that the sand blow may have formed between 800 A.D. and 1000 A.D., likely to be attributed to the 900 A.D. earthquakes (Tuttle, 1999).

One SCPTu sounding was performed close to the intersection of the two trenches, and its location is shown in Figure B.23. Results of this sounding and the inferred parameters are presented in Figure B.24.

B.7 Hueys Site

Hueys site is located north-northeast of Blytheville, Arkansas, and close to the Yarbro and Bugg site (Figure B.4). An initial survey of the site found an elliptical (plan view) sand blow, approximately 20 m wide and 30 m long. Later, a trench excavation exposed the sand blow, sand-blow crater, and related sand dikes, as shown in Figure B.25 (Tuttle, 1999). The sand dikes are very small, for the position of the trench is across the end of sand blow. The crater is filled with very fine to coarse sand. Based on archeological analysis and radiocarbon dating of materials found at this site, the liquefaction event was constrained in the time period between 800 A.D. and 1000 A.D., and was likely to be attributed to the 900 A.D. earthquakes (Tuttle, 1999).

One SCPTu sounding was performed close to the trench, and its location is shown in the aerial photo in Figure B.26. The results of the sounding and inferred soil parameters are presented in Figure B.27.

B.8 Wolf River Site

The Wolf River site is a paleoliquefaction site (Broughton et al., 2001) located east of Memphis, TN, and north of Colliersville, TN, and situated on the north bank of the Wolf River. This site has been discussed previously in Chapter 8 (Figures 8.17 to 8.27).

B.9 Walker Site

The Walker paleoliquefaction site that is located near Marked Tree, AR. On the basis of radiocarbon dating and artifact analysis, the sand blows and related dikes at this site are thought to have formed during a large New Madrid earthquake circa 1530 A.D. (Tuttle et al., 2000; Barnes, 2000). This site has been discussed previously in Chapter 6 (Figures 6.16 to 6.28).

B.10 Nodena Site

The Nodena site is a paleoliquefaction site located northeast of Wilson, Arkansas (Figure B.28). Three trenches were excavated at this site, shown as T1, T2 and T3 in Figure B.29. Logging in trench T1 is presented in Figure B.30. Although no sand dikes were observed at this trench, the sand deposits are interpreted as distal portions of sand blows, due to their similarity in sedimentary character and stratigraphic position to a sand blow deposit in trench T2 [Figure B.31 (A)]. The sand dikes in trench T2 are filled with fine sand, and some of them are connected with the overlying sand blow deposits. Radiocarbon dating and archeological analysis indicate that the liquefaction features were formed between 1450 and 1670, and likely caused by the 1530 earthquakes (Tuttle et al., 2000).

Four cone penetration soundings were performed at this site, as shown in Figure B.29. Results of the SCPTu sounding (WILS02) are representative and inferred parameters are presented in Figure B.32.

B.11 Hillhouse Site

The Hillhouse site is located at Wyatt, Missouri. According to radiocarbon dating of the deposits and analysis of artifacts found at this site, the liquefaction features were formed during the 900 A.D. earthquakes (Tuttle, 1999). This site has been discussed previously in Chapter 6 (Figure 6.29 to 6.39).

B.12 Meramec River Sites

Liquefaction features were found at several sites along lower 12 km of the Meramec River at the south side of Saint Louis, MO. The age of these features is poorly constrained, due to the lack of material for radiocarbon dating and archeological analysis (Tuttle, 1999). Hoffman (1999) suspected that these liquefaction features were resulted from earthquakes located close to St. Louis about 6500 years ago, instead of those in the New Madrid Seismic Zone.

Four cone penetration soundings were performed at paleoliquefaction sites along the Meramec River. Two of them are at the MR25W site located near US 61/67, and the other two are the MR203 site near MO 21. Figure B.33 shows the general location of the two sites. The detailed map for the MR25W site is presented in Figure B.34. Results of

the SCPTu sounding performed at this site and the inferred parameters are shown in Figure B.35. Similarly, Figure B.36 shows the detailed map for the MR203 site, and the results of the two SCPTu soundings performed at this site are shown in Figure B.37 and B.38.

B.13 St. Francis River Sites

Previous archaeological and paleoseismological investigations were performed in 1990 to 1991 at paleoliquefaction sites along St. Francis River near Dexter, Missouri. They are documented in the report by Vaughn (1994). The age of these the paleoliquefaction features was poorly constrained, but they were suspected to be associated with earthquakes that occurred more than 9000 years ago; the seismic source was speculated to be closer than those in the New Madrid Seismic Zone (Vaughn, 1994).

Six cone penetration soundings were performed at 3 different paleoliquefaction sites in this region. Two of these are at Dudley Main Ditch, two at Clodfelter Ditch, and the other two at Wilhelmina Cutoff of St. Francis River. The general locations of the test sites are shown in Figure B.39. The detailed map for the Dudley Main Ditch site is presented in Figure B.40, and results of the SCPTu sounding performed at this site are shown in Figure B.41. Similarly, the detailed map for the Clodfelter Ditch site and the SCPTu results at this site are shown in Figure B.42 and B.43, respectively, and those for the Wilhelmina Cutoff of St. Francis River are shown in Figure B.44 and B.45.

Table B.1 Summary of cone penetration tests performed at the paleoliquefaction sites in the NMSZ since 1998

Date	Sounding	Site	City	State	Latitude N°	Longitude W°	Depth (m)	GWT (m)	Type	Section
16-Sep-98	MEMPH-G	Shelby Farms	Memphis	TN	35.02913	89.70566	33.00	6.00	SCPTu2	B.1
21-Oct-98	YARB01	Yarbro Excavation	Blytheville	AR	35.98233	89.93310	28.00	4.00	SCPTu2	B.2
21-Oct-98	BUGG01	Bugg 40	Blytheville	AR	35.97277	89.90780	37.00	4.00	SCPTu2	B.3
24-Oct-98	BUGG02	Bugg 40	Blytheville	AR	35.97225	89.90792	34.75	4.00	SCPTu2	
22-Oct-98	DODD01	Dodd Farm	Steele	MO	36.09485	89.84831	31.45	4.45	SCPTu2	B.4
22-Oct-98	DODD02	Dodd Farm	Steele	MO	36.09458	89.84833	25.60	4.00	SCPTu2	
23-Oct-98	DODD03	Dodd Farm	Steele	MO	36.09423	89.84816	32.60	4.00	CPTu2	
23-Oct-98	3MS617-A	3MS617	Blytheville	AR	35.99262	89.83556	30.70	5.50	SCPTu2	B.5
24-Oct-98	3MS617-C	3MS617	Blytheville	AR	35.99276	89.83553	30.55	4.00	CPTu2	
24-Oct-98	3MS617-D	3MS617	Blytheville	AR	35.99266	89.83526	15.90	4.00	CPTu2	
25-Oct-98	JOHN01	Johnson Farm	Steele	MO	36.11920	89.84393	16.50	7.00	SCPTu2	B.6
25-Oct-98	HUEY01	Huey House	Blytheville	AR	35.98353	89.88650	26.30	4.75	SCPTu2	B.7
9-Jul-00	WOLF1	Northern Bank of Wolf River	Memphis	TN	35.09949	89.69931	26.25	6.00	SCPTu2	B.8
9-Jul-00	WOLF2	Northern Bank of Wolf River	Memphis	TN	35.09947	89.69919	28.9	6.00	CPTu2	
9-Jul-00	WOLF3	Northern Bank of Wolf River	Memphis	TN	35.09951	89.69948	25.1	6.00	CPTu2	
9-Jul-00	WOLF4	Northern Bank of Wolf River	Memphis	TN	35.09932	89.70006	20.1	6.00	CPTu2	
10-Jul-00	WOLF5	Northern Bank of Wolf River	Memphis	TN	35.09982	89.70285	31.7	6.00	SCPTu2	
10-Jul-00	WOLF6	Northern Bank of Wolf River	Memphis	TN	35.09980	89.70301	15.8	6.00	CPTu2	
10-Jul-00	WOLF7	Northern Bank of Wolf River	Memphis	TN	35.09983	89.70322	20.55	6.00	RCPTu2	

Table B.1 Summary of cone penetration tests performed at the paleoliquefaction sites in the NMSZ since 1998 (Continued)

Date	Sounding	Site	City	State	Latitude N°	Longitude W°	Depth (m)	GWT (m)	Type	Section
14-Aug-00	MTREE01	Walker Site	Marked Tree	AR	35.58316	90.38909	32.05	5.00	SCPTu2	
15-Aug-00	MTREE02	Walker Site	Marked Tree	AR	35.58324	90.38912	8.95	5.00	RCPTu2	
15-Aug-00	MTREE03	Walker Site	Marked Tree	AR	35.58320	90.38915	13.68	5.00	RCPTu2	
15-Aug-00	MTREE04	Walker Site	Marked Tree	AR	35.58317	90.38918	15.70	5.00	RCPTu2	
15-Aug-00	MTREE05	Walker Site	Marked Tree	AR	35.58313	90.38921	15.70	5.00	RCPTu1	
15-Aug-00	MTREE06	Walker Site	Marked Tree	AR	35.58311	90.38922	15.80	5.00	RCPTu1	B.9
15-Aug-00	MTREE07	Walker Site	Marked Tree	AR	35.58307	90.38924	15.57	5.00	RCPTu1	
15-Aug-00	MTREE08	Walker Site	Marked Tree	AR	35.58304	90.38925	15.73	5.00	RCPTu1	
16-Aug-00	MTREE09	Walker Site	Marked Tree	AR	35.58383	90.38992	15.55	5.00	RCPTu2	
16-Aug-00	MTREE10	Walker Site	Marked Tree	AR	35.58379	90.38997	15.65	5.00	RCPTu2	
16-Aug-00	MTREE11	Walker Site	Marked Tree	AR	35.58377	90.38999	15.80	5.00	RCPTu2	
17-Aug-00	MTREE12	Walker Site	Marked Tree	AR	35.58375	90.39002	25.93	5.00	SCPTu2	
17-Aug-00	MTREE13	Walker Site	Marked Tree	AR	35.58373	90.39005	8.05	5.00	RCPTu2	
17-Aug-00	MTREE14	Walker Site	Marked Tree	AR	35.58371	90.39009	15.48	5.00	RCPTu2	
6-Mar-01	WILS02	Nodena Site	Wilson	AR	35.60202	89.97719	21.43	6.00	SCPTu2	
6-Mar-01	WILS04	Nodena Site	Wilson	AR	35.60208	89.97722	16.20	6.00	CPTu2	B.10
6-Mar-01	WILS06	Nodena Site	Wilson	AR	35.60215	89.97715	22.93	6.00	RCPTu1	
7-Mar-01	WILS07	Nodena Site	Wilson	AR	35.60217	89.97711	16.43	6.00	CPTu2	
8-Mar-01	WYAT01	Hillhouse Site	Wyatt	MO	36.92609	89.15822	25.30	2.70	SCPTu2	
8-Mar-01	WYAT03	Hillhouse Site	Wyatt	MO	36.92685	89.15717	12.03	2.70	CPTu2	B.11
9-Mar-01	WYAT04	Hillhouse Site	Wyatt	MO	36.92706	89.15572	23.00	2.70	RCPTu2	
9-Mar-01	WYAT05	Hillhouse Site	Wyatt	MO	36.92740	89.15610	19.63	2.70	RCPTu2	

Table B.1 Summary of cone penetration tests performed at the paleoliquefaction sites in the NMSZ since 1998 (Continued)

Date	Sounding	Site	City	State	Latitude N°	Longitude W°	Depth (m)	GWT (m)	Type	Section
20-Jun-01	MER01	MR25W - Meramec River near US 61/67	St. Louis	MO	38.45882	90.35043	19.75	2.00	SCPTu2	B.12
20-Jun-01	MER02	MR25W - Meramec River near US 61/67	St. Louis	MO	38.45882	90.35043	18.68	2.00	CPTu2	
21-Jun-01	MER03	MR203 - Meramec River near MO 21	St. Louis	MO	38.46538	90.41467	12.98	2.00	SCPTu2	
21-Jun-01	MER04	MR203 - Meramec River near MO 21	St. Louis	MO	38.46502	90.41460	13.55	2.00	SCPTu2	
19-Jun-01	DEX01	DM1 - Dudley Main Ditch near St. Francis River	Dudley	MO	36.70038	90.13251	29.02	9.00	SCPTu2	B.13
19-Jun-01	DEX02	DM1 - Dudley Main Ditch near St. Francis River	Dudley	MO	36.70038	90.13251	19.33	9.00	RCPTu2	
22-Jun-01	DEX03	Clodfelter Ditch near St. Francis River	Dudley	MO	36.65318	90.13231	30.03	8.50	SCPTu2	
22-Jun-01	DEX031	Clodfelter Ditch near St. Francis River	Dudley	MO	36.65321	90.13226	28.90	8.50	RCPTu2	
22-Jun-01	DEX04	Wilhelmina Cutoff of St. Francis River	Dudley	MO	36.53725	90.17570	26.43	6.50	SCPTu2	
22-Jun-01	DEX05	Wilhelmina Cutoff of St. Francis River	Dudley	MO	36.53725	90.17570	26.50	6.50	RCPTu2	

346
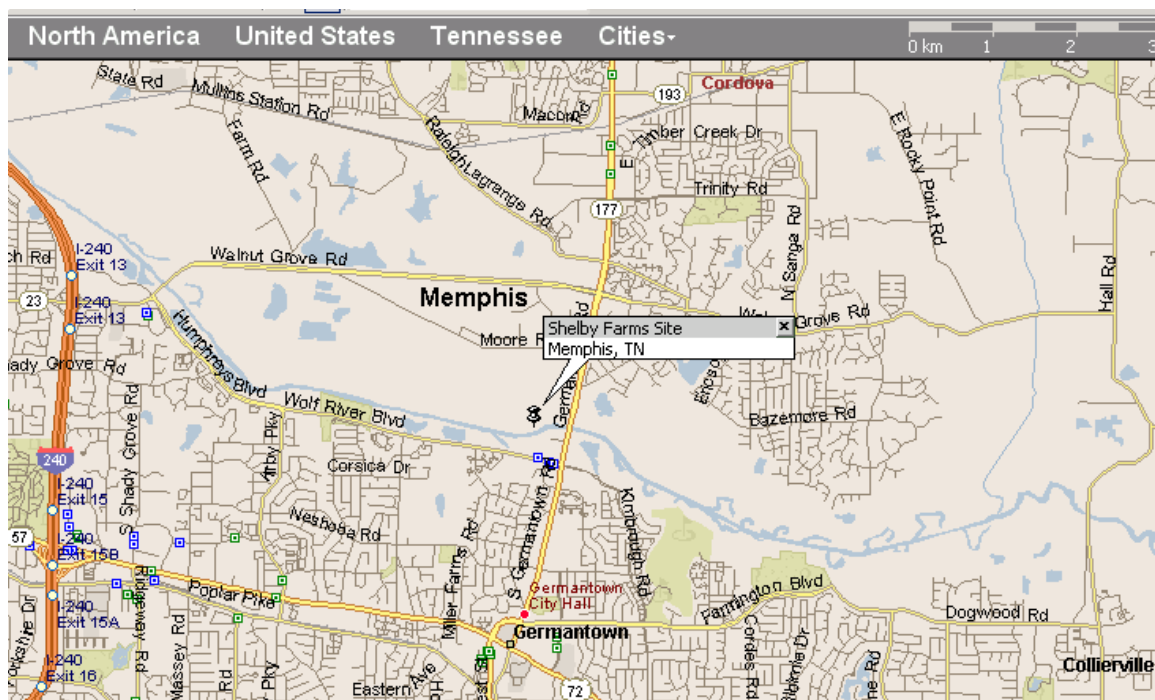
Figure B.1 Map showing the general location of the Shelby Farms site
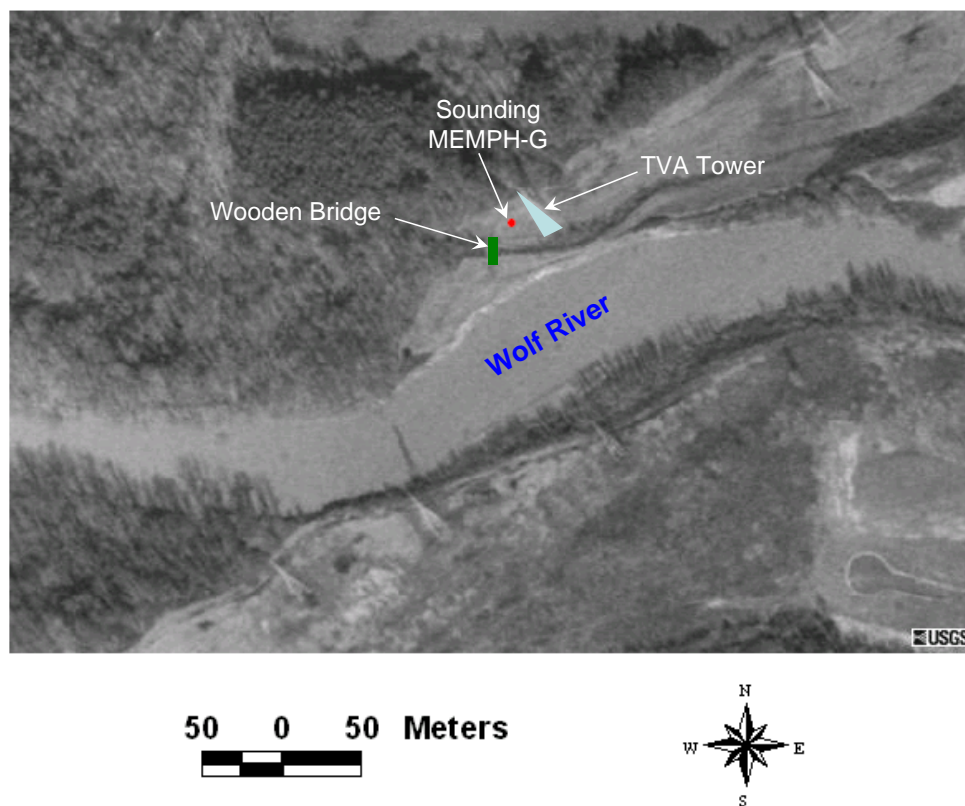
Figure B.2 Aerial photo showing the location of the SCPTu sounding (MEMPH-G) performed at the Shelby Farms site (Aerial photo from http://terraserver.microsoft.com)
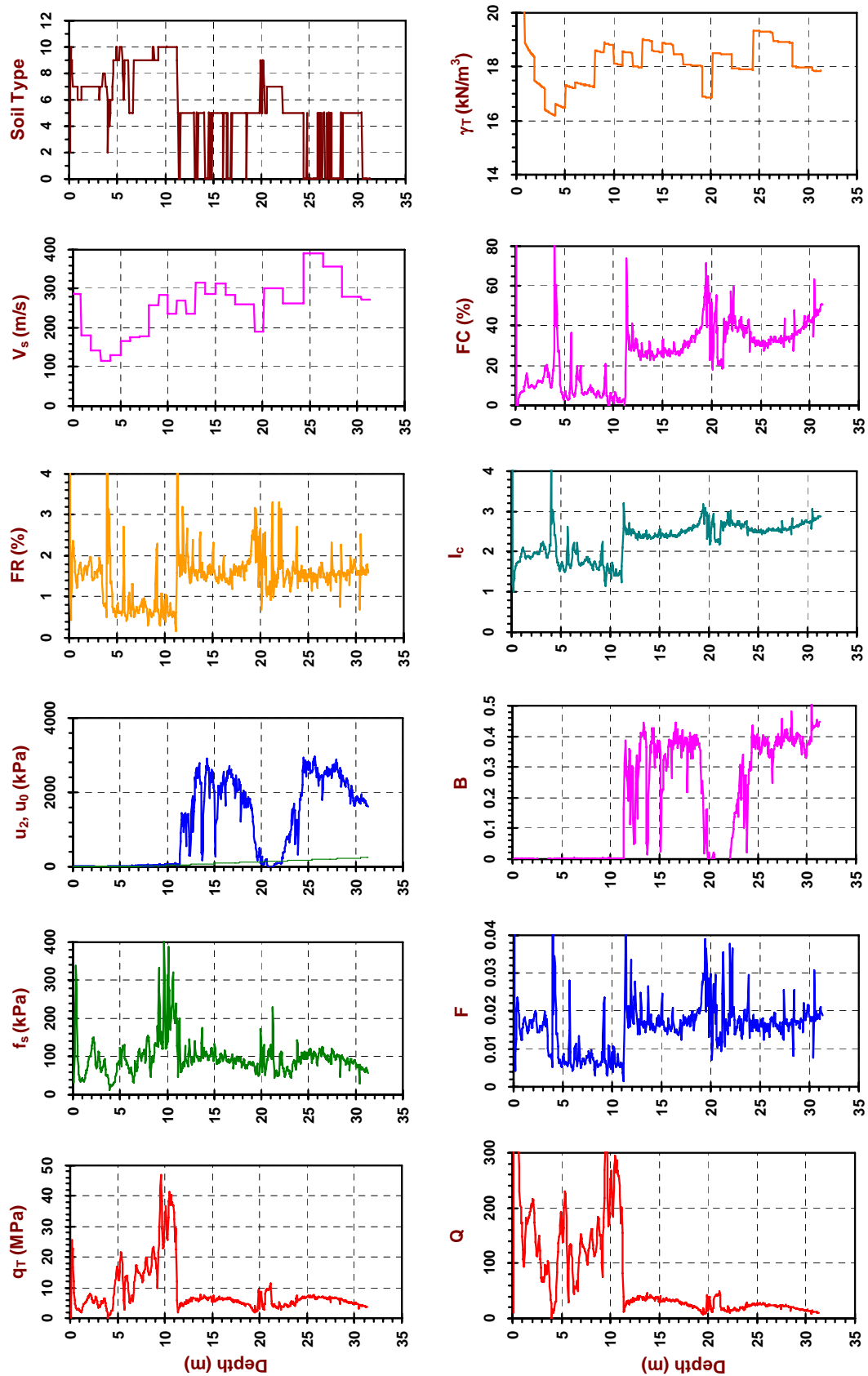
Figure B.3 Results from the SCPTu sounding (MEMPH-G) performed at Shelby Farms site in Memphis, Tennessee
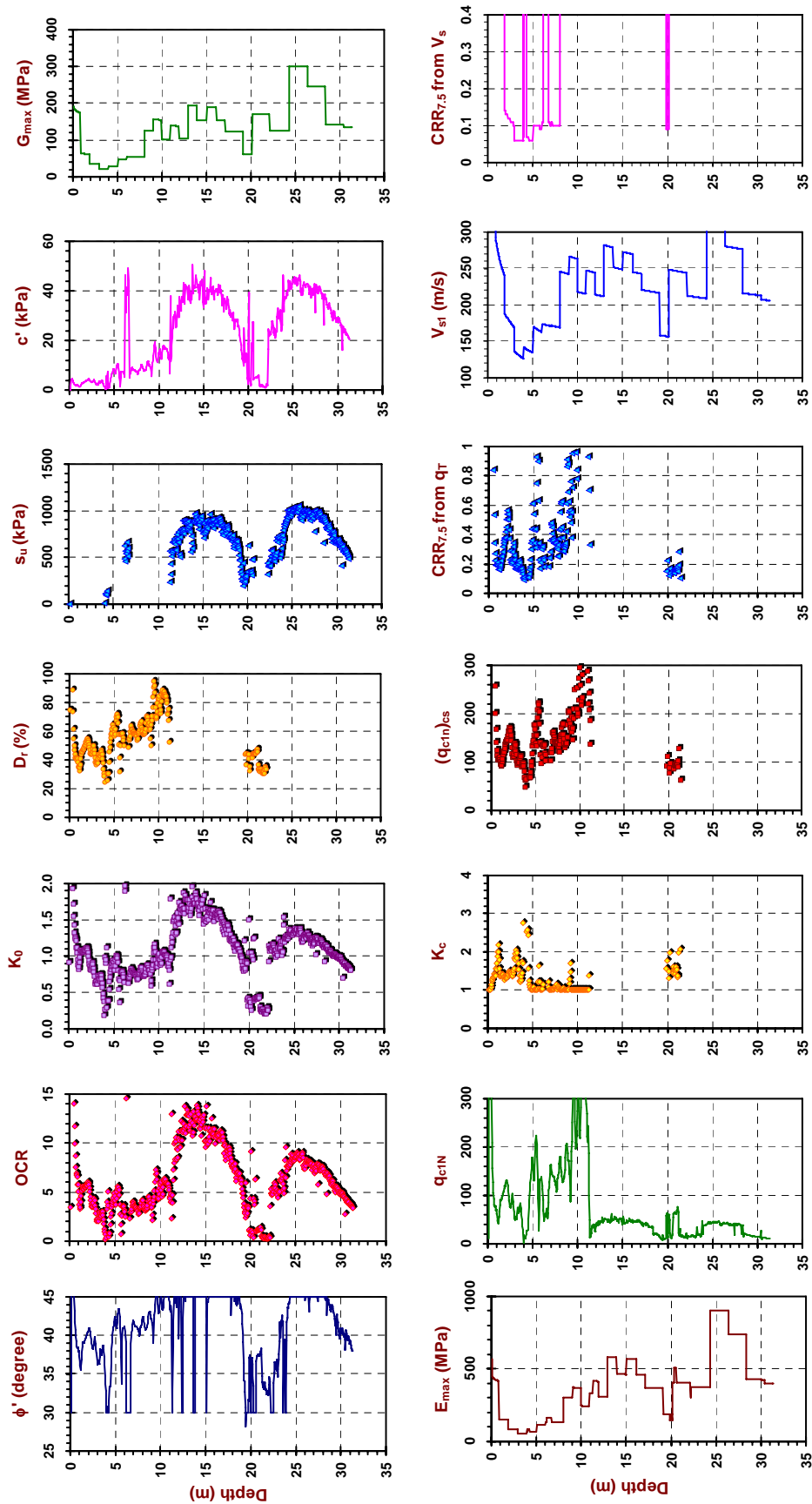
Figure B.3 Results from the SCPTu sounding (MEMPH-G) performed at Shelby Farms site in Memphis, Tennessee (Continued)
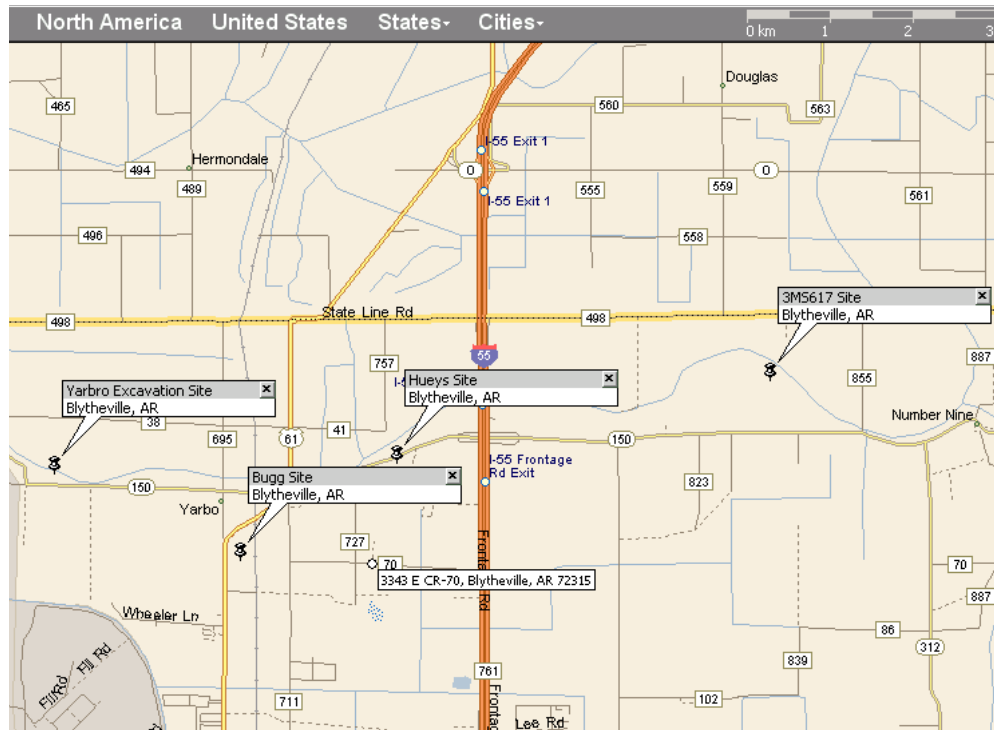
Figure B.4 Map showing the general location of Yarbro Excavation site, Bugg site, Hueys site, and 3MS617 site in Bytheville, Arkansas
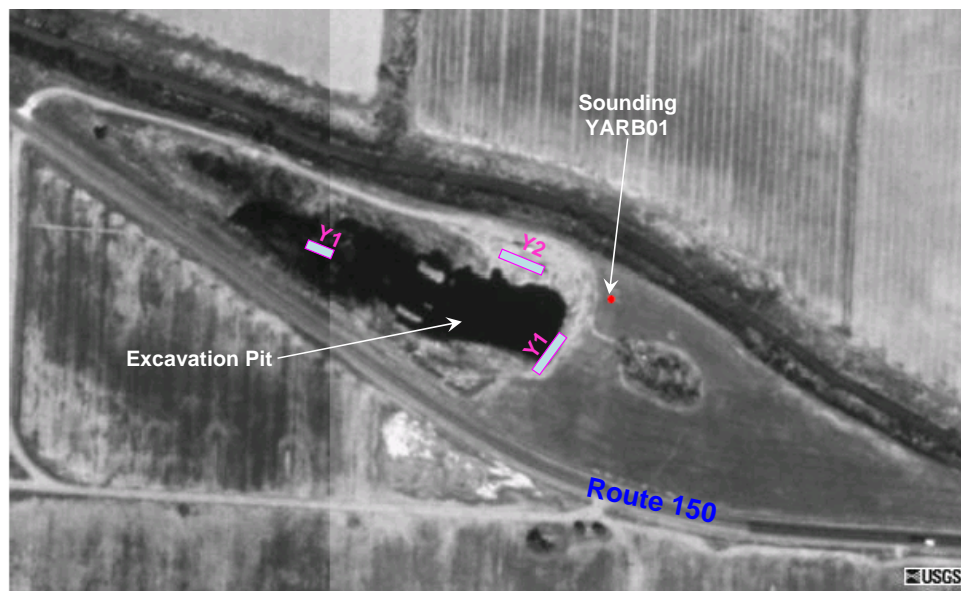
Figure B.5 Aerial photo showing the location of the logged liquefaction features and the SCPTu sounding (YARB01) performed at the Yarbro Excavation site in Blytheville, Arkansas (Photo from http://terraserver.microsoft.com)
Note: Y1, Y2, and Y3 are logged liquefaction features

350
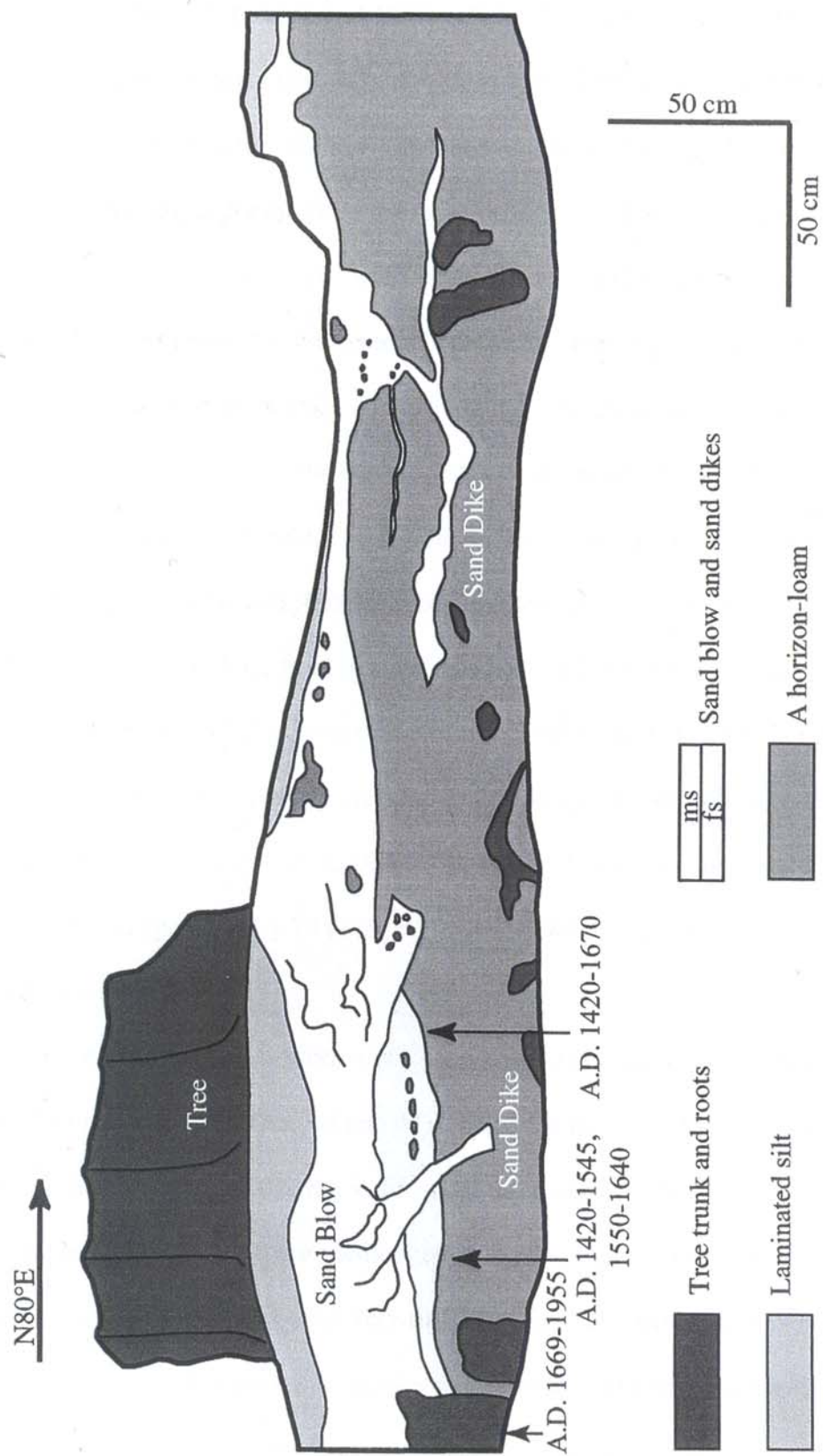
Figure B.6 Log of exposure at Y1 location of Yarbro excavation in Blytheville, Arkansas (Tuttle, 1999)
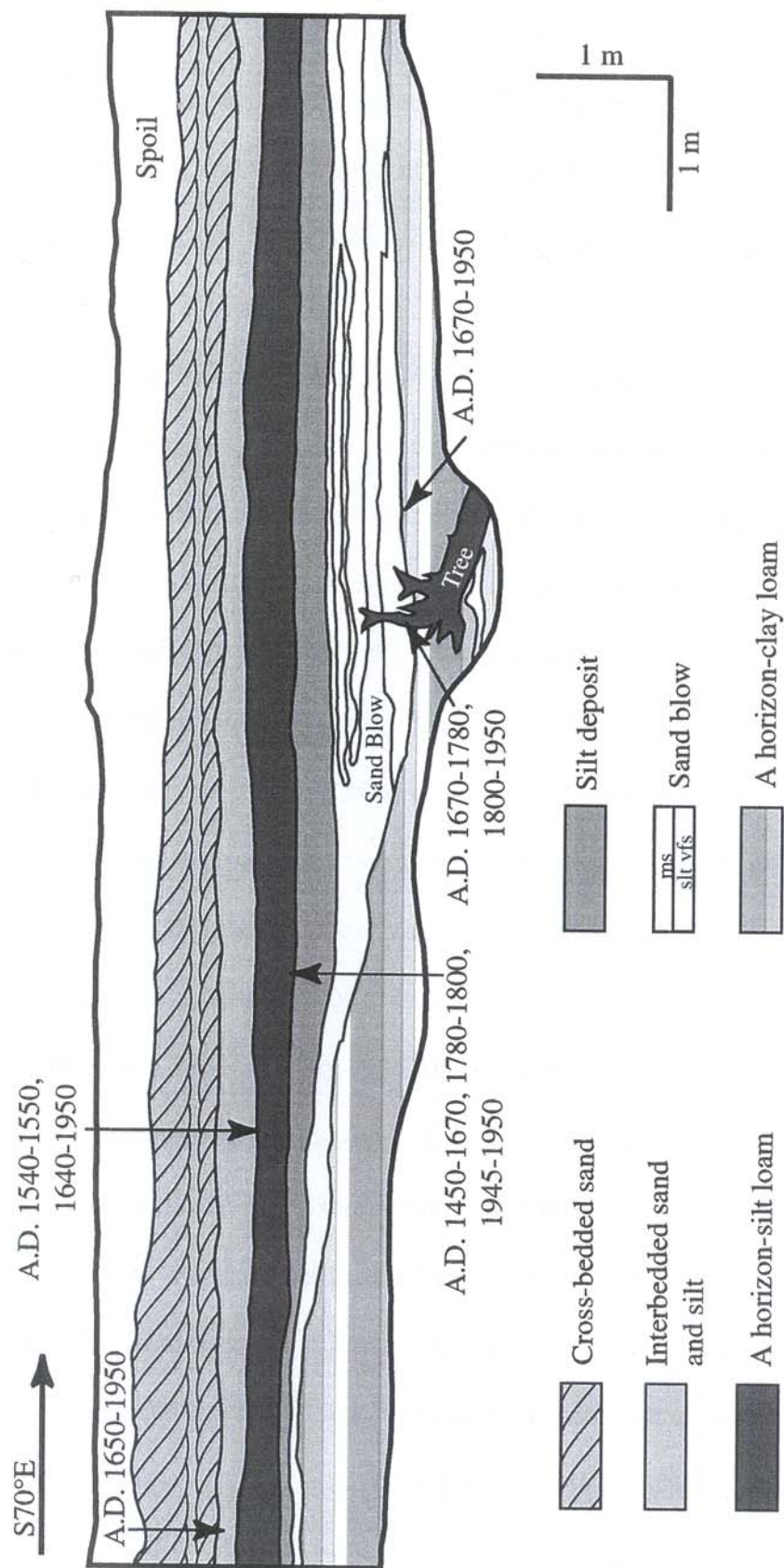
Figure B.7 Log of exposure at Y2 location of Yarbro excavation in Blytheville, Arkansas (Tuttle, 1999)

352

Figure B.8 Photo of exposure at Y3 location of Yarbro excavation in Blytheville, Arkansas (Tuttle, 1999)
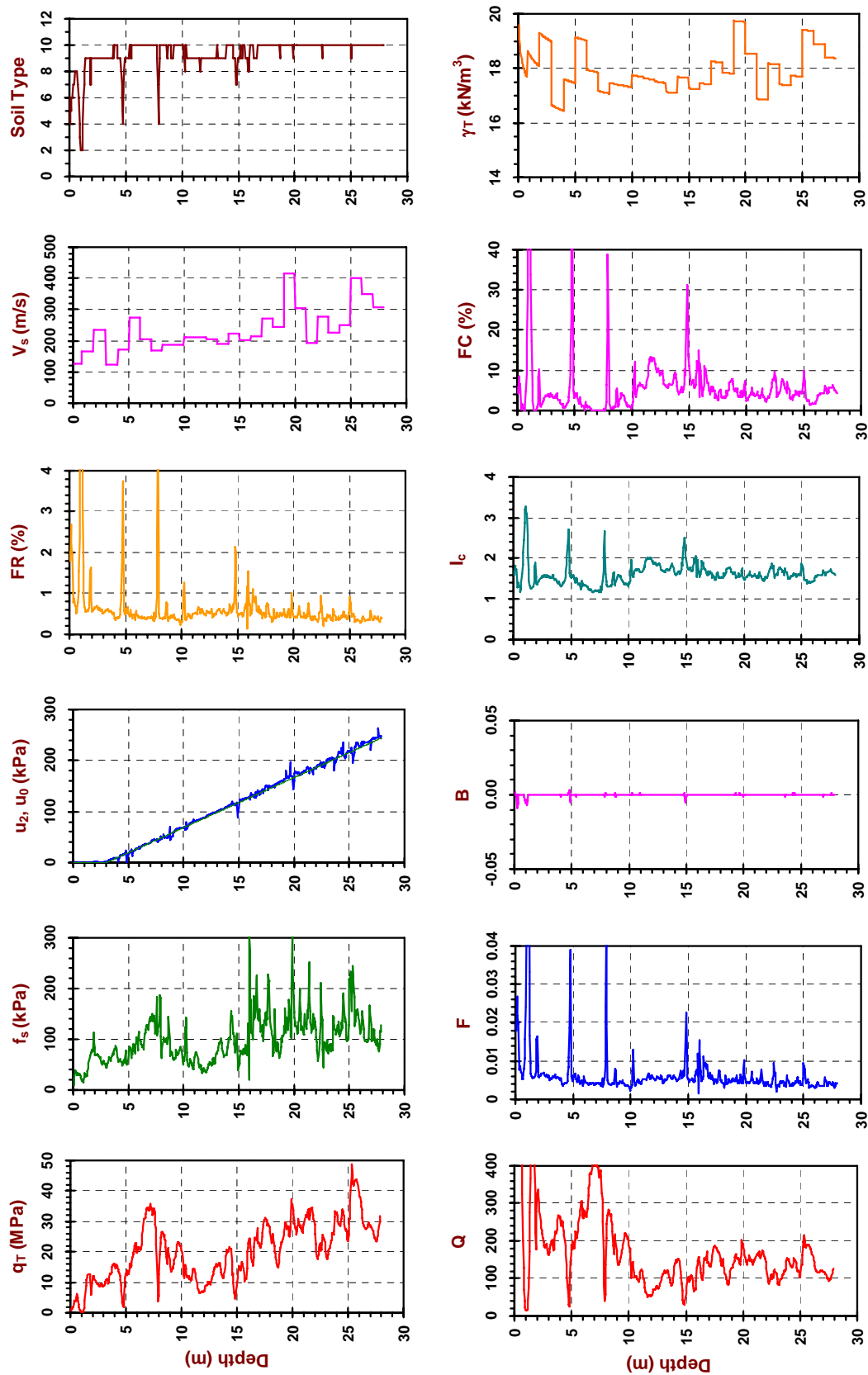
353

Figure B.9 Results from the SCPTu sounding (YARB0l) performed at the Yarbro Excavation site in Blytheville, Arkansas

354

Figure B.9 Results from the SCPTu sounding (YARB01) performed at the Yarbro Excavation site in Blytheville, Arkansas (Continued)

355
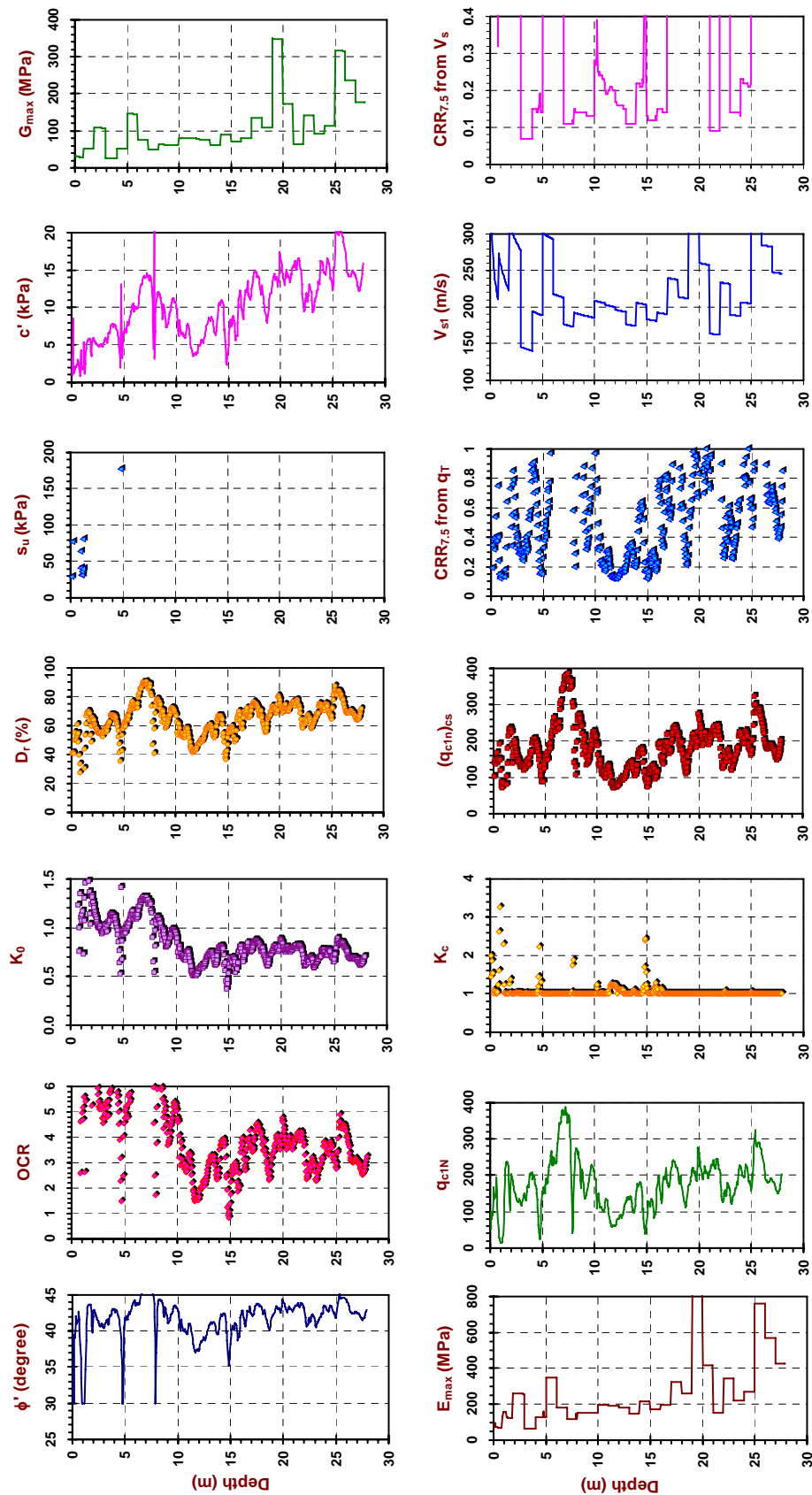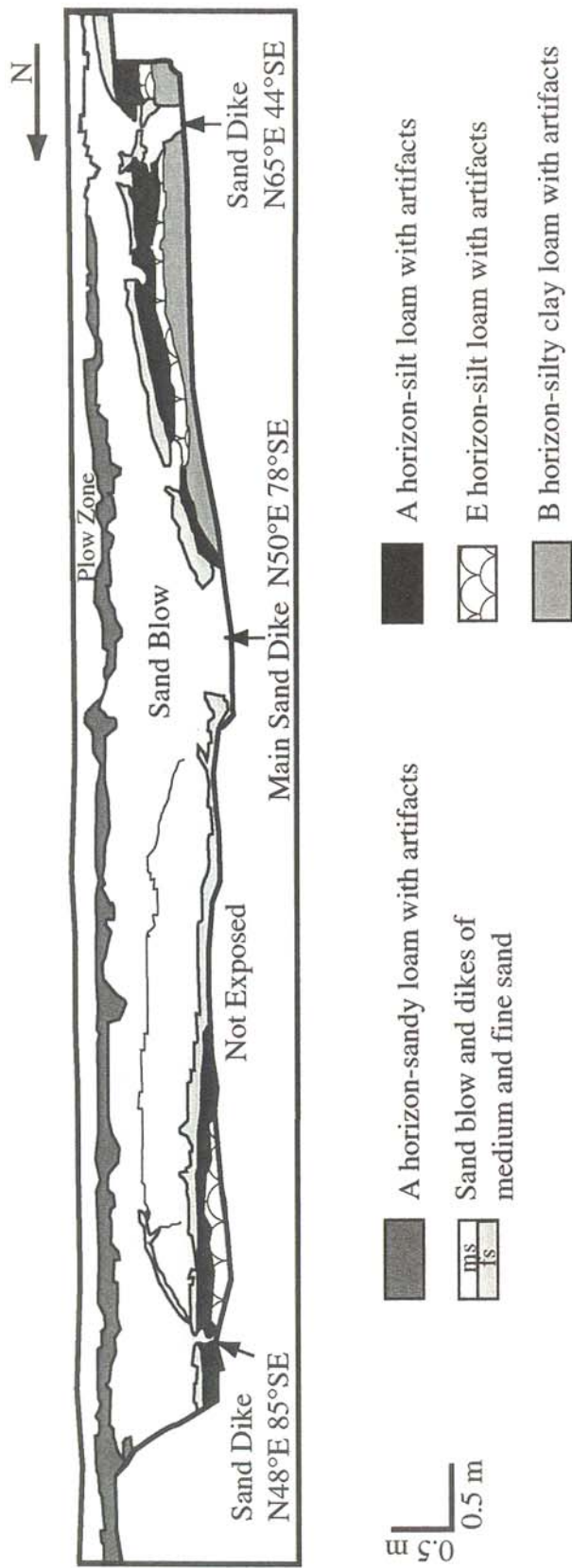
Figure B.10 Log of exposure at Bugg site in Blytheville, Arkansas (Tuttle, 1999)

356
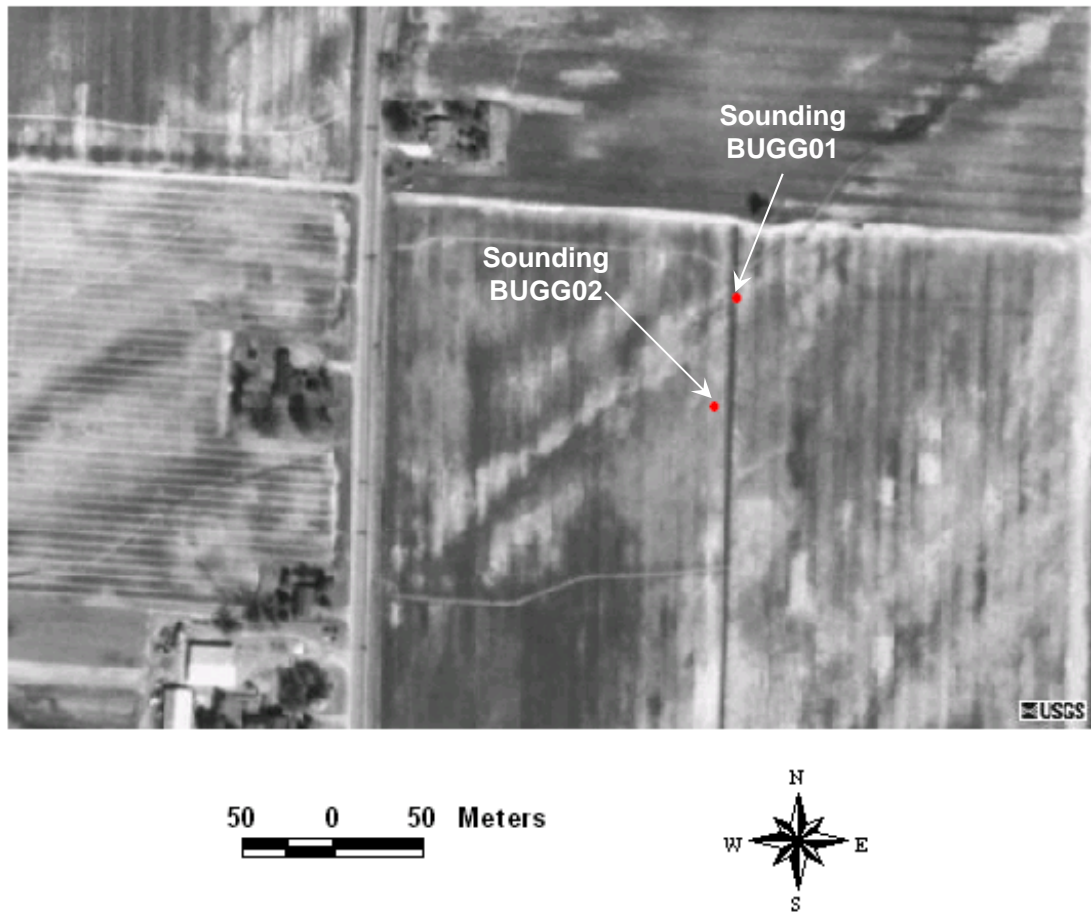
Figure B.11 Aerial photo showing the location of the SCPTu soundings (BUGG01 and BUGG02) performed at Bugg site in Blytheville, Arkansas (Photo from http://terraserver.microsoft.com)
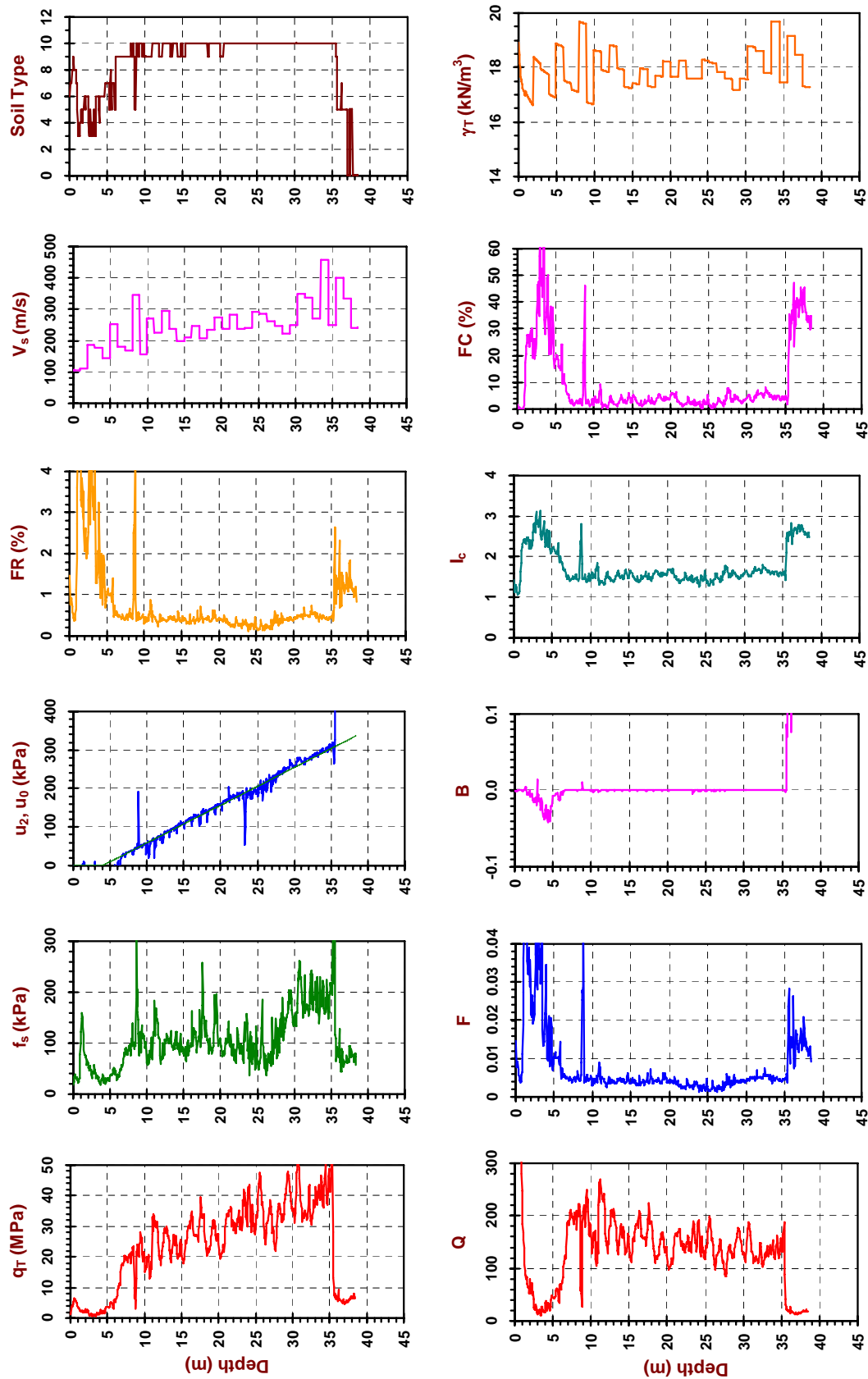
Figure B.12 Results from the SCPTu sounding (BUGG01) performed at Bugg site in Blytheville, Arkansas

358

Figure B.12 Results from the SCPTu sounding (BUGG01) performed at Bugg site in Blytheville, Arkansas (Continued)

359

Figure B.13 Results from the SCPTu sounding (BUGG02) performed at Bugg site in Blytheville, Arkansas

360

Figure B.13 Results from the SCPTu sounding (BUGG02) performed at Bugg site in Blytheville, Arkansas (Continued)

361
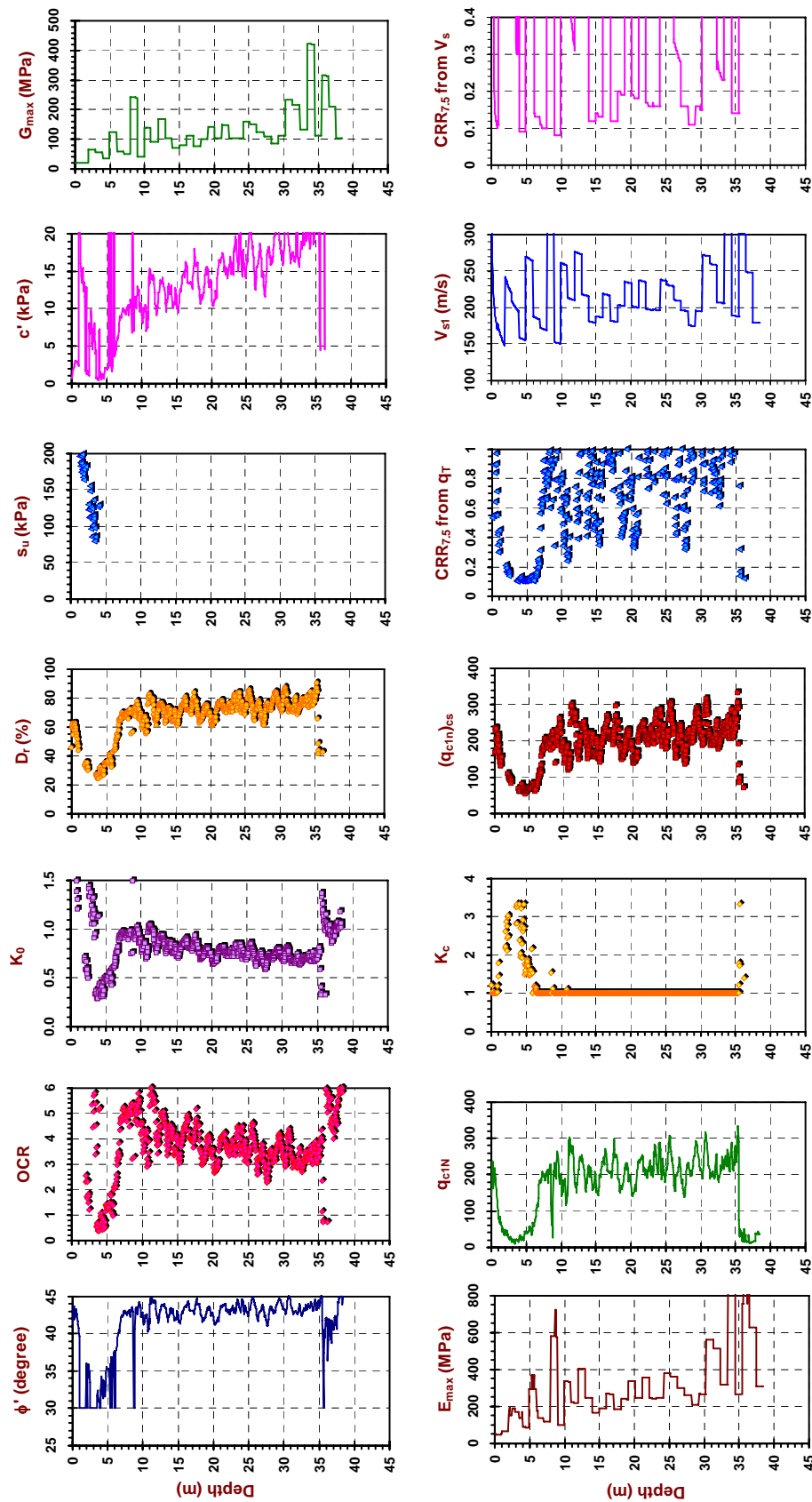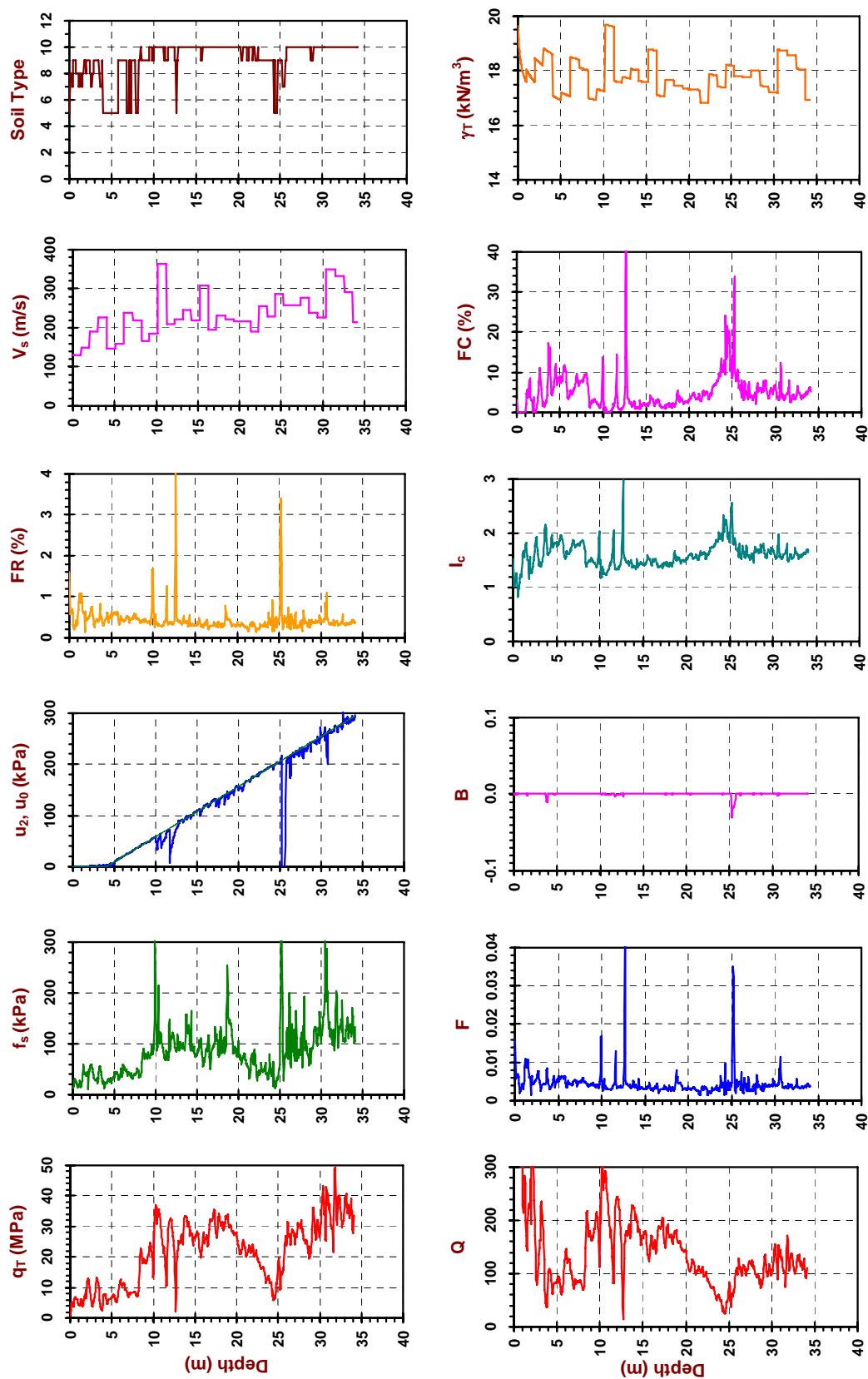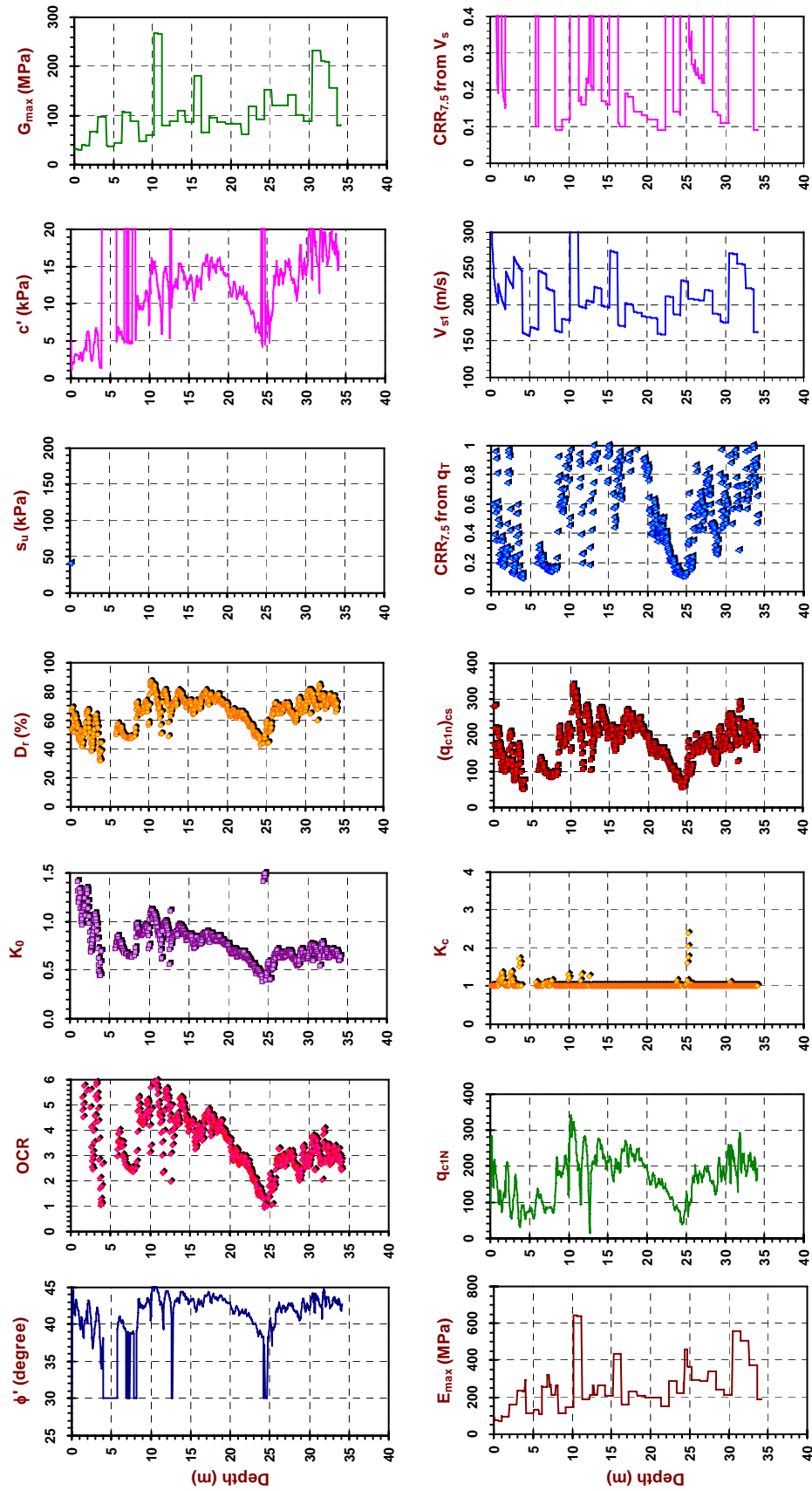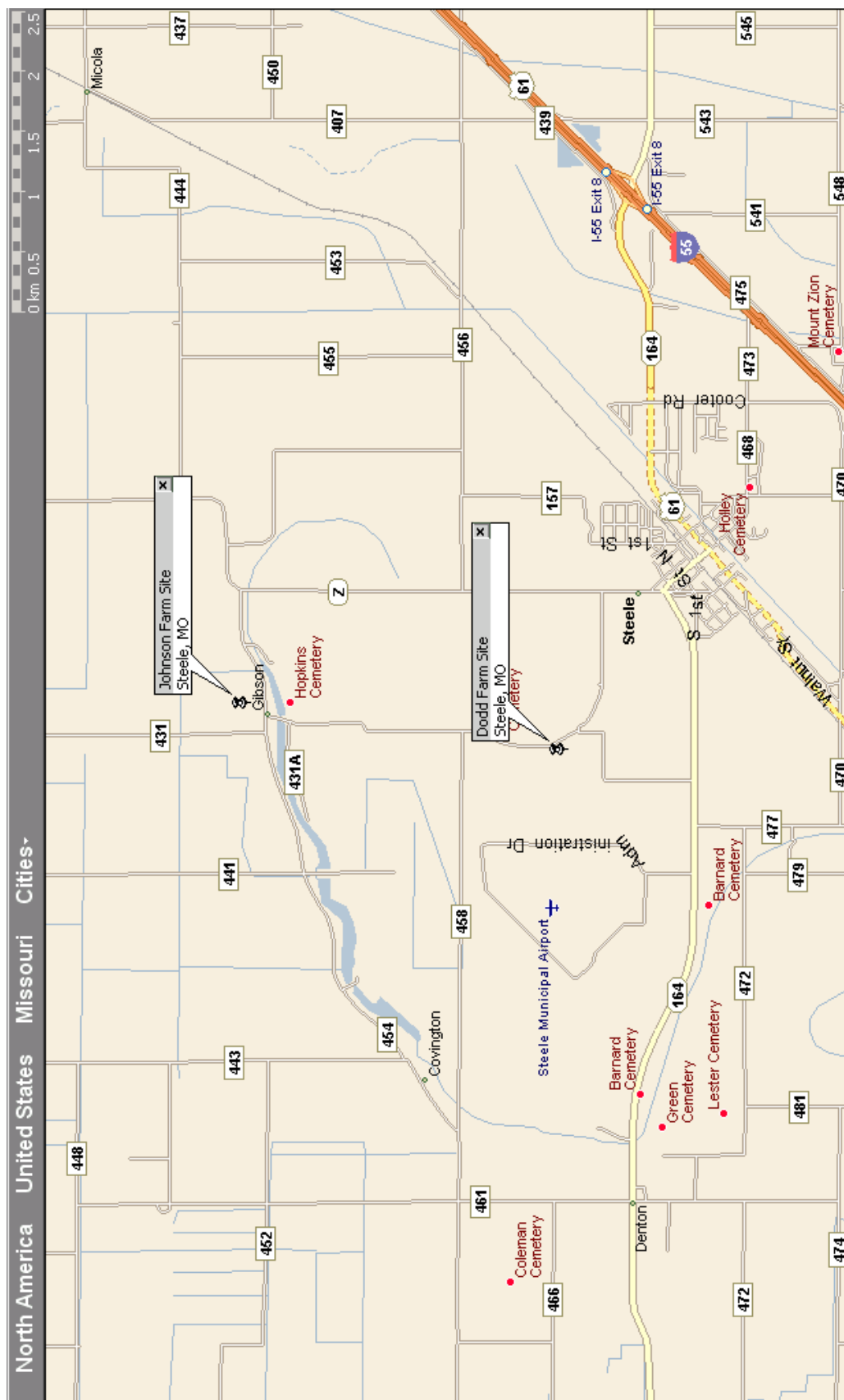
Figure B.14 Map showing the general location of the Dodd Farm site and Johnson Farm site
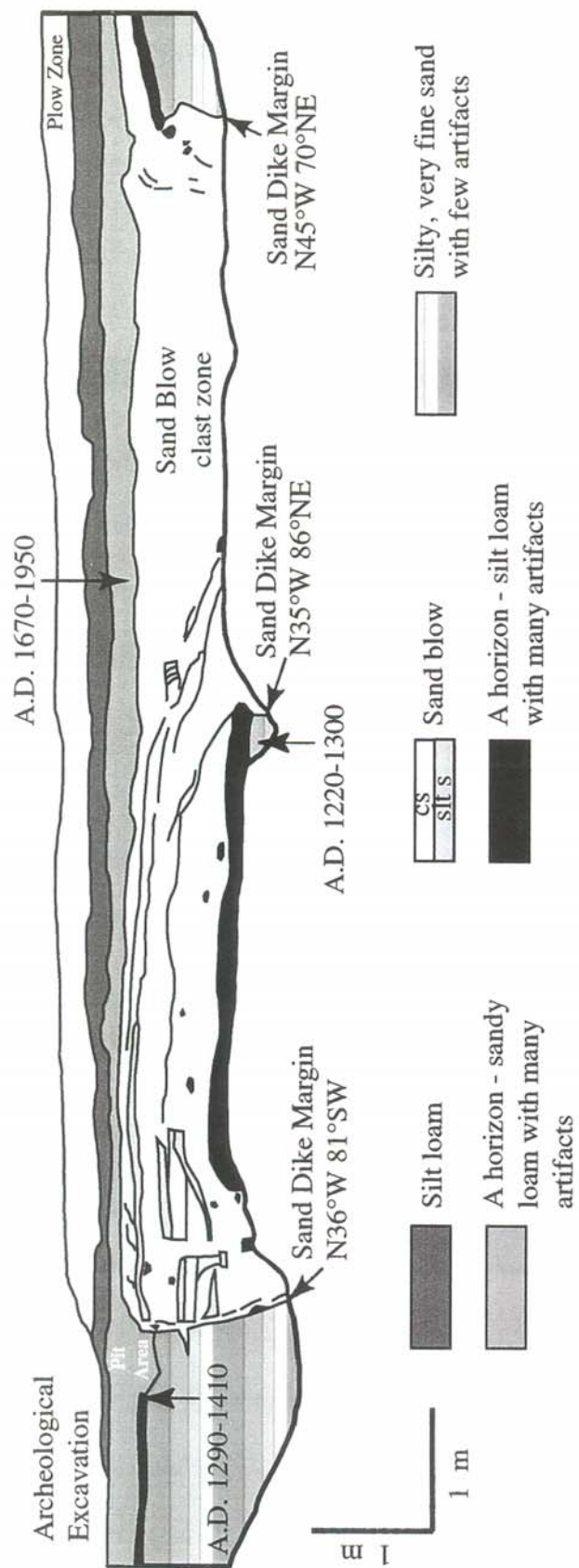
Figure B.15 Log of exposure at Dodd Farm site in Steele, Tennessee (Tuttle, 1999)
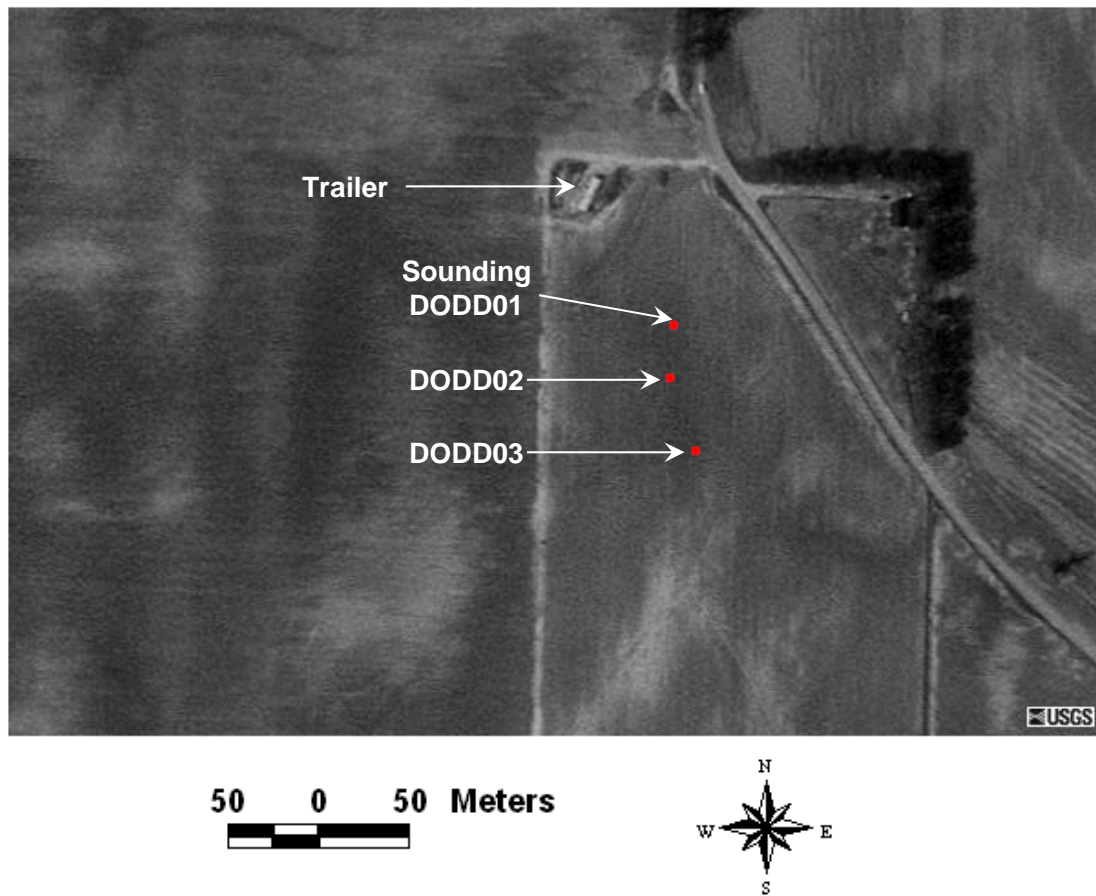
Figure B.16 Aerial photo showing the location of the SCPTu sounding performed at Dodd farm site in Steele, Tennessee (Aerial photo from http://terraserver.microsoft.com)
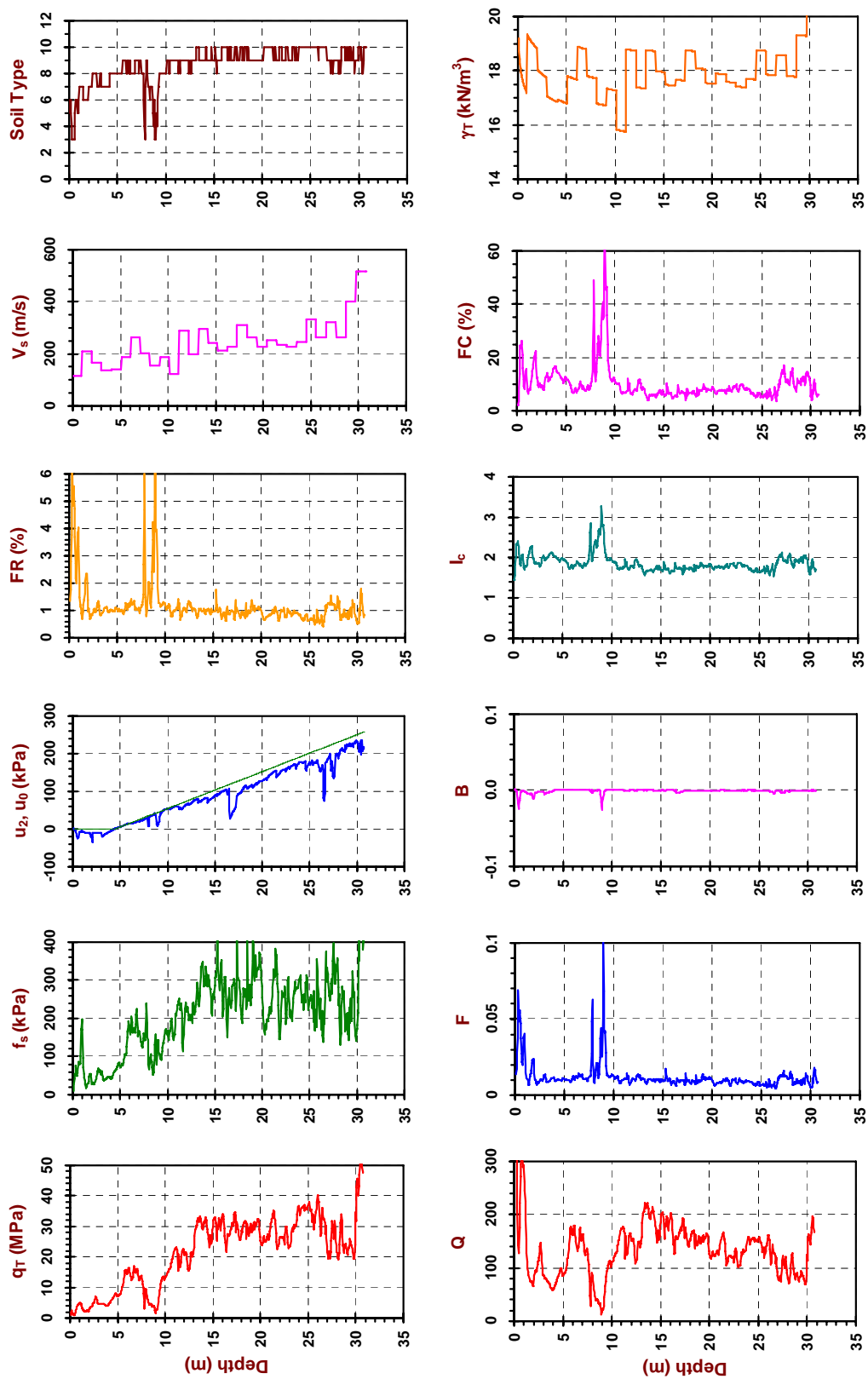
Figure B.17 Results from the SCPTu sounding (DODD01) performed at Dodd Farm site in Steele, Tennessee
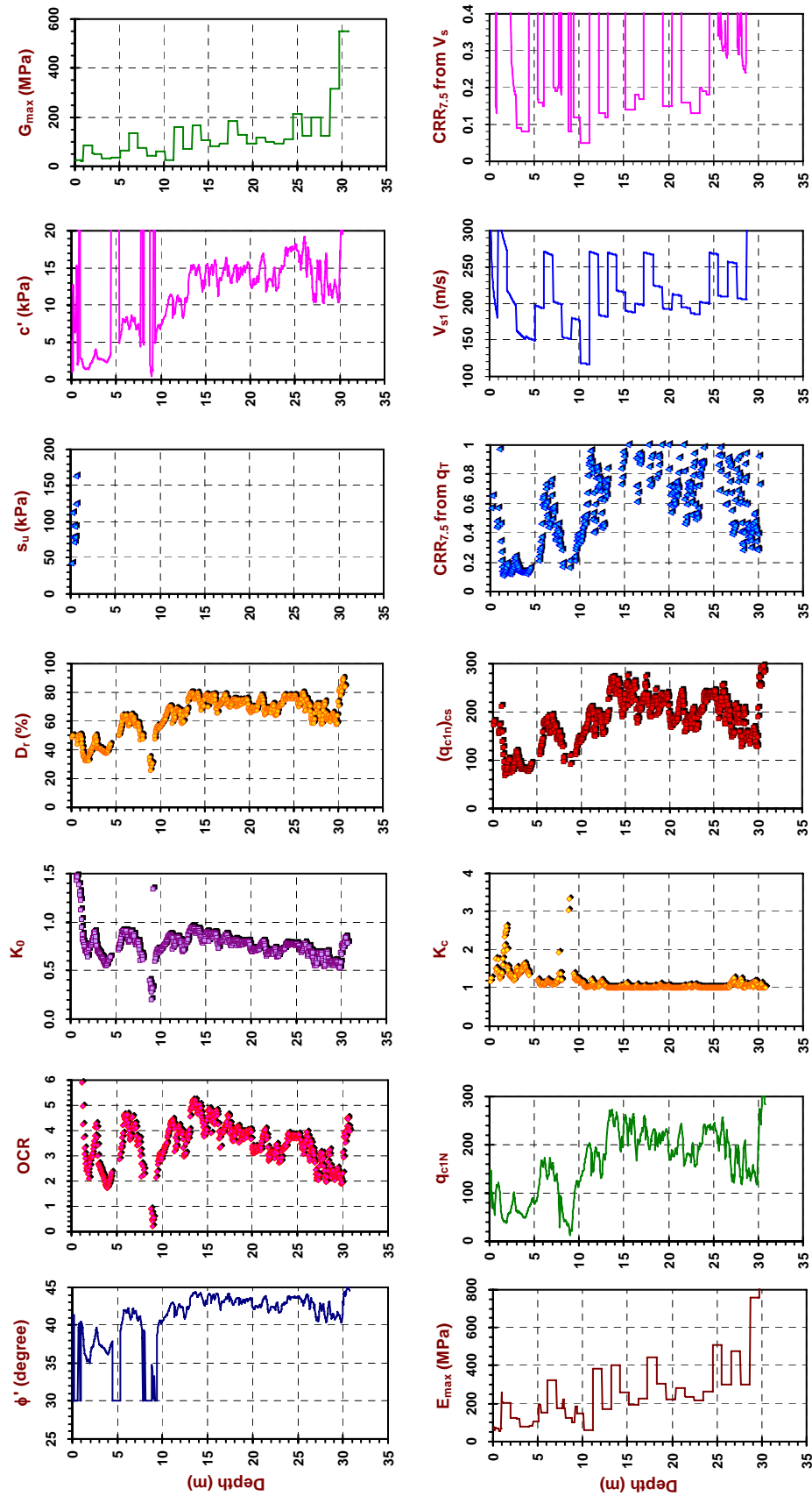
Figure B.17 Results from the SCPTu sounding (DODD01) performed at Dodd Farm site in Steele, Tennessee (Continued)
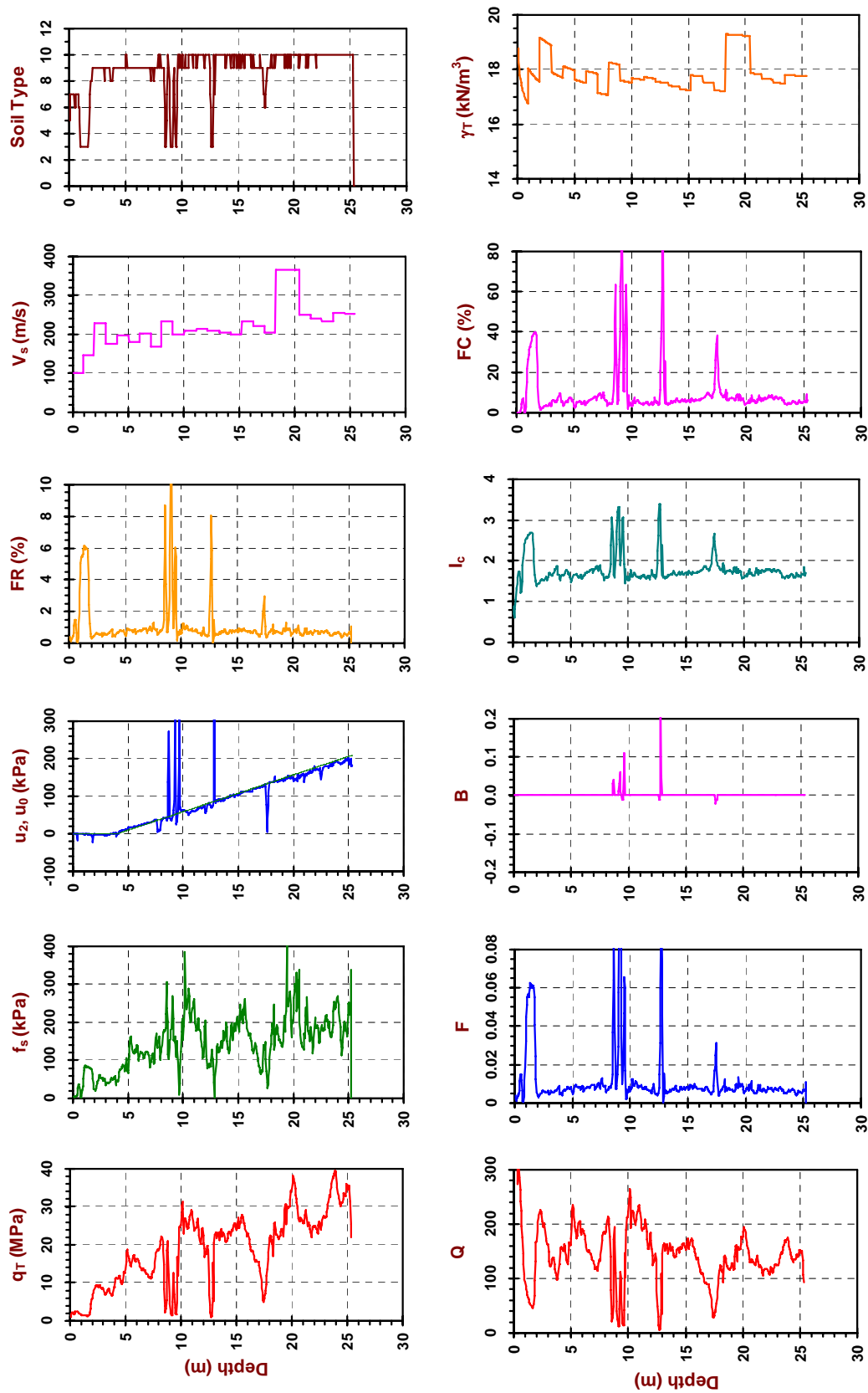
Figure B.18 Results from the SCPTu sounding (DODD02) performed at Dodd Farm site in Steele, Tennessee
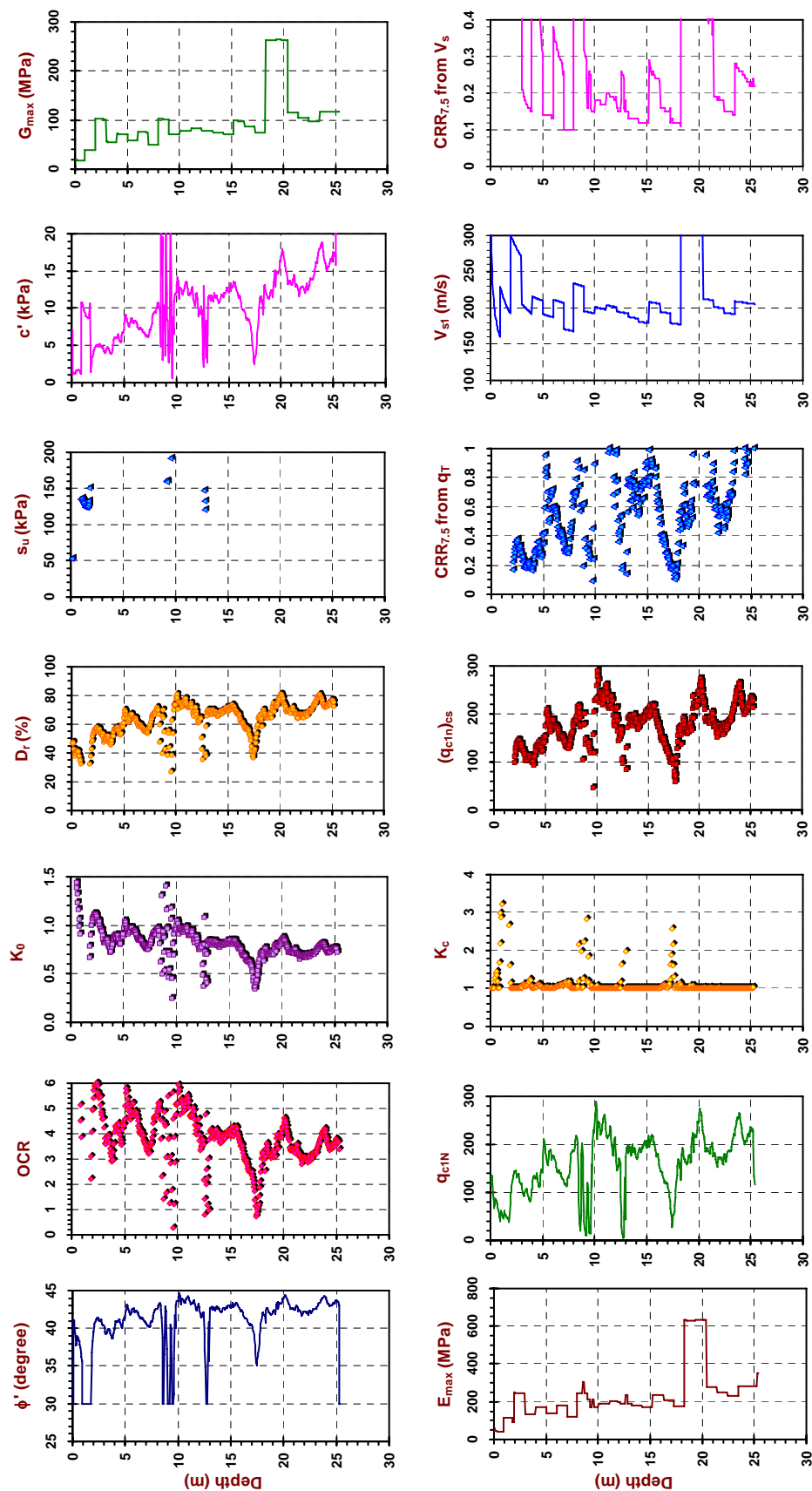
Figure B.18 Results from the SCPTu sounding (DODD02) performed at Dodd Farm site in Steele, Tennessee (Continued)
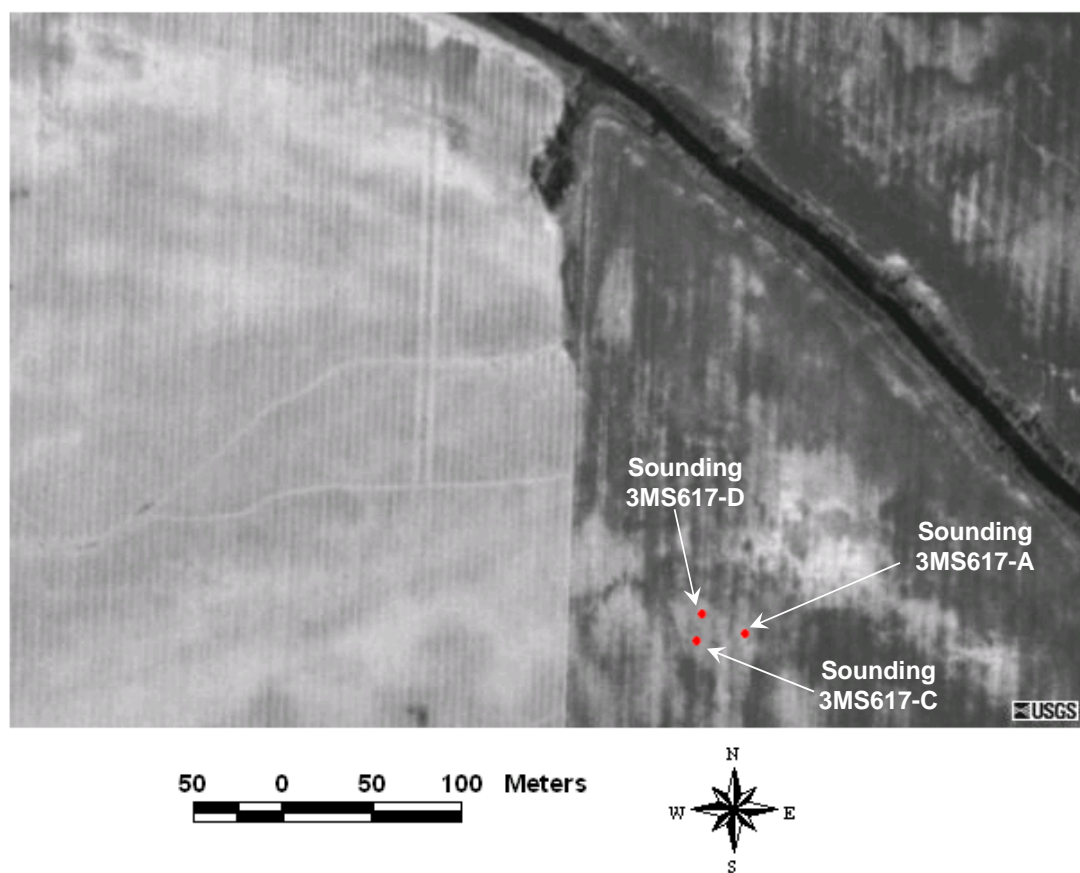
Figure B.19 Aerial photo showing the location of the cone penetration soundings performed at 3MS617 site in Blytheville, Arkansas
(Aerial photo from http://terraserver.microsoft.com)
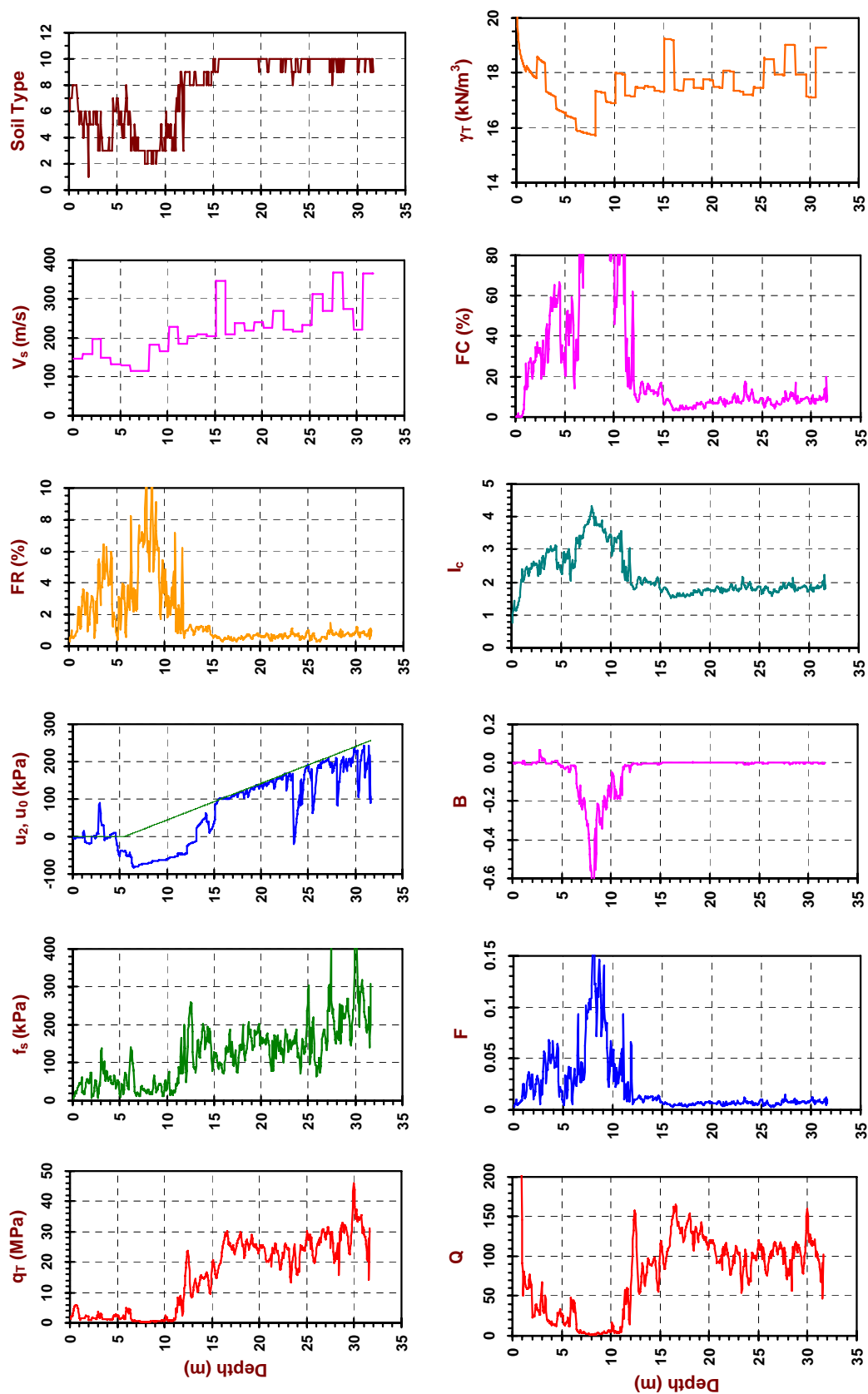
Figure B.20 Results from the SCPTu sounding (3MS617-A) performed at 3MS617 site in Blytheville, Arkansas

Figure B.20 Results from the SCPTu sounding (3MS617-A) performed at 3MS617 site in Blytheville, Arkansas (Continued)

371
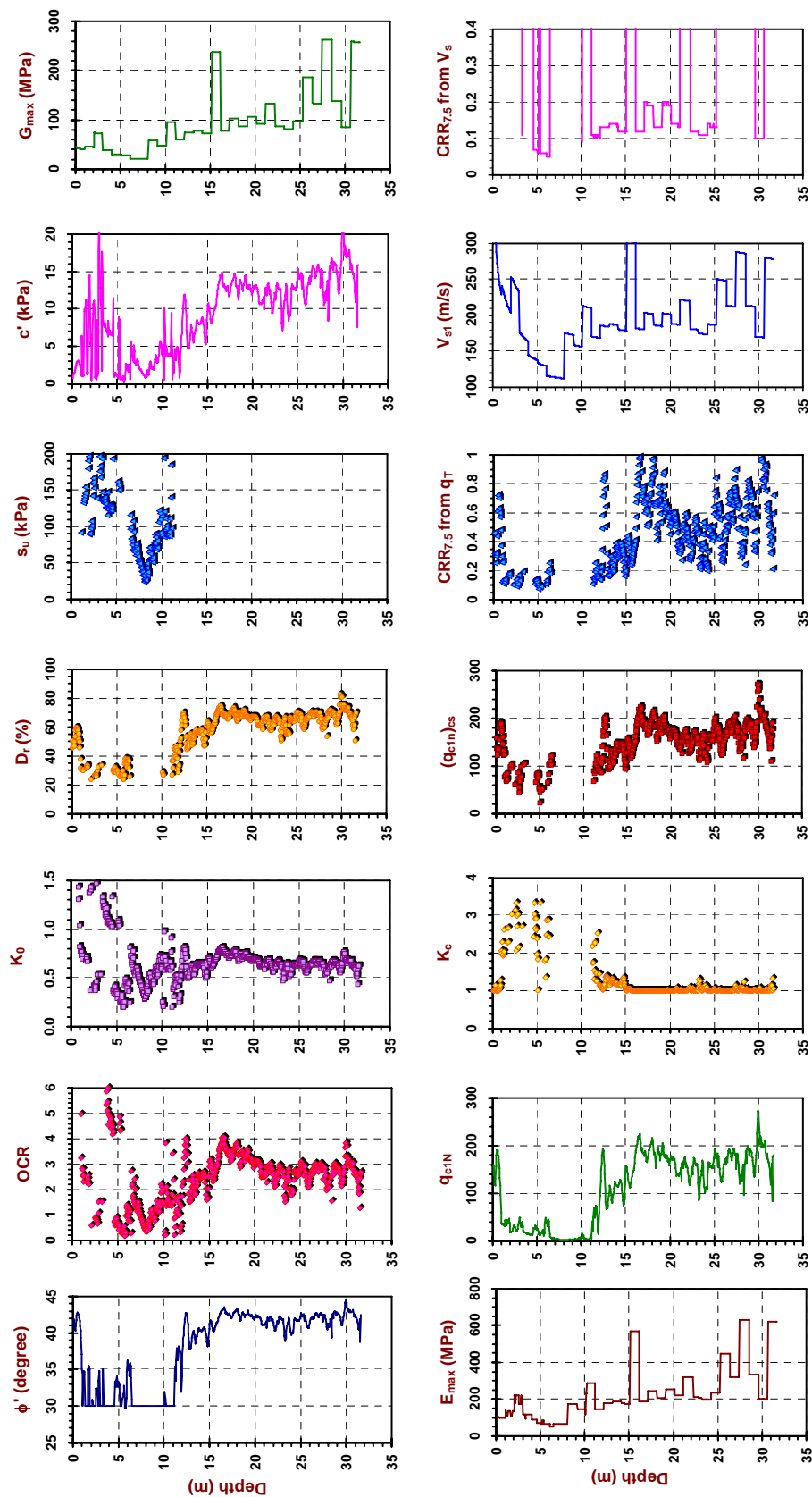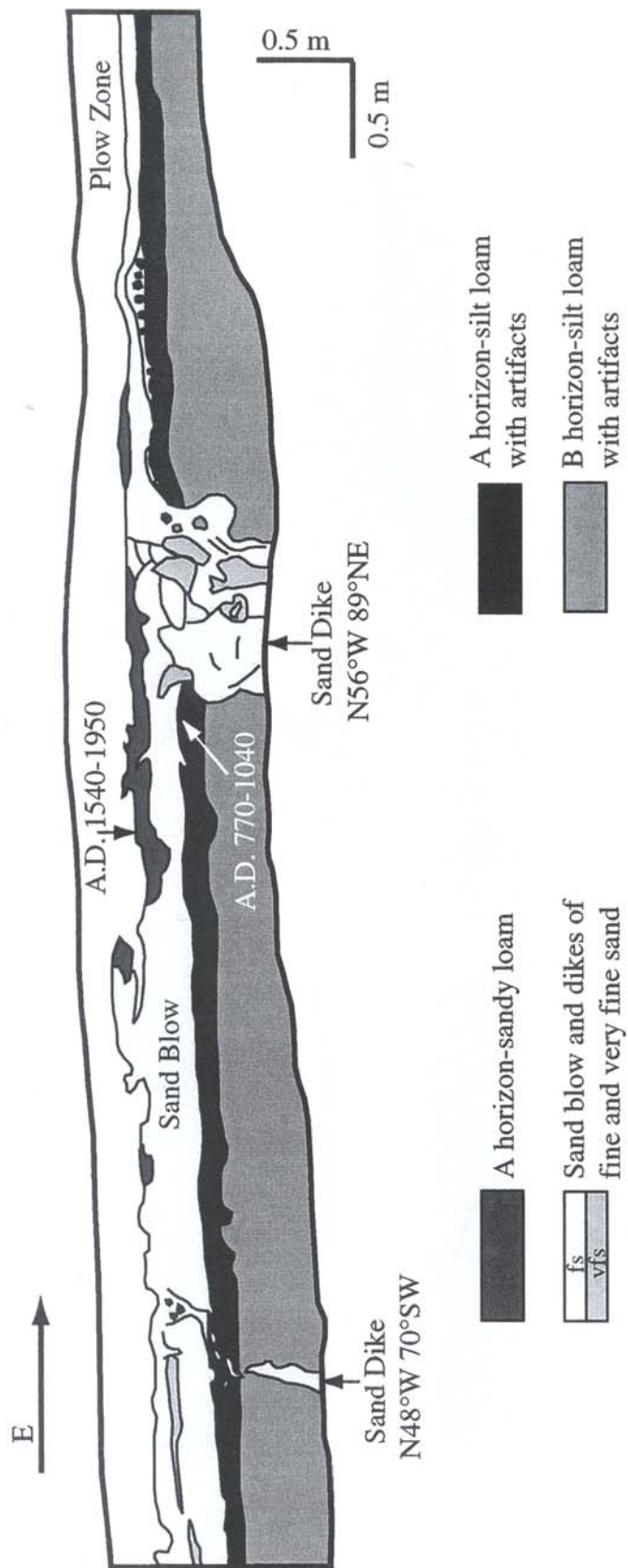
Figure B.21 Log of eastern portion of east-west oriented trench at Johnson Farm site in Steele, Missouri (Tuttle, 1999)

372

N2°E

Plow Zone

Sand Blow

Clasts

Vent Area

Sand Dike
N54°W 85°SW

0.25 m

0.25 m

fs — Sand blow-fine to coarse
vfs   sand and very fine sand

A horizon-silt loam
with artifacts

B horizon-silt loam
with artifacts
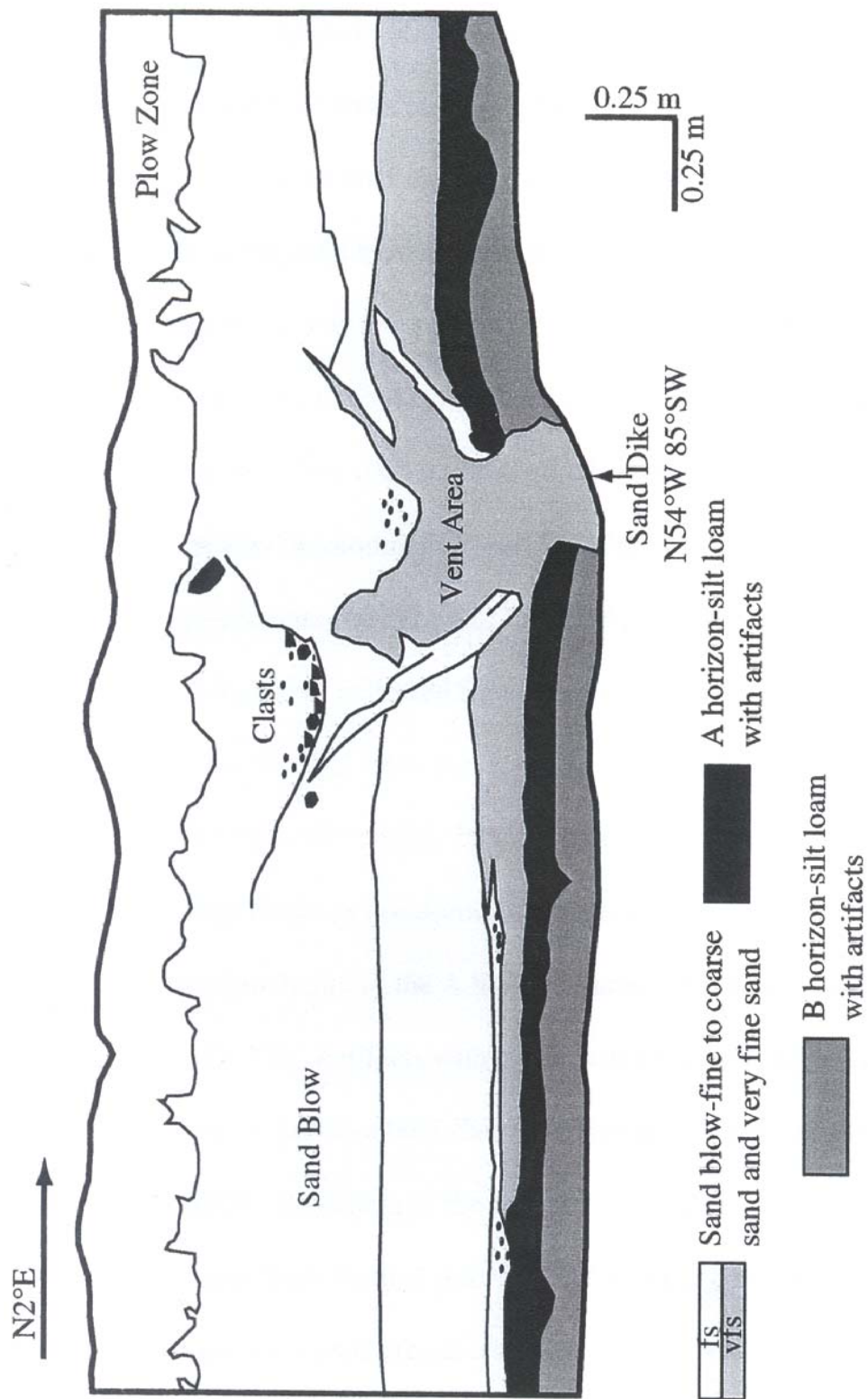
Figure B.22 Log of eastern portion of north-south oriented trench at Johnson Farm site in Steele, Missouri (Tuttle, 1999)
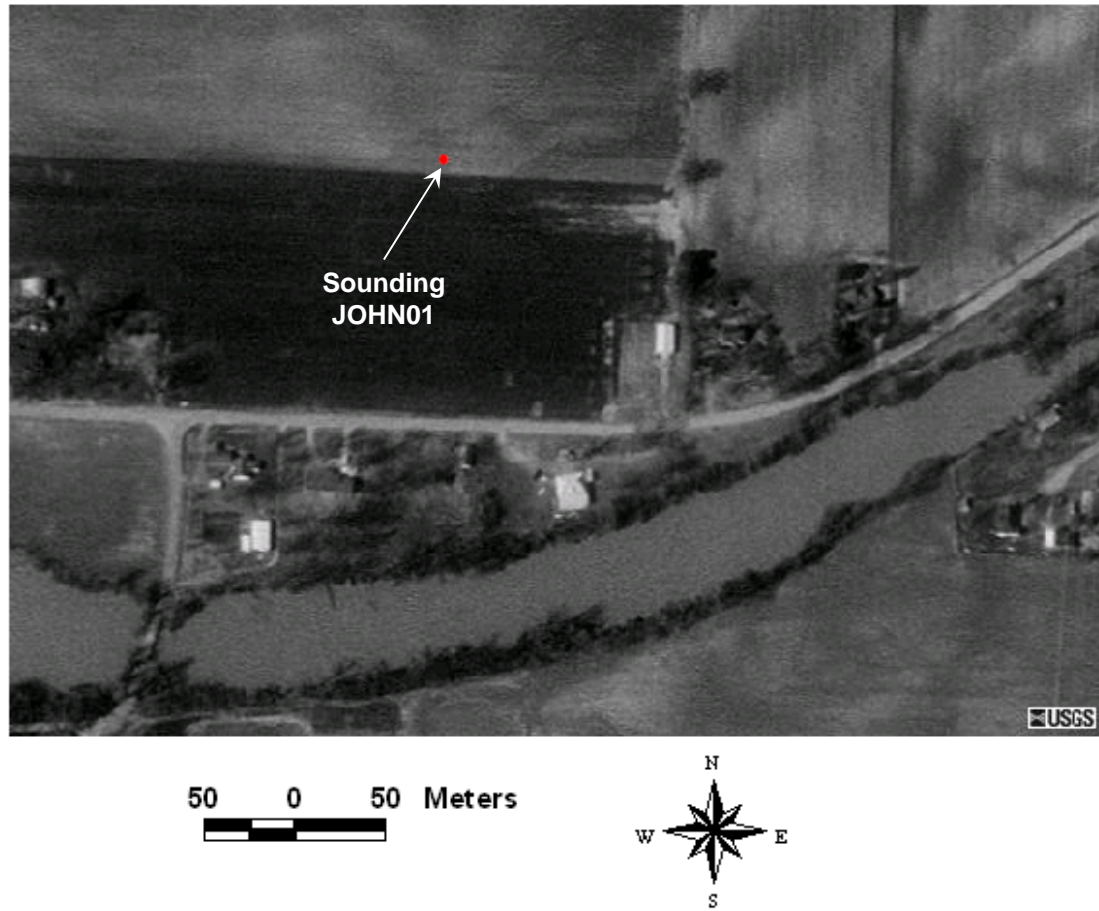
Figure B.23 Aerial photo showing the location of the SCPTu sounding (JOHN01) performed at Jonhson Farm site, Steele, Missouri (Aerial photo from http://terraserver.microsoft.com)
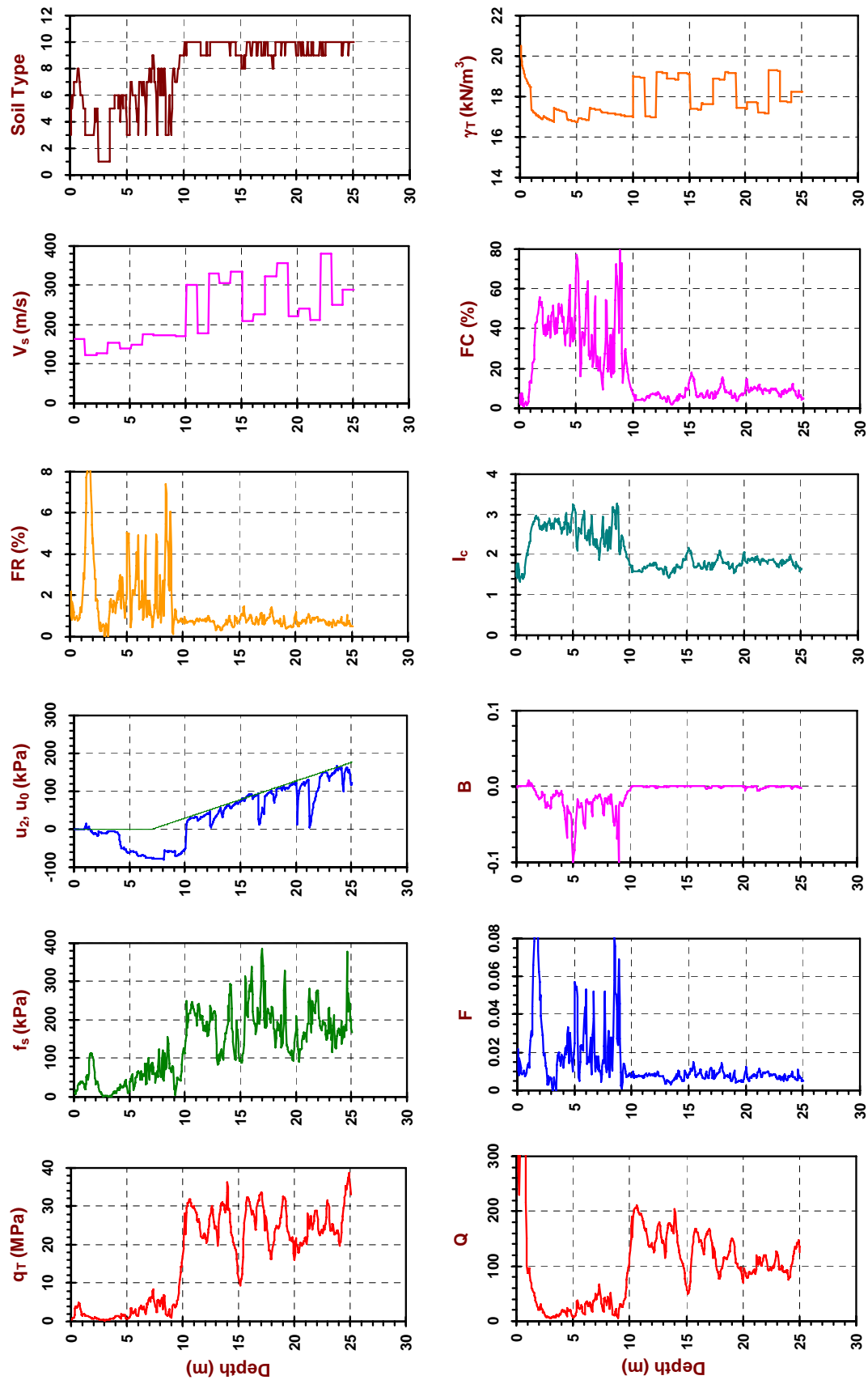
Figure B.24 Results from the SCPTu sounding (JOHN01) performed at Johnson Farm site, Steele, Missouri
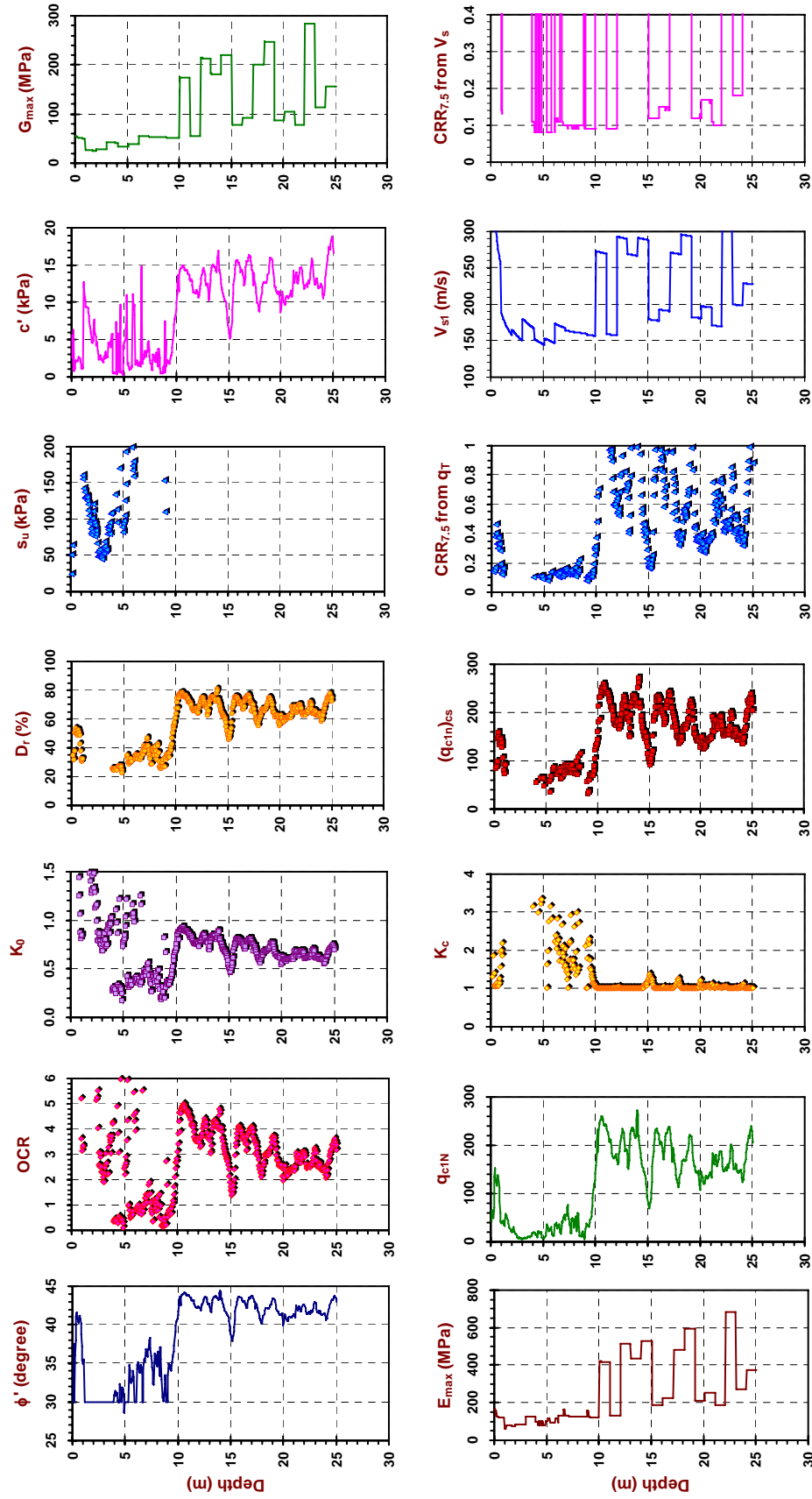
Figure B.24 Results from the SCPTu sounding (JOHN01) performed at Johnson Farm site, Steele, Missouri (continued)

376
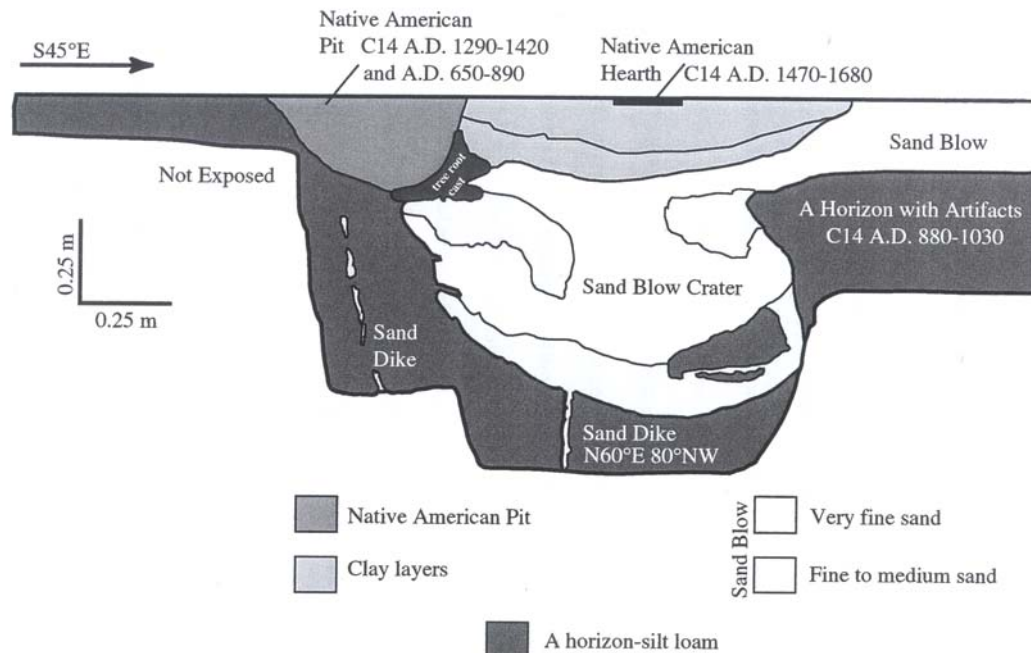
Figure B.25 Log of exposure at Hueys site in Blytheville, Arkansas (Tuttle, 1999)
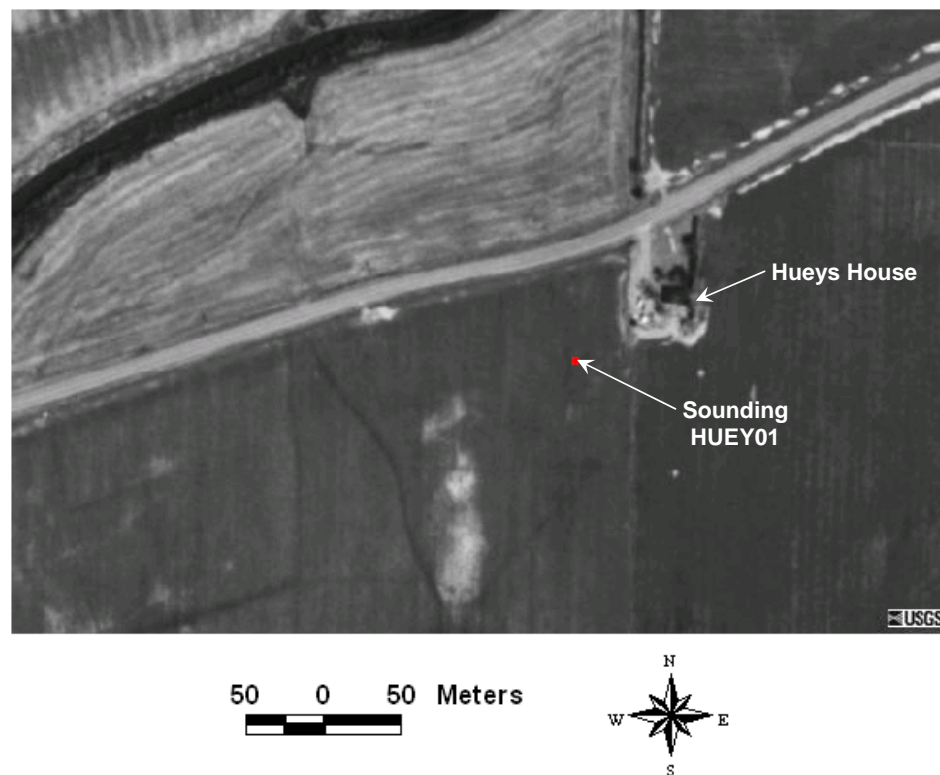
Figure B.26 Aerial photo showing the location of the SCPTu sounding (HUEY01) performed at Hueys site in Blytheville, Arkansas (Aerial photo from http://terraserver.microsoft.com)

Figure B.27 Results from the SCPTu sounding (HUEY01) performed at Hueys site in Blytheville, Arkansas

378

Figure B.27 Results from the SCPTu sounding (HUEY01) performed at Hueys site in Blytheville, Arkansas (Continued)

379
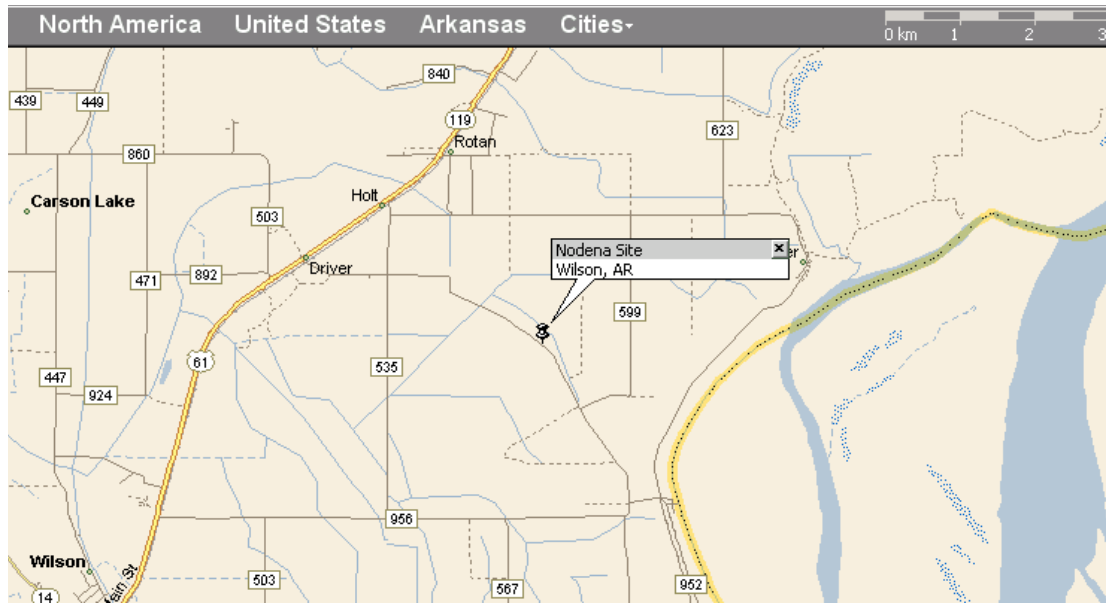
Figure B.28 Map showing the general location of the Nodena site at Wilson, Arkansas
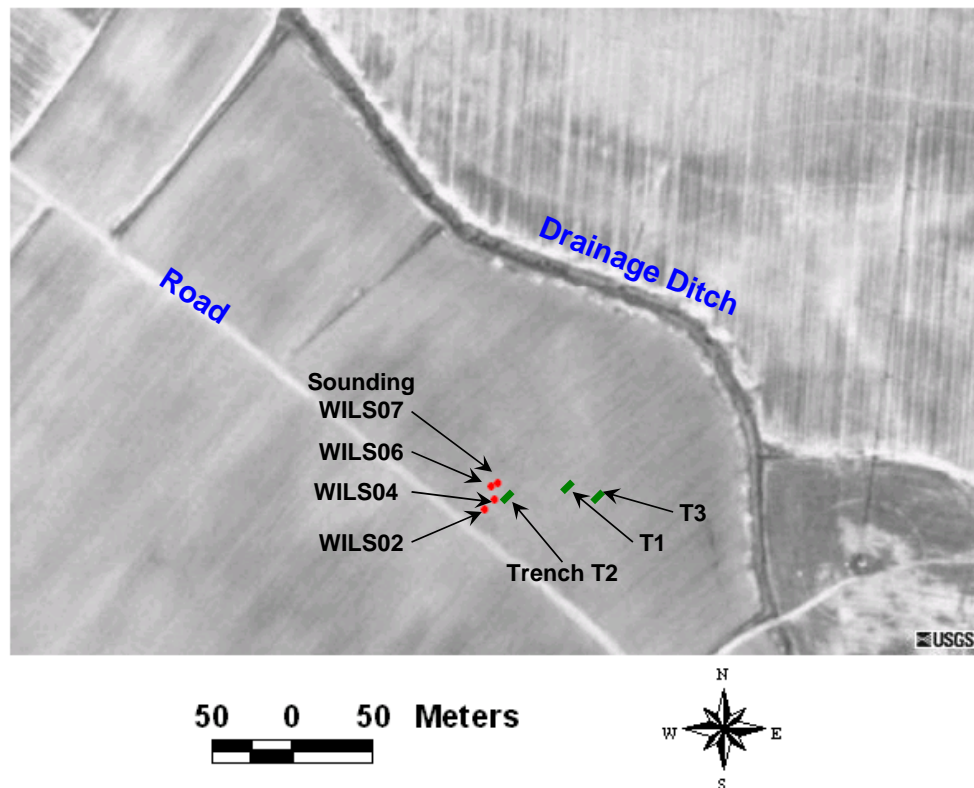
Figure B.29 Aerial photo showing the location of the soundings performed at Nodena site, Wilson, Arkansas
(Aerial photo from http://terraserver.microsoft.com)
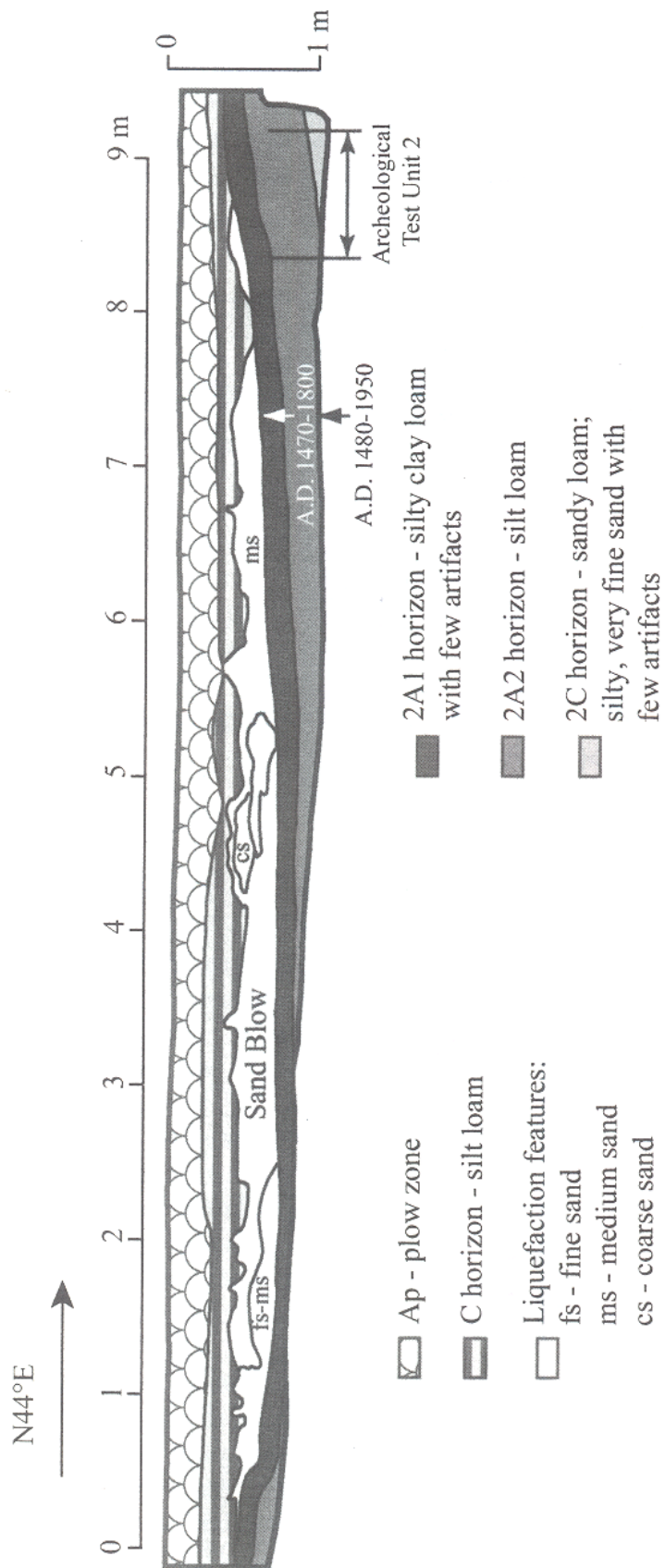
Figure B.30 Log of northwest wall of trench 1 at Nodena site near Wilson, Arkansas (Tuttle et al., 2000)
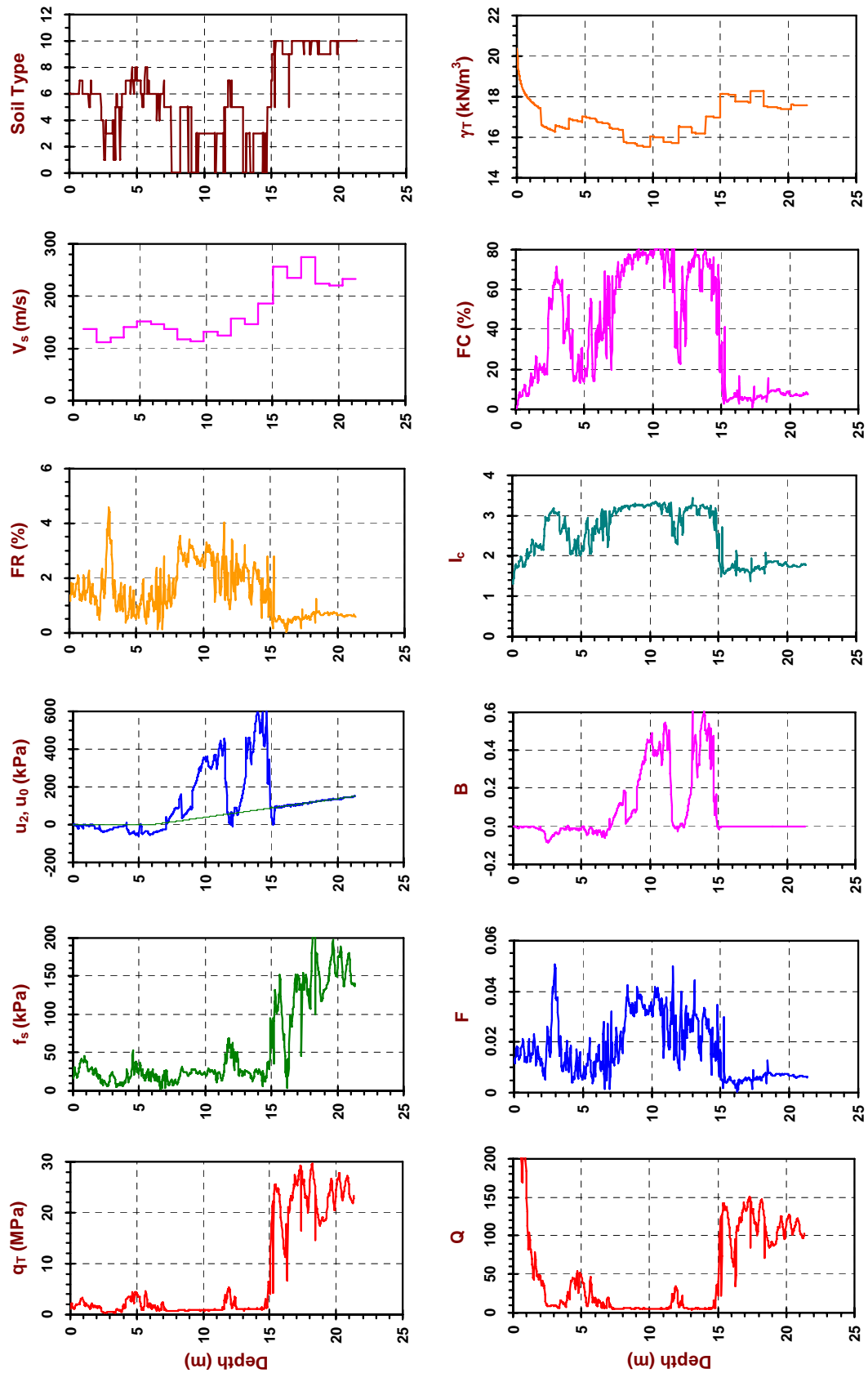
381

Figure B.31 (A) Log of southeast wall of trench 2 at Nodena site near Wilson, Arkansas; (B) Log of northwest wall at southwest end of trench 2 at Nodena site near Wilson, Arkansas (Tuttle et al., 2000)

382

Figure B.32 Results from the SCPTu sounding (WILS02) performed at Nodena site, Wilson, Arkansas
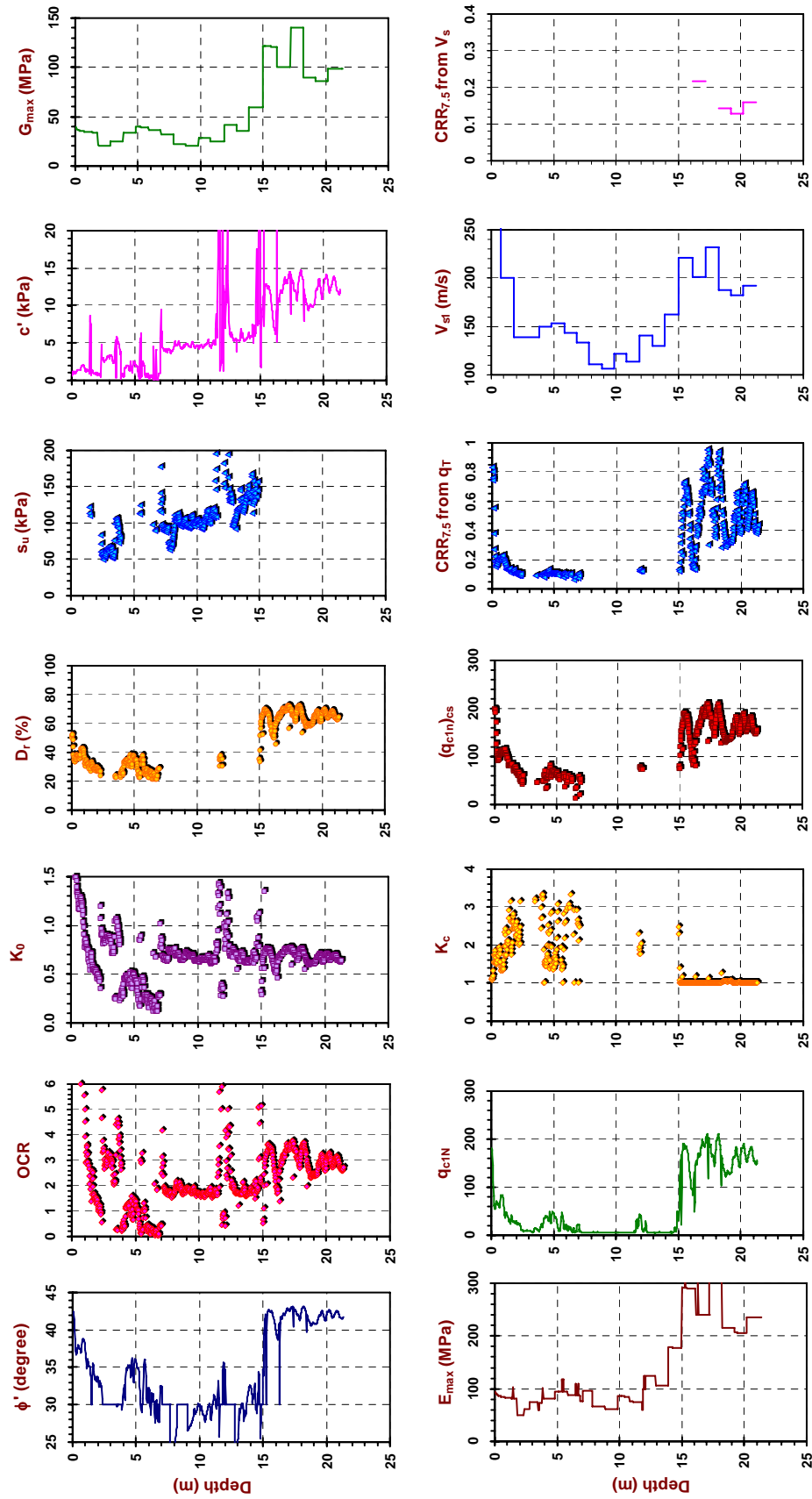
Figure B.32 Results from the SCPTu sounding (WILS02) performed at Nodena site, Wilson, Arkansas (Continued)
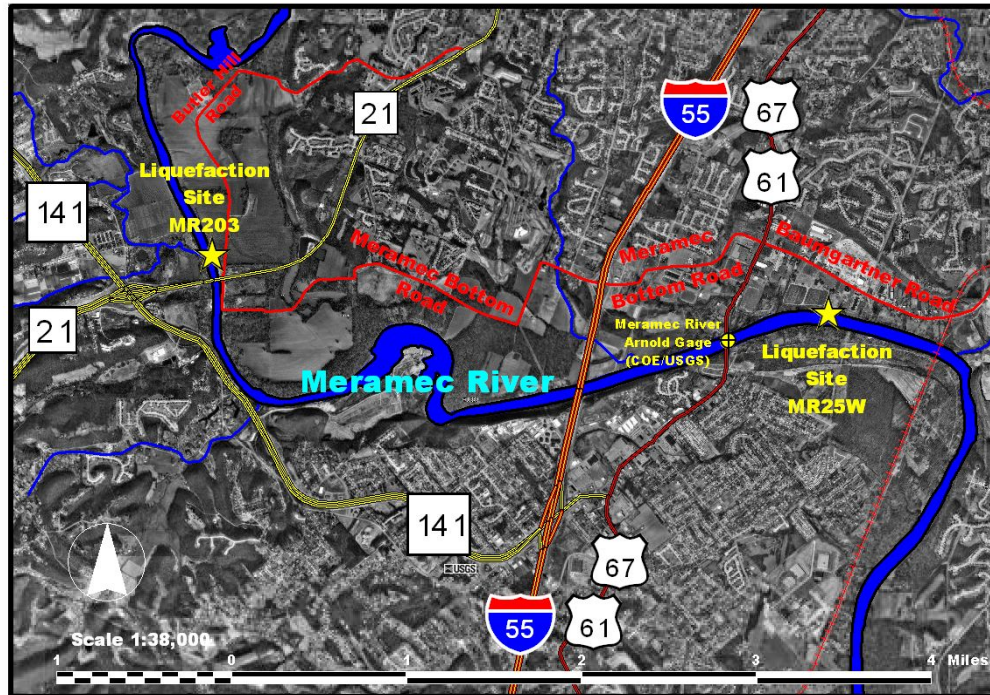
Figure B.33 Aerial photo showing the general location of the Meramec River sites (Hoffman, 2001)
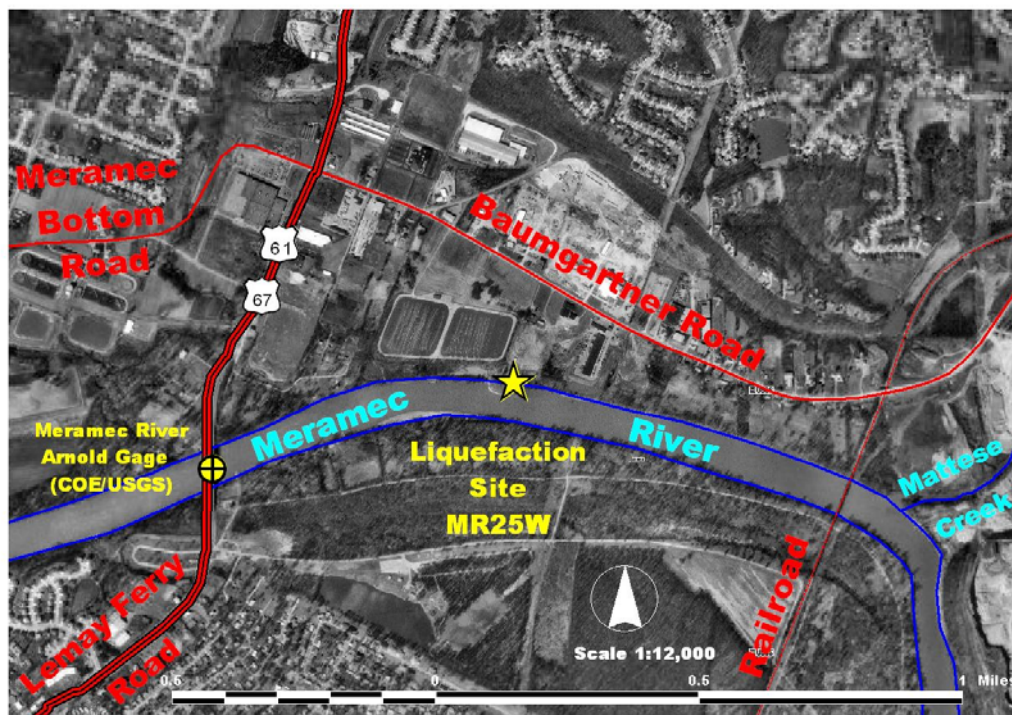
Figure B.34 Aerial photo showing the location of the MR24W site along Meramec River near St. Louis, Missouri (Hoffman, 2001)
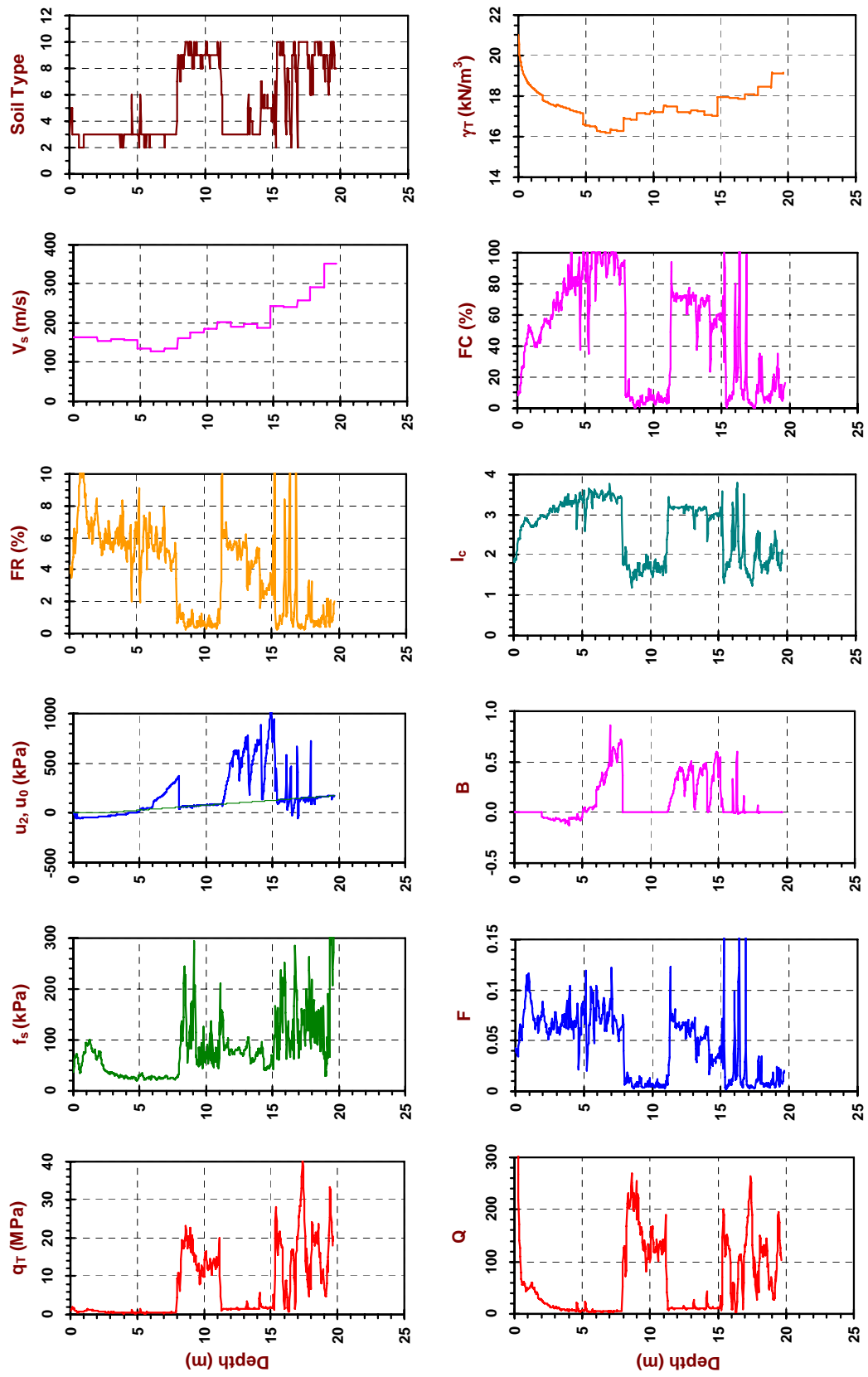
385

Figure B.35 Results from the SCPTu sounding (MER01) performed at MR24W site along Meramec River near St. Louis, Missouri

386
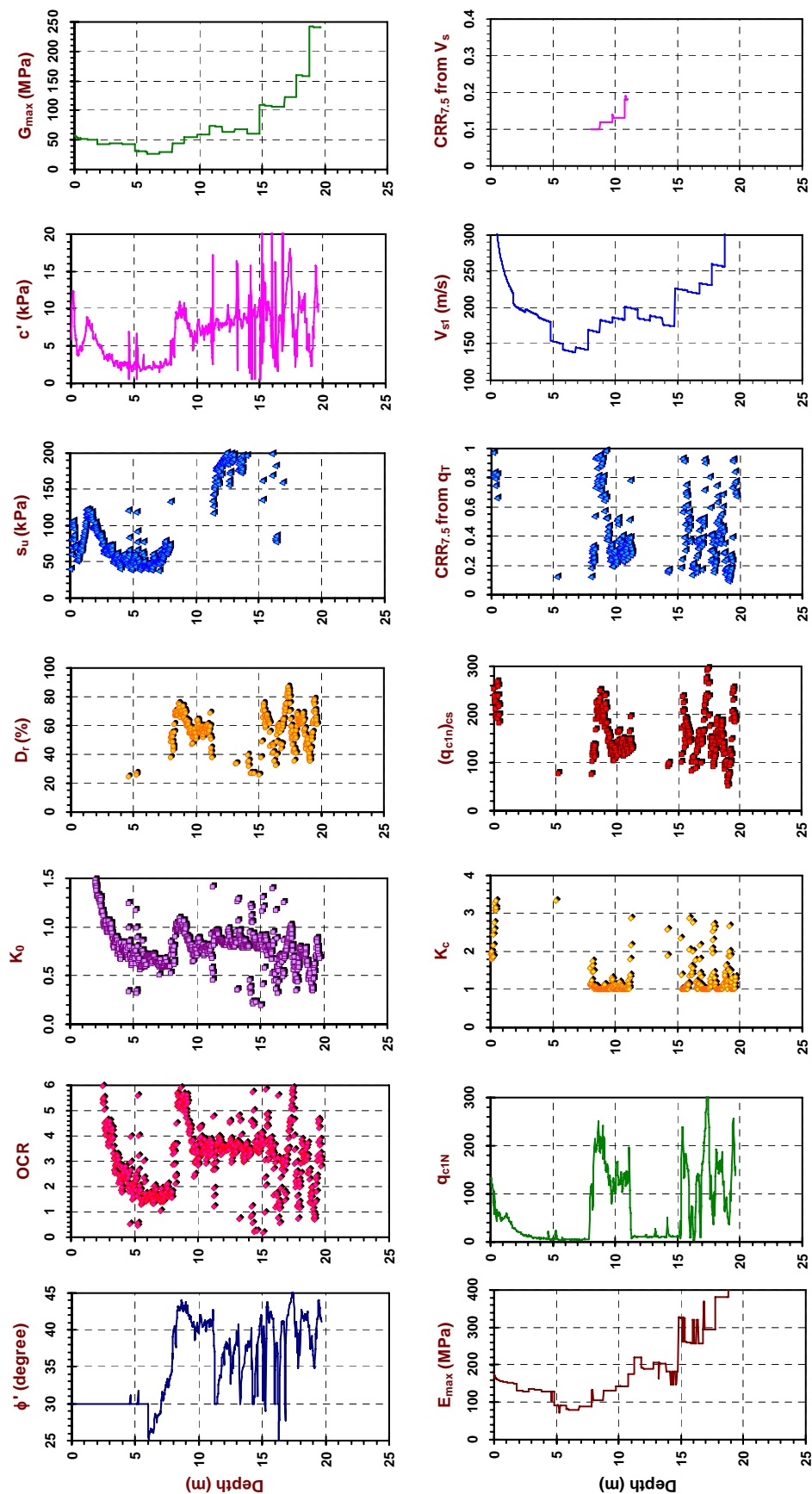
Figure B.35 Results from the SCPTu sounding (MER01) performed at MR24W site along Meramec River near St. Louis, Missouri (Continue)
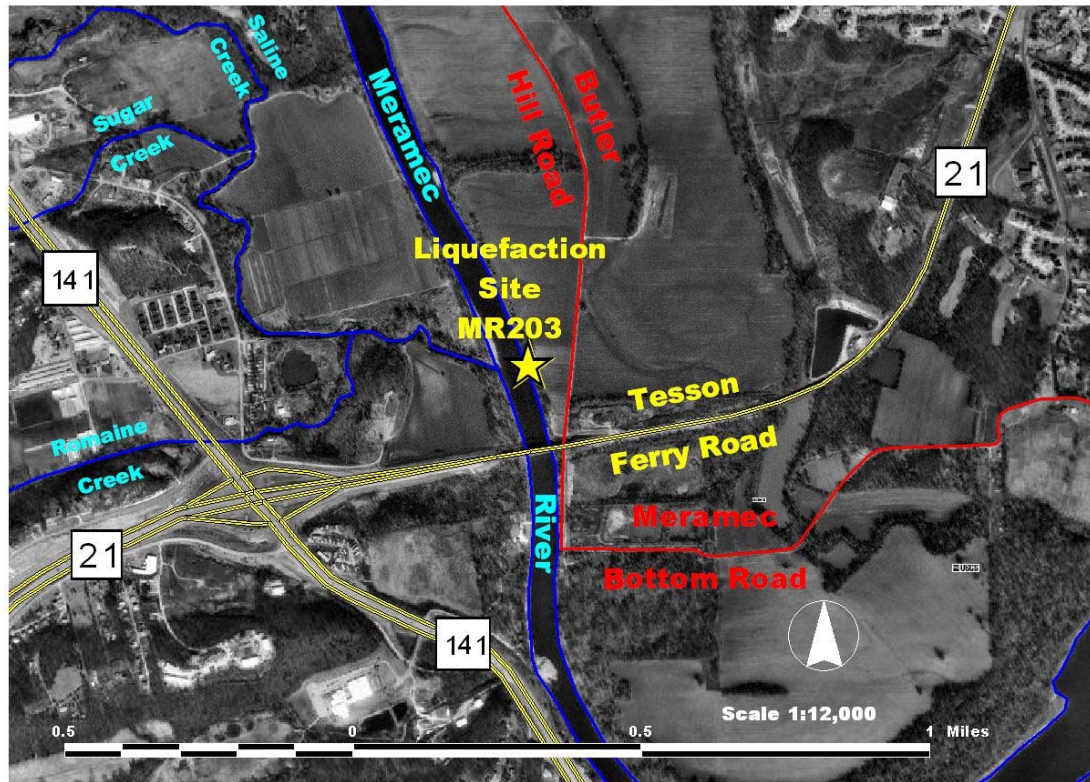
Figure B.36 Aerial photo showing the location of the MR203 site along Meramec River near St. Louis, Missouri (Hoffman, 2001)
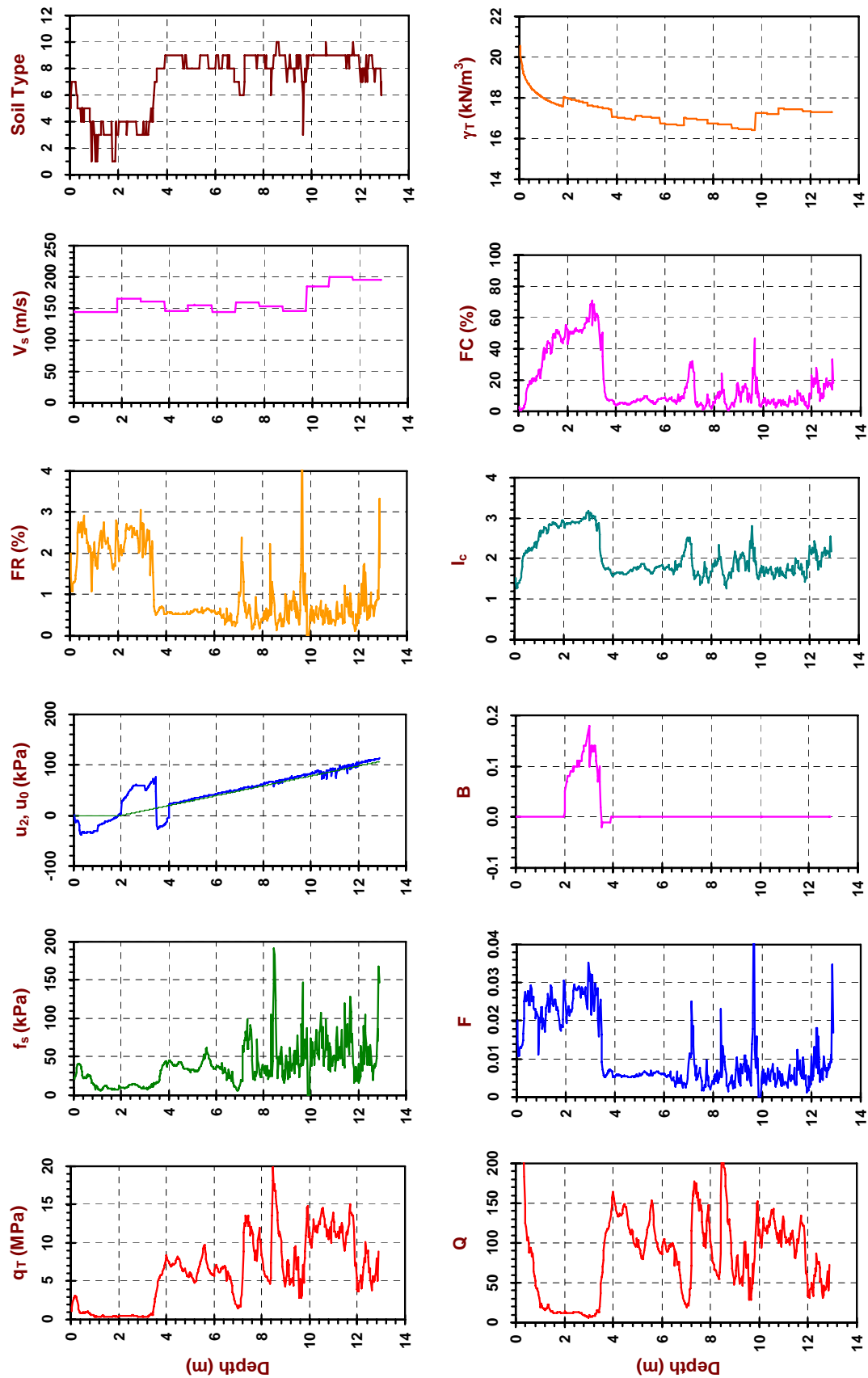
Figure B.37 Results from the SCPTu sounding (MER03) performed at MR203 site along Meramec River near St. Louis, Missouri

Figure B.37 Results from the SCPTu sounding (MER03) performed at MR203 site along Meramec River near St. Louis, Missouri (Continued)

390
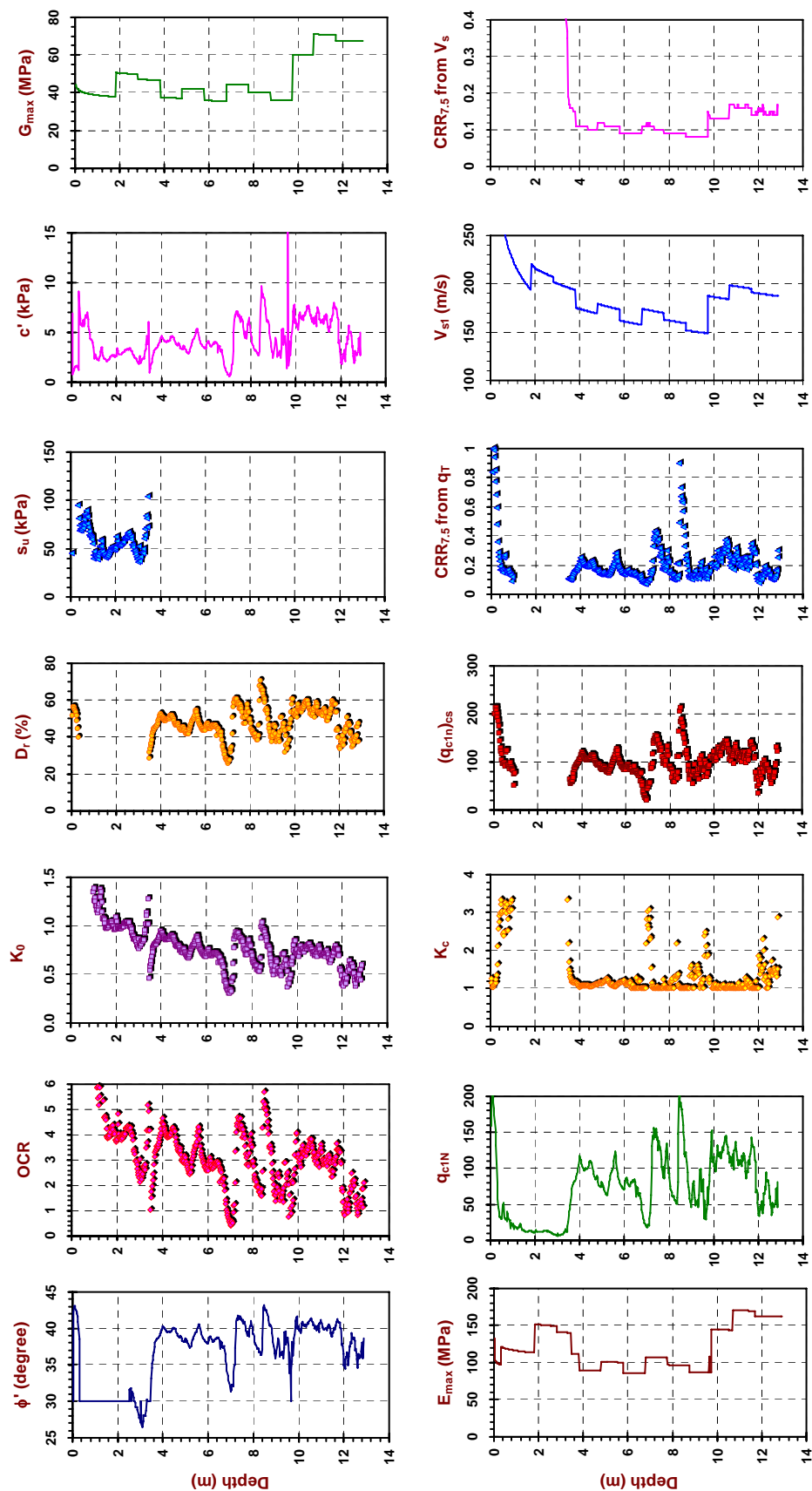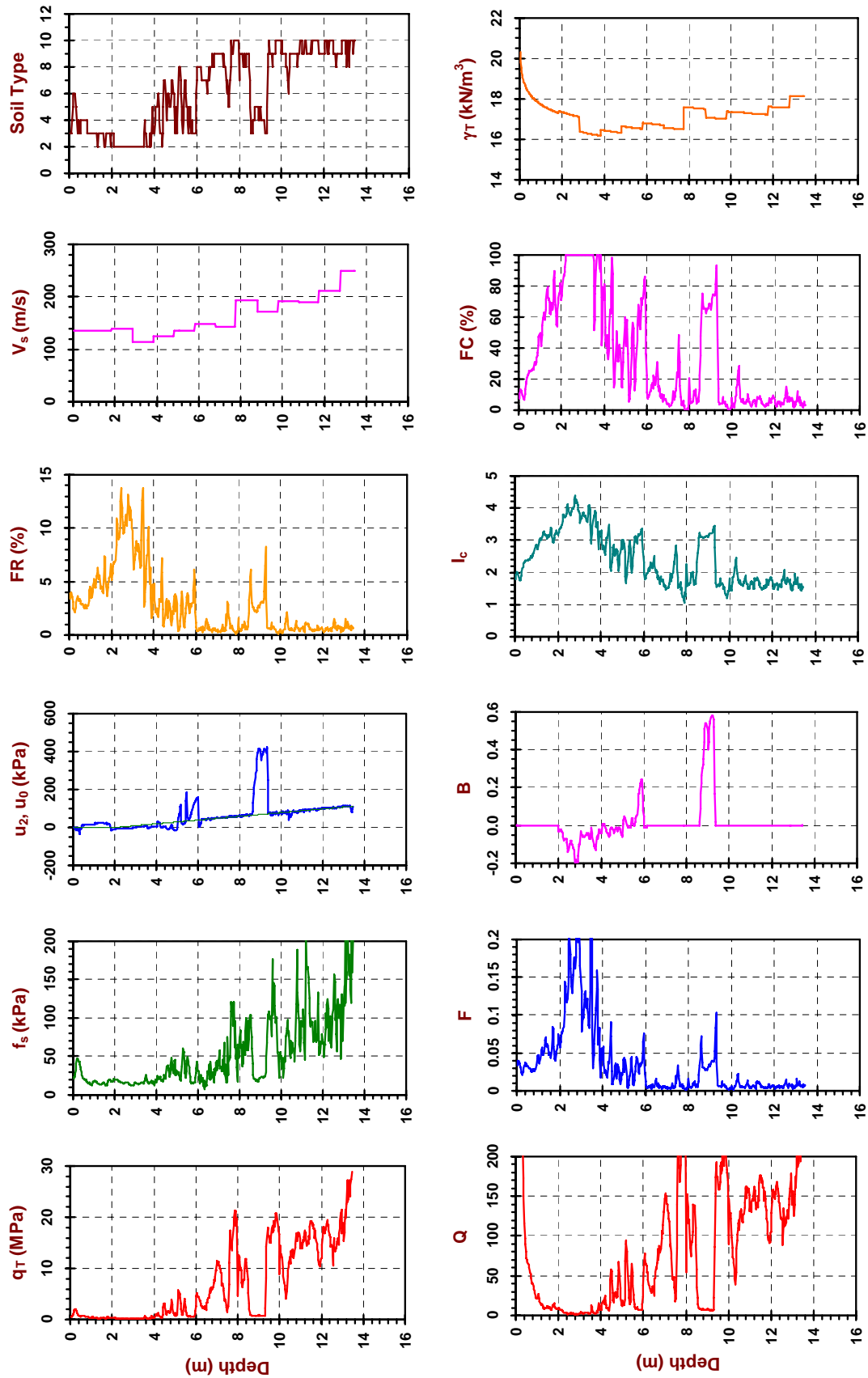
Figure B.38 Results from the SCPTu sounding (MER04) performed at MR203 site along Meramec River near St. Louis, Missouri
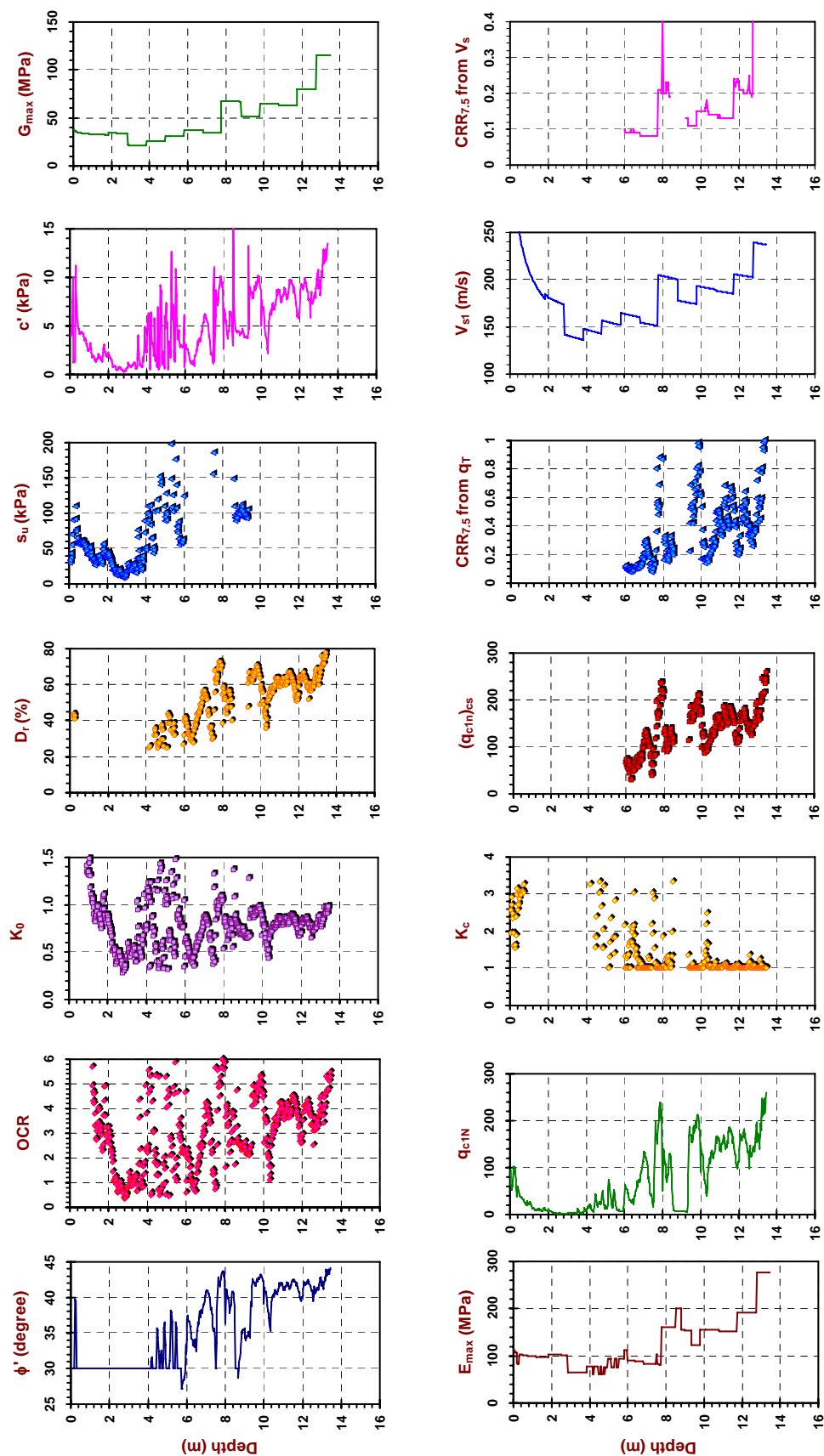
Figure B.38 Results from the SCPTu sounding (MER04) performed at MR203 site along Meramec River near St. Louis, Missouri (Continued)
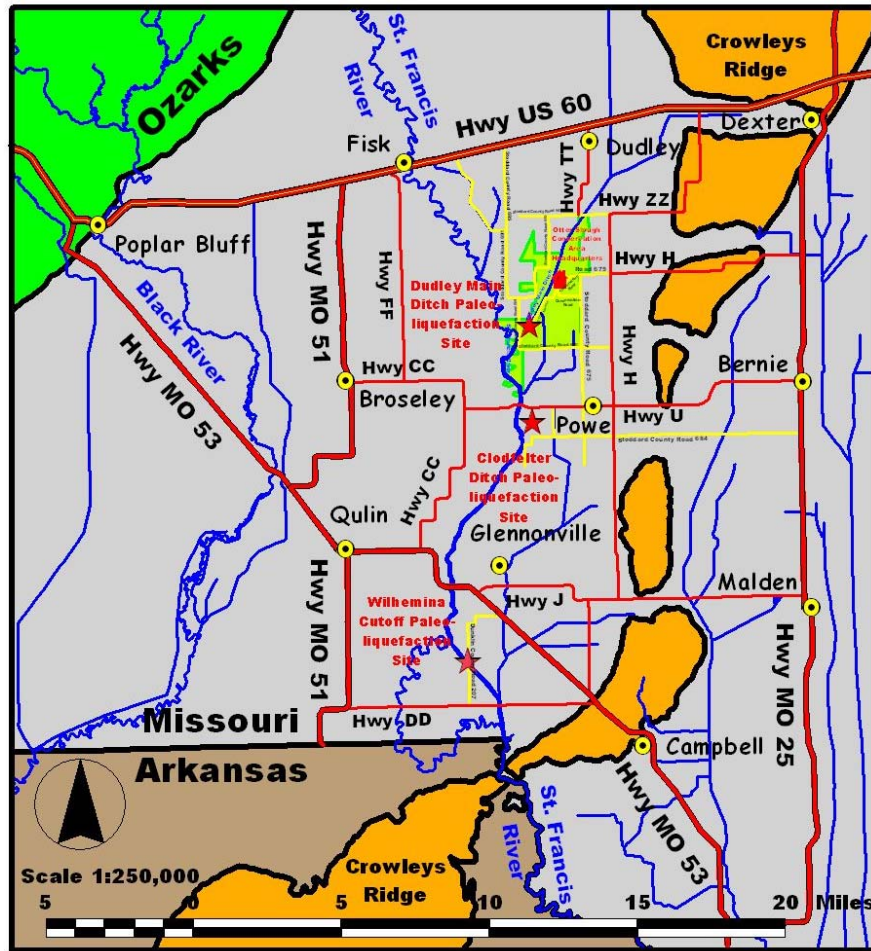
Figure B.39 Map showing the general location of the St. Francis River sites near Dexter, Missouri (Hoffman, 2001)

393

Figure B.40 Aerial photo showing the location of Dudley Main Ditch site along Meramec River near Dexter, Missouri (Hoffman, 2001)
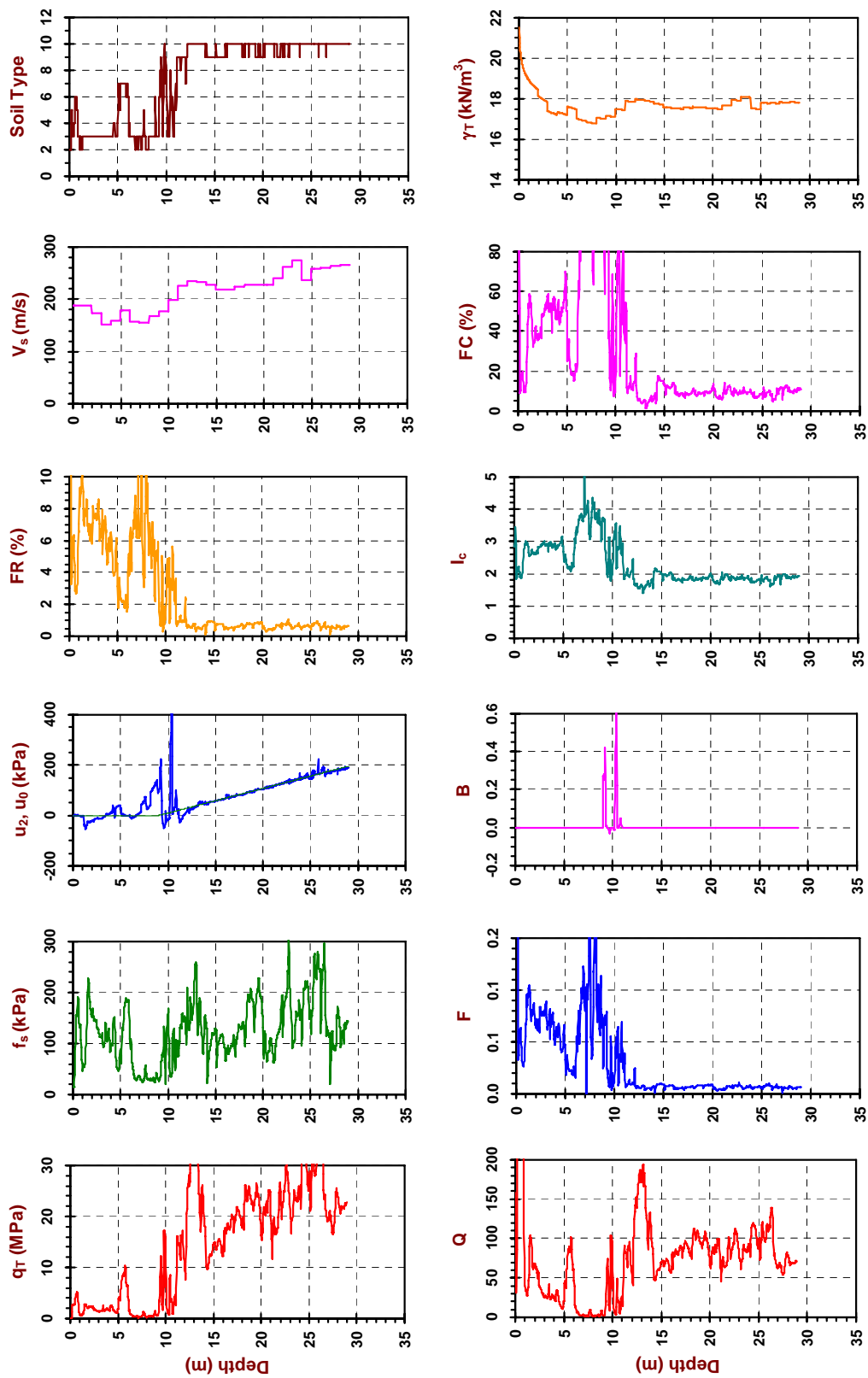
Figure B.41 Results from the SCPTu sounding (DEX01) performed at the St. Francis River site at Dudley Main Ditch near Dexter, Missouri
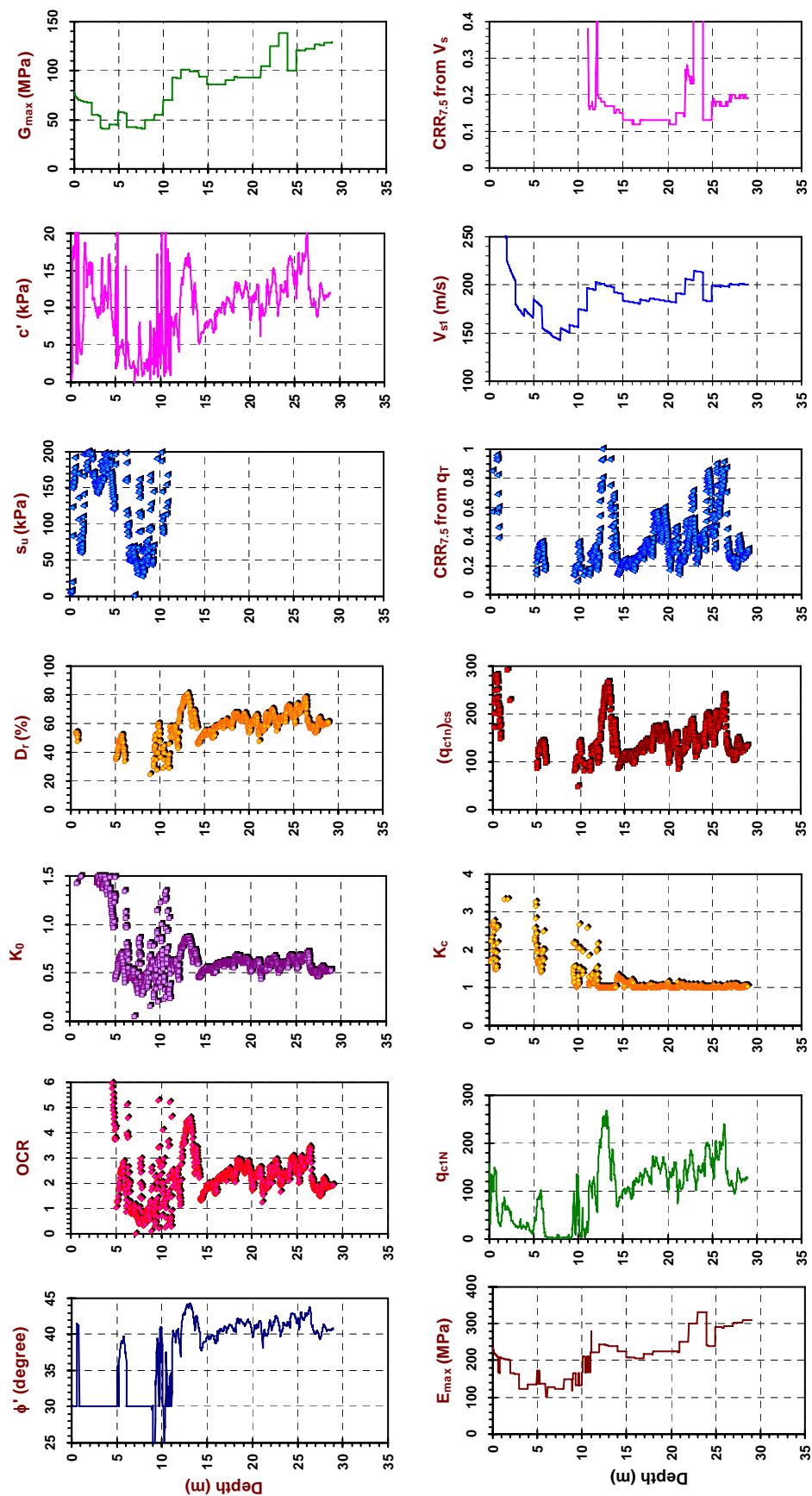
Figure B.41 Results from the SCPTu sounding (DEX01) performed at the St. Francis River site at Dudley Main Ditch near Dexter, Missouri (Continued)
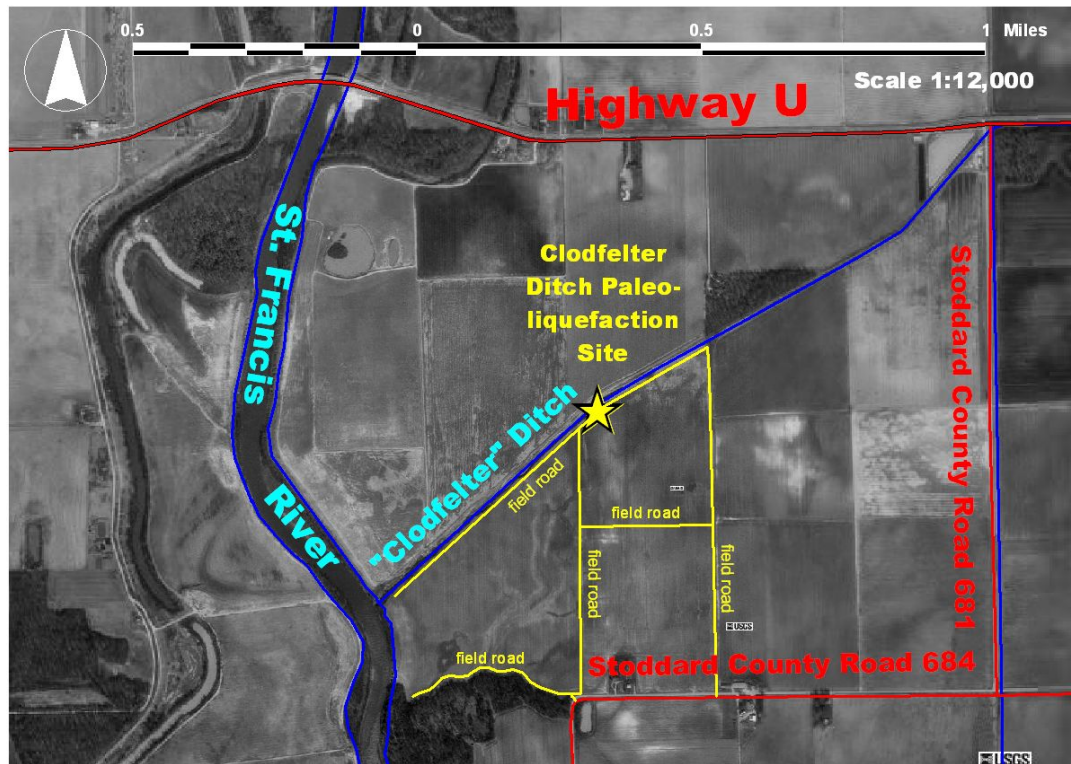
Figure B.42 Aerial photo showing the location of St. Francis River site at Clodfelter Ditch near Dexter, Missouri (Hoffman, 2001)

Figure B.43 Results from the SCPTu sounding (DEX03) performed at the St. Francis River site at Clodfelter Ditch near Dexter, Missouri

398
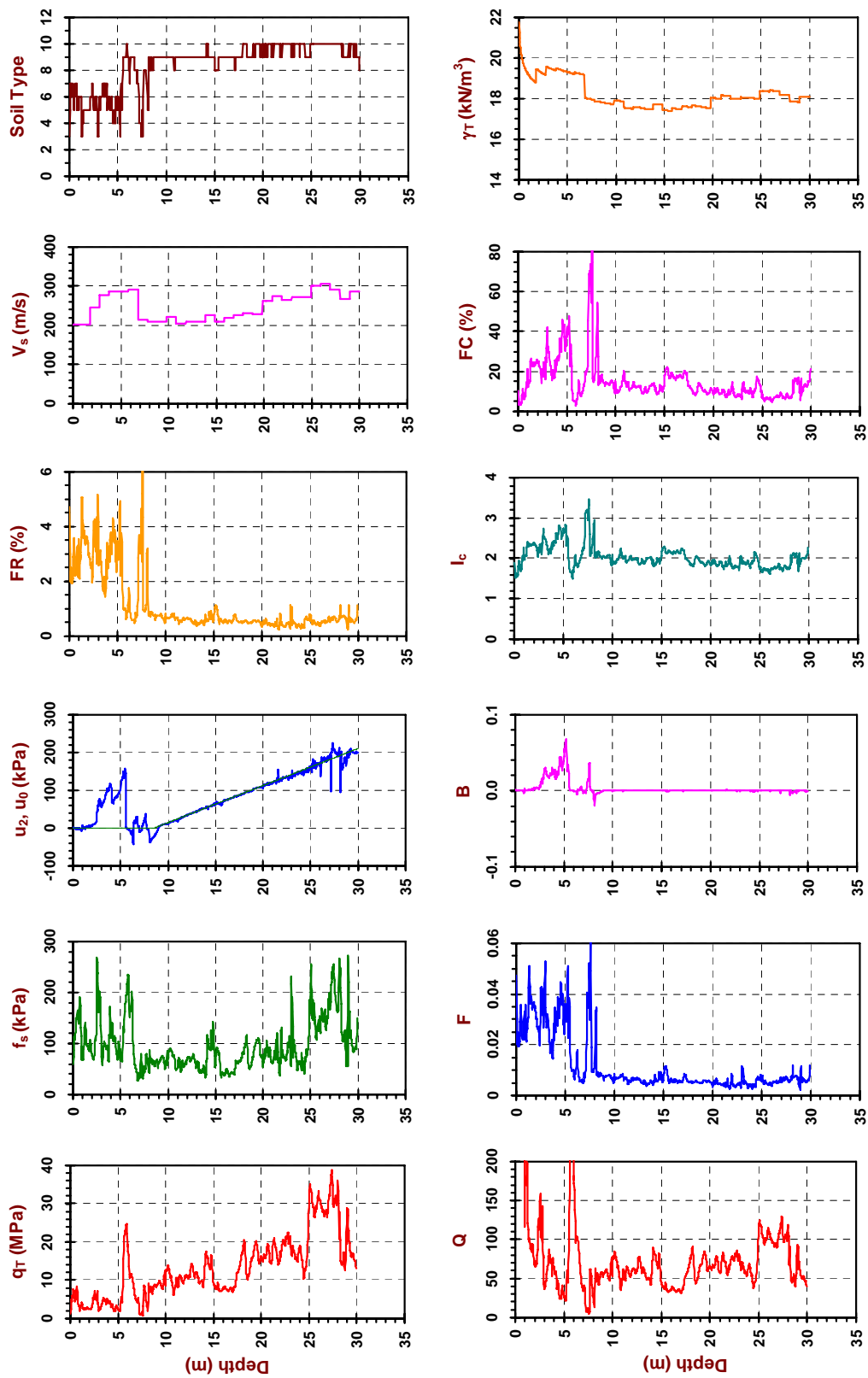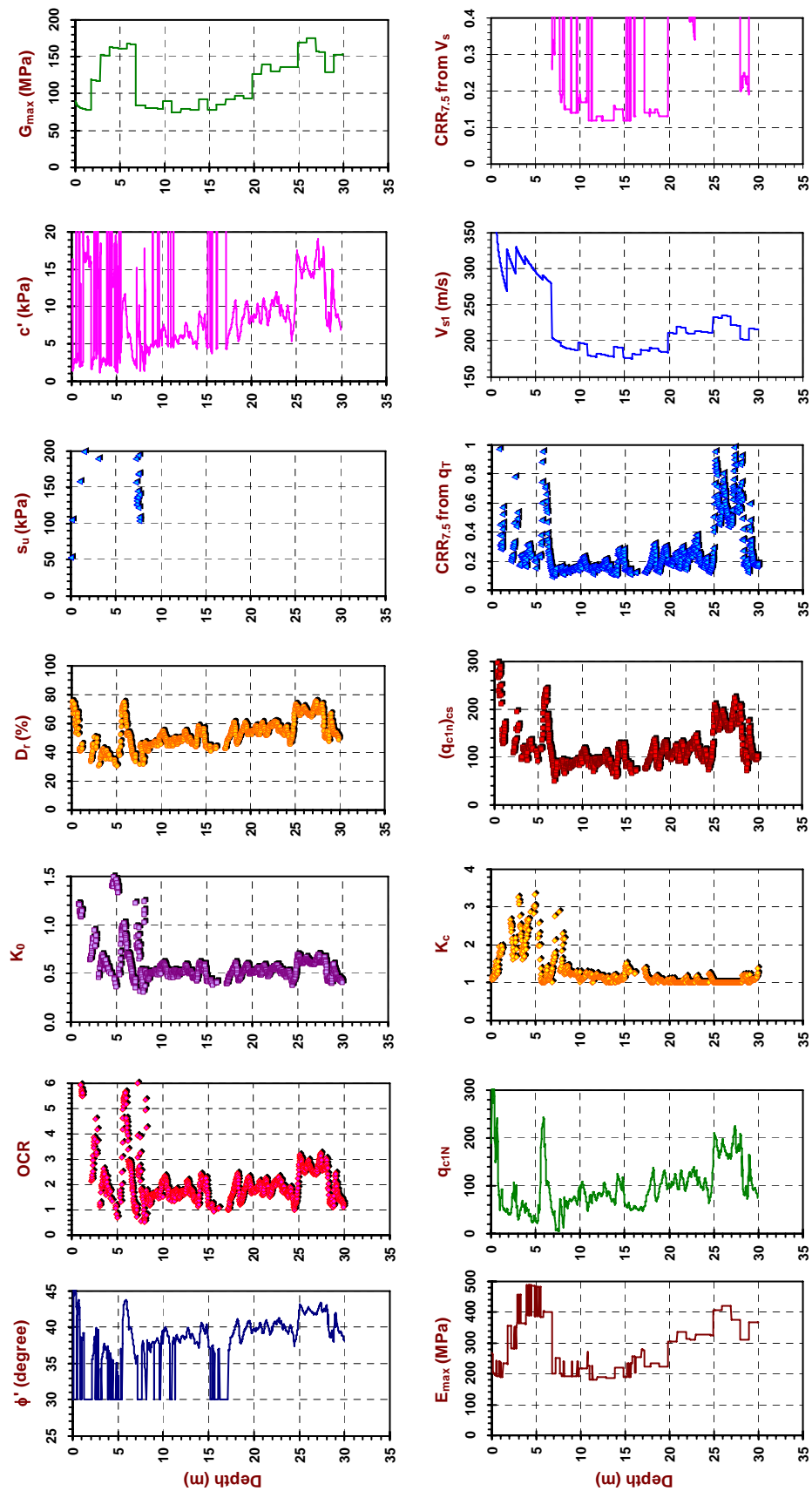
Figure B.43 Results from the SCPTu sounding (DEX03) performed at the St. Francis River site at Clodfelter Ditch near Dexter, Missouri (Continued)

Figure B.44 Aerial photo showing the location of St. Francis River site at Wilhelmina Cutoff near Dexter, Missouri (Hoffman, 2001)
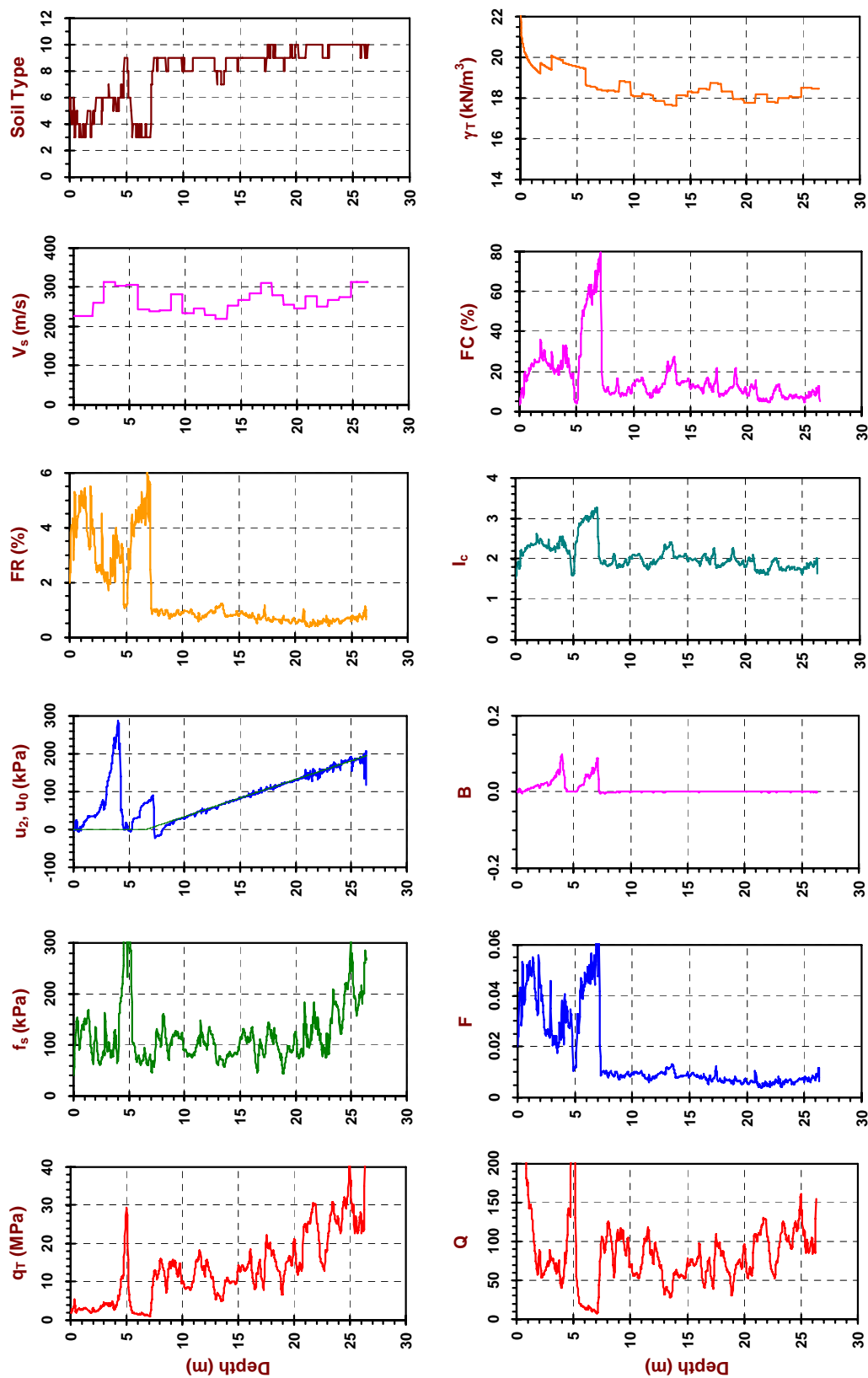
Figure B.45 Results from the SCPTu sounding (DEX04) performed at the St. Francis River site at Wilhelmina Cutoff near Dexter, Missouri

Figure B.45 Results from the SCPTu sounding (DEX04) performed at the St. Francis River site at Wilhelmina Cutoff near Dexter, Missouri (Continued)

402
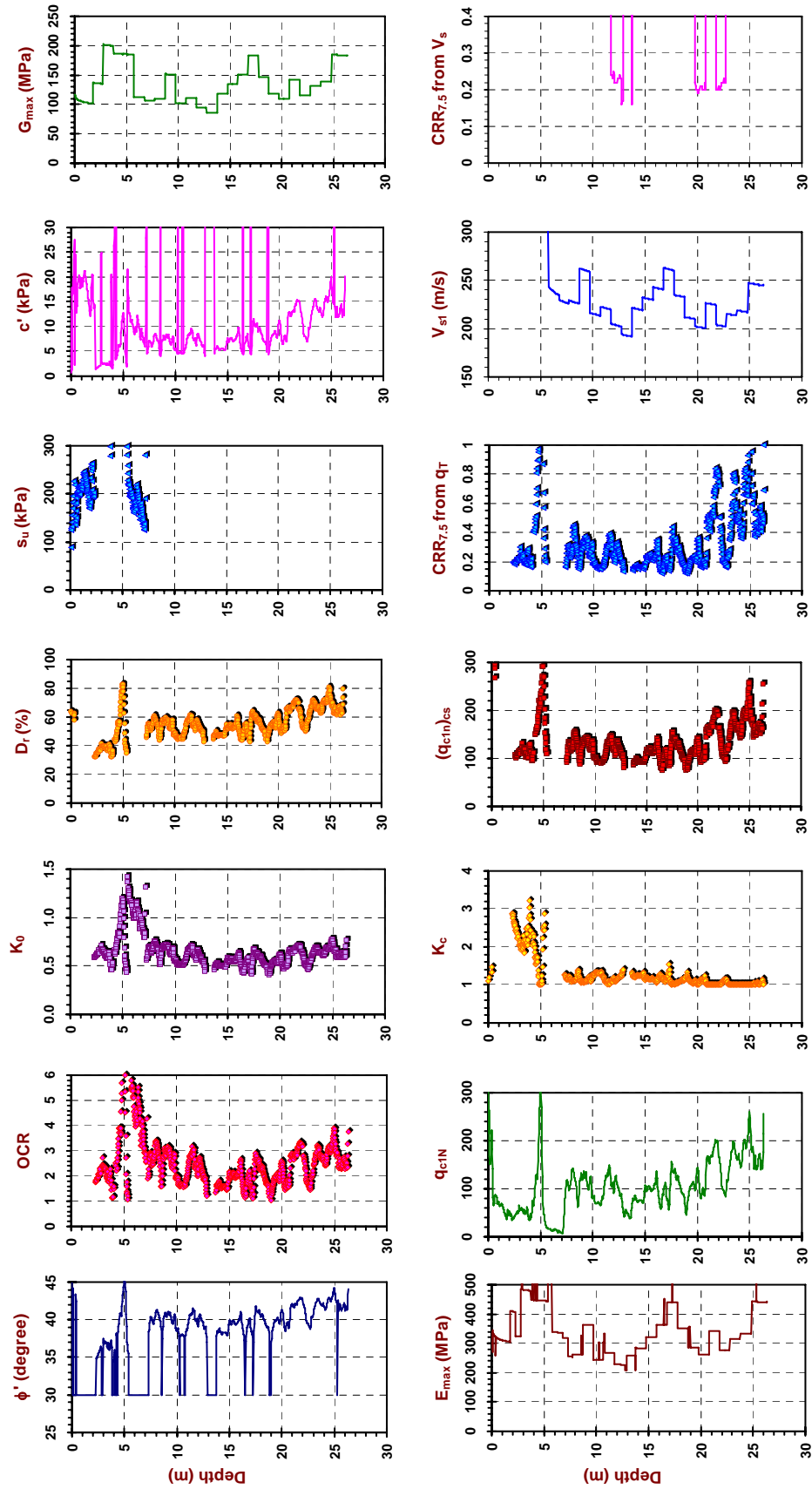
APPENDIX C

NON-PALEOLIQUEFACTION TEST SITES

Series of cone penetration tests have been performed at new sites of construction and historic sites where no apparent liquefaction evidence was found, as listed in Table C.1. Geotechnical site characterization using seismic cone penetration tests (SCPTu) at these sites identifies soils with high potential to liquefaction, and provides data for site-amplification analysis. For a specific site, the V_s in the top 30 m can be relatively accurately measured in a downhole manner by a SCPTu test, and it is of paramount significance to seismic evaluation. The 2000 IBC (Internation Building Code) emphasizes the importance of the average V_s in the top 30.5 m (100 ft) by using it to define sites with repect to their seismic vulnerability, as listed Table 6.2 in Chapter 6. Brief introduction of these sites is given in the following subsections.

C.1 Prior SCPTus By GT Team

The sites visited before year 2000 have been summarized by Schneider (1999). The Houston Levee site and the Wolf River Boulevard site are investigated, because they are in the vicinity of the Shelby Farms paleoliquefaction site discussed in Appendix A. The sediments at these sites should have been deposited in a similar manner as those at the Shelby Farms site. The Monopole Tower site is used to compare the soil profile derived from cone penetration data with soil samples collected by SPT at this site. The I-155 bridge site was studied using cone penetration tests due to concern with safety and seismic performance of the bridge during a major event. Soundings were performed at the

sites in Shelby Farms Shooting Range and Shelby Forest for the purpose of comparing shear wave velocity measurements taken by a variety of different field methods. Some introduction is given to the test sites visited since 2000 in the following sub-sections:

C.2 Mud Island Site

Mud Island, the parkland of 52 acres, was originally formed by dredge spoil taken from the Mississippi river, and the area currently forms a peninsula located on the northwestern edge of downtown Memphis, Tennessee. It is home to a growing number of apartments and houses for several thousand residents, as well as some commercial and entertainment developments. Since Mud Island has not experienced a large earthquake event due to its short period of existence, the potential damage during the probable future earthquakes is not clear. Liquefaction evaluation focusing on this island would be very helpful for estimating the damages during future earthquakes, and it can serve as a valuable guide for the future development of the island. SCPTu soundings were performed at five locations (A, B, C, D, and E) at Mud Island as shown in Figure C.1. Results of this study are documented in Liao et al. (2000).

C.3 Center for Earthquake Research and Information (CERI) Headquarters

Cone penetrations soundings were performed next to the 100-meter accelerometer array, which is installed at the headquarters of CERI in Memphis, TN. Its location is shown in Figure C.2. The soil strength characteristics and shear wave velocity obtained are necessary for analysis of the acceleration history should a seismic event occur. Results of this study are documented in Liao et al. (2001).

C.4 Test sites near Memphis, Tennessee

SCPTu tests were done at a sewage treatment plant on the banks of the Wolf River near Germantown, Tennessee, and in a small housing community on the banks of the Loosahatchee River in the northwestern part of Memphis, Tennessee. Their locations are shown in Figure C.2. While no liquefaction features were ever documented at these specific locations, the general areas are known to have experienced seismicity in the past. Results of this study are documented in Mayne (2002).

C.5 Embayment Seismic Excitation Experiment (ESEE) Sites

During the Embayment Seismic Excitation Experiments (ESEE), two test sites were selected to detonate underground explosives to generate surface waves. The first site was located in the southern NMSZ near Marked Tree, AR, and the second site selected in the northern NMSZ near Tiptonville, TN. This study has been discussed in section 6.4 of Chapter 6.

C.6 Advanced National Seismic System (ANSS) Sites

SCPTu tests were performed at monitoring sites for the Advanced National Seismic System (ANSS) in Tennessee, Arkansas, and Missouri. Locations of these sites are shown in Figures C.3 to C.5. If a significant seismic event were to occur, the soil data collected at monitoring sites would be needed to relate ground motions and deformations to the soil properties at the monitoring locations and the numerical modeling of site response. This study is documented by McGillivray et al. (2002).

Table C.1 Summary of cone penetration tests performed at the non-paleoliquefaction sites in the NMSZ since 1998

Date	Sounding	Site	City	State	Latitude N°	Longitude W°	Depth (m)	GWT (m)	Type	Section
17-Sep-98	MEMPH-H	Houston Levee	Memphis	TN	35.10833	89.73052	20.65	5.00	SCPTu2	C.1
17-Sep-98	MEMPH-I	Wolf River Boulevard	Memphis	TN	35.09927	89.80247	12.25	6.50	SCPTu2	
17-Sep-98	MEMPH-J	N 2nd Street	Memphis	TN	35.19078	90.04502	14.70	6.00	SCPTu2	
18-Sep-98	MEMPH-K	Monopole Tower	West Memphis	AR	35.15042	90.12953	32.00	4.10	SCPTu2	
28-Oct-98	I15501	I-155 Bridge	Caruthersville	MO	36.11888	89.61493	25.55	7.00	SCPTu2	
28-Oct-98	I15502	I-155 Bridge	Caruthersville	MO	36.11888	89.61493	22.00	7.00	CPTu1	
28-Oct-98	I15503	I-155 Bridge	Caruthersville	MO	36.11888	89.61493	23.00	7.00	SCPTu2	
28-Oct-98	I15505	I-155 Bridge	Caruthersville	MO	36.11888	89.61493	18.00	7.00	CPTu1	
22-Mar-99	SFSR01	Sheby Farms Shooting Range	Memphis	TN	35.12916	89.84155	30.55	2.00	SCPTu2	
22-Mar-99	SFSR02	Sheby Farms Shooting Range	Memphis	TN	35.12905	89.84030	25.50	2.00	SCPTu2	
23-Mar-99	SFOR01	Shelby Forrest	Memphis	TN	35.35780	90.01883	21.55	6.00	SCPTu2	
23-Mar-99	SFOR02	Shelby Forrest	Memphis	TN	35.35843	90.01837	21.15	6.00	SCPTu2	
4-Mar-00	MUDA	Mud Island	Memphis	TN	35.14468	90.05932	30.60	8.00	SCPTu2	C.2
5-Mar-00	MUDB	Mud Island	Memphis	TN	35.15647	90.05688	30.50	8.00	SCPTu2	
5-Mar-00	MUDC	Mud Island	Memphis	TN	35.15972	90.05642	38.00	8.00	SCPTu2	
7-Mar-00	MUDD	Mud Island	Memphis	TN	35.17568	90.05538	25.95	8.00	SCPTu2	
6-Mar-00	MUDE	Mud Island	Memphis	TN	35.17780	90.05318	24.00	8.00	SCPTu2	
8-Jul-00	CERI-MID	Center for Earthquake Research and Information	Memphis	TN	35.12372	89.93177	11.10	N/A	SCPTu2	C.3
8-Jul-00	CERI-EAST	Center for Earthquake Research and Information	Memphis	TN	35.12374	89.93186	9.85	N/A	SCPTu2	
7-Jun-01	CERI03	Center for Earthquake Research and Information	Memphis	TN	35.12366	89.93169	10.18	N/A	SCPTu2	
7-Jun-01	CERI04	Center for Earthquake Research and Information	Memphis	TN	35.12366	89.93169	21.33	N/A	SCPTu2	

406

Table C.1 Summary of cone penetration tests performed at the non-paleoliquefaction sites in the NMSZ since 1998 (Continued)

Date	Sounding	Site	City	State	Latitude N°	Longitude W°	Depth (m)	GWT (m)	Type	Section
5-Jun-01	SWG01	Sewage Treatment Plant near Wolf River	Collierville	TN	35.09335	89.71093	28.58	7.00	SCPTu2	
5-Jun-01	SWG02	Sewage Treatment Plant near Wolf River	Collierville	TN	35.09333	89.71091	30.35	7.00	SCPTu2	C.4
6-Jun-01	TRPK01	Trailer Park near Loosahatchee River	Memphis	TN	35.23957	90.02412	14.95	3.30	SCPTu2	
6-Jun-01	TRPK02	Trailer Park near Loosahatchee River	Memphis	TN	35.23957	90.02412	15.05	3.30	RCPTu1	
17-Oct-02	BLST01	Mooring Blast Site - Preblast	Mooring	TN	36.33203	89.58680	38.95	8.00	SCPTu2	
29-Oct-02	BLST05	Mooring Blast Site - 2 hour after blast	Mooring	TN	36.33203	89.58680	25.80	8.00	SCPTu2	
1-Nov-02	BLST08	Mooring Blast Site - 64 hours after blast	Mooring	TN	36.33203	89.58680	28.08	8.00	SCPTu2	
15-Jun-03	BLST11	Mooring Blast Site - 229 days after blast	Mooring	TN	36.33203	89.58680	22.93	3.50	SCPTu2	C.5
28-Oct-02	BLST04	Marked Tree Blast Site - Preblast	Marked Tree	AR	35.46024	90.56563	29.00	4.90	SCPTu2	
31-Oct-02	BLST07	Marked Tree Blast Site - 40 hours after blast	Marked Tree	AR	35.46024	90.56563	28.58	4.90	SCPTu2	
14-Jun-03	BLST09	Marked Tree Blast Site - 229 days after blast	Marked Tree	AR	35.46024	90.56563	22.15	3.50	SCPTu2	
14-Jun-03	BLST10	Marked Tree, AR - K2 array site	Marked Tree	AR	35.48452	90.55111	19.48	3.50	SCPTu2	

407

Table C.1 Summary of cone penetration tests performed at the non-paleoliquefaction sites in the NMSZ since 1998 (Continued)

Date	Sounding	Site	City	State	Latitude N°	Longitude W°	Depth (m)	GWT (m)	Type	Section
18-Oct-02	BLST02	MORT ANSS station	Mooring	TN	36.32481	89.56696	24.73	6.00	SCPTu2	
16-Jun-03	GILT01	GILT ANSS Station, STCC.	Memphis	TN	35.23019	89.98315	21.68	N/A	SCPTu2	
16-Jun-03	COLT01	COLT ANSS Station	Collierville	TN	35.03836	89.69209	11.82	N/A	SCPTu2	
17-Jun-03	RDST01	RDST ANSS station, Rhodes College	Memphis	TN	35.15775	89.98885	10.63	5.00	SCPTu2	
20-Sep-03	GSAR01	GSAR ANSS station, Gosnell High School	Gosnell	AR	35.96172	89.96940	24.10	5.00	SCPTu2	C.6
20-Sep-03	LNXT01	LNXT ANSS station	Lenox	TN	36.10192	89.49125	30.83	N/A	SCPTu2	
22-Sep-03	SHBF01	SFTN ANSS station	Memphis	TN	35.35785	90.01882	21.32	N/A	SCPTu2	
9-Aug-04	GLAT01	GLAT ANSS station	Dyesburg	TN	36.26925	89.28779	10.93	N/A	SCPTu2	
10-Aug-04	HALT01	HALT ANSS station	Dyesburg	TN	35.91071	89.33946	26.85	7.00	SCPTu2	
10-Aug-04	PEBM01	PEBM ANSS station	Steels	MO	36.11285	89.86240	25.00	2.40	SCPTu2	
11-Aug-04	PENM01	PENM ANSS station	Portageville	MO	36.44971	89.62819	34.18	4.00	SCPTu2	
11-Aug-04	HENM01	HENM ANSS station	Sikeston	MO	36.71608	89.47210	30.88	4.00	SCPTu2	
12-Aug-04	HICK01	HICK ANSS station	Hickman	KY	36.54072	89.22837	19.03	15.00	SCPTu2	

408
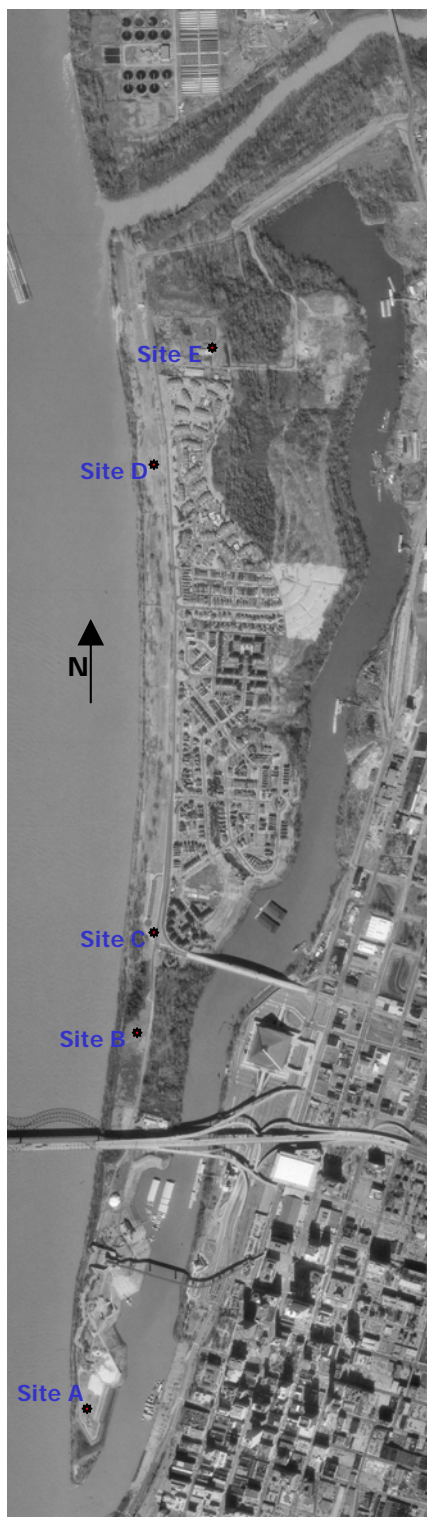
Figure C.1 Aerial photo showing the location of the tests sites at Mud Island, Memphis, Tennessee (Photo from http://terraserver.microsoft.com)

409
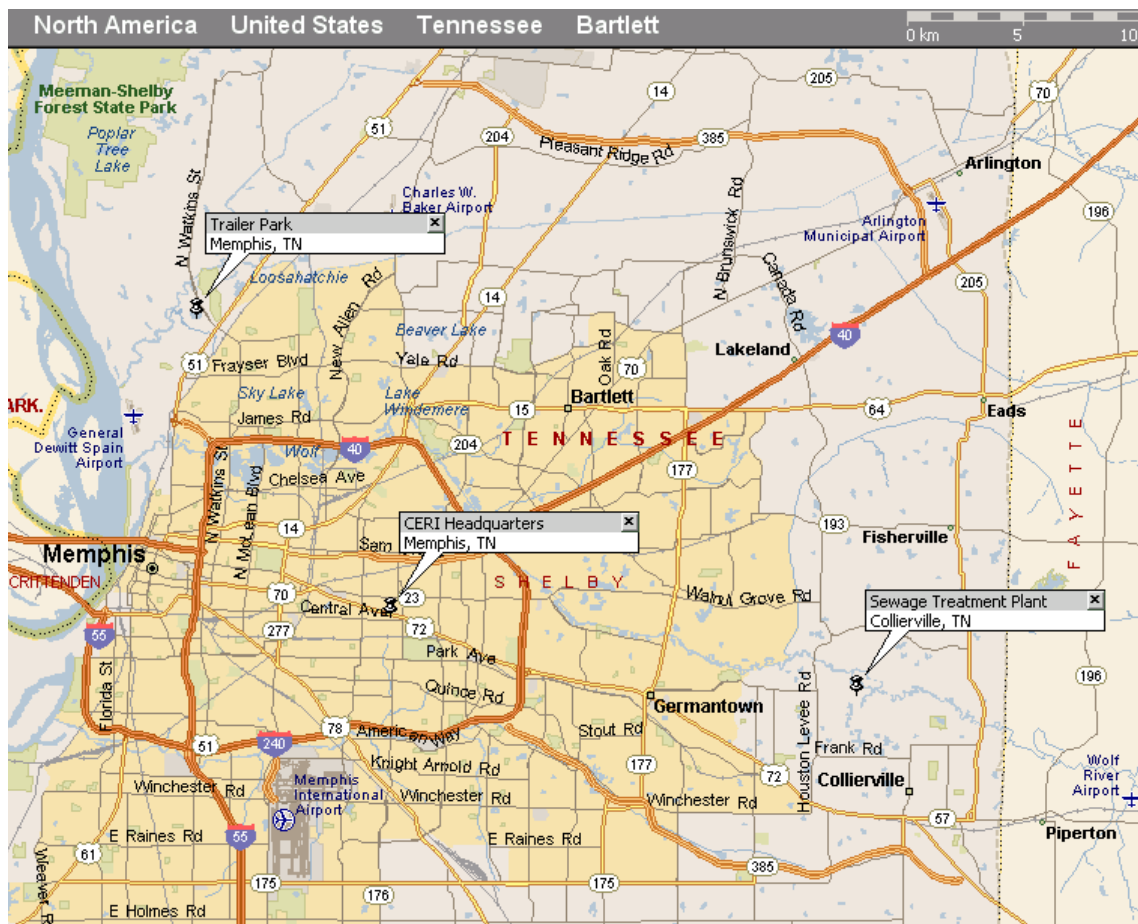
Figure C.2 Map showing the location of Center for Earthquake Research and Information (CERI) Headquarter and test sites near Memphis, TN

410
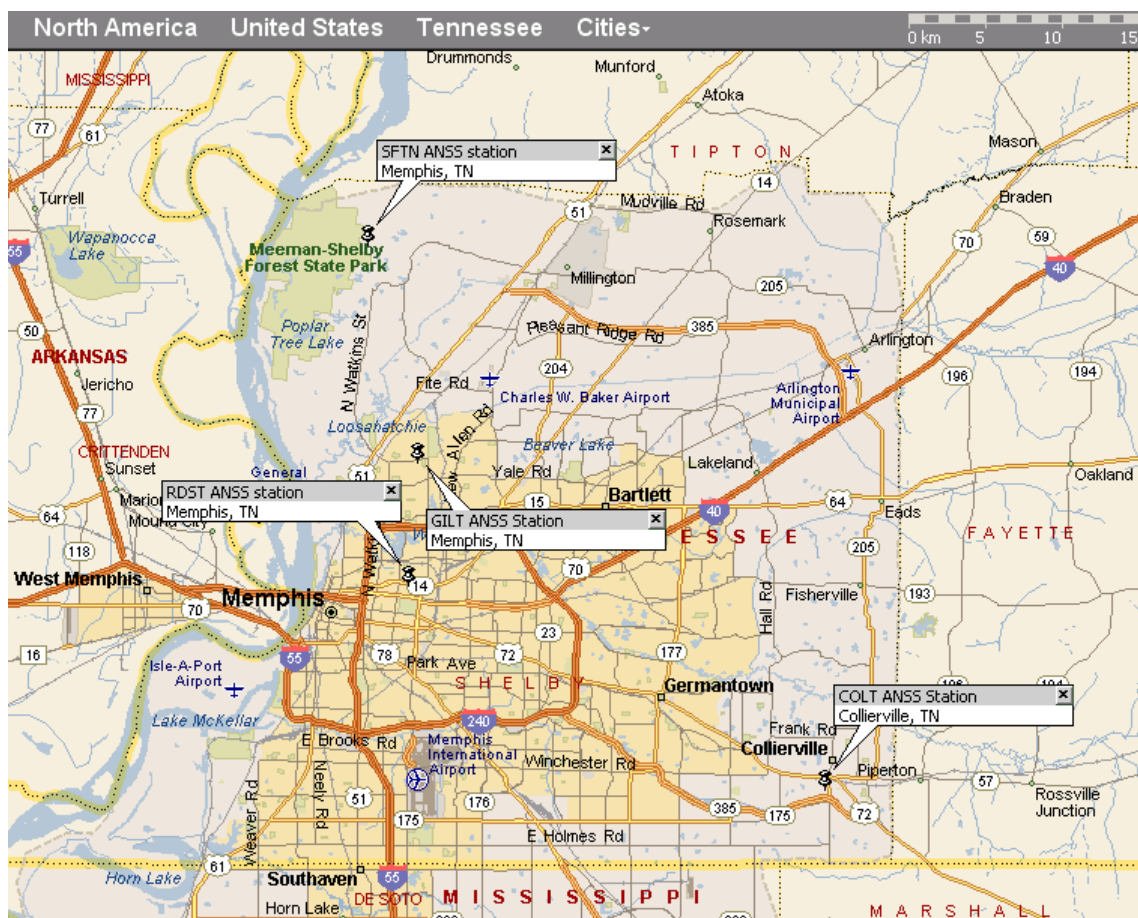
Figure C.3 Map showing ANSS station sites near Memphis, Tennessee
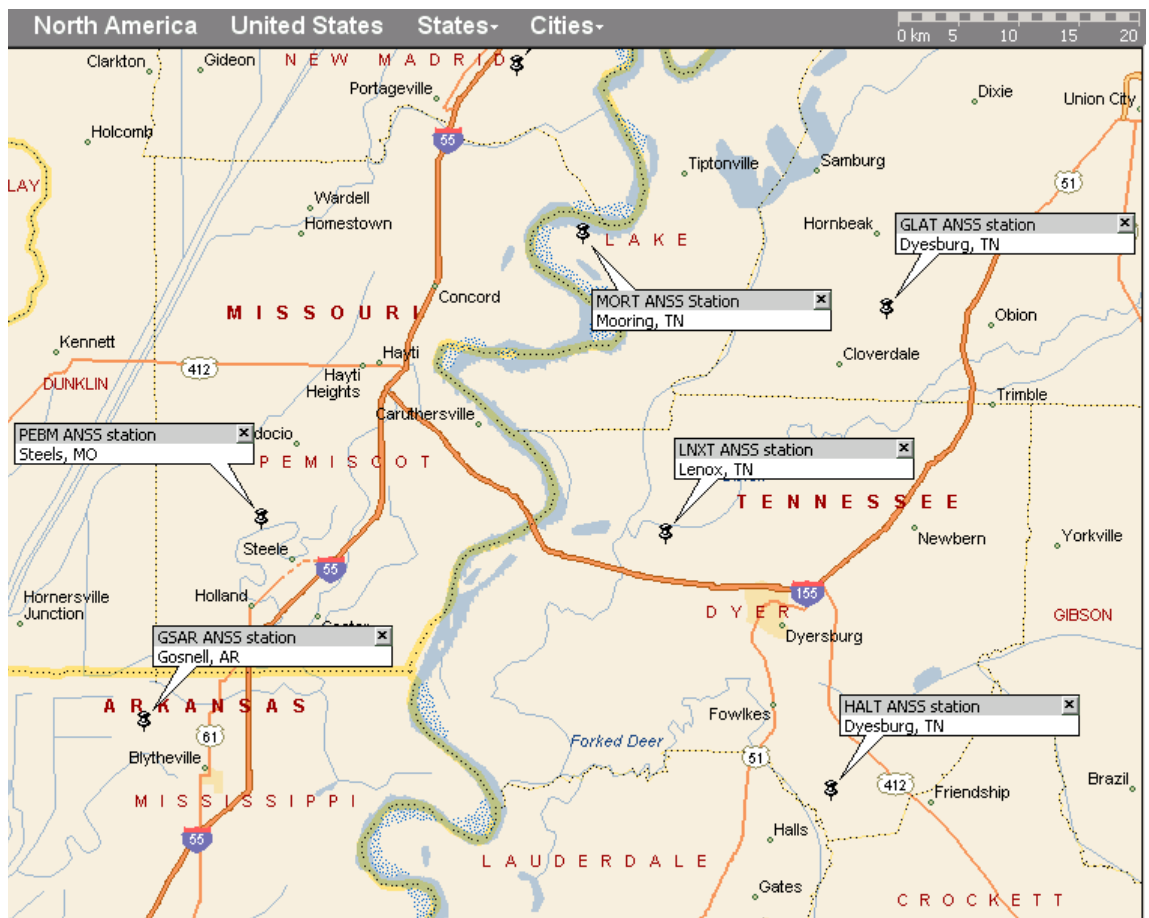
Figure C.4 Map showing ANSS station sites in Tennessee, Arkansas, and Missouri

Figure C.5 Map showing ANSS station sites in Tennessee, Arkansas, and Missouri

APPENDIX D

LIQUEFACTION EVALUATION AT
PALEOLIQUEFACTION TEST SITES IN NMSZ

For selected paleoliquefaction test sites which causative earthquakes have been dated, their liquefaction potential is evaluated using the procedures outlined in Chapter 5. The scenario earthquakes are assumed to be the same earthquake events that liquefied the test sites previously discussed.

D.1 Yarbro Excavation Paleoliquefaction Site

The large liquefaction features at Yarbro site include up to 6 m of subsidence and are believed to be formed during the 1811-1812 earthquakes (Tuttle, 1999). Figure D.1 shows the location of Yarbro site relative to the epicenters of the causative earthquakes events. It is closest to the epicenter of the $M_w = 8.1$ earthquake event (5 km), which is supposed be generate the strongest bedrock motion fot the Yarbro site. For this event, the time-history of bedrock motion generated for the Yarbro site using the program SMSIM is presented in Figure D.2. Since the empirical attenuation relationship proposed by Boore & Joyner (1991) can only be used for distance from 10 to 400 km, the CSR is computed only by DEEPSOIL. It is compared with the CRRs derived from tip resistance q_T and shear wave velocity V_s in Figure D.3 indicating fairly extensive liquefaction to 25 m depths. The probabilities of liquefaction based on q_T and V_s are shown quite high in Figure D.4.

D.2 Bugg Site and Hueys Site

The Bugg site and Hueys site are located very close together, and the liquefaction features at both sites are attributed to the 900 A.D (Tuttle, 1999). earthquake events. The distances between these two sites and the epicenters of the earthquakes events are shown in Figure D.5. According the SMSIM program, the strongest bedrock motion generated at these sites is caused by the $M_w = 7.6$ earthquake event, as shown in Figure D.6. For Bugg site, results of liquefaction analysis by deterministic and probabilistic approaches are shown in Figures G.7 and G.8, respectively. They are shown in Figures D.9 and D.10 for Hueys site.

D.3 Dodd Farm Site

Liquefaction features at Dodd Farm site are attributed to 1530 A.D (Tuttle, 1999). earthquakes, and its distances to the epicenters of the earthquake events are shown in Figure D.11. The strongest bedrock motion is generated by the $M_w = 7.6$ earthquake event, as shown in Figure D.12. The CSR is computed using the program DEEPSOIL, and it is compared with the CRR derived from q_T and V_s in Figure D.13. Results of liquefaction evaluation by probabilistic approaches are shown in Figure D.14.

D.4 Johnson Farm Site

Liquefaction features at Johnson Farm site are believed to be caused by the 900 A.D. earthquakes (Tuttle, 1999), as shown in Figure D.15. The strongest bedrock motion is generated from the $M_w = 8.1$ earthquake event (Figure D.16). Results of liquefaction

evaluation by deterministic and probabilistic approaches are shown in Figures D.17 and D.18.

D.5 Nodena Site

Liquefaction features at Nodena site is attributed to the 1530 earthquake events (Tuttle et al., 2000), as shown in Figure D.19. The strongest bedrock motion is generated from the $M_w = 7.6$ earthquake event (Figure D.20). Results of liquefaction evaluation by deterministic and probabilistic approaches are shown in Figures D.21 and D.22.
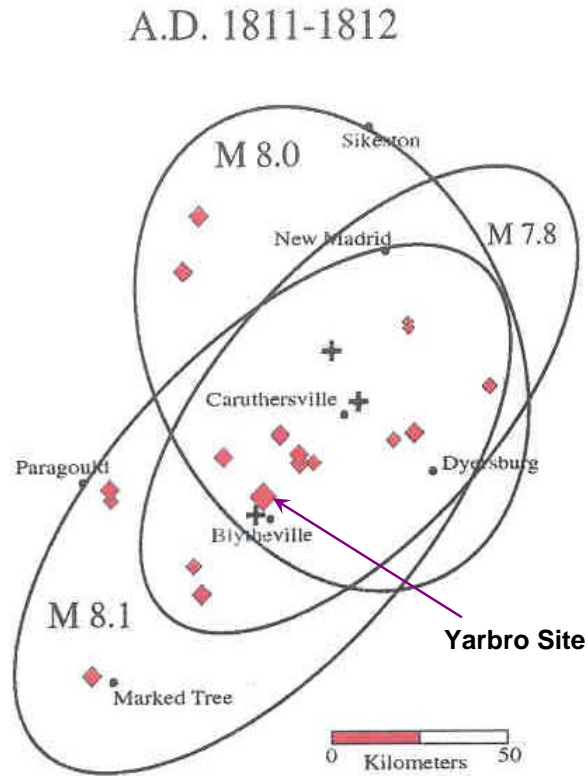
A.D. 1811-1812

Figure D.1 Yarbro site and the estimated epicenters of the seismic events that occurred in 1811 - 1812 in NMSZ (modified from Tuttle, 1999)
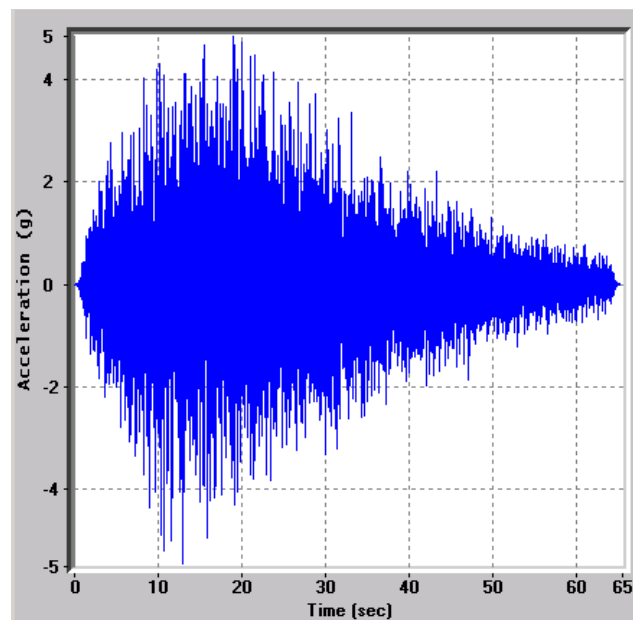
Figure D.2 Example time-history of bedrock motion generated for the Yarbro site in the event of the $M_w = 8.1$ earthquakes occurring on 12/16/1811 using the program SMSIM

417
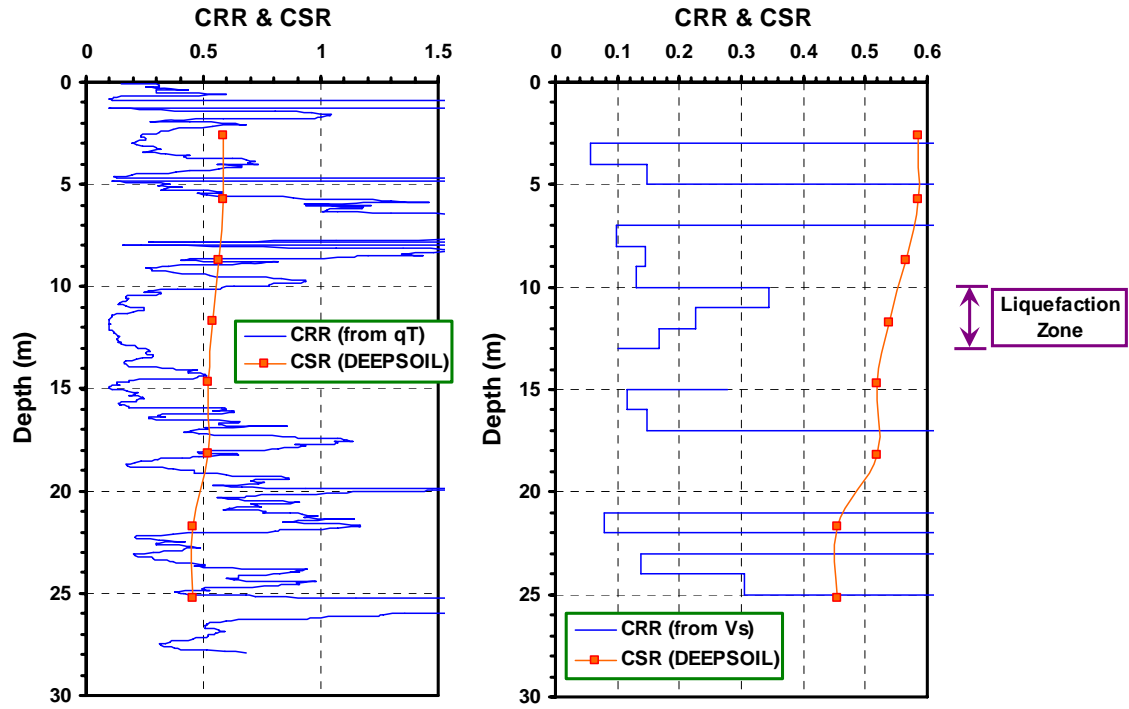
Figure D.3 Liquefaction analyses by deterministic approaches based on the SCPTu sounding performed at Yarbro site ($M_w = 8.1$, epicentral distance = 5 km)
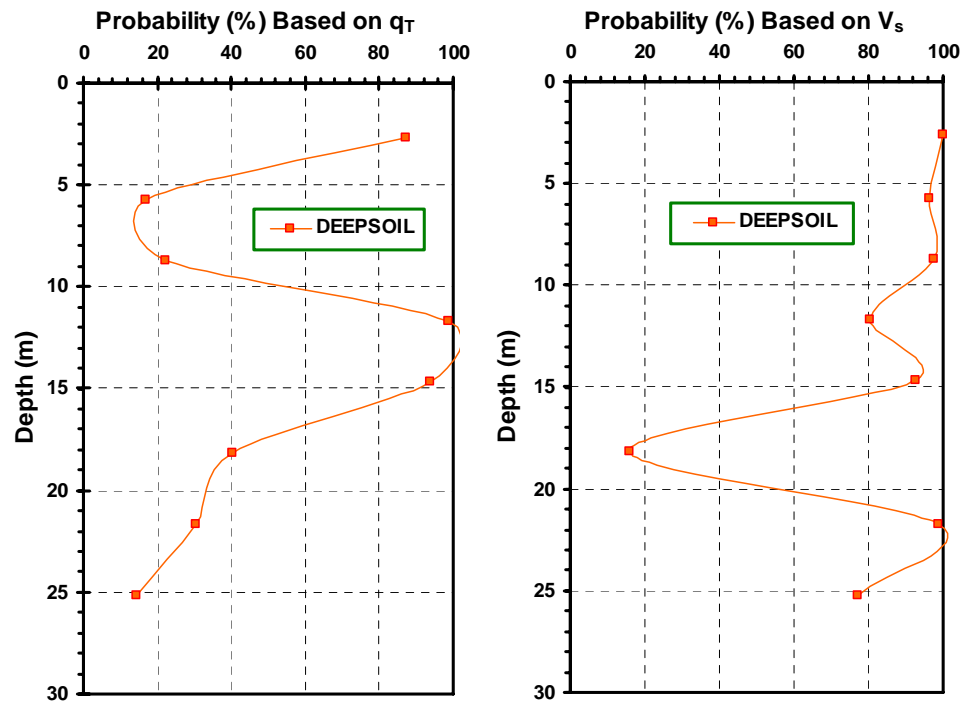
Figure D.4 Liquefaction analyses by probabilistic approaches based on the SCPTu sounding performed at Yarbro site ($M_w = 8.1$, epicentral distance = 5 km)
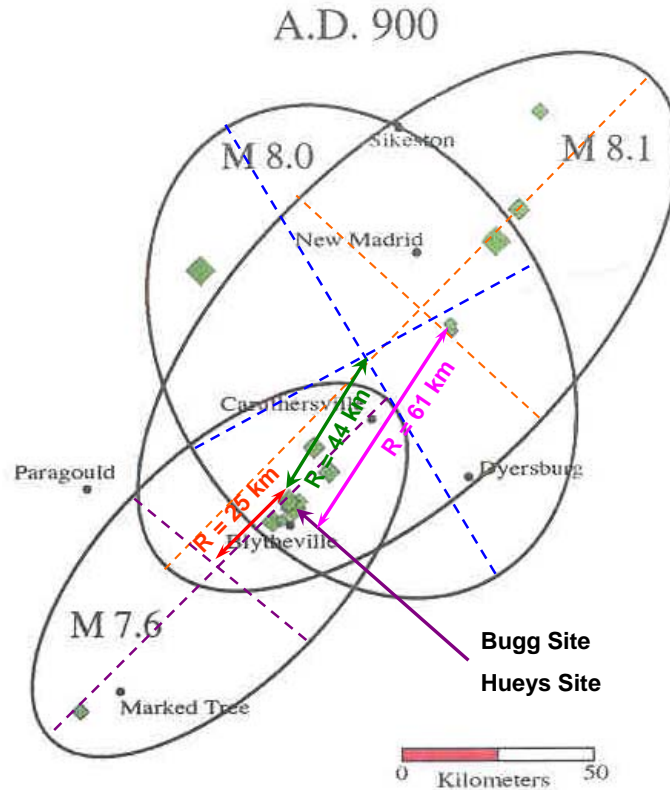
Figure D.5 Bugg site, Hueys site, and the estimated epicenters of the seismic events that occurred in 900 A.D. in NMSZ (modified from Tuttle, 1999)
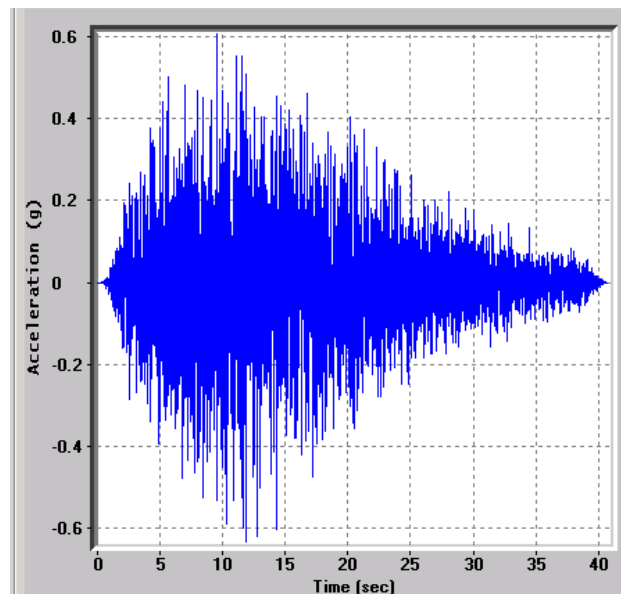
Figure D.6 Example time-histories of bedrock motion generated for the Bugg site and Hueys site in the event of the $M_w = 7.6$ earthquake occurring around 900 A.D. using the program SMSIM
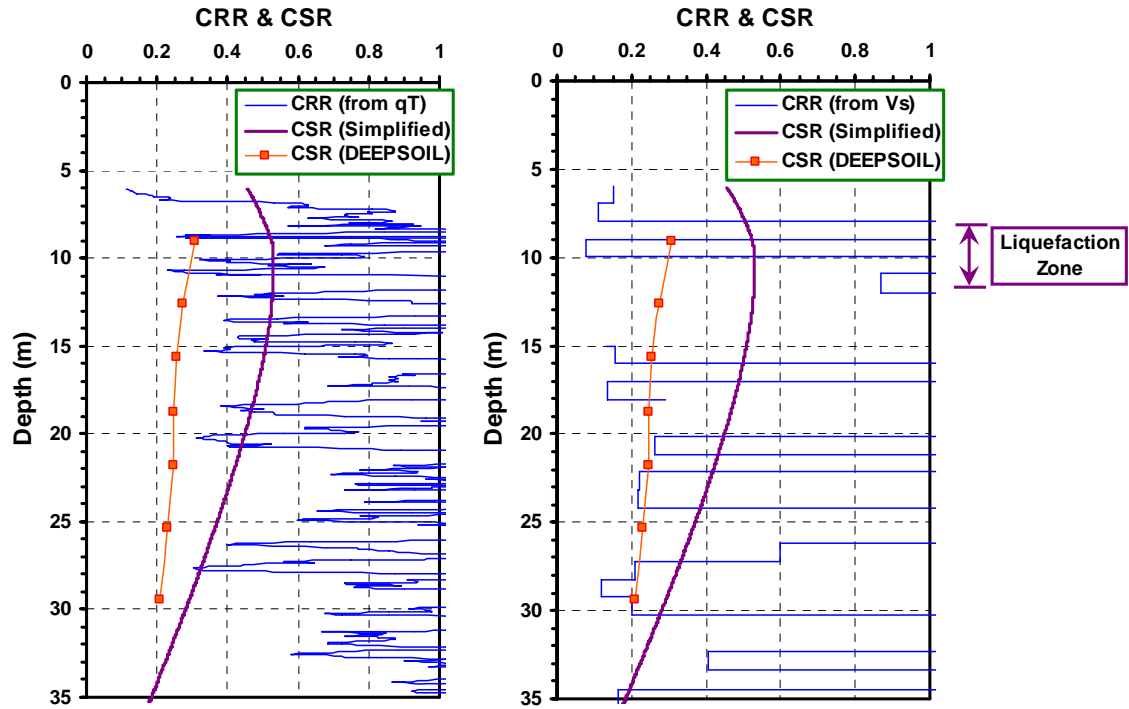
Figure D.7 Liquefaction analyses by deterministic approaches based on the SCPTu sounding (BUGG01) performed at the Bugg site ($M_w = 7.6$, epicentral distance = 25 km)
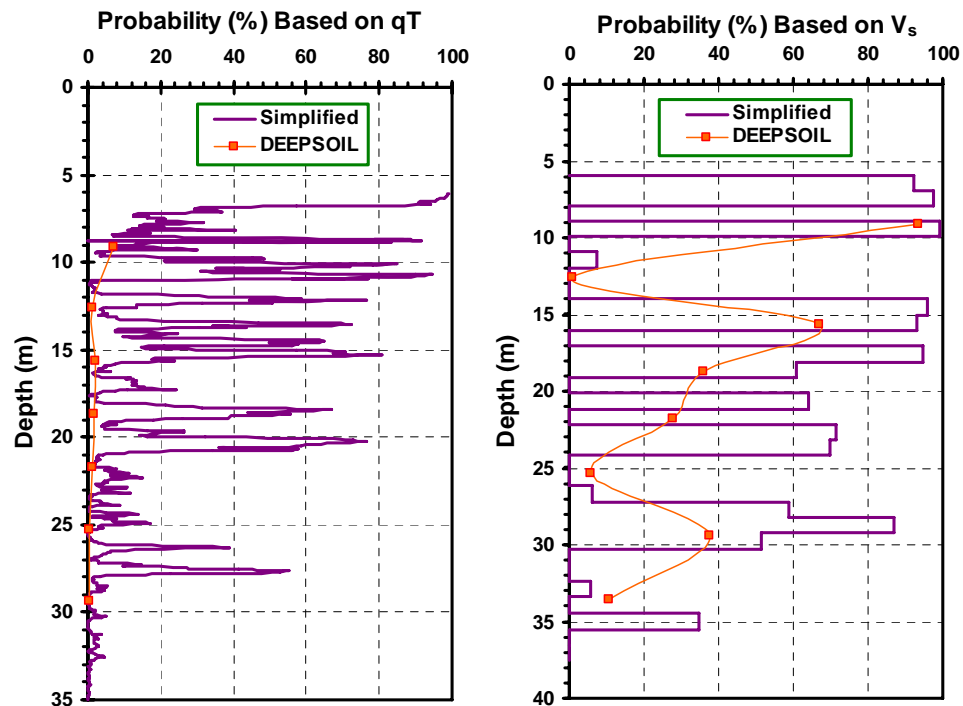
Figure D.8 Liquefaction analyses by probabilistic approaches based on the SCPTu sounding (BUGG01) performed at the Bugg site ($M_w = 7.6$, epicentral distance = 25 km)
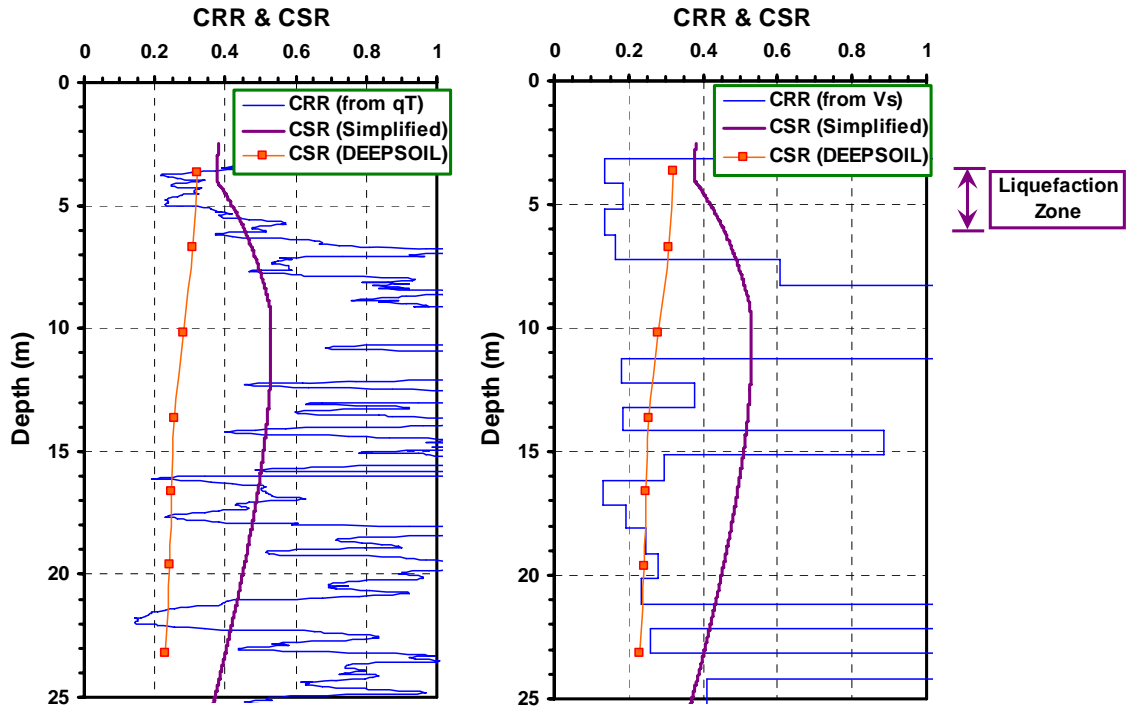
Figure D.9 Liquefaction analyses by deterministic approaches based on the SCPTu sounding (HUEY01) performed at Hueys site (M_w = 7.6, epicentral distance = 25 km)
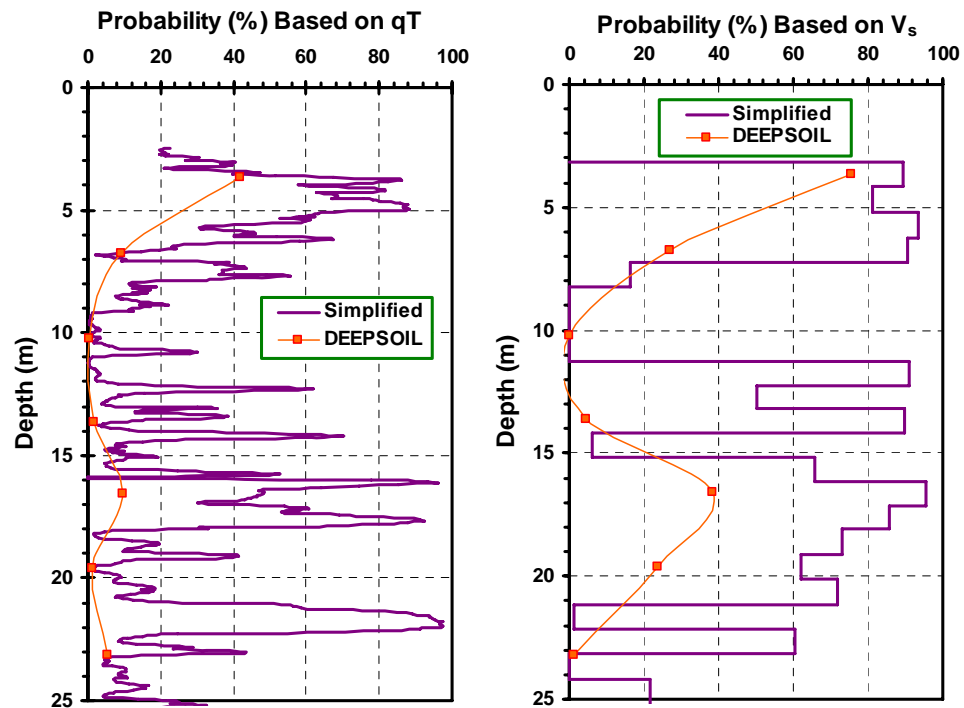
Figure D.10 Liquefaction analyses by probabilistic approaches based on the SCPTu sounding (HUEY01) performed at Hueys site (M_w = 7.6, epicentral distance = 25 km)
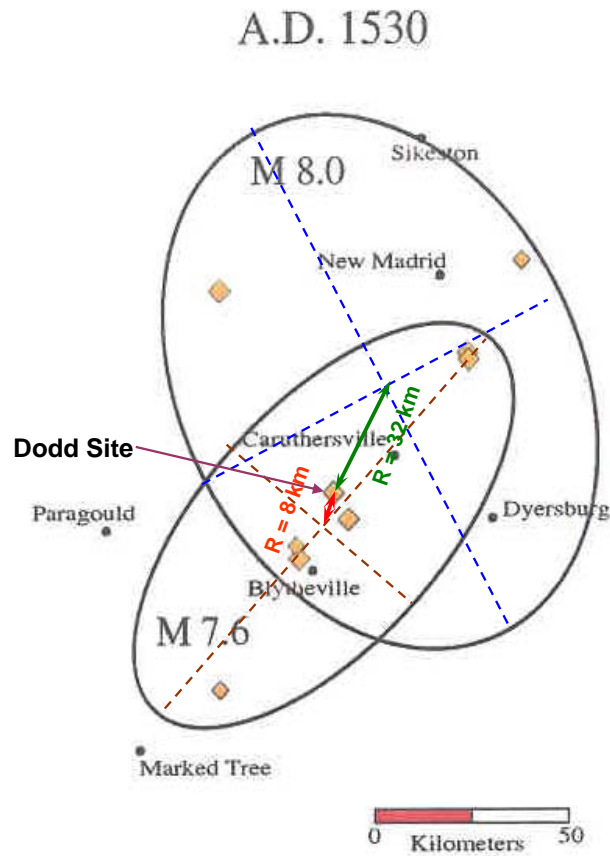
Figure D.11 Distance from Dodd Farm site to the estimated epicenters of the seismic events that occurred around 1530 A.D. in NMSZ (modified from Tuttle, 1999)
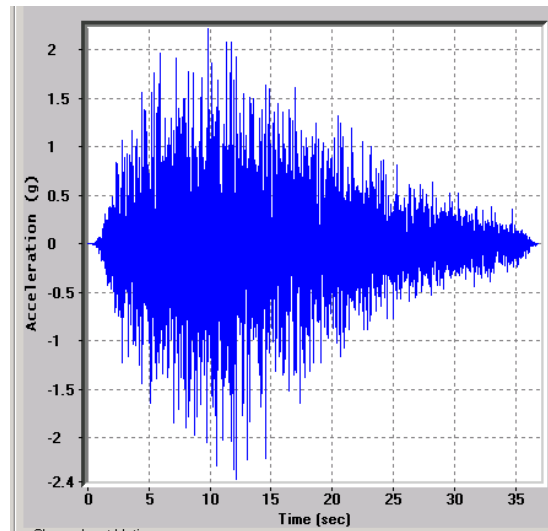
Figure D.12 Example time-history of bedrock motion generated for the Dodd Farm site in the event of the $M_w = 7.6$ earthquake event occurring around A.D 1530 using the program SMSIM
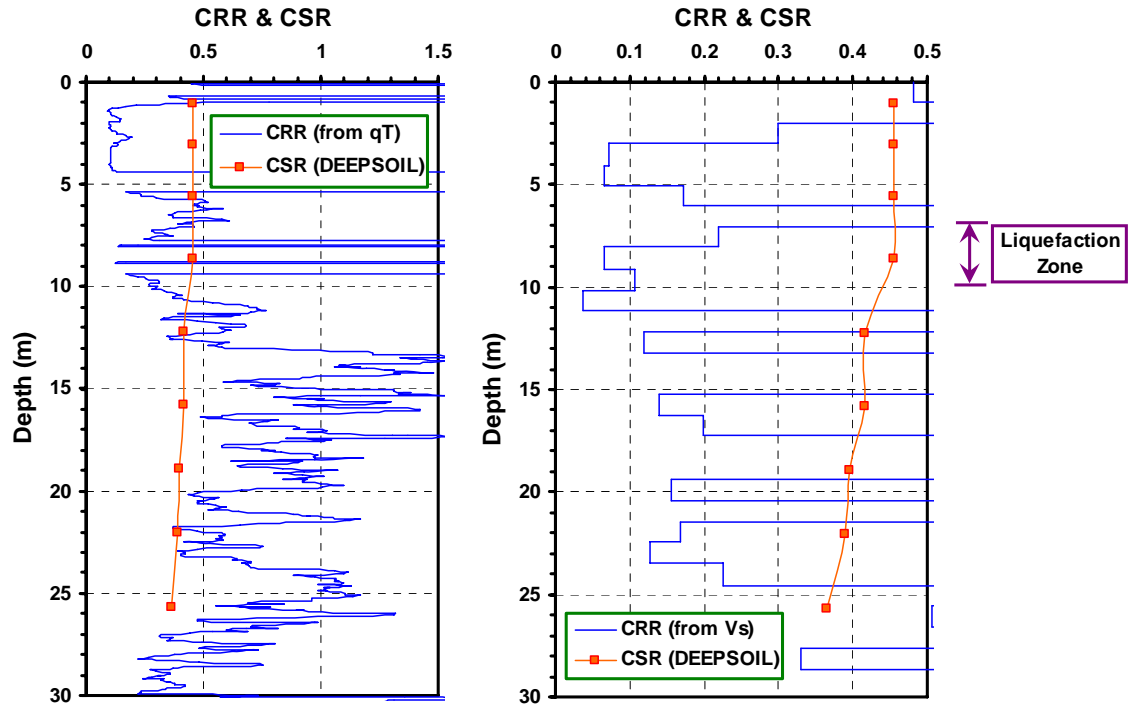
Figure D.13 Liquefaction analyses by deterministic approaches based on the SCPTu sounding performed at Dodd Farm site (M_w = 7.6, epicentral distance = 8 km)
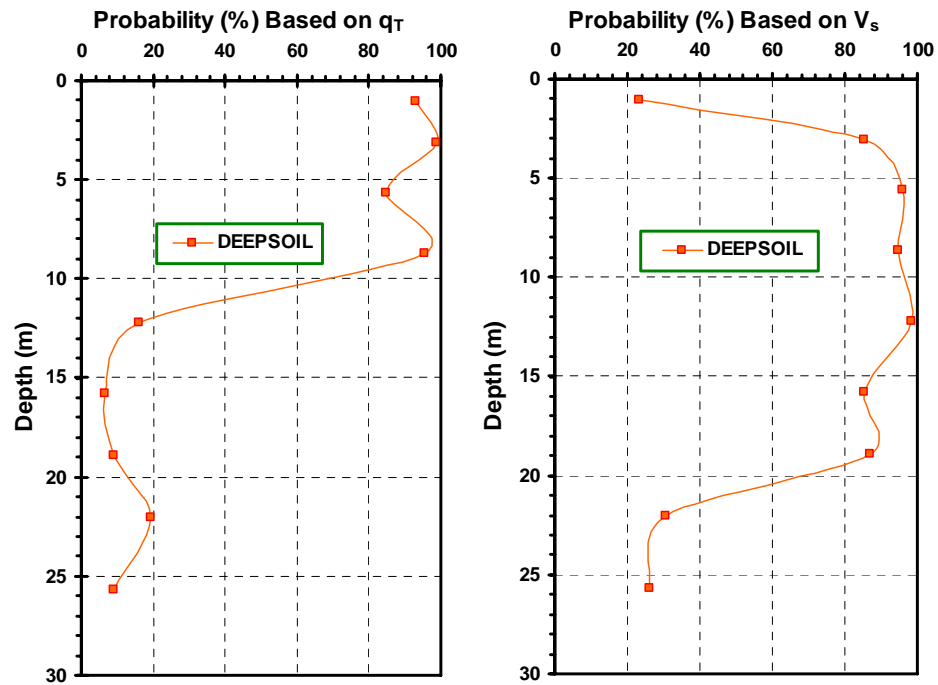
Figure D.14 Liquefaction analyses by probabilistic approaches based on the SCPTu sounding performed at Dodd Farm site (M_w = 7.6, epicentral distance = 8 km)
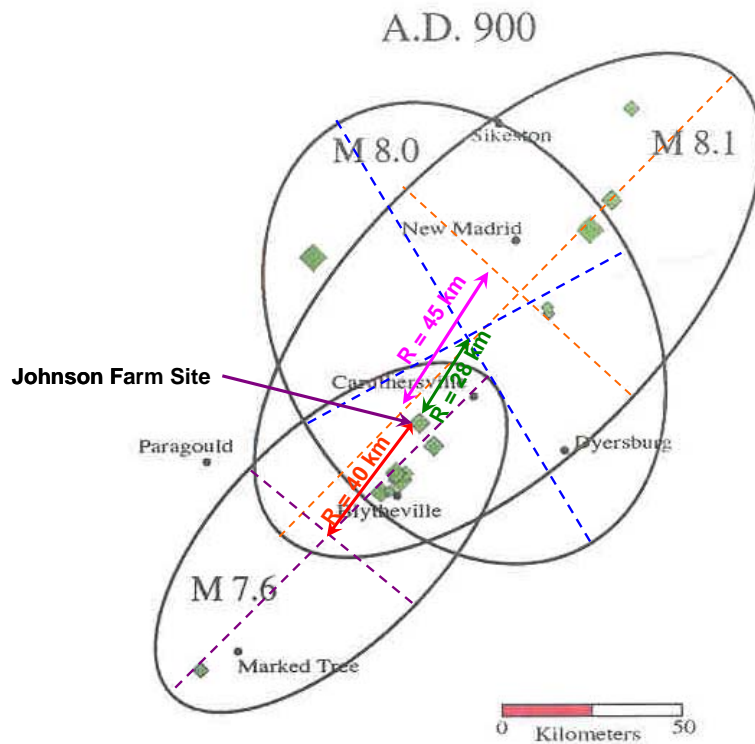
Figure D.15 Distance from Johnson Farm site to the estimated epicenters of the seismic events that occurred around 900 A.D. in NMSZ (modified from Tuttle, 1999)
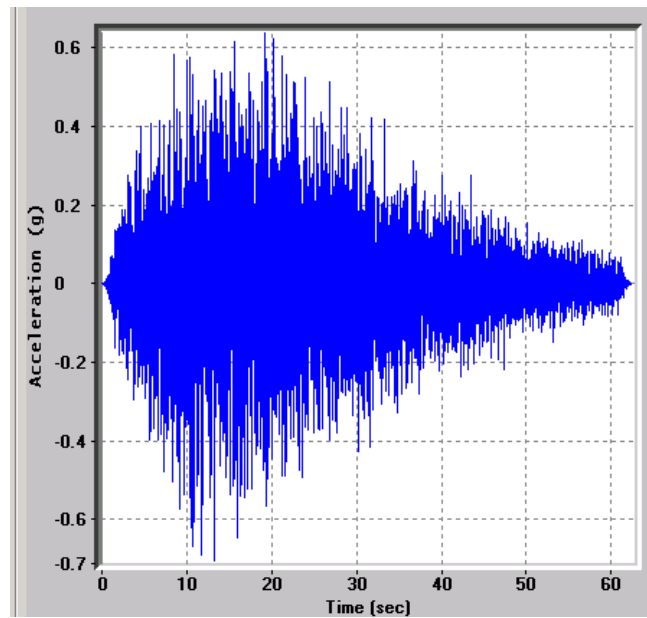
Figure D.16 Example time-histories of bedrock motion generated for the Johnson Farm site in the event of the $M_w = 8.1$ earthquakes occurring around 900 A.D. using the program SMSIM
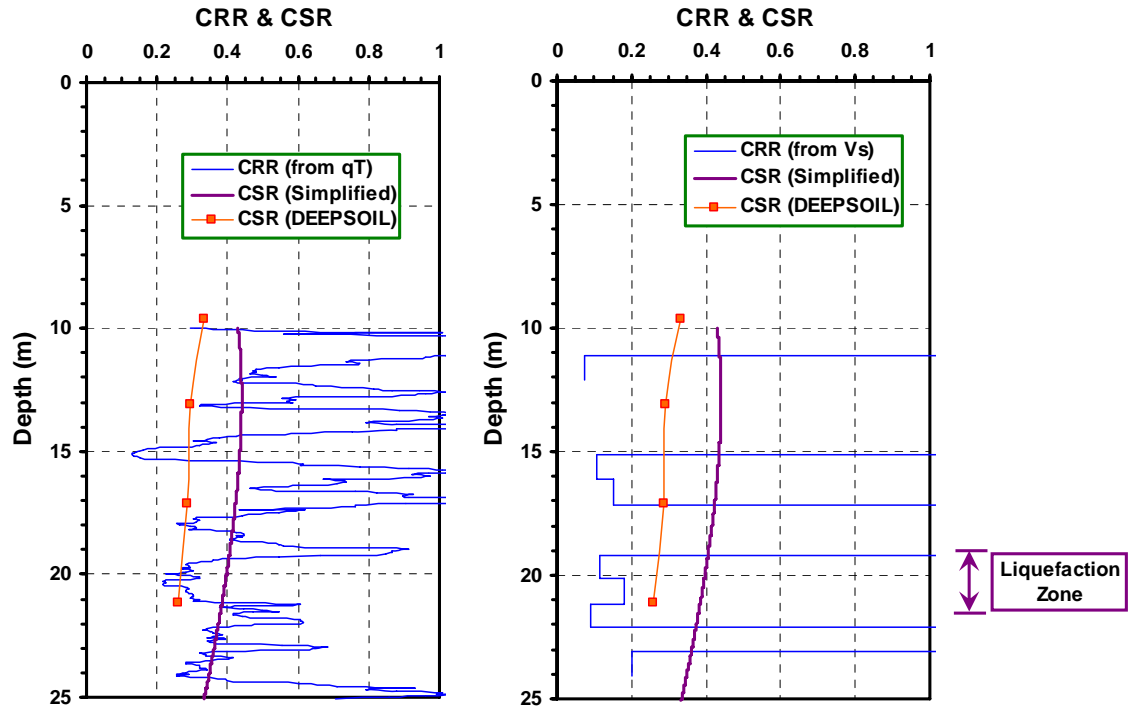
Figure D.17 Liquefaction analyses by deterministic approaches based on the SCPTu sounding performed at Johnson Farm site ($M_w = 8.1$, epicentral distance = 28 km)
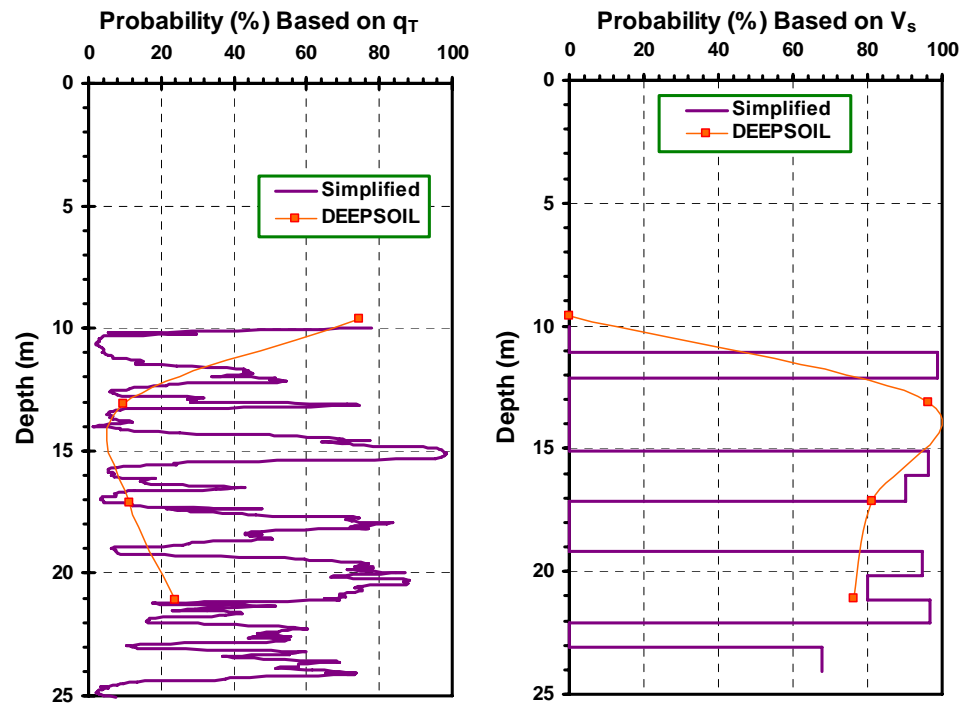
Figure D.18 Liquefaction analyses by probabilistic approaches based on the SCPTu sounding performed at Johnson Farm site ($M_w = 8.1$, epicentral distance = 28 km)
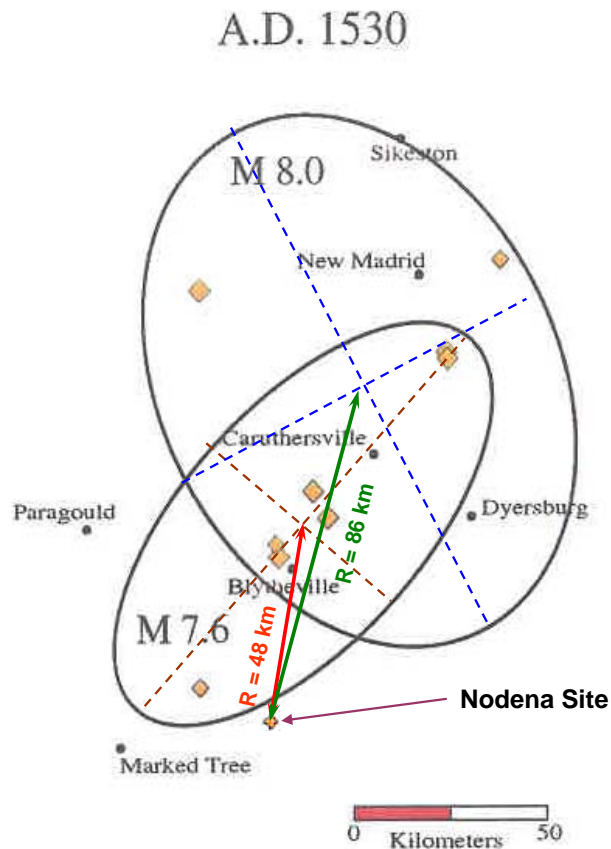
Figure D.19 Distance from the Nodena site to the estimated epicenters of the seismic events that occurred around 1530 A.D. in NMSZ (modified from Tuttle, 1999)
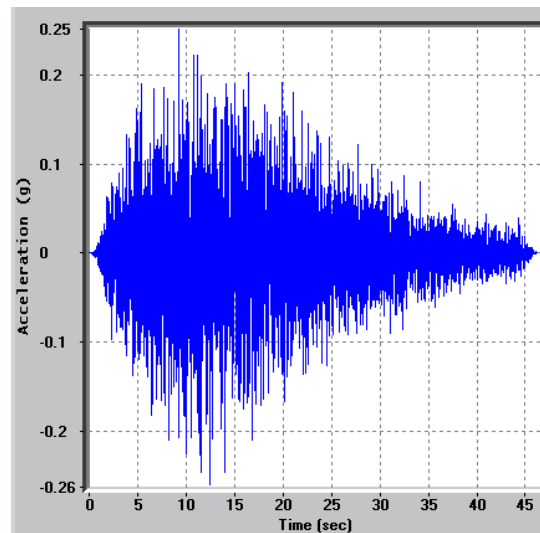
Figure D.20 Example time-histories of bedrock motion generated for the Nodena site in the event of the $M_w = 7.6$ earthquake event occurring around A.D 1530 using the program SMSIM

426
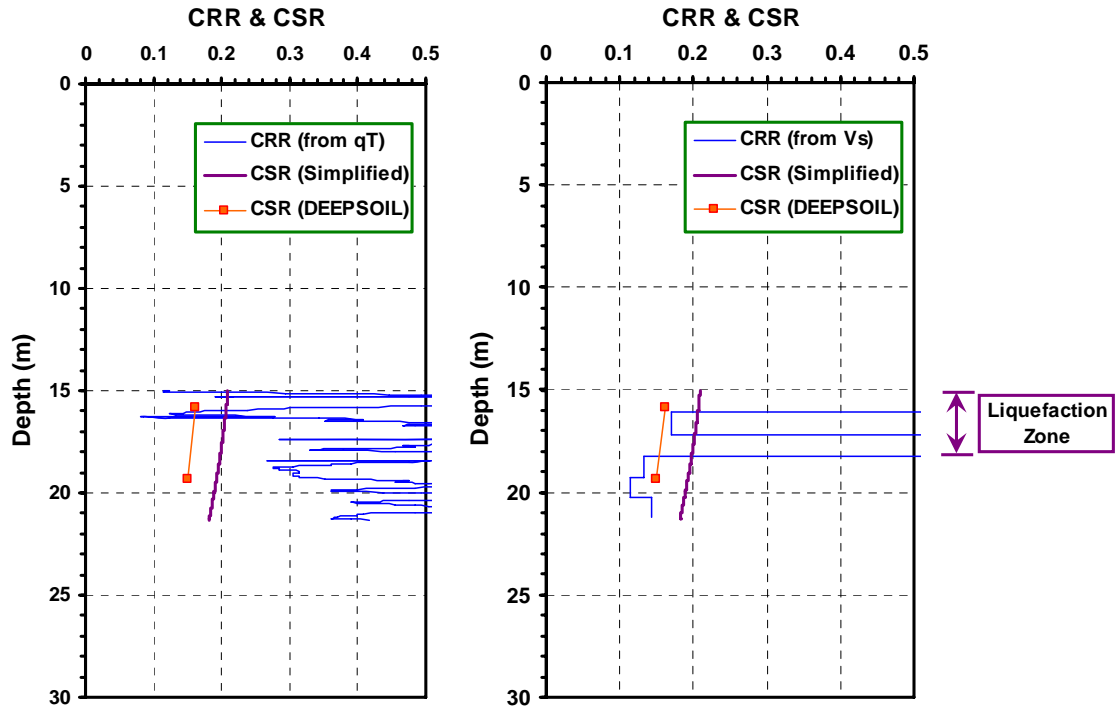
Figure D.21 Liquefaction analyses by deterministic approaches based on the SCPTu sounding performed at Nodena site (M_w = 7.6, epicentral distance = 48 km)
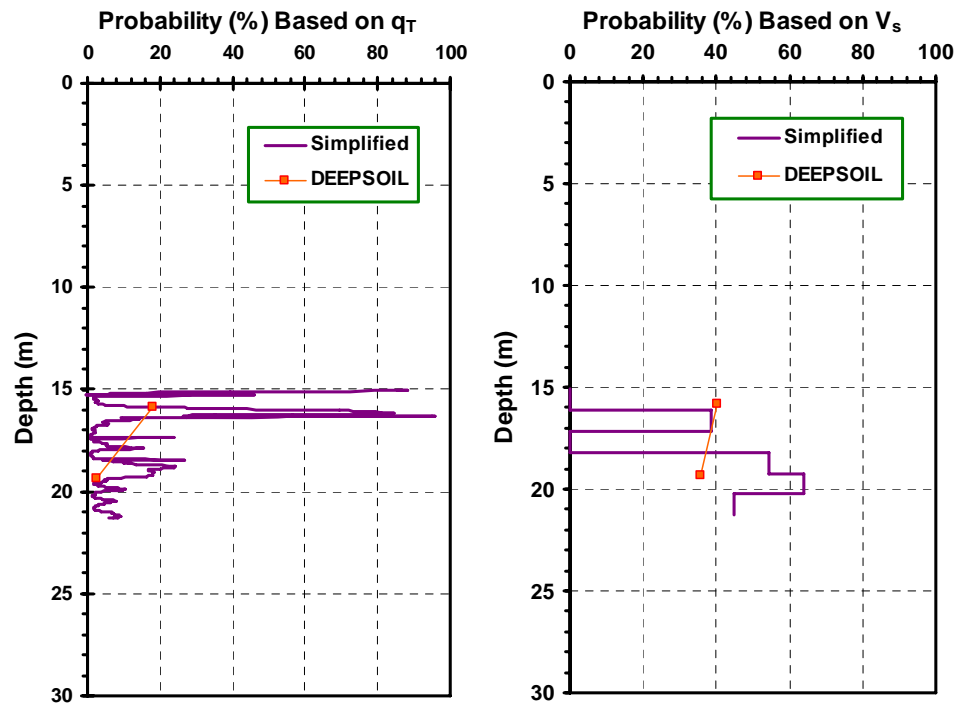
Figure D.22 Liquefaction analyses by probabilistic approaches based on the SCPTu sounding performed at Nodena site (M_w = 7.6, epicentral distance = 48 km)

APPENDIX E

INSTRUCTIONS FOR *SHEARPRO* 1.3

1. General Information

1) This program can be run on operating systems Window 95/98/2000/XP;

2) Shear wave files of the same format as the ASCII files converted from the binary files collected by Hogentogler computers are used as input, as shown in Figure E.1;

2. Install

1) Unzip/copy all the files of this program into a new folder;

2) Find the setup.exe file and set up the program on your computer;

3) The icon of ShearWavePro should appear on your Start Program Menu.

3. Configuration

After starting this program, click the menu item of "File\Configurations" to set up the necessary parameters, which include the string distance between the cone and the seismic source, and the distance between the geophone and cone tip, as shown in Figure E.2.

4. Load the files

Click the menu item of "File\Load…" and load the raw shear wave files in ASCII format. After the files are loaded, the filtered waves should appear on the screen

with the corresponding depth shown on the left of each wave train, as shown in Figure E.3.

5. Clip the waves using the window

Each wave train has a window, which consists of a left (red) bar and a right (blue) bar. These bars can be selected and dragged by the mouse to clip the waves, and only the part that is left in the window is used for future computations, as shown in Figure E.4.

6. Run

After the waves have been clipped by the window, click the menu item of "Run\Cross-Correlation" to compute the wave velocity.

7. View

1) After cross-correlation is performed, the items in the pull-down menu of "View" are enabled, and the results can be viewed by clicking these items;

2) The raw shear wave trains can be displayed on screen by clicking the item of "Original Waves";

3) The filtered shear wave trains can be displayed on screen by clicking the item of "Original Waves";

4) The computed shear wave velocity can be plotted on screen by clicking the item of "Shear Wave Velocity from Cross-Correlation";

5) The computed coefficient of determination (r^2) for cross-correlation can be plotted on screen by clicking the item of "Coef. of Determination";

6) Data of the computed velocity and coefficient of determination data can be displayed by clicking the item of "Velocity Data", and the data can be saved in a text file. Format of the saved file is shown in Figure E.5.

8. Save

After the results are generated, they can be saved in a .swp file by click the menu item of "File\Save" or "File\Save As…" And this file can be opened by click the menu item of "File\Open".

Note: User accepts all risks associated with output data and results. Authors make no claim to accuracy or reasonableness of results and possible errors.

Sounding: coke01
Depth: 1.075 meter(s)

 TIME   AMPLITUDE
 (ms)

0.025   -0.1049
0.050   -0.1006
0.075   -0.0964
0.100   -0.0964
0.125   -0.0964
0.150   -0.0899
0.175   -0.0964
0.200   -0.0921
0.225   -0.0985
0.250   -0.0964
0.275   -0.0985
 …   ….

Figure E.1 Format of input shear wave file
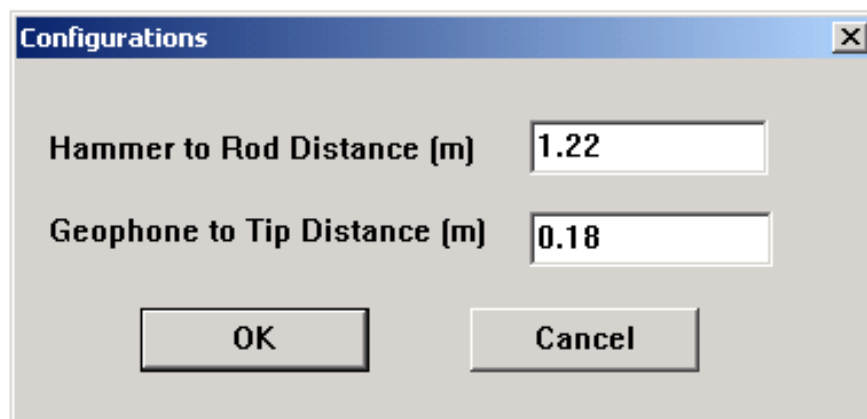
Figure E.2 Configurations at the start of the program *ShearPro*

431
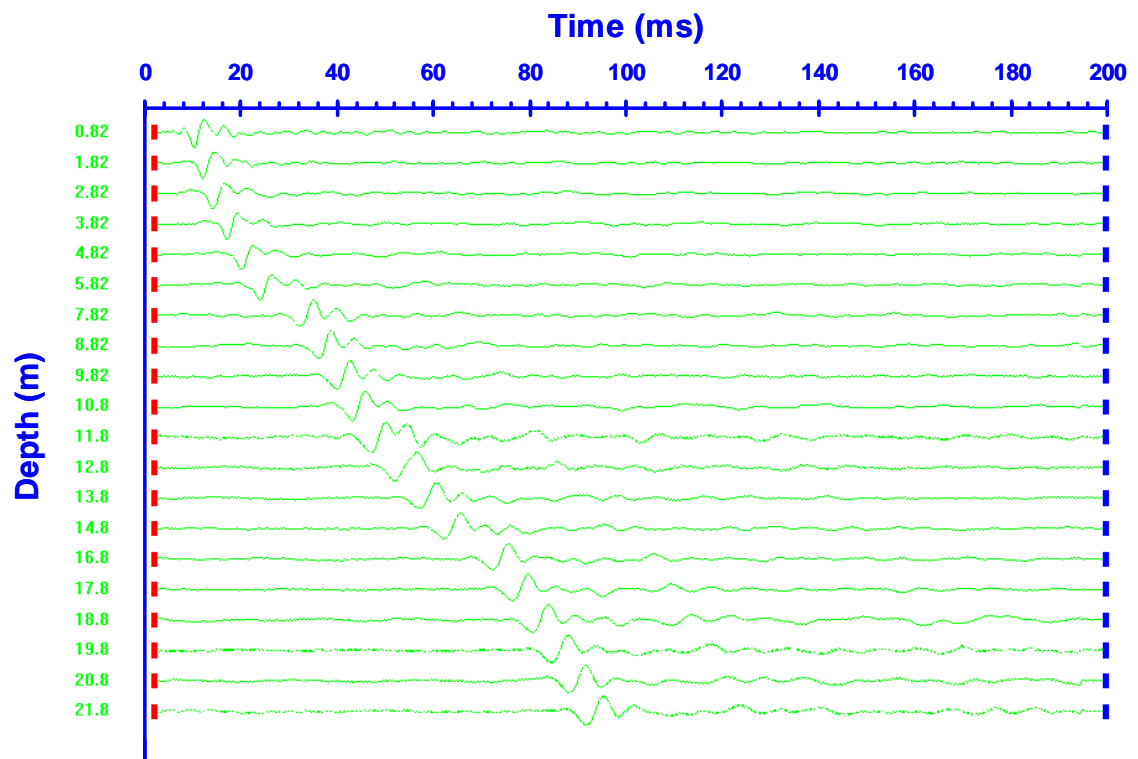
Figure E.3 Shear wave trains displayed on screen after shear wave files are loaded
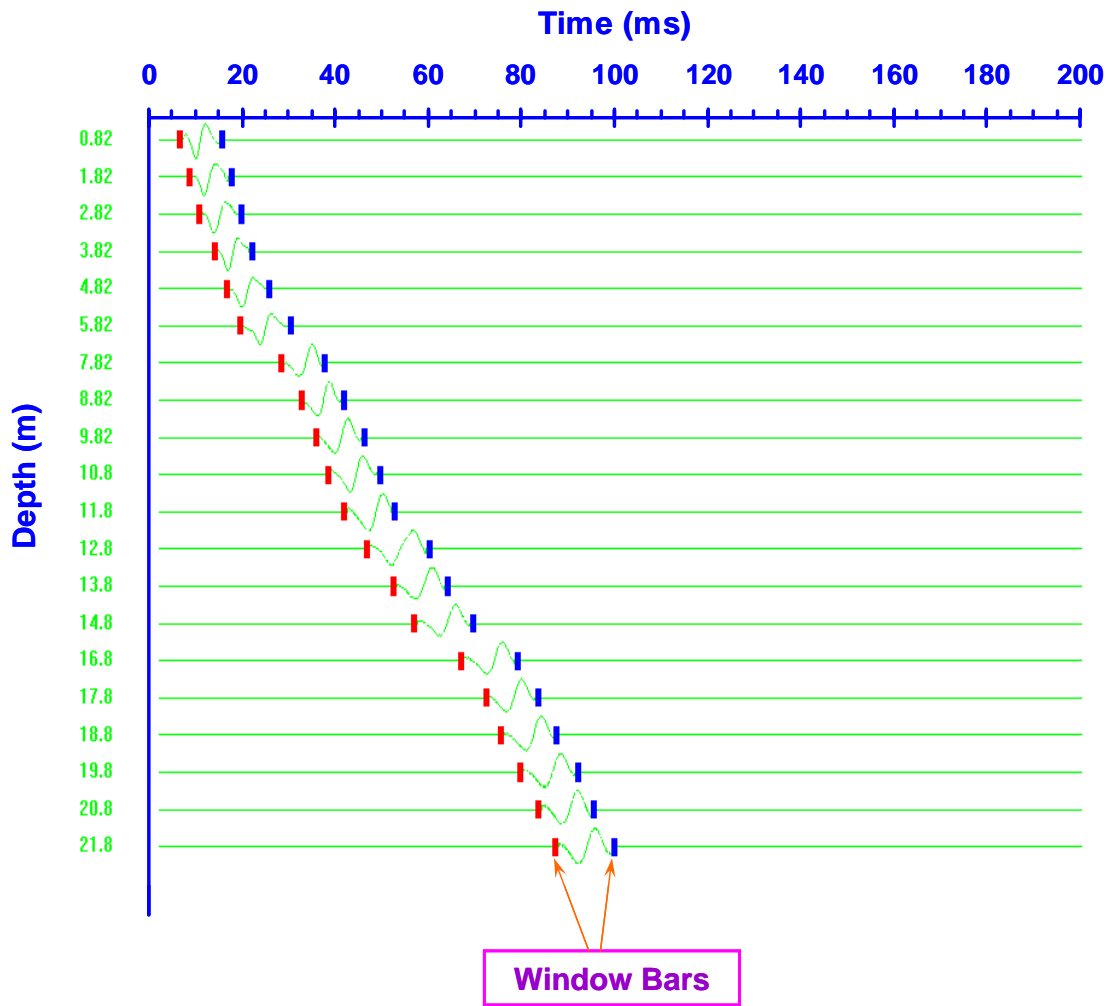
Figure E.4 Trimmed shear wave trains

Depth(m)	Velocity(m/s)	r2
1.320000	339.344360	0.756075
2.320000	375.113068	0.759930
3.320000	328.946930	0.956530
4.320000	307.812653	0.606270
5.320000	256.445557	0.857751
6.820000	226.870239	0.367164
…	…	…

Figure E.5 Format of output data of computed shear wave velocity and coefficient of determination

APPENDIX F

INSTRUCTIONS FOR *CLUSTERPRO* 1.0

1. General Information

1) This program can be run on operating systems Window 95/98/2000/XP;

2) This code is designed to process raw CPT data files of the same format as the ASCII files collected by Hogentogler computers, as shown in Figure F.1;

2. Install

1) Unzip/copy all the files of this program into a new folder;

2) Find the setup.exe file and set up the program on your computer;

3) The icon of *ClusterPro* should appear on your Start Program Menu.

3. Load the data file

Click the menu item of "File\Load…", and a window as in Figure F.2 will pop up. The CPT data file can be selected by clicking "Browse". Groundwater table also needs to be input in this window.

4. Run

After the CPT data have been loaded, click the menu item of "Run\Cluster Analysis", and a window as in Figure F.3 will pop up. By selecting "All" in the block of "Depth Range", cluster analysis will be performed for all the input CPT data. By selecting "Specify" in "Depth Range", cluster analysis will be performed

for the CPT data in the specified depth range. By selecting the data channels in the "Options" block, cluster analysis will be performed based on the selected channels. The data will be clustered into the number of clusters input through this window.

7. Results

After the cluster information is input into the program, results will be displayed on computer screen, as shown in Figure F.4. They are presented in two formats: the first format is the soil profile with the different clusters representing different soil types, and the second format includes the CPTu data points plotted in the suggested three-dimensional space as numbers corresponding to the cluster in which it belongs. The three-dimensional space in the second form can be rotated using the mouse.

Note: User accepts all risks associated with output data and results. Authors make no claim to accuracy or reasonableness of results and possible errors.

```
jag03 09-26-00 14:13 alec          Metric Absolute [SI]
opelika       hog10tu2res   1            4 0 .025 .1 .7 1 2 3 4 6
  0.03   1.96   100.5    -9.5   2.90
  0.05   2.30   151.7    -9.8   0.47
  0.08   2.79   197.6    -7.6   0.72
  0.10   3.32   231.7    -3.1   0.73
  0.13   3.49   248.1    -2.0   0.42
  0.15   3.61   255.4     3.0   0.18
  0.17   3.48   251.5    -1.1   0.47
  0.20   3.51   244.6    -1.6   0.10
  0.23   3.73   242.5    -0.3   0.05
  0.25   3.79   242.6    -0.5   0.17
   …      …      …        …      …
```

Figure F.1 Format of input file for *ClusterPro* 1.0

Note: The data columns from left to right represent depth (m), tip resistance q_c (MPa), sleeve friction f_s (kPa), porewater pressure u_2 (kPa), and inclination i.
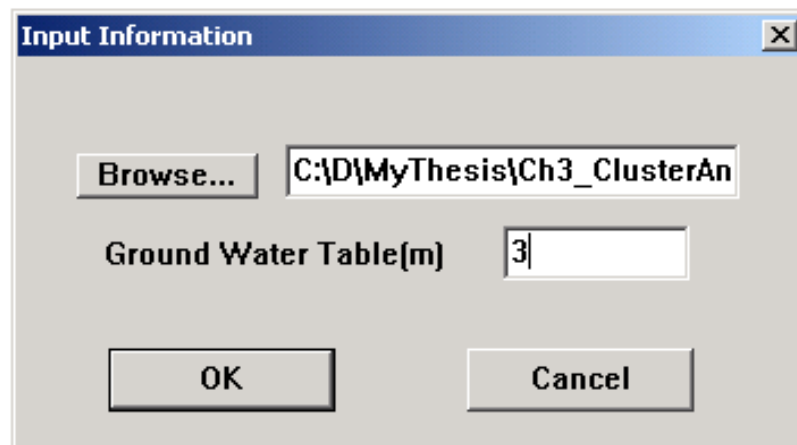
Figure F.2 Load raw CPT data and input water table into *ClusterPro* 1.0

Figure F.3 Input information for cluster analysis
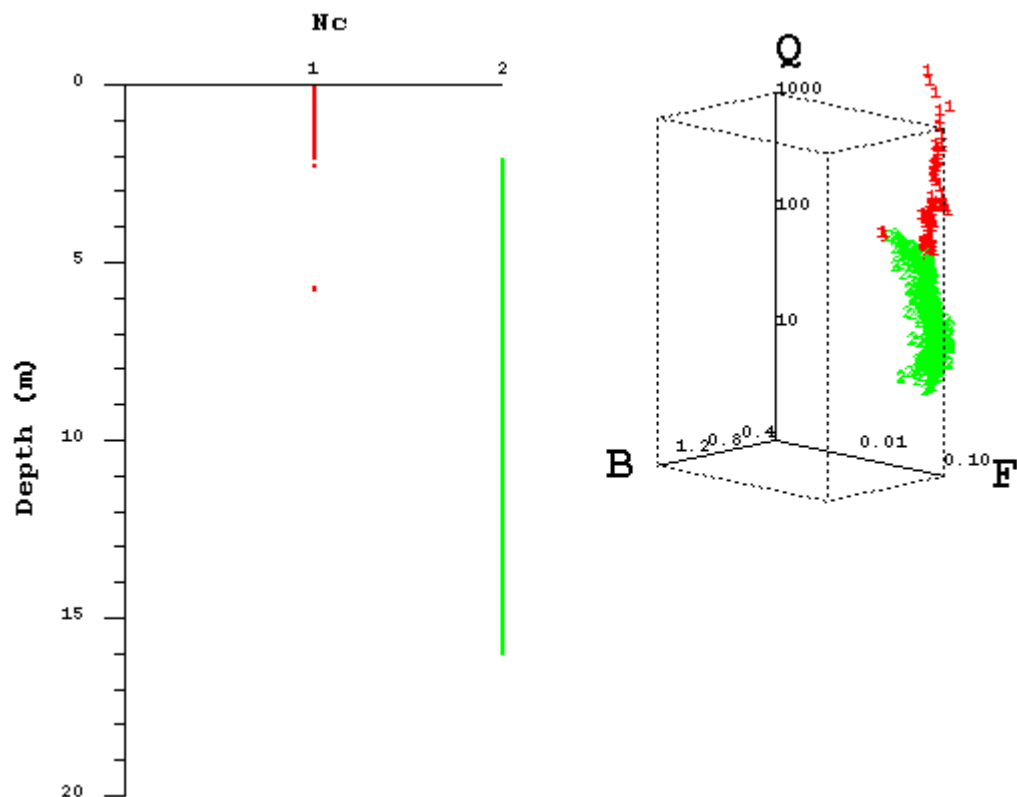
Figure F.4 Output of cluster analysis by *ClusterPro* 1.0

APPENDIX G

INSTRUCTIONS FOR *INSITUDATA* 1.0

1. General Information

1) This program can be run on operating systems Window 95/98/2000/XP;

2) This program is designed to process data from various in-situ tests, but the current version focuses on SCPTu data;

2. Install

1) Unzip/copy all the files of this program into a new folder;

2) Find the setup.exe file and set up the program on your computer;

3) The icon of *InSituData* should appear on your Start Program Menu.

3. Launch the program

When the program is started, a launcher interface (Figure G.1) pops up on the screen. By clicking the button on the launcher interface, the program continues.

4. Load the data

The raw SCPTu data can be loaded into the software from ASCII files. By clicking the tool button "Open", a window pops up for selecting the data file, as shown in Figure G.2 (a). After the file is selected, its content is displayed in the window as shown in Figure G.2 (b). By specifying the number of title lines in the data file, the header of the file that is not the SCPTu data can be excluded from

loading into the software. *InSituData* can also load the raw data by copying them from Excel spreadsheet and paste them in the program by clicking the tool button "Paste".

5. Assign names and units to the data column

After the raw SCPTu data or CPTu data are loaded into the software, the tool button "Assign" is enabled. By clicking this button, the "Assign Data Columns" window pops up, as shown in Figure G.3. By clicking on the cells in this window, the columns can be named after the selection of the user from the pull-down list and the units can be assigned. By clicking on the "Set as Default" button, the current set of column names and units are set as the default. The default names fill in the cells, if the "Load Default" button is clicked. The names can also be set by copying them from Excel spreadsheet, and then paste in this window by clicking the "Paste" button. Note that the initial default unit for the tip resistance q_T is MPa, the sleeve friction f_s is kPa, the porewater pressure is kPa, and the shear wave velocity is m/s.

6. Calculate Parameters

After the data columns are named, the "Calculate" button in the tool bar of the software is enabled. By clicking this button, the "Calculate Parameters" window pops out [Figure G.4 (a)]. The water table is input here, and the parameters of interest to the user can be selected for computation. The parameters are calculated

using the correlations recommended by the user herein. Figure G.4 (b) shows the software interface with data columns corresponding to the calculated parameters.

7. User-Defined Equations

To give the user more flexibility, the software allows the user to define the preferred correlation equations. By clicking the tool button of "Equations", the "Equations" window pops up, as shown in Figure G.5. Names of the variables, which value are available in this program, are listed on the left of the window. On the right of the window are a key pad similar to that of calculator and a list of mathematical functions. By double clicking the listed variables and functions, they can be input in the text-edit box for "Expression". Numbers and some other symbols can be input by typing or clicking on the key pad on the window. The new variable corresponding to the expression can be named in the text-edit box for "Store Result in Variable". The user-defined equations can be saved for future use by clicking the button "Save Equation". By clicking "Load Equation", the window of "Saved Equations" pops up, and shows all the equations saved previously. If any of the equations is selected, it will be shown in the "Equations" window. The equations can also be deleted by clicking the "Delete" button on the window.

8. Data Visualization

The data loaded into and calculated by this software can be plotted in charts similar to those in Excel. By clicking on the text of "Data Visualization", the

440

container for the plots is shown on the screen [Figure G.6 (a)]. Charts can be generated by clicking on the tool button "New Figure", and deleted by clicking on the tool button "Delete". By clicking "Set Default", the current charts are set as default, and the same charts are presented when the "Load Default" is clicked. The "Properties" window pops out by double clicking the charts, and properties of the charts can thus be configured. Configuring the chart properties in this software is similar to that in Excel [Figure G.6 (b)]. Similarly, the chart properties can also be set or loaded as default.

9. Export to Excel

By clicking the "Export to Excel" button on the tool bar, both the data and the charts generated in the software are output to a newly generated Excel spreadsheet.

Note: User accepts all risks associated with output data and results. Authors make no claim to accuracy or reasonableness of results and possible errors.
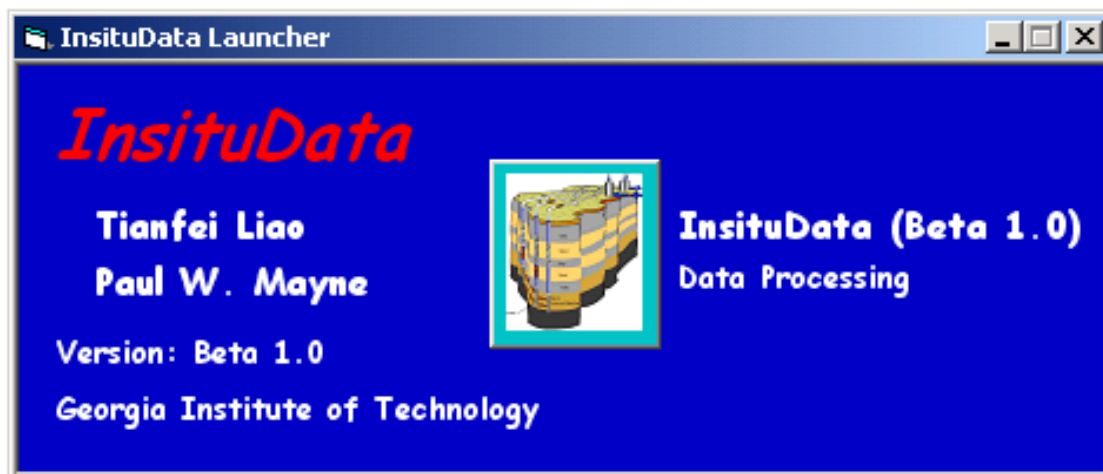
Figure G.1 Launcher interface for the software *InSituData*
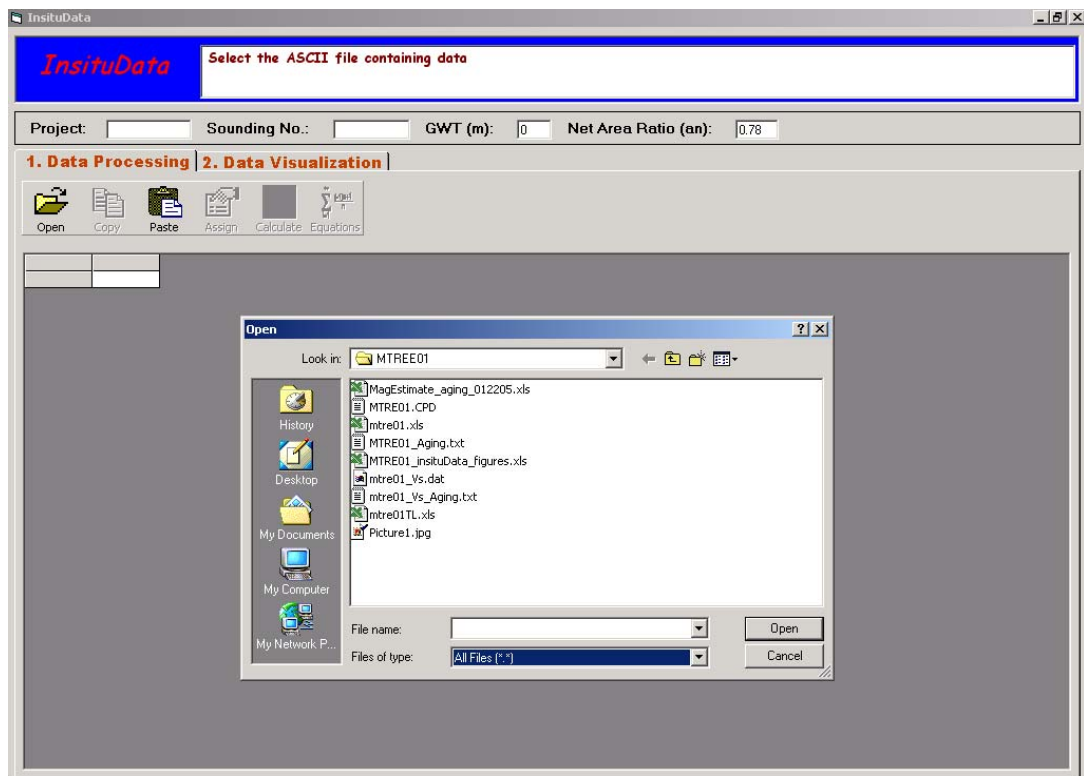
(a)
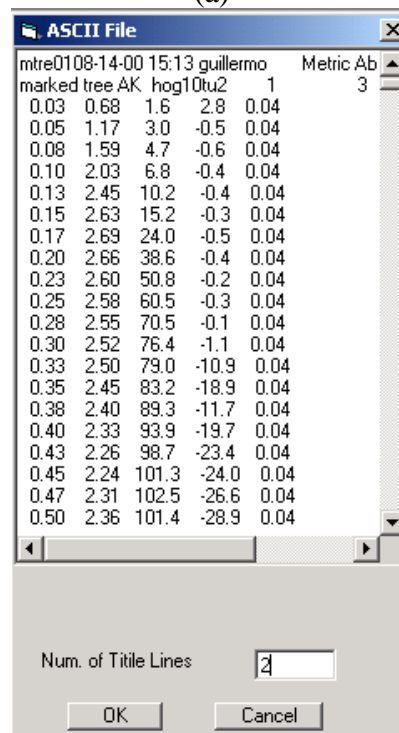
(b)

Figure G.2 Load raw CPTu data into the software *InSituData*: (a) Open the file containing raw CPTu data; (b) Displaying raw CPTu data.
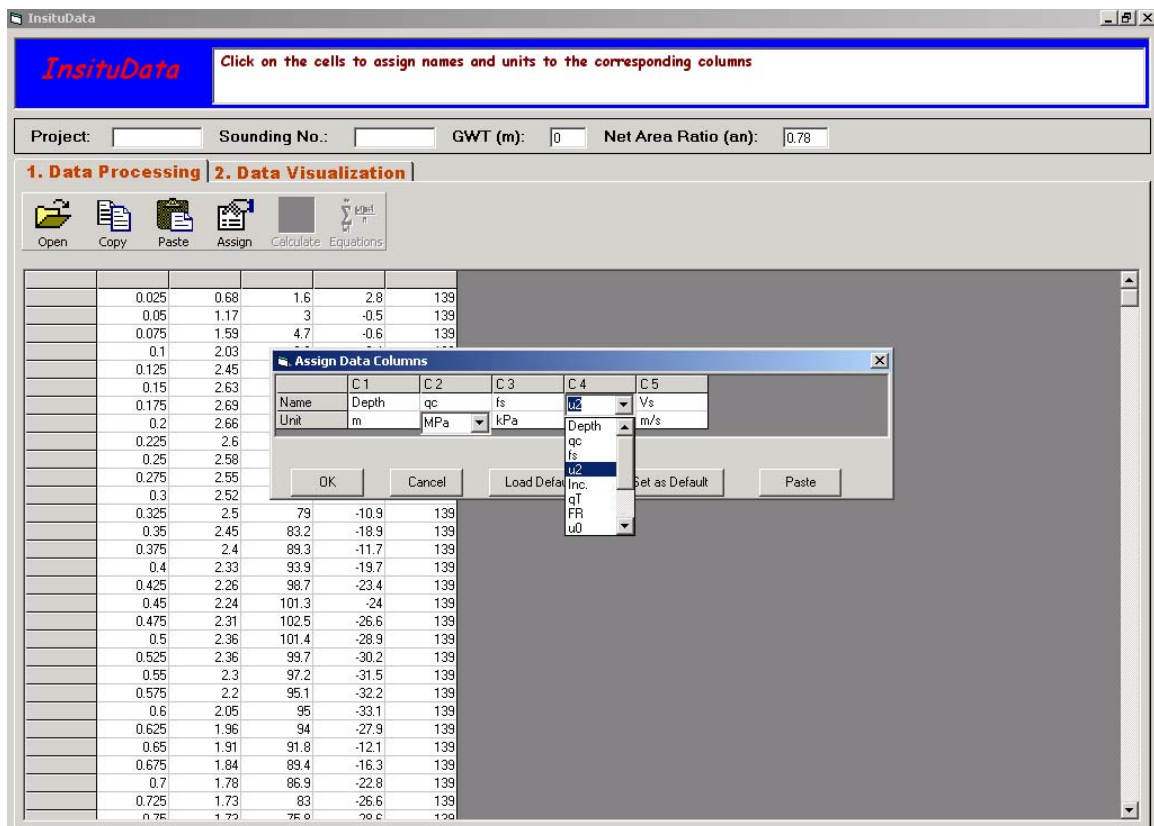
Figure G.3 Assign names and units to the data columns after they are loaded into the software *InSituData*
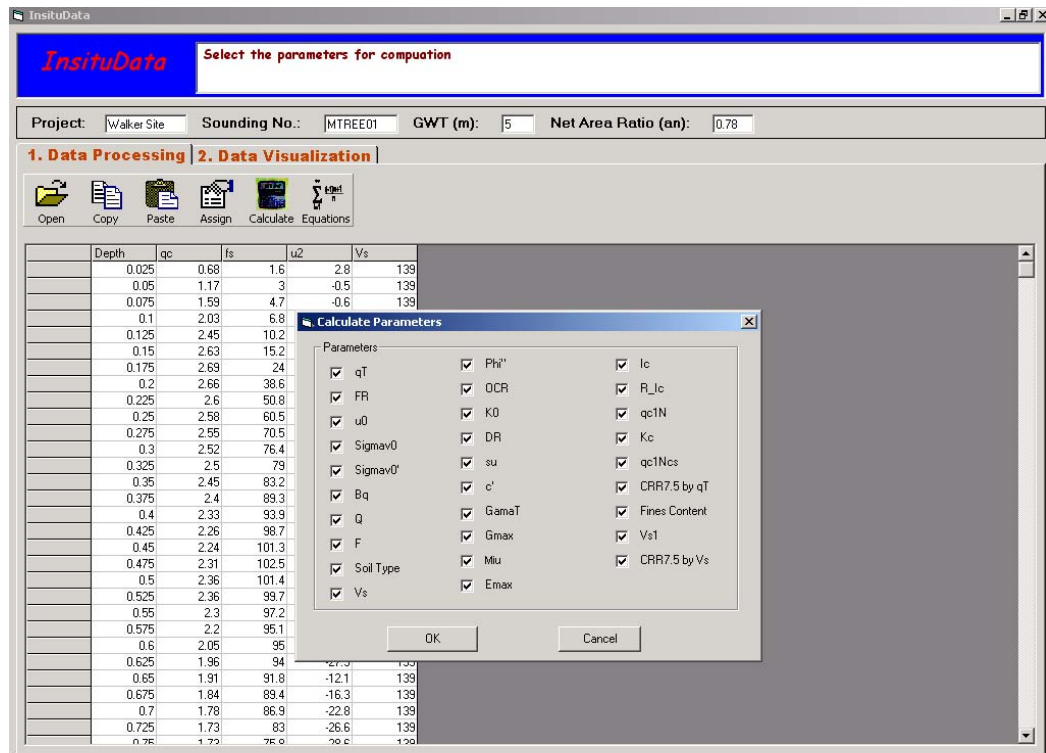
(a)
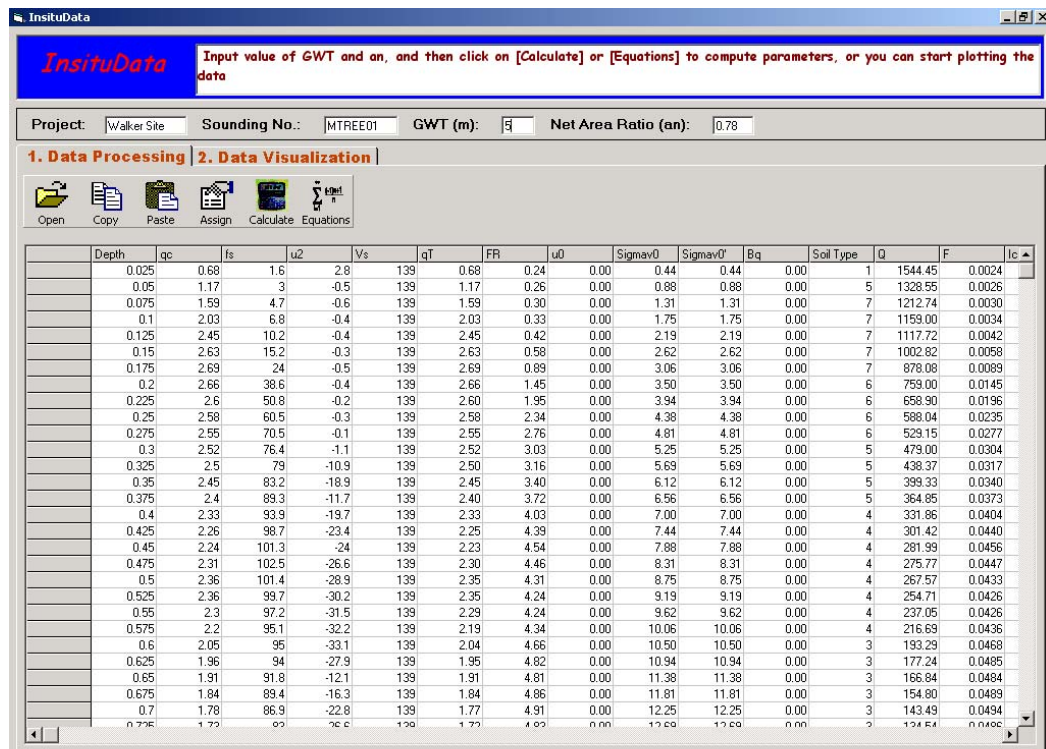
(b)

Figure G.4 Calculate parameters from the raw CPT data: (a) Select the parameters to calculate; (b) Calculated parameters displayed.

445
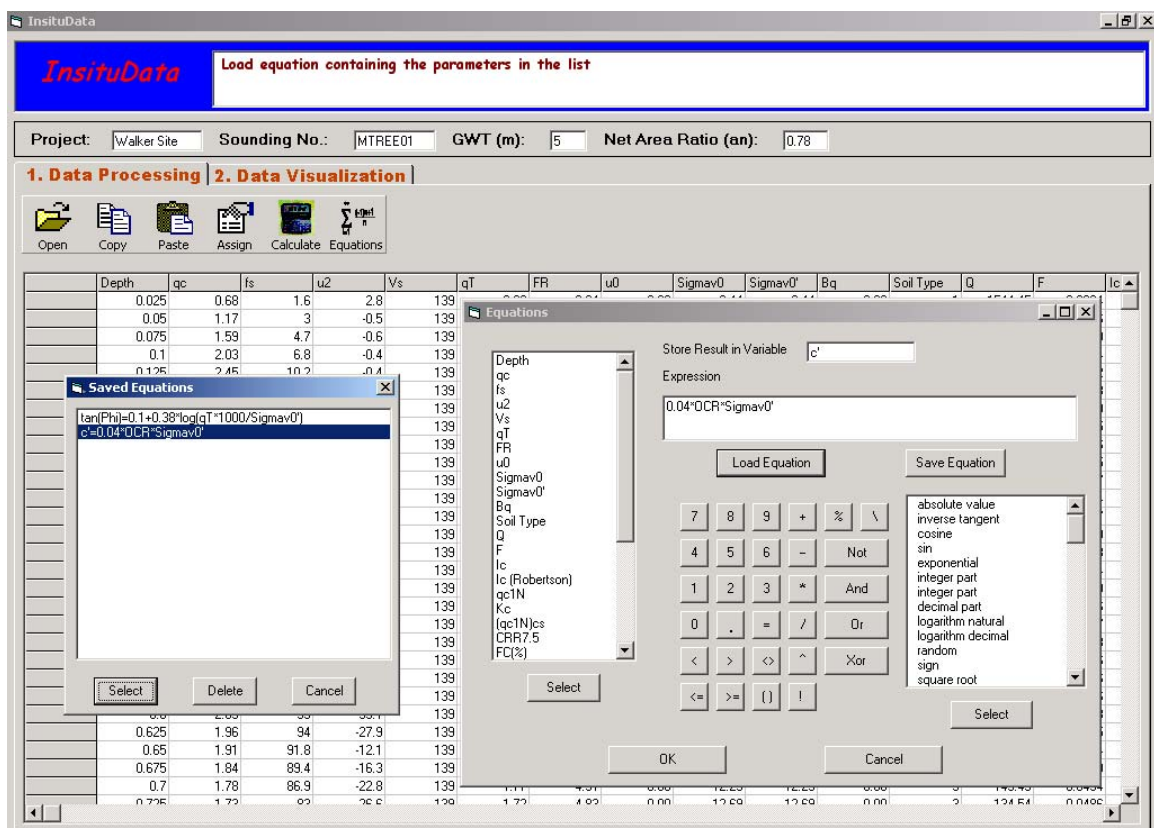
Figure G.5 Input equations into the software program *InSituData*
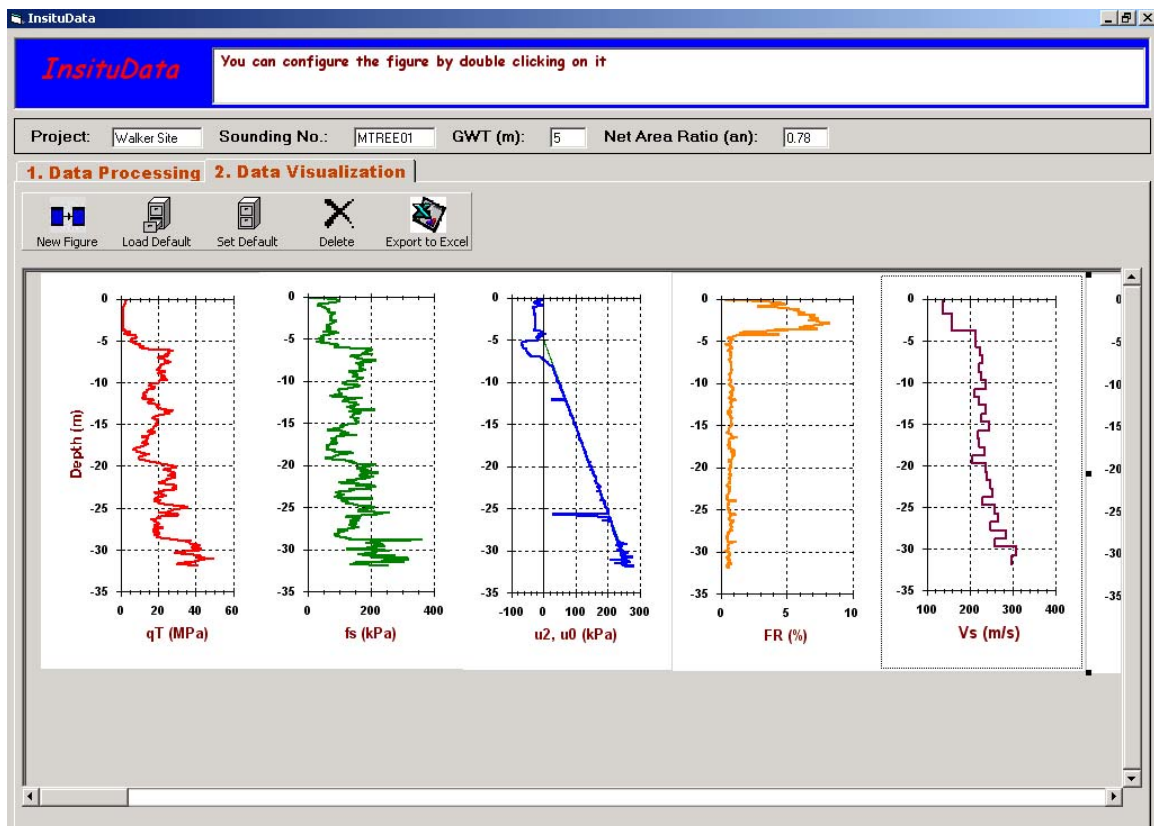
(a)
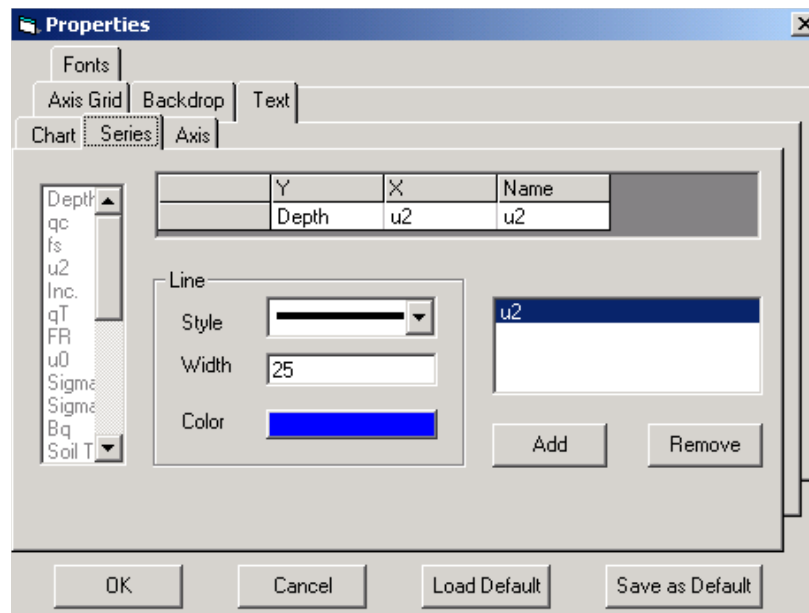
(b)

Figure G.6 Visualization of SCPTu data and derived parameters in the software *InSituData*: (a) Display of the SCPTu data and derived parameters in separate plots; (b) Configuring of the plots.

REFERENCES

Afifi, S. S., and Woods, R. D. (1971). "Long-term pressure effects on shear modulus of soils," *Journal of Soil Mechanics and Foundation Engineering*, ASCE, 97(SM10), pp. 1445-1460.

Ambraseys, N.N. (1988). "Engineering seismology, earthquake engineering and structural dynamics," *Journal of the International Association of Earthquake Engineering*, Vol. 17, pp. 1-105.

Amundsen, T., Lunne, T., Christophersen, H.P., Bayne, J.M. and Barnwell, C.L. (1985). "Advanced deep-water soil investigation at the Troll East field," *Proceedings of an International Conference, Offshore Site Investigation*, Society for Underwater Technology, London, UK, Vol. 3, pp. 165-186.

Anderson, D.G. & Stokoe, K.H. (1978). "Shear modulus: a time-dependent soil property," *Dynamic Geotechnical Testing*, ASTM STP 654, pp. 66-90.

Andrus, R.D. and Stokoe, K.H. (2000). "Liquefaction resistance of soils based on shear wave velocity," *Journal of Geotechnical & Geoenvironmental Engineering*, ASCE, 126(11), pp. 1015-1026.

Andrus, R.D., Stokoe, K.H., and Chung, R.M., (1999). "Draft Guidelines for Evaluating Liquefaction Resistance Using Shear Wave Velocity Measurements and Simplified Procedures", *Report (NISTIR) 6277*, National Insitute of Standards and Technology, p. 121.

Arias, A. (1970). "A measure of earthquake intensity," *Seismic Design for Nuclear Power Plants*, MIT Press, Cambridge, MA.

Ashford, S.A., Rollins, K.M., and Lane J.D. (2004). "Blast-induced liquefaction for full-scale foundation testing," *Journal of Geotechnical and Geoenvironmental Engineering*, ASCE, 130(8), 798-806.

Atkinson, G., Bakun, B., Bodin, P., Boore, D., Cramer, C., Frankel, A., Gasperini, P., Gomberg, J., Hanks, T., Herrmann, B., Hough, S., Johnston, A., Kenner, S., Langston, C., Linker, M., Mayne, P., Petersen, M., Powell, C., Prescott, W., Schweig, E., Segall, P., Stein, S., Stuart, B., Tuttle, M., and VanArsdale, R. (2000). "Reassessing the New Madrid seismic zone," *Transactions of the American Geophysical Union*, 81(35), pp. 402-403.

Baldi, G., Bellotti, R., Ghionna, V.N., Jamiolkowski, M., and Lo Presti, D.C.F. (1989). "Modulus of sands from CPTs and DMTs," *Proceedings of the Twelfth International Conference on Soil Mechanics and Foundation Engineering*, Vol. 1, Rio de Janeiro, pp. 165-170.

Barnes, A.A. (2000). "An interdisciplinary study of earthquake-induced liquefaction features in the New Madrid seismic zone, central United States." *M.S. Thesis*, Auburn University, Alabama, p. 266.

Baxter, C.D.P. and Mitchell, J.K. (2004). "Experimental study on the aging of sands," *Journal of Geotechnical and Geoenvironmental Engineering*, ASCE, 130(10), pp. 1051–1062.

Baziw, E.J. (2002), "Derivation of seismic cone interval velocities utilizing forward modeling and the downhill simplex method," *Canadian Geotechnical Journal*, Vol. 39, pp. 1-12.

Been, K, and M.G. Jefferies. (1985). "A state parameter for sands," *Geotechnique*, 35(2), pp. 99-112.

Been, K., Crooks, J.H.A., Becker, D.E., and Jefferies, M.G. (1985). "State parameter interpretation of the cone penetration test in sands," *Unpublished paper*.

Begemann, H. K. S. (1965). "The friction jacket cone as an aid in determining the soil profile," *Proceedings of the 6th International Conference on Soil Mechanics and Foundation Engineering*, ICSMFE, Montreal, Vol. 2, pp. 17 - 20.

Benoit, J. (2000). "The United States national geotechnical experimentation sites program: the first decaded," *National Geotechnical Experimentation Sites*, (GSP No. 93), American Society of Civil Engineers, Reston, VA, pp. 1-25.

Berrill, J.B., and Davis, R.O. (1985). "Energy dissipation and seismic liquefaction of sands: revised model," *Soils and Foundations*, 25(2), pp. 106-118.

Boore, D.M. (2002). "SMSIM — Fortran Programs for Simulating Ground Motions from Earthquakes: Version 2.0," US Geological Survey, Menlo Park, CA.

Boore, D.M. and Joyner, W.B. (1991). "Estimation of ground motion at deep-soil sites in eastern north America," *Bulletin of the Seismological Society of America*, 81(6), pp. 2167-2185.

Boulanger, R. W. (2003)."High overburden stress effects in liquefaction analyses," *Journal of Geotechnical and Geoenvironmental Engineering*, ASCE, 129(12), pp. 1071-1082.

Boulanger, R. W., Mejia, L. H., and Idriss, I. M. (1997). "Liquefaction at Moss Landing during Loma Prieta Earthquake," *Journal of Geotechnical and Geoenvironmental Engineering,* ASCE, 123(5): 453-467.

Brigham, E.O. (1988). *The Fast Fourier Transform and Its Applications*, Englewood Cliffs, NJ: Prentice-Hall, Inc., p. 448.

Broughton, A.T., Van Arsdale, R.B., and Broughton, J.H. (2001). "Liquefaction susceptibility mapping in the city of Memphis and Shelby County, Tennessee," *Engineering Geology*, Vol. 62, Nos. 1-3, pp. 207-222.

Broughton, A.T., Van Arsdale, R.B., Broughton, J.H., (2001). "Liquefaction susceptibility mapping in the City of Memphis and Shelby County, Tennessee," *Engineering Geology*, 62(1-3), pp. 207-222.

Brown, D.F. (1989). "Evaluation of the Tri Star vibrocompaction probe," *MS thesis*, University of British Columbia.

Burland, J.B. (1989). "Small is beautiful - the stiffness of soil at small strains," Ninth Laurits Bjerrum Memorial Lecture, *Canadian Geotechnical Journal*, Vol. 26, pp.499-516.

Camp, W.M. (2004). Personal communication.

Camp, W.M., Mayne, P.W., and Brown, D.A. (2002). "Drilled shaft axial design values: predicted vs. measured response in a calcareous clay," *Deep Foundations 2002*, Vol. 2, GSP No. 116, ASCE, Reston/VA, pp. 1518-1532.

Campanella, R.G. (1994). "Field methods for dynamic geotechnical testing", *Dynamic Geotechnical Testing II*, (STP 1213), ASTM, West Conshohocken, PA, pp. 3-23.

Campanella, R.G., and Stewart, W.P. (1992). "Seismic cone analysis using digital signal processing for dynamic site characterization," *Canadian Geotechnical Journal*, 29(3), pp. 477-486.

Campanella, R.G., Hitchman, R. and Hodges, W.E. (1989). "New equipment for densification of granular soils at depth," *Proceedings, 42nd Canadian Geotechnical Conference*.

Carpentier, R., De Wolfe, P., Van Damme, L., De Rouck, J. and Bernard, A. (1985). "Compaction by blasting in offshore harbor construction," *Proceedings, 11th International Conference on Soil Mechanics and Foundation Engineering (ICSMFE)*, Vol 3, San Francisco, pp. 1687 – 1692.

Carraro, J.A.H.; P. Bandini; R. Salgado (2003) "Liquefaction resistance of clean and non-lastic silty sands based on cone penetration resistance," *Journal of Geotechnical and Geoenvironmental Engineering*, ASCE, 129(11), pp. 965-976

Cetin, K.O., Seed, R.B., Der Kiureghian, A., Tokimatsu, K., Harder, L.F., Jr., Kayen, R.E., and Moss, R.E.S. (2004). "Standard penetration test-based probabilistic and deterministic assessment of seismic soil liquefaction potential," *Journal of Geotechnical and Geoenvironmental Engineering*, ASCE, 130(12), pp. 1314-1340.

Chameau, J.L., Clough, G.W., Reyna, F., and Frost, J.D. (1991a). "Liquefaction response of San Francisco bayshore fills," *Bulletin of Seismological Society of America*, 5(5), pp. 1998-2018.

Chameau, J.L., Reyna, F., and Frost, J.D. (1991b). "Ground motion analyses at several sites in San Francisco after the Loma Prieta earthquake," *Geotechnical Report 91/9*, School of Civil Engineering, Purdue University, p. 285.

Charlie, W.A., P.J. Jacobns, D.O. Doehring (1992). "Blast induced liquefaction of an alluvial sand deposit," *Geotechnical Testing Journal*, 15 (1), pp. 14-23.

Chen, C.J. and Juang, C.H. (2000). "Calibration of SPT- and CPT-based liquefaction evaluation methods," *Innovations & Applications in Geotechnical Site Characterization*, (GSP 97), ASCE. Reston/VA, pp. 49-64.

Cheng-hou, Z., Greeuw, G., Jekel, J. and Rosenbrand, W. (1990) "A new classification chart for soft soils using the piezocone test," *Engineering Geology*, Vol. 29, pp. 31-47.

Cho, G.C. and Santamarina, J.C. (2001). "Unsaturated particulate materials - particle level studies," *Journal of Geotechnical and Geoenvironmental Engineering*, 127(1), ACSE , pp. 84-96.

Cramer, C.H., Gomberg, J.S., Schweig, E.S., Waldron, B.A., and Tucker, K. (2004). "The Memphis, Shelby County, Tennessee, seismic hazard maps," U.S. Geological Survey, *Open-File Report 04-1294*, http://pubs.usgs.gov/of/2004, p. 19.

Cubrinovski, M. and Ishihara, K. (2002), "Maximum and minimum void ratio characteristics of sands," *Soils and Foundation*, vol. 42, No. 6, pp. 65-78.

Cubrinovski, M., and Ishihara, K. (1999) "Empirical correlation between SPT N-value and relative density for sandy soils," *Soils and Foundations*, Japanese Geotechnical Society, 39(5), pp. 61-71.

Davis, RO & Berrill, JB (1982). "Energy dissipation and seismic liquefaction in sands," *Earthquake Engineering and Structural Dynamics*, 10(1), pp. 59–68.

DeJong, J.T., and Frost, J.D. (2001). "Effect of CPT friction sleeve roughness and position on f_s measurement," *Proceedings of International Conference on In Situ Measurement of Soil Properties and Case Histories*, Bali, Indonesia, pp. 637-642.

Denisov, N.Y. and Dudler, I.V. (1967). "Modification de la resistance des sable sour l'effet des solicitations dynamiques," *A reprint from: Comptes Rendus de la Conference Geotechnique*, Oslo.

Denisov, N.Y., Dudler, I.V., Durante, V.A. and Khazanov, M.I. (1963). "Studies of changes of strength and compressibility of hydraulically filled sands in time," *European Conference on Soil Mechanics and Foundation Engineering*, Weisbaden, Vol 2, pp 221-225.

Douglas, B. J., and Olsen, R. S. (1981). "Soil classification using electric cone penetrometer," *Proceedings of Conference on Cone Penetration Testing and Experience*, ASCE, St. Louis, October 26 - 30, pp. 209 - 227.

Dowding, C. H., and Hryciw, R. D. (1986). "A laboratory study of blast densification of saturated sand," *Journal of Geotechnical Engineering*, ASCE, 112(2), pp.187-199.

Dumas, J.C. and Beaton, N.F. (1988). Discussion – "Practical problems from surprising soil behavior" by Mitchell, *Journal of Geotechnical Engineering*, ASCE, Vol. 114, No. 3, pp. 367-368.

EPRI (1993). "Guidelines for determining design basis ground motions," *EPRI Report Number: TR-102293*, Electric Power Research Institute, Palo Alto, CA.

Erwig, H. (1988). "The Fugro guide for estimating soil type from CPT data," *Penetration Testing in the UK*, Thomas Telford, London, pp. 261 - 263.

Eslami, A., and Fellenius, B. H. (1997). "Pile capacity by direct CPT and CPTu methods applied to 102 case histories," *Canadian Geotechnical Journal*, 34(6), pp. 880 - 898.

Everitt, B.S., Landau, S. and Leese, M. (2001). *Cluster Analysis*, Arnold, London, England, p. 237.

Facciorusso, J. and Uzielli, M. (2004). "Stratigraphic profiling by cluster analysis and fuzzy soil classification from mechanical cone penetration tests," *Geotechnical and Geophysical Site Characterization* (Proceedings ISC-2, Portugal), Millpress, Rotterdam, pp. 905 – 912.

Faris, J.R. and de Alba, P. (2000). "National geotechnical experimentation site at Treasure Island, California," *National Geotechnical Experimentation Sites*, (GSP No. 93), American Society of Civil Engineers, Reston, VA, pp. 52-71.

Farrar, J. A. (1990). "Study of in situ testing for evaluation of liquefaction resistance," *Report, R-90-06*, U.S. Department of the Interior, Bureau of Reclamation, Research and Laboratory Services Division, Geotechnical Services Branch, Denver Office.

Fear, C.E., and McRoberts, E.C. (1995). "Reconsideration of initiation of liquefaction in sandy soils," *Journal of Geotechnical Engineering*, ASCE, 121(3), pp. 249-261.

Filson, J.R., McCarthy, J., Ellsworth, W.L., and Zoback, M.L. (2003). "The USGS earthquake hazards program in NEHRP—Investing in a safer future," U.S. Geological Survey, *Fact Sheet 017-03*, http://geopubs.wr.usgs.gov/fact-sheet/fs017-03.

Finke, K., Mayne, P.W., and Klopp, R. (2001). "Piezocone penetration in Atlantic Piedmont residuum," *Journal of Geotechnical & Geoenvironmental Engineering*, ASCE, 127(1), pp. 48-54.

Fitzhardinge, C.F.R. (1990). "Dynamic compaction and slurry trench cut-off at Thap Sahao Dam, Thailand," *Proceedings, Tenth Southeastern Asian Conferenc*e, Taipei, Taiwan.

Gambin, M. (1987). "Consolidation dynamique en Thailande," *Travaus, Organe Offiel de la Federation Nationale des Travaux Publics*, No 626.

Greening, P.D., Nash, D.F.T., Benahmed, N., Ferreira, C., and Viana da Fonseca, A. (2003). "Comparison of shear wave velocity measurements in different materials using time and frequency domain techniques," *Deformation Characteristics of Geomaterials*, Vol. 1, Swets & Zeitlinger, Lisse, The Netherlands, pp. 381-386.

Gu, W.H., Morgenstern, N.R., and Robertson, P.K. (1993). "Progressive failure of lower Sand Fernando Dam," *Journal of Geotechnical Engineering*, 119(2), pp. 333-349.

Gutenberg, B. and Richter, C.F. (1956). "Magnitude and energy of earthquakes," *Annali di Geofisica*, 9(1), pp. 1-15.

Handford, G.T. (1988). "Densification of an existing dam by explosives," *Hydraulic Fill Structures*, GSP No. 21, Colorado State University, Fort Collins, pp. 751 – 762.

Hardin B.O. and Black W.L. (1969). Closure to: Vibration modulus of normally consolidated clay. *Journal of the Soil Mechanics and Foundations Division*, ASCE, Vol. 95, No. SM3, pp. 1531-1537.

Hardin, B. O., and Richart, F. E. (1963). "Elastic wave velocities in granular soils," *Journal of the Soil Mechanics and Foundations Division*, ASCE, 89(SM1), pp. 33-65.

Hardin, B.O. and Drnevich, V.P. (1972). "Shear modulus and damping in soils: measurement and parameter effects," *Journal of Soil Mechanics & Foundations Division*, 98(), pp. 603-624.

Harding Lawson Associates (1988). "Geotechnical investigation, dredging and slope improvements, Moss Landing Soth Harbor," Report Prepared for the Moss Landing Harbor District, Moss Landing, California, Concord, California.

Hashash, Y.M.A. and Park D. (2001). "Non-linear one-dimensional wave propagation in the Mississippi Embayment," *Engineering Geology*, 62 (1-3), pp. 185-206.

Hegazy, Y.A. (1998). "Delineating geostratigraphy by cluster analysis of piezocone data," *Doctor of Philosophy Thesis*, School of Civil and Environmental Engineering, Georgia Institute of Technology, p. 464.

Hegazy, Y.A. and Mayne, P.W. (1998). "Delineating geostratigraphy by cluster analysis of piezocone data," *Geotechnical Site Characterization*, Vol. 2, Proceedings of ISC-1, Atlanta, GA; Balkema, Rotterdam, pp. 1069-1074.

Hegazy, Y.A. and Mayne, P.W. (2002). "Objective site characterization using clustering of piezocone data," *Journal of Geotechnical and Geoenvironmental Engineering*, ASCE, 128 (12), pp. 986-996.

Hegazy, Y.A., Mayne, P.W., and Rouhani, S. (1997). "Three dimensional geostatistical evaluation of cone data in Piedmont residual soils," *Proceedings, 14th International Conference on Soil Mechanics & Foundation Engineering*, Vol. 1 (Hamburg), A.A. Balkema, Rotterdam, pp. 683-686.

Hegazy, Y.A., Mayne, P.W., and Rouhani, S., (1996). "Geostatistical assessment of spatial variability in piezocone tests," *Uncertainty in the Geologic Environment: From Theory to Practice* (GSP 58), Vol. 1, ASCE, New York, pp. 254-268.

Hildenbrand, T. G., Langenheim, V. E., Schweig, E., Stauffer, P.H., and Hendley II, J.W. (1996). "Uncovering hidden hazards in the Mississippi Valley," *U.S. Geological Survey Fact Sheet 200-96*; http://quake.wr.usgs.gov/prepare/factsheets/.

Hoar, R.J. and Stokoe, K.H. II (1978). "Generation and measurements of shear waves insitu," *Dynamic Geotechnical Testing*, ASTM Special Technical Publication 654, Philadelphia, pp. 3-29.

Hoffman, D. (1999). "Missouri's Earthquake Zones," *Annual Report*, Missouri Seismic Safety Commission, http://www.eas.slu.edu/SeismicSafety.

Hoffman, D. (2001). Personal communication.

Houlsby, G. (1988). "Discussion session contribution," *Penetration Testing in the U.K.*, Thomas Telford, London, pp. 141–146.

Hryciw, R.D. and Dowding, C.H. (1988). "CPT and DMT in evaluation of blast-densification of sand," *ISOPT-1 Penetration Testing*, Balkema, 1988.

Human, C.A. (1992). "Time-dependent property changes of freshly deposited or densified sands," *Ph.D. Thesis*, Civil Engineering Department, University of California, Berkeley, p. 445.

IBC (2000). *International Building Code*, prepared by International Code Council.

Idriss, I.M. (1991a). "Response of soft soil sites during earthquakes," *Proceedings, H. Bolton Seed Memorial Symposium*, Vol. 2, J.M. Duncan, ed., BiTech Publishers Ltd., Vancouver, B.C., Cananda, pp. 273-289.

Idriss, I.M. (1991b). "Earthquake ground motions at soft soil sites," *Proc., 2nd Int. Conf. on Recent Advances in Geotechnical Earthquake Engineering and Soil Dynamics*, Vol. 3, pp. 2265-2271.

Idriss, I.M. and Seed, H.B. (1968). "An analysis of ground motions during the 1957 San Francisco earthquake," *Bulletin of the Seismological Society of America*, 58(6), pp. 2013-2032.

Ishihara, K (1993). "Liquefaction and flow failure during earthquakes," *Geotechnique*, 43(3), pp. 351-415.

Ishihara, K. (1985). "Stability of natural deposits during earthquakes," *Proceedings, 11th International Conference on Soil Mechanics and Foundation Engineering*, Vol. 1, Balkema, Rotterdam, pp. 321-376.

Jamiolkowski, M., Ghionna, V.N., Lancellotta, R., and Pasqualini, E. (1988). "New correlations of penetration tests for design practice," *Penetration Testing 1988*, Proceedings of the 1st International Symposium on Penetration Testing ISOPT, Vol.1, Balkema, Rotterdam, pp. 263-296.

Jamiolkowski, M., Lo Presti, D.C.F., and Manassero, M. (2001). "Evaluation of relative density and shear strength of sands from CPT and DMT", *Soil Behavior and Soft Ground Construction*, ASCEGSP No. 119, Reston, VA, pp. 201-238.

Jefferies, M. G., and Rogers, B. T. (1993). Discussion of "Time-dependent cone penetration resistance due to blasting" by W. A. Charlie, M. F. J. Rwebyogo, and D. O. Doehring. *Journal of Geotechnical Engineering*, ASCE, 119(12), pp. 2008-2012.

Jefferies, M.G. (1991). "Explosive compaction," *Geotechnical News*, June, pp. 29 – 31.

Jefferies, M.G. and Davies, M.P. (1991). "Soil classification by the cone penetration test: Discussion," *Canadian Geotechnical Journal*, 28(1), pp. 173-176.

Jefferies, M.G., Davies, M.P. (1993). "Use of the CPTu to Estimate Equivalent SPT N_{60}," *Geotechnical Testing Journal*, 16(4), December, pp. 458-468.

Jefferies, M.G., Rogers, B.T. and Stewart, A.R. (1988). "Island construction in the Canadian Beaufort Sea," *Hydraulic Fill Structures*, GSP No. 21, Colorado State University, Fort Collins, pp. 816 – 884.

Jian, D., Xiaoling, Z., Longgen, Z., and Lianyang, Z. (1992). "Some in-situ and laboratory geotechnical test techniques used in China," *Proceedings, U.S. –China Workshop on Cooperative Research in Geotechnical Engineering* (Du Jian and

Tien H. Wu, editors), Tongji University, Shanghai and The Ohio State University, Columbus, Ohio.

Johnston, A.C. (1996). "Seismic moment assessment of stable continental earthquakes, Part III: 1811-1812 New Madrid, 1886 Charleston and 1755 Lisbon," *Geophysical Journal International*, Vol. 126, pp. 314-344.

Johnston, A.C. and Schweig, E.S. (1996). "The enigma of the New Madrid earthquakes of 1811–1812," *Annual Review of Earth and Planetary Sciences*, Vol. 24, 339-384.

Jones G. A., and Rust, E. (1982). "Piezometer penetration testing, CUPT," *Proceedings of the 2nd European Symposium on Penetration Testing*, ESOPT-2, Amsterdam, May 24 - 27, Vol. 2, pp. 607-614.

Joshi, R. C., Achari, G., Kaniraj, S. R., and Wijiweera, H. (1995). "Effect of aging on the penetration resistance of sands," *Canadian Geotechnical Journal*, 32(5), pp. 767-782.

Joyner, W.B. (1977). "NONLI3: A Fortran program for calculating nonlinear ground response," *Open File Report 77-761*, U.S. Geological Survey, Menlo Park, California.

Juang, C.H. and Jiang, T. (2000). "Assessing probabilistic methods for liquefaction potential evaluation," *Soil Dynamics & Liquefaction* (GSP 107), ASCE; Reston/VA, pp. 148-162.

Juang, C.H., Chen, C.J., and Jiang, T. (2001). "Probabilistic framework for liquefaction potential by shear wave velocity," *Journal of Geotechnical & Geoenvironmental Engineering*, ASCE; 127(8), pp. 670-678.

Kayen, R.,E., and Mitchell, J.K. (1997). "Assessment of Liquefaction Potential During Earthquakes by Arias Intensity," *Journal of Geotechnical and Geoenvironmental Engineering*, 123(12), pp. 1162-1174.

Kayen, R.E., Mitchell, J.K., Seed, R.B., Lodge, A., Nishio, S., and Coutinho, R. (1992). "Evaluation of SPT, CPT, and shear wave velocity based methods for liquefaction potential assessments using Loma Prieta data," *Proceedings, 4th Japan-U.S. Workshop on Earthquake Resistant Design of Lifeline Facilities and Countermeasures for Soil Liquefaction*, NCEER-92-0019, National Center for Earthquake Engineering, Buffalo, N.Y., pp. 177-192.

Kramer, S.L. (1996). *Geotechnical Earthquake Engineering*, Prentice Hall, Upper Saddle River, N.J., p. 653.

Kulhawy, F.H. and Mayne, P.W. (1990), "Manual on estimating soil properties for foundation design," *Report No. EL-6800*, Electric Power Research Institute, Palo Alto, CA, August 1990, 306 p.

Kulhawy, F.H. and Mayne, P.W., (1991). "Relative density, SPT, and CPT interrelationships," *Calibration Chamber Testing* (ISOCCT-1), Elsevier, New York, pp. 197-211.

La Fosse, U. and von Rosenvinge, T. (1992). "Densification of loose sands by deep blasting," *Grouting, Soil Improvement and Geosynthetics*, ASCE, GSP No 30, Vol 2, pp 954-968.

Larsson, R., and Mulabdic, M., 1991. "Piezocone tests in clay," Swedish Geotechnical Institute, SGI, *Report No. 42*, p. 240.

Law, K.T., Cao, Y.L., He, G.N. (1990). "An energy approach for assessing seismic liquefaction potential," *Canadian Geotechnical Journal*, 27(3), pp. 320-329.

Lee, M.K.W. and Finn, W.D.L. (1978). "DESRA-2, Dynamic effective stress response analysis of soil deposits with energy transmitting boundary including assessment of liquefaction potential," *Soil Mechanics Series, No. 38*, University of British Columbia, Vancouver.

Li, X. S., Z. L. Wang, and C. K. Shen. (1992). "SUMDES, a nonlinear procedure for response analysis of horizontally-layered sites subjected to multi-directional earthquake loading," Department of Civil Engineering, University of California, Davis.

Liao, S.S.C. (1996). Discussion of "Reconsideration of initiation of liquefaction in sandy soils" by C.E. Fear and E.C. McRoberts, *Journal of Geotechnical Engineering*, ASCE, 122(11), pp. 957-959.

Liao, S.S.C. and Whitman, R.V. (1986). "Overburden correction factors for SPT in sand", *Journal of Geotechnical Engineering*, ASCE, 112(3), pp. 373-377.

Liao, S.S.C., Veneziano, D., and Whitman, R.V. (1988)."Regression models for evaluating liquefaction probability," *Journal of Geotechnical Engineering*, ASCE, 114(4), pp. 389-409.

Liao, T. and Mayne, P.W. (2002). "Evaluation of Soil Liquefaction Potential and Dynamic Soil Properties by Seismic Piezocone," *Proceedings, International Conference on Advances & New Challenges in Earthquake Engineering Research (ANCER 2002)*, Polytechnic University, Hong Kong.

Liao, T. and Mayne, P.W. (2005). "Cone penetrometer measurements during Mississippi embayment seismic excitation experiment," *Proceedings, Geo-Frontiers,* Austin, Texas (in press).

Liao, T., Mayne, P.W., Tuttle, M.P., Schweig, E.S. and Van Arsdale, R.B. (2002). "CPT site characterization for seismic hazards in the New Madrid seismic zone," *Soil Dynamics and Earthquake Engineering*, Vol. 22, 943-950.

Liao, T., Zavala, G., Camp, W., McGillivray, A., and Mayne, P.W. (2000). "Results of seismic piezocone penetration tests performed in Memphis, TN," *Report* presented to U.S. Geological Survey (USGS) and Mid-America Earthquake Center (MAE), p. .

Liao, T., Zavala, G., Camp, W., McGillivray, A., and Mayne, P.W. (2000). "Results of seismic piezocone penetration tests performed in Memphis, TN," *Report* presented to U.S. Geological Survey (USGS) and Mid-America Earthquake Center (MAE).

Liao, T., Zavala, G., McGillivray, A., Camp, W., and Mayne, P.W. (2001). "Cone penetration testing for seismic hazards evaluation in Memphis & Shelby County, TN," *Report* presented to U.S. Geological Survey (USGS) and Mid-America Earthquake Center (MAE), p. 21.

Liao, T., Zavala, G., McGillivray, A., Camp, W., and Mayne, P.W. (2001). "Cone penetration testing for seismic hazards evaluation in Memphis & Shelby County, TN," *Report* presented to U.S. Geological Survey (USGS) and Mid-America Earthquake Center (MAE), p. 21.

Liu, H.P., Hu, Y., Dorman, J., Chang, T.S., and Chiu, J.M. (1997). "Upper Mississippi embayment shallow seismic velocities measured in situ," *Engineering Geology*, Vol 46, pp. 313-330.

Liu, L., and Y. Li (2001). "Identification of liquefaction and deformation features in the New Madrid seismic zone, USA, with ground penetrating radar," *Journal of Applied Geophysics*, Vol. 47, 199-215.

Lodge, A.L. (1994). "Shear Wave Velocity Measurements for Subsurface Characterization," *Ph.D. Dissertation*, University of California at Berkeley.

Luna, R. (2004). "Site response analysis including liquefaction," *Geotechnical and Bridge Seismic Design Workshop - New Madrid Seismic Zone Experience*, Cape Giarardeau, Missouri,

Lunne, T., Eidsmoen, T., Gillespie, D., and Howland, J.D. (1986). "Laboratory and field evaluation of cone penetrometers," *Use of In-Situ Tests in Geotechnical Engineering*, ASCE GSP 6, pp. 714-729.

Lunne, T., Long, M., and Forsberg, C.F. (2003). "Characterisation and engineering properties of Holmen, Drammen sand," *Characterisation and Engineering Properties of Natural Soils*, Vol.2, Swets & Zeitlinger, Lisse, pp. 1121-1148.

Lunne, T., Robertson, P.K., and Powell, J.J.M. (1997). *Cone Penetration Testing in Geotechnical Practice*, Blackie Academic and Professional., New York, Currently produced by EF-SPON, New York, p. 312.

Martin, J.R., and Clough, G.W. (1990). "Implications from a geotechnical investigation of liquefaction phenomena associated with seismic events in the charleston, SC Area," *USGS Report*, No. 14-08-001-G-1348, p. 414.

Martin, J.R., and Clough, G.W. (1994). "Seismic parameters from liquefaction evidence," *Journal of Geotechnical Engineering*, 20(8), pp. 1345-1361.

Martin, P.P. and Seed, H.B. (1978). "MASH – A computer program for the nonlinear analysis of vertically propagating shear waves in horizontally layered soil deposits," *Report No. UCB/EERC-78/23*, Earthquake Engineering Research Center, University of California, Berkeley, California.

Massarsch, K.R. and Heppel, G. (1991). "Deep vibratory of land fill using soil resonance," *Infrastructure '91*, Hong Kong Science Museum, Hong Kong, pp. 677 – 697.

Massarsch, R. and Vanneste, G. (1988). "Tri Star vibro-compaction, Annacis Island," *Franki International Technology Report*, Liege.

Matasovic, N. (1993). "Seismic response of composite horizontally-layered soil deposits," *Ph.D. dissertation*, Civil and Environmental Engineering Department, University of California, Los Angeles.

Matasovic, N., and Vucetic, M. (1995). "Seismic response of soil deposits composed of fully-saturated clay and sand layers," *First International Conference on Earthquake Geotechnical Engineering*, Tokyo, Japan, pp. 611-616.

Mayne, P.W. (1991). "Determination of OCR in clays by piezocone tests using cavity expansion and critical state concepts," *Soils and Foundations*, 31 (1), pp. 65-76.

Mayne, P.W. (2001). "Stress-strain-strength-flow parameters from enhanced in-situ tests," *Proceedings, International Conference on In-Situ Measurement of Soil Properties & Case Histories* [In-Situ 2001], Bali, Indonesia, pp. 27-48.

Mayne, P.W. (2002). "Cone penetration testing for seismic hazards evaluation in Mid-America," USGS Grant 01HQGR0039, *Report* presented to U.S. Geological Survey (USGS) and Mid-America Earthquake Center (MAE), p. 13.

Mayne, P.W. (2002). "Cone penetration testing for seismic hazards evaluation in Mid-America," USGS Grant 01HQGR0039, *Report* presented to U.S. Geological Survey (USGS) and Mid-America Earthquake Center (MAE), p. 13.

Mayne, P.W. (2005). "Integrated ground behavior: in-situ and lab tests," *Deformation Characteristics of Geomaterials*, Vol. 2 (Lyon'03), Tayler, France.

Mayne, P.W., and Rix, G.J. (1995). "Correlations between shear wave velocity and cone tip resistance in natural clays," *Soils and Foundations*, 35 (2), pp. 107-110.

Mayne, P.W., Mitchell, J.K., Auxt, J.A. and Yilmaz, R. (1995). "U.S. national report on cone penetration testing," *Proceedings, International Symposium on Cone Penetration Testing* (CPT'95), Vol. 1, Linköping, Sweden, [invited paper for US National Society of ISSMGE], pp. 263-276.

McGillivray, A., Mayne, P.W., Zavala, G., Liao, T., and Elhakim, A. (2002). "Addendum studies - Final report for MAE project HD-7a," *Report* presented to U.S. Geological Survey (USGS) and Mid-America Earthquake Center (MAE), p. 10.

McGillivray, A., Mayne, P.W., Zavala, G., Liao, T., and Elhakim, A. (2002). "Addendum studies - Final report for MAE project HD-7a," *Report* presented to U.S. Geological Survey (USGS) and Mid-America Earthquake Center (MAE), p. 10.

Mejia, L.H., Hughes, D.K., and Sun, J.I. (1992). "Liquefaction at Moss Landing during the 1989 Loma Prieta earthquake," *Proceedings, 10th World Conference on Earthquake Engineering*, A.A. Balkema, Rotterdam, The Netherlands, pp. 1435–1440.

Mesri, G., Feng, T.W., and Benak, J.M. (1990). "Postdensification penetration resistance of clean sands," *Journal of Geotechnical Engineering*, 116(7), pp. 1095-1115.

Mimura, M. (2003). "Characteristics of some Japanese natural sands - data from undisturbed frozen samples," *Characterization and Engineering Properties of Natural Soils* (2), Swets and Zeitlinger, Lisse, pp. 1149-1168.

Mitchell, J.K. (1986). "Practical problems from surprising soil behavior," *Journal of Geotechnical Engineering*, ASCE, 112(3), pp. 259 – 289.

Mitchell, J.K., and Solymar, Z.V. (1984). "Time-dependent strength gain in freshly deposited or densified sand," *Journal of Geotechnical Engineering*, ASCE, 110(11), 1559-1576.

Mitchell, J.K., and Tseng, D.-J. (1990). "Assessment of liquefaction potential by cone penetration resistance," *H. Bolton Seed Memorial Symposium*, BiTech, Vol. 2, pp. 335-350.

NEHRP (1997). *Recommended Provisions for the Development of Seismic Regulations for New Buildings*, Prepared by Building Safety Council for Federal Emergency Management Agency, Washington, D.C., Part 2 – Commentary, p. 362.

Newman, A.V., Stein, S., Dixon, T., Engeln, J.F., and Weber, J.C. (1998). "Results from GPS surveys across the New Madrid seismic zone," *American Geophysical Union*, EOS, 79(17), p. 340.

Ng, K.W., Chang, T.S., and Hwang, H. (1989). "Subsurface conditions of Memphis and Shelby County," *Technical Report NCEER-89-0021*, National Center for Earthquake Engineering Research, State University of New Yourk at Buffalo, Buffalo, N.Y.

Ng, N., Berner, P., and Covil, C. (1996). "The aging effects of sands," *Ground Engineering*, pp. 21.

Nuttli, O.W. (1979). "Seismicity in the central United State," *Geology in the Citing of Nuclear Power Plants*, Geological Society of America, Reviews in Engineering Geology, Vol. 4, pp. 67-93.

Obermeier, S. F., Martin, J. R., Frankel, A. D., Youd, T. L., Munson, P. J., Munson, C. A., and Pond, E. C., (1993). "Liquefaction evidence for one or more strong Holocene earthquakes in the Wabash Valley of southern Indiana and Illinois, with a preliminary estimate of magnitude," *U.S. Geological Survey Professional Paper 1536*, p. 27.

Obermeier, S.F. (1998). "Seismic liquefaction features: examples from paleoseismic investigations in the continental United States", *Open-file report 98-488*, U.S. Geological Survey, Reston, VA.

Obermeier, S.F. (2002). Personal communication.

Obermeier, S.F. and Pond, E.C. (1999). "Issues in using liquefaction features for paleoseismic analysis," *Seismological Research Letters*, 70(1), pp. 34-58.

Ohasaki, Y. (1969). "Effects of local soil conditions upon earthquake damage," *Proceedings of Specialty Session 2, 7th International Conference on Soil Mechanics and Foundation Engineering (ICSMFE)*, Mexico City, pp. 3-33.

Olsen, R. S. and Koester, J. P. (1995). "Prediction of liquefaction resistance using the CPT," International Symposium on Cone Penetration Testing (CPT 95), Linkoping, Sweden, pp. 251-256.

Olsen, R. S., and Malone, P. G. (1988). "Soil classification and site characterization using the cone penetrometer test," *Proceedings of First International Symposium on Cone Penetration Testing*, ISOPT-1, Orlando, Vol. 2, pp. 887 - 893.

Olsen, R.S. and Mitchell, J.K. (1995). "CPT stress normalization and predication of soil classification," *Proceedings of the International Symposium on Cone Penetration Testing* (CPT 95), Linkoping, Sweden, Swedish Geotechnical Society, Vol. 2, pp. 257-262.

Olson, S.M., Obermeier, S.F., and Stark, T.D. (2001). "Interpretation of penetration resistance for back-analysis at sites of previous liquefaction," *Seismological Research Letters*, 72(1), pp. 46-59.

Parez and Fauriel (1988). "Le piezocone ameliorations apportees a la reconnaissance de sols," *Revue Francaise de Geotech* 44, pp. 13-27.

Park, D. (2003). "Estimation of non-linear seismic site effects for deep deposits of the Mississippi embayment," *Ph.D. thesis*, University of Illinois at Urbana-Champaign, p. 311.

Park, D. and Hashash, Y.M.A. (2004). "Soil damping formulation in nonlinear time domain site response analysis," *Journal of Earthquake Engineering*, Vol. 8, (2), 249-274.

Petraborg, G.G. (1987). "A review of time-dependent changes in the strength characteristics of cohesionless soils," *MS Thesis*, University of California, Berkeley.

Pond, E.C. (1996). "Seismic parameters for the central United States based on paleoliquefaction evidence in the Wabash Valley," *Ph.D. Thesis*, School of Civil and Environmental Engineering, Virginia Polytechnic and State University.

Prevost, J.H. (1989). "DYNA1D: a computer program for nonlinear seismic site response analysis – Technical documentation," *Report NCEER-89-0025*, National Center for Earthquake Engineering Research, Buffalo, New York.

Pyke, R.M. (1985). "TESS1: A Computer Program for Nonlinear Ground Response Analysis. User's Manual," TAGA Engineering Software Services, Lafayette, California.

Qiu, Ping (1998). "Earthquake induced nonlinear ground deformation analyses," *Ph.D. Dissertation*, University of Southern California.

Richart, F.E., Hall, J.R., and Woods, R.D. (1970). *Vibrations of Soils and Foundations*, Prentic-Hall, Inc., Englewood Cliffs, New Jersey, p. 414.

Rix, G.J. (2004). Personal communication.

Robertson, P. K. and Campanella, R. G. (1983). "Interpretation of cone penetrometer tests, Part I sand," *Canadian Geotechnical Journal*, 20(4), pp. 718 - 733.

Robertson, P. K. and Fear, C. (1995). "Application of CPT to Evaluate LiquefactionPotential." *International Symposium on Cone Penetration Testing*, CPT '95, Linkoping,Sweden, Swedish Geotechnical Society, p. 57-79.

Robertson, P. K., Campanella, R. G., Gillespie, D., and Grieg, J., (1986). "Use of piezometer cone data," ASCE, In-Situ 86 Specialty Conference, *Use of In-Situ Tests in Geotechnical Engineering*, Blacksburg, June 23-25, Geotechnical Special Publication GSP No. 6, pp. 1263 - 1280.

Robertson, P. K., Fear, C. E., Woeller, D. J., and Weemees, I. A. "Estimation of sand compressibility from seismic CPT," 48th Canadian Geotechnical Conference, Vancouver, BC, 441-448.

Robertson, P.K. & Campanella, R.G. 1986. "Estimating liquefaction potential of sands using the flat plate dilatometer," *Geotechnical Testing Journal*, ASTM, 9(1), 38-40.

Robertson, P.K. (1990). "Soil classification using the cone penetration test," *Canadian Geotechnical Journal*, 27(1), pp. 151-158.

Robertson, P.K. (1991). "Soil classification using the cone penetration test: Reply," *Canadian Geotechnical Journal*, 28(1), pp. 176-178.

Robertson, P.K. and R.G. Campanella. (1985). "Liquefaction potential of sands using the CPT," *Journal of Geotechnical Engineering*, 111(3), pp. 384-403.

Robertson, P.K. and Wride, C.E. (1998). "Evaluating cyclic liquefaction potential using the cone penetration test," *Canadian Geotechnical Journal*, 35(3), pp. 442-459.

Robertson, P.K., and Wride (Fear), C.E. (1997). "Cyclic liquefaction and its evaluation based on the SPT and CPT," *Proceedings, Workshop on Evaluation of Liquefaction Resistance*, NCEER-97-0022, Multidisciplinary Center for Earthquake Engineering Research, Buffalo, NY, pp. 41-88.

Robertson, P.K., Campanella, R.G., and Wightman, A. (1983). "SPT-CPT correlations," *Journal of Geotechnical Engineering*, 109(11), pp. 1449-1459.

Robertson, P.K., Campanella, R.G., Gillespie, D., and Rice, A. (1986). "Seismic CPT to measure in-situ shear wave velocity," *Journal of Geotechnical Engineering*, ASCE, Vol. 112, pp. 791-804.

Robertson, P.K., Woeller, D.J., and Finn, W.D.L. (1992). "Seismic cone penetration test for evaluating liquefaction potential under cyclic loading," *Canadian Geotechnical Journal*, 29(4), pp. 686-695.

Romero, S.M. (2001). "Ground motion amplification of soils in the upper Mississippi embayment," *Ph.D. Dissertation*, School of Civil and Environmental Engineering, Georgia Institute of Technology, Atlanta, GA.

Romero, S.M., and Rix, G.J. (2001). "Ground motion amplification in the Upper Mississippi Embayment," *Report*, GIT-CEE/GEO-01-1, Civil and Environmental Engineering, Georgia Institute of Technology, Atlanta.

Romesburg, H.C. (1984). *Cluster Analysis for Researchers*. Wadsworth, Inc., Lifetime Learning Publications, Belmont, California, p. 334.

Sanglerat, G., Nhim, T. V., Sejourne, M., and Andina, R. (1974). "Direct soil classification by static penetrometer with special friction sleeve," *Proceedings of the First European Symposium on Penetration Testing, ESOPT-1*, Stockholm, Vol. 2.2, pp. 337 - 344.

Santamarina, J.C., Fratta, D. (1998). *Introduction to Discrete Signals and Inverse Problems in Civil Engineering,* ASCE Press, Reston, Virginia, p. 327.

Schmertmann, J. (1978), "Guidelines for Cone Penetration Test, Performance and Design," *Report No. FHWA-TS-78-209*, U.S. Dept. of Transportation, Federal Highway Administration, Washington, D.C.

Schmertmann, J.H. (1991). "The mechanical aging of soils," *Journal of Geotechnical Engineering*, 117(9), pp. 1288-1330.

Schmertmann, J.H., Baker, W., Gupta, R. and Kessler, K. (1986). "CPT/DMT QC of ground modification at a power plant," *Use of In Situ Tests in Geotechnical Engineering*, STP No. 6, pp. 985-1001.

Schmertmann, J.H., Baker, W., Gupts, R. and Kessler, K. (1986). "CPT/DMT QC of ground modification at a power plant," *Use of In-situ Tests in Geotechnical Engineering*, GSP No. 6, Virginia Tech, Blacksburg, VA, pp.985-1001.

Schnabel, P.B., Lysmer, J., and Seed, H.B. (1972). "SHAKE: a computer program for earthquake response analysis of horizontally layered sites," *Report EERC 72-12*, Earthquake Engineering Research Center, University of California, Berkeley.

Schneider (1999). "Liquefaction response of soils in Mid-America evaluated by seismic cone tests," *M.S. Thesis*, Civil and Environmental Engineering, Georgia Institute of Technology, Atlanta, GA, p. 273.

Schneider, J.A. and Mayne, P.W. (2000). "Liquefaction response of soils in mid-America evaluated by seismic cone tests," *Innovations & Applications in Geotechnical Site Characterization* (GSP No. 97), ASCE, Reston, pp. 1-16.

Schneider, J.A., Mayne, P.W., and Rix, G.J. (2001). "Geotechnical site characterization in the greater Memphis area using cone penetration tests," *Engineering Geology*, Vol. 62 (Nos. 1-3), pp. 169-184.

Schweig, E., Gomberg, J., and Hendley II, J.W. (1995). The Mississippi Valley – "whole lotta sahkin' goin' on", *U.S. Geological Survey Fact Sheet 168-95*.

Schweig, E.S., and VanArsdale, R.B. (1996). "Neotectonics of the upper Mississippi embayment," *Engineering Geology*, 45, pp. 185-203.

Seed, H. B. and de Alba, P. (1986). "Use of SPT and CPT tests for evaluating the liquefaction resistance of sands," *Use of In-Situ Tests in Geotechnical Engineering*, GSP No. 6, ASCE, New York, pp. 281-302.

Seed, H. B., and Idriss, I. M. (1982). "Ground motions and soil liquefaction during earthquakes," Earthquake Engineering Research Institute, *Monograph*, Oakland, California.

Seed, H.B. (1976). "Soil liquefaction and cyclic mobility evaluation for level ground during earthquakes," *Journal of the Geotechnical Engineering Division*, ASCE, 105, pp. 201–255. [Presented as: "Evaluation of soil liquefaction effects on level ground during earthquakes" at the ASCE Annual Convention and Exposition.]

Seed, H.B. and Idriss, I.M. (1971). "Simplified procedure for evaluating soil liquefaction potential," *Journal of the Soil Mechanics and Foundations Division*, ASCE, 97(SM9), pp. 1249-1273.

Seed, H.B., and Lee, K.L. (1967). "Liquefaction of saturated sands during cyclic loading," *Journal of the Soil Mechanics and Foundations Division*, ASCE, 92(SM6), pp. 105-134.

Seed, H.B., Idriss, I.M., Arango, I. (1983). "Evaluation of liquefaction potential using field performance data," *Journal of Geotechnical Engineering*, ASCE, 109(3), pp. 458-482.

Seed, H.B., Muraka, R., Lysmer, J., and Idriss, I.M. (1976). "Relationships between maximum acceleration, maximum velocity, distance from source and local site conditions for moderately strong earthquakes," *Bulletin of the Seismological Society of America*, 66(4), pp. 1323-1342.

Seed, H.B., Tokimatsu, K., Harder, L.F., and Chung, R.M. (1984). "Influence of SPT procedures in soil liquefaction resistance evaluations," *Report No. UCB/EERC-84/15*, Earthquake Engineering Research Center, University of California, Berkeley, California.

Seed, H.B., Tokimatsu, K., Harder, L.F., and Chung, R.M. (1985). "Influence of SPT procedures in soil liquefaction resistance evaluations," *Journal of Geotechnical Engineering*, ASCE, 111 (12), pp. 1425-1445.

Seed, R.B., Dickenson, S.E., Reimer, M.F., Bray, J.D., Sitar, N., Mitchell, J.K., Idriss, I.M., Kayen, R.E., Kropp, A., Harder, L.F., and Power, M.S. (1990). "Preliminary report on the principal geotechnical aspects of the October 17, 1989 Loma Prieta earthquake," *Report UCB/EERC-90/05*, Earthquake Engineering Research Center, University of California, Berkeley, 137 pp.

Seed, R.B., S.E. Dickenson, and I.M. Idriss (1991). "Principle geotechnical aspects of the 1989 Loma Prieta earthquake", *Soils and Foundations*, Japanese Society of Soil Mechanics and Foundation Engineering, 31(1), pp. 1-26.

Senneset, K. and Janbu, N. (1985). "Shear strength parameters obtained from static cone penetration tests," *Strength Testing of Marine Sediments, Laboratory and In Situ Measurements*, Symposium, San Diego, ASTM Special Technical Publication, STP 883, pp. 41-45.

Senneset, K. Sandven, R., Janbu, N. (1989). "Evaluation of soil parameters from piezocone tests," *Transportation Research Record* 1235, pp. 24-37.

Senneset, K., Sandven, R., and Janbu, N., 1989. "Evaluation of soil parameters from piezocone test," In-Situ Testing of Soil Properties for Transportation, Transportation Research Record, No. 1235, Washington, D. C., pp. 24 - 37.

Shibata, T., and Teparaksa, W. (1988). "Evaluation of liquefaction potentials of soils using cone penetration tests." *Soils and Foundations*, 28(2), pp. 49-60.

Silva, W. (1992). "Factors controlling strong ground motion and their associated uncertainties," *Prodeedings of Dynamic Analysis and Design Considreations for High-Level Nuclear Waste Repositories*, ASCE, Aug. 19-20, San Francisco, CA, pp. 132-161.

Sims, J.D, and Garvin, C.D (1995). "Recent liquefaction at Soda Lake, California, induced by the 1989 Loma Prieta earthquake, and 1990 and 1991 after shocks: Implications for paleoseismicity studies," *Seismological Society of America Bulletin*,Vol. 85, pp. 51-65.

Skempton, A.W. (1986). "Standard penetration test procedures and the effects in sands of overburden pressure, relative density, particle size, aging and overconsolidation," *Geotechnique*, 36(3), pp. 425-447.

Solymar (1984). "Compaction of alluvial sands by deep blasting," *Canadian Geotechnical Journal*, Vol. 21, pp. 305-321.

Solymar, S.V. (1984). "Compaction of alluvial sands by deep blasting," *Canadian Geotechnical Journal*, Vol 21, pp. 305 – 321.

Stark, T. D. and Olson, S. M. (1995). "Liquefaction resistance using CPT and field case histories," *Journal of Geotechnical Engineering*, 121(12), pp. 856-869.

Stark, T.D. (2001). "Interpretation of ground shaking from paleoliquefaction features," Report, Grand Award 01-HQ-GR-0030, Stark Consultants, Inc. p.5.

Stokoe, K.H. and Santamarina, J.C. (2000). "Seismic-wave-based testing in Geotechnical Engineering," *GeoEng 2000*, Melbourne, Australia, November, pp. 1490-1536.

Stone, W.C., Yokel, F.Y., Celebi, M., Hanks, T., and Leyendecker, E.V. (1987). "Engineering aspects of the September 19, 1985 Mexico earthquake," *NBS Building Science Series 165*, National Bureau of Standards, Washington, D.C., p. 207.

Streeter, V.L., Wylie, E.B. and Richart, F.E. (1973). "Soil motion computations by characteristics methods," *Proceedings, ASCE National Structural Engineering Conference*, San Francisco.

Suzuki, Y., Tokimatsu, K., Koyamada, K., Taya, Y., and Kubota Y. (1995). "Field correlation of soil liquefaction based on CPT data," *International Symposium on Cone Penetration Testing* (CPT 95), Linkoping, Sweden, Vol. 2, pp. 583-588.

Tanaka, H. (2002). Personal communication.

Tanaka, H., Locat, J., Shibuya, S., Tan, S-T. and Shiwatoki, R. (2001). "Characterization of Singapore, Bangkok and Ariake clays," *Canadian Geotechincal Journal*, Vol. 38, pp. 378-400.

Tatsuoka, F., Iwasaki, T., Tokida, K., Yasuda, S., Hirose, M., Imai, T. and Kon-no, M. (1980). "Standardpenetration tests and soil liquefaction potential evaluation," *Soils and Foundations*, 20(4), pp. 95-111.

Tatsuoka,F. and Shibuya,S. (1991). "Deformation characteristics of soils and rocks from field and laboratory tests," Keynote Lecture for Session No.1, Proc. of the 9th Asian Regional Conf. on Soil Mechanics and Foundation Engingeering, Bangkok, Vol. 2, pp.101-170.

Theron, M., Clayton, C.R.I., Best, A.I. (2003). "Interpretation of side-mounted bender element results using phase shift and group velocity," *Deformation Characteristics of Geomaterials*, Vol. 1, Swets & Zeitlinger, Lisse, The Netherlands, pp. 127-132.

Tokimatsu, K. and Y. Yoshimi. (1983). "Empirical correlation of soil liquefaction based on SPT N-value and fines content," *Soils and Foundations*, 23(4), pp. 56-74.

Trifunac, M.D. (1995). "Empirical criteria for liquefaction in sands via standard penetration tests and seismic wave energy," *Soil Dynamics and Earthquake Engineering*, 14(6), pp. 419-426.

Tuttle, M. P. (2001). "The use of liquefaction features in paleoseismology: Lessons learned in the New Madrid seismic zone, central United States," *Journal of Seismology,* Vol. 5, pp. 361-380.

Tuttle, M., and Barstow, N., (1996). "Liquefaction-related ground failure: A case study in the New Madrid seismic zone," *Bulletin of the Seismological Society of America*, 86(3), pp. 253-256.

Tuttle, M.P. (1999). "Late Holocene earthquakes and their implications for earthquake potential of the New Madrid seismic zone, Central United States," *PhD Dissertation*, University of Maryland, College Park, p. 250.

Tuttle, M.P., and Schweig, E.S. (1995). "Archaeological and pedological evidence for large earthquakes in the New Madrid seismic zone, central United States," *Geology*, 23(3), pp. 253-256.

Tuttle, M.P., Chester, J., Lafferty, R., Dyer-Williams, K., and Cande, R. (1999). "Paleoseismology study northwest of the New Madrid seismic zone," *Report*, NUREG/CR-5730, U.S. Nuclear Regulatory Commission, p. 96.

Tuttle, M.P., Sims, J.D., Dyer-Williams, K., Lafferty, R.H., and Schweig, E.S. (2000). "Dating of liquefaction features in the New Madrid seismic zone," Report No. *NUREG/GR-0018,* U.S. Nuclear Regulatory Commission, , p. 42.

Van Arsdale, R. (1998). "Surficial geologic and liquefaction susceptibility mapping in Shelby County, Tennessee: A pilot study," Report Abstract, Award Number 1434-HQ-98-GR-00009, University of Memphis.

Van Impe, W.F. and Meyus, L.I. (1990). "Soil compaction by blasting in the Zeebrugge harbor area," *Proceedings, First Iranian International Seminar on Soil Mechanics and Foundation Engineering*, Tehran, Iran.

Vaughn, J.D. (1994). "Paleoseismological Studies in the Western Lowlands of Southeastern Missouri," *Final Report to the U.S. Geological Survey for grant number 14-09-0001-G1931*, p. 27.

Vivatrat, V. (1978). "Cone penetration in clays," *Doctor of Philosophy Thesis*, Department of Civil Engineering, Massachusetts Institute of Technology, p. 427.

Vos, J. D. (1982). "The practical use of CPT in soil profiling," *Proceedings of the Second European Symposium on Penetration Testing, ESOPT-2,* Amsterdam, May 24 - 27, Vol. 2, pp. 933 - 939.

Vucetic, M. (1998). "Nonlinear site response due to low and high frequency base-rock motions," *Annual Report*, Southern California Earthquake Center, http://www.scec.org/research/98research.

Wickremesinghe, D. S. (1989). "Statistical characterization of soil profiles using in-situ tests," *Doctor of Philosophy Thesis*, Department of Civil Engineering, University of British Columbia, p. 288.

Wise, C.M. (1998). "Development of a prototype piezovibrocone penetrometer for in-situ evaluation of soil liquefaction susceptibility," *M.S. thesis*, School of Civil and Environmental Engineering, Georgia Institute of Technology, Atlanta, GA, p. 176.

Wolf, L., Collier, J., Bodin, P., Tuttle, M., Barstow, N., and Gomberg, J. (1996). "Geophysical and geological reconnaissance of seismically-induced sand dikes and related sand blows in the New Madrid seismic zone," *Seismological Research Letter,* 97 (2).

Woods, R.D. (1994). "Laboratory measurement of dynamic soil properties," *Dynamic Geotechnical Testing II*, ASTM STP 1213, Philadelphia, pp. 165-190.

Woodward-Clyde Consultants. (1990). "Phase I – geotechnical study, Marine Biology Laboratory, California State University, Moss Landing California," Report Prepared for California State University, San Jose, California, Oakland, California.

Wride, C.E., Robertson, P.K., Biggar, K.W., Campanella, R.G., Hofmann, B.A., Hughes, J.M.O., Kupper, A., and Woeller, D.J. (2000). "Interpretation of in situ test results from the CANLEX sites," *Canadian Geotechnical Journal*, Vol. 37, pp. 505-529.

Wroth, C.P. (1984). "Interpretation of in situ soil tests," 24th Rankine Lecture, *Geotechnique*, 34(4), pp. 449-489.

Yasuda, S., and Tohno, I. (1988). "Sites of re-liquefaction casused by the 1983 Nihonkai-Chuba earthquake," *Soils and Foundations*, 28(2), pp. 61-72.

Youd, T. L., and Noble, S. K. (1997). "Liquefaction criteria based on statistical and probabilistic analyses," *Proceedings, NCEER Workshop on Evaluation of Liquefaction Resistance of Soils*, NCEER Technical Report, No: NCEER-97-0022, pp. 201–205.

Youd, T. L., Idriss, I. M., Andrus, R. D., Arango, I., Castro, G., Christian, J. T., Dobry, R., Liam Finn, W. D., Harder, L. F., Jr., Hynes, M. E., Ishihara, K., Koester, J. P., Laio, S. S. C., Marcuson, III,W. F., Martin, G. R., Mitchell, J. K., Moriwaki, Y., Power, M. S., Robertson, P. K., Seed, R. B., Stokoe, II, K. H. (2001). ''Liquefaction resistance of soils: Summary report from the 1996 NCEER and 1998 NCEER/NSF workshops on evaluation of liquefaction resistance of soils,'' *Journal of Geotechnical and Geoenvironmental Engineering,* 127(10), pp. 817–833.

Youd, T.L. (1984). "Recurrence of liquefaction at the same site," *Proceedings of the Eighth World Conference on Earthquake Engineering*, San Francisco, CA, July 21-28, Vol. 3, pp. 231-238.

Youd, T.L. and Garris, C.T. (1995). "Liquefaction-induced ground-surface disruption," *Journal of Geotechnical Engineering*, 121(11), pp. 805-809.

Youd, T.L. and Perkins, D.M. (1987). "Mapping of liquefaction severity index," *Journal of Geotechnical Engineering*, 113(11), pp. 1374-1392.

Youd, T.L., Perkins, D.M., and Turner, W.G. (1989). "Liquefaction severity index attenuation for the Eastern United States," *Proceedings, 2nd US-Japan Workshop on Liquefaction, Large Ground Deformation and Their Effects on Lifelines*, Buffalo, NY, National Center for Earthquake Engineering Research Technical Rept. NCEER-89-0032, pp. 438-452.

Zavala, G. & Mayne, P.W. (2002). "CPT shear wave velocity sources and post processing," Poster, the 5th Annual Sowers Lecture, Georgia Institute of Technology, Atlanta, Georgia.

Zhang, Z. & Tumay, M.T (1999). "Statistical to fuzzy approach toward CPT soil classification" *Journal of Geotechnical & GeoEnvironmental Engineering*, ASCE, Vol. 125, No. 3, pp. 179-186.

Zhang, Z. (1994). "Use of uncertainty methodology in identification and classification of soils based on CPT", *Doctor of Philosophy Thesis*, Department of Civil Engineering, Louisiana State University, Baton Rouge, Louisiana, p. 199.

Ziegler, M. and Prokhorova, A. (2004). Personal communication.